Universidad de Valladolid

Escuela de Doctorado Universidad de Valladolid

PROGRAMA DE DOCTORADO EN FÍSICA

TESIS DOCTORAL:

UNDERSTANDING THE PRODUCTION PROCESS OF NANOCELLULAR POLYMERS BASED ON PMMA DRIVEN BY A HOMOGENEOUS NUCLEATION.

Presentada por Judith Martín de León para
optar al grado de
Doctora por la Universidad de Valladolid

Dirigida por:
Miguel Ángel Rodríguez Pérez

A Miguel Ángel

A papá y mamá

A Rebe

A Jose.

Agradecimientos

Cuando empecé a escribir esta tesis me enfrenté, casi con terror, a los primeros folios en blanco. Párrafos borrados, líneas reescritas, cambios de color, de estilo… estaba por aquel momento convencida de que aquellas primeras hojas serían las más difíciles. Pero qué equivocada estaba, porque si hay algo difícil, es explicar lo agradecida que me siento a todas esas personas que, de una u otra forma, tienen la culpa de que hoy esté aquí, escribiendo estos agradecimientos y con una tesis doctoral escrita. Pero allá voy…

En primer lugar, me gustaría agradecer al profesor y director de esta tesis Miguel Ángel Rodríguez Pérez. Le conocí con unos cuantos años menos sentada en la segunda fila en un aula de la torre de la antigua facultad de ciencias, expectante por la nueva optativa que comenzaba ese día "Física de Materiales". Creo que aún puedo sentir esa mezcla de alivio, ilusión y esperanza, cuando Miguel Ángel entró por la puerta y empezó a explicarnos en qué consistiría aquella asignatura, que por primera vez en lo que llevaba de carrera, consiguió entusiasmarme y hacerme pensar que había encontrado mi lugar en la Física. Después vino la charla, "la carrera científica" y cómo no, una vez más, Miguel Ángel consiguió entusiasmarme y hacerme creer que no había querido otra cosa en la vida que ser científica. Y no se equivocaba, tuve la suerte de que me admitiera en el laboratorio y me embarqué en lo que ha sido una de las mayores aventuras de mi vida, el doctorado. Así que gracias Miguel Ángel, por hacerme descubrir mi vocación, y gracias porque durante estos años de doctorado, has confiado en mí, me has enseñado un poquito de todo lo que sabes y a pensar por mí misma, me has animado a vivir experiencias maravillosas como los congresos o esa estancia que tanto me costó hacer, pero sobre todo me has enseñado a amar mi trabajo, y si alguna vez decaía la ilusión solo hacía falta una reunión contigo para salir con la motivación por las nubes. Gracias por ser mi director de tesis, ha sido un completo honor aprender de alguien como tú.

No puedo dejar de agradecer al profesor José Antonio de Saja, que, aunque nos dejó hace un par de años, sin su esfuerzo y pasión por la ciencia, CellMat no sería lo que es ahora, así que gracias por dejar tu herencia científica en nuestras manos.

Me gustaría también agradecer a esas personas que hicieron de mi estancia en Cambridge algo mejor, en especial gracias al Dr. Norman Fleck por dejarme formar parte de su laboratorio. Pero sobre todo gracias al Dr. Frederik Van Loock por toda tu ayuda, tus conocimientos y por hacer que Cambridge se convirtiera un poco más en casa cuando estaba tan lejos de la mía.

Y qué decir de todos mis compañeros, aquellos que hora tras hora se han ido convirtiendo en la gran familia que hoy CellMat es para mí. Empiezo por Emi, lo primero gracias por tu trabajo y por tu paciencia infinita. Pero, sobre todo, gracias por ser como eres, siempre digo que de mayor quiero ser como tú y es que te has convertido en alguien a quien admiro profundamente y de la que aprendo cada día solo con escucharte hablar de cualquier cosa de la vida. Ojalá de mayor pueda ser como tú.

Gracias a los técnicos de laboratorio, Puri Niño, por estar siempre dispuesta a ayudar. A la Dra. Blanca Calvo, ya en prácticas me entusiasmó todo lo que nos enseñaste, hoy te sigo mirando con admiración y con agradecimiento, sin tu ayuda y tu cariño esta tesis no habría sido posible. A Laura Izaguirre, la dulce Laura, gracias por hacerlo todo desde el corazón por ser tan cercana y hacer que me sienta cuidada en el trabajo. Javi, gracias por estar siempre dispuesto a ayudar en todo con un humor envidiable y un gran corazón. Pablo, nuestro técnico más joven, el pequeño de la familia, pero ahora el laboratorio no se entiende sin ti, sin tus fotos de SEM, y sin tu "agur yogur", gracias por hacer tu trabajo con tanto amor y con esa sonrisa, y gracias por ser más que un compañero, un amigo.

Seguimos con las doctoras Cristina Saiz y Ester Laguna. A penas he tenido la suerte de investigar con vosotras, pero eso no me ha dejado sin nada que agradeceros. Gracias Cris por compartir tan humildemente esa sabiduría, que siempre pienso que es infinita, conmigo. Gracias Ester, por esa sonrisa incansable que te acompaña por donde vas, porque haces de CellMat un lugar más dulce. Gracias a las dos por esos ratos de comidas y cafés donde se pueden olvidar todos los agobios con un millón de risas.

Gracias al Dr. Javier Pinto, por tus ganas y motivación, a la Dra. Suset Barroso, por tu sonrisa, al Dr. Alberto López, por tu simpatía, y a la Dra. Leandra Salmazo, por tus ánimos, gracias a todos por haberme ayudado siempre que lo he necesitado con una gran sonrisa.

Y sigo con la planta baja, no he podido tener unos compañeros mejores a lo largo de la tesis, me he sentido querida, valorada, y apoyada por todos y cada uno de vosotros en todos los momentos. Gracias a Josías, Alberto, Santi y Mercedes por todos los buenos ratos compartidos. Edu, porque es maravilloso verte trabajar con esa energía, ese entusiasmo y ese cariño que siempre demuestras a todos. Paula, por tu delicadeza, tu dulzura y tu cercanía, ha sido maravilloso poder pasar contigo algunas horas de trabajo. Bea, qué decir de Bea, que ojalá hubieras llegado antes y ojalá no te vayas nunca. Vas dejando un rastro de luz por donde pasas, cuando llegas a todos se nos pinta una sonrisa, y es difícil no escuchar una carcajada si estamos a tu alrededor. Has traído contigo el buen rollo, la ilusión por el trabajo, las ganas, la energía y la amistad. Gracias por ser el lazo que nos ha unido mucho más, es una suerte haberte encontrado por el camino, amiga.

Me toca mi cuarto, y se me vuelve a acelerar el corazón al máximo y se me pinta una sonrisa en la cara. No creo que hubiese mejores personas con las que compartir el trabajo. Patricia la última pieza de nuestro perfecto puzle, nos has traído tu cariño, tus abrazos y tu sonrisa, gracias por convertirte en una más. Mikel, no sé de dónde sacas la energía cada mañana para hacer todo lo que haces con tantas ganas, gracias por hacerme sentir que te puedo pedir ayuda en lo que necesite, por tu ilusión, tu alegría, no sé, por todo Mikel, eres un imprescindible en estos años de tesis. Daniiiii, el pequeño Dani con el que aprendí a dirigir un TFG, pero que fácil me lo pusiste… desde el primer momento tan trabajador, tan dispuesto, tan independiente. Desde entonces deseé que te convirtieras en uno de mis compañeros en CellMat, y así ha sido, para mi suerte, compañero de trabajo, de cuarto y amigo. Gracias Dani, es un lujo compartir el tiempo contigo.

Y ahora viene ELLA. Y no creo que haya palabras inventadas para dar las gracias a la Dra. Victoria Bernardo. Vicky, has sido mi mano en este camino cuando todo iba bien, a la que me he agarrado con fuerza cuando he sentido que me iba a caer, y la que me ha levantado cuando alguna vez he terminado por el suelo. Como científica, tengo que decirte que ha sido un HONOR, así en mayúsculas, poder beber de tus ideas, disfrutar contigo de cada experimento, has sido la suerte de mis investigaciones… y una de las SUERTES (sí, otra vez en mayúsculas) de mi vida. Me has enseñado tantas cosas que creí que no se podían llegar a aprender, que no sé cómo darte las gracias. Sólo puedo decir que te admiro, que cuando te miro veo a una de las personas más grandes que conozco y que me siento tan orgullosa de tenerte a mi lado que no he podido evitar emocionarme al escribir esto y darme cuenta de que te tengo, y tener la certeza de que te tendré. Gracias mejor amiga, gracias hermana y ojalá hubiera otra palabra, porque gracias se te queda pequeña.

Gracias también a todas esas personas que de una u otra forma han estado presentes en estos años en CellMat. A Eusebio Solorzano por tu inestimable ayuda en los primeros años de esta tesis. A la Dra. Heura Ventura por traernos tu felicidad, al Dr. Saúl Pérez por los buenos ratos de cuarto, y a todos los demás que han sido historia de estos años.

Y ahora nos vamos a los imprescindibles de la otra parte de mi vida. La aventura de la física jamás hubiese sido tan divertida sin vosotros Los Frikifísicos, tengo el orgullo de decir que mis compañeros de clase fueron mis amigos, y SON mis amigos. Gracias porque todos juntos éramos imparables, y porque 10 años más tarde seguimos unidos como parecía imposible. Gracias a todos

por quererme así, como soy; Samu, Vity, Mani, Vicky, Irene, Damián, Jose, Tolosa, Dani. Gracias por ser la mejor parte de la Física.

Sara, mi ejemplo de fuerza, de trabajo, de sacrificio y de amistad. Gracias por haber demostrado ser una incondicional. Yusta, mi prueba experimental más sólida de que una amistad puede ser eterna. Gracias, porque si alguien ha creído siempre que era capaz de escribir una tesis ese has sido tú. Gracias por confiar en mi más que yo misma, gracias por admirarme, y respetarme así, con todos mis defectos, mis locuras. Gracias Pablo, porque hoy no sería la persona que soy de no ser por ti, porque nunca has dejado que me avergüence de quien soy, gracias y gracias por regalarme tu amistad.

Papá mamá, GRACIAS. Y me quedaría así, con esa palabra en mayúsculas, porque cualquier cosa que diga desmerece a vuestro lado. Papá, mi ejemplo de que, en esta vida, si le pones ganas, pasión y amor se puede conseguir hacer cualquier cosa. Gracias por enseñarme a seguir hacia delante con la cabeza bien alta. Mamá, no sé qué habría sido de mi sin tu amor infinito, sin todas las veces que me has levantado del suelo y has intentado que olvidara que había caído. Gracias por enseñarme a vivir poniendo el corazón por delante. Gracias por vuestro apoyo, siempre, porque jamás habéis dudado de mí. Gracias porque hoy la persona que estaría escribiendo esto sería alguien muy diferente de no ser por vosotros. Me siento muy orgullosa de ser vuestra hija.

Rebe, siempre mi modelo a seguir, el espejo en el que me he mirado a lo largo de tantos años. Gracias por mirarme con esos ojos tan bonitos que me hacen sentir la hermana más lista, la más guapa, la hermana que puede con todo, que me hacen sentir fuerte, grande, orgullosa y segura de mi misma. Gracias porque sin esa mirada, yo sería mucho más pequeñita, gracias por enseñarme a crecer y a volar alto sin miedo a caer, por abrirme el camino, gracias por quererme como solo una hermana puede llegar a querer. Y gracias a esa pequeña parte de ti que ha conseguido que escribiese esta tesis con un cosquilleo en el corazón, que ha crecido a la vez que estas páginas, y que ha multiplicado mi alegría solo con imaginarme su existencia. Gracias Lucas.

Y sólo me quedas tú. Y que difícil es escribirte estas líneas. El Dr. Jose Luis Pura. Jose, mi mejor maestro, el de la paciencia infinita. Todo empezó en la carrera, cuando, por entonces siendo mi novio, te pasabas horas y horas intentando hacerme entender conceptos que parecían imposibles. Y a día de hoy todo sigue igual, cuando llamo a mi marido porque sé que él me puede ayudar con cualquier duda que se me plantee. Así que gracias, gracias por enseñarme, por crecer a mi lado y verme crecer con admiración. Hoy miro atrás y no entiendo la vida sin ti, ya no existen recuerdos de los que no formes parte. Y es que cuando yo no me siento capaz el nosotros es invencible, cuando yo me siento cansada el nosotros es incansable, y cuando me siento feliz el nosotros es pletórico. Gracias porque sabes que siempre he creído que "llegar a viejo sin haberse enamorado de verdad, en fin, es como no haber vivido" y tú me dejaste empezar a vivir a los 18, y espero que la vida no termine jamás si es a tu lado. Gracias por completar mi vida, y gracias por quererme como jamás nadie me ha querido, esta tesis sería gris sin ti.

Gracias a todos los que habéis creído en mí, y me habéis dado cariño a lo largo de este camino. Espero no haberme dejado a nadie entre estos párrafos, y haber sido capaz de que todos veáis la infinita sonrisa que tengo pintada en el corazón hoy, por vuestra culpa. Gracias, gracias y gracias.

FINANCIACIÓN

Se agradece al Ministerio de Educación, Cultura y Deporte por el apoyo económico aportado para la realización de esta tesis doctoral a través de un contrato de Formación del Personal Universitario (FPU14/02050). Además, quiero agradecer la financiación recibida por el grupo CellMat, proveniente de los siguientes proyectos de investigación:

- DESARROLLO Y FABRICACION EN CONTINUO DE AISLANTES TERMICOS AVANZADOS BASADOS EN POLIMEROS NANOCELULARES (MAT2015-69234-R). Financiado por MINECO, FEDER, UE, Programa Estatal de I+D+i Orientada a los Retos de la Sociedad.
- SENSORES BASADOS EN POLÍMEROS NANOCELULARES PARA EL ANÁLISIS DE POLIFENOLES DE INTERÉS EN ALIMENTACIÓN (VA011U16). Financiado por la Junta de Castilla y León
- NUEVAS ESTRATEGÍAS PARA EL DISEÑO DE SENSORES Y BIOSENSORES PARA LA DETECCIÓN DE POLIFENOLES Y AZÚCARES BASADOS EN POLÍMEROS TUBULARES (VA275P18). Financiado por la Junta de Castilla y León
- DESARROLLO DE PLASTICOS SUB-MICROCELULARES Y NANOCELULARES: FABRICACION, ESTRUCTURA, PROPIEDADES Y POTENCIALES APLICACIONES (MAT2012-34901). Financiado por Proyecto Plan Nacionales de Materiales.
- DESARROLLO DE UNA NUEVA GENERACIÓN DE AISLANTES TÉRMICOS AVANZADOS BASADOS EN LA OBTENCIÓN DE ESTRUCTURAS POROSAS NANOCELULARES (VA035U13). Financiado por la Junta de Castilla y León.

FUNDING

Financial support from the FPU contract (FPU14/02050) from the Spanish Ministry of Education is gratefully acknowledged. In addition, financial assistance by CellMat group provided by the following research projects is also acknowledged:

- DESARROLLO Y FABRICACION EN CONTINUO DE AISLANTES TERMICOS AVANZADOS BASADOS EN POLIMEROS NANOCELULARES (MAT2015-69234-R). Funded by MINECO, FEDER, UE, Programa Estatal de I+D+i Orientada a los Retos de la Sociedad.
- SENSORES BASADOS EN POLÍMEROS NANOCELULARES PARA EL ANÁLISIS DE POLIFENOLES DE INTERÉS EN ALIMENTACIÓN (VA011U16). Funded by Junta de Castilla y León
- NUEVAS ESTRATEGÍAS PARA EL DISEÑO DE SENSORES Y BIOSENSORES PARA LA DETECCIÓN DE POLIFENOLES Y AZÚCARES BASADOS EN POLÍMEROS TUBULARES (VA275P18). Funded by Junta de Castilla y León
- DESARROLLO DE PLASTICOS SUB-MICROCELULARES Y NANOCELULARES: FABRICACION, ESTRUCTURA, PROPIEDADES Y POTENCIALES APLICACIONES (MAT2012-34901). Funded by Proyecto Plan Nacionales de Materiales.
- DESARROLLO DE UNA NUEVA GENERACIÓN DE AISLANTES TÉRMICOS AVANZADOS BASADOS EN LA OBTENCIÓN DE ESTRUCTURAS POROSAS NANOCELULARES (VA035U13). Funded by Junta de Castilla y León.

Contents

Resumen en español

Chapter 1. Introduction

Chapter 2. State of the art

Chapter 3. Experimental section

Chapter 4. Influence of saturation parameters

Chapter 5. Influence of foaming parameters

Chapter 6. Influence of the polymeric matrix

Chapter 7. Gas dissolution process customization

Chapter 8. Properties of nanocelular materials

Chapter 9. Conclusions and future work

Resumen en español

"Tienes que intentarlo, porque si no lo intentas no habrás vivido."

William Parrish

ÍNDICE

I. Introducción

La historia de la humanidad se divide en múltiples periodos, muchos de los cuales deben su nombre a distintos materiales debido a la vital importancia que estos han tenido en la evolución. Es por tanto común oír hablar de la edad de piedra, la de bronce o la de hierro. Desde la revolución industrial se han descubierto y desarrollado cientos de diversos materiales, pero si hubiera que seleccionar un nombre para la era actual basado en uno de ellos, este sería sin duda la era del plástico.

De acuerdo con la bibliografía, se producen 300 millones de toneladas de polímeros cada año. El 10 % en peso de esa cantidad es destinado a la producción de materiales celulares poliméricos. Se estima que el mercado de los polímeros celulares alcance los 113.86 billones de euros para el año 2022 con un crecimiento anual del 5.86% [1].

Llegados a este punto y antes de continuar, es necesario definir el concepto de material celular. Un material celular es un material bifásico, en el cual una fase gaseosa está dispersa en una matriz sólida continua [2]. Tal y como muestra la **Figura I**, los materiales celulares se pueden encontrar fácilmente tanto en la naturaleza como en productos industriales. Tanto es así que prácticamente todo lo que nos rodea está conformado por una estructura celular. Se pueden encontrar estructuras celulares en el interior de un corcho, de un hueso, en la raíz de un árbol, en el ala de una mariposa, o dentro de un simple juguete.

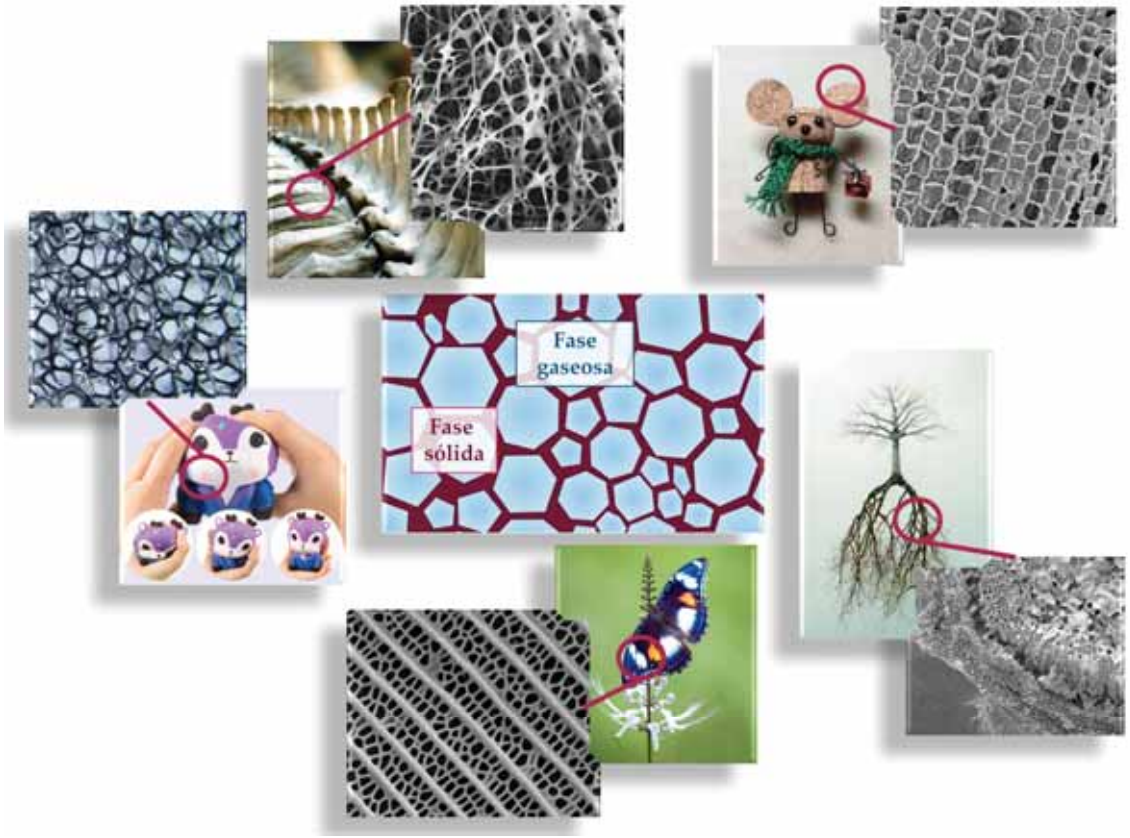

Figura I. Ejemplos de estructuras celulares. Naturales: en el interior de un hueso, un corcho, la raíz de un árbol y el ala de una mariposa. Producidas industrialmente: dentro de un juguete.

En particular, los materiales celulares poliméricos son aquellos en los que la matriz sólida está constituida por un polímero y a partir de este momento se centrará la atención en ellos [3,4].

Los materiales celulares presentan una combinación única de propiedades, lo cual explica el inusitado crecimiento del mercado de estos materiales en los últimos años. Su característica más destacable es sin duda el bajo peso que presentan, que se traduce en reducciones de coste y ahorros energéticos. Pero además de esto los materiales celulares tienen otras características que les hacen muy interesantes como son una alta relación rigidez/peso, una gran absorción de energía al impacto, una baja conductividad térmica, una gran capacidad de amortiguamiento y flotabilidad. Y no sólo eso, la selección de ciertas matrices poliméricas y estructuras celulares permite que estas estructuras puedan mostrar cualidades como permeabilidad magnética, resistencia química, excelente absorción acústica o una elevada relación superficie-volumen. Todo ello unido a su bajo peso, convierte a estos sistemas en los perfectos candidatos para múltiples aplicaciones en las que el material sólido de partida no tendría siquiera cabida [5–7].

Es esta versatilidad la que justifica la presencia de los materiales celulares en todo tipo de sectores industriales. Por ejemplo, el sector de la construcción hace uso de ellos tanto para aislamiento térmico, como para aplicaciones estructurales. Se les puede encontrar también en el sector de la automoción o en el aeronáutico, así como en aplicaciones de embalaje, en intercambiadores de calor, en sistemas de flotación, en membranas, filtros o en artículos de decoración entre otros.

Muchas de estas propiedades no serían una realidad sin el descubrimiento que tuvo lugar en 1980. En este año, Jane E. Martini-Vvedensky et al. del instituto de Tecnología de Massachusetts (MIT), desarrollaron un método para la producción de materiales microcelulares con tamaños del celda del orden de los 10 μm [8–10]. Este descubrimiento supuso una gran revolución en el mundo de los materiales celulares poliméricos. Hasta aquel momento su producción se había limitado a materiales con tamaños de celda por encima de las 100 micras, lo cual implicaba una substancial reducción de las propiedades mecánicas de estos sistemas en comparación con el sólido de partida. El objetivo perseguido por Martini-Vvedensky et al. era la producción de piezas poliméricas usando menos cantidad de material sin que ello comprometiera las propiedades mecánicas de la pieza en comparación con el sólido de partida [10].

Este descubrimiento dio lugar a un enorme crecimiento en el mundo de los materiales celulares poliméricos. Desde su nacimiento se han fabricado materiales microcelulares partiendo de múltiples polímeros como son el poliestireno (PS) [11], el policarbonato (PC) [12] o el polimetilmetacrilato (PMMA) [13] entre otros. Además, se han comprobado experimentalmente las mejores propiedades mecánicas de los materiales microcelulares frente a las de los materiales celulares convencionales. Y no solo eso, sino que se ha probado que algunos de los materiales microcelulares desarrollados exhiben propiedades superiores a las del polímero de partida. Así pues, algunos materiales microcelulares tienen una mayor resistencia al impacto, a la fatiga, una estabilidad térmica mejor, una

mayor dureza o una menor conductividad térmica que las matrices sólidas que los conforman [14–18].

Todas estas características han permitido la introducción de los polímeros celulares en sectores donde su uso era anteriormente impensable. Sin embargo, la evolución no se detiene, y las nuevas tecnologías requieren cada día de productos con mejores prestaciones. El descubrimiento de los materiales microcelulares parece sugerir que una nueva reducción del tamaño de celda es el camino correcto para seguir mejorando las propiedades de los materiales celulares.

Fue así como hace apenas 10 años nacieron los que hoy se conocen como materiales nanocelulares. Los polímeros nanocelulares se caracterizan por tener celdas en la escala nanométrica y densidades de celda por centímetro cúbico un millón de veces mayores que las de los polímeros microcelulares [19,20]. Esto, en líneas generales, se traduce en tamaños de celda alrededor de los 100 nm y densidades de celdas por encima de 10^{13} celdas/cm^3 (**Figura II**) (Ver sección 2.3 del capítulo 2).

Como se ha comentado con anterioridad, el nacimiento de los polímeros nanocelulares se ha entendido como el siguiente paso para el avance en el mundo de los materiales celulares. Es por ello por lo que han atraído la atención de multinacionales punteras como son SABIC, BASF o Dow Chemical; además de centros de investigación de reconocido prestigio que tienen líneas de investigación sobre este tema como son la Universidad de Washington (Prof. Kumar), la Universidad de Osaka (Prof. Oshima), la Universidad de Toronto (Prof. Chul Park), la Universidad de Shandong (Prof. Guilong Wang) o el laboratorio CellMat en la Universidad de Valladolid (Prof. Rodríguez-Pérez).

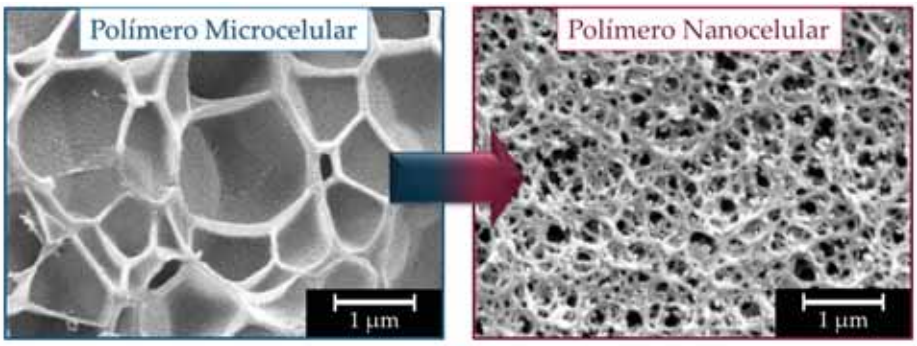

Figura II. Ejemplos de estructuras celulares de un polímero microcelular (izquierda) y uno nanocellular (derecha).

A pesar de su reciente descubrimiento, ya se ha demostrado que los polímeros nanocelulares presentan unas propiedades muy prometedoras. El factor clave para esta mejora viene dado por su estructura celular, muy distinta a la de los materiales microcelulares. En primer lugar, la fase sólida se encuentra confinada en las paredes celulares. Una cadena polimérica tiene una longitud alrededor de los 100 nm mientras que las paredes celulares rondan entre los 25 y los 40 nm [21]. Esto implica que el polímero se encuentra en un espacio restringido, lo que se conoce como confinamiento. Este fenómeno da lugar a materiales con distintas propiedades mecánicas, acústicas y dieléctricas [22–25].

Además del confinamiento de la fase sólida, la fase gaseosa de los materiales nanocelulares está también confinada dentro de las pequeñas celdas, siendo esta la principal razón de la baja conductividad térmica que presentan. Cuando las celdas tienen un tamaño similar o menor al del camino libre medio de las moléculas de aire (alrededor de 70 nm para moléculas de aire a presión atmosférica y temperatura ambiente), es más probable que las moléculas de aire choquen contra las paredes de las celdas que entre ellas y por tanto la conductividad a través de la fase gaseosa se ve reducida. Esto se conoce como efecto Knudsen y hace de estos materiales los perfectos candidatos para la creación de sistemas super aislantes [26,27].

Adicionalmente a lo previamente expuesto, se cree que el confinamiento de ambas fases podría conducir a una mejora en aplicaciones como almacenaje de gas, fenómenos de transporte o interacción radiación-materia [20].

Otro rasgo destacable de estos materiales es su gran superficie específica (alrededor de decenas de m^2/g para nanoceldas en comparación con valores que están por debajo de la unidad para microceldas), esto abre la posibilidad de utilizar los materiales nanocelulares como filtros o membranas para micro y ultrafiltración, como sensores o en aplicaciones de catálisis. [28–30].

Por otra parte, el cambio de escala de las celdas ha dado lugar a interesantes fenómenos que se han probado recientemente; si el tamaño de celda es suficientemente pequeño en comparación con la longitud de onda de la luz (por debajo de los 50 nm), los polímeros nanocelulares conservan, hasta cierto punto, la transparencia del sólido de partida [31,32].

Este gran abanico de propiedades, bajo peso, baja conductividad térmica, alto rendimiento mecánico, transparencia… podría permitir el uso de estos materiales en todo tipo de aplicaciones. Por ejemplo, como super aislantes en aeronáutica, donde se requieren bajas conductividades térmicas combinadas con altas propiedades mecánicas y bajo peso. Como aislantes en dispositivos electrónicos, como materiales estructurales en aplicaciones que demanden bajos pesos y buenas propiedades mecánicas, como ventanas super aislantes sacando partido de su transparencia y su baja conductividad térmica, como láminas protectoras para dispositivos electrónicos o como lentillas, entre muchas otras. Teniendo en cuenta además su reciente nacimiento, cabría esperar que estos materiales tengan propiedades aún por descubrir, incluso por imaginar.

La técnica de producción más prometedora hasta la fecha para su fabricación es la desarrollada en el MIT para la producción de materiales microcelulares; el espumado por disolución de gas [10].

De forma breve, el espumado por disolución de gas consiste principalmente en cuatro etapas. La primera de ellas es la saturación en la cual el polímero sólido se somete a altas presiones de gas que se encuentra a una cierta temperatura. Bajo estas condiciones, el gas difunde dentro del polímero hasta alcanzar el equilibrio, es decir la saturación. A continuación, se procede a la despresurización, en este paso se libera la presión de gas de

forma brusca desencadenando así una inestabilidad termodinámica en el polímero. Esto genera una separación de fases en el polímero, es decir la separación entre las fases sólida y gaseosa, dando lugar a lo que se conoce como puntos de nucleación. Estos puntos de nucleación son los precursores de las celdas que se forman en la tercera etapa, el espumado. Durante el espumado se incrementa la temperatura del sistema polímero-gas, dando movilidad a las cadenas poliméricas que permiten el crecimiento de los puntos de nucleación que forman las celdas que dan nombre al material celular. Por último, en la etapa de estabilización es importante estabilizar las celdas formadas, para prevenir el deterioro de la estructura celular.

Las características de la estructura celular obtenida, así como la densidad del material dependerán por tanto de todos los parámetros del proceso; la presión y la temperatura del gas durante la saturación, el ratio de despresurización, la temperatura y tiempo de espumado y decenas de otros detalles que hacen del espumado por disolución de gas un proceso de producción muy complejo de comprender y por tanto de controlar.

Las propiedades de los materiales celulares están fuertemente ligadas a las características de la estructura celular. Es por tanto que, si se desea obtener un material con determinadas propiedades, es necesario el control, por una parte, del material seleccionado y por otra del proceso de producción y de como todos sus parámetros afectan a la estructura final del material, a sus propiedades y en última instancia a sus aplicaciones.

Es este control el que se persigue en el desarrollo de esta tesis llevada a cabo en el laboratorio CellMat.

II. Marco de la tesis

Esta tesis es parte del trabajo de investigación que se lleva a cabo en el **Laboratorio de Materiales Celulares (CellMat)** [33] que forma parte del Departamento de Física de la Materia Condensada de la Universidad de Valladolid. CellMat está encabezado por el **Prof. Dr. Miguel Ángel Rodríguez Pérez** quien es al mismo tiempo el director de esta tesis doctoral.

CellMat se fundó en 1999 por el Prof. Dr. José Antonio de Saja junto con el Prof. Dr. Miguel Ángel Rodríguez Pérez, con el objetivo de crear un laboratorio dedicado a la investigación de materiales celulares.

Lo que empezó como un proyecto de caracterización de materiales celulares comerciales (principalmente espumas basadas en poliolefinas [34,35]), rápido se convirtió en un ambicioso proyecto que desde la fundación del grupo, ha investigado sobre la producción, mecanismos de espumado, estructura, propiedades, modelización y aplicaciones de los materiales celulares. Entre todo ello, cabe destacar las líneas de investigación sobre materiales celulares en base aluminio [36–38], materiales microcelulares [36,39,40], o las cinco líneas principales de investigación que actualmente se desarrollan en el laboratorio, nanocompuestos celulares [41–43], materiales celulares

basados en bioplásticos [44,45], espumas de poliuretano [46,47], materiales multifuncionales y polímeros nanocelulares [48,49].

Poco a poco el laboratorio fue desarrollando el conocimiento y las instalaciones necesarias para profundizar en el tetraedro de los materiales (**Figura III**).

Figura III. Tetraedro de los materiales.

Como se ha dicho con anterioridad, los primeros años se centraron en la caracterización de materiales celulares, evaluando de esta forma la relación existente entre estructura y propiedades. Más adelante, en 2008 el laboratorio comenzó con la producción de materiales celulares. Esta nueva línea dio como resultado la primera tesis doctoral que analizaba la relación entre producción-estructura celular y propiedades de materiales celulares. La tesis de la Dr. C. Saiz-Arroyo presentada en 2012 [50].

CellMat también ha destacado en otros aspectos como el análisis de mecanismos de espumado [51–53], la optimización de sistemas de producción o el desarrollo de nuevas tecnologías de espumado [45,50,54,55], convirtiéndose por todas estas razones en una referencia internacional en el campo de los materiales celulares.

Es importante señalar que la mayoría de la investigación que se lleva a cabo en CellMat se centra en el desarrollo de conocimiento que puede transferirse a la industria. Prueba de ello es la creación de una empresa spin-off (CellMat technologies S.L) en el año 2012 [56].

En 2014, CellMat consigue otro hito; producir sus primeros polímeros nanocelulares, añadiendo así una nueva línea de trabajo que hace de este centro uno de los pioneros en la investigación de estos materiales. Los primeros desarrollos sobre este tema se resumen en la tesis doctoral de Dr. J. Pinto Sanz [49].

Desde ese momento, se ha escrito otra tesis doctoral y se han publicado más de 15 artículos científicos sobre polímeros nanocelulares [31,48,57].

La primera tesis estaba centrada principalmente en la producción de materiales nanocelulares a partir de mezclas de PMMA con polimetilmetacritalo-b-polibutilacrilato-b-polimetilmetacrilato (MAM). Mientras que en las investigaciones posteriores se han estudiado las propiedades (mecánicas, dieléctricas, acústicas y térmicas) de estos materiales.

El trabajo de investigación que se presenta en esta tesis nació como continuidad de estos primeros trabajos y se nutre de toda la experiencia y conocimiento previo. Con la base del tetraedro ya fundada, el principal objetivo de este trabajo es fortalecer el conocimiento sobre la relación producción-estructura-propiedades, sin perder de vista las posibles aplicaciones finales de estos materiales. Para ello, se ha comenzado estudiando a fondo la relación producción-estructura utilizando PMMA como polímero de partida. El proceso de producción se ha modificado de múltiples formas, estudiando la influencia de cada uno de los parámetros de producción en la estructura celular obtenida, lo cual ha permitido un profundo entendimiento de esta relación. Además, se han estudiado algunas de sus propiedades físicas (ópticas, mecánicas y térmicas).

Las propiedades mecánicas se han medido en el "**Cambridge Centre for Micromechanics"** perteneciente al **Departamento de Ingeniería de la Universidad de Cambridge**, bajo la supervisión del **Prof. Dr. Norman A. Fleck.** Se ha realizado una estancia de tres meses de duración con el objetivo de nutrirse del avanzado conocimiento sobre propiedades mecánicas que posee este laboratorio. Fundado en 1996, el centro posee un amplio conocimiento sobre propiedades mecánicas de espumas de todo tipo. Sus líneas de investigación incluyen el modelizado del proceso de espumado, el estudio de propiedades mecánicas de materiales celulares, el análisis de los efectos de escala en la plasticidad, o la determinación de las propiedades mecánicas de juntas adhesivas, entre otras. Este centro de investigación mantiene relaciones internacionales con importantes grupos de investigación en los Estados Unidos, en Harvard, en el MIT, en Brown, en UCSB y el NIST además de centros de investigación europeos como el Institute National Polytechnique de Grenoble, Francia; la Technical University Eindhoven, Los Países Bajos; el KTH, Suecia; o el DTU en Dinamarca.

Para finalizar, cabe mencionar que esta tesis se ha desarrollado de forma paralela con otra tesis llevada a cabo en el laboratorio CellMat (Dra. Victoria Bernardo). En su trabajo se han usado materiales multifásicos en base PMMA para la producción de polímeros nanocelulares. Ambas tesis se han nutrido del conocimiento de la otra, resultando en un tándem muy beneficioso.

Esta tesis se ha desarrollado en el marco de varios proyectos de investigación financiados de forma pública (**Tabla I**) y privada (**Tabla II**).

Tabla I. Proyectos de investigación financiados a través de convocatorias competitivas de entidades públicas.

Título del proyecto	Desarrollo y Fabricación en continuo de aislantes térmicos avanzados basados en polímeros nanocelulares
Organismo de financiación	Programa Estatal de I+D+i Orientada a los Retos de la Sociedad
Duración	Desde 01/2016 hasta 12/2019
Investigador principal	Miguel Ángel Rodriguez Pérez
Presupuesto	90.750 €
Título del proyecto	Desarrollo de plásticos sub-microcelulares y nanocelulares: fabricación, estructura, propiedades y potenciales aplicaciones

Organismo de financiación	Proyecto Plan Nacionales de Materiales
Duración	Desde 01/2013 hasta 12/2015
Investigador principal	Miguel Ángel Rodriguez Pérez
Presupuesto	130.000 €
Título del proyecto	Desarrollo de una nueva generación de aislantes térmicos avanzados basados en la obtención de estructuras porosas nanocelulares
Organismo de financiación	Junta de Castilla y León
Duración	Desde 01/2013 hasta 12/2015
Investigador principal	Miguel Ángel Rodriguez Pérez
Presupuesto	30.000 €

Tabla II. Proyectos de investigación con entidades públicas o privadas.

Título del proyecto	Desarrollo de estrategias para fabricar polímeros nanocelulares en procesos industriales: extrusión y perlitas expandidas
Organismo de financiación	CellMat Technologies SL
Duración	Desde 12/2015 hasta 12/2019
Investigador principal	Miguel Ángel Rodriguez Pérez
Presupuesto	105.000 €
Título del proyecto	Desarrollo de polímeros nanocelulares avanzados
Organismo de financiación	Sabic y CellMat Technologies SL
Duración	Desde 12/2014 hasta 12/2018
Investigador principal	Miguel Ángel Rodriguez Pérez
Presupuesto	60.000 €
Título del proyecto	Desarrollo de materiales celulares ligeros y resistentes mediante el control de la composición química y estructura celular: materiales micro y nanocelulares
Organismo de financiación	CellMat Technologies SL
Duración	Desde 12/2013 hasta 12/2016
Investigador principal	Miguel Ángel Rodriguez Pérez
Presupuesto	48.000 €

III. Objetivos

Este trabajo ha sido motivado principalmente por la novedad del mundo de los materiales nanocelulares y la falta de conocimiento en esta área debido a su reciente nacimiento. Es por lo que este trabajo persigue profundizar en el campo de los polímeros nanocelulares tanto como sea posible.

Con estas miras se han definido los objetivos de esta tesis, que consisten principalmente en establecer las relaciones que se ilustran en la **Figura IV,** para materiales nanocelulares producidos a partir de nucleación homogénea. En resumen, el principal objetivo de este trabajo es establecer una conexión entre el proceso de producción de materiales nanocelulares, su estructura celular y las propiedades que presentan.

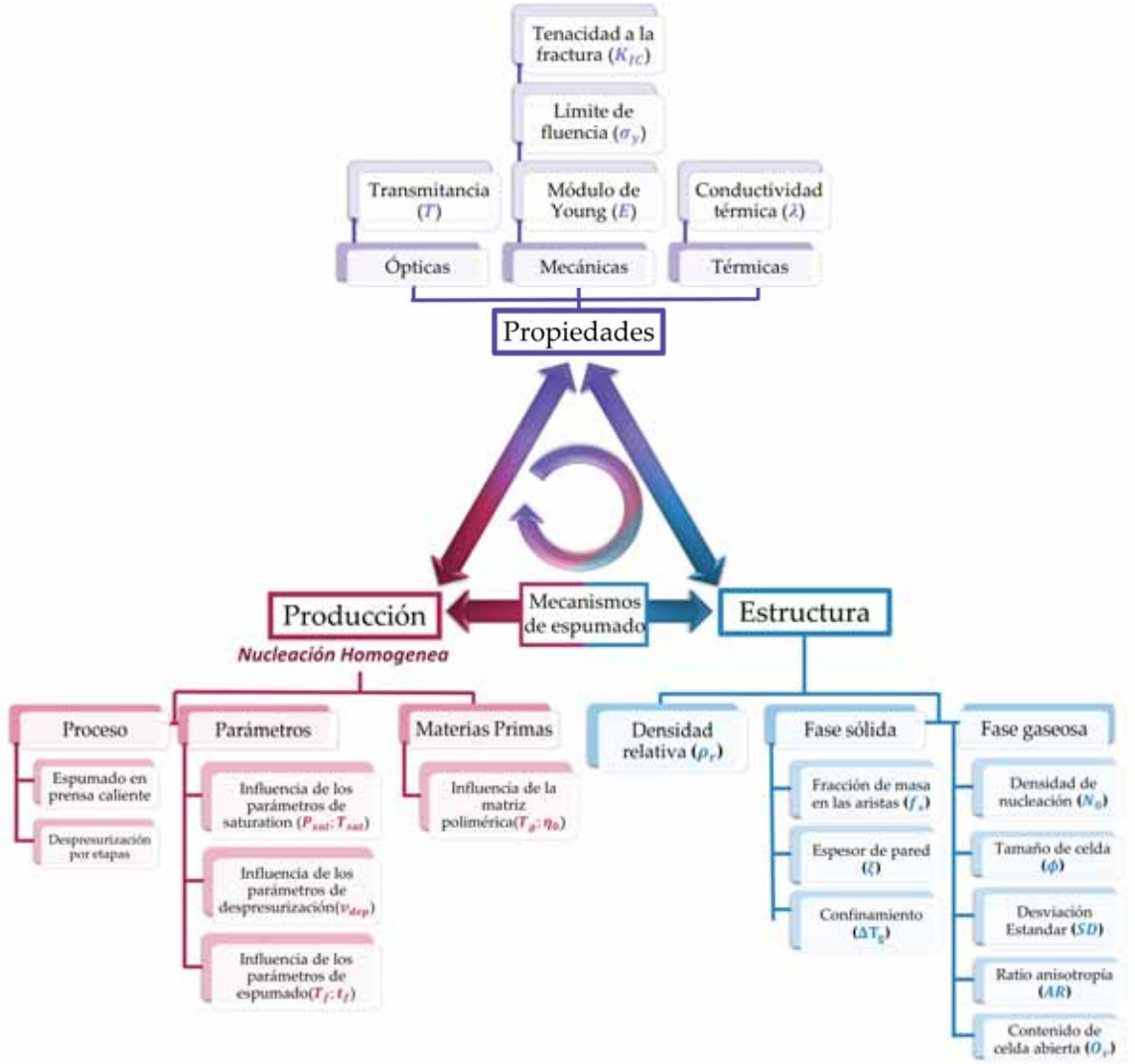

Figura IV. Esquema de las relaciones que se establecerán en esta tesis para materiales nanocelulares producidos a partir de nucleación homogénea.

Con la intención de cumplir con todo ello, se han definido los objetivos que siguen:

Analizar el efecto de modificar el proceso de producción en la estructura celular de materiales nanocelulares homogéneos.

Este primer objetivo persigue, por un lado, explorar el proceso de producción, y por otra analizar en detalle la estructura celular de los materiales obtenidos para finalmente comprender los mecanismos de espumados que gobiernan este proceso de producción. Esta investigación se ha centrado en el uso de distintos grados de PMMA libres de agentes de nucleación (es decir la investigación se centra en sistemas con nucleación homogénea). Se puede dividir por tanto este primer objetivo general en tres secundarios:

⇒ Explorar todas las posibles modificaciones del proceso de producción; como se esquematiza en la **parte izquierda de la Figura IV**, el proceso de producción

puede variar de diversas maneras, siendo las estudiadas en esta tesis la siguientes:

- Modificaciones de los parámetros de proceso: conservando el esquema original del espumado por disolución de gas en cuatro pasos, se han modificado los siguientes parámetros:
  - Parámetros de saturación: presión de saturación (P_{sat}) y temperatura de saturación (T_{sat}).
  - Parámetros de despresurización: velocidad de despresurización (v_{dep}).
  - Parámetros de espumado: temperatura de espumado (T_f), y tiempo de espumado (t_f).

Adicionalmente, el proceso como tal se puede modificar como sigue:

- Modificaciones del proceso: como se muestra en el esquema de la **Figura IV**, se han explorado dos rutas de producción alternativas:
  - Espumado en prensa: el procedimiento habitual consiste en espumar en un baño térmico, en este trabajo se analiza la posibilidad de realizar el espumado en una prensa de platos calientes. Se han usado además distintos parámetros de espumado (P_{sat}, T_{sat}) con el objetivo de establecer una comparación con el método convencional.
  - Despresurización en dos etapas: se ha modificación la etapa de despresurización en el espumado en una etapa. Así la liberación del gas se ha llevado a cabo en dos pasos en vez de en uno como es habitual. Se han modificado además la presión parcial (P), el ratio de despresurización (v_{dep}) y la temperatura de espumado (T_f) para estudiar su influencia en el resultado.

Además, se han analizado en detalle las modificaciones que se inducen al cambiar el material de partida:

- Estudio del uso de distintas matrices poliméricas para la fabricación de materiales nanocelulares; se han empleado matrices poliméricas con distintas características reológicas, temperatura de transición vítrea (T_g) y viscosidad de cero-cizalla (η_0), a la vez que se han modificado los parámetros de proceso.

Habiendo cumplido con los objetivos previos, el estudio sobre la ruta de producción se puede dar por completado siendo posible definir el siguiente objetivo parcial:

⇒ Analizar en profundidad los materiales nanocelulares obtenidos; las muestras producidas se han caracterizado de la siguiente forma (**parte derecha de la Figura IV**):

- Determinación de la densidad relativa de los materiales producidos.
- Caracterización de la estructura celular: se ha llevado a cabo un análisis completo de los parámetros que describen la estructura celular. Midiendo para ello tanto los que caracterizan la fase gaseosa como la sólida. La fase

gaseosa se ha descrito por medio del tamaño de celda (ϕ), la densidad de nucleación (N_0), la desviación estándar del tamaño de celda (SD), el ratio de anisotropía (AR), y el contenido de celda abierta (O_v). La fase sólida se ha definido a través de la fracción de masa en las aristas (f_s), el espesor de pared (ξ), y el confinamiento de la fase sólida (ΔT_g).

Tras modificar el proceso de producción y analizar en profundidad las estructuras celulares obtenidas es finalmente posible analizar los mecanismos de espumado. Es decir, el tercer objetivo parcial con respecto al proceso de producción se define como:

⇒ Entender los mecanismos de espumado que permiten relacionar los cambios producidos en la estructura celular como consecuencia de modificar el proceso de espumado.

- Se ha utilizado un modelo teórico basado en la teoría de nucleación clásica (CNT), que ha permitido entender en detalle el espumado por disolución de gas para la fabricación de espumas nanocelulares a partir de materiales homogéneos.

El primer objetivo definido permite por tanto completar todas las relaciones de la parte inferior del esquema de la **Figura IV**, quedando pendiente el estudio de las propiedades de los materiales fabricados. Esto lleva a definir el segundo objetivo principal de esta tesis:

Estudio de las propiedades de los materiales nanocelulares fabricados para obtener la relación proceso de producción-estructura celular-propiedades.

Este objetivo se basa principalmente en el estudio de las propiedades de los materiales producidos. Esto incluye el análisis de las propiedades ópticas, mecánicas y térmicas de las muestras fabricadas a lo largo de esta tesis.

⇒ Estudio de las propiedades ópticas: la transmitancia (T) de los materiales fabricados se ha determinado experimental y teóricamente:

- Experimental: a través de un amplio conjunto de medidas ha sido posible establecer la dependencia de la transmitancia con el tamaño de celda y con la longitud de onda utilizada.
- Teórica: se ha desarrollado un modelo para obtener la transmitancia de la luz visible a través de materiales nanocelulares que además permite visualizar la interacción de la luz con estas estructuras.

⇒ Estudio de las propiedades mecánicas: para caracterizar mecánicamente los materiales producidos se han medido; la resistencia a la fractura (K_{IC}), el módulo de Young (E) y el límite de fluencia (σ_y). Todas estas propiedades se han relacionado con las características del material; su densidad relativa, así como su estructura celular.

⇒ Estudio de las propiedades térmicas: se ha medido la conductividad térmica (λ) de los materiales nanocelulares fabricados.

Satisfacer estos objetivos podría permitir la producción de polímeros nanocelulares a la carta. Es decir, fabricar un material con las propiedades finales que se deseen a través de obtener una estructura celular específica controlada por el proceso de producción.

IV. Novedades

El desarrollo de esta tesis ha permitido ampliar la literatura concerniente a la producción de polímeros nanocelulares a partir de materiales homogéneos. En los párrafos que siguen se describen las novedades aportadas en esta tesis:

En cuanto a lo que el proceso de producción se refiere, se ha diseñado un montaje que permite monitorizar el proceso de difusión de gas en un sistema polimérico. **Ha sido posible medir, por primera vez de forma in-situ, parámetros como la solubilidad, la difusividad o el swelling (aumento del volumen del polímero), a través de tomografía y radiografía de neutrones.**

Además, en este trabajo **se han combinado presiones de saturación de 20 MPa con temperaturas de saturación de -32 °C por primera vez** para la fabricación de PMMA nanocelular.

Además de todo esto, **se han propuesto dos rutas alternativas para la producción de estos materiales.** La primera de ellas **modifica la etapa de espumado, sustituyendo el espumado habitual en baño térmico por un espumado en prensas**. La segunda ruta propuesta introduce la idea de **la despresurización por etapas en el proceso de espumado en una etapa.**

Aun sin salirse de las novedades incluidas en esta tesis con respecto al proceso de producción, se han utilizado **por primera vez tres matrices poliméricas con propiedades reológicas diferentes entre sí para la producción de materiales nanocelulares fabricados a través de nucleación homogénea.**

Gracias a todos estos cambios introducidos en el proceso ha sido posible la producción de materiales nanocelulares con características novedosas. Así por ejemplo, se ha conseguido **por primera vez PMMA nanocellular con tamaños de celda por debajo de los 30 nm y densidades de nucleación por encima de 10^{16} núcleos/cm^3**; estas características les convierten en **los primeros polímeros nanocelulares semitransparentes fabricados**. Asimismo, se ha elaborado, **por primera vez a través de nucleación homogénea, el polímero nanocellular que combina el menor tamaño de celda (75 nm) con la más baja densidad (0.24) reportada.**

Por medio de las rutas de producción alternativas **se han conseguido muestras planas de grandes dimensiones nunca antes documentadas**. Por otro lado, se ha

desarrollado un método para **la producción de espumas nanocelulares libres de defectos** (característicos de determinados materiales y condiciones de proceso).

Con respecto a la caracterización de los materiales, se han analizado en detalle las estructuras celulares de los sistemas fabricados, llegando a definir parámetros no documentados con anterioridad para materiales nanocelulares. **Se ha desarrollado un método para determinar la fracción de masa en las aristas en materiales nanocelulares**. Se han **aportado también datos sobre el confinamiento de la fase sólida (ΔT_g), y el contenido de celda abierta, por primera vez para materiales con tamaños de celda por debajo de los 50 nm.**

Este detallado análisis ha permitido llegar a comprender mejor los mecanismos de espumado que gobiernan el proceso de producción de materiales nanocelulares.

Finalmente, gracias a la producción de materiales con nuevas características se han podido medir las propiedades de estos por primera vez. Así pues, se ha medido **por primera vez la transmitancia de polímeros semitransparentes, desarrollando a su vez un modelo teórico novedoso que estudia la interacción de la luz con los polímeros nanocelulares. Además, se han medido también por primera vez las propiedades mecánicas y térmicas de PMMA nanocelular con tamaños de celda por debajo de los 50 nm.**

V. Estructura de esta tesis

Esta tesis se ha escrito en la modalidad de: **tesis por compendio de publicaciones**. Para ello se han enviado ocho artículos científicos a revistas internacionales (4 de ellos pendientes de aceptación) (Ver **Tabla III**). Se han añadido además algunos datos extra con el objetivo de completar o clarificar los resultados que se presentan. Asimismo, esta tesis cumple con los requisitos para obtener el **doctorado con mención internacional**.

El trabajo presentado se distribuye en **nueve** capítulos cada uno de ellos conteniendo la información que se detalla más abajo:

Capítulo 1. Introducción. Este primer capítulo aporta un breve resumen sobre los materiales celulares, más específicamente sobre los materiales nanocelulares. A continuación, se define el marco en el que se ha desarrollado la tesis, así como los objetivos propuestos y las novedades. Al mismo tiempo, se aporta un resumen con los artículos científicos, conferencias y proyectos relacionados con esta tesis. Finalmente se detalla la estructura de la tesis.

Capítulo 2. Estado del arte. En este capítulo se presenta un detallado resumen sobre los polímeros celulares, comienza con la definición de polímeros microcelulares para seguir con la de polímeros nanocelulares y los parámetros necesarios para describirlos. A continuación, se detallan los procesos de producción de materiales nanocelulares, centrando la atención en el espumado por disolución de gas y las dos estrategias usadas históricamente para producir materiales nanocelulares: nucleación heterogénea y más específicamente la utilizada en este trabajo: la nucleación homogénea. Dentro del

espumado por disolución de gas, se ha examinado en detalle la influencia de los parámetros de producción en la estructura celular final, teniendo en cuenta para ello tanto teorías de nucleación como resultados experimentales publicados con anterioridad. Así pues, se ha estudiado la influencia de los parámetros de saturación, desorción y espumado, además de la influencia de la matriz polimérica usada, en la estructura celular obtenida. Por último, se describen las propiedades ópticas, mecánicas y térmicas de los materiales nanocelulares.

Capítulo 3. Desarrollo experimental. Este capítulo describe los materiales utilizados, así como las técnicas de producción empleadas. Se focaliza en el método de fabricación de materiales celulares usado en esta tesis: el espumado por disolución de gas. Además, las técnicas de caracterización se describen en detalle, añadiendo información adicional a la que se aporta en los artículos científicos.

Capítulo 4. Influencia de los parámetros de saturación. Los resultados obtenidos se presentan por medio de dos artículos científicos, ambos analizando la etapa de saturación. En el primero de ellos, se estudia esta etapa en si misma a través de un análisis in-situ del proceso de difusión del gas dentro de los polímeros, llevado a cabo a través de tomografía de neutrones. El segundo trabajo pone de manifiesto los efectos que provocan en la estructura celular los cambios en los parámetros de saturación, especialmente se muestra el efecto de reducir la temperatura de saturación e incrementar la presión de saturación. Se aportan además datos experimentales evidenciando la influencia de la velocidad de despresurización en la estructura celular obtenida, en una sección extra.

Capítulo 5. Influencia de los parámetros de espumado. El capítulo 5 se centra en determinar cómo se ve afectada la estructura celular de PMMA nanocelular al modificar los parámetros de espumado. Los datos se presentan en un artículo científico que estudia la influencia de la temperatura y el tiempo de espumado en las estructuras obtenidas. En este trabajo la estructura celular de los materiales producidos se analiza en profundidad permitiendo comprender los mecanismos de espumado que juegan un papel en el proceso de producción de los sistemas bajo estudio.

Capítulo 6. Influencia de la matriz polimérica. Tras el estudio de la influencia de los parámetros de proceso, en este capítulo se analizan los cambios inducidos en la estructura celular como consecuencia de modificar las propiedades reológicas de la matriz utilizada. Para ello se presenta un artículo científico en el que se utilizan tres grados diferentes de PMMA para producir materiales nanocelulares que se combina además con el uso de distintas condiciones de proceso.

Capítulo 7. Modificación del espumado por disolución de gas. Adicionalmente a modificar los parámetros de producción, el proceso de producción en sí se ha modificado. Se incluyen en este capítulo dos artículos científicos que presentan dos rutas alternativas para la producción de materiales nanocelulares. La primera de ellas sustituye la etapa convencional de espumado por un espumado en prensa, permitiendo la producción de piezas planas de grandes dimensiones. La segunda permite obtener materiales libres de

defectos gracias a la introducción de una despresurización en etapas en el proceso de espumado en una etapa.

Capítulo 8. Propiedades de los materiales nanocelulares. Se presentan aquí en forma de dos publicaciones científicas, las propiedades de los materiales fabricados a lo largo de los capítulos previos (4, 5 y 6). Uno de ellos detalla las propiedades ópticas de los materiales semitransparentes fabricados, así pues, describe de manera experimental y teórica la transmitancia de los materiales celulares semitransparentes. El siguiente, estudia las propiedades mecánicas del PMMA nanocellular y su relación con la estructura celular. Finalmente, se incluyen medidas de la conductividad térmica del PMMA nanocelular en una sección extra.

Capítulo 9. Conclusiones y trabajo futuro. Para concluir se presentan los principales resultados de esta tesis, remarcando aquellos que son novedad en la literatura y relacionando todo ello con los objetivos propuestos. Finalmente se detalla el trabajo futuro.

VI. Publicaciones, conferencias y cursos.

En esta sección se resumen todas las publicaciones relacionadas con esta tesis (**Tabla III**) así como las conferencias nacionales e internacionales donde se han presentado resultados de la misma (**Tabla IV**), y la asistencia a cursos de formación (**Tabla V**) y actividades adicionales llevadas a cabo por la doctoranda (**Tabla VI**).

Tabla III. Artículos científicos que se adjuntan en la tesis.

No.	Referencia	Capítulo	Q/IF
1	Martín-de León, J.; Cimavilla-Román, P.; Bernardo, V.; Rodríguez-Pérez, M. A. Cold neutron transmission for in-situ control of gas diffusion mechanisms. **PENDING**	4	-
2	Martín-de León, J.; Bernardo, V.; Rodríguez-Pérez, M. A. Key Production Parameters to Obtain Transparent Nanocellular PMMA. *Macromolecular Materials and Engineering* **2017**, 3, 1700343.	4	Q1/2.69
3	Martín-de León, J.; Bernardo, V.; Rodríguez-Pérez, M. A. Low Density Nanocellular Polymers Based on PMMA Produced by Gas Dissolution Foaming: Fabrication and Cellular Structure Characterization. *Polymers* **2016**, *8*, 265.	5	Q1/3.364
4	Martín-de León, J. M.; Bernardo, V.; Laguna-Gutiérrez, E.; Rodríguez-Pérez, M. A. Influence of the rheological behavior of PMMA on the cellular structure of nanocellular materials. **PENDING**	6	-
5	Martín-de León, J.; Bernardo, V.; Cimavilla-Román, P.; Pérez-Tamarit, S.; Rodríguez-Pérez, M. A. Overcoming the Challenge of Producing Large and Flat Nanocellular Polymers: A Study with PMMA. *Advanced Engineering Materials*, **2019**, 1–8.	7	Q2/2.576
6	Martín-de León, J.; Bernardo, V.; Rodríguez-Pérez, M.A. Two-stage depressurization in one step foaming process: the	7	-

	production of nanocellular materials free of defects. **PENDING**		
7	Martín-de León, J.; Pura, J. L.; Bernardo, V.; Rodríguez-Pérez, M. A. Transparent nanocellular PMMA: Characterization and modeling of the optical properties. *Polymer*, **2019**, *170*, 16–23.	8	Q1/3.486
8	Martín-de León, J., Van Loock, F.; Bernardo, V.; Fleck, N.A.; Rodríguez-Pérez, M. A. The influence of cell size on the mechanical properties of nanocellular PMMA.**PENDING**	8	-

Tabla IV. Comunicaciones orales, posters y contribuciones en congresos nacionales e internacionales.

1	Martín-de León, J.; Bernardo, V.; Rodríguez-Pérez, M. A. *Influencia de la temperatura en la absorción de dióxido de carbono en espumas nanocelulares.* Escuela Nacional de Materiales Moleculares, Febrero 2014, Santa Pola, Comunidad Valenciana, España. **Talk.**
2	Martín-de León, J.; Bernardo, V.; Pérez-Tamarit, S.; Solórzano, E.; Rodríguez-Pérez, M. A. *Nanocellular foams fabrication methods by gas dissolution process.* Metfoam, Septiembre 2015, Barcelona, Cataluña, España. **Poster.**
3	Martín-de León, J.; Bernardo, V.; Rodríguez-Pérez, M. A. *Higher nucleation efficiency in polymer foams by improving gas dissolution method.* VIII European School on Molecular Nanoscience, Octubre 2015, Paris, Francia. **Talk.**
4	Martín-de León, J.; Bernardo, V.; Rodríguez-Pérez, M. A. *Influence of the process parameters in the cellular structure of low density PMMA nanocelullar polymers produced by the gas dissolution foaming route.* XIV Reunión del grupo especializado de polímeros de la RSEQ y RSEF, Septiembre 2016, Burgos, España. **Talk.**
5	Martín-de León, J.; Bernardo, V.; Rodríguez-Pérez, M. A. *Description of the process parameters for the production of ppsu nanocellular materials.* FOAMS 2016, Septiembre 2016, Seattle, Washington, Estados Unidos. **Poster.**
6	Martín-de León, J.; Bernardo, V.; Rodríguez-Pérez, M. A. *Understanding the mechanism that allow reducing density in PMMA nanocellular polymers.* FOAMS 2016, Septiembre 2016, Seattle, Washington, Estados Unidos. **Poster.**
7	Martín-de León, J.; Bernardo, V.; Rodríguez-Pérez, M. A. *Knudsen Effect: Nanocellular Polymers as thermal insulators.* Three Minutes Thesis Contest (3MT), Octubbre 2016, Valladolid, Castilla y León, España. **Talk.**
8	Martín-de León, J.; Bernardo, V.; Rodríguez-Pérez, M. A. *Nanocellular polymers: the optimal production of the thermal insulators of the future.* III Jornada Investigadoras de la UVA en "La aventura de la ciencia y la tecnología" 2017, Septiembre 2017, Valladolid, Castilla y León, España. **Talk.**
9	Martín-de León, J.; Bernardo, V.; Rodríguez-Pérez, M. A. *Semi-transparent nanocellular polymers based on PMMA: Production and characterization.* FOAMS 2017, Octubre 2017, Bayreuth, Alemania. **Talk.**

10	Martín-de León, J.; Bernardo, V.; Rodríguez-Pérez, M. A. *Controlled foaming in a hot press of flat and large parts of nanocellular PMMA.* FOAMS 2017, Octubre 2017, Bayreuth, Alemania. **Poster.**
11	Martín-de León, J.; Pura, J.L.; Bernardo, V.; Rodríguez-Pérez, M. A. *Understanding the behaviour of semi-transparent nanocellular PMMA: study of the transmittance and modelling.* CellMAT 2018, Octubre2018, Bad Staffelstein, Alemania. **Talk.**
12	Martín-de León, J.; Bernardo, V.; Rodríguez-Pérez, Pura, J.L.; M. A. *Nanocellular PMMA with tuneable cellular structure by changing the rheological behaviourof the polymer matrix.* CellMAT 2018, Octubre2018, Bad Staffelstein, Alemania. **Poster.**

Tabla V. Cursos y campañas en grandes centros de investigación.

1	*Workshop on X-RAY radioscopy and tomography.* Noviembre 2014, Berlin, Alemania.
2	*Neutron Campaign, HZB* Septiembre 2015, Berlin, Alemania
3	*Acoustic insulation in building.* 2015, Valladolid, Castilla y León, España.
4	*Seminar on characterization of materials by thermal analysis techniques: DSC, TGA.* Octubre 2015, Valladolid, Castilla y León, España.
5	*Thermal insulation in buildings.* Octubre 2015, Valladolid, Castilla y León, España.
6	*Characterization of polymeric materials.* Octubre 2016, Valladolid, Castilla y León, España.
7	*Plastic packaging, fundamentals, regulations and trends* Febrero 2018, Valladolid, Castilla y León, España.
8	*Neutron Campaign, Diamond Lightsource* Febrero 2019, Oxford, Reino Unido.

Tabla VI. Actividad adicional.

Papers	
1	Notario, B.; Pinto, J.; Solórzano, E.; Escudero, J.; Martín-de León, J; Velasco, D.; Rodríguez-Pérez, M. A. *In Situ Optical Analysis of Structural Changes in Polylactic Acid (PLA) during the Gas Dissolution Process*. Defect and Diffusion Forum **2014**, *353*, 131–136.
2	Bernardo, V.; Martín-De León, J.; Rodríguez-Pérez, M. A. *Production and characterization of nanocellular polyphenylsulfone foams.* Materials Letters 2016, 178, 155–158.
3	Bernardo, V.; Martín-de León, J.; Laguna-Gutiérrez, E.; Rodríguez-Pérez, M. A. *PMMA-sepiolite nanocomposites as new promising materials for the production of nanocellular polymers.* European Polymer Journal 2017, 96, 10–26.
4	Bernardo, V.; Martin-de León, J.; Laguna-Gutierrez, E.; Catelani, T.; Pinto, J.; Athanassiou, A.; Rodriguez-Perez, M. A. *Understanding the role of MAM molecular weight in the production of PMMA/MAM nanocellular polymers.*

	Polymer 2018, 153, 262–270.
5	Bernardo, V.; Martin-de Leon, J.; Pinto, J.; Verdejo, R.; Rodriguez-Perez, M. A. *Modeling the heat transfer by conduction of nanocellular polymers with bimodal cellular structures*. Polymer 2019, 160, 126–137.
6	V. Bernardo, J. Martin-de Leon, J. Pinto, T. Catelani, A. Athanassiou and M. A. Rodriguez-Perez, *Low-density PMMA/MAM nanocellular polymers using low MAM contents: Production and characterization*, Polymer (Guildf). 163 (2019) 115–124.
7	Martín-de León, J.; Bernardo, V.; Rodríguez-Pérez, M.A. *Nanocellular Polymers: The Challenge of Creating Cells in the Nanoscale*. Materials 2019, 12, 797.
8	V. Bernardo, J. Martin-de Leon and M. A. Rodriguez-Perez. *Anisotropy in nanocellular polymers promoted by the addition of needle-like sepiolites*, Polym. Int. 68 (2019) 1204–1214.
9	V. Bernardo, F. Loock, J. Martin-de Leon, N. A. Fleck and M. A. Rodriguez-Perez, *Mechanical Properties of PMMA-Sepiolite Nanocellular Materials with a Bimodal Cellular Structure*, Macromol. Mater. Eng. 1900041 (2019)1-12.
Conferences	
10	Bernardo, V.; Martín-de León, J.; Rodríguez-Pérez, M. A.; Pinto, J. *Nanostructure Materials and nanoporous foams.* Escuela Nacional de Materiales Moleculares, Febrero 2014, Santa Pola, Comunidad Valenciana, España. **Talk.**
11	Pérez-Tamarit, S.; Bernardo, V.; Martín-de León, J.; Solórzano, E.; Rodríguez-Pérez, M. A. *Characterization of the solid phase of cellular materials by means of X-RayμCT* Metfoam, Septiembre 2015, Barcelona, Cataluña, España. **Poster.**
12	Bernardo, V.; Martín-de León, J.; Pérez-Tamarit, S.; Solórzano, E.; Rodríguez-Pérez, M. A. *Cellular structure, properties and applications of nanoporous materials.* Metfoam, Septiembre 2015, Barcelona, Cataluña, España. **Poster.**
13	Bernardo, V.; Martín-de León, J.; Rodríguez-Pérez, M. A. *Sepiolites as nucleating agent in PMMA nanofoam.* VIII European School on Molecular Nanoscience, Octubre 2015, Paris, Francia. **Talk.**
14	Bernardo, V.; Martín-de León, J.; Rodríguez-Pérez, M. A. *Production of nanocellular materials from nanostructured polymers based on PMMA/MAM blends: Influence of the polymer molphology on the cellular structure.* XIV Reunión del grupo especializado de polímeros de la RSEQ y RSEF, Septiembre 2016, Burgos, España. **Talk.**
15	Rodríguez-Pérez, M. A.; Bernardo, V.; Martín-de León, J. *Nanocellular polymers: A new class of materials with enhanced properties.* XIV Reunión del grupo especializado de polímeros de la RSEQ y RSEF, Septiembre 2016, Burgos, España. **Plenay Talk.**
16	Bernardo, V.; Martín-de León, J.; Rodríguez-Pérez, M. A. *Needle-like nanoparticles as a new nucleating agent in CO2-foaming of nanocellular PMMA.* FOAMS 2016, Septiembre 2016, Seattle, Washington, Estados Unidos. **Poster.**
17	Bernardo, V.; Martín-de León, J.; Rodríguez-Pérez, M. A. *Nanocellular polymers based on PMMA/MAM blends: effect of the copolymer chemistry on the nanostructuration and the cellular structure.*

	FOAMS 2016, Septiembre 2016, Seattle, Washington, Estados Unidos. **Poster.**
18	Rodríguez-Pérez, M. A.; Bernardo, V.; Martín-de León, J. *Low density nanocellular foams based on PMMA: production, structure and properties.* FOAMS 2016, Septiembre 2016, Seattle, Washington, Estados Unidos. **Talk.**
19	Martín-de León, J.; Bernardo, V.; Rodríguez-Pérez, M. A. *Production and properties of low density nanocellular PMMA with controlled density and cellular structure.* Poly-Foam Conference, Abril 2017, Hilton Mainz, Alemania. **Talk.**
20	Bernardo, V.; Martín-de León, J.; Rodríguez-Pérez, M. A. *Effect of amount of block-copolymer on the density and cellular structure of nanocellular polymers based on PMMA/MAM blends.* FOAMS 2017, Octubre 2017, Bayreuth, Alemania. **Poster.**
21	Pérez-Tamarit, S.; Martín-de León, J.; Bernardo, V.; López-González, E.; Muñoz-Pascual, S.; Pinto, J.; Laguna-Gutiérrez, E.; Rodríguez-Pérez, M. A. *Transfering knodledge from the university to the industry: internships at the university of Valladolid.* EDULEARN 2018, Julio 2018, Palma de Mallorca, Illes Balears, España. **Virtual presentation.**
22	López-GonzAlez, E.; Muñoz-Pascual, S.; Bernardo, V.; Laguna-Gutiérrez, E.; Martín-de León, J.; Pérez-Tamarit, S.; Pinto, J.; Rodríguez-Pérez, M. A. *Evolution of the practical training in materials physics: from a constrained research in the polymer science field to a multidisciplinary methodology.* EDULEARN 2018, Julio 2018, Palma de Mallorca, Illes Balears, España. **Virtual presentation.**
23	Rodríguez-Pérez, M. A.; Martín-de León, J.; Bernardo, V. *Modelling Some Key Properties of Semi-Transparent Nanocellular Polymers Based on PMMA.* FOAMS 2018, Septiembre 2019, Montreal, Canada. **Talk.**
24	Santiago-Calvo, M.; Naji-Izaguirre, H.; Bernardo, V.; Martín-de León, J.; Saiani, A.; Villafañe, F.; Rodríguez-Pérez, M. A. *Production of thermoplastic polyurethane foams synthesized with different contents of hard segment and graphene nanoplatelets by the gas dissolution foaming process.* CellMAT 2018, Octubre 2018, Bad Staffelstein, Alemania. **Talk.**
25	Múgica-Izaguirre, M.; Bernardo, V.; Martín-de León, J.; Saiz-Arroyo, C.; Rodríguez-Pérez, M. A. *Production of microcellular PMMA using the bead foaming technology.* CellMAT 2018, Octubre 2018, Bad Staffelstein, Alemania. **Poster.**
26	Rodríguez-Pérez, M. A.; Martín-de León, J.; Pura, J.L.; Bernardo, V. *Nanocellular polymers. Novel approaches to produce these materials using gas dissolution foaming*. CellMAT 2018, Octubre 2018, Bad Staffelstein, Alemania. **Key-note lecture.**
27	Bernardo, V.; Martín-de León, J.; Pura, J.L.; Rodríguez-Pérez, M. A. *Nanocellular polymers based on PMMA/sepiolite nanocomposites: characterization of the mechanical behaviour*. CellMAT 2018, Octubre 2018, Bad Staffelstein, Alemania. **Poster.**
28	Bernardo, V.; Martín-de León, J.; Pura, J.L.; Rodríguez-Pérez, M. A. *Fabrication of low-density nanocellular polymers using PMMA/TPU blends.* CellMAT 2018, Octubre 2018, Bad Staffelstein, Alemania. **Talk.**

VII. Metodología de trabajo

En esta sección se describe la metodología que se ha seguido para elaborar esta tesis doctoral.

i. Selección de materiales

En primer lugar, se han seleccionado los materiales de trabajo. El material principal con el que se ha desarrollado esta tesis ha sido polimetilmetacrilato (PMMA). Se han elegido tres grados distintos de PMMA; V825T, 7N y 6N, para trabajar con matrices de diferentes características reológicas. Las características y distribuidores de todos ellos se detallan en la sección 3.2 del capítulo 3.

Por otra parte, se ha utilizado dióxido de carbono como agente espumante para el espumado por disolución de gas.

ii. Producción

Tras la selección de materiales se ha procedido a la fabricación, primero de los precursores sólidos y tras ello de los materiales celulares:

Producción de los precursores sólidos

A partir de los PMMA seleccionados se han fabricado muestras sólidas para la posterior realización de los experimentos de espumado. Para la elaboración de estos precursores sólidos se ha usado el moldeo por compresión, técnica que se explica con detalle en la sección 3.3.1 del capítulo 3.

De esta forma se han obtenido piezas sólidas que más adelante se han cortado para obtener las piezas con la geometría deseada en cada experimento.

Producción de los materiales celulares

Los materiales celulares se han fabricado a través del espumado por disolución de gas. Para ello se han utilizado dos equipos de producción. El primero de ellos, para la saturación a temperatura ambiente, y el segundo para la saturación a temperaturas por debajo de los cero grados. Ambos sistemas están provistos principalmente de un autoclave, o vaso a presión (modelo PARR 4681 y modelo PARR 4760 respectivamente, provistos por Parr Instrument Company), que permiten trabajar a altas presiones de gas, las cuales se alcanzan gracias a una bomba de presión (modelo SFT-10, Supercritical Fluid Technologies Inc.). Todos los detalles de los montajes se pueden encontrar en la sección 3.3.2 del capítulo 3.

Por otra parte, para la etapa de espumado se han usado tanto baños térmicos (J.P. Selecta Modelo 600685 del Grupo selecta) como una prensa de platos calientes siguiendo los procesos descritos en la sección 3.3.2 del capítulo 3.

iii. Caracterización

Una vez que los materiales se han fabricado se procede a la caracterización, tanto de los materiales sólidos como de los materiales celulares.

Los materiales sólidos se han descrito a través de: su temperatura de transición vítrea, medida a través de calorimetría diferencial de barrido con un Mettler DSC30 tal y como se explica en la sección 3.4.1 del capítulo 3; su densidad, determinada por medio de picnometría (AccuPyc II 1340) como se indica en la sección 3.4.2 del capítulo 3, y sus propiedades reológicas, determinadas por reología de cizalla con un reómetro AR 2000 EX (sección 3.4.7 del capítulo 3).

Para la caracterización de los materiales celulares se ha medido por una parte su densidad y por otra se ha definido su estructura celular por medio de diversos parámetros. Tras ello se han caracterizado las propiedades de estos materiales:

Densidad

La determinación de la densidad de los materiales nanocelulares se ha llevado a cabo teniendo en cuenta el método de Arquímedes y usando un kit de densidades en una balanza de precisión AT261 Mettler-Toledo tal y como se detalla en la sección 3.4.2 del capítulo 3.

Estructura celular

Para visualizar la estructura celular se ha utilizado un microscopio electrónico de barrido ESEM Scanning Electron Microscope (QUANTA 200 FEG, Hillsboro, OR, USA). Tras ello las micrografías se han analizado por medio de un software basado en el programa ImageJ/FIJI obteniendo de esta manera el tamaño de celda, la desviación estándar del tamaño de celda, la densidad de nucleación, el ratio de anisotropía, y la fracción de masa en las aristas tal y como está detallado en la sección 3.4.6 del capítulo 3.

Además, se ha medido el contenido de celda abierta a través de picnometría (sección 3.4.5 capítulo 3).

Propiedades

Por último, se han medido las propiedades de los materiales fabricados, determinando sus propiedades ópticas, mecánicas y térmicas. Así pues, para su caracterización óptica se han llevado a cabo medidas experimentales utilizando dos sistemas; con el primero de ellos se ha medido la transmitancia absoluta y consta de un láser que actúa como fuente de luz, y una esfera integradora modelo PRW0505 de Gigahertz-Optik conectada a un fotómetro modelo X94 de Gigahertz- Optik que actúan como detector. El segundo sistema, para determinar la dependencia de la transmitancia con la longitud de onda utilizada, es un espectrómetro UV-2102 PC. Tanto los sistemas como los procedimientos de medida se explican en la sección 3.4.10 del capítulo 3.

Adicionalmente se ha desarrollado un modelo teórico con COMSOL multiphysics, que permite estudiar la interacción luz/material nanocelular, así como calcular la transmitancia de cualquier sistema celular.

Las propiedades mecánicas se han determinado a través de ensayos de compresión y flexión a tres puntos gracias a una máquina de ensayos mecánicos Instron, tal y como se explica en la sección 3.4.8 del capítulo 3.

Por último, se ha determinado la conductividad térmica a través de un TPS 2500 S (Hotdisk) tal y como se describe en la sección 3.4.9 del capítulo 3.

iv. Análisis e interpretación de resultados

Tras el procedimiento experimental que permite la realización de un amplio conjunto de ensayos y la posterior caracterización de los materiales fabricados, es necesario llevar a cabo un análisis para comprender e interpretar los resultados. En esta tesis se han analizado los mecanismos de espumado que juegan un papel importante en el proceso de producción. Para ello se ha utilizado una teoría de nucleación basada en la teoría clásica de nucleación, pero adaptada a la producción de materiales nanocelulares. Por otra parte, se han analizado los posibles mecanismos físicos responsables de las propiedades que presentan estos materiales.

Todo ello ha permitido cumplir con lo propuesto en la sección de objetivos llegando por tanto a comprender la relación que existe entre proceso de producción, estructura y propiedades de los materiales nanocelulares producidos a través de nucleación homogénea en la técnica del espumado por disolución de gas.

VIII. Principales resultados y conclusiones

Esta sección se centra en describir las principales conclusiones que se han extraído durante la realización de esta tesis. En primer lugar, se describen los principales resultados obtenidos en cada capítulo. Tras ello, se resumen las principales conclusiones extraídas con respecto a los mecanismos de espumado. Además, se ha dedicado un apartado a la comparación de los resultados obtenidos con los presentados previamente en la literatura para materiales nanocelulares.

i. Capítulo 4

El capítulo 4 se centró en el estudio de la etapa de saturación y de la influencia de los parámetros de saturación y despresurización en la estructura celular de PMMA nanocelular producido a través de nucleación homogénea.

Los resultados fueron presentados a través de dos artículos científicos; el primero de ellos (P1[58]), describe un método innovador que permite la monitorización del proceso de difusión de gas en los polímeros por medio de radiografía y tomografía de neutrones. Las principales conclusiones que se han podido extraer de este estudio son las siguientes:

⇒ **Es posible monitorizar experimentos de difusión de gas en polímeros** en atmósferas de altas presiones de gas (hasta 20 MPa) **a través de radiografía y tomografía de neutrones (Figura V)**, pudiendo así determinar:

- La evolución temporal de la solubilidad de CO_2 en PMMA y PS de forma "in-situ" a través del método de calibración desarrollado.
- La evolución temporal del aumento de volumen del PMMA por medio de la monitorización de los cambios morfológicos de la muestra.
- La evolución temporal del perfil de difusión del gas en el PMMA.
- La difusividad de absorción y los tiempos de saturación.

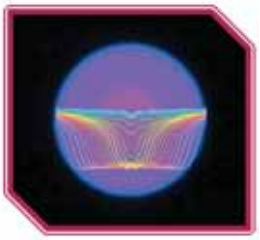

Figura V. Tomografía de neutrones de la diffusion de CO_2 enPMMA.

⇒ La solubilidad del CO_2 en PMMA:

- Crece con la presión de saturación siguiendo una ley dual para presiones de saturación desde 10 MPa a 20 MPa y 40 °C de temperatura de saturación.
- Decrece con el incremento de la temperatura de saturación, cuando se satura a 15 MPa y 40 °C y 60 °C de acuerdo con una ecuación tipo Arrhenius.

⇒ La difusividad de absorción del CO_2 en PMMA:

- Se incrementa con la presión de saturación, a través de una ley polinómica de grado dos, cuando la presión de saturación pasa de 10 MPa a 20 MPa para temperaturas de 40 °C.
- Crece con la temperatura de saturación siguiendo una ley de tipo Arrhenius (cuando se trabaja a 15 MPa y 40 y 60 °C).

⇒ Durante los experimentos de absorción, el PMMA experimenta un incremento de volumen, más conocido como swelling que:

- Se hace más notorio a medida que la solubilidad y la temperatura de espumado crecen.
- Los valores para el incremento de volumen se encuentran entre un 24 y un 30 % cuando se trabaja en un rango de presiones entre 10 MPa y 20 MPa y un rango de temperaturas entre 40 °C y 60 °C.

El Segundo artículo científico (P2 [59]) relaciona los cambios en los parámetros de saturación con los que se producen en la estructura celular, llegando a las siguientes conclusiones:

⇒ Un descenso en la temperatura de saturación de 24 °C a -32 °C (y presiones de saturación de 31 MPa y 6 MPa respectivamente) produce un incremento en la solubilidad del CO_2 en PMMA de 31 % en peso hasta 39 % en peso.

⇒ Si se mantiene constante la temperatura de saturación en -32 °C, un incremento de la presión de saturación de 6 MPa a 20 MPa, conlleva un crecimiento de la solubilidad del CO_2 en PMMA del 39 % al 48 % en peso.

⇒ Este crecimiento de la solubilidad provoca un incremento en la densidad de nucleación y una reducción del tamaño de celda:
- Solubilidades del 48 % en peso de CO_2 permiten la producción de PMMA nanocelular con densidades de nucleación de $7 \cdot 10^{16}$ núcleos/cm^3 y tamaños de celda de 14 nm.

⇒ La reducción del tamaño de celda por debajo de los 50 nm ha permitido la **producción del primer polímero nanocelular semitransparente reportado hasta la fecha** (**Figura VI**):
- Una reducción del tamaño de celda de 40 nm a 14 nm hace que la transparencia se incremente.

Figura VI. PMMA transparente

La influencia de los parámetros de despresurización se ha estudiado también brevemente en este capítulo, permitiendo concluir:

⇒ Mediante el uso de 31 MPa y 24 °C como parámetros de saturación y 25 °C y 5 min como parámetros de espumado, un incremento en la velocidad de despresurización conduce a estructuras celulares con mejores características:
- Una caída de presión de 100 MPa/s en comparación con las de 22 y 17 MPa/s conduce a celdas de menos tamaño (218 nm en comparación con 237 y 250 nm), mayores densidades de nucleación ($1.6 \cdot 10^{14}$ núcleos/cm^3 en comparación con $1.3 \cdot 10^{14}$ y $1.2 \cdot 10^{14}$ núcleos/cm^3).

ii. Capítulo 5

El capítulo cinco tiene como objetivo completar el estudio del impacto de los parámetros de producción en la estructura celular. Es por ello que en este capítulo se analiza el efecto de los parámetros de espumado (temperatura y tiempo de espumado). La estructura celular fue analizada en detalle permitiendo así entender cuáles eran los mecanismos de espumado responsables de los cambios detectados.

Los resultados se presentan en forma de artículo (P3 [60]) siendo los principales los que siguen:

⇒ Fijando las condiciones de saturación en 31 MPa de presión y 24 °C de temperatura (obteniendo así un 31 % en peso de CO_2 absorbido) un incremento en la temperatura de espumado de 40 °C a 100 °C provoca los siguientes cambios en la estructura celular:
- Un aumento en la densidad de nucleación de $2 \cdot 10^{14}$ núcleos/cm^3 cuando se espuma a 40 °C hasta casi $4 \cdot 10^{14}$ núcleos/cm^3 cuando se espuma a 100 °C.
- Prácticamente ningún cambio en el tamaño de celda, obteniéndose valores en torno a los 225 nm para todos los materiales producidos.
- Una reducción de la densidad relativa desde valores en torno a 0.4 para las temperaturas de espumado más bajas hasta valores de 0.24 cuando se espuma a 100°C.

⇒ 110 °C es la temperatura límite para producir PMMA nanocelular en estas condiciones de saturación: cuando se espuma a esta temperatura durante 5 minutos la estructura nanocelular colapsa, reduciéndose el tamaño de celda hasta los 184 nm y aumentando la densidad relativa hasta 0.54.

⇒ Un incremento en el tiempo de espumado de 1 a 5 minutos tiene la misma influencia en la estructura que un incremento en la temperatura de espumado. Por ejemplo, para una temperatura de espumado de 40 °C un aumento del tiempo de espumado de 1 a 5 minutos conlleva una reducción en la densidad relativa de 0.47 a 0.37, un incremento de la densidad de nucleación de $1.8 \cdot 10^{14}$ núcleos/cm^3 a $2.2 \cdot 10^{14}$ núcleos/cm^3, mientras que el tamaño de celda se mantiene constante en valores entre 212 y 225 nm.

⇒ La reducción de la densidad relativa provoca cambios adicionales en la estructura celular del PMMA nanocelular:

- El contenido de celda abierta aumenta al disminuir la densidad relativa hasta obtener una estructura completamente interconectada para valores de densidad relativa por debajo de 0.3.
- Mientras que el tamaño de pared permanece constante en los 25 nm, **la fracción de masa en las aristas, medida por primera vez en este trabajo para materiales nanocelulares (Figura VII),** se reduce con la disminución de la densidad relativa.

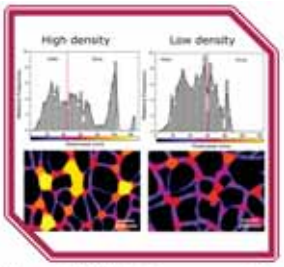

Figura VII. Técnica para medir la fracción de masa en las aristas.

⇒ El análisis de los resultados obtenidos a llevado a un mejor entendimiento de los mecanismos de espumado:

- La reducción de la densidad relativa ocurre como consecuencia del aumento del número de puntos de nucleación. La densidad relativa se reduce a la mitad al incrementar la temperatura de espumado de 40 °C a 100 °C debido a que la densidad de nucleación se dobla mientras que el tamaño de celda permanece constante.
- La densidad relativa no alcanza valores por debajo de 0.24 debido a que la total interconexión entre celdas frena su reducción. Como consecuencia a que la estructura está completamente abierta, el gas difunde fuera del material imposibilitando que siga expandiendo.
- Una reducción de la densidad provoca un descenso en la fracción de masa en las aristas que resulta en un incremento del confinamiento de la fase sólida en los materiales fabricados. Este confinamiento es cuantificado a través del aumento de la temperatura de transición vítrea y llega a alcanzar los 11 °C para los materiales de menor densidad.

iii. Capítulo 6

Una vez estudiada la influencia de los parámetros de producción en la estructura celular del PMMA producido, la influencia de modificar las propiedades de la matriz

polimérica usada se analizó en el capítulo 6. Los resultados se presentan en un artículo científico (P4 [61]) donde se usan tres matrices de PMMA diferentes (con viscosidades desde 1587 Pa·s a 7095 Pa·s y temperaturas de transición vítrea desde los 99 °C hasta los 114 °C). Los parámetros de producción fueron modificados a su vez.

Las conclusiones extraídas de este capítulo son las que siguen:

⇒ La solubilidad se ve fuertemente afectada tanto por los parámetros de proceso como por la matriz utilizada:
- Una viscosidad inferior y/o una temperatura de transición vítrea inferior resulta en mayores solubilidades especialmente cuando se trabaja a temperatura ambiente de saturación.
- Cuando se utilizan condiciones de saturación de 31 MPa y 24 °C la solubilidad cambia del 31 % en peso para el polímero más viscoso, al 36 % para el menos. Mientras que cuando las condiciones de saturación son de 20 MPa y -32 °C la solubilidad crece hasta el 45 % en peso para todos los polímeros viéndose las diferencias entre ellos muy reducidas.

⇒ La difusividad de desorción se incrementa con la solubilidad independientemente de la viscosidad de la matriz polimérica. Desde valores alrededor de $7 \cdot 10^{-8}$ cm^2/s hasta valores en torno a $2 \cdot 10^{-7}$ cm^2/s.

⇒ La estructura celular se ve fuertemente afectada por la solubilidad siendo las tendencias observadas similares para todos los polímeros bajo estudio:
- La densidad de nucleación se incrementa en dos órdenes de magnitud cuando la solubilidad cambia entre el menor y el mayor valor:
  - Para los grados de PMMA HV y MV la densidad de nucleación se incrementa desde los 10^{14} núcleos/cm^3 hasta los 10^{16} núcleos/cm^3 para un aumento de solubilidad entre 31 % a 45 %.
  - Para el PMMA LV se incrementa desde los 10^{13} núcleos/cm^3 hasta los 10^{16} núcleos/cm^3 cuando crece la solubilidad del 36 % en peso al 44 %.
- El tamaño de celda se reduce en un factor 10 diez, reduciéndose desde los cientos de nanómetros hasta las decimas de nanómetros cuando la solubilidad cambia del menor al mayor valor.
- La densidad relativa es más difícil de reducir cuando la solubilidad se incrementa.
- El contenido de celda abierta se incrementa con la solubilidad hasta alcanzar valores del 100%.
  - Para los dos polímeros con mayor viscosidad esto ocurre para solubilidades por encima del 38 %.
  - La estructura celular del material menos viscoso se interconecta de forma más gradual con el incremento en solubilidad. Así pues, para valores de la solubilidad en torno al 36 % el contenido de celda abierta es de un 20 %, valor que aumenta al 50 % para una solubilidad del 40% y que alcanza el 80 % cuando la solubilidad es del 44% en peso.

⇒ Los parámetros de espumado modifican las estructuras celulares de forma similar independientemente de la viscosidad de la matriz y de la solubilidad:

- Un incremento de la temperatura de espumado de 25 °C a 80 °C reduce la densidad relativa.
  - Para el grado de PMMA HV con un 31 % en peso de gas, este aumento implica una reducción en la densidad relativa de 0.50 a 0.30. Mientras que con un 45 % en peso de gas, se reduce de 0.55 a 0.38.
  - Para el grado PMMA LV con un 36 % en peso de gas decrece de 0.30 a 0.20, y con un 45 % de solubilidad de 0.45 a 0.35.
- Un aumento en la temperatura de espumado provoca un crecimiento en la densidad de nucleación, mientras que el tamaño de celda permanece constante.
  - Con un aumento de la temperatura de espumado entre 25 °C y 80 °C y una solubilidad del 31 % en peso de CO_2, el PMMA de mayor viscosidad ve incrementada la densidad de nucleación de $1.7{\cdot}10^{14}$ núcleos/cm^3 a $3.6{\cdot}10^{14}$ núcleos/cm^3. Mientras que para una solubilidad del 45 % en peso la densidad de nucleación crece de los $2.3{\cdot}10^{16}$ núcleos/cm^3 a los $3.5{\cdot}10^{16}$ núcleos/cm^3.
  - Para el grado de menor viscosidad, con una solubilidad del 36 % en peso la densidad de nucleación pasa de ser $1.8{\cdot}10^{13}$ núcleos/cm^3 a ser $3.3{\cdot}10^{13}$ núcleos/cm^3. Cuando la solubilidad se incrementa al 45 % este aumento es de $7.9{\cdot}10^{15}$ núcleos/cm^3 a $1.8{\cdot}10^{16}$ núcleos/cm^3.

⇒ Aunque las tendencias observadas son las mismas para los tres grados de PMMA, la viscosidad afecta de una forma muy importante a la estructura celular del PMMA nanocelular:

- Independientemente de la solubilidad, una viscosidad menor permite alcanzar menores densidades relativas, mientras que una viscosidad mayor resulta en tamaños de celda más pequeños y densidades de nucleación mayores.

⇒ Combinando el uso de altas solubilidades y distintas viscosidades **se han fabricado materiales nanocelulares con estructuras no documentadas hasta la fecha para nucleación homogénea:**

- El PMMA de menor viscosidad ha permitido la producción de un material nanocelular con **75 nm de tamaño de celda y una densidad de nucleación de 10^{15} núcleos/cm^3 valores combinados con una densidad relativa de 0.24** (**Figura VIII**).
- El PMMA de mayor viscosidad permite fabricar un material con **14 nm de tamaño de celda y $3.5{\cdot}10^{16}$ núcleos/cm^3, con densidades relativas de 0.4** (**Figura VIII**).

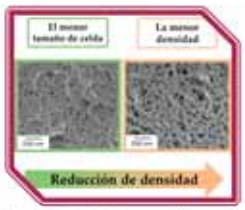

Figura VIII. Mejores polímeros nanocelulares homogeneos producidos.

⇒ Se han analizado los mecanismos de espumado llegando a las siguientes conclusiones:

- La reducción de densidad que se observa cuando se incrementa la temperatura de espumado es consecuencia del crecimiento de puntos de nucleación.

- Las estructuras de celda abierta frenan el crecimiento resultando en materiales con mayores densidades relativas.
- Las diferencias entre las estructuras celulares que se encuentran al usar distintas matrices polimétricas son atribuidas al control que tiene la viscosidad sobre el Volumen de Influencia (VI).
  - Una mayor viscosidad frena el crecimiento de IV prolongando el tiempo de nucleación y provocando en consecuencia densidades de nucleación superiores.
  - La viscosidad juega un papel muy importante en el proceso de crecimiento logrando mayores expansiones cuanto menor sea la viscosidad. Este efecto es más notorio para bajas solubilidades.

iv. Capítulo 7

En el capítulo 7 se analizaron distintas modificaciones del espumado por disolución de gas convencional.

Dos artículos científicos han sido incluidos en este capítulo presentando alternativas al proceso de producción original que afectan a las estructuras celulares de los materiales fabricados.

El primero de ellos (P5 [62]) detalla la producción de piezas de material nanocelular espumadas en una prensa de platos calientes en vez de en un baño térmico como es habitual. Se han realizado una serie de experimentos que han llevado a concluir lo siguiente:

⇒ **Es posible fabricar piezas planas de grandes dimensiones de PMMA nanocelular (100 x 100x 6 mm³) a través del espumado por disolución de gas mediante el espumado en una prensa de platos calientes** (**Figura IX**). Se han fabricado estructuras nanocelulares de PMMA con tamaños de celda por debajo de los 250 nm y densidades relativas menores de 0.3.

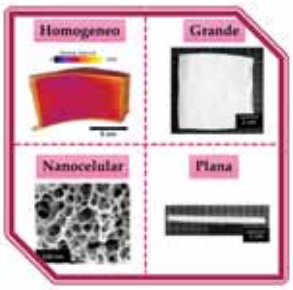

Figura IX. Muestras grandes y planas de PMMA nanocelular.

⇒ La estructura celular de las muestras fabricadas de este modo es homogénea y comparable a la de los materiales espumados en baño térmico (**Figura IX**). Las pequeñas diferencias encontradas son expuestas a continuación:

- Las muestras presentan un ligero decrecimiento de densidad de nucleación debido a la presión aplicada durante el espumado. Así pues, la densidad de nucleación obtenida tras el espumado en prensa varía entre los $1.5 \cdot 10^{14}$ núcleos/cm³ y los $2.8 \cdot 10^{14}$ núcleos/cm³ mientras que para el espumado en baño estos valores se encuentran entre los $1.8 \cdot 10^{14}$ núcleos/cm³ y los $3.6 \cdot 10^{14}$ núcleos/cm³.
- El tamaño de celda es ligeramente inferior al usar este espumado alternativo, con celdas entre los 240 nm y los 270 nm mientras que en el baño térmico los valores oscilan entre los 204 nm y los 261 nm.

⇒ Un incremento de la temperatura de espumado tiene el mismo efecto que se observa al espumar en baño térmico:
  - Una mayor densidad de nucleación. El valor crece desde los $1.5 \cdot 10^{14}$ núcleos/cm^3 al espumar a 40 ˚C hasta los $2.8 \cdot 10^{14}$ núcleos/cm^3 cuando se espuma a 80 ˚C.
  - Una reducción de densidad causada por el aumento de puntos de nucleación desde 0.5 hasta 0.31.
  - Una reducción de la fracción de masa en las aristas, desde 0.66 hasta 0.42.
  - Un incremento del contenido de celda abierta desde un 6 % al espumar a 40 ˚C hasta un 77 % al espumar a 80 ˚C.

En el segundo artículo científico (P6 [63]), se presenta otra modificación del proceso. En este caso se modifica la despresurización del proceso de espumado en una etapa. Así pues, se presenta un proceso en el cual la despresurización ocurre en dos pasos. Este trabajo permite obtener los siguientes resultados:

⇒ **Es posible eliminar los defectos de tamaño micrométrico que aparecen al producir PMMA nanocelular con algunas matrices y ciertas condiciones de proceso, a través de una despresurización parcial en dos etapas.** **(Figura X)**

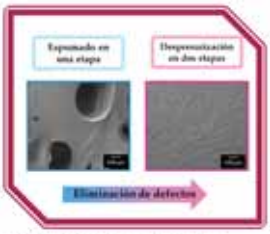

Figura X. Eliminación de defectos microcelulares.

⇒ La estructura nanocelular que se obtiene a través de este proceso es comparable con la que se obtiene al espumar a través de un espumado es una etapa convencional, aunque:
  - El tamaño de celda es superior y la densidad de nucleación inferior:
    - Para los grados HV y MV el tamaño de celda pasa de los 200 nm a estar por encima de los 300 nm cuando se espuma a 50 ˚C. Mientras que la densidad de nucleación disminuye de $1 \cdot 10^{14}$ núcleos/cm^3 hasta $3 \cdot 10^{13}$ núcleos/cm^3.
    - Para el grado de PMMA LV, el tamaño de celda se incrementa desde los 500 nm hasta los 800 nm cuando se espuma a 50 ˚C, mientras que la densidad de nucleación decrece desde los $1 \cdot 10^{13}$ núcleos/cm^3 a los $3 \cdot 10^{12}$ núcleos/cm^3.

⇒ Al modificar los parámetros de producción en el nuevo proceso se obtiene lo que sigue:
  - El resultado de utilizar una presión residual mayor depende de la viscosidad de la matriz utilizada, así pues:
    - Para el PMMA con una viscosidad mayor, la densidad de nucleación se incrementa.
    - Para bajas viscosidades, la densidad de nucleación disminuye.

⇒ El análisis de los mecanismos de espumado para este proceso en particular ha permitido entender mejor el espumado de polímeros nanocelulares:
  - Para evitar la formación de defectos microcelulares es beneficioso que la presión del gas durante el crecimiento del material sea baja.

- Cuando se lleva a cabo el proceso de despresurización en dos etapas, existe una fuerte competición entre los parámetros que gobiernan la nucleación y el espumado. Compitiendo entre sí, la difusividad, la velocidad de despresurización y la viscosidad.
  - Mientras que altas velocidades de despresurización y altas viscosidades son beneficiosas para la densidad de nucleación una alta difusividad perjudica este valor. El resultado final dependerá de esta competición.

Tras los estudios llevados a cabo en los capítulos 4, 5, 6 y 7 se puede dar por satisfecha la relación que se muestra en la **Figura XI**. El proceso de producción para materiales nanocelulares ha sido estudiado a fondo. Se han modificado los parámetros de proceso, la matriz utilizada, así como el proceso en sí mismo, a la vez que se han analizado meticulosamente las estructuras celulares obtenidas.

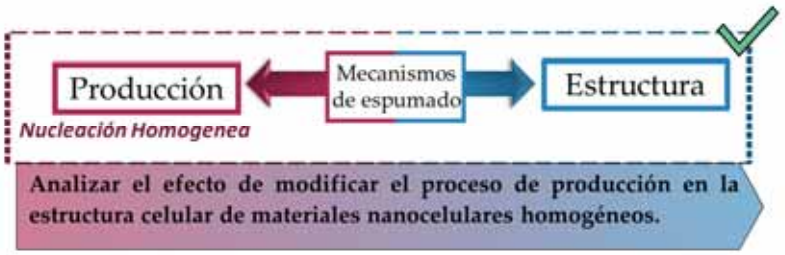

Figura XI. Relaciones completadas en los Capítulos 4, 5, 6 y 7.

Se han estudiado por otra parte los mecanismos de espumado que actúan durante el proceso de producción de PMMA nanocelular a través de teorías de nucleación.

El primer objetivo propuesto en esta tesis ha sido satisfecho.

v. Capítulo 8

Una vez que el objetivo uno se ha cumplido, en el capítulo 8 se ha tratado de satisfacer el segundo de los objetivos propuestos en la sección III.

Así pues, se han descrito las propiedades ópticas, mecánicas y térmicas de los materiales nanocelulares producidos gracias al conocimiento adquirido en los capítulos previos.

Las propiedades ópticas del PMMA semitransparente se presentan a través de un artículo científico (P7 [64]) que ha llevado a obtener los siguientes resultados:

⇒ La transmitancia del PMMA nanocelular experimentalmente medida depende de:

- El tamaño de celda; la transmitancia presenta valores cercanos a cero para tamaños de celda en torno a los 225 nm mientras que alcanza 0.94 para el menor tamaño de celda (14 nm) y una densidad relativa de 0.45 con láminas de 0.05 mm de espesor.
- La longitud de onda utilizada elevada a la potencia menos cuatro, lo cual indica la presencia de dispersión Rayleigh en las espumas nanocelulares.

⇒ **Se ha desarrollado por primera vez un modelo teórico que permite visualizar los mecanismos físicos que ocurren en la interacción luz-material** (**Figura XII**):

- Cuando el tamaño de celda es inferior a un décimo de la longitud de onda utilizada, la luz viaja preferiblemente a través de la fase gaseosa.
- Los valores y tendencias medidas experimentalmente son reproducidas correctamente con el modelo desarrollado.
- Es posible calcular la transmitancia para cualquier material, tamaño de celda, espesor, densidad y longitud de onda utilizada.

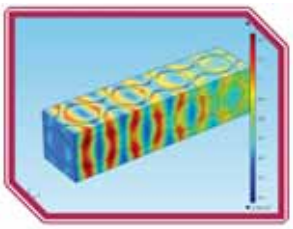

Figura XII. Primer modelo teórico para la transmisión de luz en PMMA.

Con respecto a las propiedades mecánicas, se han llevado a cabo diferentes experimentos para PMMA nanocelular con distintas estructuras celulares que se presentan en el segundo artículo científico de este capítulo (P8 [65]). Así pues, se han estudiado las propiedades mecánicas de materiales celulares con densidades similares y tamaños de celda que van desde la micro hasta la nano escala (de 3 micras a 30 nm). Las principales conclusiones son las que siguen:

⇒ El módulo de Young relativo y el límite de fluencia relativo son independientes del tamaño de celda en el rango estudiado y para densidades relativas de 0.4.

⇒ La tenacidad a la fractura prácticamente se duplica cuando el tamaño de celda decrece de la micro a la nano escala.

Por último, se han determinado las propiedades térmicas de materiales nanocelulares con celdas desde las 20 micras a los 25 nm, concluyendo que:

⇒ Las muestras con tamaños de celda en el tango nanométrico presentan efecto Knudsen siendo su conductividad térmica menor que la que muestras los materiales microcelulares.

⇒ Se ha observado una reducción adicional en la conductividad térmica atribuida al confinamiento de la fase sólida.

Figura XIII. Relaciones establecidas en esta tesis.

En conclusión, se han determinado experimentalmente las propiedades de los materiales nanocelulares, demostrando que estas son distintas a las que presentan los polímeros microcelulares.

Estos resultados permiten establecer la relación que existe entre las propiedades de los materiales nanocelulares y su estructura celular. Esto junto con la correlación previamente establecida entre la estructura celular y el proceso de producción lleva a la cumplimentación del segundo objetivo de esta tesis (**Figura XIII**).

IX. Mecanismos de espumado

Para comprender las conclusiones previas, **se han analizado los mecanismos de espumado que gobiernan la nucleación y el crecimiento a través de una teoría de nucleación**, concluyendo lo que sigue:

⇒ Para entender los mecanismos de espumado en materiales nanocelulares es necesario mejorar la teoría de nucleación homogénea (CNT):
- En esta tesis se ha introducido el concepto de volumen de influencia, para poder considerar el impacto de parámetros como la difusividad, el ratio de despresurización o la viscosidad.
- Introducir el concepto de volumen de influencia implica asumir que la nucleación no ocurre de forma instantánea:
  - Un crecimiento más lento del volumen de influencia resulta en tiempos de nucleación superiores y por tanto densidades de nucleación mayores.

⇒ Para estimar correctamente las características de la estructura celular se deben considerar paralelamente la teoría de nucleación clásica y el cambio en el volumen de influencia:
- La densidad de nucleación se maximiza y el tamaño de celda se minimiza a través de:
  - Un incremento de solubilidad ya sea dado por una alta presión o una baja temperatura de saturación.
  - Un crecimiento lento del volumen de influencia que se puede conseguir a través de:
    - Altos ratios de despresurización.
    - Altas viscosidades.
    - Difusividades de desorción lentas.
- La densidad relativa se minimiza a través de:
  - Altas temperaturas de espumado.
  - Bajas viscosidades.

⇒ Se puede conseguir el equilibrio perfecto combinando todo el conocimiento previo, siendo así posible fabricar materiales nanocelulares a la carta con las características deseadas.

Tabla VII. Esquema de la influencia de los parámetros de producción del espumado por disolución de gas en dos etapas y de la matriz usada en la producción de materiales nanocelulares de baja densidad. El signo – indica que no hay una influencia directa.

	Saturación		Despresurización		Espumado		Matriz	
	P_{sat}	T_{sat}	v_d	t_d	T_f	t_f	η	T_g
Máx. N_0	↑	↓	↑	↓	↑*	↑*	↑	↑
Min. ϕ	↑	↓	↑	↓	-	↑*	↑	↑
Min. ρ_r	-	-	-	-	↑*	↑*	↓	↓

***** Estos parámetros deben de maximizarse hasta cierto límite donde ocurre la degeneración de la estructura celular.

Lo concluido con anterioridad se puede resumir en la **Tabla VII.** En ella se muestran los requerimientos para fabricar un material nanocelular a partir de un polímero homogéneo por la vía del espumado por disolución de gas. Se ha considerado que se desea obtener un material con la máxima densidad de nucleación, el menor tamaño de celda y la menor densidad posible.

Aquellos parámetros con una mayor influencia en comparación con los demás se han marcado con flechas en negrita de un mayor tamaño. En resumen, el material nanocelular óptimo se puede fabricar por medio de la maximización de la presión de saturación, la velocidad de despresurización, la temperatura y el tiempo de espumado, y una minimización de la temperatura de saturación el tiempo de desorción y el uso de un polímero con una viscosidad y una temperatura de transición vítrea balanceadas que permitan una buena expansión sin comprometer la densidad de nucleación y el tamaño de celda.

X. Comparación con los datos de la literatura

Los materiales fabricados en esta tesis han sido comparados con los materiales nanocelulares de la literatura fabricados siguiendo nucleación homogénea o heterogénea. El tamaño de celda frente a la densidad relativa de todos ellos está representado en la **Figura XIV.**

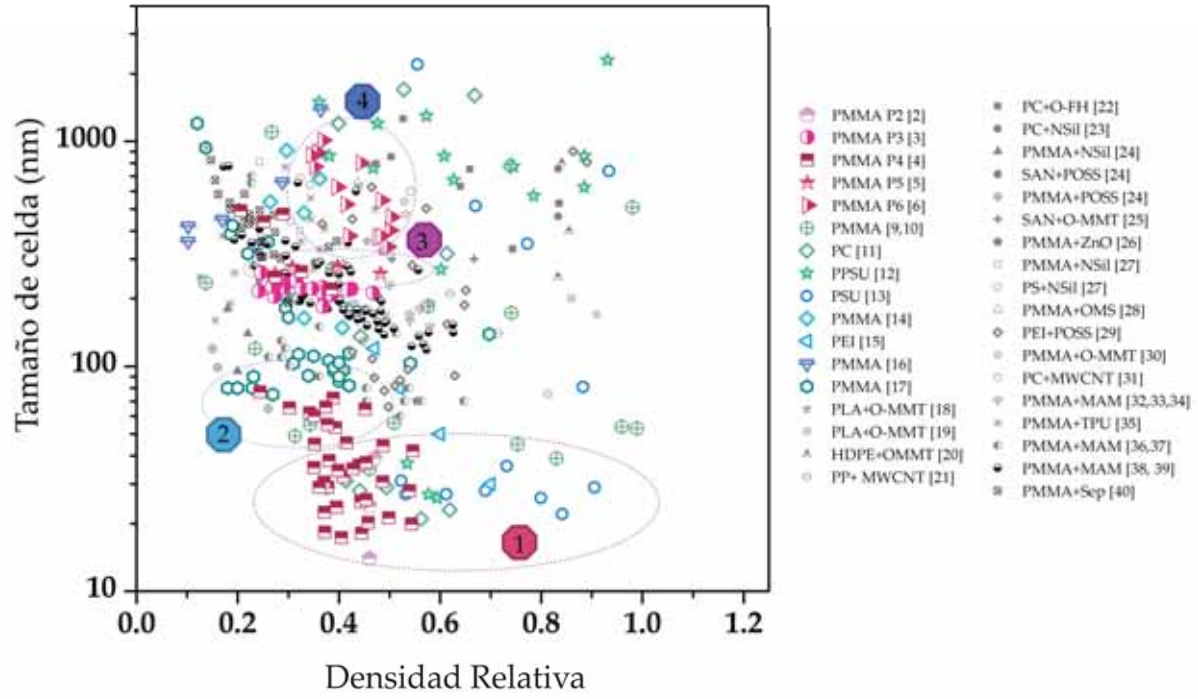

Figura XIV. Tamaño de celda en función de la densidad relativa tanto para los materiales nanocelulares fabricados en esta tesis como para los documentados previamente en la literatura producidos usando tanto nucleación homogénea como heterogénea.

En el mapa puede verse como los materiales nanocelulares producidos en esta tesis (representados por los puntos rosáceos) comparten características con los materiales publicados previamente en la literatura. Es por tanto que en el mapa de la **Figura XIV**, la mayoría de los puntos correspondientes a los materiales fabricados en esta tesis, se encuentran en regiones que habían sido previamente cubiertas por otros autores. Sin embargo, alguno de los materiales fabricados presenta una combinación de tamaños de celda y densidades relativas no documentadas hasta la fecha. Si se centra la atención en la zona de tamaños de celda inferiores **(1)**, se puede ver, que los materiales fabricados en los artículos científicos P2 y P4 muestran tamaños de celda por debajo de los 20 nm, por primera vez para polímeros nanocelulares [2,4]. En ambos trabajos, estos bajos tamaños de celda se han alcanzado gracias al uso combinado de bajas temperaturas de saturación y altas presiones. En la literatura, los materiales presentados por Guo et. al [11] son los que se acercan más a los datos aportados en esta tesis. Así pues, mediante el uso de policarbonato y usando nucleación homogénea presenta unas estructuras nanocelulares con un tamaño de celda de 21 nm y una densidad relativa de 0.56. Usando PSU y PPSU como matrices poliméricas Guo et al. reportaron también materiales con 22 nm y 26 nm de tamaño de celda respectivamente y densidades relativas de 0.84 y 0.59 [12,13].

Además de superar la barrera inferior de tamaño de celda, el PMMA nanocelular de esta tesis presenta densidades relativas por debajo de 0.4 por primera vez para celdas menores de 30 nm como puede verse en la región 1 de la **Figura XIV.**

Si se presta atención a la zona **2** del mapa, se puede apreciar que los materiales nanocelulares del artículo P4 con un tamaño de celda de 75 nm y una densidad relativa de 0.24, pueden competir con aquellos materiales de la literatura que muestran el menor tamaño de celda combinado con la menor densidad relativa. Para empezar, se van a considerar los fabricados a través de nucleación homogénea, Costeux et al. documentan un PMMA nanocelular producido a partir de un copolímero de PMMA-co- EA, con una densidad de 0.18 y un tamaño de celda de 80 nm. Sin embargo, al reducir el tamaño de celda a 75 nm la densidad aumenta hasta 0.27 [17]. Es por tanto que se puede considerar que el PMMA nanocelular producido en esta tesis tiene el tamaño de celda más bajo combinado con la menor densidad jamás conseguido para materiales nanocelulares producidos a partir de nucleación homogénea. Por otro lado, cuando al trabajar con nucleación heterogénea (PMMA con nanopartículas de POSS) Costeux et. al presentan un tamaño de celda de 65 nm con una densidad relativa de 0.26, datos que mejoran a los presentados en esta tesis [24].

Además de las regiones ya comentadas, en esta tesis se ha producido PMMA nanocelular con estructuras comparables a las de materiales fabricados previamente que se encuentran en la literatura, pero con mejores características (regiones **3** y **4**). Así pues, en el artículo P5 se presentaron por primera vez, muestras planas de grandes dimensiones. Estas muestras poseen estructuras celulares (tamaños de celda en torno a los 250 nm y densidades relativas entre 0.5 y 0.3) comparables con las de otros polímeros nanocelulares de la literatura. Por ejemplo, estos materiales son comparables con los producidos por Bernardo et. al [39,40] mediante el uso de nucleación heterogénea (usando PMMA como matriz y MAM como agente nucleante) con tamaños de celda entre 200 nm y 300 nm, densidades relativas entre 0.23 y 0.47 y dimensiones de 20 x 10 x 4 mm^3. Por otro lado, Pinto et. al, reportaron sistemas de PMMA/MAM con unos 250 nm de tamaño de celda densidades relativas en torno a 0.5 y unas dimensiones de tan solo 50 x 15 x 3 mm^3 [33].

Finalmente, la región **4** agrupa PMMA nanocelular libre de defectos (producido a partir de matrices con las que previamente se había demostrado la aparición de los mismos (P4)), con tamaños de celda entre los 300 nm y la micra y densidades relativas desde 0.5 hasta 0.34. Características comparables a las de otros polímeros nanocelulares de la literatura, producidos a través de nucleación homogénea como el PMMA de Costeux et. al [14] o a través de nucleación heterogénea como el PMMA con TPU presentado por Wang et. al [35].

XI. Referencias

[1] http://www.marketsandmarkets.com/Market-Reports/foams-market-1011.html 06/03/2019.

[2] Gibson, L. J.; Ashby, M. F. *Cellular solids: Structure and Properties*; 2nd ed.; Cambridge: Cambridge University Press.: United States, **1997**.

[3] Mills, N. J. Handbook of polymeric foams and foam technology. *Polymer* **1993**, *34*, 2237.

[4] Eaves, D. *Handbook of Polymer Foams*; Rapra Technology Limited: Shawbury, Shrewsbury, Shropshire, UK, **2004**.

[5] Rodriguez-Perez, M. A. Crosslinked polyolefin foams: Production, structure, properties, and applications. *Advances in Polymer Science* **2005**, *184*, 97–126.

[6] Saiz-Arroyo, C.; Rodriguez-Perez, M. A.; Tirado, J.; López-Gil, A.; de Saja, J. A. Structure-property relationships of medium-density polypropylene foams. *Polymer International* **2013**, *62*, 1324–1333.

[7] Prabhu, S.; Raja, V. K. B.; Nikhil, R. Applications of Cellular Materials – An Overview. *Applied Mechanics and Materials* **2015**, *766–767*, 511–517.

[8] Martini-Vvedensky, J. J. E.; Suh, N. N. P.; Waldman, F. F. a. Microcellular closed cell foams and their method of manufacture. *US Patent 4,473,665* **1984**.

[9] Kumar, V.; Weller, J. E. A Process to Produce Microcellular PVC. *International Polymer Processing* **1993**, *1*, 73–80.

[10] Kumar, V.; Suh, N. P. A process for making microcellular thermoplastic parts. *Polymer Engineering and Science* **1990**, *30*, 1323–1329.

[11] Arora, K. A.; Lesser, A. J.; McCarthy, T. J. Preparation and Characterization of Microcellular Polystyrene Foams Processed in Supercritical Carbon Dioxide. *Macromolecules* **1998**, *31*, 4614–4620.

[12] Kumar, V.; Weller, J. Production of Microcellular Polycarbonate Using Carbon Dioxide for Bubble Nucleation. *Journal of Engineering for Industry* **1994**, *116*, 413–420.

[13] Reglero Ruiz, J. A.; Viot, P.; Dumon, M. Microcellular foaming of polymethylmethacrylate in a batch supercritical CO 2 process: Effect of microstructure on compression behavior. *Journal of Applied Polymer Science* **2010**, *118*, 320–331.

[14] Kumar, V. Microcellular Polymers: Novel materials for the 21st century. *Progress in Rubber and Plastics Technology* **1993**, *9*, 54–70.

[15] Shimbo, M.; Higashitani, I.; Miyano, Y. Mechanism of strength improvement of foamed plastics having fine cell. *Journal of Cellular Plastics* **2007**, *43*, 157–167.

[16] Kumar, V.; VanderWel, M.; Weller, J.; Seeler, K. a. Experimental Characterization of the Tensile Behavior of Microcellular Polycarbonate Foams. *Journal of Engineering Materials and Technology* **1994**, *116*, 439.

[17] Nadella, K.; Kumar, V. Tensile and flexural properties of solid-state microcellular ABS panels. *Experimental Analysis of Nano and Engineering* **2007**, *22*, 765–766.

[18] Sun, H.; Sur, G. S.; Mark, J. E. Microcellular foams from polyethersulfone and polyphenylsulfone: Preparation and mechanical properties. *European Polymer Journal* **2002**, *38*, 2373–2381.

[19] Costeux, S. CO 2 -blown nanocellular foams. *Journal of Applied Polymer Science* **2014**, *131*, n/a-n/a.

[20] Notario, B.; Pinto, J.; Rodriguez-Perez, M. A. Nanoporous polymeric materials: A new class of materials with enhanced properties. *Progress in Materials Science* **2016**, *78–79*, 93–139.

[21] Kumaki, J. Observation of polymer chain structures in two-dimensional films by atomic force microscopy. *Polymer Journal* **2016**, *48*, 3–14.

[22] Notario, B.; Ballesteros, A.; Pinto, J.; Rodriguez-Perez, M. A. Nanoporous PMMA : A novel

system with different acoustic properties. *Materials Letters* **2016**, *168*, 76–79.

[23] Notario, B.; Pinto, J.; Verdejo, R.; Rodríguez-Pérez, M. A. Dielectric behavior of porous PMMA: From the micrometer to the nanometer scale. *Polymer* **2016**, *107*, 302–305.

[24] Miller, D.; Kumar, V. Microcellular and nanocellular solid-state polyetherimide (PEI) foams using sub-critical carbon dioxide II. Tensile and impact properties. *Polymer* **2011**, *52*, 2910–2919.

[25] Merlet, S.; Marestin, C.; Schiets, F.; Romeyer, O.; Mercier, R. Preparation and characterization of nanocellular poly(phenylquinoxaline) foams. A new approach to nanoporous high-performance polymers. *Macromolecules* **2007**, *40*, 2070–2078.

[26] Notario, B.; Pinto, J.; Solorzano, E.; De Saja, J. A.; Dumon, M.; Rodriguez-Perez, M. A. Experimental validation of the Knudsen effect in nanocellular polymeric foams. *Polymer (United Kingdom)* **2015**, *56*, 57–67.

[27] Forest, C.; Chaumont, P.; Cassagnau, P.; Swoboda, B.; Sonntag, P. Polymer nano-foams for insulating applications prepared from CO2 foaming. *Progress in Polymer Science* **2015**, *41*, 122–145.

[28] Li, L.; Schulte, L.; Clausen, L. D.; Hansen, K. M.; Jonsson, G. E.; Ndoni, S. Gyroid nanoporous membranes with tunable permeability. *ACS Nano* **2011**, *5*, 7754–7766.

[29] Pinto, J.; Dumon, M.; Rodriguez-Perez, M. A.; Garcia, R.; Dietz, C. Block Copolymers Self-Assembly Allows Obtaining Tunable Micro or Nanoporous Membranes or Depth Filters Based on PMMA; Fabrication Method and Nanostructures. *The Journal of Physical Chemistry C* **2014**, *118*, 4656–4663.

[30] Lu, G. Q.; Zhao, X. S. Nanoporous Materials — An Overview. In *Nanoporous materials: Science and engineering*; Imperial Collegue Press: London, **2004**.

[31] Pérez-Tamarit, S.; Notario, B.; Solórzano, E.; Rodriguez-Perez, M. A. Light transmission in nanocellular polymers: Are semi-transparent cellular polymers possible? *Materials Letters* **2018**, *210*, 39–41.

[32] Martín-de León, J.; Bernardo, V.; Rodríguez-Pérez, M. Á. Key Production Parameters to Obtain Transparent Nanocellular PMMA. *Macromolecular Materials and Engineering* **2017**, *3*, 1700343.

[33] CellMat http://cellmat.es/.

[34] Rodríguez-Pérez, M. A. Propiedades térmicas y mecánicas en espumas de poliolefinas. *Ph.D. Thesis, University of Valladolid* **1998**.

[35] Arcos y Rábago, L. O. Propiedades térmicas y mecánicas de espumas de poliolefinas fabricadas en un proceso de moldeo por compresión, **2002**.

[36] Solorzano, E. Espumas de Aluminio: Proceso de Espumado, Estructura Celular y Propiedades. *Ph.D. Thesis, University of Valladolid* **2008**.

[37] Lazaro Nebreda, J. Optimización de la estructura celular en espumas de aluminio. *Ph.D. Thesis, University of Valladolid* **2014**, 326.

[38] Ruiz-Reglero, A. J. Fabricación y caracterización de espumas de aluminio: aplicaciones en el sector aeronáutico. *Ph.D. Thesis, University of Valladolid* **2007**, 429.

[39] Reglero-ruiz, J. A.; Saiz-Arroyo, C.; Dumon, M.; Rodríguez-Pérez, M. Á.; Gonzalez, L. Production, cellular structure and thermal conductivity of microcellular (methyl methacrylate)–(butyl acrylate)–(methyl methacrylate) triblock copolymers. *Polymer International* **2010**, *60*, 146–152.

[40] Lobos Martín, J. Improving the stiffness and strength of porous materials by enhancement of

the matrix microstructure and cellular morphology. *Ph.D. Thesis, University of Valladolid*.

[41] Reglero Ruiz, J. A.; Dumon, M.; Pinto, J.; Rodriguez-Pérez, M. A. Low-density nanocellular foams produced by high-pressure carbon dioxide. *Macromolecular Materials and Engineering* **2011**, *296*, 752–759.

[42] Bernardo, V.; Martín-de León, J.; Laguna-Gutiérrez, E.; Rodríguez-Pérez, M. Á. PMMA-sepiolite nanocomposites as new promising materials for the production of nanocellular polymers. *European Polymer Journal* **2017**, *96*, 10–26.

[43] Saiz-Arroyo, C.; Rodriguez-Pérez, M. A.; de Saja, J. A. Improving the Structure and Physical Properties of LDPE Foams using Silica Nanoparticles as an Additive. *Cellular polymers* **2011**, *30*.

[44] López Gil, A. *Development of Environmentally Friendly Cellular Polymers for Packaging and Structural Applications . Study of the Relationship Cellular Structure-Mechanical Properties*; **2016**.

[45] Salmazo, L. O. Cinéticas de espumación y control de la estructura celular en materiales basados en caucho natural y poliolefinas. *Ph.D. Thesis, University of Valladolid* **2015**.

[46] Acuña, P.; Santiago-Calvo, M.; Villafañe, F.; Rodriguez-Pérez, M. A.; Rosas, J.; Wang, D. Impact of expandable graphite on flame retardancy and mechanical properties of rigid polyurethane foam. *polymer composites* **2018**.

[47] Santiago-Calvo, M.; Blasco, V.; Ruiz, C.; Paris, R.; Villafañe, F.; Rodriguez-Pérez, M. A. Improvement of thermal and mechanical properties by control of formulations in rigid polyurethane foams from polyols functionalized with graphene oxide. *Journal of Applied Polymer Science* **2019**, *136*.

[48] Collado, N. Fabricación y Caracterización de las Propiedades Físicas de Polímeros Nanocelulares : Transición de la Escala Micro a la Nano. *Ph.D. Thesis, University of Valladolid*.

[49] Pinto Sanz, J. Fabricación y Caracterización de Materiales Poliméricos Submicrocelulares a partir de Polímeros Nanoestructurados. *Ph.D. Thesis, University of Valladolid* **2014**.

[50] Saiz-Arroyo, C. Fabricación de materiales celulares mejorados basados en poliolefinas. Relación procesado-composición-estructura-propiedades. *Ph.D. Thesis, University of Valladolid* **2012**.

[51] Saiz-Arroyo, C.; De Saja, J. A.; Velasco, J. I.; Rodríguez-Pérez, M. Á. Moulded polypropylene foams produced using chemical or physical blowing agents: Structure-properties relationship. *Journal of Materials Science* **2012**, *47*, 5680–5692.

[52] Pardo, S. X-Ray Imaging Applied to the Characterization of Polymer Foams' Cellular Structure and its Evolution. *Ph.D. Thesis, University of Valladolid* **2014**.

[53] Perez-Tamarit, S.; Solórzano, E.; Pardo-Alonso, S.; Mokso, R.; Rodriguez-Pérez, M. A. Pore Nucleation and Growth in Cellular Polymers Analysed By Time Resolved Synchrotron X-Ray M - Ct. *International conference on tomography of materials and structures* **2017**, 3–4.

[54] Rodriguez-Pérez, M. A.; de Saja, J. A.; Tirado, J.; lopez gil, A. Procedimiento de Fabricación de Materiales Celulares de Matriz Termoplástica **2013**.

[55] Rodriguez-Pérez, M. A.; de Saja, J. A.; Escudero, J.; Vazquez, J. . Sistema y Procedimiento de Moldeo de Piezas con Moldes Autoportantes **2012**.

[56] http://www.cellmattechnologies.com/ http://www.cellmattechnologies.com/.

[57] Notario, B.; Pinto, J.; Rodriguez-Perez, M. a. Towards a new generation of polymeric foams: PMMA nanocellular foams with enhanced physical properties. *Polymer* **2015**, *63*, 116–126.

[58] Martín-de León, J.; Cimavilla-Román, P.; Bernardo, V.; Solórzano, E.; Rodríguez-Pérez, M. A. Cold neutron transmission for in-situ analysis of gas diffusion in polymers. *Paper sent* **2019**.

[59] Martín-de León, J.; Bernardo, V.; Rodríguez-Pérez, M. Á. Key Production Parameters to Obtain Transparent Nanocellular PMMA. *Macromolecular Materials and Engineering* **2017**, *302*.

[60] Martín-de León, J.; Bernardo, V.; Rodríguez-Pérez, M. Low Density Nanocellular Polymers Based on PMMA Produced by Gas Dissolution Foaming: Fabrication and Cellular Structure Characterization. *Polymers* **2016**, *8*, 265.

[61] León, J. M.; Bernardo, V.; Laguna-gutiérrez, E.; Rodríguez-pérez, M. Á. Influence of the rheological behaviour of PMMA on the cellular structure of nanocellular materials. *Paper sent* 1–16.

[62] Martín-de León, J.; Bernardo, V.; Cimavilla-Román, P.; Pérez-Tamarit, S.; Rodríguez-Pérez, M. Á. Overcoming the Challenge of Producing Large and Flat Nanocellular Polymers: A Study with PMMA. *Advanced Engineering Materials* **2019**, 1–8.

[63] Martín-de León, J.; Bernardo, V.; Rodríguez-pérez, M. Á. Two stage depressurization in one step foaming process: the production of nanocellular materials free of defects. *Paper sent* **2019**.

[64] Martín-de León, J.; Pura, J. L.; Bernardo, V.; Rodríguez-Pérez, M. Á. Transparent nanocellular PMMA: Characterization and modeling of the optical properties. *Polymer* **2019**, *170*, 16–23.

[65] Martín-de León, J.; Van Loock, F.; Bernardo, V.; Fleck, N. A.; Rodríguez-Pérez, M. A. The influence of cell size on the mechanical properties of nanocellular PMMA.

Chapter 1

Introduction

"Algunas palabras eran así. Tenían añadidas vidas enteras. Fantasmas, vidas, éxtasis y penas."

Paulina Simons

INDEX

1.1. Introduction

The history of humanity has been divided into multiple periods; some of them owe their name to different materials due to the vital importance they had in human evolution. Thus, it is common to hear about the stone age, the copper age, the bronze age, or the iron age. Multiple materials have been discovered and developed since the industrial revolution, but if a materials' name should be given to the last decades, it must be the plastic age.

According to the bibliography, 300 million tons of plastic are produced per year. 10 wt.% of this amount is used to produce polymeric cellular materials. It is estimated that the cellular polymer market will reach $126.08 billion by 2022, presenting an annual growth rate of 5.86%. [1]

Before going any further, cellular materials should be introduced. They are defined as two-phase materials, in which a gaseous phase is dispersed in a continuous solid matrix [2]. Hundreds of examples of these structures can be found either in nature or in industrial products, as is shown in **Figure 1.1**. Almost wherever we are looking at, a cellular material can be found; inside a cork, a bone, a root, a butterfly wing, or a simple toy.

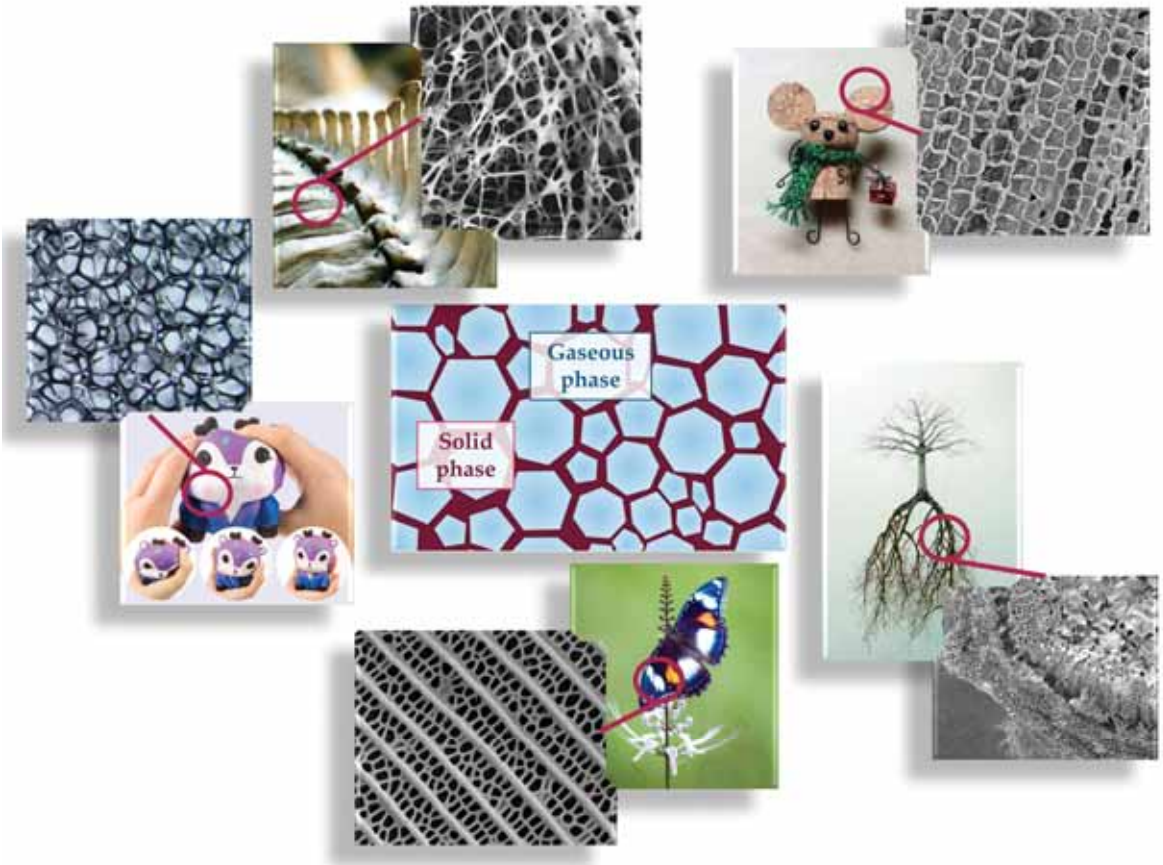

Figure 1.1. Some examples of cellular structures. Natural ones: inside a human bone, a cork, a tree root, and a butterfly wing. Industrially produced: inside a toy.

Particularly, cellular polymers are those in which the solid matrix is a polymer and on which attention will be focused from now on [3,4].

The reason for the fast-spreading and growing of these materials in the last decades rely on their exciting properties. If something characterizes cellular materials is its low weight, that leads to energy and cost savings. Moreover, among its properties, it can be highlighted their high stiffness and strength to weight ratio, crash energy absorption, low thermal conductivity, cushioning performance, and buoyancy. Additionally, by selecting specific polymeric matrixes and cellular structures, other attractive properties such as magnetic permeability, no water absorption, chemical resistance, acoustic absorption, and a high specific surface can be achieved. This enormous range of features along with the low weight makes cellular polymers suitable for applications which cannot easily be filled by the former solid [5–7].

All this explains the widespread of cellular polymers in all kind of industrial sectors. The building sector takes advantage of cellular materials both for structural applications and thermal insulation ones. They can also be found in the automotive industry and the aeronautical one, as well as in packaging applications, heat exchangers, marine flotation, membranes, filters, decoration, and cushioning, among others.

In order to understand how cellular polymers have come to be so present in all kind of sectors, it is necessary to look back in history to a critical year for the development of cellular materials; 1980. In this year Jane E. Martini-Vvedensky et al. from the Massachusetts Institute of Technology (MIT) conceived a method to produce microcellular plastics with cell diameters on the order of 10 μm [8–10]. This was a breakthrough technology over conventional foaming processes which produced cellular materials with cell size typically higher than 100 μm. Up to that moment, the production of foams implied a substantial reduction in the mechanical properties of the material. Therefore, the primary objective of Martini-Vvedensky et al. was the production of polymeric parts with a reduced amount of plastic but with mechanical properties similar to those of the former polymer [10].

This was only the prelude to all the advance after this discovery. Microcellular materials were produced since then by using different polymers such as polystyrene (PS) [11], polycarbonate (PC) [12] or polymethylmethacrylate (PMMA) [13], among others. Moreover, it was widely proved that they significantly improve the mechanical properties of conventional cellular polymers. Plus that, in comparison with solid plastics, some of the microcellular polymers developed showed higher impact strength, fatigue life, thermal stability, Charpy impact strength, toughness, and lower thermal conductivity [14–18].

Thanks to all these properties and the advances in production methods, cellular polymers were introduced in sectors where it was not possible to use them before. Nevertheless, human evolution does not stop, and new applications demand products with increasingly better properties. Microcellular polymers discovery suggested that a further reduction in the cell size could be a very promising path for an additional improvement of properties.

That is how nanocellular polymers were born around fifteen years ago. Nanocellular polymers are those presenting cells in the nanometric scale and with a density of cells per

cubic centimeter at least ten thousand times larger than the one shown by microcellular polymers [19,20]. That means, in general terms, that the cell sizes of nanocellular polymers can be defined to be lower than 300 nm along with cell densities higher than 10^{13} cells/cm^3 (**Figure 1.2**). This general definition presents some subtleties that are explained in Chapter 2, section 2.3.

The change from macrocellular to microcellular polymers (**Figure 1.2**) implied a significant change in the properties of these materials and therefore opens the possibility of using them in new applications. The appearance of nanocellular polymers has been perceived as the next step for improvement in cellular materials world. For this reason, they have attracted the attention of leading multinationals in the polymer's world such as SABIC, BASF, or Dow Chemical, and also of research centres of recognized prestige such as the University of Washington (Prof. Kumar), the University of Osaka (Prof. Oshima), the University of Toronto (Prof. Chul Park), the University of Shandong (Prof. Guilong Wang) or the CellMat Laboratory in the University of Valladolid (Prof. Rodríguez-Pérez).

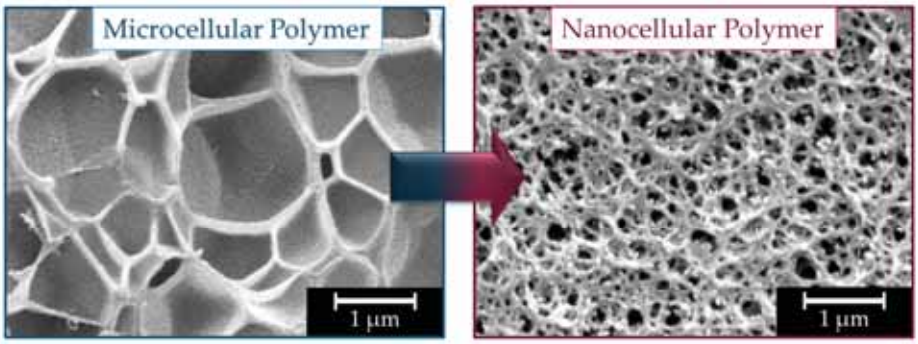

Figure 1.2. Examples of cellular structures of a microcellular polymer (left) and a nanocellular polymer (right).

Although its discovery is quite recent, it has already been shown that they present promising properties. In fact, it has been proved that their different cellular structure grants unique qualities to nanocellular polymers. To begin with, the solid phase is distributed in such thin cell walls (around 25 nm to 40 nm) that the polymer chains are confined due to the chain length is usually higher than 100 nm [21]. This effect results in different mechanical, acoustic, and dielectric properties for those cellular materials in comparison with microcellular ones [22–25]. In addition to the solid phase, the gaseous phase is also confined inside the nanocells, being this fact the reason for the reduced thermal conductivity of nanocellular polymers. When cells present a size of the order of magnitude or smaller than the mean free path of the gas molecules (around 70 nm for air, at atmospheric pressure and room temperature) the heat conduction through the gaseous phase is reduced because it is more likely that the molecules interact with the cell walls than between them. This effect is known as Knudsen effect and turns these materials into promising materials to build super-insulating structures [26,27].

Additionally, it is believed that the confinement of both phases, solid and gaseous one, could result in an enhancement of these materials in comparison with current

materials for applications such as gas storage, transport phenomena or radiation-matter interaction [20].

Another important characteristic of nanocellular polymers is its high specific area (above tens of m^2/g for cells ranging the nanometers in comparison with values smaller than the unity for microcells). This opens the possibility of using these materials as filters or membranes for micro and ultrafiltration, and also in sensors or catalysis applications [28–30].

The change of scale in the size of the cells is also the cause of amazing features that have been recently proved; when the cell size is small enough in comparison with the light wavelength (lower than 50 nm), nanocellular polymers preserve, up to some extent, the transparent character of the solid precursor [31,32].

This outstanding compendium of properties, low weight, reduced thermal conductivity, high mechanical responses, high surface area, or transparency, could open the possibility of using these materials in many applications. For example, as super-insulators for aeronautical use where high insulation, high mechanical response, and low weight is required. As insulation materials for electronic devices, for structural applications demanding low weights and high mechanical properties, as super thermal insulation windows taking advantage of their transparency and low conductivity, as protective layers for electronic devices, lenses, and much more. Also, considering the short period since its appearance, it seems that, in addition to the properties already proven, nanocellular foams have much more to offer that has not been still discovered, or even imagined.

The production method developed in the MIT to produce microcellular polymers, the gas dissolution foaming process [10], is the most promising one, until date, for the production of the materials concerning this work.

In a brief description, gas dissolution foaming process consists of mainly four steps, each one governed by multiple parameters. First of all, saturation, where the solid polymers are subjected to a high-pressure atmosphere of gas at a specific saturation temperature. Under these conditions, the gas diffuses inside the sample until reaching equilibrium, it means until saturation. In the second step, the depressurization, the gas is fast released, leading the polymer to an instability stage that makes possible the formation of nucleation points. Those nucleation points are the precursors for the final cells that are grown in the foaming step in which growing is promoted by increasing the temperature of the material containing the gas phase. Finally, the cells are stabilized, preventing further growing and degeneration of the cellular structure.

As it can be supposed, the final result, it means, the final cellular structure and density of the material depend on the pressure and the temperature of the gas during saturation, on the rate of depressurization, on the temperature and the time used during the foaming. In addition to tens of other details that make this production process very difficult to understand and therefore to control.

The properties of the cellular material are closely linked to the characteristics of their cellular structure. Therefore, if a material wants to be designed with specific properties, the control should be focused on the raw materials used, in the production process, and on the knowledge of how each process parameter affects to the final product, therefore the final properties and ultimately the applications.

All the explained before has encouraged to develop this thesis, pursuing the objectives defined in section 1.3, and that is part of the investigation carried out in CellMat Laboratory, as explained in the following section.

1.2. Framework of this thesis

This thesis is part of the research work developed in the **Cellular Materials Laboratory (CellMat)** [33] belonging to the Condensed Matter Physics Department of the University of Valladolid. The leader of this group is **Prof. Miguel Ángel Rodríguez Pérez,** who is at the same time the director of this Ph.D. thesis.

CellMat was founded in 1999 by Prof. Dr. José Antonio de Saja and by Prof. Dr. Miguel Ángel Rodríguez Pérez, pursuing the objective of creating a research laboratory about cellular materials.

What began as the characterization of commercial cellular materials (mainly polyolefin-based foams) [34,35], quickly became an ambitious project that since its foundation has covered investigations on the production, foaming mechanisms, structure, properties, modeling, and applications of cellular materials. Among which it is worth mentioning, the investigations on aluminium based cellular materials [36–38], microcellular materials [36,39,40], or the five main research topics of the laboratory; cellular nanocomposites [41–43], bioplastic based cellular materials [44,45], polyurethane foams [46,47], multifunctional cellular materials and nanocellular polymers [48,49].

Step by step, the laboratory developed the know-how and facilities necessary to work on the materials tetrahedron for cellular materials **(Figure 1.3**).

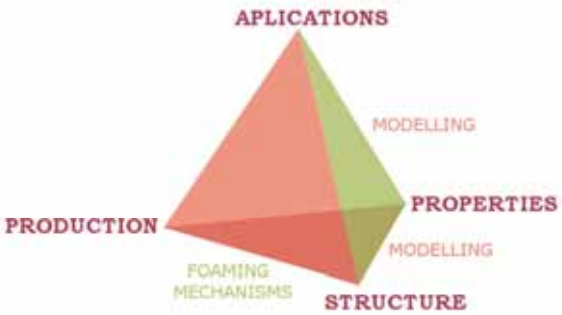

Figure 1.3. Materials tetrahedron

As aforementioned, research in CellMat started with investigations focused on the characterization of cellular materials, evaluating the structure-properties relationship. Then, in 2008, the laboratory started to produce its own foamed materials. This resulted in the first Ph.D. thesis relating the production process with the cellular structure and with

the properties. The thesis on polyolefin-based cellular polymers by Dr. C. Saiz- Arroyo was presented in 2012 [50].

In addition, CellMat laboratory has also stood out to analyze the foaming mechanisms [51–53], optimizing of the current production systems or developing new foaming processes [45,50,54,55] becoming for all these reasons an international reference in the field of cellular materials.

Another essential aspect to mention is that most of the research in CellMat is focused on developing knowledge that could be transferred to the industry. Proof of this is the creation of a spin-off company (CellMat Technologies S.L) in 2012 [56].

It was in 2014 when another key milestone for this thesis was achieved. Nanocellular polymers were produced for the first time in CellMat, and this topic was added as a new research line, making the laboratory a pioneer center in the investigations related to these novel materials. The initial developments were summarised in the Ph.D. Thesis of Dr. J. Pinto Sanz [49].

Since this moment, another Ph.D. thesis and more than 15 papers about this topic have been published [31,48,57].

The first thesis mainly studied the production of nanocellular polymers obtained from blends of PMMA and poly(methyl methacrylate)-b-poly(butyl acrylate)-b-poly(methyl methacrylate) (MAM). While further investigations have been focused on the study of the properties (mechanical, dielectric, acoustic, and thermal) of those produced materials.

The research work presented in this thesis was born as a continuation of those first works and benefits from all the expertise developed before. Having laid the foundations of the tetrahedron, the main objective of this thesis is to make our knowledge on the base of the tetrahedron for nanocellular polymers stronger, without losing sight of the final possible applications. Thus, firstly an in-depth study of the production-structure relationship has been carried out by using PMMA as raw polymer. The production process has been modified using different approaches, searching for the influence of each production parameter on the final cellular structure, resulting in an in-depth knowledge of this relationship. Also, some physical properties (optical, mechanical, and thermal) have been characterized.

The measurement of the mechanical properties has been carried out in the **Cambridge Centre for Micromechanics** belonging to the **Engineering Department of the University of Cambridge**, under the supervision of **Prof. Dr. Norman Fleck.** A three months stay was carried out in this laboratory aiming at taking advantage of the advanced knowledge about mechanical properties they have. Opened in 1996, this center has vast expertise on the mechanics of lattice materials and foams, including modeling of the foaming process, cell mechanics, size effects in plasticity, mechanics of adhesive joints, among others. This research center is internationally linked with major US groups at Harvard, Massachusetts Institute of Technology, Brown, University of California Santa Barbara and the National Institute of Standards and Technology and European research centers including the

Institute National Polytechnique de Grenoble, France; the Technical University of Eindhoven, The Netherlands; KTH, Sweden and the Technical University of Denmark.

Moreover, this thesis has been developed in parallel with another thesis in CellMat (Dra. Victoria Bernardo). In such work multiphasic polymers also based on PMMA have been used for the production of nanocellular polymers. Several synergies between both theses benefit both of them.

This thesis has been developed in the framework of several research funded projects, both public (**Table 1.1**) and private (**Table 1.2**):

Table 1.1. Research projects funded through competitive calls of public entities.

Project Title	Development and continuous manufacturing of advanced thermal insulators based on nanocellular polymers
Funding Body	State Program of R & D Oriented towards the Challenges of Society
Duration	From 01/2016 to 12/2019
Principal Investigator	Miguel Ángel Rodriguez Pérez
Budget	90.750 €
Project Title	Development of sub-microcellular and nanocellular plastics: manufacturing, structure, properties and potential applications
Funding Body	Project National Materials Plan
Duration	From 01/2013 to 12/2015
Principal Investigator	Miguel Ángel Rodriguez Pérez
Budget	130.000 €
Project Title	Development of a new generation of advanced thermal insulators based on obtaining nanocellular porous structures
Funding Body	Regional government of Castile-Leon
Duration	From 01/2013 to 12/2015
Principal Investigator	Miguel Ángel Rodriguez Pérez
Budget	30.000 €

Table 1.2. Research projects with public or private entities.

Project Title	Development of strategies to manufacture nanocellular polymers in industrial processes: extrusion and expanded beads
Funding Body	CellMat Technologies SL
Duration	From 12/2015 to 12/2019
Principal Investigator	Miguel Ángel Rodriguez Pérez
Budget	120.000 €
Project Title	Development of advanced nanocellular polymers
Funding Body	Sabic and CellMat Technologies SL
Duration	From 12/2014 to 12/2018
Principal Investigator	Miguel Ángel Rodriguez Pérez
Budget	60.000 €

Project Title	Development of light and resistant cellular materials by controlling the chemical composition and cellular structure: micro and nanocellular materials
Funding Body	CellMat Technologies SL
Duration	From 12/2013 to 12/2016
Principal Investigator	Miguel Ángel Rodriguez Pérez
Budget	48.000 €

1.3. Objectives

The novelty of nanocellular materials and therefore, the lack of knowledge in this area have motivated this work with the aim of delve into this field as much as possible.

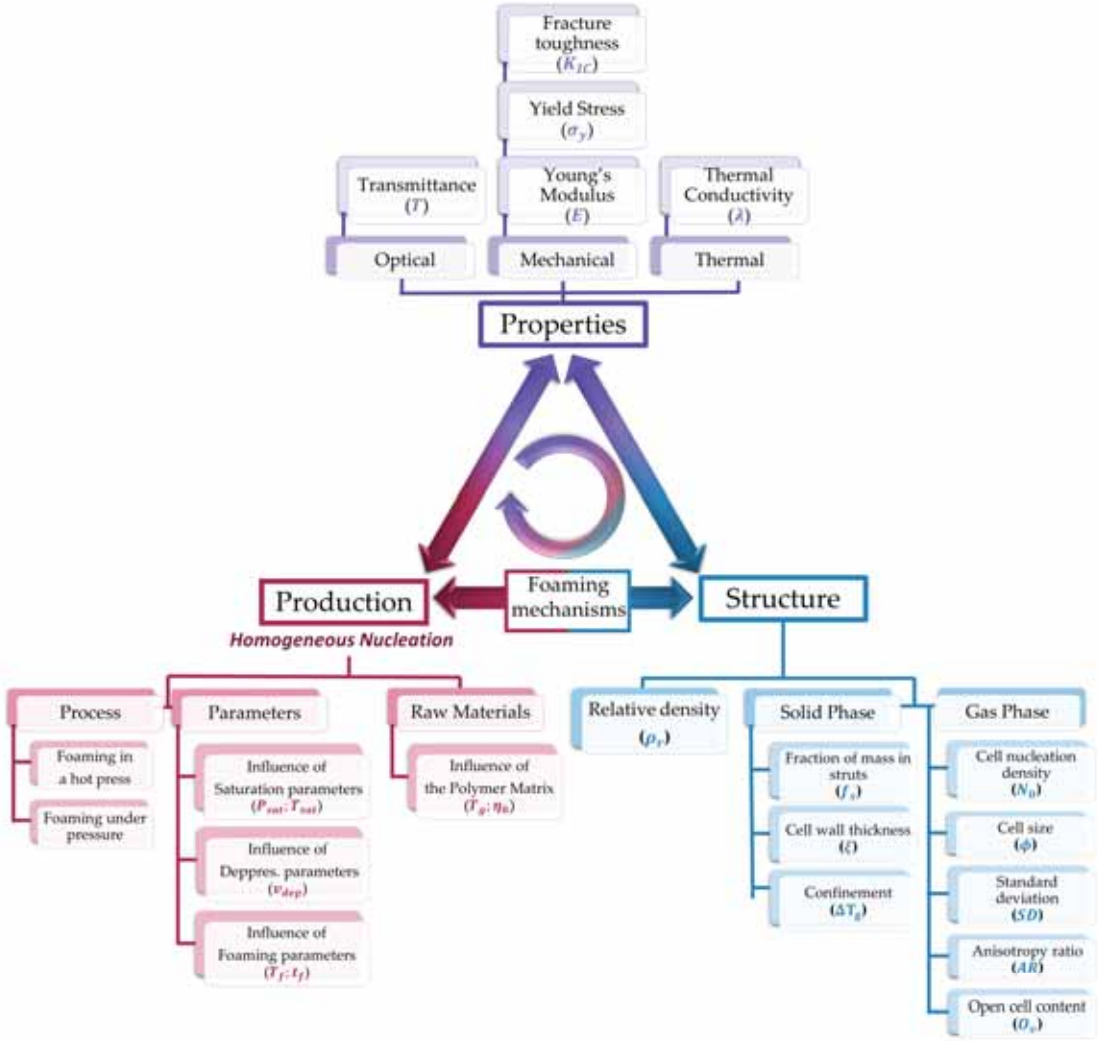

Figure 1.4. Scheme of the relationship that will be established in this thesis for nanocellular materials.

This has led to defining the objectives of this thesis, that mainly consists of generating new knowledge on the relationships shown in **Figure 1.4** for nanocellular materials. Thus, a connection between the production process, the obtained cellular structure and the final

properties of the produced materials aim to be established in this work, as explained below by defining the objectives of this thesis.

Analyze the effect of modifying the production process on the final cellular structure of homogeneous nanocellular polymers.

This first objective aims, on the one hand, at exploring the production process, and on the other hand, at analyzing in-deep the obtained cellular structure, and finally, at understanding the foaming mechanisms. The research work has been focused on the use of several grades of PMMA, without the use of nucleating agents (i.e., all the research is focused on systems that have homogeneous nucleation). So, this first general objective can be divided into three secondary ones:

⇒ Explore all the possible modification of the production process. As schematized in **the left of Figure 1.4**, the production process can be modified by following different routes, the ones explored in this thesis are:

- Modifications of the process parameters: while preserving the original scheme of the four steps of the gas dissolution foaming process. Modifications of the following parameters have been studied:
  - Saturation parameters: saturation pressure (P_{sat}), and saturation temperature (T_{sat}).
  - Depressurization parameters: pressure drop rate or depressurization velocity (v_{dep}).
  - Foaming parameters: foaming temperature (T_f), and foaming time (t_f).

Additionally, it is possible to introduce some changes in the process itself as described below:

- Modifications of the process itself. As showed in the scheme, two different routes have been herein explored:
  - Foaming in a hot press: foaming in a thermal bath is the standard procedure for the third step in gas dissolution foaming process, herein the possibility of foaming the samples in a hot press is studied. Foaming parameters of this step were explored (P_{sat}, T_{sat}) with the aim of comparison with the conventional method.
  - Two-stage depressurization: the saturation and the foaming step were combined in order to explore a modified one-step process. Thus, depressurization is carried out in two steps instead of the single-step usually employed. Modifications in the partial depressurizations (P), as well as in the pressure drop rate (v_{dep}) and the foaming temperature (T_f) have been explored.

In addition, the modifications induced by changing the raw materials have been analyzed in detail:

- Explore different polymer matrices for the production of nanocellular materials; polymer matrices with different rheological characteristics, glass transition temperatures (T_g) and zero- shear viscosities (η_0), have been used in experiments by employing, at the same time, different process parameters.

After the previous steps, the production route is explored, being possible to describe the next partial objective:

⇒ In-deep analysis of the obtained nanocellular materials. Samples produced by following the different routes previously described have been analyzed using the following steps (**right part in Figure 1.4**):

- Relative density determination of the produced materials.
- Characterization of the cellular structure: to obtain a comprehensive description of the cellular structure parameters defining both, the main characteristics of the gas and the solid phase have been measured. Thus, gas-phase was defined through the cell size (ϕ), the cell nucleation density (N_0), the standard deviation of the cell size distribution (SD), the anisotropy ratio (AR), and the open cell content (O_v), while the solid phase was described with the fraction of mass in struts (f_s), the cell wall thickness(ξ), and the solid confinement (ΔT_g)

After modifying the production process and analyze the cellular structure, it is possible to analyze the foaming mechanisms. This is the third partial objective connected to the production process:

⇒ Understanding the foaming mechanisms that relate the changes in the cellular structure induced by the modification of the production process.

- A modified classical nucleation theory has been used for the understanding of the obtained results, contributing to an in-deep knowledge of the gas dissolution foaming process in homogeneous polymers.

The first objective leads to fulfilling all the relationships raised in the bottom scheme of **Figure 1.4**, so only the study of the properties of the produced materials remains pending. This leads to the definition of the second main objective of this thesis.

Study of the properties of the produced nanocellular material to stablish the relationship formulation - production process - cellular structure - properties.

The main part of this goal is the study of some of the properties of the produced materials. This includes the analysis of the optical, mechanical, and thermal properties of the samples developed in this work.

⇒ Study of the optical properties: the transmittance (T) of the developed materials has been analyzed from both experimental and theoretical points of view.
  - Experimental: a complete set of measurements of the transmittance of the produced materials has been done stablishing the dependence of this property with the cell size and the used wavelength.
  - Theoretical: a novel theoretical model has been developed, to obtain the transmittance of the light through nanocellular materials as well as to study the interaction of visible light with those structures. The physical mechanisms controlling this property have been analyzed.

⇒ Study of the mechanical properties: the mechanical properties of the produced materials; the fracture toughness (K_{IC}), the Young´s modulus (E) and the yield stress (σ_y) were measured. Those were related to two key parameters defining the cellular structure: cell size, and relative density.

⇒ Study of the thermal properties: the thermal conductivity (λ) of the produced nanocellular materials was measured and evaluated in terms of the structure of the material.

By satisfying these objectives, it could be possible to produce nanocellular materials on-demand, with the desired final properties thanks to the control of their cellular structure through the production process.

1.4. Novelties

The development of this thesis has contributed to the scientific literature of nanocellular polymers produced from homogeneous materials with some novelties explained in the following paragraphs.

In terms of the production process, a method that enables monitoring of the diffusion process of gas inside polymeric systems has been developed. Thus, parameters such as **solubility, diffusivity, or swelling have been in-situ measured through neutron radiography and tomography for the first time**.

Besides **saturation pressures as high as 20 MPa combined with minimum saturation temperatures of -32 °C have been used for the first time** in the production of nanocellular PMMA.

Additionally, **two innovative production routes for nanocellular PMMA are herein presented.** The first one modifies the foaming route, **changing the foaming in a thermal bath by foaming in a hot press.** The second one integrates the idea of **partial depressurization in one step foaming.**

While staying in the novelties referring to the production process, **three polymer matrixes with different rheological properties have been firstly used for the production of nanocellular materials driven by homogeneous nucleation. This has allowed widening the range of relative densities and cellular structures produced.**

Due to those modifications in the production process, cellular structures with characteristics never reported before have been created. Thus, **nanocellular PMMA with cell sizes smaller than 30 nm and cell nucleation densities higher than 10^{16} nuclei/cm^3 have been produced for the first time**, resulting those structures, in the **firsts semi-transparent nanocellular polymer ever produced**. Additionally, **nanocellular materials with extremely small cells sizes and low relative densities, 0.24 have been produced by using homogeneous nucleation**.

By using the alternative gas dissolution process methods, **flat pieces of nanocellular PMMA with dimensions never reported before were fabricated.** On the other hand, **a technique for removing defects appearing in some materials for particular production conditions have been developed herein.**

Cellular structure of the produced materials has been in-deep analyzed, leading to measurements of some parameters not previously reported. Thus, **a method for the analysis of the fraction of mass in the struts in nanocellular materials has been developed**. Also, **values for the solid confinement (ΔT_g), or the open cell content has been firstly measured for materials with cell sizes below 50 nm.**

This in-deep analysis of the cellular structure leads to a better understanding of the foaming mechanisms governing the production of nanocellular materials.

Finally, thanks to the production of specific nanocellular materials, some of them never reported before, it has been possible to measure the properties of these materials for the first time. Thus, the **transmittance of semi-transparent nanocellular polymers is measured in this thesis for the first time, and a theoretical model studying the interaction light/nanocellular polymers have been newly developed. Additionally, the mechanical and thermal properties for PMMA with cell sizes below 50 nm have also been firstly measured in this thesis.**

1.5. Structure of this thesis

This thesis is written as a **compendium of publications**. Eight scientific papers have been sent to international journals (4 of them are pending of acceptance) (See **Table 1.3**). Additionally, some unpublished results have been added to provide a better understanding of the presented results. Also, this thesis fulfills the requirements to obtain the degree of **Doctor in Philosophy (Ph. D)** with an **International Mention**.

The work presented in this thesis is divided into **nine** chapters; each of them containing the following information:

Chapter 1. Introduction. A brief introduction of cellular materials and more specifically of nanocellular materials is given in this first chapter. This is followed by the framework of this thesis, the pursued objectives, and the novelties. A summary of the scientific articles, conferences, and projects concerning this work is also presented. Finally, the structure of this thesis is included.

Chapter 2. State of the art. This chapter offers a complete overview of cellular polymers, starting from the definition of microcellular polymers and continuing with the description of nanocellular polymers and all the needed parameters to describe those materials. Then, the production process of nanocelular materials is defined, focussing the attention on the gas dissolution foaming process and the two main followed strategies historically used to produce nanocellular materials: heterogeneous nucleation and particularly the one used in this work; homogeneous nucleation. While staying in the gas dissolution foaming process, the influence of all the production parameters on the final cellular structure is examined in detail, taking into account results previously published. That is the influence of saturation, depressurization, and foaming parameters, apart from the impact of the polymeric matrix on the final material. Finally, a description of the optical, mechanical, and thermal properties of nanocellular materials is given.

Chapter 3. Experimental section. Herein a description of the used materials and all the production and characterization techniques is offered. The attention in this chapter is given to the gas dissolution foaming process. Most of the characterization techniques are explained in detail in the different scientific papers. However, an in-deep description is herein provided, giving additional information.

Chapter 4. Influence of the saturation parameters. The findings on this topic are distributed in two papers; both of them to analyze the saturation process. In the first one, the saturation step is studied itself by in-situ analysis of the diffusion process of the gas inside the polymers thanks to neutron tomography. The second one highlights the effect of changing the saturation parameters on the final cellular structure. This work is focused on the effect of reducing the saturation temperature and increasing the saturation pressure. Moreover, an extra section adds experimental results on the influence of the depressurization rate on the cellular structure.

Chapter 5. Influence of the foaming parameters. Chapter 5 is focused on the study of the influence of the foaming parameters on the final cellular structure of nanocellular PMMA. Reported data is presented in a scientific paper focused on the effect of the foaming temperature and time on the final produced material. In this work, the cellular structure of the produced materials is in-deep analyzed, obtaining a comprehensive understanding of the foaming mechanisms playing a role in the foaming process.

Chapter 6. Influence of the polymeric matrix. After the investigation of the modification of the production process, this section is dedicated to study how the rheological properties of the used polymeric matrix affect the final cellular structure. This was carried out by using different PMMA grades presenting different rheological properties. This study has been complemented with the use of different production parameters and is presented in the form of a scientific paper.

Chapter 7. Gas dissolution process customization. In addition to modifying the production parameters, gas dissolution process can be customized itself. Two papers are herein included presenting two innovative routes to produce nanocellular materials. The first one changes the standard foaming process by using a hot-press for foaming, allowing

to produce flat samples of large dimensions. The second one leads to the production of nanocellular materials free of defects, by tuning the depressurization step in a one-step foaming process. Thus, a two-stage depressurization is carried out, and results are compared with those obtained with the standard one-step process.

Chapter 8. Properties of nanocellular materials. By using the nanocellular PMMAs produced in previous chapters (4, 5 and 6), different properties have been characterized and are presented in the form of two scientific articles. One concerning the optical properties of the transparent and semi-transparent nanocellular PMMA produced, herein experimental and theoretical measurements are shown. The second one shows the results obtained concerning the mechanical properties of nanocellular PMMA and the relationship of those results with the cellular structure of the nanocellular material. Finally, an extra section includes the thermal conductivity of materials in a wide range of cell sizes and relative densities.

Chapter 9. Conclusions and future work. Main findings of this thesis are presented in this last chapter. The novel results are highlighted and related to the proposed objectives and compared with the previous data in the literature. Finally, future work and new research topics are suggested.

1.6. Publications, conferences, and courses

This section comprises all the publications related to this thesis (**Table 1.3**) as well as the national and international conferences where results concerning this thesis were presented by the Ph.D. candidate (**Table 1.4**), the training courses and experiments performed in large scale scientific facilities (**Table 1.5**) and additional activities (**Table 1.6**) carried out by the Ph.D. candidate.

Table 1.3. Scientific articles presented in this thesis.

No.	Article Reference	Chapter	Q/IF
1	Martín-de León, J.; Cimavilla-Román, P.; Bernardo, V.; Rodríguez-Pérez, M. A. Cold neutron transmission for in-situ control of gas diffusion mechanisms. **PENDING**	4	-
2	Martín-de León, J.; Bernardo, V.; Rodríguez-Pérez, M. A. Key Production Parameters to Obtain Transparent Nanocellular PMMA. *Macromolecular Materials and Engineering* **2017**, 3, 1700343.	4	Q1/2.69
3	Martín-de León, J.; Bernardo, V.; Rodríguez-Pérez, M. A. Low Density Nanocellular Polymers Based on PMMA Produced by Gas Dissolution Foaming: Fabrication and Cellular Structure Characterization. *Polymers* **2016**, *8*, 265.	5	Q1/3.364
4	Martín-de León, J. M.; Bernardo, V.; Laguna-Gutiérrez, E.; Rodríguez-pérez, M. A. Influence of the rheological behavior of PMMA on the cellular structure of nanocellular materials. **PENDING**	6	-
5	Martín-de León, J.; Bernardo, V.; Cimavilla-Román, P.; Pérez-Tamarit, S.; Rodríguez-Pérez, M. A. Overcoming the Challenge of Producing Large and Flat Nanocellular	7	Q2/2.576

	Polymers: A Study with PMMA. *Advanced Engineering Materials,* **2019**, 1–8.		
6	Martín-de León, J.; Bernardo, V.; Rodríguez-Pérez, M.A. Two-stage depressurization in one step foaming process: the production of nanocellular materials free of defects. **PENDING**	7	-
7	Martín-de León, J.; Pura, J. L.; Bernardo, V.; Rodríguez-Pérez, M. A. Transparent nanocellular PMMA: Characterization and modeling of the optical properties. *Polymer,* **2019**, *170*, 16–23.	8	Q1/3.486
8	Martín-de León, Van Loock, F.; Bernardo, V.; Fleck, N.A.; Rodríguez-Pérez, M. A. The influence of cell size on the mechanical properties of nanocellular PMMA *Polymer.* **ACCEPTED**	8	Q1/3.486

Table 1.4. Oral communications, posters and contributions to international and national conferences.

1	Martín-de León, J.; Bernardo, V.; Rodríguez-Pérez, M. A. *Influencia de la temperatura en la absorción de dióxido de carbono en espumas nanocelulares.* Escuela Nacional de Materiales Moleculares, February 2014, Santa Pola, Comunidad Valenciana, Spain. **Talk.**
2	Martín-de León, J.; Bernardo, V.; Pérez-Tamarit, S.; Solórzano, E.; Rodríguez-Pérez, M. A. *Nanocellular foams fabrication methods by gas dissolution process.* Metfoam, September 2015, Barcelona, Cataluña, Spain. **Poster.**
3	Martín-de León, J.; Bernardo, V.; Rodríguez-Pérez, M. A. *Higher nucleation efficiency in polymer foams by improving gas dissolution method.* VIII European School on Molecular Nanoscience, October 2015, Paris, France. **Talk.**
4	Martín-de León, J.; Bernardo, V.; Rodríguez-Pérez, M. A. *Influence of the process parameters in the cellular structure of low density PMMA nanocelullar polymers produced by the gas dissolution foaming route.* XIV Reunión del grupo especializado de polímeros de la RSEQ y RSEF, September 2016, Burgos, Spain. **Talk.**
5	Martín-de León, J.; Bernardo, V.; Rodríguez-Pérez, M. A. *Description of the process parameters for the production of PPSU nanocellular materials.* FOAMS 2016, September 2016, Seattle, Washington, United States. **Poster.**
6	Martín-de León, J.; Bernardo, V.; Rodríguez-Pérez, M. A. *Understanding the mechanism that allow reducing density in PMMA nanocellular polymers.* FOAMS 2016, September 2016, Seattle, Washington, United States. **Poster.**
7	Martín-de León, J.; Bernardo, V.; Rodríguez-Pérez, M. A. *Knudsen Effect: Nanocellular Polymers as thermal insulators.* Three Minutes Thesis Contest (3MT), October 2016, Valladolid, Castilla y León, Spain. **Talk.**
8	Martín-de León, J.; Bernardo, V.; Rodríguez-Pérez, M. A. *Nanocellular polymers: the optimal production of the thermal insulators of the future.*

	III Jornada Investigadoras de la UVA en "La aventura de la ciencia y la tecnología" 2017, September 2017, Valladolid, Castilla y León, Spain. **Talk.**
9	Martín-de León, J.; Bernardo, V.; Rodríguez-Pérez, M. A. *Semi-transparent nanocellular polymers based on PMMA: Production and characterization.* FOAMS 2017, October 2017, Bayreuth, Germany. **Talk.**
10	Martín-de León, J.; Bernardo, V.; Rodríguez-Pérez, M. A. *Controlled foaming in a hot press of flat and large parts of nanocellular PMMA.* FOAMS 2017, October 2017, Bayreuth, Germany. **Poster.**
11	Martín-de León, J.; Pura, J.L.; Bernardo, V.; Rodríguez-Pérez, M. A. *Understanding the behaviour of semi-transparent nanocellular PMMA: study of the transmittance and modelling.* CellMAT 2018, October 2018, Bad Staffelstein, Germany. **Talk.**
12	Martín-de León, J.; Bernardo, V.; Rodríguez-Pérez, Pura, J.L.; M. A. *Nanocellular PMMA with tuneable cellular structure by changing the rheological behaviourof the polymer matrix.* CellMAT 2018, October 2018, Bad Staffelstein, Germany. **Poster.**

Table 1.5. Training courses and campaigns in large scientific facilities.

1	*Workshop on X-RAY radioscopy and tomography.* November 2014, Berlin, Germany.
2	*Neutron Campaign, HZB* September 2015, Berlin, Germany
3	*Acoustic insulation in buildings.* 2015, Valladolid, Castilla y León, Spain.
4	*Seminar on characterization of materials by thermal analysis techniques: DSC, TGA.* October 2015, Valladolid, Castilla y León, Spain.
5	*Thermal insulation in buildings.* October 2015, Valladolid, Castilla y León, Spain.
6	*Characterization of polymeric materials.* October 2016, Valladolid, Castilla y León, Spain.
7	*Plastic packaging, fundamentals, regulations and trends* February 2018, Valladolid, Castilla y León, Spain.
8	*Neutron Campaign, Diamond Lightsource* February 2019, Oxford, United Kingdom.

Table 1.6. Additional activities

Papers	
1	Notario, B.; Pinto, J.; Solórzano, E.; Escudero, J.; Martín-de León, J; Velasco, D.; Rodríguez-Pérez, M. A. *In Situ Optical Analysis of Structural Changes in Polylactic Acid (PLA) during the Gas Dissolution Process*. Defect and Diffusion Forum **2014**, *353*, 131–136.
2	Bernardo, V.; Martín-De León, J.; Rodríguez-Pérez, M. A. Production and characterization of nanocellular polyphenylsulfone foams. *Materials Letters* **2016**, *178*, 155–158.

3	Bernardo, V.; Martín-de León, J.; Laguna-Gutiérrez, E.; Rodríguez-Pérez, M. A. PMMA-sepiolite nanocomposites as new promising materials for the production of nanocellular polymers. *European Polymer Journal* **2017**, *96*, 10–26.
4	Bernardo, V.; Martin-de Leon, J.; Laguna-Gutierrez, E.; Catelani, T.; Pinto, J.; Athanassiou, A.; Rodriguez-Perez, M. A. Understanding the role of MAM molecular weight in the production of PMMA/MAM nanocellular polymers. *Polymer* **2018**, *153*, 262–270.
5	Bernardo, V.; Martin-de Leon, J.; Pinto, J.; Verdejo, R.; Rodriguez-Perez, M. A. Modeling the heat transfer by conduction of nanocellular polymers with bimodal cellular structures. *Polymer* **2019**, *160*, 126–137.
6	Bernardo, V.; Martin-de Leon, J.; Pinto, J.; Catelani, T.; Athanassiou, A.; Rodriguez-Perez, M. A. Low-density PMMA/MAM nanocellular polymers using low MAM contents: Production and characterization. *Polymer* **2019**, *163*, 115–124.
7	Martín-de León, J.; Bernardo, V.; Rodríguez-Pérez, M. Nanocellular Polymers: The Challenge of Creating Cells in the Nanoscale. *Materials* **2019**, *12*, *797*.
8	Bernardo, V.; Martin-de Leon, J.; Rodriguez-Perez, M. A. Anisotropy in nanocellular polymers promoted by the addition of needle-like sepiolites. *Polymer International* **2019**, *68*, 1204–1214.
9	Bernardo, V.; Loock, F.; Martin-de Leon, J.; Fleck, N. A.; Rodriguez-Perez, M. A. Mechanical Properties of PMMA-Sepiolite Nanocellular Materials with a Bimodal Cellular Structure. *Macromolecular Materials and Engineering* **2019**.
Conferences	
10	Bernardo, V.; Martín-de León, J.; Rodríguez-Pérez, M. A.; Pinto, J. *Nanostructure Materials and nanoporous foams.* Escuela Nacional de Materiales Moleculares, February 2014, Santa Pola, Comunidad Valenciana, Spain. **Talk.**
11	Pérez-Tamarit, S.; Bernardo, V.; Martín-de León, J.; Solórzano, E.; Rodríguez-Pérez, M. A. *Characterization of the solid phase of cellular materials by means of X-RayμCT* Metfoam, September 2015, Barcelona, Cataluña, Spain. **Poster.**
12	Bernardo, V.; Martín-de León, J.; Pérez-Tamarit, S.; Solórzano, E.; Rodríguez-Pérez, M. A. *Cellular structure, properties and applications of nanoporous materials.* Metfoam, September 2015, Barcelona, Cataluña, Spain. **Poster.**
13	Bernardo, V.; Martín-de León, J.; Rodríguez-Pérez, M. A. *Sepiolites as nucleating agent in PMMA nanofoam.* VIII European School on Molecular Nanoscience, October 2015, Paris, France. **Talk.**
14	Bernardo, V.; Martín-de León, J.; Rodríguez-Pérez, M. A. *Production of nanocellular materials from nanostructured polymers based on PMMA/MAM blends: Influence of the polymer molphology on the cellular structure.* XIV Reunión del grupo especializado de polímeros de la RSEQ y RSEF, September 2016, Burgos, Spain. **Talk.**
15	Rodríguez-Pérez, M. A.; Bernardo, V.; Martín-de León, J. *Nanocellular polymers: A new class of materials with enhanced properties.* XIV Reunión del grupo especializado de polímeros de la RSEQ y RSEF, September 2016, Burgos, Spain. **Plenay Talk.**
16	Bernardo, V.; Martín-de León, J.; Rodríguez-Pérez, M. A. *Needle-like nanoparticles as a new nucleating agent in CO2-foaming of nanocellular PMMA.*

	FOAMS 2016, September 2016, Seattle, Washington, United States. **Poster.**
17	Bernardo, V.; Martín-de León, J.; Rodríguez-Pérez, M. A. *Nanocellular polymers based on PMMA/MAM blends: effect of the copolymer chemistry on the nanostructuration and the cellular structure.* FOAMS 2016, September 2016, Seattle, Washington, United States. **Poster.**
18	Rodríguez-Pérez, M. A.; Bernardo, V.; Martín-de León, J. *Low density nanocellular foams based on PMMA: production, structure and properties.* FOAMS 2016, September 2016, Seattle, Washington, United States. **Talk.**
19	Martín-de León, J.; Bernardo, V.; Rodríguez-Pérez, M. A. *Production and properties of low density nanocellular PMMA with controlled density and cellular structure.* Poly-Foam Conference, April 2017, Hilton Mainz, Germany. **Talk.**
20	Bernardo, V.; Martín-de León, J.; Rodríguez-Pérez, M. A. *Effect of amount of block-copolymer on the density and cellular structure of nanocellular polymers based on PMMA/MAM blends.* FOAMS 2017, October 2017, Bayreuth, Germany. **Poster.**
21	Pérez-Tamarit, S.; Martín-de León, J.; Bernardo, V.; López-GonzAlez, E.; Muñoz-Pascual, S.; Pinto, J.; Laguna-Gutiérrez, E.; Rodríguez-Pérez, M. A. *Transfering knowledge from the university to the industry: internships at the university of Valladolid.* EDULEARN 2018, July 2018, Palma de Mallorca, Illes Balears, Spain. **Virtual presentation.**
22	López-GonzAlez, E.; Muñoz-Pascual, S.; Bernardo, V.; Laguna-Gutiérrez, E.; Martín-de León, J.; Pérez-Tamarit, S.; Pinto, J.; Rodríguez-Pérez, M. A. *Evolution of the practical training in materials physics: from a constrained research in the polymer science field to a multidisciplinary methodology.* EDULEARN 2018, July 2018, Palma de Mallorca, Illes Balears, Spain. **Virtual presentation.**
23	Rodríguez-Pérez, M. A.; Martín-de León, J.; Bernardo, V. *Modelling Some Key Properties of Semi-Transparent Nanocellular Polymers Based on PMMA.* FOAMS 2018, September 2019, Montreal, Canada. **Talk.**
24	Santiago-Calvo, M.; Naji-Izaguirre, H.; Bernardo, V.; Martín-de León, J.; Saiani, A.; Villafañe, F.; Rodríguez-Pérez, M. A. *Production of thermoplastic polyurethane foams synthesized with different contents of hard segment and graphene nanoplatelets by the gas dissolution foaming process.* CellMAT 2018, October 2018, Bad Staffelstein, Germany. **Talk.**
25	Múgica-Izaguirre, M.; Bernardo, V.; Martín-de León, J.; SAiz-Arroyo, C.; Rodríguez-Pérez, M. A. *Production of microcellular PMMA using the bead foaming technology.* CellMAT 2018, October 2018, Bad Staffelstein, Germany. **Poster.**
26	Rodríguez-Pérez, M. A.; Martín-de León, J.; Pura, J.L.; Bernardo, V. *Nanocellular polymers. Novel approaches to produce these materials using gas dissolution foaming.* CellMAT 2018, October 2018, Bad Staffelstein, Germany. **Key-note lecture.**
27	Bernardo, V.; Martín-de León, J.; Pura, J.L.; Rodríguez-Pérez, M. A. *Nanocellular polymers based on PMMA/sepiolite nanocomposites: characterization of the mechanical behaviour.* CellMAT 2018, October 2018, Bad Staffelstein, Germany. **Poster.**
28	Bernardo, V.; Martín-de León, J.; Pura, J.L.; Rodríguez-Pérez, M. A. *Fabrication of low-density nanocellular polymers using PMMA/TPU blends.*

CellMAT 2018, October 2018, Bad Staffelstein, Germany. **Talk.**

1.7. References

[1] http://www.marketsandmarkets.com/Market-Reports/foams-market-1011.html 06/03/2019.

[2] Gibson, L. J.; Ashby, M. F. *Cellular solids: Structure and Properties*; 2nd ed.; Cambridge: Cambridge University Press.: United States, **1997**.

[3] Mills, N. J. Handbook of polymeric foams and foam technology. *Polymer* **1993**, *34*, 2237.

[4] Eaves, D. *Handbook of Polymer Foams*; Rapra Technology Limited: Shawbury, Shrewsbury, Shropshire, UK, **2004**.

[5] Rodriguez-Perez, M. A. Crosslinked polyolefin foams: Production, structure, properties, and applications. *Advances in Polymer Science* **2005**, *184*, 97–126.

[6] Saiz-Arroyo, C.; Rodriguez-Perez, M. A.; Tirado, J.; López-Gil, A.; de Saja, J. A. Structure-property relationships of medium-density polypropylene foams. *Polymer International* **2013**, *62*, 1324–1333.

[7] Prabhu, S.; Raja, V. K. B.; Nikhil, R. Applications of Cellular Materials – An Overview. *Applied Mechanics and Materials* **2015**, *766–767*, 511–517.

[8] Martini-Vvedensky, J. J. E.; Suh, N. N. P.; Waldman, F. F. a. Microcellular closed cell foams and their method of manufacture. *US Patent 4,473,665* **1984**.

[9] Kumar, V.; Weller, J. E. A Process to Produce Microcellular PVC. *International Polymer Processing* **1993**, *1*, 73–80.

[10] Kumar, V.; Suh, N. P. A process for making microcellular thermoplastic parts. *Polymer Engineering and Science* **1990**, *30*, 1323–1329.

[11] Arora, K. A.; Lesser, A. J.; McCarthy, T. J. Preparation and Characterization of Microcellular Polystyrene Foams Processed in Supercritical Carbon Dioxide. *Macromolecules* **1998**, *31*, 4614–4620.

[12] Kumar, V.; Weller, J. Production of Microcellular Polycarbonate Using Carbon Dioxide for Bubble Nucleation. *Journal of Engineering for Industry* **1994**, *116*, 413–420.

[13] Reglero Ruiz, J. A.; Viot, P.; Dumon, M. Microcellular foaming of polymethylmethacrylate in a batch supercritical CO 2 process: Effect of microstructure on compression behavior. *Journal of Applied Polymer Science* **2010**, *118*, 320–331.

[14] Kumar, V. Microcellular Polymers: Novel materials for the 21st century. *Progress in Rubber and Plastics Technology* **1993**, *9*, 54–70.

[15] Shimbo, M.; Higashitani, I.; Miyano, Y. Mechanism of strength improvement of foamed plastics having fine cell. *Journal of Cellular Plastics* **2007**, *43*, 157–167.

[16] Kumar, V.; VanderWel, M.; Weller, J.; Seeler, K. a. Experimental Characterization of the Tensile Behavior of Microcellular Polycarbonate Foams. *Journal of Engineering Materials and Technology* **1994**, *116*, 439.

[17] Nadella, K.; Kumar, V. Tensile and flexural properties of solid-state microcellular ABS panels. *Experimental Analysis of Nano and Engineering* **2007**, *22*, 765–766.

[18] Sun, H.; Sur, G. S.; Mark, J. E. Microcellular foams from polyethersulfone and polyphenylsulfone: Preparation and mechanical properties. *European Polymer Journal* **2002**, *38*, 2373–2381.

[19] Costeux, S. CO 2 -blown nanocellular foams. *Journal of Applied Polymer Science* **2014**, *131*, n/a-n/a.

[20] Notario, B.; Pinto, J.; Rodriguez-Perez, M. A. Nanoporous polymeric materials: A new class of materials with enhanced properties. *Progress in Materials Science* **2016**, *78–79*, 93–139.

[21] Kumaki, J. Observation of polymer chain structures in two-dimensional films by atomic force microscopy. *Polymer Journal* **2016**, *48*, 3–14.

[22] Notario, B.; Ballesteros, A.; Pinto, J.; Rodriguez-Perez, M. A. Nanoporous PMMA : A novel system with different acoustic properties. *Materials Letters* **2016**, *168*, 76–79.

[23] Notario, B.; Pinto, J.; Verdejo, R.; Rodríguez-Pérez, M. A. Dielectric behavior of porous PMMA: From the micrometer to the nanometer scale. *Polymer* **2016**, *107*, 302–305.

[24] Miller, D.; Kumar, V. Microcellular and nanocellular solid-state polyetherimide (PEI) foams using sub-critical carbon dioxide II. Tensile and impact properties. *Polymer* **2011**, *52*, 2910–2919.

[25] Merlet, S.; Marestin, C.; Schiets, F.; Romeyer, O.; Mercier, R. Preparation and characterization of nanocellular poly(phenylquinoxaline) foams. A new approach to nanoporous high-performance polymers. *Macromolecules* **2007**, *40*, 2070–2078.

[26] Notario, B.; Pinto, J.; Solorzano, E.; De Saja, J. A.; Dumon, M.; Rodriguez-Perez, M. A. Experimental validation of the Knudsen effect in nanocellular polymeric foams. *Polymer (United Kingdom)* **2015**, *56*, 57–67.

[27] Forest, C.; Chaumont, P.; Cassagnau, P.; Swoboda, B.; Sonntag, P. Polymer nano-foams for insulating applications prepared from CO2 foaming. *Progress in Polymer Science* **2015**, *41*, 122–145.

[28] Li, L.; Schulte, L.; Clausen, L. D.; Hansen, K. M.; Jonsson, G. E.; Ndoni, S. Gyroid nanoporous membranes with tunable permeability. *ACS Nano* **2011**, *5*, 7754–7766.

[29] Pinto, J.; Dumon, M.; Rodriguez-Perez, M. A.; Garcia, R.; Dietz, C. Block Copolymers Self-Assembly Allows Obtaining Tunable Micro or Nanoporous Membranes or Depth Filters Based on PMMA; Fabrication Method and Nanostructures. *The Journal of Physical Chemistry C* **2014**, *118*, 4656–4663.

[30] Lu, G. Q.; Zhao, X. S. Nanoporous Materials — An Overview. In *Nanoporous materials: Science and engineering*; Imperial Collegue Press: London, **2004**.

[31] Pérez-Tamarit, S.; Notario, B.; Solórzano, E.; Rodriguez-Perez, M. A. Light transmission in nanocellular polymers: Are semi-transparent cellular polymers possible? *Materials Letters* **2018**, *210*, 39–41.

[32] Martín-de León, J.; Bernardo, V.; Rodríguez-Pérez, M. Á. Key Production Parameters to Obtain Transparent Nanocellular PMMA. *Macromolecular Materials and Engineering* **2017**, *3*, 1700343.

[33] CellMat http://cellmat.es/.

[34] Rodríguez-Pérez, M. A. Propiedades térmicas y mecánicas en espumas de poliolefinas. *Ph.D. Thesis, University of Valladolid* **1998**.

[35] Arcos y Rábago, L. O. Propiedades térmicas y mecánicas de espumas de poliolefinas

fabricadas en un proceso de moldeo por compresión, **2002**.

[36] Solorzano, E. Espumas de Aluminio: Proceso de Espumado, Estructura Celular y Propiedades. *Ph.D. Thesis, University of Valladolid* **2008**.

[37] Lazaro Nebreda, J. Optimización de la estructura celular en espumas de aluminio. *Ph.D. Thesis, University of Valladolid* **2014**, 326.

[38] Ruiz-Reglero, A. J. Fabricación y caracterización de espumas de aluminio: aplicaciones en el sector aeronáutico. *Ph.D. Thesis, University of Valladolid* **2007**, 429.

[39] Reglero-ruiz, J. A.; Saiz-Arroyo, C.; Dumon, M.; Rodríguez-Pérez, M. Á.; Gonzalez, L. Production, cellular structure and thermal conductivity of microcellular (methyl methacrylate)–(butyl acrylate)–(methyl methacrylate) triblock copolymers. *Polymer International* **2010**, *60*, 146–152.

[40] Lobos Martín, J. Improving the stiffness and strength of porous materials by enhancement of the matrix microstructure and cellular morphology. *Ph.D. Thesis, University of Valladolid*.

[41] Reglero Ruiz, J. A.; Dumon, M.; Pinto, J.; Rodriguez-Pérez, M. A. Low-density nanocellular foams produced by high-pressure carbon dioxide. *Macromolecular Materials and Engineering* **2011**, *296*, 752–759.

[42] Bernardo, V.; Martín-de León, J.; Laguna-Gutiérrez, E.; Rodríguez-Pérez, M. Á. PMMA-sepiolite nanocomposites as new promising materials for the production of nanocellular polymers. *European Polymer Journal* **2017**, *96*, 10–26.

[43] Saiz-Arroyo, C.; Rodriguez-Pérez, M. A.; de Saja, J. A. Improving the Structure and Physical Properties of LDPE Foams using Silica Nanoparticles as an Additive. *Cellular polymers* **2011**, *30*.

[44] López Gil, A. *Development of Environmentally Friendly Cellular Polymers for Packaging and Structural Applications . Study of the Relationship Cellular Structure-Mechanical Properties*; **2016**.

[45] Salmazo, L. O. Cinéticas de espumación y control de la estructura celular en materiales basados en caucho natural y poliolefinas. *Ph.D. Thesis, University of Valladolid* **2015**.

[46] Acuña, P.; Santiago-Calvo, M.; Villafañe, F.; Rodriguez-Pérez, M. A.; Rosas, J.; Wang, D. Impact of expandable graphite on flame retardancy and mechanical properties of rigid polyurethane foam. *polymer composites* **2018**.

[47] Santiago-Calvo, M.; Blasco, V.; Ruiz, C.; Paris, R.; Villafañe, F.; Rodriguez-Pérez, M. A. Improvement of thermal and mechanical properties by control of formulations in rigid polyurethane foams from polyols functionalized with graphene oxide. *Journal of Applied Polymer Science* **2019**, *136*.

[48] Collado, N. Fabricación y Caracterización de las Propiedades Físicas de Polímeros Nanocelulares : Transición de la Escala Micro a la Nano. *Ph.D. Thesis, University of Valladolid*.

[49] Pinto Sanz, J. Fabricación y Caracterización de Materiales Poliméricos Submicrocelulares a partir de Polímeros Nanoestructurados. *Ph.D. Thesis, University of Valladolid* **2014**.

[50] Saiz-Arroyo, C. Fabricación de materiales celulares mejorados basados en poliolefinas. Relación procesado-composición-estructura-propiedades. *Ph.D. Thesis, University of Valladolid* **2012**.

[51] Saiz-Arroyo, C.; De Saja, J. A.; Velasco, J. I.; Rodríguez-Pérez, M. Á. Moulded polypropylene foams produced using chemical or physical blowing agents: Structure-properties relationship. *Journal of Materials Science* **2012**, *47*, 5680–5692.

[52] Pardo, S. X-Ray Imaging Applied to the Characterization of Polymer Foams' Cellular Structure and its Evolution. *Ph.D. Thesis, University of Valladolid* **2014**.

[53] Perez-Tamarit, S.; Solórzano, E.; Pardo-Alonso, S.; Mokso, R.; Rodriguez-Pérez, M. A. Pore Nucleation and Growth in Cellular Polymers Analysed By Time Resolved Synchrotron X-Ray M - Ct. *International conference on tomography of materials and structures* **2017**, 3–4.

[54] Rodriguez-Pérez, M. A.; de Saja, J. A.; Tirado, J.; lopez gil, A. Procedimiento de Fabricación de Materiales Celulares de Matriz Termoplástica **2013**.

[55] Rodriguez-Pérez, M. A.; de Saja, J. A.; Escudero, J.; Vazquez, J. . Sistema y Procedimiento de Moldeo de Piezas con Moldes Autoportantes **2012**.

[56] http://www.cellmattechnologies.com/ http://www.cellmattechnologies.com/.

[57] Notario, B.; Pinto, J.; Rodriguez-Perez, M. a. Towards a new generation of polymeric foams: PMMA nanocellular foams with enhanced physical properties. *Polymer* **2015**, *63*, 116–126.

Chapter 2

State of the art

"El mundo era tan reciente, que muchas cosas carecían de nombre y para mencionarlas había que señalarlas con el dedo."

Gabriel García Márquez

INDEX

2.1. Introduction

This chapter collects the essential concepts and definitions for the understanding of this thesis and a complete analysis of the state of the art by collecting prior works previously published regarding nanocellular polymers.

Thus, a complete description of cellular polymers, particularly nanocellular polymers, is given by defining the parameters of the cellular structure. Additionally, the production route used in this thesis, the gas dissolution foaming process is described. Finally, a revision of the properties of nanocellular polymers is given. Optical, mechanical, and thermal properties are studied.

2.2. Cellular Polymers

Cellular polymers are a group of materials inside of those called cellular solids. Cellular solids are commonly defined as materials composed by two phases, a continuous gaseous phase dispersed in a matrix (**Figure 2.1**) [1]. As it was mentioned in the introduction, cellular solids surround us, they can be found almost everywhere in nature, so there is no doubt of their importance. *Cellular polymers* are those in which the solid matrix is a polymer. They were produced artificially for the first time around 1920, after a new attempt by men to imitate nature [2].

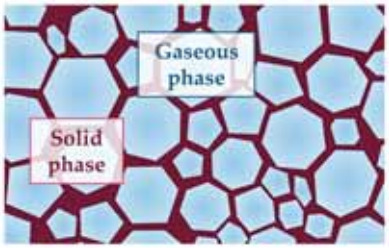

Figure 2.1. Scheme of the cellular structure of a cellular polymer.

After their development, their use has been widespread in all kind of applications, due to a noncommon combination of properties. In addition to their most remarkable feature, their reduced density in comparison with the former solid, cellular polymers are characterized by presenting properties such as high energy absorption under impacts, low thermal conductivity, buoyancy, or excellent cushioning performance among others. Those properties can be broadened by selecting the adequate polymer matrix, being possible to have cellular structures with magnetic permeability, no water absorption, with chemical resistance, acoustic absorption or high specific surface [3–5]. This explains their presence in the automotive sector, the building industry, as well as in comfort applications, packaging, thermal and acoustic insulation, etc.

Cellular materials can be classified attending to different characteristics; one of the most common ones is the one referring to their cell size. Those cellular polymers showing the biggest pores are known as conventional cellular polymers and cover a range of cell sizes from few millimeters to tens of micrometers. When the pore size is below ten micrometers, cellular polymers are known as microcellular polymers. And finally, when they present cell sizes in the nanometric range, their name is nanocellular polymers.

2.3. Nanocelular polymers

Nanocellular polymers were developed as an attempt of improving microcellular polymers. Those last ones were produced for the first time in the earlies 1980s at the Massachusetts Institute of Technology (MIT) [6,7]. Their discovery involved a significant improvement of the mechanical properties of cellular materials allowing to reduce the weight of the former polymers and therefore their cost, without compromising in a significant extent the mechanical properties. This made possible to spread the use of cellular materials in sectors where it was unthinkable to find them previously.

This evolution in cellular materials suggested that further improvement could be reached by a new reduction of the cell size. This was the driving force to develop *nanocellular polymers*.

Nanocellular polymers implied a reduction of the cell size from a few micrometers to the nanometric scale, and an increase of the cell density, it means the number of cells per unit volume, from 10^{10}-10^{12} cells/cm^3 to cell densities higher than 10^{13} cells/cm^3 [8,9]. However, this is a broad definition. The change from micro to nanocellular materials is interesting as far as this change in scale leads to changes in the properties of those materials. Depending on the selected property, this size barrier changes. Thus, for instance, changes in mechanical properties have been observed when cell size decreases below 200 nm for some systems (see section 2.5.1).

On the other hand, the change of behavior in the thermal conductivity when changing from the micro to the nanoscale starts to be significant for cell sizes smaller than 100 nm (see section 2.5.2). While when studying optical properties, modifications are observed when decreasing the cell size below 50 nm (see section 2.5.3). Therefore, a better approach is to define nanocellular materials according to the studied property, and defining the threshold value when significant modifications of the property under study are detected.

So far, when defining nanocellular polymers only two characteristics of those materials have been taken into account, the cell size and the cell density. However, materials under study are much more complex, and in order to define them accurately, a set of parameters defining their cellular structure are needed. The next section is focused on the description of those parameters.

2.3.1. Parameters defining cellular polymers

Relative density, ρ_r

Relative density is a macroscopic descriptor of cellular polymers, and it is one of the most important parameters when defining a cellular material. Is defined as the ratio between the density of the cellular material (ρ_f) and the density of the former solid (ρ_s), as it is shown in **Equation 1**.

$$\rho_r = \frac{\rho_f}{\rho_s} \qquad (1)$$

Considering this parameter, nanocellular polymers can be classified as high-density ones when $\rho_r > 0.6$, medium density when $0.6 > \rho_r < 0.3$ and low-density ones when $\rho_r < 0.3$.

It is also common to find the definition of porosity V_f in the bibliography; this is defined as one minus the relative density ($V_f = 1 - \rho_r$) and it accounts for the volume fraction of the gas phase.

Once the relative density is determined, the cellular structure needs to be analyzed using microscopic descriptors. As it was aforementioned, cellular materials are formed by two different phases (**Figure 2.1**), the solid and the gaseous one, and both of them need to be described. While cell size, the standard deviation of the cell size, the anisotropy ratio, the cell density, and the cell nucleation density refer to the gaseous phase, the cell wall thickness, the fraction of mass in struts and the open cell content concern to the solid phase. The definition of all of them is included in the next paragraphs.

Cell size, ϕ

Figure 2.2. ϕ

This parameter refers to the gaseous phase and defines the dimensions of the pores conforming the cellular material (**Figure 2.2**). The cell size is determined as the average value of the diameter of the cells forming the cellular material.

As commented above, cellular polymers starting to be considered nanocellular polymers when the cell size is on the nanometric scale.

Standard deviation of the cell size distribution, SD

Figure 2.3. SD

Most cellular materials present a cell size distribution, i.e., cells with different diameters are forming the structure. An important parameter to define is the standard deviation of this cell size distribution that indicates its width (**Figure 2.3**). Another usually given parameter is SD/ϕ, which reveals the homogeneity of the cellular material. The smaller is this parameter the most homogeneous is the cellular structure.

Anisotropy ratio, AR

Figure 2.4. AR

It is also important to know the isotropy of the cells. In order to determine if cells present a preferential direction of growth, the anisotropy ratio is defined as the ratio between the cell size in two perpendicular directions (**Figure 2.4**).

$$AR = \frac{\phi_z}{\phi_x} \quad (2)$$

Cell density, N_v

Figure 2.5. N_v

This parameter determines the number of cells per unit of volume of the cellular material (**Figure 2.5**). It can be calculated by following the Kumar's approximation shown in **Equation 3** [6], from a 2D image of the cellular material and by assuming an isotropic bubble distribution.

$$N_v = \left(\frac{nM}{A}\right)^{\frac{3}{2}} \quad (3)$$

Where A is the area of the micrograph, n is the number of cells in this area, and M is the magnification factor of the micrograph.

Nanocellular polymers are characterized by presenting cell densities higher than 10^{13} cells/cm^3 [8](see section 2.3 for additional details).

Cell nucleation density, N_0

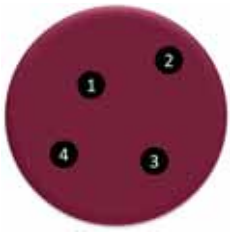

Figure 2.6. N_0

Cell nucleation density is defined as the number of nucleation sites per cubic centimeter of the solid polymer (**Figure 2.6**), and it is calculated from the cell density of the material by supposing no degeneration mechanisms, it means assuming that each final cell corresponds to a unique nucleation point. This value can be calculated using the following equation:

$$N_0 = \frac{N_v}{\rho_r} \quad (4)$$

Cell nucleation density for nanocellular polymers is established to be higher than 10^{13} nuclei/cm^3 [9] (see section 2.3 for additional details).

Fraction of mass in the struts, f_s

Figure 2.7. f_s

In a polyhedral cell, it can be distinguished between three elements; walls, edges, and vertexes. The solid part separating two cells is the cell wall while the sum of vertexes and edges constitute the struts (**Figure 2.7**). Fraction of mass in the struts defines how the solid phase is distributed in the cellular material. It is set as the ratio between the amount of solid material placed in the struts and the total amount of solid phase, as it can be seen in equation 5.

$$f_s = \frac{m_{struts}}{m_{struts} + m_{walls}} \quad (5)$$

Cell wall thickness, ξ

Figure 2.8. ξ

To characterize the solid phase between two cells, the average cell wall thickness is used.

The cell wall thickness is defined as the thickness of the solid part that separates two cells measured in the central area of the cell wall (which is typically the area where this value reaches a minimum for a given cell wall) (**Figure 2.8**). Inside a cellular material, there are different cells and different cell walls; therefore, this parameter is not constant (there is a cell wall thickness distribution), so it has to be measured and averaged over a significant number of cell walls.

Nanocellular polymers are characterized by presenting cell wall thickness in the nanometric range, usually smaller than the cell size.

Open cell content, OC

Figure 2.9. OC

In a cellular material, cells can be completely isolated, wholly connected by a solid structure only consisting in struts, or intermediately connected by broken cell walls (**Figure 2.9**). The percentage of open cells is defined as the volume fraction of interconnected cells, and it is known as open cell content.

The specific methods used to experimentally measure all those parameters are explained in detail in section 3.4.

2.4. Production methods

Although microcellular polymers were discovered more than 40 years ago, their production at industrial scale did not occur until 20 years later [10], and even now very few companies distributed them, being their production still studied at laboratory scale and producing high impact publications [11–14].

Considering the evolution over time of microcellular polymers, it is comprehensible that the production of nanocellular polymers remains yet at a laboratory scale, being up to date one of the leading topics in cellular materials research.

Nanocellular polymers have been produced by using a wide variety of polymeric matrices. Thus nanocellular polymers in base polycarbonate (PC)[15], polyphenylsulfone (PPSU) [16], thermoplastic polyurethane (TPU) [17], polyetherimide (PEI) [18], polypropylene (PP) [19], or PMMA [20,21] can be found in the bibliography. Besides, single-phase polymer systems, nanocellular polymers based on miscible blends, nanocomposites, multiphase polymer systems or immiscible blends [22–25], have also been produced since the discovery of those materials. With this wide variety of cited nanocellular polymers, it would appear that their research is already covered, but nanocellular materials can be considered as very young materials.

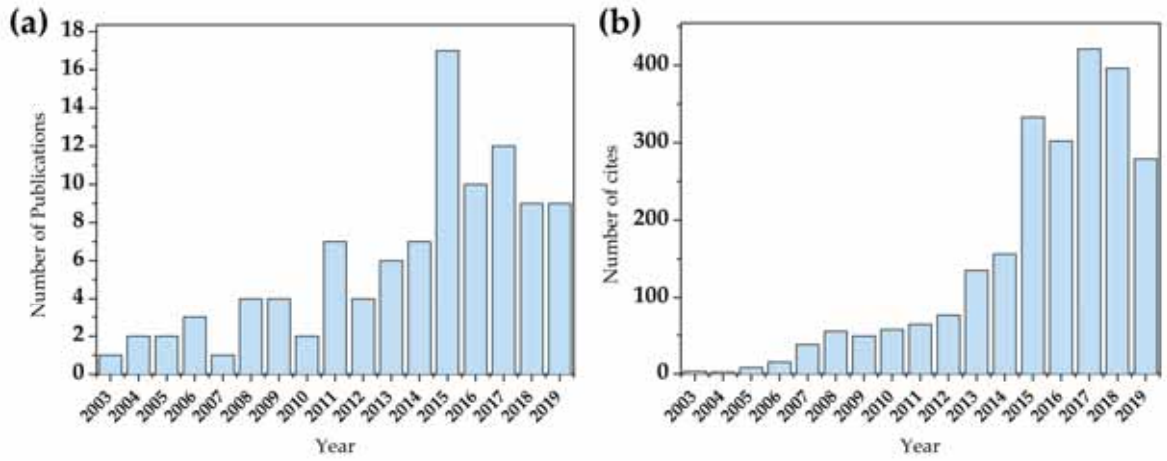

Figure 2.10. **a)** Number of publications regarding nanocellular polymers per year. **b)** Number of cites regarding nanocellular polymers per year (founded in Scopus with nanocellular polymer as topic).

As it is shown in **Figure 2.10,** first publications about this topic date from 2003 (**Figure 2.10a**), and it is not until 2013 when appears an increasing interest for those materials rising both the number of publications as well as the number of cites per year (**Figure 2.10b**). So, there is a great deal of further work still to be done. For example, nanocellular systems based in a single phase of polystyrene has not been produced except for small thicknesses; on the other hand, nanocellular systems previously mentioned are not any closer to being optimum. Their density, cell size, or their scaling up should be improved, and therefore, the production methods need to be further investigated.

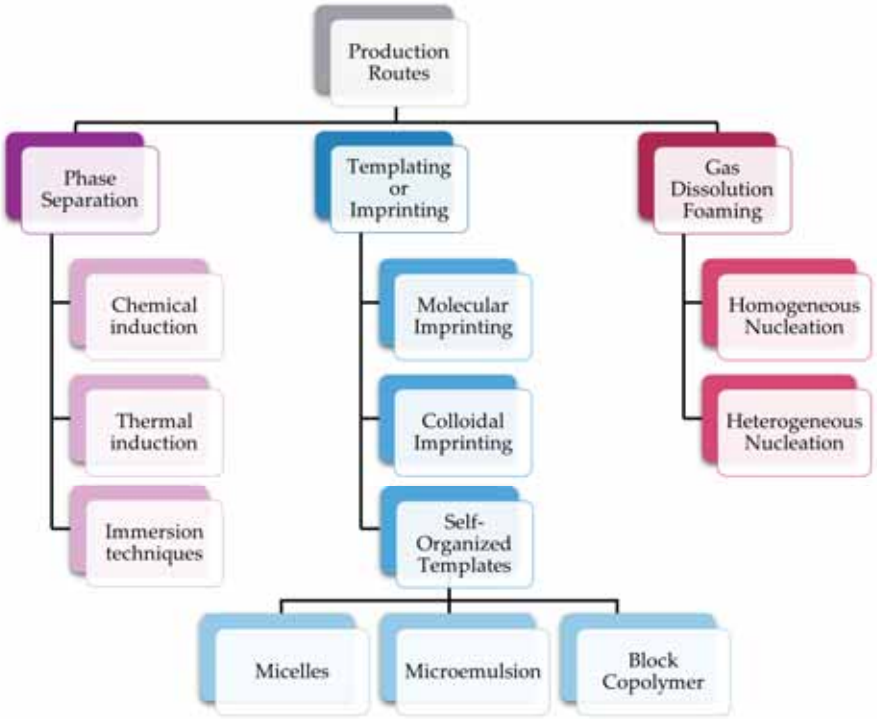

Figure 2.11. Nanocellular polymers production routes scheme.

The jump from the micro to the nanoscale implies a reduction in a hundred times in the cell size and an increment of the density of cells per cubic centimeter of ten thousand. This reduction in size is equivalent to the difference in size between a gothic cathedral and a mobile phone. Herein the difficult task is to generate such enormous amount of cells in the nanometric range. That means that previously used routes to manufacture microcellular polymers need to be reinvented or redefined.

Up to date, a large number of techniques have been used aiming at producing polymers with cell sizes in the nanometric range. The most important ones are summarized in **Figure 2.11** As it can be seen production routes can be classified into three different groups: phase separation techniques, imprinting or templating approaches and finally the gas dissolution foaming method [26].

Phase separation techniques

This method consists of inducing a phase separation between the polymer and the gas phase, either through chemical or thermal techniques or using immersion techniques.

When talking about the *chemical induction phase separation* (CIPS) the phase separation is triggered by a chemical quench [27,28], while in the *thermal induction phase separation* (TIPS) the phase separation is stimulated by an abrupt change in the temperature, that means a quenching [29,30].

However, the most promising phase separation technique for the production of nanocellular polymers is the *immersion technique*. In *immersion techniques,* a polymer solution precipitates at a constant temperature in a non-solvent bath or a solvent/non-solvent mixture (**Figure 2.12**). The phase separation is triggered by the diffusion of the solvent out of the polymer film to the bath and the non-solvent from the bath to the polymer [31]. This method have allowed to produce thin nanocellular membranes from different polymers such as polyamide (PA) [32], polycarbonate (PC) [31], polystyrene (PS) and poly(2-vinyl pyridine)[33] or polymethylmethacrylate (PMMA) [34], reaching with this last one nanocellular layers with nanocellular pores of around 100 nm.

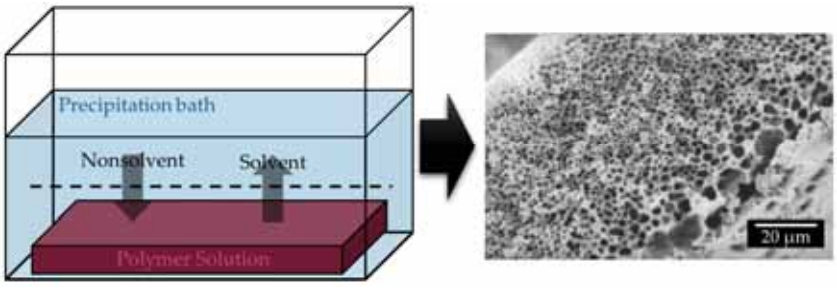

Figure 2.12. Immersion technique scheme an example of a PC membrane with nanocellular structure [31].

Imprinting or templating techniques

As their name suggests, in this second group of fabrication techniques, the cellular material is generated from a previous template that acts as porogen of the desired

polymer. Inside this group, three different techniques are included, molecular imprinting, colloidal imprinting, and self-organized templates, all of them following the same scheme (**Figure 2.13**).

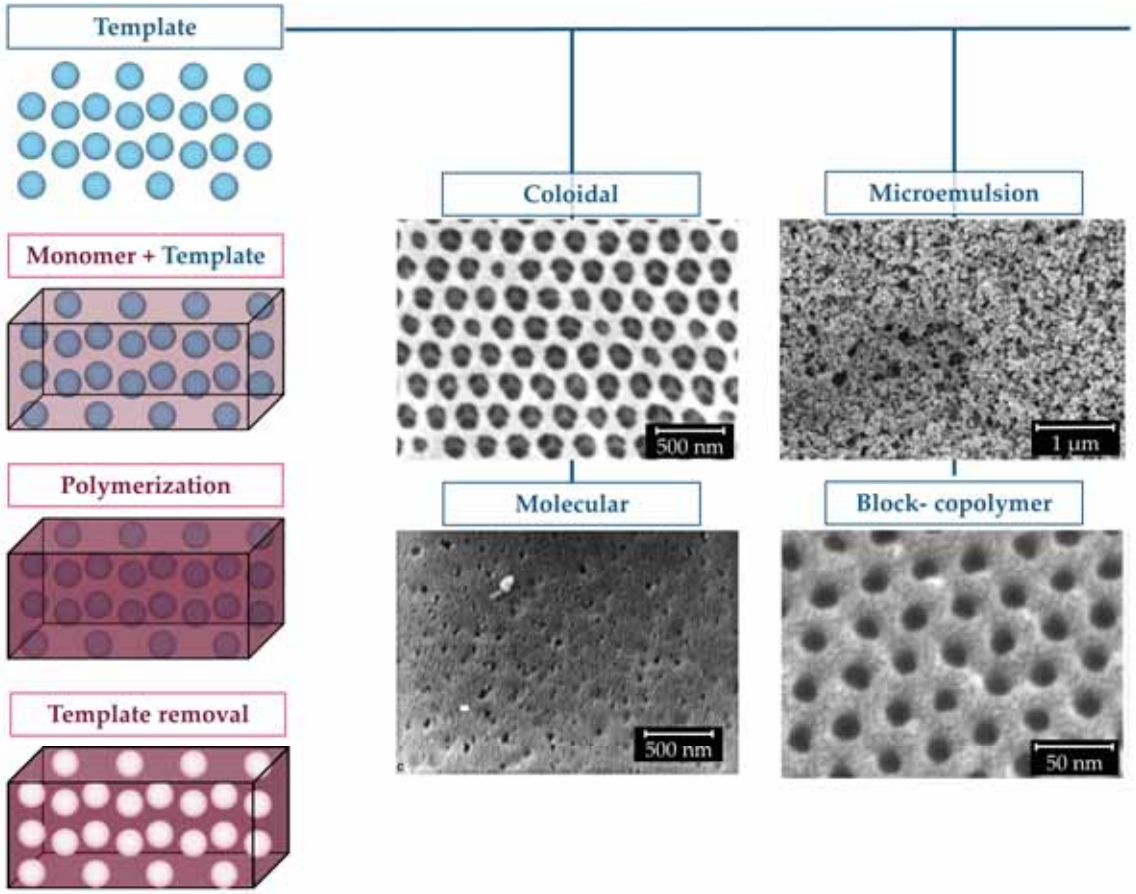

Figure 2.13. Scheme of imprinting or templating techniques, showing different nanocellular structures achieved [35–39]**.**

The initial monomer is mixed together with the porogene (it means the phase that acts as a generator of the cells) working as a template; the next step is the polymerization of the mix where the monomers merge around the given porogene. Finally, the template needs to be removed either chemically, thermally, or with some other extraction method, leading to the desired nanocellular polymer.

The main parameter changing between methods is the porogene. In the case of *molecular imprinting* a molecule is acting as "nanometric mould", this method allows the creation of cellular polymers with cell sizes ranging 10 nm that can act as sensors targeting small molecules or biological receptors, but the process is always limited to membranes no thicker than hundreds of microns [35,40,41].

In the case of *colloidal imprinting,* the template is given by a colloidal crystal that after the whole process should be removed in this case by extraction, dissolution, or calcination. This imprinting technique has led to the production of membranes with a microcellular structure in base polyurethane (PU) or polystyrene (PS) [36,42]. Moreover, also membranes with a nanocellular structure have been produced using polystyrene or

divinylbenzene (DVB) or ethylenglycoldimethacrylate (EDMA) as polymer matrixes [36,43].

Finally, as it was shown in the scheme of **Figure 2.11**, *self-organized templates techniques* is an additional process to take into account. For this technique, micelles, microemulsions, or block copolymers can be used as porogene.

In the first case, non-polar micelles are well dispersed in a mixture with the monomers and the cross-linking agents. Water is added as a medium to control the size of these micelles. In this case, a crosslinking process is carried out, and finally, the water is extracted, having a porous membrane with pore sizes from 10 to 50 nm as the final result [37,44].

Microemulsions and block copolymer techniques are, on the other hand, the two more common self-organized templates techniques.

A microemulsion is a mixture of two immiscible liquids by means of surfactants that makes possible to have a stable microstructure. This mixture group into domains that can act as porogene in the process previously schematized. Following this method materials presenting cell sizes from 65-400 nm have been produced [38], or thin membranes of Poly(Ethylene Oxide) (PEO) with pores as small as 2.5 nm [45].

At last, a block copolymer is suitable to act also as porogene. A block copolymer is a copolymer formed when two monomers cluster together forming blocks of repeating units. In this case, by choosing the correct mixture of polymers, it is possible to select the stable one as the matrix and the labile one as the dispersed phase, being possible to remove this last one chemically or thermally, leaving a nanocellular polymer as a result. This technique leads to thin films with cell sizes around 10 nm [46,47]. Moreover, a mixture of PS-PLA has been reported to reach pore sizes between 15 and 45 nm with thicknesses up to 1 mm [39].

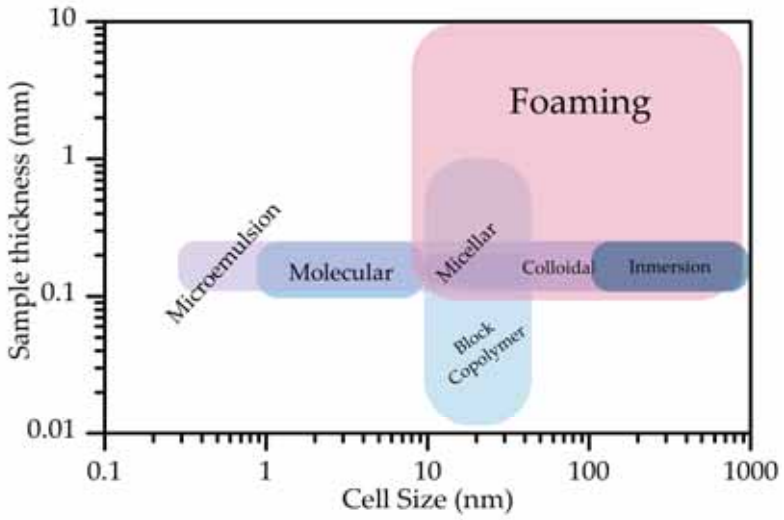

Figure 2.14. Nanocellular materials characteristics as a function of the different production techniques.

The previous techniques, allow the production of nanocellular polymeric structures but present two major drawbacks, the first one is the use of organic solvents that need to be removed after the whole process. The second one is shown in **Figure 2.14**, the production of nanocellular polymers with such techniques is limited to thin membranes of 1 millimeter at most.

Figure 2.14 also includes the range of cell size and thicknesses that can be reached with the gas dissolution foaming technique. As it can be seen, samples with a much higher thickness can be produced through this method, as explained in the next section.

2.4.1. Gas dissolution foaming process

The most promising foaming process, to date, for the production of thick samples of nanocellular polymers is the gas dissolution foaming process that is usually carried out by using carbon dioxide (CO_2) as physical blowing agent [6].

Use CO_2 as blowing agent is an excellent choice due to the good diffusion characteristics that it presents in its supercritical state and the easily accessible conditions for reaching this state (31 °C and 7.3 MPa). Additionally, it is a green solvent; it means it can be removed without leaving any residue or produce any pollutant compound [48].

Gas dissolution foaming is a physical foaming process, with the gas acting as the blowing agent. This process can be carried out in two different ways; the so-called two-step process and the one-step process. The two-step foaming process consists of four stages, saturation, depressurization, foaming, and stabilization that are carefully explained and schematized in the following paragraphs.

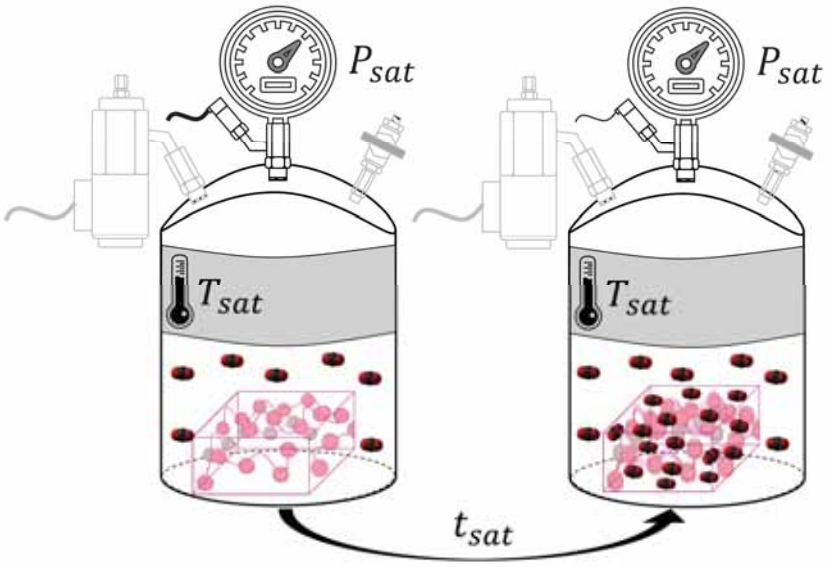

Figure 2.15. Scheme of the saturation step.

The process starts with the saturation (**Figure 2.15**). The initial solid polymer is placed inside a pressure vessel, where the gas is introduced at a specific pressure and temperature conditions, the so-called saturation pressure (p_{sat}) and saturation temperature (T_{sat}), and the diffusion process starts. CO_2 diffuses inside the solid polymer, occupying its free

volume; as it is shown in **Figure 2.17.** The gas is incorporated between the polymer chains at the molecular scale, forming a homogeneous single-phase system. As it can also be seen in **Figure 2.17** when carbon dioxide is introduced between the polymeric chains, it induces a higher mobility; this effect results in a decrease of the initial glass transition temperature of the polymer (T_g) to a lower one, the effective glass transition temperature ($T_{g_{eff}}$). The diffusion process continues up to saturation; it means until the polymer does not admit more amount of gas at the given conditions of pressure and temperature. The amount of supported gas is given by the solubility limit defined as the maximum concentration for which only a single phase occurs, this limit depends on the polymer/gas system. After the saturation time (t_{sat}) the first step can be considered complete.

The second part of this technique is the depressurization step (**Figure 2.16**). Herein the pressurized gas is fast released at a certain depressurization velocity (v_{dep}) leading to a thermodynamical instability inside the polymer. When the polymer is subjected to high pressures, it admits a higher amount of gas, decreasing such pressure to atmospheric leads to a supersaturation state of the polymer. It means the polymer no longer supports such amount of gas due to the solubility limit decreases at those conditions and the equilibrium between the gas and the polymer is broken leading to, on the one hand, the diffusion of the gas outside (governed by the desorption diffusivity D_{des}) of the polymer and, on the other hand, to phase separation. As it schematized in the third step of **Figure 2.17**, the gas phase is now clustered in small nucleation points that will be essential for the formation of the final cellular material.

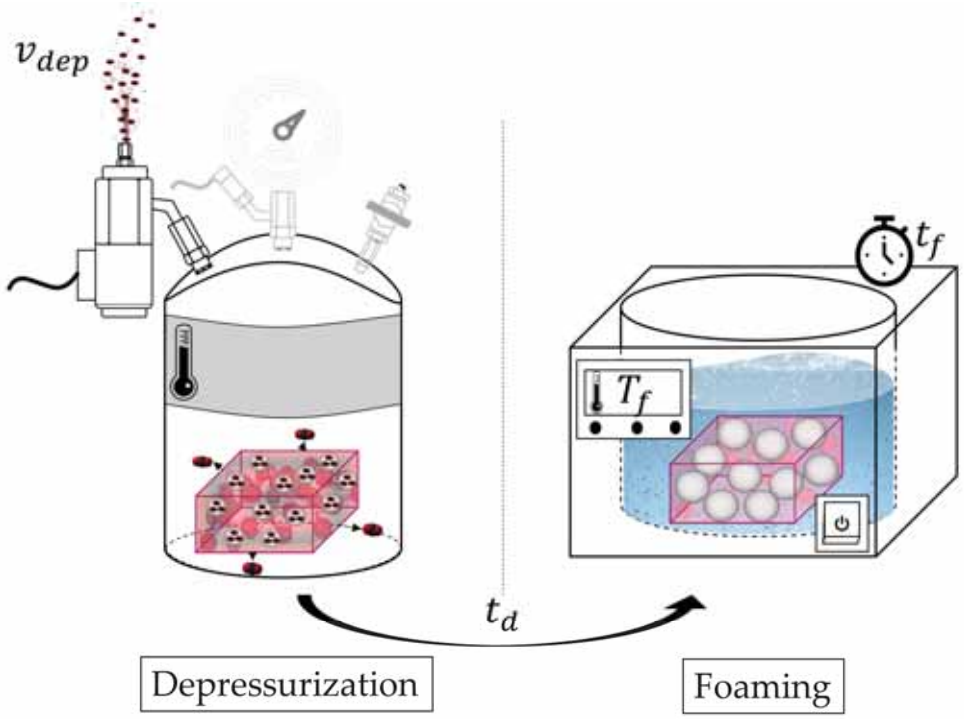

Figure 2.16. Scheme of the depressurization and foaming steps.

After the desorption time (t_d) (time between the depressurization and the beginning of the foaming) the polymer is heated, usually in a thermal bath, thus starting the foaming

step (**Figure 2.16**). In this stage, the polymer is heated at the foaming temperature (T_f), higher than the effective glass transition temperature reached in the previous step, during some time (foaming time, t_f). This foaming temperature makes the polymer to be in a plasticized state; the increase in temperature gives the polymeric chains enough mobility to allow the nucleation points growing into the cells.

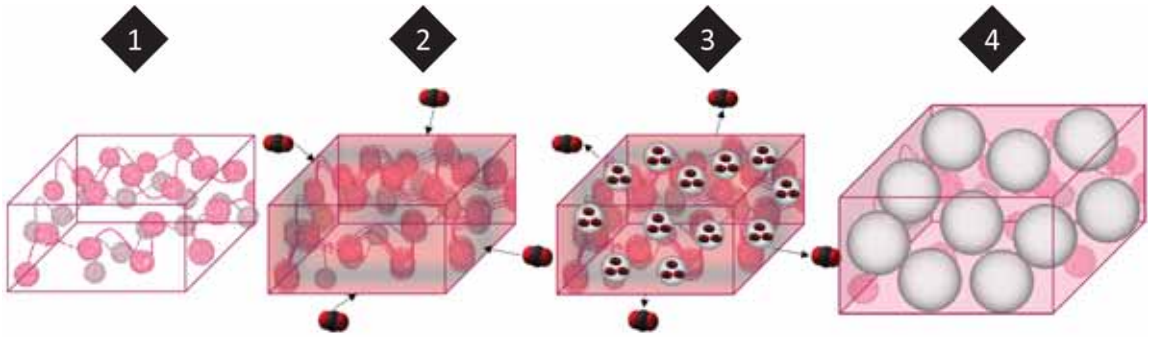

Figure 2.17. Evolution of a polymer sample under the gas dissolution foaming process.

It should be highlighted that although those three steps have been described as separate processes, the boundaries between them are not always so clear, and some of the steps could co-occur. For example, it has been explained that nucleation points are created due to a thermodynamic instability, but an increase in the temperature can also trigger this process. For this reason, the nuclei formation can be happening due to both depressurization and foaming as it will be later explained.

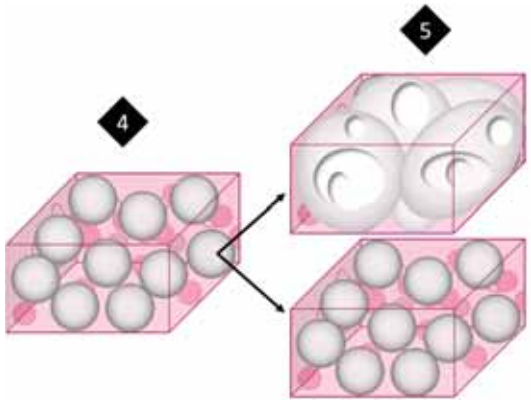

Figure 2.18. Scheme of the stabilization step of the gas dissolution foaming process.

Once the cellular polymer is created, it is essential to consider the fourth and last step, the stabilization of the cellular structure. As long as the temperature is higher than the effective glass transition of the polymer, the material continues growing. If this situation enlarges, it can lead to degeneration mechanisms resulting in the deterioration of the original cellular structure when the cell walls are broken, and many cells have joined together reducing the final number of cells and increasing its size (**Figure 2.18**). Those degeneration mechanisms group coalescence, drainage, or coarsening. To prevent such phenomena, the cellular structure should be freezing to stop further foaming, that means, at the end of the foaming process the material has to be cooled down at a temperature lower than the effective glass transition.

As previously said, gas dissolution foaming process could be done in an alternative way, the one step-foaming, where the depressurization and foaming steps are merged into a unique one. This is achieved by increasing the saturation temperature above the $T_{g_{eff}}$, allowing the polymer to foam during the depressurization step.

During this apparently simple method, complex physical processes take place, so to obtain the desired final result, it is essential to understand them. It should be recalled that the ultimate purpose of this research was the creation of nanocellular polymers, that is cellular polymers with cell sizes in the nanometric scale. Considering the relationship between cell density (N_v), the porosity $V_f = 1 - \rho_r$, and the cell size (ϕ) (**Equation 6**), if a nanocellular material wants to be produced with cell sizes ranging 200 nm and assuming a porosity higher than 0.5, the cell density should be of the order of 10^{14} cells/cm^3.

$$N_v = \frac{6\,V_f}{\pi \phi^3} \tag{6}$$

Or what is the same, assuming no coalescence, the number of nucleation points created in the solid materials (**Equation 7**) should also be of the order of 10^{14} nuclei/cm^3.

$$N_0 = \frac{N_v}{\rho_r} \tag{7}$$

Therefore, the first step for obtaining such materials is to create this enormous amount of nucleation points; afterward, those points should be growing into cells avoiding at the same time the degeneration mechanisms.

Therefore one key aspect of this research is to understand the different possibilities for the generation of the required number of nucleation points.

As it was described, during saturation, the gas dissolves inside the polymer, and it is not until the depressurization when the polymer-gas system can give place to the nucleation points. In order for those nuclei to appear, phase separation is needed. There are two possibilities: spinodal decomposition and nucleation.

In spinodal decomposition, both phases, gaseous and solid one are split without the appearance of nucleation points, creating an interconnected gas phase and therefore a co-continuous cellular structure. This happens at high supersaturations and specific saturation conditions, where the polymer-gas mixture is unstable, then the energy characterized for the nuclei formation (Gibbs free energy (**Equation 12**)) vanishes and gas molecules immediately form clusters which rapidly grow and coalesce [49].

In all the other cases, phase separation occurs by nucleation, that is the method studied in this thesis. Inside this mechanism, two different approximation can be followed, homogeneous nucleation or heterogeneous one. This distinction is not always easy to establish, but in general, homogeneous materials can be considered those in which a second phase is not intentionally added, while heterogeneous materials are those in which

a second phase has been inserted with the aim of using this phase as preferent nucleation sites.

Materials in this thesis have been created by using homogeneous nucleation, but due to their importance, both approaches will be explained in the next section, although greater attention will be paid to homogeneous nucleation. Classical Nucleation Theory (CNT), initially developed for nucleation in liquid/vapor systems [50], has been historically used for the explanation of phenomena taking place during microcellular foaming [51,52]. However, its use for nanocellular polymers has been proved to be limited. Although the trends are correctly explained by this theory [53], it predicts the absolute values of the final number of nucleation points poorly [54,55]. Moreover, this theory does not consider the effect that factors such as the viscosity of the polymer has in the nucleation process. For this reason, a more detailed theory based in CNT will be used in this thesis (*see section Homogeneous Nucleation*).

I. Heterogeneous Nucleation

As previously explained, the nucleation is considered to be heterogeneous when a second phase is intentionally added in the polymer mixture aiming at promoting nucleation in the interphase between the two phases or in the second phase.

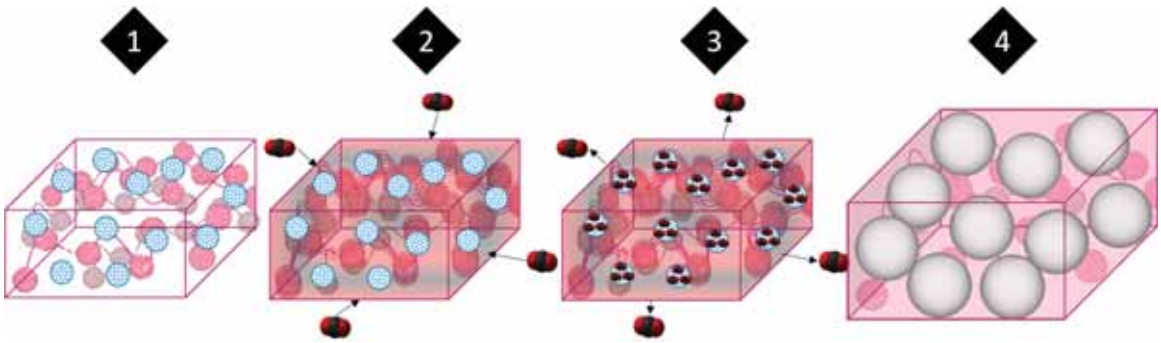

Figure 2.19. Scheme of a heterogeneous sample under the gas dissolution foaming process.

Considering the gas dissolution foaming process, the scheme in **Figure 2.17** should be modified as **Figure 2.19** shows. In this case, the second phase, already present in the solid matrix, is the preferred site of the gas to nucleate the cells when a thermodynamic instability takes place. In this situation, it can be said that the nucleation is mainly governed by this second phase.

Attending to the Classical Nucleation Theory, the rate of heterogeneous nucleation, defined as the number of nucleus per unit of solid volume and time is given by **Equation 8** [56].

$$N_{het} = f_1 C_1 \exp\left(-\frac{\Delta G_{het}}{k_B T}\right) \quad (8)$$

Where C_1 is the concentration of gas in the polymer, f_1 is the frequency factor of gas molecules joining the nucleus, k_B is the Boltzmann constant, T is the gas temperature in Kelvin and ΔG_{het} is the energy barrier for heterogeneous nucleation.

This equation given by the CNT is helpful to understand the differences between the heterogeneous nucleation and homogeneous one. It can be considered that the equation governing the nucleation in the heterogeneous process is essentially the same that for homogeneous nucleation except for the expression of the energy barrier.

As it was already explained, in order to form a nucleus, it is necessary to overcome an energy barrier. The addition of a second phase is a strategy to reduce this energy in comparison with the one needed when talking about homogeneous nucleation.

$$\Delta G_{het} = \frac{16\pi\gamma^3}{3\Delta p^2} f(\theta) = \Delta G_{hom} f(\theta) \quad (9)$$

Thus, the Gibbs free energy barrier for heterogeneous nucleation (**Equation 9**) depends on the surface tension between the pore and the polymer phase (γ), the pressure difference between gas and solid (Δp), factors common to the homogeneous nucleation, and an extra one, $f(\theta)$, that is a function defining the ratio between homogeneous and heterogeneous nucleation. This function takes values equal or smaller than one, introducing this way the contribution given by the interphase. This is a function of the wetting angle of the polymer-additive-gas interface **Equation 10** [56]**.**

$$f(\theta) = \frac{1}{4}(2 + cos\theta)(1 - cos\theta)^2 \quad (10)$$

It can be concluded then that a second phase reduces the energy necessary to create a nucleus, but in order to obtain a nanocellular polymer, it should be taken into account that the final cell nucleation density should be higher than 10^{13} nuclei/cm^3. Which means that the interphase should be dispersed along the polymeric matrix with a density similar to the one desired for the cells. Then it is mandatory to introduce a minimum of 10^{13} nucleation species per cubic centimeter of the solid material.

Nanocellular materials by using heterogeneous nucleation have been achieved up to now with two types of additives acting as nucleating species, inorganic particles, or organic phases. When talking about inorganic particles, nanosilicas are the most popular additive [23,57], but also multi-wall carbon nanotubes (MWCNT) [58], organo-modified fluorohectorite (OMS)[59], polyhedral oligomeric silsesquioxane (POSS) [60,61] or organophilic montmorillonite (O-MMT) [62,63] among others have been used. Those particles have been added in polymers such as PLA[62,64], high density polyethylene (HDPE)[65], styrene-co-acrylonitrile (SAN)[66], PS [57], PC, or the most used one PMMA [59,67,68] or PMMA based copolymers such as; random copolymer 50% ethyl methacrylate (PMMA-co-EMA), random copolymer 9% ethyl acrylate (PMMA-co-EA)[60]. Among all those systems and added particles, the most promising results are those achieved by Costeux by mixing PMMA and PMMA-co-EA with nanosilicas leading to nanocellular materials with relative densities smaller than 0.23 and minimum cell sizes of 95 nm. Moreover, by mixing PMMA-co-EMA with POSS nanocellular materials with cell sizes ranging 100 nm combined with a relative density of 0.16 have been achieved [60]. Bernardo et al. produced bimodal cellular structures [69] using PMMA with sepiolites as

nucleating agent. Samples with relative densities around 0.24 and nanocellular populations of 300 nm were achieved [68].

On the other hand, when using nanostructured polymers, although other examples can be found ([25,66,70–74]) the most used system, in this case, is PMMA with a second dispersed polymer such as MAM [75–79] or TPU, herein the most promising results are those presented by Wang, in the PMMA/TPU system with cell sizes around 250 nm and relative densities of 0.125 [80].

Taking into account these works, especially the ones carried out in the Ph.D Thesis of V. Bernardo [69,81,82], it is clear that the final cellular structure is critically determined by the second phase and parameters related with it; such as the amount of particles/micelles, the dispersion in the matrix, the interaction of the second phase with the blowing agent or in the case of nanostructured polymers the molecular weight of the dispersed one, among others. In these systems, the production parameters are less critical (i.e., nanocellular polymer can be produced with a wide range of processing parameters).

The situation radically changes when homogeneous nucleation is considered, in this case, the only players are the gas and the polymer, and the only way to interact with the gas/polymer system is by controlling the production process using the production parameters as it is explained in the next section.

II. Homogeneous Nucleation

Homogeneous materials have been claimed to be those in which no second phase or nanostructuration is intentionally added. So, it can be said that, in this context, homogeneous materials are those presenting a single phase, in which cells are created without any help but the gas itself. Or if there are additional phases, they are not playing a critical role during nucleation. Those materials are the ones used for developing this thesis. Therefore the understanding of the process taking place in them during gas dissolution foaming is mandatory. An in-depth study about the influence of all the process parameters on the final cellular structure will be carried out in this section while mentioning all the previous works dealing with this topic.

As it was explained before, the formation of stable nuclei requires to exceed an energy barrier. Clusters of gas are formed due to the induced instability, then, as it is shown in the scheme of **Figure 2.20**, the evolution of this cluster into a stable nucleus giving place to a cell, is associated to the free energy.

The radius of a cluster of gas will evolve becoming higher with higher given energy, if the free energy is high enough and reach the value known as free energy barrier (ΔG_{hom}) then the radius of the nuclei will reach the size r_c, known as critical radius, and additional gas molecules will join this nucleus, starting the formation of a bubble. Conversely, if the energy is not enough, this cluster will be re-dissolved.

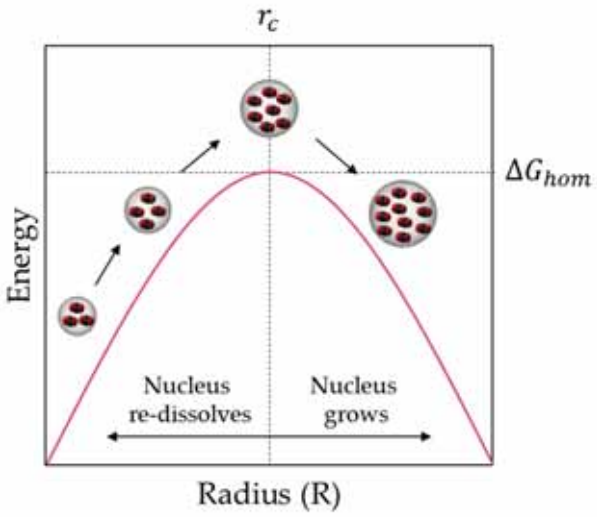

Figure 2.20. Scheme of the evolution of a nucleus of radius R indicating the energy barrier (ΔG_{hom}).

The Gibbs free energy barrier and the critical radius are both magnitudes related with the interfacial tension between the gas bubble and the polymer, γ, and the difference between the gas pressure and the solid one, ΔP. Their expressions are given in **Equations 11 and 12**.

$$\Delta G_{hom} = \frac{16\pi\gamma^3}{3\Delta P^2} \tag{11}$$

$$r_c = \frac{2\gamma}{\Delta P} \tag{12}$$

The homogeneous ratio of nucleation defined as the number of nucleation points per unit of solid volume and unit of time is then related to those quantities. According to the homogeneous nucleation theory, developed by Colton and Suh [56,83], the cell nucleation density for homogeneous materials (N_{hom}) can be described with **Equation 13**.

$$N_{hom} = f_0 C_0 \exp\left(-\frac{\Delta G_{hom}}{k_B T_f}\right) \tag{13}$$

Where f_0 is the frequency factor of gas molecules joining the nucleus, C_0 the concentration of gas in the polymer, k_B the Boltzmann constant, T_f the gas temperature during the foaming and ΔG_{hom} is the already described Gibbs free energy barrier **Equation 11)**.

As it has been mentioned, CNT overestimates the value of cell nucleation density. This is due to the fact that CNT is not taking into account viscoelastic effects and other mechanisms potentially contributing to the creation, stabilization, or destruction of nuclei.

To correctly predict nucleation and growth in nanocellular materials, different theories have been developed over time. The first ones were able to model single bubble growth; the simplest was established by Street et al. and more complex dynamics were added in further models (Amon et al. or Venerus et al.) [84–88]. It was not until 1996 when Shafi et al. were able to simulate nucleation and growth at the same time [89,90], thanks to the introduction of a new concept: the Influence Volume, that will be later explained. This model permitted to introduce the effect of parameters such as the depressurization velocity or the viscosity on the cellular structure evolution. From this moment, different models have tried to combine the Influence Volume concept with the CNT trying to correctly simulate the production process of polymeric cellular materials [91–93]. The most detailed model, up to date, for nanocellular materials, is the one developed by Costeux et al. [49,94].

Although all those theories have successfully predicted some experimental results, they have only studied the effect of one parameter each time on the final cellular structure. Thus, for example, Costeux et al. were able to model the impact of the saturation pressure and temperature on the final cellular structure or the effect of the depressurization velocity on the cell size, the cell nucleation density, and the cell size distribution by maintaining constant the rest of the parameters.

However, during the production process of nanocellular materials, the production parameters affect simultaneously to the cellular structure, that is, there exists competition between parameters such as saturation pressure, diffusivity, pressure drop rate or viscosity, being difficult to determine the real contribution of each one separately. Throughout this thesis, different experiments have been carried out, trying to clarify the effect of each production parameter on the characteristics of the produced material, taking into account the mentioned simultaneous effects. The obtained results have been deeply studied and related to the theoretical models in the literature. This comprehensive analysis has led to developing this state of the art where the theories have been carefully selected to theoretically explain the individual influence of all the production parameters on the cellular structure as well as the competition between them, analysis that have not been previously reported.

The primary model used herein is based on the one developed by Costeux et al.[49] that rely on CNT but introduces some necessary changes for the understanding of nanocellular foaming.

This model is built on the approach proposed by Shafi et al. that consider both nucleation and bubble growth to predict values of cell size and porosity. As previously

commented, this model introduces a new concept, the influence volume (IV) that will be explained in the following paragraphs. The first steps, followed by the gas/polymer system, are assumed to be conceptually the same that those described by the CNT. The gas phase is dissolved into the polymer matrix up to depressurization where instability is induced, resulting in gas cluster formations that will grow into cells. The influence volume is then defined. When a stable nucleus is formed, it means when $R > r_c$, then surrounding gas molecules are attracted to it and start to diffuse into this nucleus. This situation causes a gas concentration gradient from the bubble surface as it is showed in **Figure 2.21a**. The concentration inside the new cell is represented by the pinkish tone; near the surface of the nascent cell, the concentration of gas is small, becoming higher as moving away up to reach the maximum gas concentration value again. This halo of diffusing gas is called influence volume.

This innovative concept changes the perspective of nucleation theory in two essential points. The first one is to assume, that each new nucleation point created inside this influenced volume, cannot evolve into a new cell due to gas molecules diffuse preferably to the one already created stable nucleus. So new nuclei can only appear in the non-influenced volume (UV). This reduces the rate of nucleation and allows obtaining more accurate predictions.

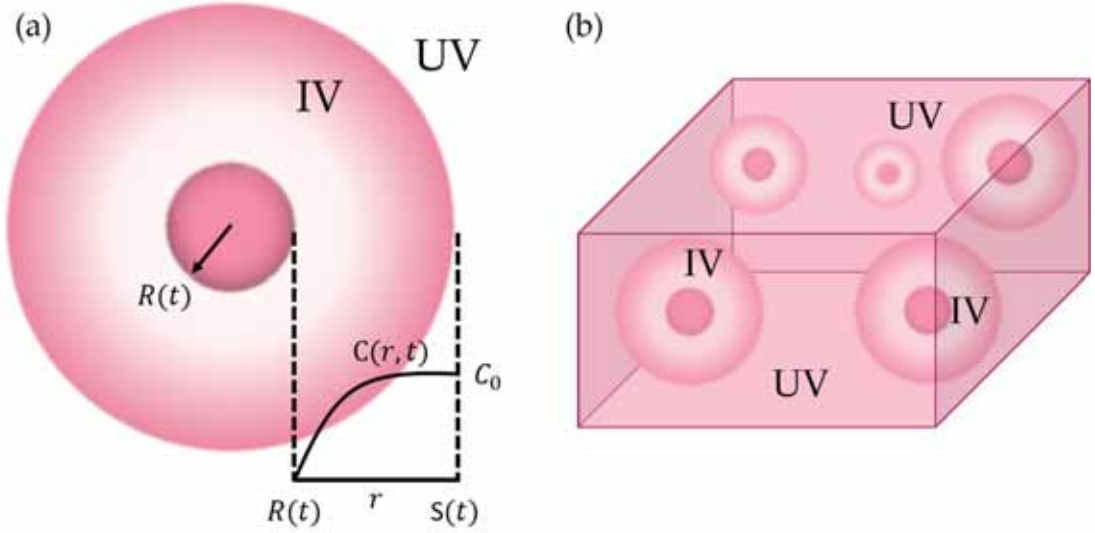

Figure 2.21. a) Scheme of the gas concentration profile near a nascent cell. **b)** Scheme of the influence volume inside a polymer while nucleation and growing.

Moreover, Influence Volume enables to consider a nucleation time, it means, this model assumes that nucleation does not occur instantaneously, and it takes some time to trigger it. This allows introducing the influence of parameters not taken into account by CNT such as viscosity, diffusivity, or pressure drop rate in the final number of nucleation points.

Then the main equations governing this model are the ones describing the total number of nucleation points as well as the cell growth. Thus, the number of created nuclei is given by **Equation 14:**

$$N_0 = \int_0^t N_{hom} V_L dt \tag{14}$$

Where N_{hom} is given by the CNT equation (**Equation 13**), and V_L is the non-influenced volume available at a time t, that is defined with **Equation 15**:

$$V_L = V_{L0} - \int_0^t N_{hom}\,(t-\tau) V_L(t-\tau) V_{cb}(\tau) d\tau \tag{15}$$

With V_{L0} being the total polymer volume when $t = 0$ and V_{cb} is the influence volume that surrounds each cell.

On the other hand, cell growth is defined by assuming the conservation of mass and momentum both inside the cell and the IV, and the expression is the one showed in Equation 16:

$$\frac{dR}{dt} = \frac{\Delta P \cdot R}{4\eta} - \frac{\gamma}{2\eta} \tag{16}$$

With η being the viscosity of the polymer/gas mixture, and γ the interfacial tension between the gas bubble and the polymer.

These conceptual modifications make possible a better understanding of the influence of each process parameter on the final cellular structure. Following sections will be focused on how each process parameter affect the characteristics of the cellular structure giving experimental and theoretical results, based on the model described.

⟹ *Saturation Parameters Influence*

Saturation step is governed by the saturation pressure, saturation temperature, and saturation time. Going back to **Equation 11** and **13**, a discussion about the importance of $\boldsymbol{P_{sat}}$ and $\boldsymbol{T_{sat}}$ in the creation of the desired number of nucleation points will be carried out.

$$\Delta G_{hom} = \frac{16\pi\gamma^3}{3(\boldsymbol{P_{sat}} - P_{atm})^2} \tag{11}$$

$$N_{hom} = f_0 \boldsymbol{C_0} \exp\left(-\frac{\Delta G_{hom}}{k_B T_f}\right) \tag{13}$$

Firstly, a higher saturation pressure will increase the pressure drop reducing the free energy barrier and consequently enhancing the nucleation. Secondarily, attending to **Equation 16**, an increase in the pressure drop will lead to faster growth of the cells during foaming, a fact that will be discussed later.

On the other hand, the number of nucleation points is related with C_0, that as explained before is the amount of gas uptake, that is, the solubility of the gas in the polymer, being this parameter a function of the pressure and the temperature of gas $C_0(P_{sat}, T_{sat})$.

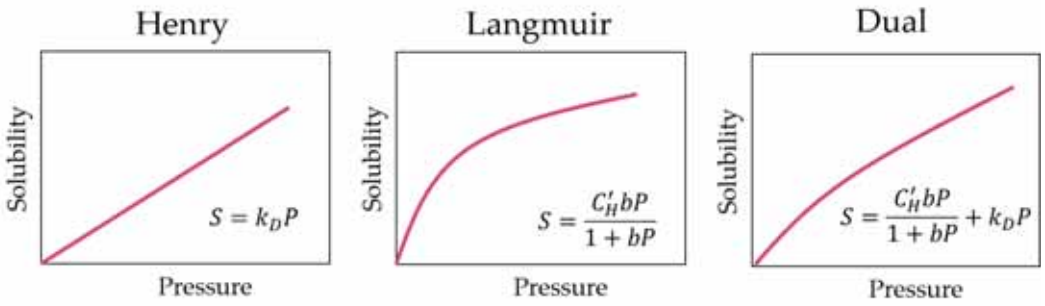

Figure 2.22. Dependence of the solubility with the gas pressure.

To start with, a common trend of solubility with saturation pressure is given by Henry's law (**Figure 2.22**). In this model, solubility depends linearly on saturation pressure being k_D the correlation parameter. This linearity is useful for some pressure ranges and a wide variety of polymers, however, it is usually necessary to enhance this model being the Langmuir's law and the Dual model more general equations (**Figure 2.22**) [95–97]. Despite the used law, the increase of the solubility with the saturation pressure is clear in all the models. Then, keeping in mind that the main objective is maximizing the number of cells, it can be concluded that. **Cell nucleation density is maximized by increasing the saturation pressure.**

The increase in the number of nucleation points implies a decrease in cell size. Supposing no coalescence conditions and two samples with the same relative density, in the same volume less number of cells can grow higher than a large number of them. So secondarily **an increase in the saturation pressure minimizes the cell size.**

Relative density depends on both the number of nucleation points as well as the cell size, an increase of both parameters leads to a reduction of relative density, so when producing nanocellular materials, while the increase in N_0 reduces the relative density the decline of the cell size results in an increase of it. So, the final result depends on the competition of both parameters. It can be said that **saturation pressure does not have a direct effect on the relative density of nanocellular materials**, because other effects need to be taken into account.

This dependence has been already proven in the bibliography for nanocellular materials produced from homogeneous polymers. Thus, as it can be seen in **Figure 2.23a**, Guo et al. determined the effect of the saturation pressure in the production of cellular

PPSU, showing that when saturating at a constant temperature of 20 °C, an increase of the saturation pressure from 1 to 7 MPa leads to an increase in the cell nucleation density, as the proposed theory predicts. This increase comes hand-in-hand with a decrease in the cell size (**Figure 2.23b**). This way PPSU with N_0 ranging 10^{14} nuclei/cm^3 and cell sizes around 20 nm were produced by increasing the saturation pressure to 7 MPa [98]. The results obtained by Costeux et al. in a blend of PMMA-co-EA also leads to the same conclusion; the increase of saturation pressure from 30 to 36 MPa at different saturation temperatures (55 and 35 °C) leads to an increase in the cell nucleation density and a reduction of the cell size while no direct effect is observed in the relative density. This maximization leads to homogeneous nanocellular polymers with a cell size of 164 nm and almost $9{\cdot}10^{14}$ nuclei/cm^3[49].

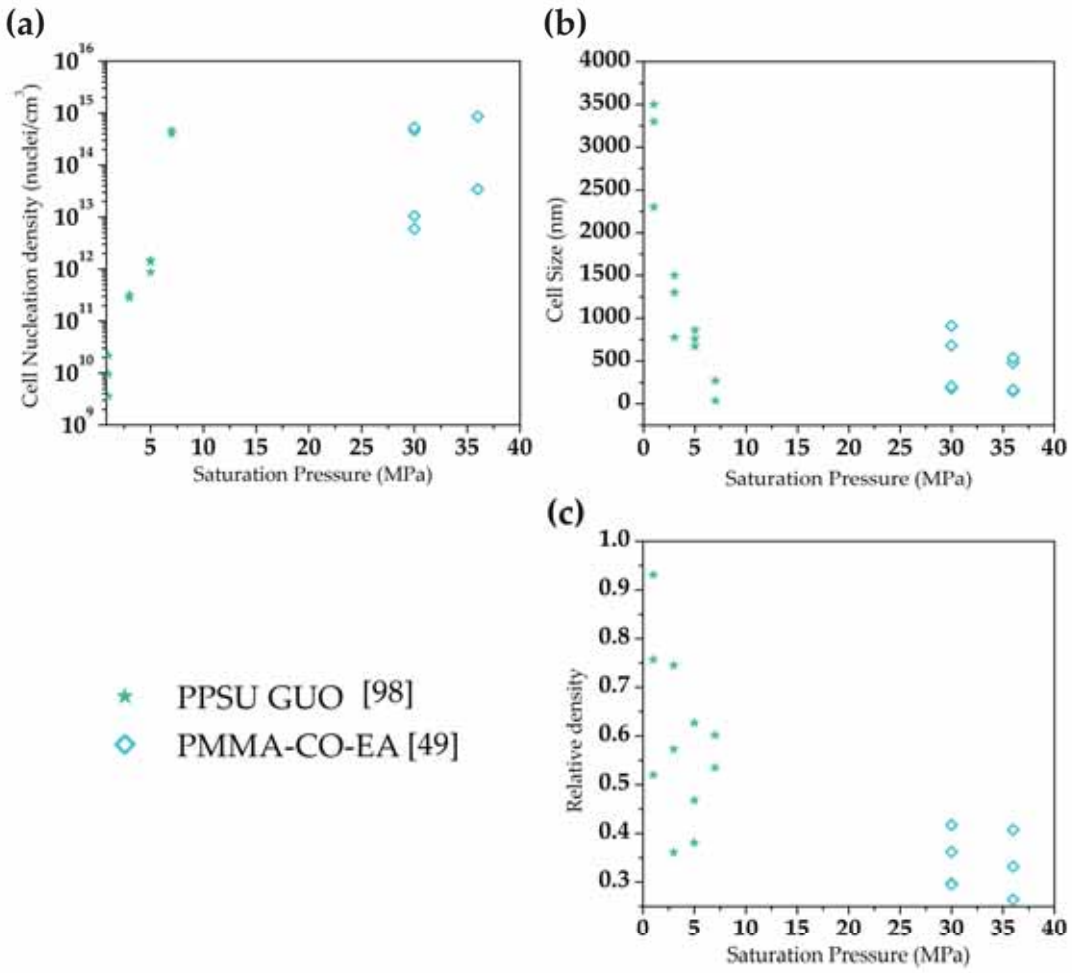

Figure 2.23. a) Cell nucleation density as a function of the saturation pressure for literature data. **b)** Cell size as a function of the saturation pressure for literature data. **c)** Relative density as a function of the saturation pressure for literature data.

On the other hand, the saturation temperature is also affecting the solubility, as indicated before. This dependence is given by Arrhenius equation:

$$S = S_0 \exp\left(-\frac{\Delta H_s}{R\boldsymbol{T_{sat}}}\right) \tag{17}$$

where S_0 is the preexponential factor, ΔH_s is the heat of sorption, R is the gas constant, and T_{sat} is the saturation temperature. The value of the heat of sorption depends on the used gas/polymer system, and also on the range of pressures and temperatures used due to the phase changes of gas. However, for CO_2-philic materials, that is, polymers with affinity for carbon dioxide, this value is negative. It means that an increase in the solubility is promoted by decreasing the saturation temperature. Therefore, the second requirement for the maximization of the nucleation points has been found. **Cell nucleation density is enhanced by the use of reduced saturation temperatures.**

The same way it was explained for saturation pressure herein a **decrease in the saturation temperature leads to smaller cell sizes and no direct effect on the relative density of nanocellular materials produced from homogeneous polymer is expected.**

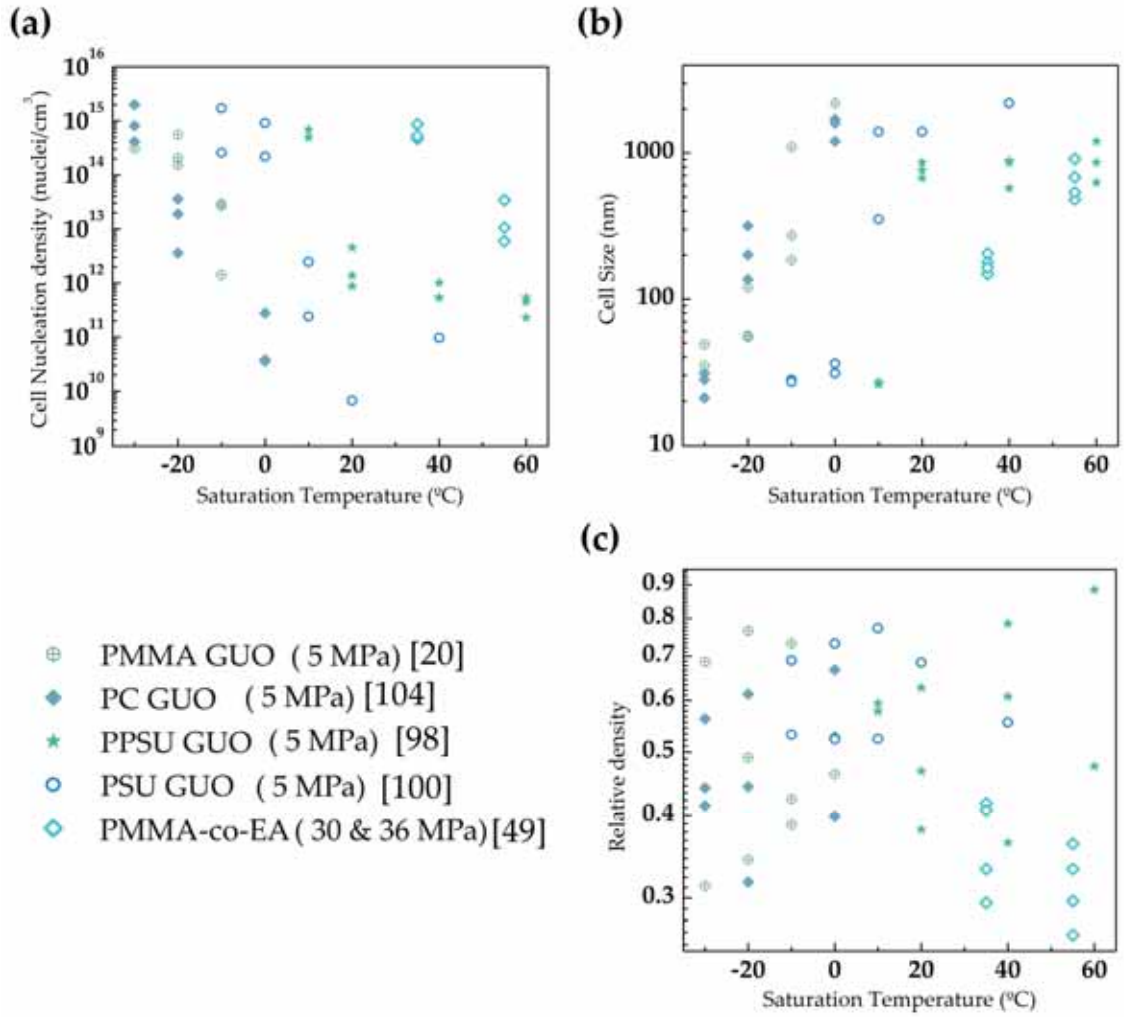

Figure 2.24. a) Cell nucleation density as a function of the saturation temperature for literature data. **b)** Cell size as a function of the saturation temperature for literature data. **c)** Relative density as a function of the saturation temperature for literature data.

Attending to the literature data, these assumptions can be confirmed (**Figure 2.24**). As it can be seen, several authors have observed those effects [15,49,98–100]. Thus, the increase of the cell nucleation density and the decrease of the cell size with the reduction

of the saturation temperature is evident in **Figure 2.24a** and **b**. Materials produced at -30 °C can be herein highlighted. Thus, PC with 21 nm and $4 \cdot 10^{14}$ nuclei/cm^3 was obtained and PMMA with 35 nm, and $3 \cdot 10^{14}$ nuclei/cm^3 were produced by this decrease in the saturation temperature.

Saturation time is given by the second Fick's law (**equation 18**). The solution of this equation depends mainly on the geometry of the sample and on the sorption diffusivity ($D_{sor}(T_{sat}, P_{sat})$) that depends on the gas/polymer system and is also influenced by saturation temperature and saturation pressure.

$$\frac{\delta C}{\delta t} = D \frac{\delta^2 C}{\delta x^2} \tag{18}$$

The dependence of the diffusivity with those two parameters is similar to the ones observed for the solubility. The pressure influence is given by **Equation 19** although normally it is enough with the linear term in pressure meaning that an increase in the saturation pressure leads to an increase in the absorption diffusivity of the gas in the polymer.

$$D = a + bP + cP^2 \tag{19}$$

The influence of the saturation temperature is also described with an Arrhenius law, as follows:

$$D = D_0 \exp\left(-\frac{\Delta H_D}{RT}\right) \tag{20}$$

where D_0 is the pre-exponential factor and ΔH_D is the activation energy for the diffusion process. Although in some temperature range and for some gas/polymer systems, this activation energy presents a negative value [20], the usual behavior is a positive value of this constant for the absorption process. That means that a decrease in the saturation temperature leads to a reduction of the diffusivity, which is reflected in an increase in the saturation time.

In conclusion, the requirements found up to now for the production of nanocellular polymers that is, maximum saturation pressures and minimum saturation temperatures, have the opposite effect in the diffusivity. High pressures will enhance the rate of absorption, while low temperatures reduce this rate. So, these two parameters will compete in the determination of this saturation time.

In any case, absorption diffusivity is important as far as the sample is fully saturated, once the whole saturation is achieved, this parameter should not affect the final cellular structure.

⟹ *Depressurization Parameters Influence*

When depressurization is carried out at a temperature lower than the effective glass transition (two-step process), it can be considered that this step is only affecting nucleation and not growing.

The main parameters to consider herein are the pressure drop rate ($\boldsymbol{\Delta P/\Delta t}$) or depressurization velocity, $\boldsymbol{v_d}$ and the desorption time $\boldsymbol{t_d}$. As it was shown in the previous step, the pressure drop itself, $\boldsymbol{\Delta P}$ affects the nucleation density, being beneficial to maximize this value. As it was explained before, nucleation is not an instantaneous process, that means that if depressurization takes too long, the pressure drop in each instant of time, will be smaller, leading to less number of nucleation points. So the ideal situation is to drop from the saturation pressure to the atmospheric one as fast as possible to maximize $\Delta P/\boldsymbol{\Delta t}$, which means that the depressurization should be quick. **Cell nucleation density is increased when the pressure drop rate is maximum.**

This fact has been only proved for microcellular polymers and theorized to have the same effect for nanocellular ones [101,102].

When foaming in one step, nucleation and growing co-occur, so the previous situation remarkably changes. In this case, the nucleation and the growing will compete for the available gas, playing the depressurization velocity a vital role in the final result. Herein, while nucleation, gas starts to diffuse into the stable nuclei for growing, this leads to an important change in the influence volume that will affect nucleation.

This is easily understandable considering a particular situation with two materials starting from the same conditions but subjected to different depressurization rates. **Figure 2.25** shows a scheme of two systems with the same initial amount of gas achieved through identical saturation conditions, but the depressurization velocity in the first case v_1 is higher than in the second one, v_2.

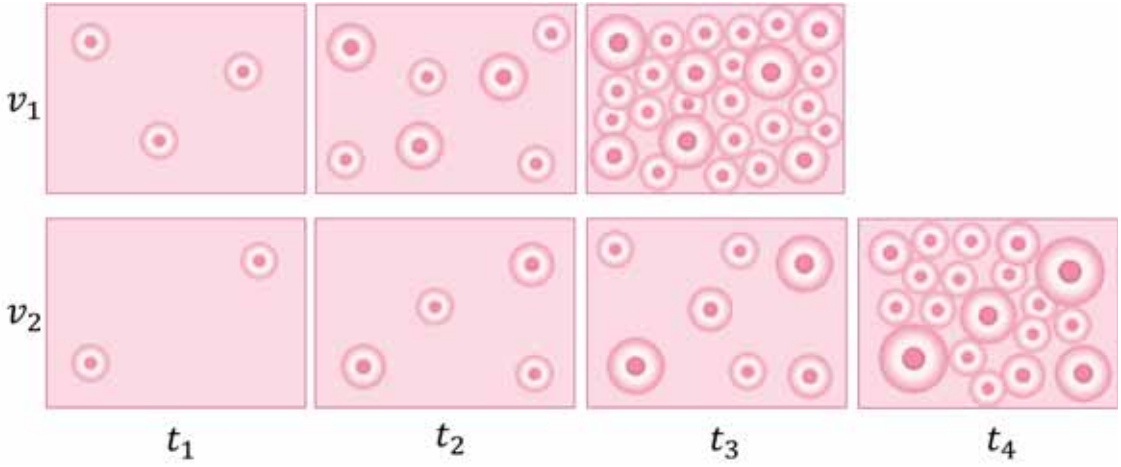

Figure 2.25. Nucleation and growth evolution of two materials with the same initial amount of gas but different depressurization velocities $v_1 > v_2$.

After a time t_1 from the initial pressure release, the achieved pressure drop rate in material 1 is higher than in the material 2, so the number of nucleation points is also higher.

The growth rate is even faster in material one. The higher nucleation rate, together with, the faster-growing results in a quicker increase of IV in material 1 than in material 2. It must be taken into account that whereas the growth rate is linearly proportional to the pressure drop the nucleation rate is equivalent to the exponential of $1/\Delta P^2$. So, the imbalance between material 1 and 2 is higher for nucleation density than for the size of the cells. Summarizing these differences in the drop rate leads to the following for each instant of time during depressurization:

$$v_1 > v_2 \begin{cases} \Delta P_1 \gg \Delta P_2 \rightarrow N_{0_1} \gg N_{0_2} \\ \dfrac{\delta R_1}{\delta t} > \dfrac{\delta R_1}{\delta t} \end{cases} IV_1 > IV_2 \tag{21}$$

The exponential increase of nucleation points together with the faster growing observed in material 1, reduces the time available for nucleation. So, at t_3 the influence volume of all the created cells are touching each other, with no more uninfluenced volume available, then nucleation stops. While material 2 is still growing, at a lower rate, so nucleation time enlarges to the final situation t_4 where the limit is achieved, with a final balance of a smaller number of bigger bubbles. That means that the same amount of gas has been used in material one preferably for nucleation and in material two for growing.

Moreover, when talking about one step foaming diffusivity must also be considered in this step. If simultaneously with a different depressurization rate, there exists a different diffusivity, then the final number of nucleation points will be influenced by the competition of these two parameters. This contribution can be quantified with the non-dimensional number N_p defined as follows [49]:

$$N_p = \frac{r_c^2}{D}\frac{dP_g}{dt} \tag{22}$$

Where P_g is the gas pressure in each instant of time. Then, if the depressurization rate is faster than the diffusivity, that means if the change of pressure is more rapid than the diffusion of gas into the cells; then the IV will grow slower than in the opposite situation when the diffusion of gas into the nascent cells is so fast that soon the UV dominates over the pressure drop, decreasing the cell nucleation density.

Additionally, to the depressurization velocity, the description of the effect of the desorption time is still pending. As explained before, simultaneously to nucleation, the gas starts to diffuse out after the release of the pressure. Diffusion velocity is determined by the desorption diffusivity ($\boldsymbol{D_{des}}$), that as D_{sor} increases with pressure (**Equation 19**). The growing phase requires the presence of gas, for this reason, it is essential not to enlarge $\boldsymbol{t_d}$ more than necessary to have available gas for the foaming stage. When the polymer is fully saturated the concentration of gas is equal through the thickness, when the gas starts to diffuse out of the material, the level of gas starts to decrease, this decrease is sharpest at the edge of the samples, leading to a concentration profile as that shown in **Figure 2.26a.**

As the gas concentration is critical for both nucleation and foaming, this concentration profile usually leads to the formation of both, a solid skin and a gradient from higher to

smaller cells. In the center of the sample where the concentration is maximum, the cellular structure will correspond to the one given for the used saturation and foaming conditions. When this concentration decreases near the surface, the nucleation will decrease, leading to a less number of larger cells, this situation continues leading to a gradient cellular structure from the center to the edges (**Figure 2.26b**). When reaching the outer part of the material, the concentration of gas is so small that during the foaming the effective glass transition is not low enough to allow the growing, leading to the so-called solid skin.

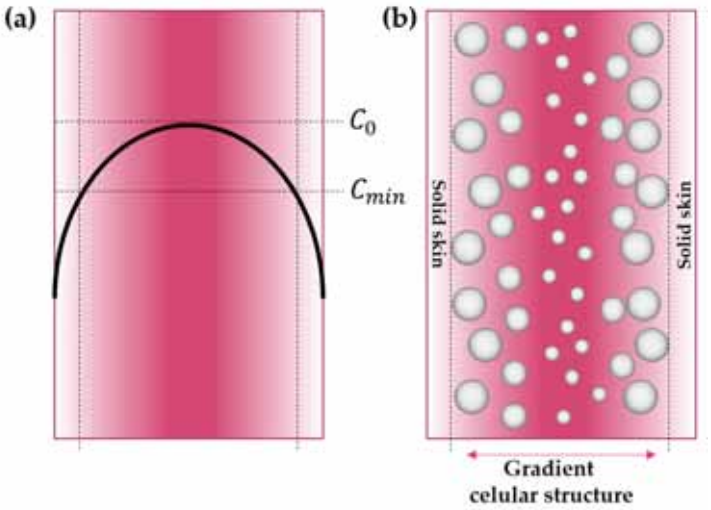

Figure 2.26. a) Gas concentration profile in the sample thickness. **b)** Solid skin and gradient cellular structure due to the gas concentration profile in the sample thickness.

If the desorption time enlarges the solid skin becomes thicker, and the volume of the sample with small cells is reduced. Due to this if the objective is maximizing cell density**, the desorption time, t_d has to be minimum.**

⇒ *Foaming Parameters Influence*

In this step, the parameters to consider are the foaming temperature $\boldsymbol{T_f}$ and the foaming time $\boldsymbol{t_f}$. As commented before the first requirement for the foaming temperature is to be higher than the effective glass transition temperature of the polymer. Additionally, resorting again to **Equation 13**, it can be seen that T_f has a direct influence on the number of nucleation points.

$$N_{hom} = f_0 C_0 \exp\left(-\frac{\Delta G_{hom}}{k_B \boldsymbol{T_f}}\right) \tag{13}$$

Therefore, **the number of nucleation point is maximized when increasing the foaming temperature.**

On the other hand, to reach the maximum expansion, the foaming time should be enough to consume the uninfluenced volume completely. **Foaming time should be high enough to achieve maximum expansion.**

The influence of the foaming temperature has been widely studied in the bibliography, as **Figure 2.27** shows. The general tendency is an increase in the number of cells when the foaming temperature rises. So independently on the used polymer, increasing the foaming temperature favors the creation of nucleation points. For each system, there is a foaming temperature for which N_0 is maximum. Further increase of this temperature leads to the degeneration of the cellular structure (those points were removed from the graph to observe clear tendencies). Accordingly to these previous publications, nanocellular PMMA reaches the maximum cell nucleation density when foaming at 50 °C [103] nanocellular PC when foaming at 110 °C, PSU when foaming at 150 °C, and PPSU at 200 °C [15,98–100]. Taking this data into account, it seems clear that this maximum foaming temperature is related to the original T_g of the polymer, fact that will be discussed in the *matrix influence* section.

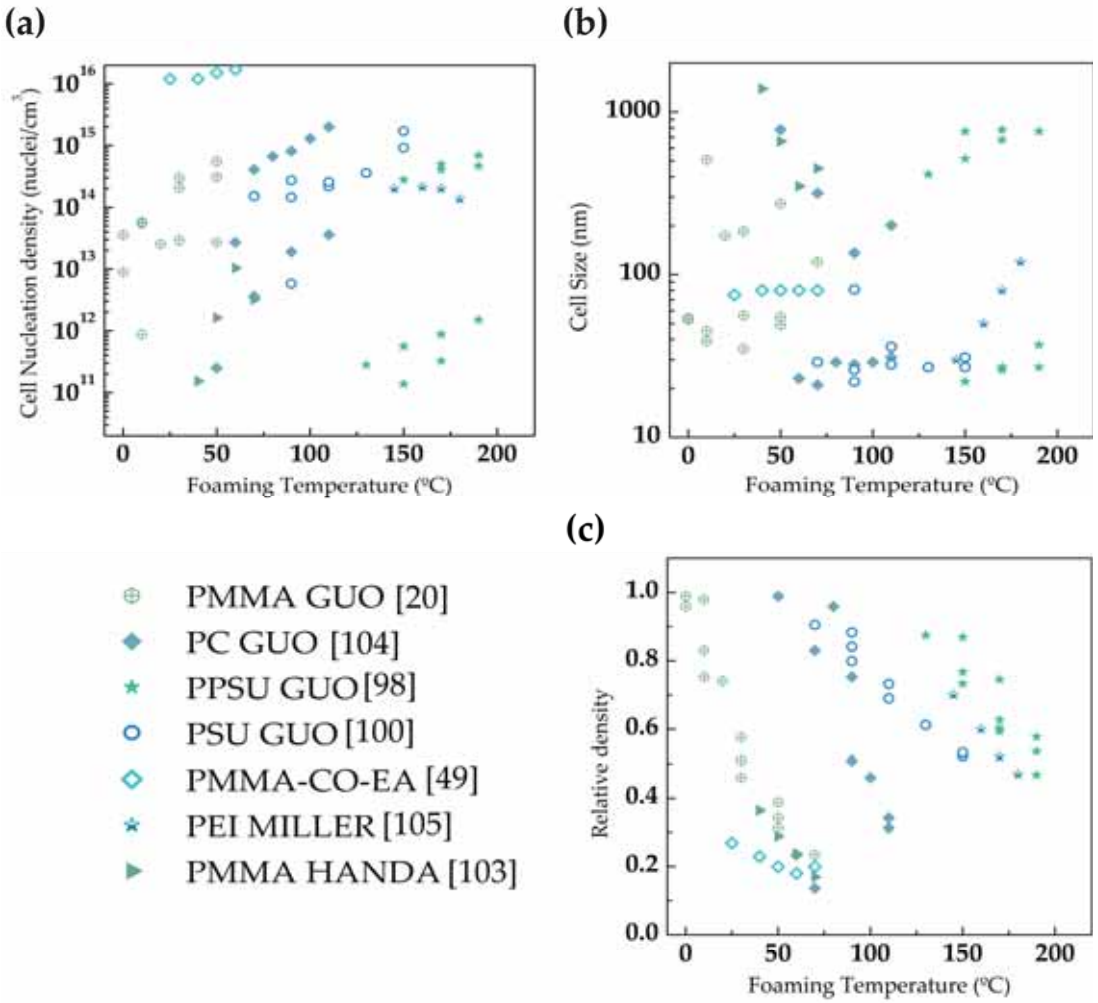

Figure 2.27. a) Cell nucleation density as a function of the foaming temperature for literature data. **b)** Cell size as a function of the foaming temperature for literature data. **c)** Relative density as a function of the foaming temperature for literature data.

By contrast to the observed when talking about the saturation parameters, herein the increase of the cell nucleation density is not accompanied by a decrease in the cell size (**Figure 2.27b**). This can be explained because several facts play a role in cell size. A higher

number of nucleation points should lead to smaller cell size, but an increase in the foaming temperature is also producing extra mobility to the polymeric chains, making it easier for them to grow. Both effects can compensate each other, and the cell size could be constant, in the range of foaming temperatures where N_0 growths. When degeneration happens at higher temperatures, cell size increases (those points were removed from the graph to observe clear tendencies). It can be then stated that **foaming temperature does not affect cell size in certain processing windows.**

So, for example, Guo showed that nanocellular PC saturated at 5 MPa and -30 °C, showed an increasing cell nucleation density from $2.70 \cdot 10^{13}$ nuclei/cm^3 when foaming at 60 °C to $2 \cdot 10^{15}$ nuclei/cm^3 when foaming at 110 °C while cell size remains almost constant having values around 25 nm [104]. On the other hand, an example of degeneration can be seen in the paper on PEI from Miller et al. [105], where N_0 decreases from 2 to $1.36 \cdot 10^{14}$ nuclei/cm^3, and cell size increases from 30 to 120 nm when foaming temperature increases from 145 to 180 °C.

The combination of both effects leads to the results observed in **Figure 2.27c**, a rise in the cell nucleation density while maintaining constant the cell size leads to a clear **decrease in the relative density when the foaming temperatures increases**

⟹ *Stabilization Parameters Influence*

Once the cellular structure has the desired characteristics, it is necessary to stop the growing abruptly to avoid degeneration mechanisms. Thus, the foaming temperature should be decreased up to situate it below the effective glass transition. Since depressurization, the gas diffuses out of the sample resulting in a progressive increase of $T_{g_{eff}}$. If $T_{g_{eff}}$ is higher than room temperature at the end of the foaming step, then it is enough to stabilize the material at room temperature. On the contrary, when the effective glass transition is still below room temperature, the sample should be maintained at a lower temperature prolonging this situation until the effective glass transition is again above room temperature. **The final material should be stabilized at a temperature below the effective glass transition temperature.**

⟹ *Matrix Influence*

Up to this point, the influence of the process parameters have been studied, but the final obtained foam will also depend on the properties of the used polymeric matrix. The properties of this matrix will also affect the obtained material. Thus, parameters such as the initial $\boldsymbol{T_g}$ of the material or its viscosity $\boldsymbol{\eta}$ would affect the cellular structure.

After the previous discussion the effect of the $\boldsymbol{T_g}$ on the material seems obvious; it will mainly affect in the foaming step. A smaller initial glass transition temperature will lead to a lower effective glass transition, being the difference between the foaming temperature and the $T_{g_{eff}}$ higher. **In conclusion, a polymer with a smaller glass transition will need a lower foaming temperature and a smaller temperature for stabilization.**

As it was observed in **Figure 2.27**, the optimum temperature varies for each system, so PPSU presenting a glass transition temperature of near 220 °C needs a higher foaming temperature for properly expansion while PMMA with a T_g of 114 °C expands with much smaller temperatures.

Additionally, the introduced model allows introducing the effect of the viscosity of the polymer matrix on the final cellular structure. Once more, the concept of the Influence Volume is essential to understand the impact of this parameter over the obtained foam. As mentioned before, in this model, the nucleation is assumed not to be instantaneous, meaning that cells nucleated first grow in detriment of the surrounding ones. That means that a slow growth rate of initial nuclei will enhance the creation of additional stable nuclei, and here is where the viscosity plays its role; a higher viscosity promotes a slower growth. **Therefore, to maximize the number of nucleation points, a higher viscosity is needed.**

This contribution also competes with the diffusivity, due to both are affecting the evolution of influence volume, and is defined by the Schmidt number [106] described as follows:

$$N_{Sc} = \frac{\mu}{\rho D} \tag{23}$$

Where μ is the viscosity of the polymer/gas mixture, ρ is the density, and D is the diffusion parameter. When the viscosity is high enough to slow down the diffusion of the gas to the nascent cells, the influence volume maintains small longer, and the number of nucleation points increases. When the viscosity is not enough, the diffusivity contributes to the fast enlarge of the cells and therefore the reduction of UV available, thus reducing the nucleation time. (This effect can be explained with the same scheme of **Figure 2.25** but changing the different depressurization rates by different viscosities where $\eta_1 > \eta_2$).

On the other hand, the used polymeric matrix also affects the growing phase. As it is predicted by **equation 16**, a smaller viscosity contributes to a higher growth rate. This would lead to a faster increase in the influence volume with the consequent reduction of nucleation points and the rise of the cell size. **Therefore, it is expected that a lower viscosity will enhance a higher expansion at the cost of a smaller number of higher cells.**

This effect was studied by Costeux et al. using different polymer blends [22]. In this paper, the viscosity of the different blends is used to explain the cellular structure changes. It is essential to point out that the used mixtures behave differently under gas pressure, so one of the polymers reduced their viscosity to a greater extent than the others. That means that to understand the behavior of those blends, the data of this viscosity under gas should be studied. **Figure 2.28** shows the different cellular structure characteristics as a function of zero shear viscosity of the SAN-MMA-EA (Styrene Acrylonitrile-Methyl Methacrylate-co-Ethyl Acrylate) system under gas pressure.

The discussed above is herein clear, an increase in the viscosity leads to an increase in the cell nucleation density and a decrease in the cell size. Herein both parameters are

affecting the relative density, and the range of variation is not very wide, being not possible to observe a clear tendency. On the other hand, taking into account another work of Costeux et al., working with PMMA-co-EMA [49], it can be seen how a decrease in the glass transition temperature of the used system (the glass transition is intimately related with the viscosity) leads to an increase in the cell nucleation density a decrease in the cell size and an increase in the achieved relative density.

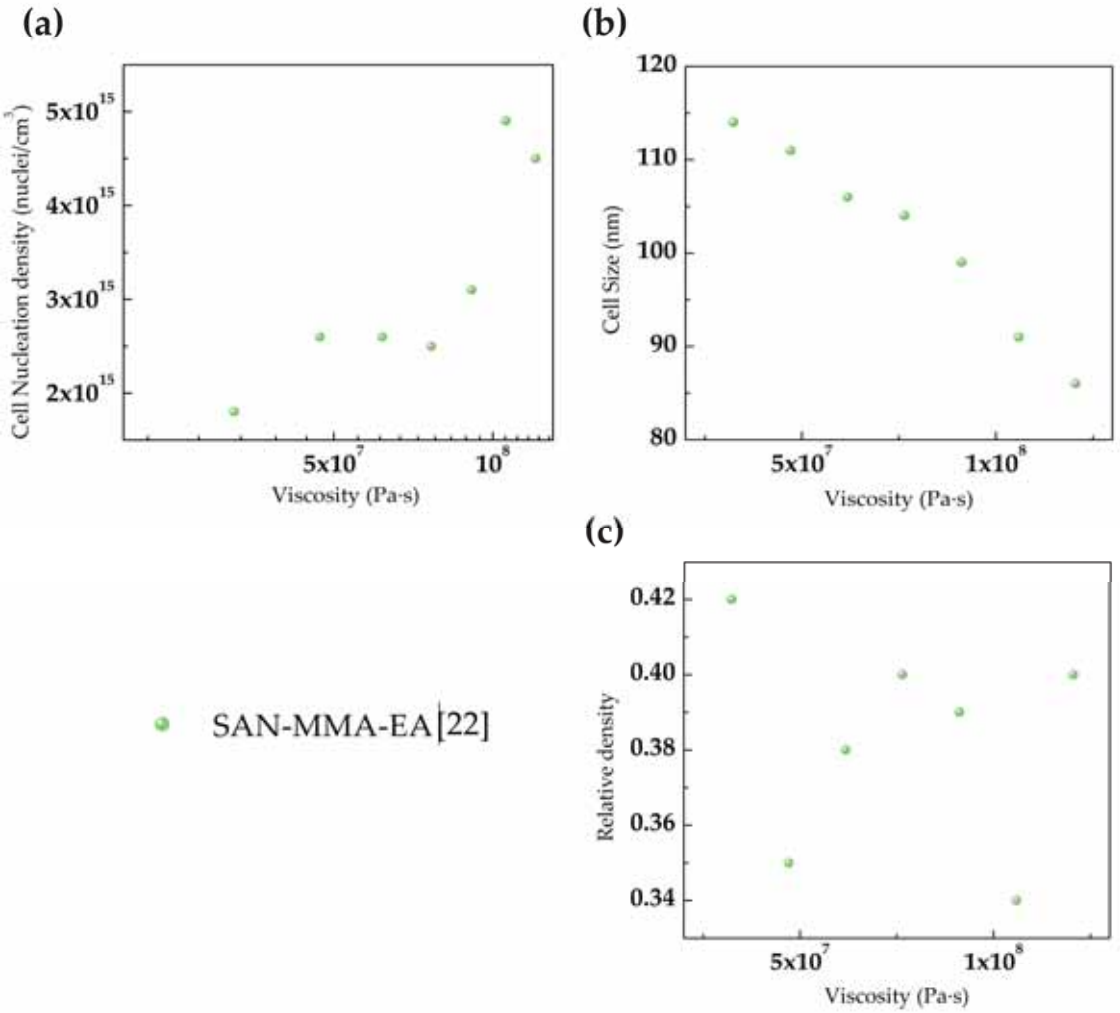

Figure 2.28. a) Cell nucleation density as a function of the viscosity for literature data. **b)** Cell size as a function of the viscosity for literature data. **c)** Relative density as a function of the viscosity for literature data.

2.5. Properties

Ultimately, the control of the cellular structure is essential to manipulate the properties of the created material. Thus, all the parameters listed before influence the final properties of the material, and therefore, they are defining the applications where cellular materials could be used.

As already highlighted, the importance of nanocellular polymers relies on their different properties in comparison with cellular materials presenting larger cell sizes, such

as micro or macrocellular materials. Microcellular materials have been already proven to perform better than macrocellular ones mainly when focusing on mechanical properties.

Nanocellular materials present promising characteristics that make them suitable for their use in applications where cellular polymers cannot be used. Nanocellular polymers can be used as membranes for micro and ultrafiltration or in catalysis and sensors applications due to their high specific area [78,107,108]. Moreover, it has been reported their potential use for surface nano-functionalization for biomedical applications [109–111]. However, for nanocellular materials, there is a long way to go, there are several theories about how those should perform. Some of those theories have been already proven or partially proved. However, the truth is that experimental facts are scarce; this opens a whole new world of possibilities for nanocellular materials still to be explored.

Some of the most exciting properties are related to their mechanical, thermal, and optical properties. The following sections describe the expected response of these materials, including the experimental data in the literature:

2.5.1. Optical Properties

The ability of a material to be transparent to visible light is given by the capacity of the waves to pass through without interfering with the material. When entering a medium visible light can be absorbed or scattered, depending on the magnitude of both phenomena all the incident light, a fraction or any of it will be transmitted.

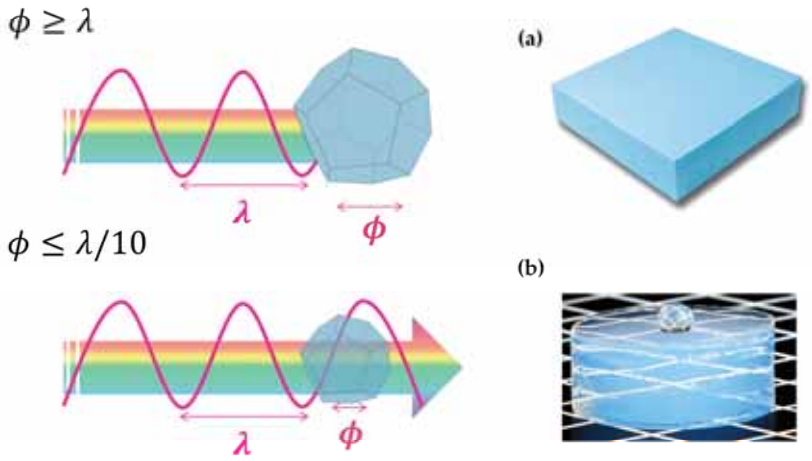

Figure 2.29. Scheme of the transmission of light through cells of different sizes. **a)** PU foam representing a cellular material with microcells. **b)** Silica aerogel showing a cellular material with nanocells.

When talking about polymeric cellular materials, while any absorption takes place in the polymer matrix, the pores act as scatters of visible light. The amount of scattered light and therefore of the transmitted one depends on the cell size (**Figure 2.29**).

The wavelength of visible light ranges from 450 nm to 750 nm. When the cell size is similar or higher than this wavelength (higher than a tenth of the used wavelength), it is not easy for the light to trespass the pores. When the light enters the bubble suffers a high scattering, that means that the light is dispersed instead of transmitted, resulting in an

opaque material (**Figure 2.29a**). But this situation can reverse if the pore reduces to values smaller than a tenth of the visible light (**Figure 2.29b**). Then the total amount of the scattered light becomes negligible, and it could be said that the pore is so small that it is almost invisible for visible light.

In conclusion, when the cell size is much bigger than the wavelength, no light dispersion is observed. When becoming comparable to the wavelength, the amount of scattered light raises, leading to opaque materials. Further reduction of the cell size results in a decrease in the total amount of scattered light up to minimal values that allows visible light to transmit again through the cellular material.

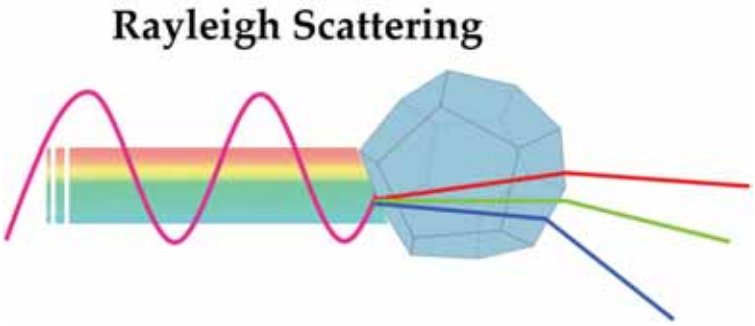

Figure 2.30. Scheme of Rayleigh Scattering in a cell smaller than a tenth of the visible wavelength.

When the size of the scatter changes not only the amount of light that is scattered is modified, but the direction in which the light is scattered. Thus, when the wavelength and the cell size are similar, the observed scattering is the so-called Mie scattering. In this case, most of the light is scattered forward at small angles. A reduction of the cell size below a tenth of the wavelength leads to a selective scattering that is known as Rayleigh Scattering. In this case, the light with smaller wavelengths (bluish colors) is greater scattered than those with higher wavelengths (reddish colors) (**Figure 2.30**).

This behavior is characteristic of silica aerogels. Silica aerogels are ultra-porous materials formed by small silica particles (2-50 nm of diameter) agglomerated into spherical secondary particles forming a matrix with pores smaller than 100 nm and ultra-low densities. Those materials have been widely proven to show a transparent character [112–116]. Nanocellular polymers show numerous similarities with aerogels, so it is reasonable to think that when presenting cell sizes smaller than 50 nm, they will behave similarly for visible light transmission.

Although this has been lately claimed in different works, there are few experimental pieces of evidence of the transparency of nanocellular polymers. Thus, Guo presented a film of nanocellular PC with an average cell size of 28 nm that shows transmittance of nearly 20% for red light, while a microcellular film of PC is entirely opaque for any wavelength [104]. Additionally, Pérez-Tamarit et al. showed that the transmittance of 1 mm in thickness cellular PMMA, increases from 0, when the cell size is around 500 nm, to values higher than 20% when the cell size is 20 nm. This work also reveals a significant

dependence with the wavelength, being the transmittance much smaller for a blue laser than for a red one [117].

2.5.2. Mechanical Properties

One of the main drawbacks for conventional cellular polymers is the loss of their mechanical properties in comparison with the former solid. This restricts their use for structural applications.

This problem seems to be solved by the development of microcellular materials in the latest 80s. Since their discovery, it has been proved for several systems that this range of cell sizes granted cellular materials with improved mechanical properties than those presented by polymers with larger cell sizes. Thus, where conventional materials were demonstrated to perform much worse than the solid, microcellular polymers have been proved to equal the specific mechanical properties of the former solid or, in some specific cases, even improve them. This has been experimentally proved up to now with numerous systems, the failure energy of polyvinyl chloride (PVC) with cell sizes around 3 μm was studied as a function of the relative density, over a range between 1 and 0.6 [118]. In this study, a linear dependence of the failure energy with the relative density is reported, while the common behavior for conventional foams states that the loss in the properties with the relative density should be quadratic. Sun et al. [119], proved that polyethersulfone (PESF) and polyphenylsulfone (PPSF) perform better than the proposed models for the Young´s modulus and the yield stress measured in compression and tension tests. Also, microcellular polycarbonate (PC) with cell sizes from 10 to 40 microns and relative densities higher than 0.7 was tested, showing a higher Izod impact strength than the solid [120,121]. This behavior was attributed to a change from brittle to ductile behavior of the material as a result of the introduction of microbubbles. This improvement with respect to the solid was also reported for the tensile strength of microcellular materials of blends of polyethylene and isotactic polypropylene (HDPE/i-PP) [122].

So, the improvement with respect to conventional foams was proved. However, the effect of the cell size in those properties is not clear in the literature. For example, Barlow et al. reported that microcellular PC with a constant relative density of 0.7 and cell sizes between 8-18 microns perform similarly when talking about impact strength independently on the cell size [120]. Similar results were presented for expanded polystyrene (EPS) in a range of 3 to 300 microns [123]. Conversely, polyethyleneterephthalate (CPET) and polypropylene (PP) shows improved tensile fracture stress with reduced cell sizes in a range between 3 to 1 micron, although the relative density is not reported being a possible cause of this change [124].

A further reduction in the cell size has been reported in several studies to be the next step for the improvement of the mechanical properties of cellular materials. This effect has been attributed to solid confinement within the cell walls.

Nanocellular materials present cell sizes in the nanometric range, which implies that the cell walls are also reduced to this scale. In fact, several works report cell walls smaller

than 20 nm when the pore size is below 200 nm [82,125]. This reduction of the solid phase forces the polymer chains to pack into the available volume (**Figure 2.31**). This confinement reduces the mobility of polymer chains, leading to an increase in the glass transition temperature of the polymer that could indicate a higher stiffness of the solid phase. This fact has been though to positively contribute to the mechanical strength of nanocellular polymers [102]. However, literature regarding this topic is not very large, and the results are not yet conclusive.

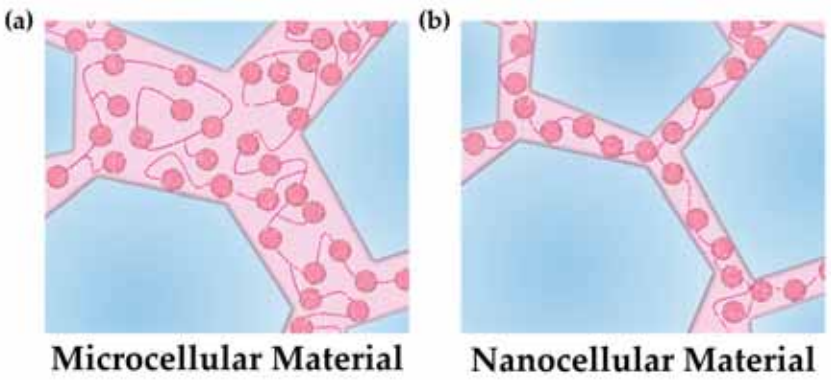

Figure 2.31. a) Scheme of the distribution of the polymer chains within the solid phase of a microcellular material. **b)** Scheme of the distribution of the polymer chains within the solid phase of a nanocellular material.

Nevertheless, results obtained up to now seems to indicate that, in general, the mechanical properties such as the Young´s modulus and the yield stress are independent of the cell size, while properties such as the tensile or fracture toughness increase significantly when reducing the cell size to the nanoscale.

In this regard, Guo tested micro and nanocellular PC with a relative density around 0.5 and cell sizes of 5 to 8 microns for the microcellular materials and 17 to 25 nm for the nanocellular ones [104]. The measured properties under tensile tests show that Young's modulus, yield stress, stress at break, strain at break, and toughness are similar for both ranges of cell sizes. Additionally, Bernardo et al. found that Young's modulus, yield strength and fracture toughness of nanocellular composites made of PMMA and sepiolite particles were dependent upon the concentration and the dispersion of the particles, but independent of cell size when working with microcellular materials ranging the 4 μm of cell size and nanomaterials with 300-500 nm [126]. On the contrary, Miller and Kumar tested micro and nanocellular PEI with cell sizes of 5 microns and 40 nm respectively through uniaxial tensile test. They found that both perform similarly for yield strength and the modulus of elasticity while tensile toughness is increased in a factor 2 to 3 when working with nanocellular PEI [127]. Additionally, Sharudin and Ohshima reported that the tensile yield strength of polypropylene-based (PP) nanocellular foams with a relative density between 0.5-0.8 and cell sizes smaller than 250 nm, is close to the yield strength of the former solid polymer, though the tensile failure strain of the nanocellular foam was found to be lower than the tensile failure strain of the solid polymer [71]. Ultimately, Notario et al. found that when working with microcellular polymers of 11 microns and nanocellular polymers rounding the 200 nm of cell size, the material performance index

for a light, stiff beam in bending $E^{1/2}/\rho$, where E is the Young's modulus and ρ is the density, and the impact resistance measured by Charpy tests for a polymethyl methacrylate (PMMA) nanocellular foam exceeded that for a microcellular PMMA foam [128].

Although presented results can result confusing, it can be extracted that for each material, there exists a different threshold of cell size that should be trespassing to find an effect on the mechanical properties. Although more in-depth analysis is needed, the initial results on this topic promising.

2.5.3. Thermal Properties

Nanocellular polymers are well known for their potential as thermal insulators. Cellular polymers have been historically used for this purpose; in fact, the main insulator in buildings is projected polyurethane (PU) presenting thermal conductivities around 21-25 mW/mK. Even though this is a low value for thermal conductivity, smaller thermal conductivities are required to reduce the energy consumption in space heating. At present, the energy consumption in households represents 25% of the total energy consumption of western countries; more than 50% of this is a consequence of the heating[129]. The European Union, in their fight against the climatic change, proposed a reduction of 20 % of these values before 2020 [130].

The low thermal conductivity of cellular materials is due to the reduced thermal conductivity of the gaseous phase in comparison with the solid one. So, increasing the amount of gas phase, that means the reduction of the density of the cellular polymer is essential to further reduce the thermal conductivity of cellular polymers. Thermal conductivity values in PU foams are in the lower limit being challenging to improve them. Herein is where nanocellular polymers acquire an important role.

Thermal conductivity λ_t for cellular materials is given by the following expression:

$$\lambda_t = \lambda_g + \lambda_s + \lambda_c + \lambda_r \quad (24)$$

where λ_g and λ_s represent the conduction through the gas phase and the solid phase respectively, λ_c is the convection inside the pores, and λ_r is the thermal radiation term. In order to understand how nanocellular polymers improve this total thermal conductivity, the fourth terms are discussed in the following paragraphs.

Firstly, λ_c can be neglected for pores smaller than 4 mm or 2 mm depending on working with close cells or open cells materials [131,132]. In any case, this contribution does not have relevance for nanocellular polymers.

On the other hand, the radiation term does not have influence for relative densities higher than 0.2, independently on the cell size. When the relative density if smaller than 0.2, this term starts to contribute and can play an important role in micro and macrocellular materials. Radiation can account for 20-30% of the total thermal conductivity for low-density foams. In addition, several authors have suggested that this

term will have even higher importance in nanocellular materials with low relative densities [133], although, for nanocellular materials with relative densities higher than 0.2, it can also be neglected [134,135]. So, in practical terms, when talking about nanocellular polymers, the total conductivity is reduced to the conduction through both phases.

According to Ashby´s model, the thermal conductivity due to conduction can be expressed as follows:

$$\lambda_t = \lambda_g + \lambda_s = g\lambda_s' \left(1 - V_g\right) + \lambda_g' V_g \tag{25}$$

being V_g the volume fraction of voids and g a structural factor that considers changes in the solid phase such as tortuosity and ranges between 1/3 and 1.

Equation 25 is valid for microcellular materials, but it should be modified for nanocellular ones. To understand the reason, the concept of mean free path is needed. The mean free path is the minimum distance that a gas molecule has to travel, on average, to collide with another one (**Figure 2.32a**). For air molecules at atmospheric pressure and room temperature this value is around 70 nm. That means that in microcellular materials with cell sizes much larger than 70 nm air molecules freely move inside the cells, colliding with each other and contributing to the thermal conduction (**Figure 2.32b**). When cell size becomes smaller, the probability of those molecules to collide with another is reduced (**Figure 2.32c**) up to become negligible when the cell size is of the same order of magnitude that the mean free path (**Figure 2.32d**). In this case, it is more likely for the gas to find a cell wall that another molecule to bump into. Thus, it can be said that the gas phase is confined in nanocellular materials, giving as a result a different contribution to the thermal conductivity.

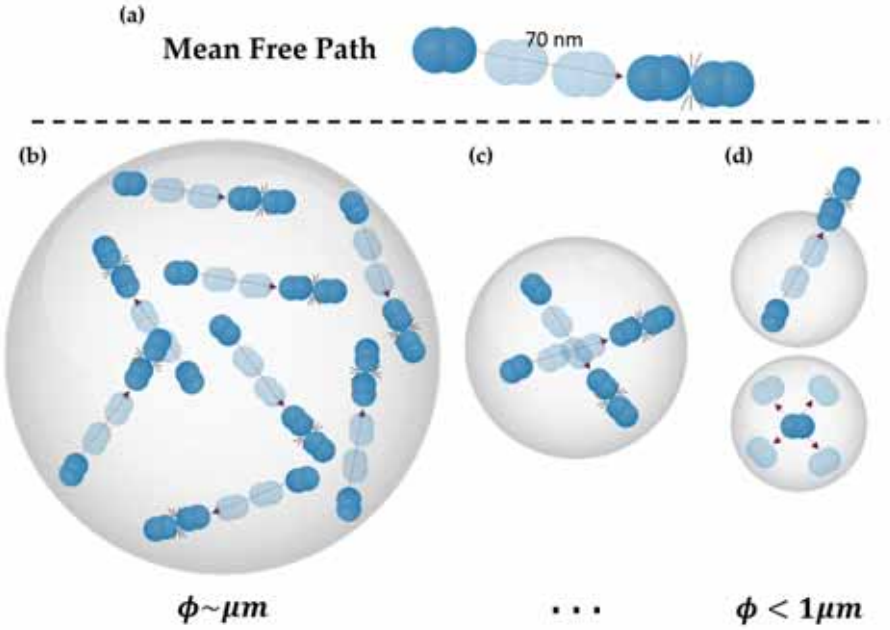

Figure 2.32. a) Scheme of the mean free path. **b) c) d)** Scheme of gas behavior inside a cell of different sizes from the micrometric to the nanometric range.

This lack of collisions leads to the reduction of the thermal conductivity through the gaseous phase, a fact that is well known as Knudsen effect [136,137]. To take into account this effect, the thermal conductivity of the gaseous phase can be described as follows:

$$\lambda'_g = \frac{\lambda'_{g0} V_g}{(1 + 2\beta k_n)} \tag{26}$$

where λ'_{g0} is the thermal conductivity of the gas (26 mW/m·K for air at room temperature and atmospheric pressure), β is a parameter that considers the energy transfer when a gas molecule collides with the solid phase (about 1.64 for air) and k_n is the Knudsen number defined as the mean free path of the gas molecules, l_g (70 nm for air at room temperature and atmospheric pressure) divided by the cell size:

$$k_n = \frac{l_g}{\phi} \tag{27}$$

Is this Knudsen number which accounts for the reduction of the gas conduction when decreasing the cell size. As it is shown in **Figure 2.33**, the predicted reduction is significant when trespassing below the micron. According to this, thermal conductivity associated with the gaseous phase can be almost neglected when cell sizes are smaller than 20 nm.

Knudsen effect has been already experimentally proven in nanocellular polymers by Notario et al. [138] showing that nanocellular PMMA with cell sizes around 200 nm has a reduced gas thermal conductivity.

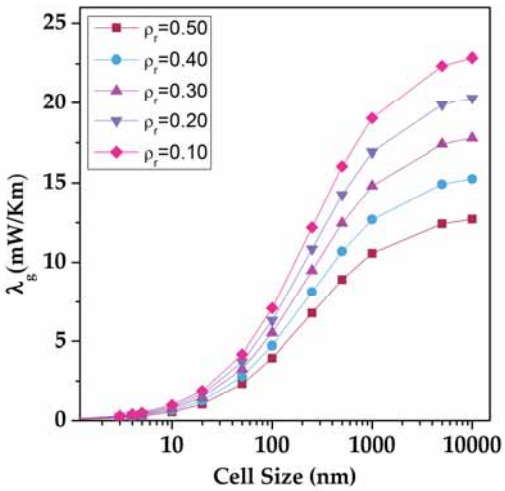

Figure 2.33. Gaseous conductivity considering the Knudsen contribution for materials with different relative densities.

On the other hand, several authors proposed that the reduction of the cells to the nanometric scale do not have only an effect on the gaseous term, but in the conduction through the solid phase. As it was explained in section 2.5.2, the solid phase is confined within the cell walls, this together with the presumption of an increased tortuosity when decreasing the solid phase to this scale [139], leads some authors to theorize that λ_s is also reduced in nanocellular polymers. This is attributed to phonon scattering. The same way cell size is on the order of magnitude of the mean free path of air molecules, the size of the

cell walls is of the order of magnitude of the phonon wavelength. In this case, this situation leads to the phonons to a lower effective mean path, meaning that they scatter with the solid interphases being more difficult to travel through the material, and thus reducing the conductivity of the solid phase [140,141]. This reduction in the solid phase was also experimentally proved in the work of Notario et al. [138]. The experimental thermal conduction of the solid phase was founded to be smaller than the predicted by Equation 25. It is then that although the origin of this last reduction is still to be confirmed the reduction of the cell size to the nanoscale leads to a reduction in the conductivity of both phases.

2.6. References

[1] Gibson, L. J.; Ashby, M. F. *Cellular solids: Structure and Properties*; 2nd ed.; Cambridge: Cambridge University Press.: United States, **1997**.

[2] Buist, J. M. Cellular Polymers. In *Fire and Cellular Polymers*; Springer, Dordrecht, **1986**; pp. 5–23.

[3] Rodriguez-Perez, M. A. Crosslinked polyolefin foams: Production, structure, properties, and applications. *Advances in Polymer Science* **2005**, *184*, 97–126.

[4] Saiz-Arroyo, C.; Rodriguez-Perez, M. A.; Tirado, J.; López-Gil, A.; de Saja, J. A. Structure-property relationships of medium-density polypropylene foams. *Polymer International* **2013**, *62*, 1324–1333.

[5] Eaves, D. *Handbook of Polymer Foams*; Rapra Technology Limited: Shawbury, Shrewsbury, Shropshire, UK, **2004**.

[6] Kumar, V.; Suh, N. P. A process for making microcellular thermoplastic parts. *Polymer Engineering and Science* **1990**, *30*, 1323–1329.

[7] Kumar, V.; Weller, J. E. A Process to Produce Microcellular PVC. *International Polymer Processing* **1993**, *1*, 73–80.

[8] Costeux, S. CO 2 -blown nanocellular foams. *Journal of Applied Polymer Science* **2015**, *132*, n/a-n/a.

[9] Notario, B.; Pinto, J.; Rodriguez-Perez, M. A. Nanoporous polymeric materials: A new class of materials with enhanced properties. *Progress in Materials Science* **2016**, *78–79*, 93–139.

[10] Microgreen polymers Inc. https://web.archive.org/web/20060518124632/http://www.microgreeninc.com/.

[11] Laguna-Gutierrez, E.; Escudero, J.; Kumar, V.; Rodriguez-Perez, M. A. Microcellular foaming by using subcritical CO 2 of crosslinked and non-crosslinked LDPE/clay nanocomposites. *Journal of Cellular Plastics* **2018**, *54*, 257–282.

[12] Qiang, W.; Hu, D.; Liu, T.; Zhao, L. Strategy to control CO2 diffusion in polystyrene microcellular foaming via CO2-philic additives. *The Journal of Supercritical Fluids* **2019**, *147*, 329–337.

[13] Ruiz, J. A. R.; Vallejos, S.; Pascual, B. S.; Ramos, C.; Beltrán, S.; García, F. C.; García, J. M. Microcellular polymer films based on cross-linked 1-vinyl-2-pyrrolidone and methyl methacrylate. *The Journal of Supercritical Fluids* **2018**, *140*, 270–278.

[14] Xu, G.; Gao, R.; Jin, W.; Zou, J.; Xiong, X.; Li, X.; Zeng, X. Regulation of pore cell structures of coal-based carbon foams based on the nucleation mechanism of microcellular polymer. *Ceramics*

International **2018**, *44*, 11077–11087.

[15] Guo, H.; Kumar, V. Some thermodynamic and kinetic low-temperature properties of the PC-CO2 system and morphological characteristics of solid-state PC nanofoams produced with liquid CO2. *Polymer* **2015**, *56*, 46–56.

[16] Bernardo, V.; Martín-De León, J.; Rodríguez-Pérez, M. A. Production and characterization of nanocellular polyphenylsulfone foams. *Materials Letters* **2016**, *178*, 155–158.

[17] Yeh, S. K.; Liu, Y. C.; Chu, C. C.; Chang, K. C.; Wang, S. F. Mechanical Properties of Microcellular and Nanocellular Thermoplastic Polyurethane Nanocomposite Foams Created Using Supercritical Carbon Dioxide. *Industrial and Engineering Chemistry Research* **2017**, *56*, 8499–8507.

[18] Miller, D.; Chatchaisucha, P.; Kumar, V. Microcellular and nanocellular solid-state polyetherimide (PEI) foams using sub-critical carbon dioxide I. Processing and structure. *Polymer* **2009**, *50*, 5576–5584.

[19] Bao, J.; Liu, T.; Zhao, L.; Barth, D.; Hu, G.; France, I. U. De; Universit, M. Supercritical Carbon Dioxide Induced Foaming of Highly Oriented Isotactic Polypropylene. **2011**, 13387–13395.

[20] Guo, H.; Kumar, V. Solid-state poly(methyl methacrylate) (PMMA) nanofoams. Part I: Low-temperature CO2 sorption, diffusion, and the depression in PMMA glass transition. *Polymer* **2015**, *57*, 157–163.

[21] Pinto, J.; Reglero-Ruiz, J. A.; Dumon, M.; Rodriguez-Perez, M. A. Temperature influence and CO2 transport in foaming processes of poly(methyl methacrylate)–block copolymer nanocellular and microcellular foams. *The Journal of Supercritical Fluids* **2014**, *94*, 198–205.

[22] Costeux, S.; Bunker, S. P.; Jeon, H. K. Homogeneous nanocellular foams from styrenic-acrylic polymer blends. *Journal of Materials Research* **2013**, *28*, 2351–2365.

[23] Zhai, W.; Yu, J.; Wu, L.; Ma, W.; He, J. Heterogeneous nucleation uniformizing cell size distribution in microcellular nanocomposites foams. *Polymer* **2006**, *47*, 7580–7589.

[24] Otsuka, T.; Taki, K.; Ohshima, M. Nanocellular Foams of PS/PMMA Polymer Blends. *Macromolecular Materials and Engineering* **2008**, *293*, 78–82.

[25] Yokoyama, B. H.; Li, L.; Nemoto, T.; Sugiyama, K. Tunable Nanocellular Polymeric Monoliths Using Fluorinated Block Copolymer Templates and Supercritical Carbon Dioxide. *Advanced Materials* **2004**, *16*, 1542–1546.

[26] Hentze, H. P.; Antonietti, M. Porous polymers and resins for biotechnological and biomedical applications. *Reviews in Molecular Biotechnology* **2002**, *90*, 27–53.

[27] Li, J.; Du, Z.; Li, H.; Zhang, C. Porous epoxy monolith prepared via chemically induced phase separation. *Polymer* **2009**, *50*, 1526–1532.

[28] Kiefer, J.; Hilborn, J. G.; Hedrick, J. L. Chemically induced phase separation: A new technique for the synthesis of macroporous epoxy networks. *Polymer* **1996**, *37*, 5715–5725.

[29] Nam, Y. S.; Park, T. G. Biodegradable polymeric microcellular foams by modified thermally induced phase separation method. *Biomaterials* **1999**, *20*, 1783–1790.

[30] Mehta, R. H.; Madsen, D. A.; Kalika, D. S. Microporous membranes based on poly(ether ether ketone) via thermally-induced phase separation. *Journal of Membrane Science* **1995**, *107*, 93–106.

[31] Di Luccio, M.; Nobrega, R.; Borges, C. . Microporous anisotropic phase inversion membranes from bisphenol-A polycarbonate: study of a ternary system. *Polymer* **2000**, *41*, 4309–4315.

[32] Chenc, L.; Dwan, A.; Cryte, C. C. Membrane Formation by Isothermal Precipitation in of Membrane Morphology I. Description of Membrane Morphology. *Journal of Polymer Science Part B: Polymer Physics* **1995**, *33*, 211–222.

[33] Li, L.; Shen, X.; Hong, S. W.; Hayward, R. C.; Russell, T. P. Fabrication of Co-continuous nanostructured and porous polymer membranes: Spinodal decomposition of homopolymer and random copolymer blends. *Angewandte Chemie - International Edition* **2012**, *51*, 4089–4094.

[34] Walheim, S.; Bradley, R. S.; Jones, P. D.; Routledge, E. Nanophase-Separated Polymer Films as High-Performance Antireflection Coatings. *Science* **2009**, *520*, 520–523.

[35] Ramström, O.; Ansell, R. J. Molecular imprinting technology: Challenges and prospects for the future. *Chirality* **1998**, *10*, 195–209.

[36] Gates, B.; Yin, Y.; Xia, Y. Fabrication and characterization of porous membranes with highly ordered three-dimensional periodic structures. *Chemistry of Materials* **1999**, *11*, 2827–2836.

[37] Menger, F. M.; Tsuno, T.; Hammond, G. S. Cross-Linked Polystyrene Incorporating Water Pools. *Journal of the American Chemical Society* **1990**, *112*, 1263–1264.

[38] Du Fresne Von Hohenesche, C.; Schmidt, D. F.; Schädler, V. Nanoporous melamine - Formaldehyde gels by microemulsion templating. *Chemistry of Materials* **2008**, *20*, 6124–6129.

[39] Zalusky, A. S.; Olayo-Valles, R.; Wolf, J. H.; Hillmyer, M. A. Ordered nanoporous polymers from polystyrene-polylactide block copolymers. *Journal of the American Chemical Society* **2002**, *124*, 12761–12773.

[40] Steinke, J. H. G.; Dunkin, I. R.; Sherrington, D. C. Molecularly imprinted anisotropic polymer monoliths. *Macromolecules* **1996**, *29*, 407–415.

[41] Wackerlig, J.; Lieberzeit, P. A. Molecularly imprinted polymer nanoparticles in chemical sensing - Synthesis, characterisation and application. *Sensors and Actuators, B: Chemical* **2015**, *207*, 144–157.

[42] Park, S. H.; Xia, Y. Fabrication of Three-Dimensional Macroporous Membranes with Assemblies of Microspheres as Templates. *Chemistry of Materials* **1998**, *10*, 1745–1747.

[43] Johnson, S. A.; Johnson, S. A.; Ollivier, P. J.; Mallouk, T. E. 19999-Ordered Mesoporous Polymers of Tunable Pore Size from Colloidal Silica Templates.pdf. **2011**, *963*, 10–13.

[44] Zhu, X. X.; Banana, K.; Yen, R. Pore size control in cross-linked polymer resins by reverse micellar imprinting. *Macromolecules* **1997**, *30*, 3031–3035.

[45] Liu, J.; Teo, W. K.; Chew, C. H.; Gan, L. M. Nanofiltration membranes prepared by direct microemulsion copolymerization using poly(ethylene oxide) macromonomer as a polymerizable surfactant. *Journal of Applied Polymer Science* **2000**, *77*, 2785–2794.

[46] Volksen, W.; Yoon, D. Y.; Hawker, C. J.; Trollsås, M.; Hedrick, J. L.; Miller, R. D.; Carter, K. R. Templating Nanoporosity in Thin-Film Dielectric Insulators. *Advanced Materials* **2002**, *10*, 1049–1053.

[47] Hedrick, J. L.; Russell, T. P.; Labadie, J.; Lucas, M.; Swanson, S. High temperature nanofoams derived from rigid and semi-rigid polyimides. *Polymer* **1995**, *36*, 2685–2697.

[48] Jacobs, L. J. M.; Kemmere, M. F.; Keurentjes, J. T. F. Sustainable polymer foaming using high pressure carbon dioxide: a review on fundamentals, processes and applications. *Green Chemistry* **2008**, *10*, 731.

[49] Costeux, S.; Khan, I.; Bunker, S. P.; Jeon, H. K. Experimental study and modeling of nanofoams formation from single phase acrylic copolymers. *Journal of Cellular Plastics* **2014**, *51*, 197–221.

[50] Blander, M.; Katz, J. L. Bubble nucleation in liquids. *AIChE Journal* **1975**, *21*, 833–848.

[51] Goel, S. K.; Beckman, E. J. Generation of microcellular polymeric foams using supercritical carbon dioxide. I: Effect of pressure and temperature on nucleation. *Polymer Engineering and Science* **1994**, *34*, 1137–1147.

[52] Krause, B.; Mettinkhof, R.; Van Der Vegt, N. F. A.; Wessling, M. Microcellular foaming of amorphous high-Tg polymers using carbon dioxide. *Macromolecules* **2001**, *34*, 874–884.

[53] Costeux, S.; Jeon, M. H.; Bunker, T. S.; Khan, I. Nanocellular foams from acrylic polymers : experiments and modeling. *FOAMS 2012 Conference* **2012**, 1–6.

[54] Xu, X.; Cristancho, D. E.; Costeux, S.; Wang, Z.-G. Bubble nucleation in polymer–CO2 mixtures. *Soft Matter* **2013**, *9*, 9675.

[55] Kim, Y.; Park, C. B.; Chen, P.; Thompson, R. B. Origins of the failure of classical nucleation theory for nanocellular polymer foams. *Soft Matter* **2011**, *7*, 7351.

[56] Colton, J. S.; Suh, N. P. Nucleation of microcellular foam: Theory and practice. *Polymer Engineering & Science* **1987**, *27*, 500–503.

[57] Liu, S.; Zoetebier, B.; Hulsman, L.; Zhang, Y.; Duvigneau, J.; Vancso, G. J. Nanocellular polymer foams nucleated by core-shell nanoparticles. *Polymer* **2016**, *104*, 22–30.

[58] Ameli, A.; Nofar, M.; Park, C. B.; Pötschke, P.; Rizvi, G. Polypropylene/carbon nanotube nano/microcellular structures with high dielectric permittivity, low dielectric loss, and low percolation threshold. *Carbon* **2014**, *71*, 206–217.

[59] Yang, J.; Huang, L.; Zhang, Y.; Chen, F.; Fan, P.; Zhong, M.; Yeh, S. A new promising nucleating agent for polymer foaming: Applications of ordered mesoporous silica particles in polymethyl methacrylate supercritical carbon dioxide microcellular foaming. *Industrial and Engineering Chemistry Research* **2013**, *52*, 14169–14178.

[60] Costeux, S.; Zhu, L. Low density thermoplastic nanofoams nucleated by nanoparticles. *Polymer* **2013**, *54*, 2785–2795.

[61] Yu, H.; Lei, Y.; Yu, X.; Wang, X.; Liu, T.; Luo, S. Solid-state polyetherimide (PEI) nanofoams: the influence of the compatibility of nucleation agent on the cellular morphology. *Journal of Polymer Research* **2016**, *23*, 121.

[62] Fujimoto, Y.; Ray, S. S.; Okamoto, M.; Ogami, A.; Yamada, K.; Ueda, K. Well-Controlled Biodegradable Nanocomposite Foams : From Microcellular to Nanocellular. *Macromolecular Rapid Communications* **2003**, *24*, 457–461.

[63] Monnereau, L.; Urbanczyk, L.; Thomassin, J.-M.; Alexandre, M.; Jérôme, C.; Huynen, I.; Bailly, C.; Detrembleur, C. Supercritical CO2 and polycarbonate based nanocomposites: A critical issue for foaming. *Polymer* **2014**, *55*, 2422–2431.

[64] Ema, Y.; Ikeya, M.; Okamoto, M. Foam processing and cellular structure of polylactide-based nanocomposites. *Polymer* **2006**, *47*, 5350–5359.

[65] Lee, Y. H.; Park, C. B.; Wang, K. H. HDPE-Clay Nanocomposite Foams Blown with Supercritical CO2. *Journal of Cellular Plastics* **2005**, *41*, 487–502.

[66] Urbanczyk, L.; Calberg, C.; Detrembleur, C.; Jérôme, C.; Alexandre, M. Batch foaming of

SAN/clay nanocomposites with scCO2: A very tunable way of controlling the cellular morphology. *Polymer* **2010**, *51*, 3520–3531.

[67] Pinto, J.; Morselli, D.; Bernardo, V.; Notario, B.; Fragouli, D.; Rodriguez-Perez, M. A.; Athanassiou, A. Nanoporous PMMA foams with templated pore size obtained by localized in situ synthesis of nanoparticles and CO 2 foaming. *Polymer* **2017**, *124*, 176–185.

[68] Bernardo, V.; Martín-de León, J.; Laguna-Gutiérrez, E.; Rodríguez-Pérez, M. Á. PMMA-sepiolite nanocomposites as new promising materials for the production of nanocellular polymers. *European Polymer Journal* **2017**, *96*, 10–26.

[69] Bernardo, V.; Martin-de Leon, J.; Pinto, J.; Verdejo, R.; Rodriguez-Perez, M. A. Modeling the heat transfer by conduction of nanocellular polymers with bimodal cellular structures. *Polymer* **2019**, *160*, 126–137.

[70] Dutriez, C.; Satoh, K.; Masami, K.; Yokoyama, H. Nanocellular foaming of fluorine containing block copolymers in carbon dioxide : the role of glass transition in carbon dioxide. *RSC Advances* **2012**, *2*, 2821–2827.

[71] Sharudin, R. W. B.; Ohshima, M. CO2-Induced Mechanical Reinforcement of Polyolefin-Based Nanocellular Foams. *Macromolecular Materials and Engineering* **2011**, *296*, 1046–1054.

[72] Nemoto, T.; Takagi, J.; Ohshima, M. Control of Bubble Size and Location in Nano-/Microscale Cellular Poly(propylene)/Rubber Blend Foams. *Macromolecular Materials and Engineering* **2008**, *293*, 574–580.

[73] Nemoto, T.; Takagi, J.; Ohshima, M. Nanoscale Cellular Foams from a Poly(propylene)-Rubber Blend. *Macromolecular Materials and Engineering* **2008**, *293*, 991–998.

[74] Hideaki Yokoyama*, † and; Sugiyama‡, K. Nanocellular Structures in Block Copolymers with CO2-philic Blocks Using CO2 as a Blowing Agent: Crossover from Micro- to Nanocellular Structures with Depressurization Temperature. **2005**.

[75] Forest, C.; Chaumont, P.; Cassagnau, P.; Swoboda, B.; Sonntag, P. CO2 nano-foaming of nanostructured PMMA. *Polymer* **2015**, *58*, 76–87.

[76] Forest, C.; Chaumont, P.; Cassagnau, P.; Swoboda, B.; Sonntag, P. Nanofoaming of PMMA using a batch CO2 process: Influence of the PMMA viscoelastic behaviour. *Polymer* **2015**, *77*, 1–9.

[77] Pinto, J.; Dumon, M.; Pedros, M.; Reglero, J.; Rodriguez-Perez, M. A. Nanocellular CO2 foaming of PMMA assisted by block copolymer nanostructuration. *Chemical Engineering Journal* **2014**, *243*, 428–435.

[78] Pinto, J.; Dumon, M.; Rodriguez-Perez, M. A.; Garcia, R.; Dietz, C. Block Copolymers Self-Assembly Allows Obtaining Tunable Micro or Nanoporous Membranes or Depth Filters Based on PMMA; Fabrication Method and Nanostructures. *The Journal of Physical Chemistry C* **2014**, *118*, 4656–4663.

[79] Reglero Ruiz, J. A.; Dumon, M.; Pinto, J.; Rodriguez-Pérez, M. A. Low-density nanocellular foams produced by high-pressure carbon dioxide. *Macromolecular Materials and Engineering* **2011**, *296*, 752–759.

[80] Wang, G.; Zhao, J.; Mark, L. H.; Wang, G.; Yu, K.; Wang, C.; Park, C. B.; Zhao, G. Ultra-tough and super thermal-insulation nanocellular PMMA/TPU. *Chemical Engineering Journal* **2017**, *325*, 632–646.

[81] Bernardo, V.; Martín-de León, J.; Laguna-Gutiérrez, E.; Rodríguez-Pérez, M. Á. PMMA-

sepiolite nanocomposites as new promising materials for the production of nanocellular polymers. *European Polymer Journal* **2017**, *96*, 10–26.

[82] Bernardo, V.; Martin-de Leon, J.; Laguna-Gutierrez, E.; Catelani, T.; Pinto, J.; Athanassiou, A.; Rodriguez-Perez, M. A. Understanding the role of MAM molecular weight in the production of PMMA/MAM nanocellular polymers. *Polymer* **2018**, *153*, 262–270.

[83] Colton, J. S.; Suh, N. N. P. The nucleation of microcellular thermoplastic foam with additives: Part II: Experimental Results and discussion. *Polymer Engineering and Science* **1987**, *27*, 493–499.

[84] Street, J. R. The Rheology of Phase Growth in Elastic Liquids. *Journal of Rheology* **1968**, *12*, 103.

[85] Street, J. R.; Fricke, A. L.; Reiss, L. P.; Fricke, A. L.; Reiss, L. P. Dynamics of Phase Growth in Viscous, Non-Newtonian Liquids: Initial Stages of Growth. *Industrial and Engineering Chemistry Fundamentals* **1971**, *10*, 54–64.

[86] Amon, M.; Denson, C. D. A study of the dynamics of foam growth: Analysis of the growth of closely spaced spherical bubbles. *Polymer Engineering & Science* **1984**, *24*, 1026–1034.

[87] Venerus, D. C.; Yala, N.; Bernstein, B. Analysis of diffusion-induced bubble growth in viscoelastic liquids. *Journal of Non-Newtonian Fluid Mechanics* **1998**, *75*, 55–75.

[88] Arefmanesh, A.; Advani, S. G.; Michaelides, E. E. An accurate numerical solution for mass diffusion-induced bubble growth in viscous liquids containing limited dissolved gas. *International Journal of Heat and Mass Transfer* **1992**, *35*, 1711–1722.

[89] Shafi, M. A.; Joshi, K.; Flumerfelt, R. W. Bubble size distributions in freely expanded polymer foams. *Chemical Engineering Science* **1997**, *52*, 635–644.

[90] Shafi, M. a; Lee, J. G.; Flumerfelt, R. W. Prediction of cellular structure in free expansion polymer foam processing. *Polymer Engineering and Science* **1996**, *36*, 1950–1959.

[91] Taki, K. Experimental and numerical studies on the effects of pressure release rate on number density of bubbles and bubble growth in a polymeric foaming process. *Chemical Engineering Science* **2008**, *63*, 3643–3653.

[92] Leung, S. N.; Park, C. B.; Li, H. Numerical simulation of polymeric foaming processes using modified nucleation theory. *Plastics, Rubber and Composites* **2006**, *35*, 93–100.

[93] Feng, J. J.; Bertelo, C. A. Prediction of bubble growth and size distribution in polymer foaming based on a new heterogeneous nucleation model. *Journal of Rheology* **2004**, *48*, 439–462.

[94] Khan, I.; Adrian, D.; Costeux, S. A model to predict the cell density and cell size distribution in nano-cellular foams. *Chemical Engineering Science* **2015**, *138*, 634–645.

[95] Sato, Y.; Fujiwara, K.; Takikawa, T.; Sumarno; Takishima, S.; Masuoka, H. Solubilities and diffusion coefficients of carbon dioxide and nitrogen in polypropylene, high-density polyethylene, and polystyrene under high pressures and temperatures. *Fluid Phase Equilibria* **1999**, *162*, 261–276.

[96] Doroudiani, S.; Chaffey, C. E.; Kortschot, M. T. Sorption and diffusion of carbon dioxide in wood-fiber/polystyrene composites. *Journal of Polymer Science, Part B: Polymer Physics* **2002**, *40*, 723–735.

[97] Williams, M. M. R. The mathematics of diffusion. *Annals of Nuclear Energy* **1977**, *4*, 205–206.

[98] Guo, H.; Nicolae, A.; Kumar, V. Fabrication of high temperature polyphenylsulfone nanofoams using high pressure liquid carbon dioxide. *Cellular Polymers* **2016**, *35*, 119–142.

[99] Guo, H.; Nicolae, A.; Kumar, V. Solid-state poly(methyl methacrylate) (PMMA) nanofoams.

Part II: Low-temperature solid-state process space using CO2 and the resulting morphologies. *Polymer* **2015**, *70*, 231–241.

[100] Guo, H.; Nicolae, A.; Kumar, V. Solid-state microcellular and nanocellular polysulfone foams. *Journal of Polymer Science, Part B: Polymer Physics* **2015**, *53*, 975–985.

[101] Park, C. B.; Baldwin, D. F.; Suh, N. P. Effect of the Pressure Drop Rate on Cell Nucleation in Continuous Processing of Microcellular Polymers Effect of the Pressure Drop Rate on Cell Nucleation filters for separation processes, surface modifiers for low friction, and biomedical materials. A ty. *Polymer Engineering and Science* **1995**, *35*, 432–440.

[102] Costeux, S. CO2 -blown nanocellular foams. *Journal of Applied Polymer Science* **2015**, *132*, 41293–41293.

[103] Handa, Y. P.; Zhang, Z. A New Technique for Measuring Retrograde Vitrification in Polymer – Gas Systems and for Making Ultramicrocellular. **1999**, 11–13.

[104] Guo, H. Solid-state Polymer Nanofoams, **2015**.

[105] Miller, D.; Kumar, V. Microcellular and nanocellular solid-state polyetherimide (PEI) foams using sub-critical carbon dioxide II. Tensile and impact properties. *Polymer* **2011**, *52*, 2910–2919.

[106] Bergman, T. L.; Incropera, F. P. *Fundamentals of heat and mass transfer.*; Wiley, **2011**.

[107] Li, L.; Schulte, L.; Clausen, L. D.; Hansen, K. M.; Jonsson, G. E.; Ndoni, S. Gyroid nanoporous membranes with tunable permeability. *ACS Nano* **2011**, *5*, 7754–7766.

[108] Lu, G. Q.; Zhao, X. S. Nanoporous Materials — An Overview. In *Nanoporous materials: Science and engineering*; Imperial Collegue Press: London, **2004**.

[109] Kyzioł, A.; Kyzioł, K. Surface Functionalization With Biopolymers via Plasma-Assisted Surface Grafting and Plasma-Induced Graft Polymerization—*Materials for Biomedical Applications*; Elsevier: Amsterdam, The Nederlands, **2017**.

[110] Kumar Thakur, V.; Kumari Thakur, M.; Kessler, M. R. *Handbook of composites from renewable materials*; Wiley, **1985**.

[111] Liu, X.; Chu, P. K.; Ding, C. Surface nano-functionalization of biomaterials. *Materials Science and Engineering R: Reports* **2010**, *70*, 275–302.

[112] Pisal, A. A.; Venkateswara Rao, A. Development of hydrophobic and optically transparent monolithic silica aerogels for window panel applications. *Journal of Porous Materials* **2017**, *24*, 685–695.

[113] Riffat, S. B.; Qiu, G. A review of state-of-the-art aerogel applications in buildings. *International Journal of Low-Carbon Technologies* **2013**, *8*, 1–6.

[114] Yokoyama, H.; Li, L.; Nemoto, T.; Sugiyama, K. Tunable nanocellular polymeric monoliths using fluorinated block copolymer templates and supercritical carbon dioxide. *Advanced Materials* **2004**, *16*, 1542–1546.

[115] Reim, M.; Reichenauer, G.; Körner, W.; Manara, J.; Arduini-Schuster, M.; Korder, S.; Beck, a.; Fricke, J. Silica-aerogel granulate - Structural, optical and thermal properties. *Journal of Non-Crystalline Solids* **2004**, *350*, 358–363.

[116] Soleimani Dorcheh, A.; Abbasi, M. H. Silica aerogel; synthesis, properties and characterization. *Journal of Materials Processing Technology* **2008**, *199*, 10–26.

[117] Pérez-Tamarit, S.; Notario, B.; Solórzano, E.; Rodriguez-Perez, M. A. Light transmission in

nanocellular polymers: Are semi-transparent cellular polymers possible? *Materials Letters* **2018**, *210*, 39–41.

[118] Juntunen, R. P.; Kumar, V.; Weller, J. E.; Bezubic, W. P.; Mi, J. Impact Strength of High density microcellular poly(vinyl chloride) foams. **2000**, *6*, 93–99.

[119] Sun, H.; Sur, G.; Mark, J. Microcellular foams from polyethersulfone and polyphenylsulfonePreparation and mechanical properties. *European Polymer Journal* **2002**, *38*, 2373–2381.

[120] Barlow, C.; Kumar, V.; Flinn, B.; Bordia, R. K.; Weller, J. Impact Strength of High Density Solid-State Microcellular Polycarbonate Foams. *Journal of Engineering Materials and Technology* **2002**, *123*, 229.

[121] Collias, D. I.; Baird, D. G.; Borggreve, R. J. . Impact toughening of polycarbonate by microcellular foaming. *Polymer* **1994**, *35*, 3978–3983.

[122] Doroudiani, S.; Park, C. B.; Kortschot, M. T. Processing and characterization of microcellular foamed high-density polyethylene/isotactic polypropylene blends. *Polymer Engineering and Science* **1998**, *38*, 1205–1215.

[123] Doroudiani, S.; Kortschot, M. T. Polystyrene foams. II. Structure-impact properties relationships. *Journal of Applied Polymer Science* **2003**, *90*, 1421–1426.

[124] Shimbo, M.; Higashitani, I.; Miyano, Y. Mechanism of strength improvement of foamed plastics having fine cell. *Journal of Cellular Plastics* **2007**, *43*, 157–167.

[125] Pardo-Alonso, S.; Solórzano, E.; Brabant, L.; Vanderniepen, P.; Dierick, M.; Van Hoorebeke, L.; Rodríguez-Pérez, M. A. 3D Analysis of the progressive modification of the cellular architecture in polyurethane nanocomposite foams via X-ray microtomography. *European Polymer Journal* **2013**, *49*, 999–1006.

[126] Bernardo, V.; Martín-de León, J.; Laguna-Gutiérrez, E.; Rodríguez-Pérez, M. Á. PMMA-sepiolite nanocomposites as new promising materials for the production of nanocellular polymers. *European Polymer Journal* **2017**, *96*, 10–26.

[127] Nadella, K.; Kumar, V. Tensile and flexural properties of solid-state microcellular ABS panels. *Experimental Analysis of Nano and Engineering* **2007**, *22*, 765–766.

[128] Notario, B.; Pinto, J.; Rodriguez-Perez, M. a. Towards a new generation of polymeric foams: PMMA nanocellular foams with enhanced physical properties. *Polymer* **2015**, *63*, 116–126.

[129] Eurostat Energy consumption in households http://www.mof.gov.cy/cystat (accessed Jun 11, 2019).

[130] Watts, N.; Stott, R.; Rafferty, A. M. Combating climate change. *Bmj* **2015**, *351*, h6178–h6178.

[131] Alvarez-Lainez, M.; Rodriguez-Perez, M. A.; DE Saja, J. A. Thermal conductivity of open-cell polyolefin foams. *Journal of Polymer Science Part B: Polymer Physics* **2008**, *46*, 212–221.

[132] Holman, J. P.; Boggs, J. H. Heat Transfer to Freon 12 Near the Critical State in a Natural-Circulation Loop. *Journal of Heat Transfer* **1960**, *82*, 221.

[133] Saja, J. A. D. E.; Almanza, O. A.; Rodriguez-Perez, M. A. Prediction of the radiation term in the thermal conductivity of crosslinked closed cell polyolefin foams. *Journal of Polymer Science Part B: Polymer Physics* **2000**, *38*, 993–1004.

[134] Solórzano, E.; Rodriguez-Perez, M. A.; Lazaro, J.; De Saja, J. A. Influence of solid phase

conductivity and cellular structure on the heat transfer mechanisms of cellular materials: Diverse case studies. *Advanced Engineering Materials* **2009**, *11*, 818–824.

[135] Ferkl, P.; Pokorný, R.; Bobák, M.; Kosek, J. Heat transfer in one-dimensional micro- and nano-cellular foams. *Chemical Engineering Science* **2013**, *97*, 50–58.

[136] Lu, X.; Caps, R.; Fricke, J.; Alviso, C. T.; Pekala, R. W. Correlation between structure and thermal conductivity of organic aerogels. *Journal of Non-Crystalline Solids* **1995**, *188*, 226–234.

[137] Schmidt, D.; Raman, V. I.; Egger, C.; du Fresne, C.; Schädler, V. Templated cross-linking reactions for designing nanoporous materials. *Materials Science and Engineering: C* **2007**, *27*, 1487–1490.

[138] Notario, B.; Pinto, J.; Solorzano, E.; De Saja, J. A.; Dumon, M.; Rodriguez-Perez, M. A. Experimental validation of the Knudsen effect in nanocellular polymeric foams. *Polymer (United Kingdom)* **2015**, *56*, 57–67.

[139] Pinto, J.; Notario, B.; Verdejo, R.; Dumon, M.; Costeux, S.; Rodriguez-Perez, M. A. Molecular confinement of solid and gaseous phases of self-standing bulk nanoporous polymers inducing enhanced and unexpected physical properties. *Polymer* **2017**, *113*, 27–33.

[140] Sundarram, S. S.; Li, W. On thermal conductivity of micro- and Nanocellular polymer foams. **2012**, *47*, 935068.

[141] Prasher, R. Thermal conductivity of composites of aligned nanoscale and microscale wires and pores. *Journal of Applied Physics* **2006**, *100*.

CHAPTER 3

Experimental section

"Ilusos que hoy arrojan a la fuente sus monedas, realistas que no dudan en mojarse y cogerlas."

LOVG

INDEX

3.1. Introduction

This third chapter focuses on the description of the experimental aspects related to this thesis.

Firstly, a detailed description of the used materials and their properties is given. Moreover, the used production methods for the solid and cellular materials and the used set-ups are clearly described.

Finally, a list of all the different characterization methods used in this work is provided. Consequently, characterization methods used to study both the starting solids and the cellular structures produced, are described. Additionally, the techniques used for the characterization of optical, mechanical, and thermal properties of the produced materials are explained.

3.2. Materials

Poly (methyl methacrylate) (PMMA) is the main polymer used for the development of this thesis.

PMMA is a thermoplastic resin obtained from the polymerization of methyl methacrylate. Its chemical formula is $(C_5O_2H_8)_n$ that can be schematized as follows:

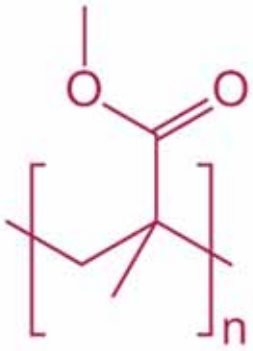

Figure 3.1. Chemical structure of Poly (methyl methacrylate).

Since their discovery in 1928, this polymer has been widely used in hundreds of applications due to its attractive properties. PMMA is a strong, tough, and lightweight polymer; moreover, its impact strength is higher than the one of glass or polystyrene. Furthermore, it is a transparent polymer, having a visible light transmittance higher than 92% for a thickness of 3 mm, and it allows to filter ultraviolet radiation. Despite other polymers, it offers high environmental stability [1].

Attending to all those properties is understandable its widespread use in all kind of industrial sectors. Thus, PMMA can be found as glass substitute in buildings or lenses of exterior lights of automobiles. Besides, it is also employed in the medical sector for lenses, bone cement in orthopedic surgery, or artificial teeth [1]. Those are only a few examples of its multiple applications. Additionally, apart from the thousands of uses in daily-life applications, this polymer is also employed in more specific applications, as in optical

fibers, it is also sensitive to ionizing radiation being used as dosimeter [2], or as high resolution resist in photolithographic processes [3].

However, as far as this thesis concerns, PMMA will be used as the raw matrix for the production of nanocellular materials using the gas dissolution foaming process.

In this thesis, three different degrees of PMMA have been used. V825T, 7N, and 6N. The materials have been provided in the form of pellets. V825T was kindly supplied by ALTUGLAS® International (Colombes, France) and 7N and 6N by PLEXIGLAS® Evonik Industries (Essen, Germany).

The characteristics of these polymers are shown in **Table 3.1**.

Table 3.1. Characteristics of the three polymethylmethacrylates used in this thesis, with ρ the density, M_n the number average molecular weight, M_w the weight average molecular weight, T_g the glass transition temperature, MFI the melt flow index and η_0 the zero shear viscosity.

Material	ρ (g/cm³)	M_n (g/mol)	M_w (g/mol)	T_g (°C)	MFI (g/10 min)	η_0 (Pa·s)
V825T (HV)	1.186	43157	83221	114.4	1.92	7095
7N (MV)	1.187	45119	83621	109.3	3.64	3800
6N (LV)	1.190	34149	77255	98.6	8.20	1587

Density, measured as explained in section 3.4.2, is around 1.19 g/cm³ for the three materials. Molecular weights have been determined by gel permeation chromatography (GPC) in the "Instituto de Ciencia y Tecnología de Polímeros" in Madrid. As shown in **Table 3.1**, molecular weights differ depending on the polymer; being the 6N grade, the one presenting the smaller values, while molecular weights for V825T and 7N are very close to each other.

On the other hand, other characteristics such as glass transition temperature, the melt flow index and the zero-shear viscosity (see sections 3.4.1 and 3.4.7 for the methods used to obtain these properties), have been considered, being the three grades different. Thus, V825T is the one with the highest glass transition temperature, accompanied by the smallest melt flow index and therefore, the highest viscosity. Conversely, 6N has the lowest T_g and the highest MFI and consequently the lowest viscosity. Material 7N presents intermediate values. In order to become aware of those properties, materials will be named accordingly with their viscosity. So, from now on, V825T will be identified as high viscosity (HV) PMMA, 7N as medium viscosity (MV) PMMA and 6N as low viscosity (LV) PMMA.

Medical grade of carbon dioxide (CO_2) with a 99.9% of purity was selected as the blowing agent for the gas dissolution foaming experiments.

3.3. Production methods

In this section, the production methods for the solid parts as well as the ones used for the production of nanocellular materials are explained.

3.3.1. Solid samples production

Solid sheets of different thicknesses have been produced in this thesis (from 0.5 mm to 4 mm) from the initial pellets to perform the different experiments. The production route is the same independently on the used PMMA.

Solid precursors were produced by compression molding through a hot plate press from Remtex (Barcelona, Spain) (**Figure 3.3b**). The initial pellets are firstly dried at 80 °C during 4 hours in a vacuum drying oven at 0.015 MPa (Model VacioTem TV, from JP Selecta) to remove the moisture.

Afterward, those pellets are placed inside the desired mold located between two aluminum foil sheets and two steel plates, as **Figure 3.3a** shows. This assembly is positioned inside the press, and the compression molding process starts.

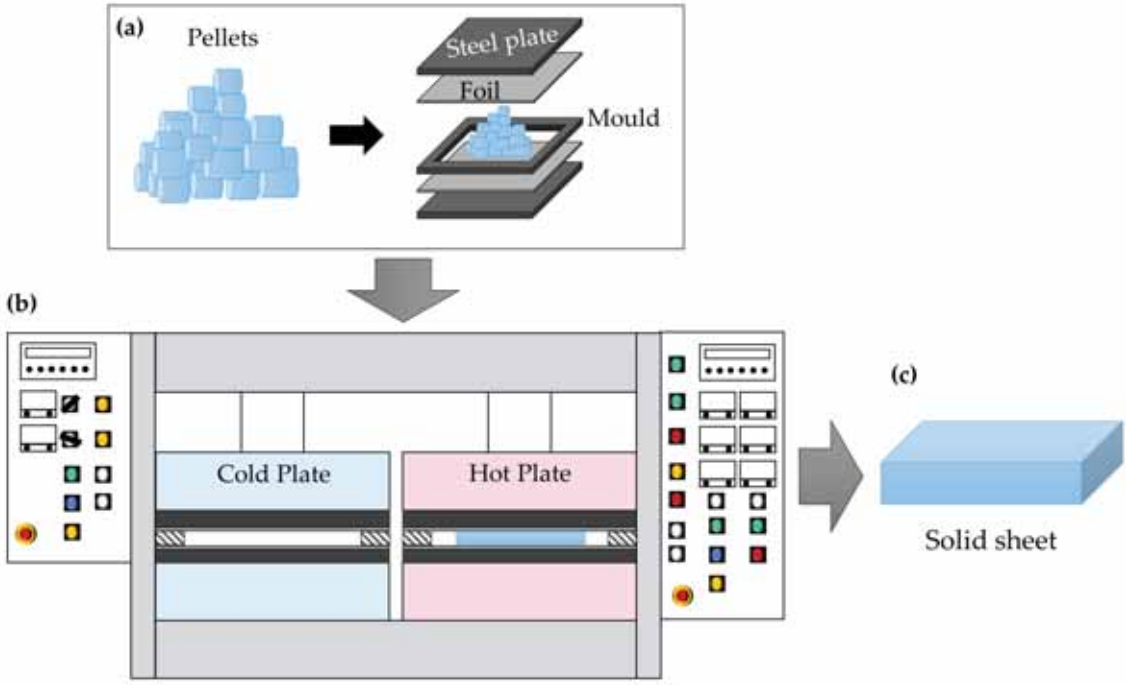

Figure 3.3. Scheme of the compression molded process. **a)** Scheme of the pellets positioning for the compression molded process. **b)** Scheme of hot plate press. **c)** Scheme of the produced solid sheet.

Firstly, the mould is placed on the hot plate, being the polymer heated at 250°C for 9 min without applying any pressure. During these 9 minutes, the material softens due to the used temperature, that is higher than its T_g. Then, a certain pressure is applied during one additional minute, allowing the soften PMMA to acquire the shape of the mold. The

applied pressure will be different for each thickness and mold dimensions and will be indicated in each specific experiment (see the experimental section of the scientific articles, from P1 to P8, in chapters from 4 to 8). Finally, the material is cooled down at room temperature in the cold plates under the same pressure used for compression for 4 minutes.

The obtained solid sheets are usually cut into the desired dimensions for the corresponding experiment.

3.3.2. Foaming tests

Gas dissolution foaming experiments have been carried out in two different set-ups. The first one was used to perform saturation at temperatures above room temperature, and the second one for saturating at low temperatures.

The room temperature set-up is schematized in **Figure 3.4a**; the system comprises a pressure vessel (5) (model PARR 4681) provided by Parr Instrument Company (Moline, IL, USA) with a capacity of 1 liter. This pressure vessel is provided with two metal clamps (6) and twelve screws, ensuring the seal of the system. This model allows working at 41 MPa of maximum pressure combined with 350 °C of temperature.

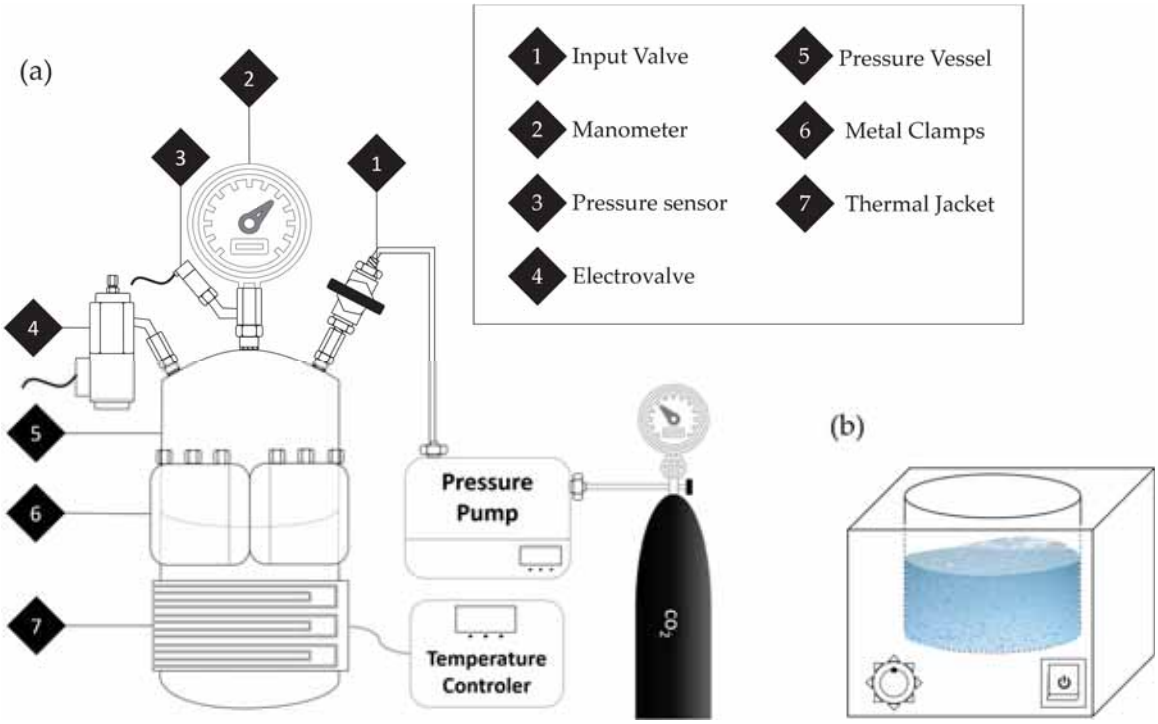

Figure 3.4. a) Scheme of the pressure system set-up. **b)** Scheme of the thermal bath

In order to provide the vessel with the required pressure, a pressure pump (model SFT-10) supplied by Supercritical Fluid Technologies Inc. (Newark, DE, USA) is used. It can work up to maximum pressures of 68.9 MPa at a maximum flow rate of 24 ml/min. On the other hand, the control of the temperature is accomplished through a thermal jacket of 1200 W (7) connected to a temperature controller (CAL 3000).

The gas goes into the pressure vessel through the input valve (1) and goes out through an electrovalve (4) with K_v = 1.1 L/min, allowing the system to release the gas fast.

Summing up, the gas comes out of the gas bottle at a pressure of 6 MPa and is pressurized through a pressure pump, that conducts this gas to the input valve (1) and therefore to the pressure vessel (5). The manometer (2) gives the pressure in every moment, and the clamp heater (7) along with the temperature controller provides the desired saturation temperature. Finally, after saturation, the gas is released through the electrovalve (4).

Additionally, the system is provided with sensors (3) allowing data acquisition in a computer, so the pressure and the temperature can be monitored during the whole process.

The set-up for the saturation at below zero temperatures is very similar to the previously described one. The main difference is that the pressure vessel is placed inside a freezer (Liebherr comfort), allowing to saturate from -15 °C to -32 °C. In this case, the pressure vessel is the model PARR 4760 with a volume of 0.3 liters that allows to work up to 30 MPa and 275 °C. Moreover, the depressurization medium is a needle-like valve with K_v = 0.3 L/min. The thermal jacket and temperature controller are no needed in this set-up because the temperature is controlled by the freezer. The rest of the assembly, as the manometer or the pressure pump, is equivalent to the one previously described.

Two different foaming setups have been used for the foaming step. The most common one is the foaming in a thermal bath (schematized in **Figure 3.4b**). Thermal baths used in this thesis are the J.P. Selecta Model 600685, provided by Grupo Selecta (Barcelona, Spain).

Alternatively, the hot press presented in section 3.3.1 has also been used for the foaming step. In this case, only the hot plate is used. For this foaming process, the hot plate and the steel sheets are preheated at the desired foaming temperature while the aluminum foil is maintained at room temperature. After the depressurization, the sample is placed between the different sheets. The cold aluminum foil prevents the sample from starting foaming before placing it in the hot plate. The set of layers containing the material is then introduced between the hot plates and foamed under a certain pressure, temperature and time. Then, the pressure is released, and the material is stabilized at room temperature. More details of this process are included in chapter 7 (paper P5).

3.4. Characterization methods

Solids and cellular materials properties have been studied by using a set of characterization methods described in the following sections.

3.4.1. Differential scanning calorimetry

To determine the glass transition temperature of the different samples, a Mettler DSC30 differential-scanning calorimeter, previously calibrated with indium, has been used.

The used program comprises three steps, a first heating cycle performed between 20 °C and 160 °C at 10 °C/min. Afterward, the sample is maintained at 160 ºC for 3 minutes and then cooled from 160 °C to 20 °C at -10 °C/min. The third stage consists of a heating cycle identical to the first one.

The first heating cycle of the three PMMA considered is represented in **Figure 3.5**; the glass transition temperature is then calculated as the mid-point of the drop that characterizes this temperature. The one determined in this first cycle corresponds to the T_g of the material under study with all its thermal history.

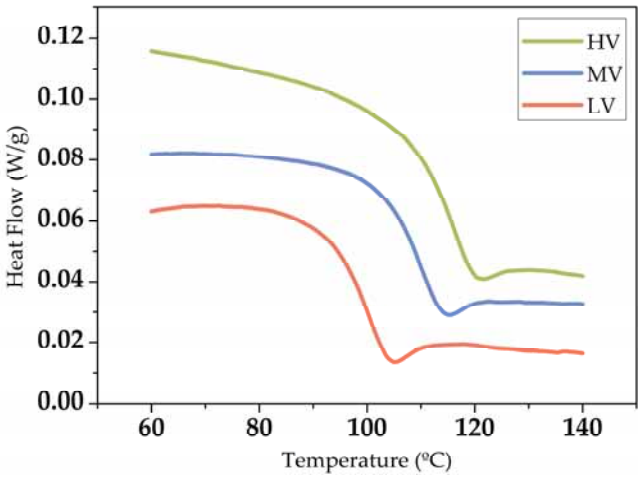

Figure 3.5. Differential scanning calorimeter thermogram of the first heating cycle for the three solid PMMAs used.

In the second heating cycle, it is possible to determine the T_g of the material without any thermal history (see paper P3 in chapter 5).

3.4.2. Density

The density of both solid and cellular materials have been measured in this thesis by following two different approaches.

The density of solid materials was determined through gas pycnometry, using a gas pycnometer model AccuPyc II 1340, supplied by Micromeritics.

Conversely, for cellular materials, the water-displacement method based on Archimedes principle has been used. Measurements were carried out in an AT261 Mettler-Toledo balance provided with a density determination kit.

Cellular materials present a solid skin characteristic of the gas dissolution foaming process (see section 2.4.1 of Chapter 2). This solid skin has been removed previously to the density measurements, using a polisher model LaboPOl2-LaboForce3 supplied by Struers. For each sample, enough amount was removed to eliminate the whole thickness corresponding to the solid skin. In this way, the density of the nanocellular structure is always measured.

3.4.3. Depressurization velocity

In order to determine the depressurization rate, the pressure in the moment of the gas release has been monitored as it is shown in **Figure 3.6**.

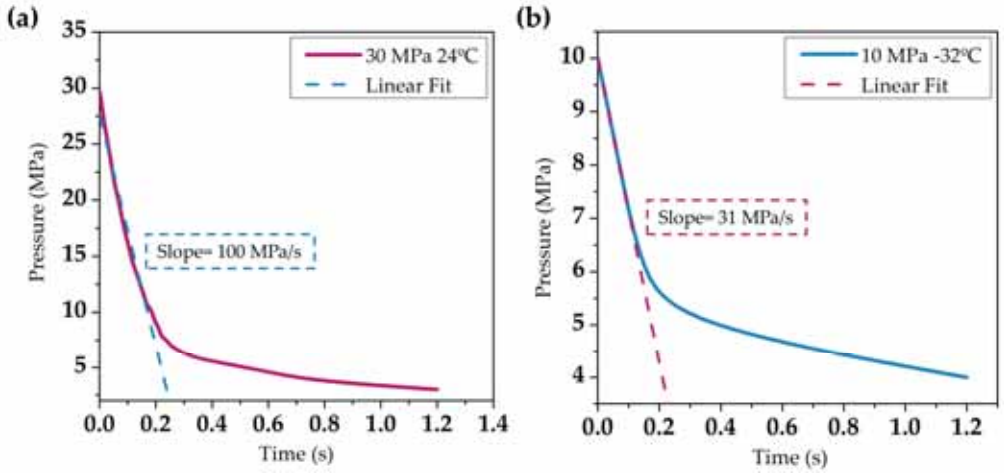

Figure 3.6. Pressure drop rates for two different saturation conditions **a)** Saturation pressure of 30 MPa and saturation temperature of 24 °C (set up for room temperature). **b)** Saturation pressure of 10 MPa and saturation temperature of -32 °C (set up for low temperature).

The pressure drop rate was calculated as the slope of the curve in the first linear part. Two examples are included in **Figure 3.6.** This information has been included in the research papers later included in different chapters.

3.4.4. Solubility and diffusivity

Solubility is defined as the total amount of gas uptake by the polymer when it is fully saturated. It can be calculated as the percentage of weight increment of the solid sample due to gas sorption:

$$CO_2 uptake\ (wt\%) = \frac{m_f - m_0}{m_0} \cdot 100 \qquad (3.1)$$

Where m_0 and m_f are the mass of the sample before and immediately after the saturation, respectively. The initial mass is determined by weighting the polymer before the saturation experiment. However, the determination of the final mass is more complicated. As it was described in section 2.4.1 of chapter 2, since depressurization, the gas starts to diffuse out of the sample. This loss should be considered to determine the exact final mass of the polymer. For this purpose and after saturation, the mass vs. time is monitored as it is shown in **Figure 3.7**.

The first linear part of the depressurization curve is considered to calculate the mass of the polymer in the moment of depressurization, that means when it is fully saturated

and therefore has the maximum amount of gas (m_f) [4]. By considering this linear part; the final mass is calculated as the intercept of this curve with the y-axis (i.e., for time 0).

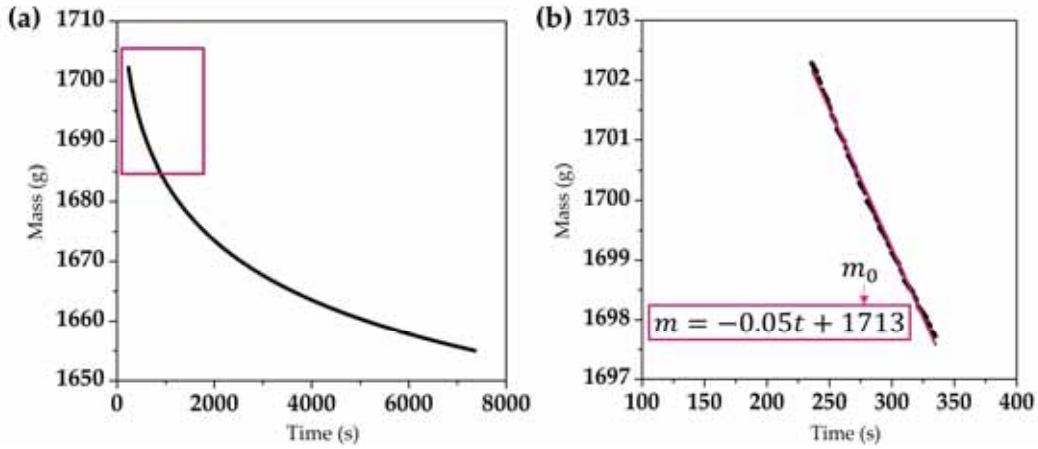

Figure 3.7. Graphs for the grade V825T PMMA saturated at 31 MPA and 24 ºC. **a)** Mass vs. time after depressurization. **b)** linear part of the mass loss graph at initial times.

The same desorption curve (**Figure 3.7a**) can also be used to determine de desorption diffusivity using the slope method [5]. At short times the evolution of the mass with time can be described with the following equation [6]:

$$\frac{m(t)}{m_f} = \frac{4}{l}\left(\frac{Dt}{\pi}\right)^{0.5} \tag{3.2}$$

being $m(t)$ the amount of gas in the polymer at time t, l, the thickness of the used polymer and D the desorption diffusivity. Then, by plotting $m(t)/m_f$ vs $t^{0.5}/l$, the desorption diffusivity can be derived from the slope (R) of the curve as follows:

$$D = \frac{\pi R^2}{16} \tag{3.3}$$

3.4.5. Open cell content

The open cell content was measured through gas pycnometry, using a pycnometer Model AccuPyc II 1340, Micromeritics. According to ASTM D6226-10 standard, the open cell content can be calculated as:

$$O_v = \frac{V - V_p - V_s}{V(1 - \rho_r)} \tag{3.3}$$

where V is the geometric volume, determined using the weighted mass and the density of the material (determined as explained in section 3.4.2) ($V = m/\rho$). V_s is a factor considering the exposed cells at the surface of the sample, and that is negligible for nanocellular materials. And finally, V_p is the pycnometric volume. To determine this quantity, a pressure scanning from 0.2 to 1.3 MPa is performed while measuring the volume for each pressure value. When this value is constant (**Figure 3.8**) that means that no more gas can penetrate the cells, the pycnometric volume can be deduced from the mean value of the final constant data (see **Figure 3.8**).

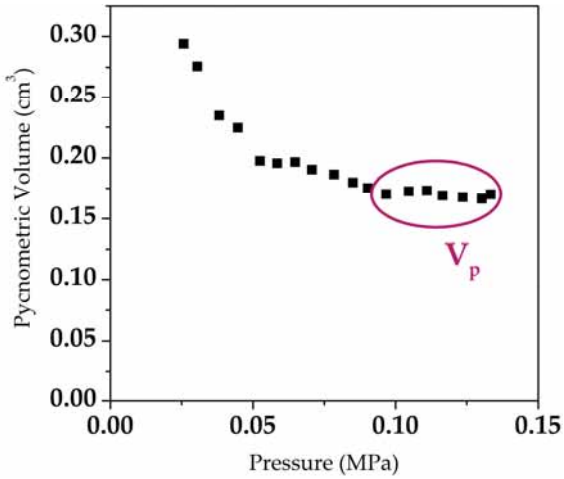

Figure 3.8. Volume measured by the pycnometer as a function of the pressure. The last data at high pressure are used to obtain an average value of V_p. (Graph corresponding to the sample 15 of the paper P3).

3.4.6. Scanning electron microscopy

The cellular structure of the produced cellular polymers has been visualized thanks to an ESEM Scanning Electron Microscope (QUANTA 200 FEG, Hillsboro, OR, USA). Prior to visualization, it is necessary to follow the next procedure. Firstly, samples are fractured after immersion in liquid nitrogen. That ensures the preservation of the cellular structure. After that, the visualization surface is coated with a layer of a thickness between 5 and 10 nm of gold or iridium using a sputter coater (model SDC 005, Balzers Union, Balzers, Liechtenstein). When coating with gold, aggregations of gold with sizes larger than 20 nm can be observed in the SEM image, so when the cell size is smaller than this value, iridium was chosen as the coating metal due to this metal hardly aggregates. After the coating, cellular structures are ready for visualization.

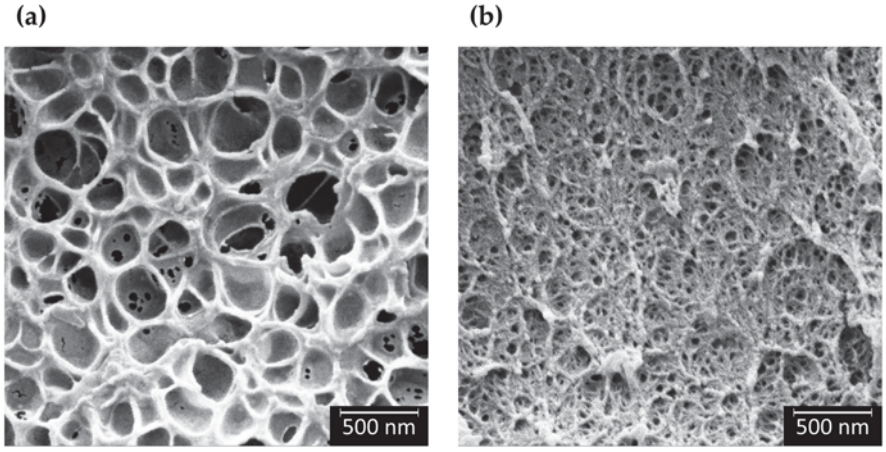

Figure 3.9. SEM micrographs of two different nanocellular PMMA with different cell size. **a)** Sample produced at 31 MPa and 24 ºC (sample of HV PMMA from P3) coated with gold. **b)** Sample produced at 10 MPa and -32 ºC (sample of HV PMMA from P8) coated with iridium.

Micrographs, as those shown in **Figure 3.9,** are obtained using this procedure. Images are then analyzed with ImageJ/FIJI. When the mean cell size is large enough that the cells are discernible (**Figure 3.9a**), it is possible to perform a mask of the cellular structure. That means to obtain an image as that shown in **Figure 3.10a**. This type of image allows using a software-based on ImageJ/FIJI to obtain quantitative data of the cellular structure [7]. This software allows obtaining the cell size (Φ), the standard deviation of the cell size distribution (SD), and the cell nucleation density (N_0) (calculated by using Kumar's method [8]). Moreover, the anisotropy ratio (AR), that is, the ratio of the cell size in the compression direction during precursors production (set as z-axis) and the cell size in a direction perpendicular to it (x-direction) can also be obtained.

As described in section 2.3.1 of chapter 2, a full description of the cellular structure requires a considerable number of parameters. So, apart from the previously described ones, a more in-depth analysis has been done for particular samples in which the cell wall thickness and the mass fraction in the struts were also determined.

The methodology of analysis is illustrated in **Figure 3.10.** The same mask used for the initial analysis is binarized (**Figure 3.10b),** where the solid phase is colored in white and gas phase in black. Through this image, it is possible to evaluate the local thickness of the solid phase, resulting in a color map (**Figure 3.10c**) indicating the differences in thickness.

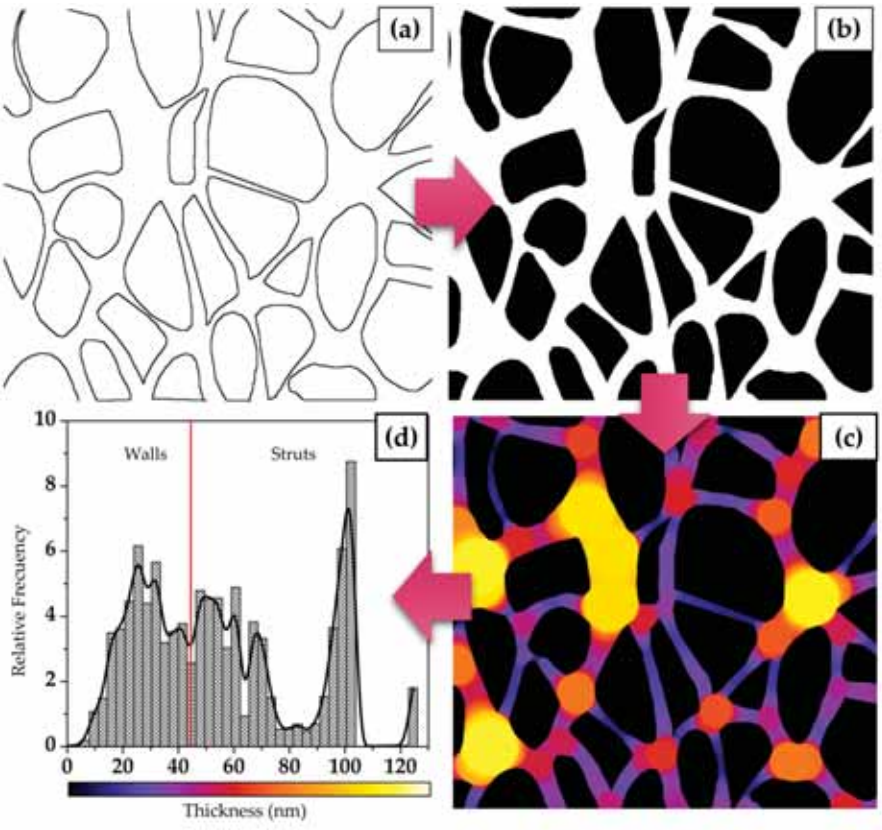

Figure 3.10. a) Mask drew from the SEM micrograph. **b)** Binarized mask of the cell micrograph **c)** Local thickness image obtained from a SEM micrograph. **d)** Histogram of the size distribution of the solid phase, including walls and struts.

From this image, the histogram of **Figure 3.10d** can be obtained quantifying the relative frequency corresponding to each thickness. In the histogram, it is possible to distinguish two different distributions; one corresponding to the solid part distributed in cell walls and the second one corresponding to the solid phase placed in the struts.

The smallest value of strut thickness is then located in the local thickness image and selected as the threshold value to divide the two distributions.

The fraction of mass in the struts is the ratio between the mass situated in the struts with respect to the total solid mass. So, from the histogram f_s is simply the sum of the relative frequencies corresponding to the struts distribution (see P3 in chapter 5 for further details).

The cell wall thickness can be obtained either by directly measuring it from the SEM image or the histogram, calculating the mean thickness of the cell wall distribution.

On the other hand, with cellular structures as those shown in **Figure 3.9b**, a different analysis should be done. In this case, it is not possible to create a mask from the image, so the cell nucleation density is also determined using the Kumar's method by marking all the cells in the software based on ImageJ/FIJI. However, due to the absence of a mask, the cell size is not automatically obtained and should be directly measured from the micrograph. In order to do that, the diameter of more than one hundred of cells is measured in different directions, by introducing the scale of the image it is possible to determine the 2D value for the cell size, that averaging all the measurements provide the mean cell size. Afterward, this value is converted to the 3D cell size by multiplying by 1.273 [7].

3.4.7. Polymers Rheology

Shear rheology tests were carried out in a stress-controlled rheometer, AR 2000 EX from TA Instruments.

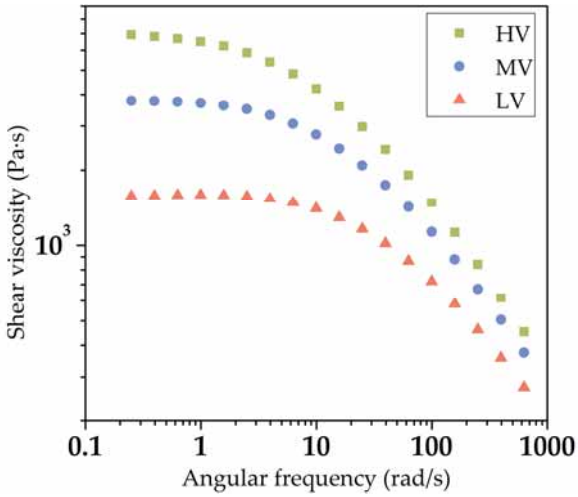

Figure 3.11. Shear viscosity of the three used PMMA as a function of the angular frequency.

To carried out this technique, solid cylindrical samples of each polymer were produced by compression molding with the procedure explained in section 3.3.1 by applying a pressure of 11 MPa.

With the produced samples, dynamic shear viscosity measurements were performed at 230 °C under a nitrogen atmosphere. A parallel plates geometry of R = 25 mm in diameter and a fixed gap of h = 1 mm has been used with an angular frequency range of $0.01 < w < 100\ rad/s$, and a strain of 6%.

Following this procedure, the curves of **Figure 3.11** have been obtained. From these curves, it is possible to calculate the zero shear viscosity as the value of the complex viscosity at low frequencies in the Newtonian plateau [9]. This zero shear viscosity has been included in **Table 3.1**. As it was previously mentioned the rheological properties of the polymers used is very different.

3.4.8. Optical properties

Optical properties of cellular materials have been determined both, experimentally and theoretically. Both techniques are explained in the following paragraphs.

I. Experimental measurements

To experimentally evaluate the optical properties of the materials, two different measurements were carried out, one to measure the total transmittance of the samples and the other to determine the dependence of the transmittance with the used wavelength.

⇒ *Absolute Transmittance*

Transmittance is defined as the light intensity passing through a material (I) divided by the initial intensity emitted by the source (I_0):

$$T = \frac{I}{I_0} \tag{3.4}$$

Before perfoming these measurements, plane parallel layers of different thicknesses were cut using a precision cutting machine Mod.1000 IsoMet (**Figure 3.12a**).

To perform those measurements, the set-up shown in **Figure 3.12b** has been used. Three lasers, with wavelengths of 450 nm, 532nm, and 650nm, were used as a light source. The detector consists of a photodiode joined to an integrating sphere with a 12.5 mm window (model PRW0505 provided by Gigahertz-Optik) connected to a photometer (model X94 provided by Gigahertz- Optik). The laser-detector distance is 30 mm, being the size of the laser beam at the surface of the sample of 2 mm. The initial intensity (I_0) was measured with any sample while the transmitted intensity (I) was measured by placing the sample immediately before to the sphere window, to collect all the light passing through the sample.

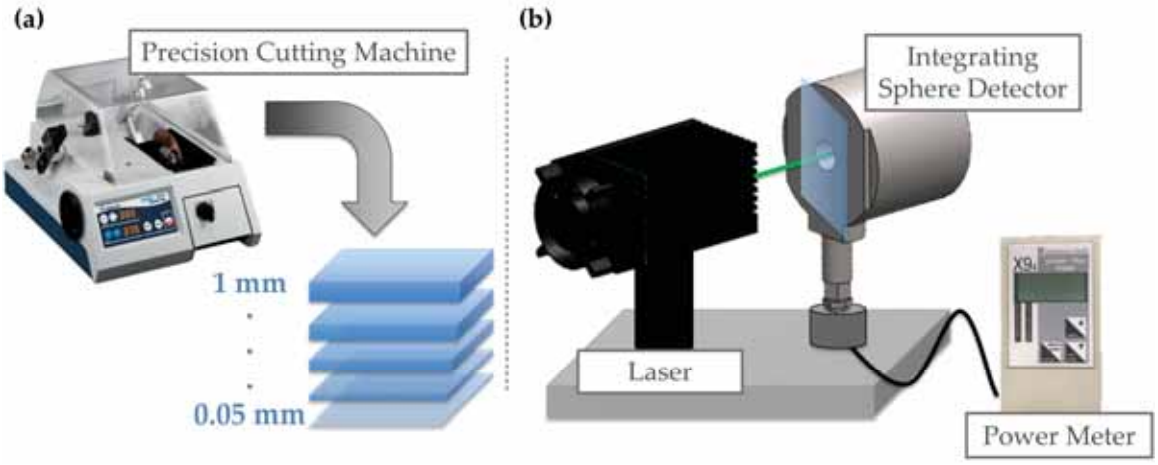

Figure 3.12. a) Precision cutting machine for the production of different thickness layers (from 0.05 to 1 mm). **b)** Scheme of the set-up for the absolute transmittance measurements.

⇒ *Wavelength dependence*

The wavelength dependence was determined using an ultraviolet spectrometer model UV-2102 PC, supplied by Shimadzu. This spectrometer emits in a range from 400 nm to 800 nm.

The configuration of the apparatus leads the sample to be around 2 cm away from the detector, being not possible to collect all the light passing through the sample due to scattering. This join with the weak intensity of the spectrometer made impossible to - measure absolute transmittance values with this set-up. Therefore, only the effect of the wavelength on the transmittance has been measured with this set-up.

To obtain a signal amplification, the energy mode was used with a gain factor of two. Then the transmittance through a solid was taken as the initial intensity. Then the transmittance was determined as the intensity through a cellular material divided by the one of the obtained for the solid.

II. Theoretical model

The modeling of the transmittance was carried out by means of the commercial software COMSOL Multiphysics (version 5.0) that allows studying the interaction between visible light and nanocellular PMMA.

This process comprises three different steps. Firstly, model the cellular material itself, secondly generate a mess allowing performing the calculations and finally solving the interaction light material.

⇒ *Modeling the cellular material*

Nanocellular material is modeled as **Figure 3.13** shows, with two phases corresponding to the solid PMMA and the air. The information regarding the refraction index and the dielectric constant of both phases are introduced in the model using the data of the PMMA used for the experimental measurements. The pores were defined as spheres

with fcc packaging. Therefore, the cell size and the density can be defined as well as the thickness of the material.

Symmetry conditions in z and y directions are therefore applied to this parallelepiped to simulate an infinite plane sample. This method allows maintaining the computational costs at a minimum. The thickness of the material is fixed in a value of 1.27 μm.

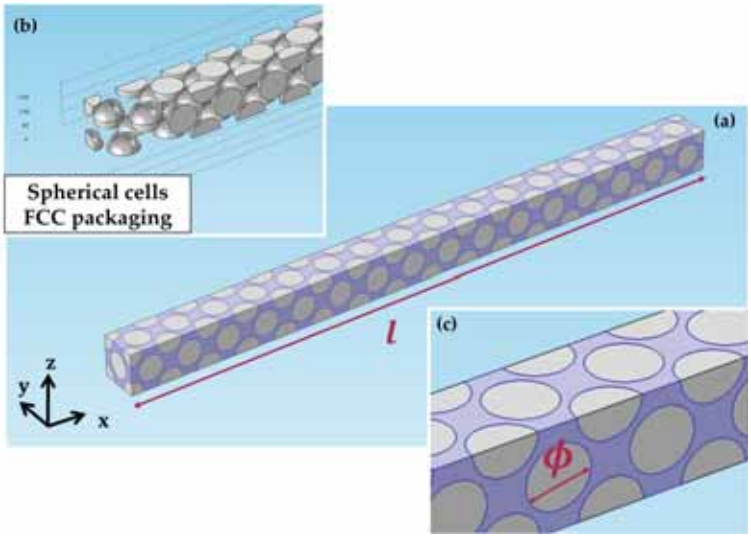

Figure 3.13. a) Modeled parallelepiped of a nanocellular material with thickness l.27 μm **b)** Gaseous phase with spherical cells and fcc packaging. **c)** Cell size of the modeled material.

⇒ *Generate the mess*

In order to perform the calculations, it is needed to generate a mess in the defined material. In order to correctly solve the interaction of the visible light with the elements of the nanocellular material, it is needed to define a size of the mess smaller than a tenth of the visible wavelength and smaller than the corresponding cell size (**Figure 3.14a**). Otherwise, the predictions will not be accurate. Once the size is defined the geometry of the mess was selected to be an automatically generated tetrahedral mess with more elements in the interfaces to obtain the highest resolution with the minimum computational cost.

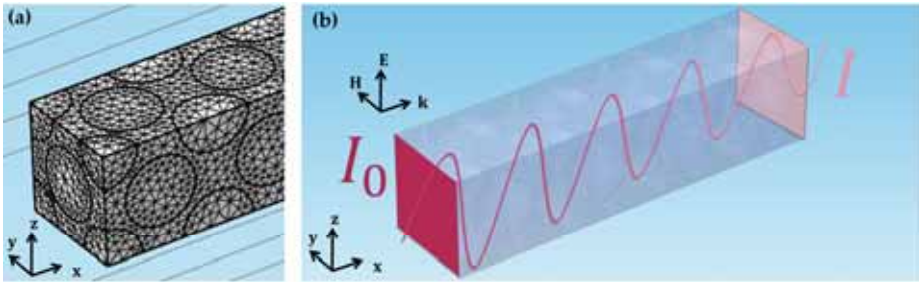

Figure 3.14. a) Meshing of the material. **b)** Representation of the electromagnetic field and the initial and final intensities.

⇒ *Solve the interaction light-material*

Finally, a polarized plane wave of a selected wavelength is introduced in the modeled material (**Figure 3.14b**), and the software is able to solve the Maxwell equations. Being finally possible to calculate the transmittance by dividing the intensity at the end of the infinite plane sample by the introduced intensity.

The obtained transmittance is mathematically processed in order to compare the obtained values with the experimental ones, as explained in chapter 8.

3.4.9. Mechanical Properties

The testing of mechanical properties was performed in the Engineering Department of the University of Cambridge. All the tests were conducted in a screw-driven test bench (Instron 5584 electromechanical testing machine) at room temperature. Two kinds of experiments were carried out by using this equipment, uniaxial compression tests, and single edge notch three-point bending (SENB) tests.

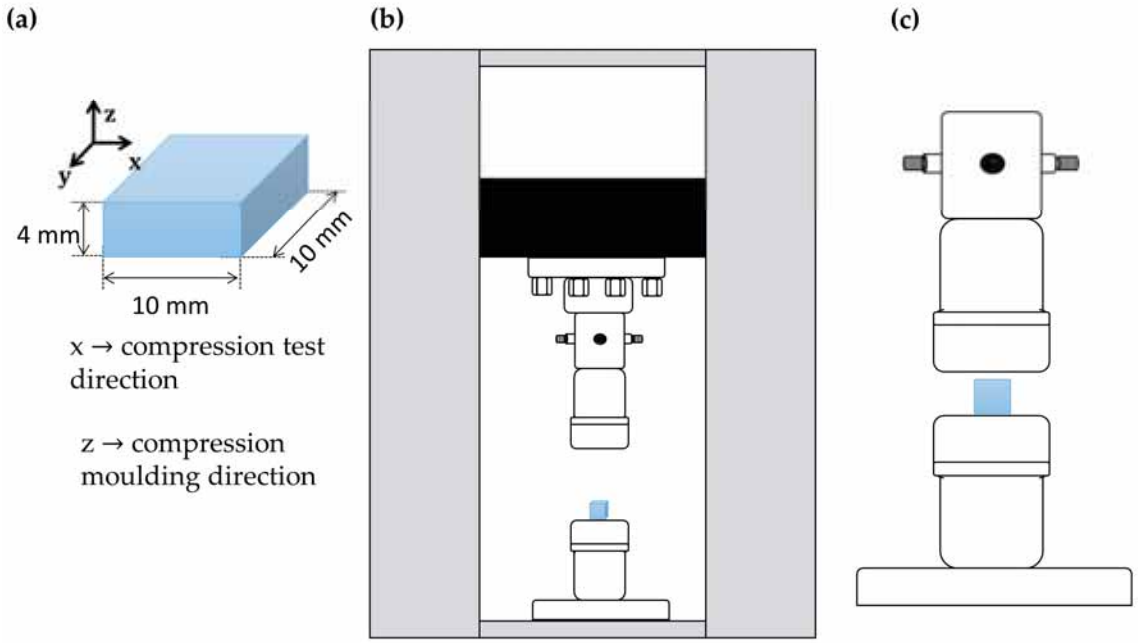

Figure 3.14. a) Scheme of the sample used for compression tests. **b)** Scheme of the Instron with the compression assembly**. c)** Zoom of the compression assembly**.**

Before both experiments, samples were dried in an oven at 50 °C overnight. The assembly for uniaxial compression test is schematized in **Figure 3.14.** After removing the solid skin, samples were machined at 10 x 10 x 4 mm^3 and experiments were carried out by compressing the samples perpendicularly to the compression-molded direction (as the samples are entirely homogeneous same results are expected in the compression-molded direction, see P8 for further details). The chosen experiment parameters were a cross-head speed of 0.083 mm s^{-1}, resulting in a strain rate equal to 8.3 x 10^{-4} s^{-1} for all compression tests. On the other hand, the displacement along the compression direction was measured with a laser extensometer.

This experiment leads to stress vs. strain curves as that shown in **Figure 3.16a**. From which the Young´s modulus (E) and the yield stress (σ_y) can be extracted. The Young´s modulus is calculated as the slope of the first linear part of the curve. The yield stress is calculated as the intersect of the extrapolation of the two fits of the linear regions (**Figure 3.16a**).

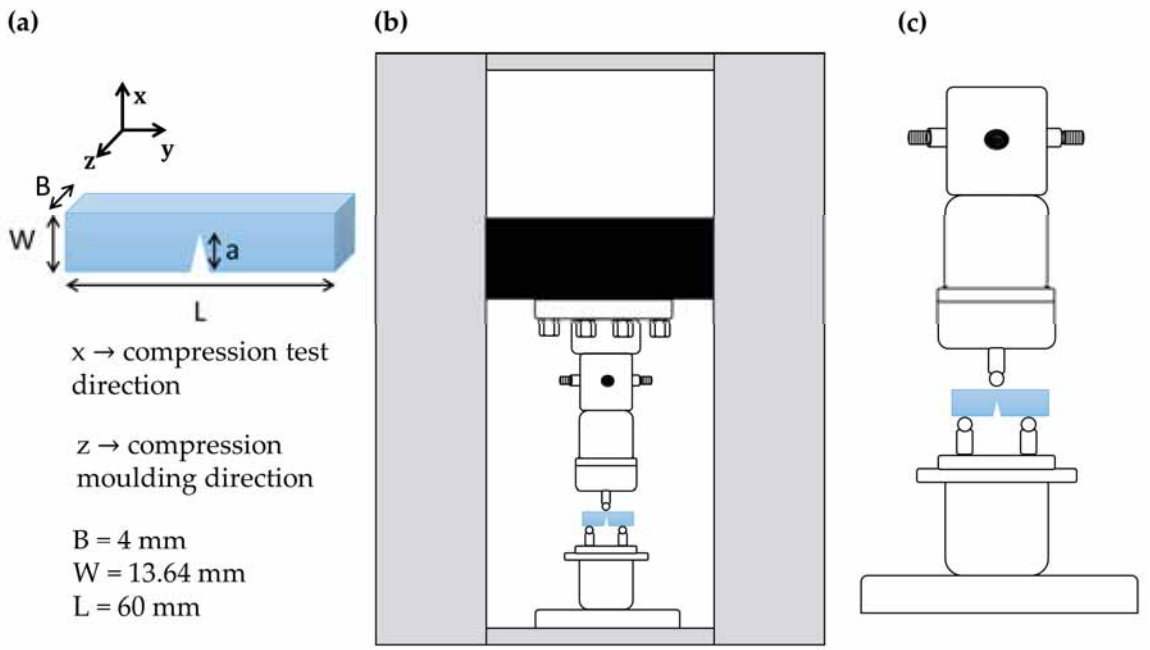

Figure 3.15. a) Scheme of the sample used for three-point bending tests. **b)** Scheme of the Instron with the three-point bending assembly**. c)** Zoom of the three-point bending assembly**.**

Conversely, SENB tests were carried out with the configuration schematized in **Figure 3.15** and by following the ASTM D5045-14 standard [10]. According to this standard, samples dimensions were chosen to be 60 x 13.6 x 4 mm^3. The initial sharp pre-crack with dimensions $0.45 < a/W < 0.55$, was made at the end of a sawed notch by tapping with a razor blade. Graphs as that shown in **Figure 3.16b** are obtained as a result of this experiment (See paper P8 in chapter 8 for further details).

From this graph, it is possible to extract the value of fracture toughness, as indicated in equation 3.5.

$$K_{IC} = \left(\frac{P_Q}{BW^{\frac{1}{2}}}\right) f(x) \tag{3.5}$$

where B and W are the thickness and width of the sample (**Figure 3.15a**), and f(x) the function that follows:

$$f(x) = 6x^{1/2}\,\frac{[1.99 - x(1-x)(2.15 - 3.93x + 2.7x^2]}{(1+2x)(1-x)^{3/2}} \tag{3.6}$$

with $x = a/W$.

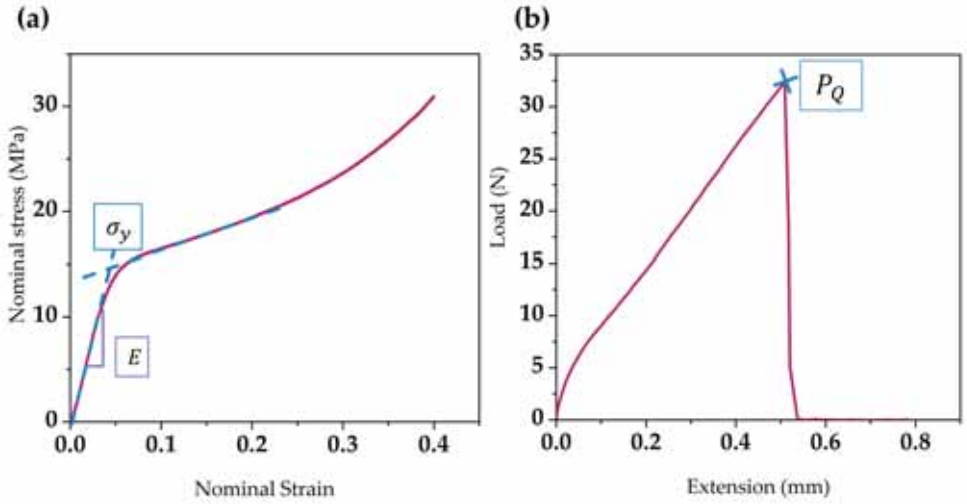

Figure 3.16. a) Example of stress vs. strain curve obtained from the uniaxial compression tests and the measured parameters E and σ_y (experiment for a sample of HV PMMA with 26 nm of cell size of P8) . **b)** Example of a load vs. extension curve obtained from the SENB experiments (sample of the grade MV PMMA with 35 nm of cell size P8).

3.4.10. Thermal Properties

Thermal conductivity was measured using a thermal conductivity meter TPS 2500 S (Hotdisk) by following the Transient Plane Source (TPS) technique [11].

The main principle of this technique relies on a plane element, acting both as temperature sensor and heat source. This element consists of a Nickel electrical conductor in the form of a double spiral placed between two Kapton layers.

This sensor is located between two identical samples of the material under study. Therefore a constant electric pulse is applied during a specific time. The change in the temperature during this period is determined by measuring the changes in the resistance of the sensor. Finally, the conductivity can be derived from the temperature of the sensor vs. time plot by solving the heat conduction equation [12].

In this thesis, both measurements under atmospheric pressure and vacuum conditions were carried out after polishing the solid skin. Measurements have been done using a TPS sensor of 3.189 mm of radius. For the ambient pressure ones, samples were measured five times with a time span of 30 minutes to avoid temperature drift. Measurements time of 40 s and power between 6-7 mW were used.

Prior to the thermal conductivity measurements, samples were dried at 50 °C overnight to remove the moisture.

3.5. References

[1] Ali, U.; Karim, K. J. B. A.; Buang, N. A. A Review of the Properties and Applications of Poly (Methyl Methacrylate) (PMMA). *Polymer Reviews* **2015**, *55*, 678–705.

[2] Takehisa, M.; Sato, Y.; Sasuga, T.; Haneda, N.; Haruyama, Y.; Sunaga, H. Gamma-ray response of a clear, crosslinked PMMA dosimeter, Radix W. *Radiation Physics and Chemistry* **2007**, *76*, 1619–

1623.

[3] Mejia, I.; Estrada, M. Characterization of Polymethyl Methacrylate (PMMA) layers for OTFTs gate dielectric. *Proceedings of the Sixth International Caribbean Conference on Devices, Circuits and Systems, ICCDCS 2006 - Final Program and Technical Digest* **2006**, 375–377.

[4] Tang, M.; Du, T.-B.; Chen, Y.-P. Sorption and diffusion of supercritical carbon dioxide in polycarbonate. *The Journal of Supercritical Fluids* **2004**, *28*, 207–218.

[5] Guo, H.; Kumar, V. Some thermodynamic and kinetic low-temperature properties of the PC-CO2 system and morphological characteristics of solid-state PC nanofoams produced with liquid CO2. *Polymer* **2015**, *56*, 46–56.

[6] Crank, J. *The mathematics of diffusion*; Oxford University Press, **1975**.

[7] Pinto, J.; Solorzano, E.; Rodriguez-Perez, M. a.; de Saja, J. a. Characterization of the cellular structure based on user-interactive image analysis procedures. *Journal of Cellular Plastics* **2013**, *49*, 555–575.

[8] Kumar, V.; Suh, N. P. A process for making microcellular thermoplastic parts. *Polymer Engineering and Science* **1990**, *30*, 1323–1329.

[9] Laguna-Gutierrez, E.; Van Hooghten, R.; Moldenaers, P.; Angel Rodriguez-Perez, M. Effects of extrusion process, type and content of clays, and foaming process on the clay exfoliation in HMS PP composites. *Journal of Applied Polymer Science* **2015**, *132*, 1–12.

[10] International, A. D5045 − 14. Standard Test Methods for Plane-Strain Fracture Toughness and Strain Energy Release Rate of Plastic Materials.

[11] International, A. ASTM D5930-17, Standard Test Method for Thermal Conductivity of Plastics by Means of a Transient Line-Source Technique. **2017**.

[12] Saja, J. A. D. E.; Almanza, O.; Rodri, M. A. Applicability of the Transient Plane Source Method To Measure the Thermal Conductivity of Low-Density. *Polymer* **2003**, 1226–1234

Chapter 4

Influence of saturation parameters

"No hay nada en el mundo más difícil de mantener que la franqueza y nada más cómodo que la adulación."

Fiódor Dostoyevski

INDEX

4.1. Introduction

Saturation parameters include saturation pressure P_{sat}, saturation temperature T_{sat} and saturation time t_{sat} as it was explained in Chapter 2, section 2.4.1. The impact of those ones in the resulting cellular material was illustrated in Chapter 2. This chapter aims at measuring the diffusion kinetics of CO_2 in PMMA and at proving the effect of those parameters in the cellular structure and optical properties of nanocellular PMMA.

Two papers are herein presented to fulfil this objective. The first one, "Martín-de León, J.; Cimavilla-Román, P.; Bernardo, V.; Solórzano, E.; Rodríguez-Pérez, M. A. Cold neutron transmission for in-situ control of gas diffusion mechanisms. *Paper sent* **2019**." introduces an innovative technique allowing to perform tomography experiments under high pressures of gas. So, radiography and tomography data are obtained during the diffusion process.

This makes possible to in-situ monitoring the diffusion kinetics of CO_2 inside polymers, particularly PMMA. Saturation conditions have been changed, using saturation pressures from 10 to 20 MPa and saturation temperatures of 40 °C and 60 °C. By monitoring the process, it has been possible to determine the influence of P_{sat} and T_{sat} in the solubility, **S**, and diffusivity, **D** experimentally. Moreover, morphological changes during the experiment, such as swelling S_w, are also in-situ visualized and related to saturation conditions. In conclusion, $S(P_{sat}, T_{sat})$; $D(P_{sat}, T_{sat})$; $S_w(P_{sat}, T_{sat})$ are herein determined, as **Figure 4.1** shows.

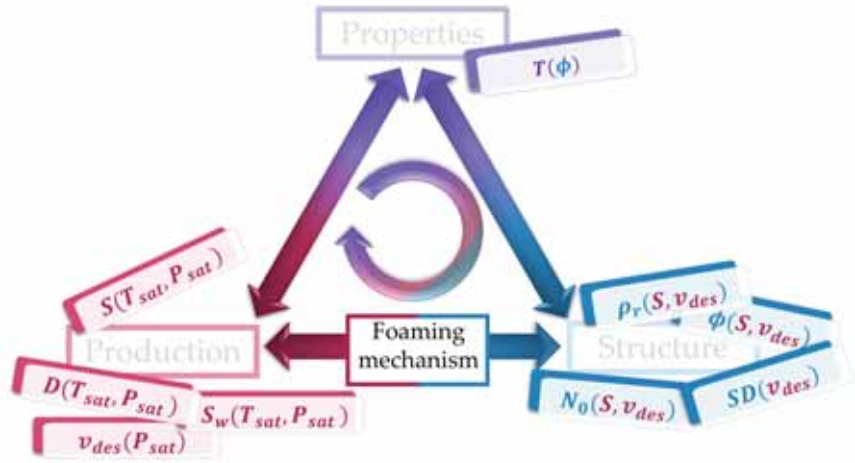

Figure 4.1. Established relationships in Chapter 4.

In the second paper; "Martín-de León, J.; Bernardo, V.; Rodríguez-Pérez, M. Á. Key Production Parameters to Obtain Transparent Nanocellular PMMA. *Macromolecular Materials and Engineering* **2017**, *3*, 1700343" changes in the solubility (as a result of the saturation parameters modifications) are related to the obtained cellular structure. So, the solubility is enhanced from 31 wt% to 48 wt% by sharply decreasing the saturation temperature from room temperature to -32 °C, and using a high saturation pressure up of 20 MPa. Those changes entail modifications in the cell nucleation density, the cell size and relative density that are in-deep studied ($N_0(S)$; $\phi(S)$; $\rho(S)$) (See **Figure 4.1**).

Additionally, those changes in the cellular structure have strong relevance on the final properties of nanocellular PMMA, particularly in the optical properties. So herein the transmittance, T of the produced materials is determined and related to the parameters defining the cellular structure, $T(\phi)$.

Finally, a brief description of the influence of the depressurization parameters on the final cellular structure is presented $\phi\ (v_{des}), N_0(v_{des}), SD(v_{des})$.

In conclusion, this chapter establishes the importance of the saturation parameters on the solubility and how modifying the solubility affects the cellular structure and physical properties (in this chapter, the optical properties).

4.2. Cold neutron transmission for in-situ control of gas diffusion mechanisms.

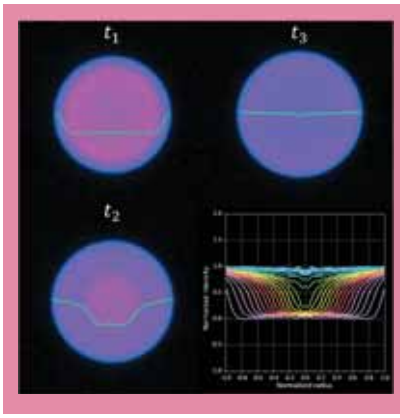

A novel set-up for monitoring gas diffusion process has been developed. Neutron radiography and tomography of polymeric materials under high pressures of gas were carried out. Information about the absorption kinetics of supercritical CO_2 was obtained. Additionally, solubility, diffusivity and morphological changes can be in-situ obtained through the developed measurement technique.

COLD NEUTRON TRANSMISSION FOR IN-SITU ANALYSIS OF GAS DIFFUSION IN POLYMERS.

J. Martín-de León,[1] P. Cimavilla-Román,[1], V. Bernardo[1], E. Solórzano,[2] M.A. Rodriguez-Pérez[1]

Cellular Materials Laboratory (CellMat), Universidad de Valladolid, 47011, Spain

Correspondence to: Judith Martín-de León (E-mail: *jmadeleon@fmc.uva.es*)

Abstract

A novel set-up for monitoring gas diffusion process has been developed. Neutron radiography and tomography of polymeric materials under high pressures of gas were carried out. Information about the absorption kinetics of supercritical CO_2 was obtained. Additionally, solubility, diffusivity, and macroscopic changes in the dimensions of the samples can be in-situ obtained through the developed measurement technique.

Gas diffusion is a universal phenomenon that happens all over daily life. From minor issues such as the gas losses in soft-drinks to the breathing process without which humans could not live. The physics behind the diffusion phenomena is essential for the understanding of all of these processes.

Besides in nature, gas diffusion has become an essential process in some industrial technologies. Particularly, methods based on diffusion of supercritical carbon dioxide (sc-CO_2) are widely used in sectors such as automotive, building, or pharmaceutical, among others. For example, pharmacology takes advantage of sc-CO_2 by dissolving different drugs into their final porous matrixes employing a diffusion process, usually called solvent impregnation method. For instance, ketoprofen has been inserted into

poly(vinylpyrrolidone) micro containers [1], as well as ibuprofen, aspirin, and alendronate, have been loaded on amino-functionalized silicas [2–4]. Furthermore pharmacology benefits from this process also for particle engineering, where sc-CO_2 is used as solvent or antisolvent for drug processing [5,6].

In addition to the pharmacological applications, gas diffusion is used to produce microcellular polymers that are industrially manufactured for all kind of applications. MuCell Extrusion LLC distributes microcellular polymers products in the form of films, sheets or blow molding pieces, that meet the needs from several applications such as food packaging to the production of structural parts, bags, ducts or industrial pipes [7–9]. Expanded polypropylene (EPP) parts are also produced via a CO_2 diffusion-based method [10,11]. Gaming pieces, furniture parts or lightweight construction components are made of EPP, but especially the automotive sector cannot be understood nowadays without these materials; car bumpers, battery covers, roof pillars or seat bracing are developed from this microcellular polymer and distributed by companies all around the world (Gumotex, BASF SE, Kaneka Belgium N.V.). Still, in the cellular polymer's framework, the gas diffusion process is also used for the production of new and promising materials such as are nanocellular polymers [12,13].

In addition to the previous applications, sc-CO_2 diffusion processes can be employed in environmental applications. As an example, it is used for the extraction of contaminants from post-consumer polymers[14–16].

The control of the diffusion process parameters (such as used pressure, temperature, and depressurization rate) is critical for the characteristics of the final product in all the mentioned applications. When talking about microcellular polymers, parameters such as the final density or the final cell size of the cellular material are strongly affected by the diffusion conditions [18–20]. Referring to the impregnation methods, the amount of medicament dissolved inside the polymer depends on the saturation pressure, temperature and time [6,21,22]; or in the case of the particle engineering methods, the final size of the particle, as well as the distribution of particle size, strongly depends upon the production parameters [5,6,23,24].

To understand and control those diffusion process, it is key to develop experimental methods that could in-situ visualize the diffusion process. However, all those supercritical CO_2 diffusion processes are carried out following a batch process inside a pressure vessel suitable for achieving the high-pressure atmosphere required. This constitutes a major drawback for the analysis of these processes because pressure vessel is typically made of heavy elements such as steel what makes difficult the use of historical non-destructive imaging systems, such as X-rays due to the high attenuation when passing through these heavy elements and the low contrast between the gas and the background [25]. On the other hand, cold neutrons offer the perfect alternative due to their weak interaction with matter what makes them very penetrating, being possible to visualize what is happening inside a metal cell. Additionally, the interaction of neutrons with chemical elements varies randomly across the periodic table, leading to high contrast [26].

In this letter, a pioneering set-up to perform in situ radiography and tomography experiments of the gas dissolution process under high-pressure atmospheres is presented (**Figure 1**). This system allows monitoring the whole process thanks to the use of cold neutrons, gathering information about the sc-CO_2 absorption kinetics. Furthermore, it allows obtaining information about the morphological changes in 3D in the saturated system.

Experiments were performed at the neutron imaging instrument at the BER-2 research reactor of the Helmholtz-Zentrum Berlin, CONRAD 2 [27,28]. This curved guide filters the high energy neutrons and gammas from the core of the reactor achieving a neutron spectrum at the end of the guide that presents a maximum in 2.5 Å, that is, cold neutrons, that allow performing high-resolution tomographies. For this study, a pinhole diameter of 2 cm was used reflected in collimating ratios L/D of 500. A high-resolution detector system with a pixel size of 13.5 μm yielded a spatial resolution of 23.36 μm with a field of view of 30 x 30 cm^2. The detector exposure time was fixed in 1 s, and each tomography experiment consisted of a set of 600 projections covering an angular interval of 360°. One tomography was completed every 10 minutes resulting in total measuring times from 8 to 14 hours.

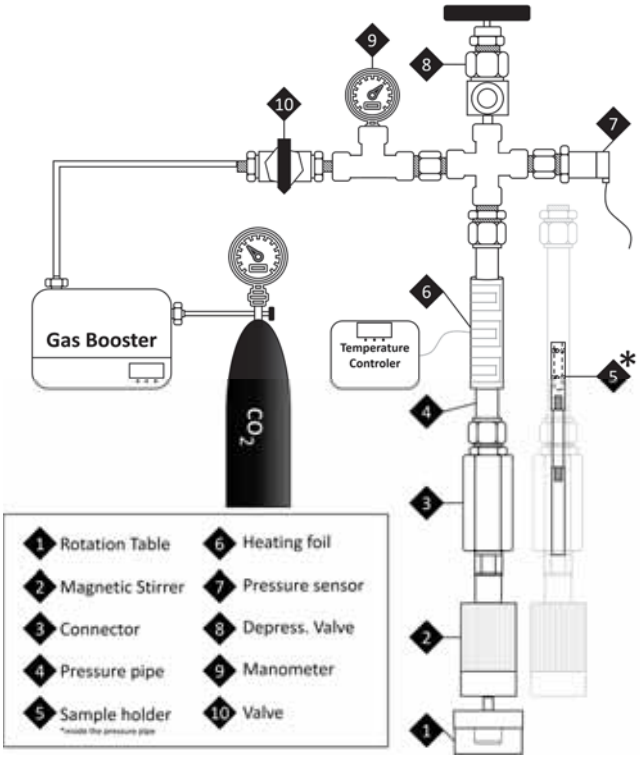

Figure 1. Scheme of the used set-up to perform the in-situ diffusion experiments.

The set-up to perform the diffusion experiments is shown in **Figure 1**. It was placed on the rotation table at the end of the line being the neutron beam pointing at the pressure pipe where the sample of interest is placed. The novelty of this apparatus relies on the possibility of performing high-resolution tomographies of a rotating sample under high pressures of gas. Credit is due to, on the one hand, the small eccentricity achieved with the rotation system, and on the other hand to the whole self-constructed set-up that allows

reaching high pressures while the sample is rotating. As shown in **Figure 1**, the rotation system attached to the rotation table comprises a magnetic stirrer (2) (Mini 100 from premex gmbh) connected to a self-constructed sample holder (5), through a connector ensuring the non-eccentric rotation (3). The sample holder is provided with some screws guaranteeing the immobility of the sample during the whole experiment. This sample holder is placed inside the aluminum pipe acting as pressure vessel (4), that joins together with a CO_2 bottle and a gas booster that allows the system to work up to pressures of 20 MPa. Additionally, a heating blanket (6) (12V/12W) join with a temperature controller makes possible to reach temperatures up to 80 °C.

The whole installation allows performing experiments with a wide range of saturation parameters (gas pressure and temperature). Different saturation conditions induce different behaviors in the gas/polymer system; for example, higher pressures lead to higher solubilities and diffusivities, while higher temperatures imply lower solubilities but also an increase of the velocity of diffusion of the gas [29–32]. Furthermore, polymers suffer an increase in their volume when gas diffuses inside them, an effect known as swelling. Swelling is dependent on the saturation conditions as well as on the polymer nature[33,34]. To evaluate the sensibility of the developed measurement method to all these changes, a set of diffusion experiments at different saturation conditions were carried out by using two different polymers, commonly used for the applications mentioned above. Thus, cylindrical polymeric samples of polystyrene (PS) and polymethylmethacrylate (PMMA) with diameters around 4 mm were subjected to pressures ranging 10 to 20 MPa and temperatures of 40°C and 60°C. Samples were placed inside the described assembly, and the system was pressurized at the desired conditions. Immediately after this, the tomography experiment was launched to track the whole diffusion process. Tomography experiments have been analyzed, aiming at measuring the differences between the different conditions and establish the resolution of the proposed method.

The attenuation of a neutron beam passing through a polymer is due to coherent and incoherent scattering and absorption of neutrons by the nuclei conforming the polymer chains (carbon, oxygen, and hydrogen). So, the transmission of neutrons T, through a polymer can be described by Beer's law [35]: $T = I/I_0 = e^{-\mu \cdot l}$. Where I is the intensity through the sample, I_0 is the incident intensity, μ is the attenuation coefficient and l is the radius of the sample. The introduction of a new phase inside the polymer, such as CO_2, leads to a decrease of the total transmission and therefore an increase in the attenuation coefficient, due to the scattering and absorption of neutrons by the gas, being now the attenuation coefficient a combination of the contributions given by the polymer and the introduced gas [36].

On the other hand, the diffusion of the gas inside a polymer is described by the Fick's second law, $\delta C/\delta t = D\delta^2 C/\delta x^2$, where C is the concentration of gas and D is the diffusion coefficient [37]. According to the solution of this differential equation for a cylindrical sample when working with a diffusion coefficient dependent on the gas concentration, the gas is slowly penetrating the polymer from the surface of the sample to the center of it.

Therefore, the sorption process of gas inside the polymer should result in a change of the transmittance and the attenuation coefficient that can be related with the parameters defining the diffusion process, such as solubility, i.e., the amount of absorbed gas, or diffusivity, the rate at which gas penetrates the polymer.

The proposed set-up, together with the acquisition method and data processing, allow to in-situ measure for the first time in 3D all those changes taking place in a polymer subjected to a sc-CO2 diffusion process. To obtain the maximum amount of information, the acquired tomographies have been analyzed in two different ways. Firstly, the projection images, this is, the raw data obtained during the beam time has been investigated obtaining images like that shown in **Figure 2a**. These projection images, initially obtained as a 16-bit grayscale map, were later treated to produce color images improving this way the visual dynamic range. The transmission through the cylinder has been calculated by considering the intensity I as the average gray value of a region of interest inside the sample and the initial intensity I_0 as the mean gray value of the region of interest outside of the sample but inside the pipe vessel (**Figure 2a**). Five images per tomography for every tomography have been analyzed by following the same procedure, calculating this way the temporal evolution of transmissivity of the gas-polymer system. This will be corrected by swelling, as explained later.

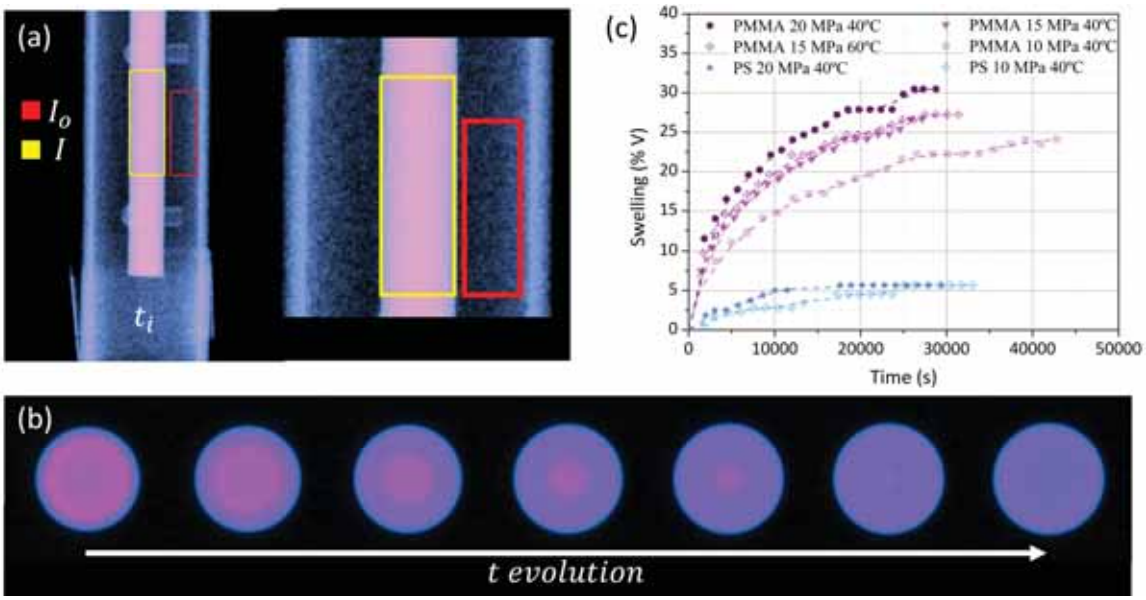

Figure 2. a) Initial and final images for the radiography analysis of the samples. Two examples of the region of interest considered in determining the transmittance are showed. **b)** Time evolution of the cross-section images obtained through tomography analysis for the sample saturated at 10 MPa and 40 ˚C. **c)** Time evolution of swelling for the different experiments.

Conversely, tomography experiments were reconstructed using the filtered back-projection algorithm implemented in the commercial software tool Octopus [38]. Due to polymers are strong absorbers of cold neutrons, the reconstructed cross-section of the material shows a central region darker than the edge. This lack of linearity in the line profile through the sample is caused by the beam hardening effect. Therefore prior to the

tomography reconstruction, it is necessary to apply a beam hardening correction algorithm implemented in Octopus. Afterward, a noise filter is used, and the position of the center of rotation is calculated as well as the offset angle of the same axis of rotation[39]. Afterward, a noise filter is applied, and the alignment of the vertical slices is carried out. Each tomography reconstruction consists in a set of 1000 cross-section images that are later averaged, resulting in a single cross-section image per tomography showing the radial profile of the attenuation coefficient. As it is shown in **Figure 2b**, by following the same procedure for each tomography, the temporal evolution of the radial profile of the attenuation coefficient can be obtained. The tomography analysis also allows monitoring any structural change taking place during the test.

The in-depth analysis described has led to the visualization of the whole diffusion process and the quantification of the parameters defining it. Firstly, morphologic changes in the polymer due to gas diffusion were quantified. As **Figure 2b** illustrates, gas absorption involves an increase in the total diameter of the sample (swelling). By knowing the initial radius of the cylinder, it is possible to quantify the percentage of volume increase of the sample during the whole diffusion experiment (**Figure 2c**). Changes between saturation conditions and between polymers are detected. Moreover, the final obtained values agree with those shown in the bibliography [40,41], concluding that our method has enough resolution to detect structural changes during gas diffusion process (see appendix).

As explained before, the swelling is directly related to the diffusion of gas inside the polymer. This absorption of gas, besides a change in volume, leads to a change in the neutron transmittance through the cylinder that can be calculated with the radioscopy analysis. To obtain the evolution of the transmittance with time, it is necessary to process the radioscopy data jointly with the swelling measurements previously obtained. The radius (l) of the sample is increasing during the experiment, so to obtain comparable transmittance values along time, a factor considering this radius increase was introduced normalizing this way all the transmittance values to the initial diameter of the sample (l_0). Thus the normalized transmittance, T_0, can be calculated from the transmittance T measured in any instant corresponding as follows $T_0 = T^{r_0/r}$. After this procedure graphs as that shown in **Figure 3a** were obtained. It can be seen how the method allows detecting the decrease of the transmittance due to gas diffusion, the introduction of the second phase is leading to a higher neutron absorption reflected in the measured transmittance values. This huge change gives us the chance to quantify the total amount of gas absorbed, that is, the solubility in the sample, in each instant of time. The initial transmittance (T_i) is related to the initial amount of gas C_i, it means zero, and the final value of transmittance, T_f is linked with the final amount of CO_2 uptake C_f. This final amount was calculated as the percentage of weight increment of the gas-polymer mixture concerning the initial weight of the polymer by means of weighting the sample immediately after the whole experiment in a precision balance and extrapolating the data to zero desorption time [22]. Then, the amount of gas inside the sample for each instant of time (C_i) can be defined as $C_i = C_f \cdot (T_i - T_0)/(T_f - T_0)$, as shows in **Figure 3b**. This solubility curve is observed in-

situ for the first time as far as authors know and fit accurately with experimental data obtained in ex-situ analysis (see appendix).

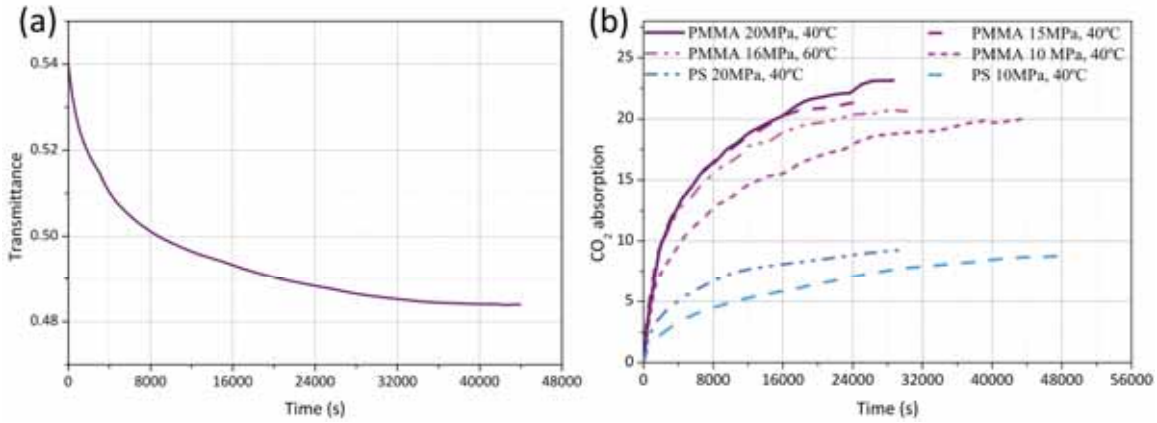

Figure 3. **a)** Example of the transmittance evolution with time for the sample of PMMA saturated at 10 MPa and 40 ˚C. **b)** Solubility values during the whole experiment for all the test carried out.

Finally, the analysis of the reconstructed tomography slices culminates in the obtention of the temporal evolution of the diffusion profile of gas inside of the polymer, and the determination of the diffusivity and the saturation time. As it was shown in **Figure 2 b**, the cross-section of the sample shows, on the one hand, radial changes in the absorption coefficient, and on the other hand, the temporal evolution of this radial profile. These differences are due to the gas penetrating the sample, the lighter shades are signal of the lack of gas in the solid, while the darkest ones mark the presence of this second phase inside the polymer. It is clear how the gas advances radially from the surface of the sample to the center up to reach the full saturation when the tones inside the cylinder are homogeneous. The radial and temporal evolutions can be quantified by merely representing the radial profile of gray values for each tomography (**Figure 4a**). This normalized radial profile represents the solution of the Fick law for the diffusion of a gas inside a cylinder with a diffusion coefficient dependent on the pressure [42]. Therefore, it is possible to experimentally determine the concentration distribution of gas inside the cylinder and to in-situ follow the evolution of this profile, thanks to the method developed in this work.

The evolution of the concentration profile is related to the velocity of penetration of the gas inside of the polymer. This evolution is well known to be linear with the square root of time and can be studied by studying the evolution of the position of the neutron intensity curve as a function of time. To do that the point where the derivate function changes its sign is selected and its position inside the cylinder is represented as a function of the square root of time. The slope of this curve let to determine the value for the square root of the diffusivity for the different polymers and saturation conditions. Obtained values agree with those shown in bibliography measured following ex-situ methods[43,44](see appendix). Additionally, the intersection with the x-axes is indicating

the required time for the gas to reach the center of the sample; it means the saturation time (see appendix for further data).

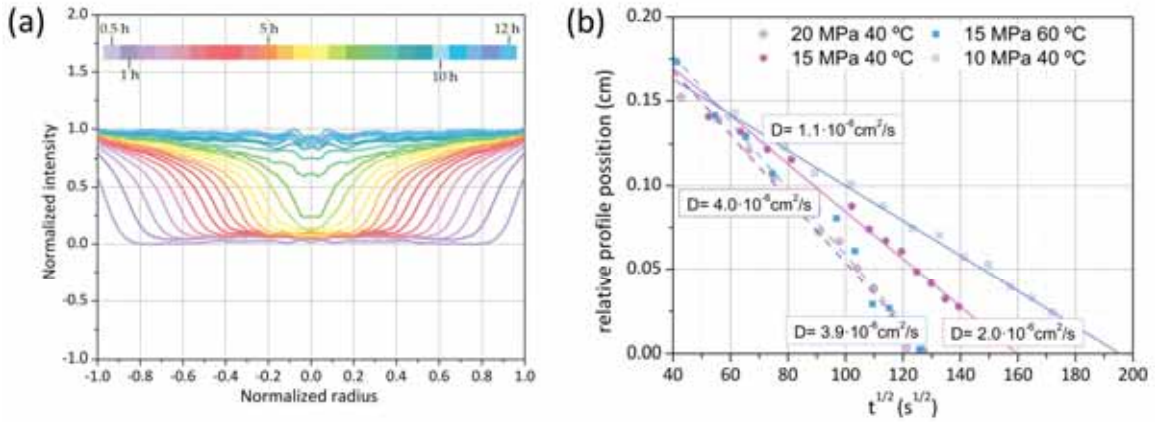

Figure 4. a) Time evolution of the neutron intensity along the radius of the sample of PMMA saturated at 10 MPa and 40 ˚C. **b)** Representation for the determination of diffusivity and saturation times.

To sum up, the developed set up together with the followed analysis make it possible to in-situ follow the diffusion process of a gas inside a solid leading to both qualitative and quantitative results. Thus, structural changes such as swelling can be followed and measured, as well as the evolution of the solubility during the whole experiment while the concentration profile or the diffusivity and saturation time can be determined.

This method would be constructive for the understanding and therefore, control of the applications aforementioned where diffusion of gas plays a major role. Thus, morphological changes in samples, critical for the production of structural cellular polymers, could be controlled, and process times accurate adjusted. In pharmacologic applications, this method would enable to monitor the solubility of the medicaments inside the polymer or its distribution inside the capsule thanks to the concentration profile. Additionally, phenomena taking place during depressurization process, essential for impregnation processes and particle engineering could be visualized. Ultimately, the developed method allows visualizing and measuring in-situ all the physical process of the diffusion phenomenon, that up to now were hidden for us, being possible to understand and finely control the diffusion process in many applications.

Acknowledgments:

Financial assistance from MINECO, FEDER, UE (MAT2015-69234-R), the Junta of Castile and Leon (VA275P18) and Spanish Ministry of Science, Innovation and Universities (RTI2018-098749-B-I00) are gratefully acknowledged. Financial support from FPU grant FPU14/02050 (V. Bernardo) from the Spanish Ministry of Education and Junta of Castile and Leon grant (J. Martín-de León and P. Cimavilla-Román) are gratefully acknowledged.

1. References

[1] Marizza, P.; Pontoni, L.; Rindzevicius, T.; Alopaeus, J. F.; Su, K.; Zeitler, J. A.; Keller, S. S.; Kikic, I.; Moneghini, M.; De Zordi, N.; Solinas, D.; Cortesi, A.; Boisen, A. Supercritical

impregnation of polymer matrices spatially confined in microcontainers for oral drug delivery: Effect of temperature, pressure and time. *Journal of Supercritical Fluids* **2016**, *107*, 145–152.

[2] Nieto, A.; Balas, F.; Colilla, M.; Manzano, M.; Vallet-Regí, M. Functionalization degree of SBA-15 as key factor to modulate sodium alendronate dosage. *Microporous and Mesoporous Materials* **2008**, *116*, 4–13.

[3] Gao, L.; Sun, J.; Li, Y. Functionalized bimodal mesoporous silicas as carriers for controlled aspirin delivery. *Journal of Solid State Chemistry* **2011**, *184*, 1909–1914.

[4] Szegedi, A.; Popova, M.; Goshev, I.; Mihály, J. Effect of amine functionalization of spherical MCM-41 and SBA-15 on controlled drug release. *Journal of Solid State Chemistry* **2011**, *184*, 1201–1207.

[5] Tabernero, A.; Martín del Valle, E. M.; Galán, M. A. Supercritical fluids for pharmaceutical particle engineering: Methods, basic fundamentals and modelling. *Chemical Engineering and Processing: Process Intensification* **2012**, *60*, 9–25.

[6] Shoyele, S. A.; Cawthorne, S. Particle engineering techniques for inhaled biopharmaceuticals. *Advanced Drug Delivery Reviews* **2006**, *58*, 1009–1029.

[7] Wu, H.; Wintermantel, E.; Haugen, H. J. The effects of mold design on the pore morphology of polymers produced with mucell technology. *Journal of Cellular Plastics* **2010**, *46*, 519–530.

[8] Hyde, L. J.; Kishbaugh, L. A. The MuCell ® Injection Molding Process : A Strategic Cost Savings Technology for Electronic Connectors. *Proceedings of International Institute of Connector and Interconnection Technology, Inc. (IICIT) Annual Symposium* **2003**.

[9] Milan, D.; Peal, D. (12) Patent Application Publication (10) Pub . No .: US 2002/0187020 A1. **2013**, *1*.

[10] Carley, M.; Shoper, S. R. Vehicle bumper energy absorber system and method **2012**, *1*.

[11] Tang, E.; Wa Leung, S. K. Molding method for expandable polypropylene **2012**, *1*, 1–4.

[12] Notario, B.; Ballesteros, A.; Pinto, J.; Rodriguez-Perez, M. A. Nanoporous PMMA : A novel system with different acoustic properties. *Materials Letters* **2016**, *168*, 76–79.

[13] Costeux, S. CO 2 -blown nanocellular foams. *Journal of Applied Polymer Science* **2015**, *132*, n/a-n/a.

[14] Guerra, R. M.; Marán, M. L.; Sánchez, A.; Jiménez, A. Analysis of citrates and benzoates used in poly(vinyl chloride) by supercritical fluid extraction and gas chromatography. *Journal of Chromatography A* **2002**, *950*, 31–39.

[15] Smith, S. H.; Taylor, L. T. Extraction of various additives from polystyrene and their subsequent analysis. *Chromatographia* **2002**, *56*, 165–169.

[16] Thilén, M.; Shishoo, R. Optimization of experimental parameters for the quantification of polymer additives using SFE/HPLC. *Journal of Applied Polymer Science* **2000**, *76*, 938–946.

[17] Li, S.; Qiao, C.; Li, Z.; Hui, Y. The effect of permeability on supercritical CO2 diffusion coefficient and determination of diffusive tortuosity of porous media under reservoir conditions. *Journal of CO2 Utilization* **2018**, *28*, 1–14.

[18] Miller, D.; Chatchaisucha, P.; Kumar, V. Microcellular and nanocellular solid-state polyetherimide (PEI) foams using sub-critical carbon dioxide I. Processing and structure. *Polymer* **2009**, *50*, 5576–5584.

[19] Kumar, V.; Weller, J. Production of Microcellular Polycarbonate Using Carbon Dioxide for Bubble Nucleation. *Journal of Engineering for Industry* **1994**, *116*, 413–420.

[20] Kumar, V.; Weller, J. E. A model for the unfoamed skin on microcellular foams. *Polymer Engineering and Science* **1994**, *34*, 169–173.

[21] Pavlínek, P. Transformation of the Czech Automotive Components Industry Through Foreign Direct Investment. *Eurasian Geography and Economics* **2008**, *44*, 184–209.

[22] Gorle, B. S. K.; Smirnova, I.; Arlt, W. Adsorptive crystallization of benzoic acid in aerogels from supercritical solutions. *The Journal of Supercritical Fluids* **2010**, *52*, 249–257.

[23] Reverchon, E. Supercritical antisolvent precipitation of micro- and nano-particles. *The Journal of Supercritical Fluids* **1999**, *15*, 1–21.

[24] Gurikov, P.; Smirnova, I. Amorphization of drugs by adsorptive precipitation from supercritical solutions: A review. *Journal of Supercritical Fluids* **2018**, *132*, 105–125.

[25] Satija, R.; Jacobson, D. L.; Arif, M.; Werner, S. A. In situ neutron imaging technique for evaluation of water management systems in operating PEM fuel cells. *Journal of Power Sources* **2004**, *129*, 238–245.

[26] Roland, C. M. Neutron Scattering in the Analysis of PolymersUpdate based on the original article by D. G. Bucknall, Encyclopedia of Analytical Chemistry , © 2000, John Wiley & Sons, Ltd. . *Encyclopedia of Analytical Chemistry* **2012**, 1–27.

[27] Kardjilov, N.; Hilger, A.; Manke, I.; Banhart, J. CONRAD-2: The neutron imaging instrument at HZB. *Neutron News* **2014**, *25*, 23–26.

[28] Kardjilov, N.; Hilger, A.; Manke, I.; Woracek, R.; Banhart, J. CONRAD-2: The new neutron imaging instrument at the Helmholtz-Zentrum Berlin. *Journal of Applied Crystallography* **2016**, *49*, 195–202.

[29] Han, X.; Koelling, K. W.; Tomasko, D. L.; Lee, L. J. Continuous microcellular polystyrene foam extrusion with supercritical CO2. *Polymer Engineering & Science* **2002**, *42*, 2094–2106.

[30] Tang, M.; Du, T.-B.; Chen, Y.-P. Sorption and diffusion of supercritical carbon dioxide in polycarbonate. *The Journal of Supercritical Fluids* **2004**, *28*, 207–218.

[31] Sato, Y.; Yurugi, M.; Fujiwara, K.; Takishima, S.; Masuoka, H. Solubilities of carbon dioxide and nitrogen in polystyrene under high temperature and pressure. *Fluid Phase Equilibria* **1996**, *125*, 129–138.

[32] Nadella, K.; Guo, H.; Weller, J.; Kumar, V. Sorption and Desorption of CO 2 in Polycarbonate (PC) and Acrylonitrile Butadiene Styrene (ABS) in the Solid State Microcellular Process.

[33] Wissinger, R. G.; Paulaitis, M. E. Swelling and sorption in polymer–CO2 mixtures at elevated pressures. *Journal of Polymer Science Part B: Polymer Physics* **1987**, *25*, 2497–2510.

[34] Tomasko, D. L.; Li, H. B.; Liu, D. H.; Han, X. M.; Wingert, M. J.; Lee, L. J.; Koelling, K. W. A review of CO(2) applications in the processing of polymers. *Industrial & Engineering Chemistry Research* **2003**, *42*, 6431–6456.

[35] Bostain, D. A.; Brenizer, J. S.; Norris, P. M. Neutron radioscopic measurement of water adsorption coefficients in aerogels. *Research in Nondestructive Evaluation* **2002**, *14*, 47–57.

[36] Melnichenko, Y. B.; Wignall, G. D.; Cole, D. R.; Frielinghaus, H. Adsorption of supercritical CO 2 in aerogels as studied by small-angle neutron scattering and neutron transmission

techniques. *Journal of Chemical Physics* **2006**, *124*, 1–11.

[37] Williams, M. M. R. The mathematics of diffusion. *Annals of Nuclear Energy* **1977**, *4*, 205–206.

[38] Vlassenbroeck, J.; Masschaele, B.; Cnudde, V.; Dierick, M.; Pieters, K.; Van Hoorebeke, L.; Jacobs, P. Octopus 8: A High Performance Tomographic Reconstruction Package for X-ray Tube and Synchrotron micro-CT. *Advances in X-ray Tomography for Geomaterials* **2010**, 167–173.

[39] Vlassenbroeck, J.; Dierick, M.; Masschaele, B.; Cnudde, V.; Van Hoorebeke, L.; Jacobs, P. Software tools for quantification of X-ray microtomography at the UGCT. *Nuclear Instruments and Methods in Physics Research, Section A: Accelerators, Spectrometers, Detectors and Associated Equipment* **2007**, *580*, 442–445.

[40] Rajendran, A.; Bonavoglia, B.; Forrer, N.; Storti, G.; Mazzotti, M.; Morbidelli, M. Simultaneous Measurement of Swelling and Sorption in a Supercritical CO 2 -Poly (methyl methacrylate) System. *Work* **2005**, 2549–2560.

[41] Bonavoglia, B.; Storti, G.; Morbidelli, M. Modelling of the Sorption and Swelling Behavior of Semi-crystalline Polymers in Supercritical CO 2. *October* **2005**, 41–44.

[42] Crank, J. *The mathematics of diffusion*; Oxford University Press, **1975**.

[43] Handa, Y. P.; Zhan, Z.; Wong, B. Solubility, diffusivity, and retrograde vitrification in PMMA-CO2, and development of sub-micron cellular structures. *Cellular polymers 20*, 1–16.

[44] Webb, K. F.; Teja, A. S. Solubility and diffusion of carbon dioxide in polymers. *Fluid Phase Equilibria* **1999**, *158–160*, 1029–1034.

4.2.1. Appendix

I. Solubility

Solubility as a function of time was calculated for each experiment as shown in **Figure 3** of the manuscript (paper P1) thanks to the calibration performed. To verify this calibration, an ex-situ experiment was carried out with PMMA by saturating at 15 MPa and 60 °C of saturation pressure and temperature respectively.

The experiment was carried out in the set-up described in section 3.3.2. Five saturation experiments were performed with different saturation times from 30 minutes to 14 hours as it shows **Figure 4.2a**. After each experiment, the amount of gas uptake was determined by doing an extrapolation of the mass at zero time, as explained in section 3.4.4. Finally, the obtained experimental points were compared with the obtained curve with the neutron transmission calibration. As can be seen in **Figure 4.2a,** an accurate fitting is obtained.

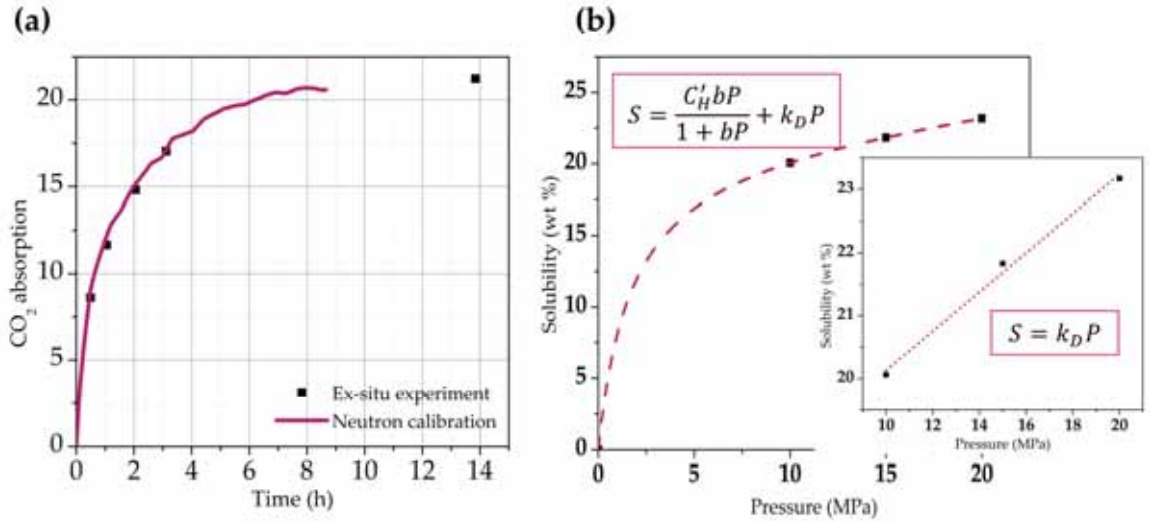

Figure 4.2. a) Comparison between ex-situ sorption experiments with the in-situ solubility curve obtained with the proposed method. **b)** Linear relationship between solubility and pressure in the studied range.

On the other hand, solubility data can be related to the used saturation conditions. As it can be seen in **Figure 4.2b** and **Table 4.1** when fixing the saturation temperature in 40 °C, an increase in the saturation pressure from 10 MPa to 20 MPa results in a raise of solubility from 20 % of gas uptake to 23 wt% of gas uptake.

Different models give the dependence of solubility with pressure. The simplest one is Henry model that relates solubility linearly with pressure through the Henry constant k_D. Although this relationship fits for a wide range of process parameters and polymers, non-linear models are sometimes needed like Langmuir or Dual models [1–3].

Figure 4.2b shows the fitting for the obtained data in this work. Assuming the 0 MPa, 0 wt% of gas point, data points adjust to the dual model, by using $C'_H = 21.5, b = 0.59$ *and* $k_D = 0.17$. In addition, in the range of used pressures points fits with Henry equation by using a value of $k_D = 0.3$.

Conversely, when maintaining the saturation pressure at 15 MPa, the increase in the saturation temperature from 40 °C to 60 °C is translated in a solubility reduction (**Table 4.1**). Attending to Equation 17, the dependence of the solubility with temperature is given by Arrhenius equation[4]:

$$S = S_0 \exp\left(-\frac{\Delta H_s}{RT_{sat}}\right) \quad (17)$$

Where S_0 is the preexponential factor, ΔH_s is the heat of sorption, R is the gas constant, and T_{sat} is the saturation temperature. Taking into account that the heat of sorption is negative for CO_2/PMMA system[5], an increase in the saturation temperature results in a decrease in the solubility.

Table 4.1. Data for the PMMA experiments.

Saturation Pressure (MPa)	Saturation Temp.(°C)	Saturation Time (h)	Solubility (wt %)	Diffusivity (cm^2/s)	Swelling (% Volu)
10	40	10.6	20.06	$1.1 \cdot 10^{-6}$	24.10
15	40	7.1	21.86	$2.0 \cdot 10^{-6}$	26.66
20	40	4.7	23.17	$4.0 \cdot 10^{-6}$	30.47
15	60	4.7	21.23	$3.9 \cdot 10^{-6}$	27.22

Although solubility would depend on the characteristics of the used PMMA, data in the literature for saturation temperatures between 40 and 60 °C, range between 20 and 25 wt% similarly to the obtained data in this work [6,7].

II. Diffusivity

Saturation conditions also affect diffusivity, so the dependence with pressure is given by the following equation [8]:

$$D = a + bP + cP^2 \quad (4.1)$$

Figure 4.3 shows the data obtained in this work fitted with equation 4.1, with constant values of $a = 1.0 \cdot 10^{-8}$; $b = 8.4 \cdot 10^{-9}$; $c = 2.4 \cdot 10^{-8}$. It is clear that an increase in the pressure results in a faster absorption diffusivity, translating in smaller saturation times (**Table 4.1**).

Conversely, the dependence with the temperature is given by an Arrhenius type equation [5].

$$D = D_0 \exp\left(-\frac{\Delta H_D}{RT}\right) \quad (4.2)$$

where D_0 is the pre-exponential factor and ΔH_D is the activation energy for the diffusion process. Although some exceptions have been reported [5], activation energy is usually positive for gas/polymer systems, so an increase in the temperature leads to higher sorption diffusivities.

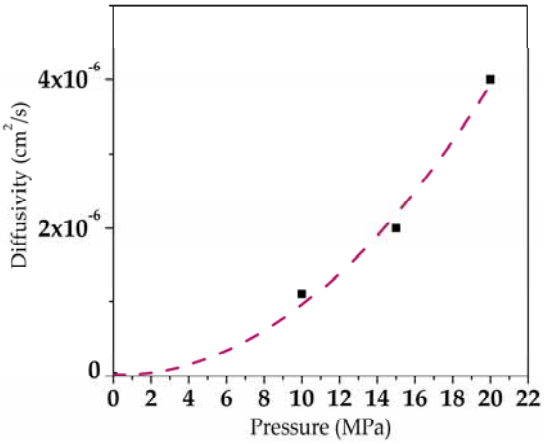

Figure 4.3. Diffusivity as a function of saturation pressure, adjusted with equation 4.1.

That is the case in this work (**Table 4.1**), where an increase of the temperature from 40 to 60 °C doubles the diffusivity. The change is, in fact, equivalent to increase the pressure from 15 to 20 MPa.

Obtained data fits with those previously reported, PMMAs with different molecular weights present sorption diffusivities ranging 10^{-6} - 10^{-7} cm^2/s [6,7].

III. Swelling

The change in the volume as a consequence of gas diffusion is closely related to the amount of gas uptake. A higher amount of gas uptake results in a higher increase in the volume of the material.

PMMA in the bibliography is reported to increase its volume between 20% and 30% when using similar saturation conditions.

This volume increment is also affected by the saturation temperature. An increase in saturation temperature leads to higher mobility of polymeric chains, leading to a slightly higher swelling for similar solubilities.

To sum up, higher saturation pressures lead to higher solubilities accompanied by higher swelling and higher absorption diffusivities. Conversely, increase the saturation temperature leads to smaller solubilities but higher swelling and absorption diffusivity.

References

[1] Sato, Y.; Fujiwara, K.; Takikawa, T.; Sumarno; Takishima, S.; Masuoka, H. Solubilities and diffusion coefficients of carbon dioxide and nitrogen in polypropylene, high-density polyethylene, and polystyrene under high pressures and temperatures. *Fluid Phase Equilibria* **1999**, *162*, 261–276.

[2] Doroudiani, S.; Chaffey, C. E.; Kortschot, M. T. Sorption and diffusion of carbon dioxide in wood-fiber/polystyrene composites. *Journal of Polymer Science, Part B: Polymer Physics* **2002**, *40*, 723–735.

[3] Williams, M. M. R. The mathematics of diffusion. *Annals of Nuclear Energy* **1977**, *4*, 205–206.

[4] Guo, H.; Kumar, V. Some thermodynamic and kinetic low-temperature properties of the PC-

CO2 system and morphological characteristics of solid-state PC nanofoams produced with liquid CO2. *Polymer* **2015**, *56*, 46–56.

[5] Guo, H.; Kumar, V. Solid-state poly(methyl methacrylate) (PMMA) nanofoams. Part I: Low-temperature CO2 sorption, diffusion, and the depression in PMMA glass transition. *Polymer* **2015**, *57*, 157–163.

[6] Webb, K. F.; Teja, A. S. Solubility and diffusion of carbon dioxide in polymers. *Fluid Phase Equilibria* **1999**, *158–160*, 1029–1034.

[7] Nikitin, L.; Said-Galiyev, E.; Vinokur, R. A.; Khokhlov, A. R. Poly (methyl methacrylate) and Poly (butyl methacrylate) Swelling in Supercritical Carbon Dioxide. *Macromolecules* **2002**, *35*, 934–940.

[8] Crank, J. *The mathematics of diffusion*; Oxford University Press, **1975**.

4.3. Key production parameters to obtain transparent nanocellular PMMA

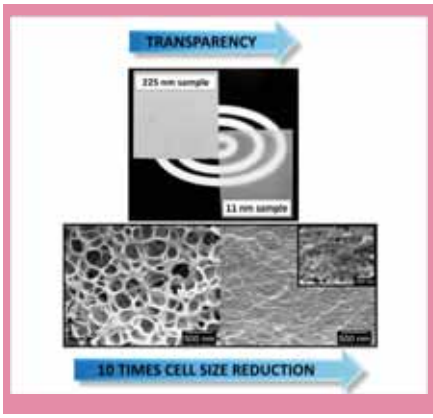

Transparent nanocellular PMMA has been produced for the first time. The key parameters needed for its production are low saturation temperatures (-32 °C) combined with high saturation pressures (6-20MPa). The materials obtained by using this method present homogeneous cellular structures, with cell nucleation densities, higher than 10^{16} nuclei/cm^3, and cell sizes clearly below 50 nm.

KEY PRODUCTION PARAMETERS TO OBTAIN TRANSPARENT NANOCELLULAR PMMA.

Judith Martín-de León, Victoria Bernardo, Miguel Ángel Rodríguez-Pérez

Cellular Materials Laboratory (CellMat), Universidad de Valladolid, 47011, Spain

Correspondence to: Judith Martín-de León (E-mail: *jmadeleon@fmc.uva.es*)

Abstract

Transparent nanocellular polymethylmethacrylate (PMMA) with relative densitiy around 0.4 has been produced for the first time by using the gas dissolution foaming technique. The processing conditions and the typical characteristics of the cellular structure needed to manufacture this novel material has been discovered.

It has been proved that low saturation temperatures (-32 °C) combined with high saturation pressures (6 MPa, 10 MPa, 20 MPa) allow increasing the solubility of PMMA up to values not reached before. In particular, the highest CO_2 uptake ever reported for PMMA, (i.e. 48 wt%) has been found for a saturation pressure of 20 MPa and a saturation temperature of -32°C. Due to these processing conditions cell nucleation densities of 10^{16} nuclei/cm^3 and cell sizes clearly below 50 nm has been achieved. The nanocellular polymers obtained, with cell sizes 10 times smaller than the wavelength of visible light and very homogeneous cellular structures, show a significant transparency.

1. Introduction

Cellular polymers have aroused much interest since the discovery of microcellular polymers in the 1980s at Massachusetts Institute of Technology (MIT),[1] because they present better mechanical properties than materials with bigger cell sizes. [2] In order to further improve these materials, cell sizes were reduced up to the nanometric range, [3]

leading to nanocellular materials (cell sizes below 500 nm) which present interesting properties that make them suitable for their use as insulating materials [4], filters and sensors, among others. [5] In addition, nanocellular materials produced from amorphous polymers are expected to keep ,up to some extent ,the transparent character of the former solid, unlike microcellular materials that are all of them opaque. This potential transparency is due to the fact that if the cells are small enough compared to the wavelength of light, the material will transmit the light rather than scatter it (as occurs in microcellular materials).[6] Transparent nanocellular materials could be potentially used to create transparent thermal insulators that could find a wide range of applications in windows of the construction and transport industries, leading to huge energy savings. [7] As far as we know, there are no precedents of transparent nanocellular polymers produced from the gas dissolution foaming process, but previous studies carried out with silica aerogels (nanostructured materials presenting transparent character [8]) suggest that pore sizes should be around 10 times smaller than the wavelength of light, and in addition the cell size distribution should be very narrow.

Previous papers have dealt with the reduction of cell sizes below 50 nm following different strategies. Some of them are the use of self-assembled order copolymers that can provide nanocellular structures from 100 nm [9] to 10 nm[10], the use of homopolymers based on PC that can produce materials with cell sizes of 20- 30 nm [7] or the use of PPSU as raw material that allows producing cellular polymers with cell sizes of 20 to 30 nm[11] However, the authors of these papers did not analyse the possible transparency of these systems. On the other hand, one of the most studied systems for the production of nanocellular materials has been PMMA due to its high affinity with CO2. In order to reduce the cell size of this system the solubility of PMMA homopolymer have been improved by means of two different strategies, increasing the saturation pressure (psat) [12] or decreasing saturation temperature (Tsat) (reaching cell sizes of 35 nm). [13] But the combination of the two previous strategies at the same time has not been explored.

Taking the previous information in mind, the objective of this work is to produce transparent nanocellular materials based on a PMMA homopolymer. In order to do that the CO2 solubility in the material has been maximized by using Tsat of -32 °C and psat of 6, 10 and 20 Mpa simultaneously, exploring these limits for the first time. This method results in an improvement in cell nucleation densities of two orders of magnitude and smaller cell sizes compared with results obtained up to date. Moreover, the materials with cell sizes below 40 nm show a signficant degree of transparency

2. Experimental section

2.1. Materials

Polymethylmethacrylate (PMMA) V825T was kindly supplied by ALTUGLAS® International (Colombes, France) in the form of pellets. The material used presents a density (ρ) of 1.19 g/cm^3 (measured at 23 °C and 50% HR), a melt flow index of 1.92 g/10 min (230°C/2.16 kg) and a glass transition temperature (T_g) of 114.5 °C measured by DSC.

Medical grade CO_2 (99.9% purity) was used as blowing agent.

2.2. Samples production

The PMMA pellets were processed by using a hot plate press so as to obtain cylindrical 2mm thick sheets. The material was first heated at 250 °C during 9 minutes without applying any pressure. Afterwards, it was pressed under a constant pressure of 2.2 MPa for one minute. Finally, the material was cooled down at room temperature under the same pressure.

These sheets were later cut in order to obtain 20 x 20 x 2 mm^3 samples for the foaming tests.

2.3. Foaming test

Foaming tests have been carried out in a high pressure vessel (model PARR 4760) provided by Parr Instrument Company (Moline, IL, USA). In order to work up to 20 MPa, the pressure system comprises an accurate pressure pump controller (model SFT-10) provided by Supercritical Fluid Technologies Inc. (Neward, DE, USA). The pressure vessel is placed inside a freezer which allows controlling the saturation temperature from 0 °C to -32 °C. Thermal baths (J.P. Selecta Model 600685, Grupo Selecta, Barcelona, Spain) have been used for the foaming after the saturation of the samples. A set of gas dissolution foaming experiments have been done by using this set up. Gas dissolution foaming process consists of three steps, saturation, desorption and foaming. Samples are initially saturated under certain conditions of CO_2 pressure and temperature. Pressure gas is fast released in the second step, and after the desorption time (td) samples are immersed in a thermal bath for foaming.

In this work, Tsat has been fixed to be -32 °C in all the experiments. On the other hand, psat has been varied (6 MPa, 10 MPa and 20 MPa) in order to study its influence on the final cellular structure. Saturation time was 5 days for every experiment in order to ensure the complete saturation of the samples [14]. Pressure was released at a ratio of 1MPa/s. td was 2 minutes for all the experiments. For the foaming step, three different foaming temperatures (Tf) (25 °C, 40 °C and 60 °C) have been used. Foaming time (tt) was 2 minutes.

2.4. Characterization techniques

2.4.1. Density

Density of solid samples (ρ_s) was determined by means of a gas pycnometer (Mod. AccuPyc II 1340, Micromeritics, Norcross, GA, USA). Density of foamed samples (ρ_f) was measured with the water displacement method, based on Archimedes' principle. A density determination kit for an AT261 Mettler-Toledo balance has been used for this purpose. Relative density (ρ_r) has been calculated as the ratio between ρ_f and ρ_s($\rho_r = \rho_f/\rho_s$). The solid skin, characteristic of this process and presenting maximum values of 50μm, has been removed by means of a polisher (model LaboPOl2-LaboForce3, Struers (Ballerup, Dinamarca))before measuring ρ_f. 200 μm has been removed on each side of the sample.

2.4.2. Amount of gas uptake

The amount of CO2 uptake has been calculated as the percentage of weight increment of the sample due to the gas sorption. The final weight of the samples was extrapolated to zero time using the desorption curve (mass lost vs. time plot), which was registered with a Mettler-Toledo balance. The value of mass when the curve is extrapolated to zero desorption time is considered as the mass of the sample under the saturation conditions used, i.e. the solubility of the material. [15]

2.4.3. Scanning electron microscopy

In order to maintain the cellular structure for SEM visualization, samples were cooled down in liquid nitrogen and then cut using a Leica microtome at -120 °C. Then they were coated with around 10 nm of gold by using a sputter coater (model SDC 005, Balzers Union, Balzers, Liechtenstein). An ESEM Scanning Electron Microscope (QUANTA 200 FEG, Hillsboro, OR, USA) has been used to obtain images of the cellular structure. In order to analyse the SEM micrographs, a software based on ImageJ/FIJI [16] has been used. Cell nucleation density (N0) has been measured by using the Kumar method [17] while the tridimensional cell size (ϕ) has been calculated by averaging the cell size measurement of a satisfactory number of cells (more than 200). The cell size distribution as well as the standard deviation of the cell size distribution (SD) has been also measured for each material. Finally, the standard deviation divided by the cell size (SD/ϕ) has been calculated in order to characterize the homogeneity of the cellular structure

Due to the small cell size of the samples, some aspects need to be taken into account regarding the values of this structure characteristic. On the one hand, the gold coating is reducing the measured cell size in approximately 20 nm. On the other hand, the gold coating is covering the smaller cells. Therefore, the reported cell size is an average of the sizes of visible cells. Despite these two facts, the provided values are comparable with those reported using the same methodology.

2.4.4. Transparency

In order to test the transparency of each material, 1 mm thick samples have been cut off by from the foamed materials by means of a precision cutting machine (Mod.1000 IsoMet). Samples obtained are completely plane parallel and present a homogenous thickness.

3. Results and discussion

3.1. Gas uptake

As expected, solubility increases as saturation pressure becomes higher (**Figure 1 (Left)**). [18] A extremely high solubility (39 wt.%) was obtained by decreasing Tsat up to -32 °C and using 6 MPa of psat. [14] By maintaining this low Tsat but increasing the psat up to 20 MPa, it has been possible to achieve a solubility of 48 wt.%, which is to our knowledge, the highest CO_2 solubility ever reported for PMMA.

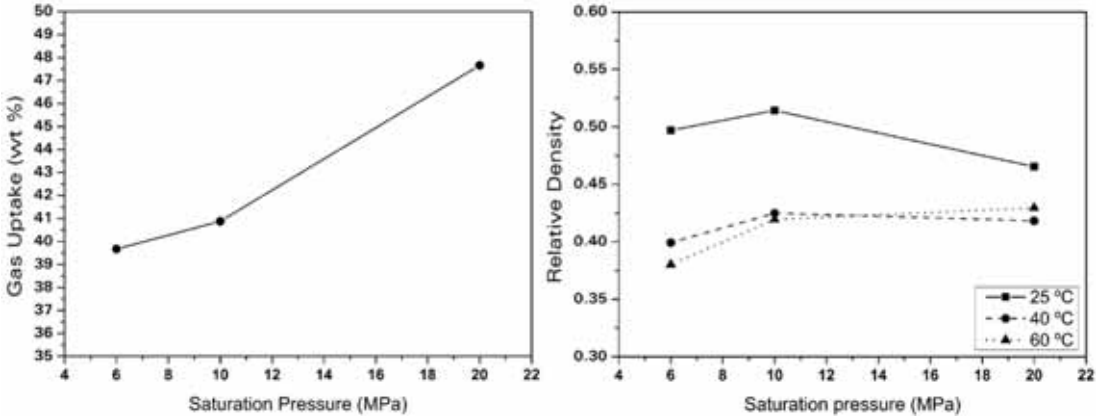

Figure 1. Gas uptake as a function of saturation pressure for a constant saturation temperature of -32 °C. (Left) Relative density as a function of the saturation pressure for different foaming temperatures. (Right)

3.2. Relative density

Figure 1 (Right) shows that relative density hardly changes with psat while it sharply decreases by increasing the Tf from 25 to 40 °C, but when the temperature is increased to 60 °C relative density is no longer reduced. It can be also observed that for 20 MPa, ρ_r is almost constant for all the foaming conditions.

In order to analyse the effect of psat in the final cellular structure samples foamed at 40 °C have been selected.

3.2. Cellular structure

SEM micrographs of the cellular structures obtained as well as the cell size distribution are shown in **Figure 2** while the rest of the obtained data are presented in **Figure 3** and **Table 1. Figure 2** shows a significant reduction of cell size when saturation pressure is increased.

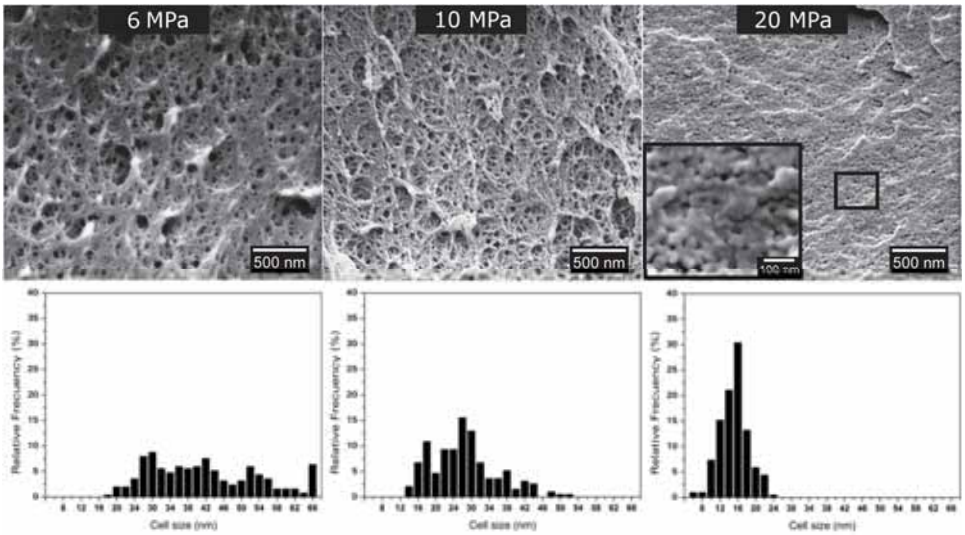

Figure 2. SEM micrographs (up) and cell size distributions (down) of samples foamed at 40 °C during 2 minutes for the three different saturation pressures.

As it can be seen in **Figure 3** and **Table 1**, the increase of the amount of gas uptake from 39 wt% to 48 wt% implies an increase of N_0 from $1.2 \cdot 10^{16}$ nuclei/cm^3 to $6.9 \cdot 10^{16}$ nuclei/cm^3.Otherwise cell size decreases remarkably from 40 nm to almost 10 nm.

On the other hand, changes in the cell size distribution (**Figure 2**, down) can be also observed. As ϕ becomes smaller the width of the cell size distribution (quantified by SD/ϕ) decreases from 0.3 to 0.2, which means that the cell size distribution is more homogeneous.

It can be concluded that it is possible to obtain samples with the same relative density but with different N_0 and ϕ, only by changing the amount of gas absorbed. Using a p_{sat} of 20 MPa and a T_{sat} of -32 °C , values of N_0 as high as $7 \cdot 10^{16}$ nuclei/cm^3 and ϕ around 10 nm can be obtained. These values have not been reported for PMMA before.

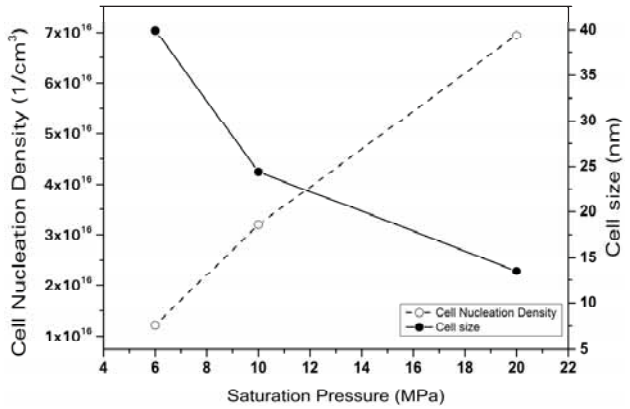

Figure 3. Cell nucleation density and cell size as a function of saturation pressure for samples foamed at 40 °C during 2 minutes.

Table 1. Cell nucleation density, cell size and SD/ Φ for the samples foamed at 40 °C during 2 minutes for the three different pressures.

Saturation pressure [MPa]	N_0 [nuclei/cm^3]	Cell Size [nm]	SD/ Φ
6	$1.2 \cdot 10^{16}$	39	0.27
10	$3.2 \cdot 10^{16}$	24	0.23
20	$6.9 \cdot 10^{16}$	14	0.19

3.4. Transparency

Figure 4 shows a comparison between the 1mm thick samples of this study and one sample produced at 31 MPa of saturation pressure and 25 °C of saturation temperature [12] . This sample has a cell size of 225 nm and relative density of 0.43.

As it is shown in this figure, while the material with a cell size of 250 nm is fully opaque, the materials produced in this research are transparent and as expected transparency increases as cell size becomes smaller.

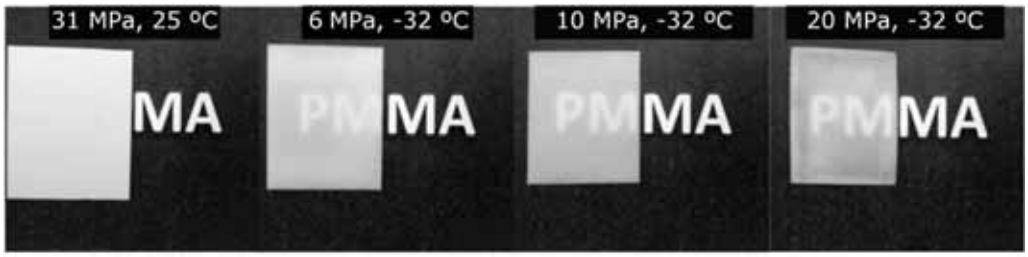

Figure 4. Transparency of the samples produced at three different saturation pressures, compared with a sample of 225 nm of cell size and the same relative density.

As it has been previously reported for aerogels, to obtain transparent nanocellular polymers cell size should be clearly below the wavelength of visible light (400-750 nm). It is needed to reach cells sizes around 40 nm for relative densities of around 0.4 to achieve an appreciable transparency (**Figure 4**).

The material showing the higher transparency is the one showing a smaller cell size and the more homogeneous cell size distribution. It seems that in materials with higher average cell size the presence of cells with diameters bigger than 60 nm are presumably increasing the scattering and therefore reducing the transparency of the material.

4. Conclusions

Nanocellular materials based on PMMA have been produced by using a T_{sat} of -32 °C and three different p_{sat} (6 MPa, 10 MPa and 20 MPa). Changes the saturation pressure increases the amount of gas uptake from 39 wt% to 48 wt% which has permitted to rise cell nucleation densities of $7 \cdot 10^{16}$ nuclei/cm^3 at 20 MPa and to decrease of the cell size to 14 nm. The effect of changing the foaming conditions has been also studied. Higher relative density are obtained with a T_f of 25 °C, while 40 and 60 °C produce materials with smaller and similar relative densities (0.4). In addition, thanks to the reduced cell size obtained (10 times lower than the wavelength of visible light) and the very homogenous cellular structure, transparent nanocellular polymers have been successfully produced for the first time. The possibility of producing transparent nanocellular polymer opens a wide range of potential applications for these novel materials.

Acknowledgments:

Financial assistance from MINECO, FEDER, UE (MAT2015-69234-R), and the Junta de Castile and Leon (VA011U16) are gratefully acknowledged. Financial support from Junta of Castile and Leon grant Q4718001C (J.M.L.) and FPU grant FPU14/02050 (V.B.) from the Spanish Ministry of Education is gratefully acknowledged.

5. References

[1] Eaves, D. *Handbook of Polymer Foams*; Rapra Technology Limited: Shawbury, Shrewsbury, Shropshire, UK, **2004**.

[2] Nadella, K.; Kumar, V. Tensile and flexural properties of solid-state microcellular ABS panels. *Experimental Analysis of Nano and Engineering …* **2007**, *22*, 765–766.

[3] Bureau, M. N. Fracture Toughness of High Density Polycarbonate Microcellular Foams. *Journal of Cellular Plastics* **2006**, *42*, 229–240.

[4] Forest, C.; Chaumont, P.; Cassagnau, P.; Swoboda, B.; Sonntag, P. Polymer nano-foams for insulating applications prepared from CO2 foaming. *Progress in Polymer Science* **2015**, *41*, 122–145.

[5] Costeux, S. CO2 -blown nanocellular foams. *Journal of Applied Polymer Science* **2015**, *132*, 41293–41293.

[6] Hunt, A. J.; Berdahl, P. Structure data from light scattering studies of aerogel. *Materials Research Society Symposium Proceeding* **1984**, *32*, 275–280.

[7] Guo, H.; Kumar, V. Some thermodynamic and kinetic low-temperature properties of the PC-CO2 system and morphological characteristics of solid-state PC nanofoams produced with liquid CO2. *Polymer* **2015**, *56*, 46–56.

[8] Schmidt, M.; Schwertfeger, F. Applications for silica aerogel products. *Journal of Non-Crystalline Solids* **1998**, *225*, 364–368.

[9] Shinkai, T.; Ito, M.; Sugiyama, K.; Ito, K.; Yokoyama, H. Ordered and foam structures of semifluorinated block copolymers in supercritical carbon dioxide. *Soft Matter* **2012**, *8*, 5811–5817.

[10] Dutriez, C.; Satoh, K.; Masami, K.; Yokoyama, H. Nanocellular foaming of fluorine containing block copolymers in carbon dioxide : the role of glass transition in carbon dioxide. *RSC Advances* **2012**, *2*, 2821–2827.

[11] Bernardo, V.; Martín-De León, J.; Rodríguez-Pérez, M. A. Production and characterization of nanocellular polyphenylsulfone foams. *Materials Letters* **2016**, *178*, 155–158.

[12] Martín-de León, J.; Bernardo, V.; Rodríguez-Pérez, M. Low Density Nanocellular Polymers Based on PMMA Produced by Gas Dissolution Foaming: Fabrication and Cellular Structure Characterization. *Polymers* **2016**, *8*, 265.

[13] Guo, H.; Nicolae, A.; Kumar, V. Solid-state poly(methyl methacrylate) (PMMA) nanofoams. Part II: Low-temperature solid-state process space using CO2 and the resulting morphologies. *Polymer* **2015**, *70*, 231–241.

[14] Guo, H.; Kumar, V. Solid-state poly(methyl methacrylate) (PMMA) nanofoams. Part I: Low-temperature CO2 sorption, diffusion, and the depression in PMMA glass transition. *Polymer* **2015**, *57*, 157–163.

[15] Tang, M.; Du, T.-B.; Chen, Y.-P. Sorption and diffusion of supercritical carbon dioxide in polycarbonate. *The Journal of Supercritical Fluids* **2004**, *28*, 207–218.

[16] Pinto, J.; Solorzano, E.; Rodriguez-Perez, M. a.; de Saja, J. a. Characterization of the cellular structure based on user-interactive image analysis procedures. *Journal of Cellular Plastics* **2013**, *49*, 555–575.

[17] Kumar, V.; Suh, N. P. A process for making microcellular thermoplastic parts. *Polymer Engineering and Science* **1990**, *30*, 1323–1329.

[18] Webb, K. F.; Teja, A. S. Solubility and diffusion of carbon dioxide in polymers. *Fluid Phase Equilibria* **1999**, *158–160*, 1029–1034.

4.4. Influence of the depressurization parameters

The main parameter governing the depressurization step in gas dissolution foaming process is the pressure drop rate or depressurization velocity (v_{dep}). In order to experimentally determine its influence on the final cellular structure of nanocellular polymethylmethacrylate (PMMA), a set of experiments were carried out.

4.4.1. Experimental section

PMMA V825T (Chapter 3, section 3.2) was used for this study. Solid samples with a thickness of 4 mm have been produced for the foaming experiments by compression molding (Chapter 3 section 3.3.1).

Then, those samples were employed for the production of nanocellular materials by means of gas dissolution foaming process by using the set-up described in Chapter 3 section 3.3.2 and schematized in **Figure 3.4**.

Saturation parameters were chosen to be 31 MPa and 24 °C, in order to obtain a solubility of 31 %, reported to lead to nanocellular structures in PMMA [1]. Three different depressurization velocities were used in this work. In order to change the depressurization velocity, an electrovalve of with K_v= 1.1 L/min has been used to obtain the maximum depressurization ratio. Afterward, a ball valve was used to limit the flow of the electrovalve. Thus three depressurization velocities have been obtained, 98 MPa/s, 22 MPa/s and 17 MPa/s (measured as explained in Chapter 3 section 3.4.3).

Foaming parameters were selected to be 25 °C for the foaming temperature and 5 min for the foaming time.

4.4.2. Characterization techniques

To characterize the produced cellular materials, the relative density was determined by following the procedure in Chapter 3 section 3.4.2. Moreover, the cell size and the cell nucleation density were measured as explained in Chapter 3, section 3.4.6.

4.4.3. Results

The relative density of the obtained samples is 0.51 for the ones produced by using depressurization rates of 98 and 22 MPa/s and 0.48 for the sample produced with a depressurization ratio of 17 MPa/s. So it could be said that relative density presents a constant value of around 0.5.

SEM micrographs of the obtained cellular structures are shown in **Figure 4.2**. The three materials present a homogeneous cellular structure, but some differences can be appreciated between them.

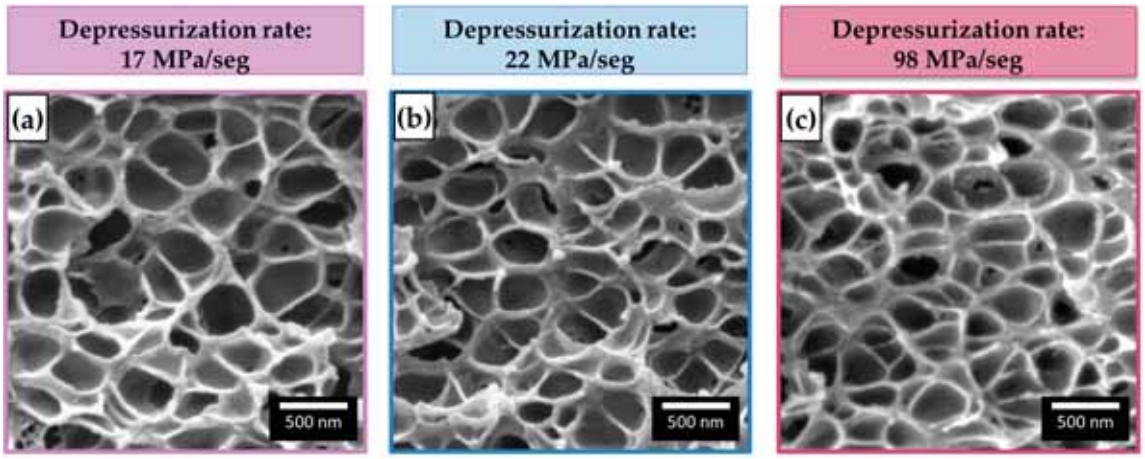

Figure 4.2. SEM images for the samples produced by releasing the gas at different depressurization rates.

The sample produced with the lowest depressurization velocity presents larger cells in comparison with the one produced through a depressurization velocity of 98 MPa/s. This can be confirmed by looking at the obtained data (**Figure 4.2a**). The cell nucleation density increases as depressurization velocity raises while the cell size decreases.

Thus, a pressure drop rate of 100 MPa/s leads to a cell nucleation density of $1.6 \cdot 10^{14}$ nuclei/cm^3 and a cell size of 217 nm, while for a pressure drop rate of 17 MPa the cell nucleation density is $1.2 \cdot 10^{14}$ nuclei/cm^3 and the cell size 250 nm.

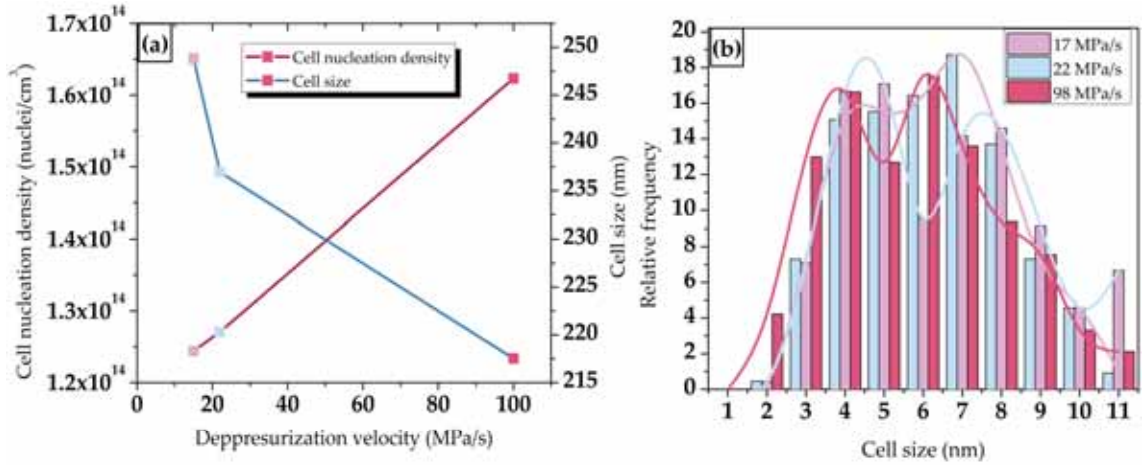

Figure 4.3. a) Cell size and cell nucleation density of the samples as a function of the depressurization velocity. **b)** Cell size distribution of the samples.

Additionally, the cell size distribution has been studied, obtaining the results shown in **Figure 4.3b**. Decreasing the depressurization velocity leads to a cell size distribution shifted to the right, that means to larger cell size values, but similar cell size distribution widths. To quantify the width of the cell size distribution, the magnitude SD/ϕ can be analyzed. For 100 MPa/s of depressurization rate, a value of 0.51 was measured while 0.45 and 0.48 are the values corresponding to the samples produced with v_{des} of 22 and 17 MPa/s respectively. So, similar values were measured.

It can be concluded that a faster depressurization velocity is beneficial to obtain a higher number of smaller cells when producing nanocellular materials from homogeneous polymers. However, it is important to point out that in the range of pressure drop rates analyzed (with a factor of around 5 times between the minimum and maximum pressure drop rate used) and for the saturation and foaming conditions under study, although the effect is clear, the cell size reduction and the cell nucleation density increase are moderate.

Obtained results agree with that discussed in section 2.4.1 about the influence of depressurization velocity in the cellular structure. The proposed model introduces the concept of influence volume, meaning that nucleation does not occur instantaneously, but there exists a nucleation time. Then considering equation 4.1, where the nucleation ratio is given:

$$N_{hom} = f_0 C_0 \exp\left(-\frac{16\pi\gamma^3}{3\Delta P k_B T}\right) \tag{4.1}$$

as a function of f_0 that is the frequency factor of gas molecules joining the nucleus, C_0 the concentration of gas in the polymer, γ the interfacial tension between the gas bubble and the polymer, ΔP the difference between the gas pressure and the solid one, k_B the Boltzmann constant, and T is the gas temperature.

It can be seen that an increase in the pressure drop leads to an increment in the cell nucleation density. If depressurization is slow, the pressure drop in each instant of time is smaller, resulting in a small number of nucleation points. However, if depressurization is almost instantaneous, the value of the pressure drop maximizes, thus the number of nucleation points. Then, when working at $v_{des} = 98\ MPa/s$ creates higher instantaneous instabilities in the polymer/gas systems leading to a more efficient nucleation and therefore smaller cells.

4.5 References

[1] Martín-de León, J.; Bernardo, V.; Rodríguez-Pérez, M. ángel Low density nanocellular polymers based on PMMA produced by gas dissolution foaming: Fabrication and cellular structure characterization. *Polymers* **2016**, *8*.

Chapter 5

Influence of foaming parameters

"La verdad es una cosa terrible y hermosa, y por lo tanto debe ser tratada con gran cuidado."

J.K. Rowling

INDEX

5.1. Introduction

Once the influence of the saturation parameters on the cellular structure has been determined (chapter 4), those parameters have been fixed to study the impact of the foaming parameters.

As it was described in chapter 2 section 2.4.1, the foaming step is governed by the foaming temperature, T_f, and the foaming time, t_f, therefore, the goal of this chapter is to understand the effect of those two parameters on the cellular structure of nanocellular PMMA.

Figure 2.25 in chapter 2 illustrates data of different authors demonstrating how foaming affect cell nucleation density, cell size, and relative density [1–6]. However, in order to understand the foaming mechanisms taking place when foaming temperature and time are changed, a more in-deep analysis was needed.

To fulfill this objective, the article "Martín-de León, J.; Bernardo, V.; Rodríguez-Pérez, M. A. Low density nanocellular polymers based on PMMA produced by gas dissolution foaming: Fabrication and cellular structure characterization. *Polymers* **2016**, *8*, 265." is included in this chapter.

In this article, nanocellular PMMA is produced by using a constant solubility and a wide range of foaming temperatures and times. Saturation parameters are fixed at 31 MPa of saturation pressure and 24 °C of foaming temperature leading to a 31 wt.% of gas uptake for all the experiments. With those conditions foaming temperatures from 40 °C to 110 °C and foaming times from 1 to 5 minutes are used.

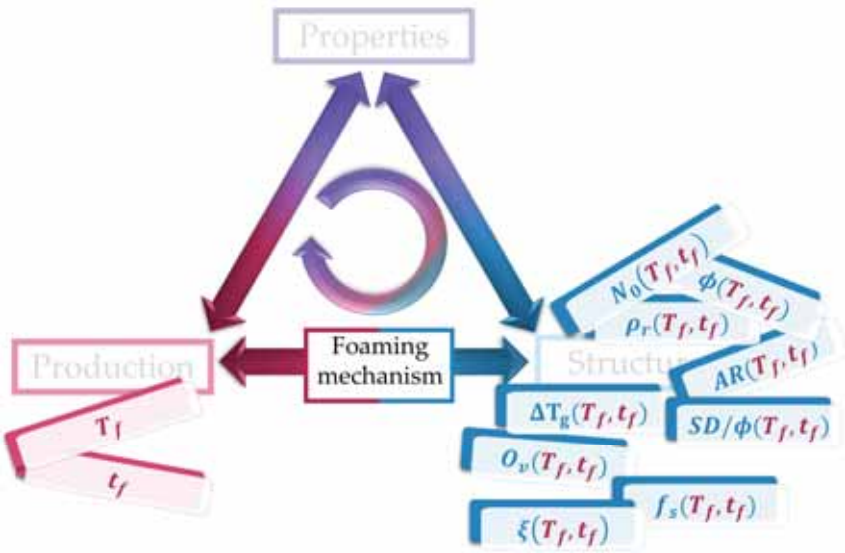

Figure 5.1. Established relationships in Chapter 5.

Obtained cellular structures are then in-deep analyzed. Common parameters such as relative density, $\rho_r(T_f,t_f)$, cell size, $\phi\ (T_f,t_f)$ or cell nucleation density, $N_0\ (T_f,t_f)$ are related to modifications in the foaming parameters. Additionally, to obtain a complete understanding, advanced parameters defining both the gas and the solid phase of the

cellular structure (see chapter 2 section 2.3.1) have also been measured. Thus the gaseous phase has also been characterized by the standard deviation of the cell size, $SD(T_f, t_f)$, the anisotropy ratio, $AR\ (T_f, t_f)$, and the open cell content $O_v(T_f, t_f)$. On the other hand, the solid phase is defined through the fraction of mass in struts, $f_s\ (T_f, t_f)$, the cell wall thickness, $\xi(T_f, t_f)$, and the solid phase confinement, $\Delta T_g(T_f, t_f)$.

This comprehensive analysis allows relating the parameters defining the cellular structure between them, as well as how they are linked with the production process, particularly the foaming step (**Figure 5.1**).

Also, the foaming mechanisms taking place when modifying the foaming parameters, foaming temperature, and foaming time, are discussed in Chapter 5.

5.2. Low density nanocellular polymers based on PMMA produced by gas dissolution foaming: fabrication and cellular structure characterization.

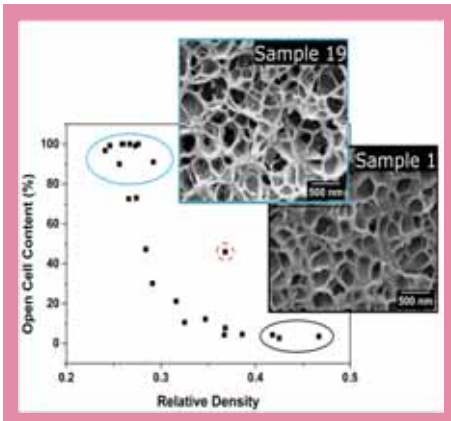

In this paper low density nanocellular polymers based on Polymethylmethacrylate (PMMA) are produced. To produce these materials the processing parameters of the gas dissolution process are optimized. A deep study of the cellular structure is carried out in order to establish the relationship between process and structure. Finally, the confinement effect of the solid phase, previously observed for these materials is also analyzed.

LOW DENSITY NANOCELLULAR POLYMERS BASED ON PMMA PRODUCED BY GAS DISSOLUTION FOAMING: FABRICATION AND CELLULAR STRUCTURE CHARACTERIZATION.

J. Martín-de León, V. Bernardo, M.A. Rodriguez-Pérez

Cellular Materials Laboratory (CellMat), Universidad de Valladolid, 47011, Spain

Correspondence to: Judith Martín-de León (E-mail: *jmadeleon@fmc.uva.es*)

Abstract

This paper describes the processing conditions needed to produce low density nanocellular polymers based on polymethylmethacrylate (PMMA) with relative densities between 0.45 and 0.25, cell sizes between 200 and 250 nm and cell densities higher than 10^{14} cells/cm^3. To produce these nanocellular polymers, the foaming parameters of the gas dissolution foaming technique using CO_2 as blowing agent have been optimized. Taking into account previous works, the amount of CO_2 uptake was maintained constant (31% by weight) for all the materials. Foaming parameters were modified between 40 °C and 110 °C for the foaming temperature and from 1 to 5 min for the foaming time. Foaming temperatures in the range of 80 to 100 °C and foaming times of 2 min allow for production of nanocellular polymers with relative densities as low as 0.25. Cellular structure has been studied in-depth to obtain the processing-cellular structure relationship. In addition, it has been proved that the glass transition temperature depends on the cellular structure. This effect is associated with a confinement of the polymer in the cell walls, and is one of the key reasons for the improved properties of nanocellular polymers.

Keywords: nanocellular polymer; nanocellular foam; gas dissolution foaming; confinement; PMMA.

1. Introduction

The research on cellular polymers is a popular topic in material science since the development of microcellular polymers in the 1980s at Massachusetts Institute of Technology (MIT) [1]. Nowadays, microcellular polymers (with cell sizes in the range of a few microns and cell densities around 10^9 cells/cm^3) are well known multiphasic materials. There are papers on the fabrication and characterization of different systems: polysulfone (PSU) [2], polystyrene (PS) [3], polyvinyl (chloride) (PVC) [4], polyurethane (PU) [5], polyethylene (PE) [6], polymethylmethacrylate (PMMA) [7], and polycarbonate (PC) [8]. The key reason that explains the interest in microcellular materials is that these materials improve the mechanical properties of conventional cellular polymers. This has been reported by different authors for different systems such as poly (ethylene terephthalate) (PET) [9], acrylonitrile butadiene styrene (ABS) [10], PVC [11] or PC [12]. In fact, these materials present better tensile and impact properties than conventional cellular polymers. To further improve the mechanical properties of these systems, there are two promising strategies: (1) improving the cellular structure by means of increasing the homogeneity of the cellular structure; and (2) reducing the average cell size [13],[14]. This is one of the reasons that explains the significant interest that has appeared in the last few years in the development of nanocellular polymers. Nanocellular polymers are characterized by cell sizes below 300 nm and cell densities higher than 10^{14} cells/cm^3 [15],[16]. It is expected that a reduction in cell size to the nanoscale will provide materials with superior properties. In fact, the high potential of these materials has been recently reported for different systems. Miller et al. have proven that cell size reduction to the nanoscale in polyetherimide (PEI) results in an increase in strain to failure and tensile toughness [17]. In addition, it has been proved that nanocellular PMMA presents higher modulus of elasticity, higher impact strength and improved hardness than microcellular PMMA [18]. In addition, another interesting fact recently proved for nanocellular PMMA is that cell size reduction allows for decreasing the thermal conductivity due to the Knudsen effect [19],[20].

Mechanical properties of cellular polymers depend on the cellular structure but relative density also plays an important role [21]. Therefore, it is essential to design production methods able to control both the cellular structure (generating cells with sizes in the nanoscale) as well as the density.

Several methods have been proposed to produce nanocellular polymers. For instance, pattern-transfer techniques have been used to obtain thin film nanocellular polymeric materials [22]. Another approach is the use of solvent based techniques in which nanocellular polymers are fabricated from block copolymers with thermally stable blocks and thermally labile blocks. The thermally labile blocks are removed by using organic solvents leaving nanopores behind [23]. This route works with high T_g polymers/copolymers systems. However, one of the most promising techniques in the

production of bulk nanocellular polymers is the gas dissolution foaming process, usually using CO_2 as blowing agent. This technique involves the saturation of the polymer by the gas phase in high pressure atmospheres and the release of the pressure when the polymer is saturated. When the polymer is under atmospheric pressure again, its super saturation state results in a nucleation process. The nucleation sites are able to grow, typically by heating the polymer over its effective glass transition temperature [24]. There are several studies that have used this technique to create nanocellular polymers. Nanocellular materials produced from pure polymers can be found in systems such as PEI, studied by Sundarram and Li [25]. They were able to produce nanocellular PEI with relative densities around 0.3 and 200 nm of cell size, using 8 MPa and 35 °C as saturation parameters. Nanocellular PMMA with 120 nm of cell size and a relative density of 0.23 has been fabricated by Guo et al. using a saturation process carried out at low temperatures (−20 °C) [22]. The same method has been also used by Guo et al. for polycarbonate, achieving 200 nm of cell size and 0.38 of relative density [26]. Another approach to produce nanocellular polymers using the gas dissolution technique is the use of nano-structured polymers as precursors for the foaming process. These materials have shown, to date, to be more appropriate for obtaining high cell densities using low saturation pressures and high saturation temperatures, but, on rare occasions, they present low relative densities. For instance, nanocellular PMMA/MAM (triblock copolymers poly(methyl methacrylate)-poly(butyl acrylate)-poly(methyl methacrylate)) blends produced by Pinto et al. had relative densities of 0.41 and a cell sizes around 200 nm [27]. They used 30 MPa and 25 °C as saturation conditions. Another PMMA copolymer, PMMA-oEA/SAN(styrene-acrylonitrile copolymer), studied by Costeux et al. was able to produce nanocellular polymers with relative densities of 0.4 and cell sizes of 100 nm. They used saturation conditions of 33 MPa and 30 °C [28]. Another strategy has been the introduction of nanoparticles as nucleating sites. Nanocellular polymers from PC with silica nanoparticles were fabricated by Zhai achieving cells with average sizes of 400 nm and 0.8 of relative density [29]. In addition, by using simultaneously homogeneous and heterogeneous nucleation mechanisms in PMMA-*co*-EMA containing nanoparticles, it has been possible to reduce relative density up to values of 0.2 obtaining cell sizes of 80 nm using 30 MPa as saturation pressure [30].

As it was described in the previous paragraphs, several types of nanocellular polymers have been fabricated up to now by using different systems. However, low relative densities are hardly found and, in the cases they were obtained, complex polymeric matrices such copolymers containing nanoparticles or they have used non-conventional processing parameters such as low saturation temperatures (i.e., saturation temperatures clearly below room temperature) have been used. In addition, in the previous published papers, the process-density-cellular structure relationship has not been analyzed in detail. In particular, the effect of reducing the density on structural characteristics such as cell size, cell nucleation density, cell size distribution, anisotropy ratio, fraction of mass in the struts or open cell content have not been described in detail in previous publications.

Taking the previous information into account, this paper has two main goals. The first one is to obtain nanocellular polymers with low relative density using a conventional PMMA homopolymer and saturation conditions that do not require low temperatures. The second one is to analyze in detail the process-density-cellular structure relationships for these novel materials.

2. Materials and methods

2.1. Materials

Polymethylmethacrylate (PMMA) V 825T was kindly supplied by ALTUGLAS® International (Colombes, France) in the form of pellets. The material used presents a density (ρ) of 1.19 g/cm^3 (measured at 23 °C and 50% HR) and a glass transition temperature (T_g) of 114.5 °C measured by DSC. Medical grade CO_2 (99.9% purity) was used as blowing agent.

2.2. Methods

2.2.1. Precursors production

The as received PMMA was processed into sheets of (155 × 75 × 4 mm^3) using a hot plate press. The process consists of three stages. The pellets were first heated at 250 °C during 9 min in the hot plates without applying any pressure. Then, they were pressed under a constant pressure of 2.2 MPa for another minute. Finally, the sheet was cooled down at room temperature under the same pressure.

These sheets were cut into 20 × 10 × 4 mm^3 samples that were used as precursors for the foaming experiments.

2.2.2. Foaming tests

Foaming experiments were performed in a high pressure vessel (model PARR 4681) provided by Parr Instrument Company (Moline, Illinois,USA). The system to supply the gas pressure comprises an accurate pressure pump controller (model SFT-10) provided by Supercritical Fluid Technologies Inc (Newark, Delaware, USA). Thermal baths (J.P. Selecta Model 6000685, Grupo Selecta, Bercelona, Spain) have been used to heat the samples after saturation with CO_2. A set of foaming experiments have been performed with this set-up using the so-called gas dissolution foaming process [24]. This production route consists of three stages, the saturation step, the desorption step and the foaming step. Samples are introduced in the pressure vessel under a high pressure atmosphere up to saturation. Then, the pressure is released and after some time (desorption time) samples are immersed in a thermal bath for foaming.

Saturation parameters have been chosen to achieve a 31 wt.% of CO_2 uptake, an amount suitable to produce nanocellular materials in PMMA [18],[31]. Saturation pressure (p_{sat}) was fixed at 31 MPa and saturation temperature (T_{sat}) at 25 °C. Saturation time was 24 h for all the experiments. After saturation, the pressure was released by using a fast depressurization rate (100 MPa/s), achieved by using an electrovalve with K_v = 1.1 L/min. Desorption time for all the experiments was 3 min. Foaming temperatures were modified

from 40 °C to 110 °C and foaming times from 1 min to 5 min in order to study the influence of these parameters in the density and cellular structure.

2.2.3. Amount of Gas Uptake

Gas uptake was calculated as the percentage of weight increment of the sample due to the gas sorption. The final weight of the samples after the whole saturation process was evaluated from the desorption vs. time curve, which was registered with a Mettler–Toledo balance (Mettler-Toledo, Columbus, Ohio, USA). This curve can be extrapolated to zero desorption time in order to obtain the total amount of gas uptake during saturation [32]. As it has been previously mentioned, the gas uptake for all the experiments was 31 ± 0.3 % by weight.

2.2.4. Density

Density of solid samples (ρ_s) was measured with a gas pycnometer (Mod. AccuPyc II 1340, Micromeritics, Norcross, Georgia, USA), and density of cellular samples (ρ_f) was determined using the water-displacement method based on Archimedes' principle. A density determination kit for an AT261 Mettler–Toledo balance has been used for this purpose. Relative density (ρ_r) has been calculated as ρ_f/ρ_s. The solid skin of nanocellular samples (that present maximum values of 100 μm) has been removed with a polisher (model LaboPOl2-LaboForce3, Struers (Ballerup, Dinamarca), by removing 200 μm on each side. This polishing process was performed before measuring the material density ρ_f.

2.2.5. Open Cell Content

The percentage of open cells (O_v %) was measured with a gas pycnometer (Mod. AccuPyc II 1340, Micromeritics), according to ASTM D6226-10. The equation to calculate the open cell content is:

$$O_v(\%) = \frac{V - V_p - V_s}{V(1 - \rho_r)}, \quad (1)$$

where V is the geometric volume of the sample, V_p is the volume measured by the pycnometer and V_s takes into account the exposed cells at the surface of the sample. The external volume, V, was determined from the cellular material density (and its mass (m) (measured with an AT261 Mettler– Toledo balance) as $V = m/\rho$. In order to determine V_p, a pressure scan (from 0.2 MPa to 1.3 MPa) with the gas pycnometer has been performed measuring the pycnometric volume for each pressure. From a certain pressure, the volume remains constant, which demonstrates that no more gas can enter inside the cellular material. V_p has been considered as the mean value of these last constant values measured.

As V_s is proportional to the cell size, this value becomes negligible for nanocellular materials and can be neglected in these measurements.

2.2.6. Scanning Electron Microscopy

To prepare the samples for SEM visualization, they were cooled down with liquid nitrogen and then fractured. In addition, they were coated with gold using a sputter coater (model SDC 005, Balzers Union, Balzers, Liechtenstein). An ESEM Scanning Electron Microscope (QUANTA 200 FEG, Hillsboro, Oregon, USA) has been used to obtain images of the cellular structure. The homogeneity of the cellular structure of the samples was analysed by taking different micrographs through the thickness. It was observed that samples were very homogeneous once the external solid skin was removed.

Cellular structure of each material was characterised with a software based on ImageJ/FIJI [33]. Structural parameters such as cell nucleation density (N_0), calculated using the Kumar's method, average cell size(ϕ), cell size distribution, standard deviation of the cell size distribution (SD), and anisotropy ratio (AR) calculated as the ratio of the cell size in the compression direction during precursors production (set as z-axis) and the cell size in a direction perpendicular to it (x direction) have been obtained [34]. A total of two micrographs randomly obtained have been used for the analysis of each material. Therefore, more than 300 cells have been considered for each specimen.

With the aim of obtaining a more complete description of the cellular structure, some advanced cellular structure descriptors such as mean cell wall thickness (ξ) and mass fraction in the struts (f_s) have been measured. Mean cell wall thickness has been measured directly from the micrographs. More than sixty cell walls have been measured per type of material. The average value has been used to characterize the material. This is a 2D characterization method, so broken walls cannot be easily detected in micrographs, thus the measured mean cell wall thickness values correspond to visible (non-broken) cell walls. f_s has been calculated using ImageJ/FIJI and the method explained in **Figure 1**. First of all, a representative region of the micrograph was cropped, then cells were marked in order to create a mask (**Figure 1a**). The second step consists of binarizing the created mask to isolate the solid phase and the gaseous one, marking the first one in white and the second one in black (**Figure 1b**). Local thickness can be analysed from this image, obtaining a local thickness image of the original cellular material (**Figure 1c**). In this image, due to the difference in thickness that struts and walls present, it is possible to distinguish these two different structural elements and to obtain a local thickness histogram (**Figure 1d**). This histogram quantifies the relative frequency corresponding to each thickness. In order to evaluate the fraction of material in the struts, a threshold value has been chosen as the minimum thickness corresponding to a strut (**Figure 1d**).

This minimum thickness was chosen by measuring the thickness of different struts directly from the micrographs and selecting the minimum value as threshold. For each image, it was confirmed that this threshold value was selected properly to avoid an overlapping of the two distributions, i.e., to avoid computing cell walls as struts. Finally, the fraction of mass in the struts can be determined as the total sum of relative densities corresponding to struts thickness. Some samples (those with lower densities) did not present sufficient differences in thickness between struts and cell walls (the two distributions showed a significant overlap), so for these particular samples, it was not possible to apply this quantification approach.

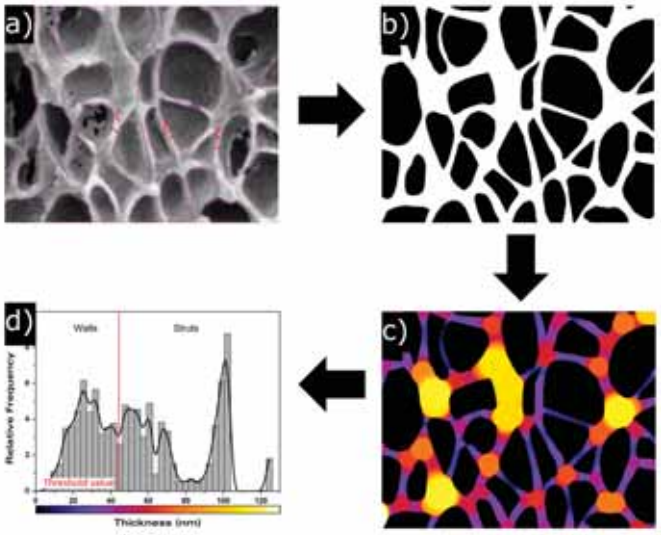

Figure 1. Description of the method to measure the fraction of mass in the struts (f_s). (**a**) cell mask; (**b**) binarized cell mask; (**c**) local thickness cell image; (**d**) local thickness histogram.

2.2.7. Differential Scanning Calorimetry

Glass transition temperature (T_g) has been measured by using a Mettler DSC30 differential-scanning calorimeter (Mettler-Toledo, Columbus, Ohio, USA) previously calibrated with indium. The T_g was taken as the mid-point of the change in the DSC thermogram that characterizes this transition. The weights of the samples were approximately 5 mg. To study the glass transition temperature of the as processed samples a first heating step was performed between 20 °C and 160 °C at 10 °C/min. Later on, samples were maintained at 160 °C for 3 min to erase any thermal history, and then they were cooled from 160 °C to 20 °C at −10 °C/min. Finally, the initial cycle of heating from 20 °C to 160 °C at 10 °C/min was performed again to determine the glass transition temperature of samples with the same thermal history. These experiments were done on the cellular materials and on the solid sheets. T_g increment (ΔT_g), defined as the difference between the T_g of the cellular material in the first heating step and that of the solid material in the same heating step, was calculated for each material. The same calculation was performed for the second heating step defining ΔT_{g_2}.

3. Results

3.1. Influence of the Foaming Temperature and Time

3.1.1. Relative Density

To study the influence of the foaming parameters on the final cellular structure, different foaming temperatures have been used, from 40 °C to 110 °C, increasing in intervals of 10 °C. Furthermore, the influence of the foaming time has been determined using 1, 2 and 5 min of foaming time for each temperature. Relative density of each sample has been measured. As it can be seen in **Figure 2**, the relative density has a clear tendency with both the foaming temperature and the foaming time.

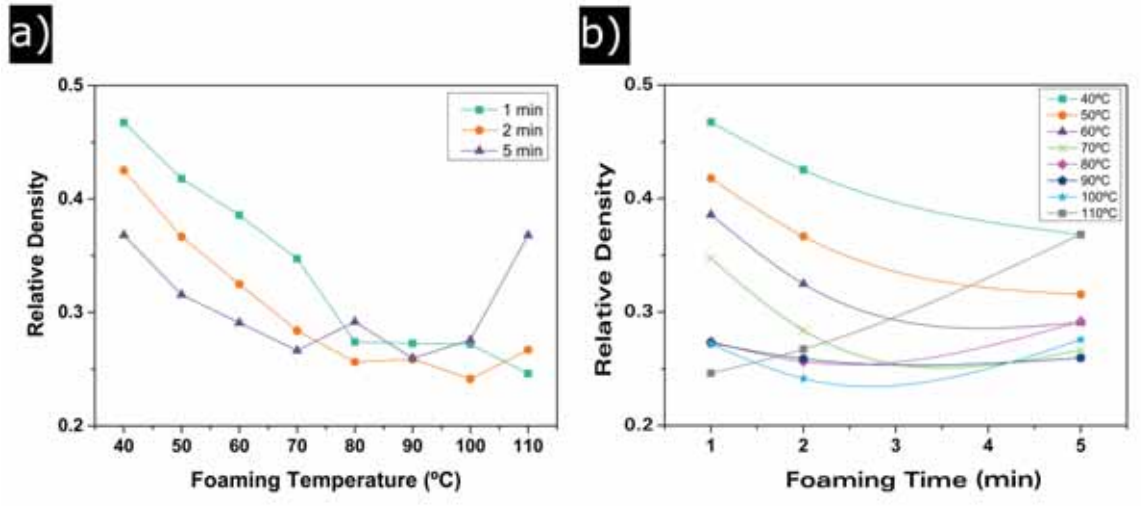

Figure 2. (**a**) relative density evolution with foaming temperature; (**b**) relative density evolution with foaming time.

Relative density experiences an important decay from 0.46 at 40 °C of foaming temperature to a minimum of around 0.24 when the temperature increases. This decay seems to reach equilibrium at 80 °C. No significant differences in relative density are observed between samples foamed at 80 °C and the ones foamed at 90 °C and 100 °C. This is also true for samples foamed at 110 °C for foaming times of 1 and 2 min, but for 5 min relative density suffers a sharp increase (**Figure 2a** and **Table 1**).

Figure 2b shows the effect of foaming time. An increase in the foaming time results in a decrease in the relative density for temperatures from 40 °C to 80 °C. At this last temperature, the equilibrium reached by ρ_r is also detected. For higher temperatures, 90 °C and 100 °C, densities are similar for times between 1 and 5 min. It can be observed again that the experiments performed at 110 °C of foaming temperature do not follow the general trend; the lowest density is reached at 1 minute and then the relative density increases to values above 0.35.

It can be concluded that, for these saturation conditions, there exist a minimum relative density of 0.25 that can be reached using temperatures between 80 °C and 100 °C and foaming times between 2 and 5 min. Moreover, 110 °C seems to be the upper limit for the foaming temperature because at 5 min of foaming time, the relative density increases significantly. This is a consequence of the very close value of this temperature and the T_g of the used polymer.

Table 1. Production parameters and main characteristics of the materials under study.

S.	t_f (min)	T_f (°C)	ρ_r	N_0 (1/cm³)	ϕ (nm)	SD/ϕ	AR	ξ (nm)	f_s	OC (%)	ΔT_g (°C)	ΔT_{g_2} (°C)
1	1	40	0.47	1.78×10^{14}	212	0.45	1.24	26	0.60	4	4.9	0.1
2	2	40	0.43	1.55×10^{14}	220	0.37	1.22	30	0.54	3	6.4	2.1
3	5	40	0.37	2.17×10^{14}	225	0.39	1.26	24	0.54	8	7.3	0.7
4	1	50	0.42	1.74×10^{14}	219	0.40	1.30	24	0.57	4	5.9	0.5
5	2	50	0.37	2.24×10^{14}	213	0.41	1.32	26	0.47	4	8.5	0.8

6	5	50	0.32	2.16×10^{14}	241	0.41	1.27	24	0.54	21	9.9	0.3
7	1	60	0.39	2.38×10^{14}	207	0.42	1.21	26	0.46	5	8.3	1.6
8	2	60	0.33	2.34×10^{14}	221	0.40	1.27	26	0.36	11	10.0	−0.7
9	5	60	0.29	2.12×10^{14}	236	0.47	1.26	23	0.38	30	9.6	1.4
10	1	70	0.35	2.27×10^{14}	221	0.44	1.24	24	0.39	12	7.8	1.2
11	2	70	0.28	2.19×10^{14}	229	0.46	1.20	30	0.36	47	10.5	1.5
12	5	70	0.27	2.73×10^{14}	221	0.44	1.28	25	0.34	73	10.3	0.3
13	1	80	0.27	3.56×10^{14}	208	0.45	1.21	23	0.35	73	10.5	0.7
14	2	80	0.26	3.15×10^{14}	227	0.40	1.14	26	-	90	11.6	2.2
15	5	80	0.29	2.81×10^{14}	224	0.41	1.23	29	0.35	91	11.3	2.4
16	1	90	0.27	3.04×10^{14}	222	0.40	1.12	29	0.35	99	10.0	0.5
17	2	90	0.26	3.13×10^{14}	222	0.44	1.14	26	-	100	10.3	1.0
18	5	90	0.26	2.79×10^{14}	234	0.40	1.09	28	-	100	10.5	0.6
19	1	100	0.27	3.44×10^{14}	204	0.41	1.18	28	0.31	100	10.9	21.9
20	2	100	0.24	3.60×10^{14}	216	0.46	1.03	26	-	97	10.7	2.5
21	5	100	0.28	2.67×10^{14}	234	0.43	1.16	29	0.308	100	11.4	1.1
22	1	110	0.25	2.23×10^{14}	261	0.43	1.19	28	-	99	10.9	1.4
23	2	110	0.27	2.99×10^{14}	227	0.43	1.04	33	0.32	100	10.9	1.0
24	5	110	0.37	3.10×10^{14}	184	0.40	1.17	36	0.54	46	4.9	2.0

*S= Sample; t_f= foaming time; T_f= foaming temperature;

3.1.2. Cellular Structure

One example of the typical cellular structures obtained is shown in **Figure 3**.

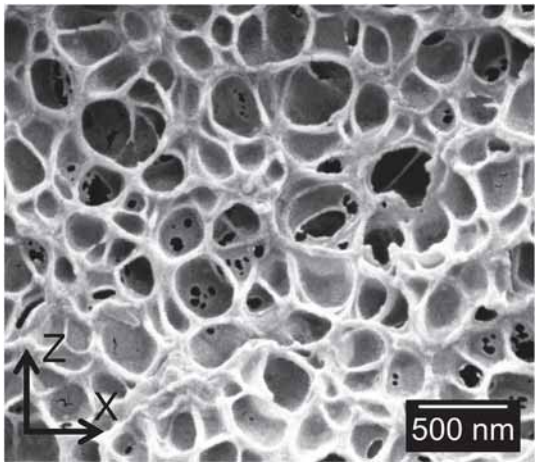

Figure 3. Micrograph of cellular structure of Sample 7.

As it has been previously mentioned, samples present cell sizes in the nanometric range. The high homogeneity of the cellular structure, as well as a slight anisotropy of the cells in *z*-direction, can also be observed.

Figure 4 shows the evolution of the cell size (a) and cell nucleation density (b) with foaming time and foaming temperature. Between 40 °C and 100 °C of foaming time, cell sizes slightly increase from 205 to 240 nm (**Figure 4a**); consequently, only a small variation of 35 nm is detected. For a foaming temperature of 110 °C, only samples foamed during 1 and 2 min follow the general trend, whereas the cell size of the sample foamed during the

5 min experiment reduction due to the higher density of this material. It is also remarkable that the standard deviation of the cell size distribution divided by the average cell size (SD/Φ) (**Table 1**) remains constant for all temperatures and foaming times, with values near 0.4. Therefore, the homogeneity of the cellular structure does not depend on the foaming parameters, obtaining homogeneous cellular materials for all the foaming conditions.

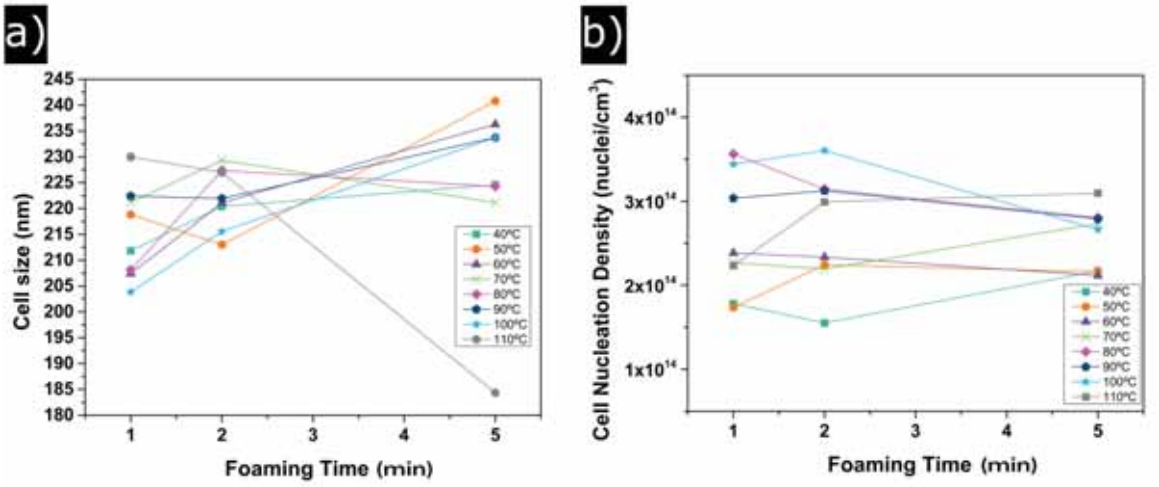

Figure 4. (**a**) evolution of the cell size with foaming time; (**b**) evolution of cell nucleation density with foaming time.

Cell nucleation density tendencies are shown in **Figure 4b**. Two different behaviours can be distinguished. On the one hand, for foaming temperatures of 40 °C, 50 °C and 60 °C, the values of N_0 are below 2 × 10^{14} cm^{-3}. On the other hand, samples corresponding to foaming temperatures between 80 °C and 110 °C show higher values of N_0 (above 3 × 10^{14} nuclei/cm^{-3}). For instance, N_0 increases from 1.5 × 10^{14} nuclei/cm^3 for 40 °C of foaming temperature and 2 min of foaming time to 3.5 × 10^{14} nuclei/cm^3 for 100 °C of foaming temperature and the same foaming time.

Table 1 also shows the other characteristics measured: anisotropy ratio, cell wall thickness, mass fraction in the struts, open cell content and glass transition temperature increments. The anisotropy ratio (AR) is higher than one for all the materials under study. This indicates that cells are slightly elongated in the *z*-direction (i.e., the direction of the applied pressure during the production of the solid precursors). In addition, the obtained at temperatures below 60 °C are between 1.2 and 1.3, while for foaming temperatures higher than 60 °C AR are slightly reduced to values between 1.0 and 1.2. The values of cell wall thickness are in a range between 22 nm and 30 nm, except for sample 24 (the one foamed at high temperature and with high foaming times) that presents a higher value of 36nm. Therefore, ξ seems to remain almost constant with foaming temperature as well as with foaming time. In fact, there is no a clear trend of this parameter with foam density. Otherwise, mass fraction in the struts changes significantly with foaming temperature; the values are reduced from 0.6 to 0.3 when temperature is increased. As already discussed, this magnitude was not measured in some samples (low density samples) because of the similarities between the sizes of cell walls and struts.

3.1.3. Open Cell Content

The evolution of open cell content with foaming conditions is shown in **Figure 5**. Up to 80 °C of foaming temperature, O_v increases from 3% at 40 °C to 91% at 80 °C. Temperatures of foaming higher than 80 °C yield to completely open cell structures. A tendency with the foaming time is also observed, and open cell content increases with this parameter. Cellular materials foamed during 5 min present higher open cell content than those foamed during 1 or 2 min. Once again, the nanocellular material produced at 110 °C of foaming temperature and 5 min of foaming time presents an anomalous behaviour. Due to the higher density and change in the internal cellular structure, the sample does not present a completely open cell structure.

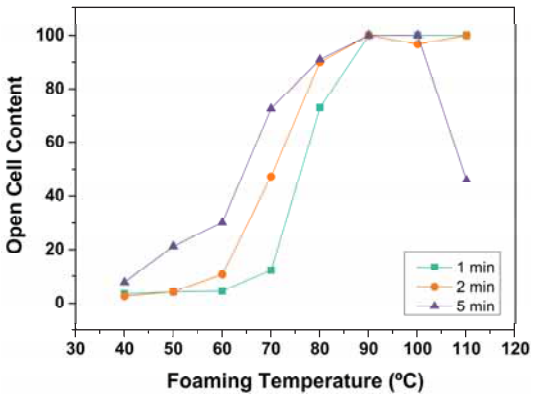

Figure 5. Open cell content as a function of foaming temperature.

3.1.4. Glass Transition Temperature

Table 1 shows that when the glass transition temperature is measured in the first heating step, there are differences up to 11 °C between the glass transition of the nanocellular polymer and that of the solid precursor, while these differences disappear when the glass transition temperature is measured in the second heating step.

4. Discussion

As it has been described in the previous section, nanocellular polymers with a wide range of relative densities (from 0.47 to 0.24) have been produced. Consequently, the cellular structure of these cellular materials is different. In this section, the correlations found between density and the parameters that define the cellular structure are discussed. The section is divided into two parts; firstly the analysis of the characteristics related to the gaseous phase and secondly the study of the parameters connected to the solid phase.

4.1. Gaseous Phase

In order to analyze the relationship between relative density and the changes in gaseous phase, obtained results for the cell size and cell nucleation density should be discussed.

As mentioned above, the relative density changes in a factor of nearly 2, from 0.47 for the material with the highest density (sample 1) to 0.24 for the material with the lowest density (sample 20).

If the number of cells is constant, a change of a factor of two in relative density should be translated in a change of 1.26 ($2^{1/3}$) in the cell size. However, the ratio of cell sizes between these samples (1 and 20) is only 1.02 (**Table 1**). This is just an example of the general trend observed (**Figure 6**).

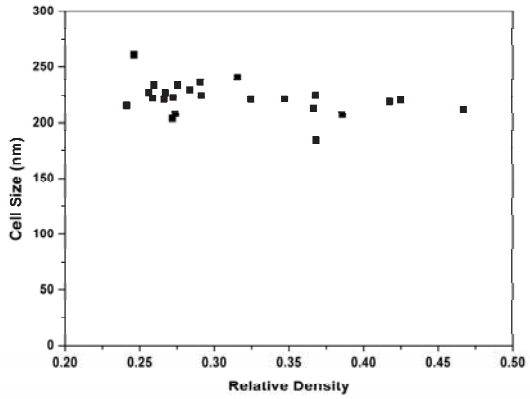

Figure 6. Average cell size as a function of relative density.

Even though the range of relative densities is wide, almost all the samples have cell sizes in the same range.

Cell nucleation density has also been analyzed. N_0 changes from 1.5×10^{14} for samples produced at low temperatures to 3.5×10^{14} nuclei/cm^3 for samples produced at high temperatures, that is, N_0 doubles its value when the foaming temperature is modified (**Figure 7a**).

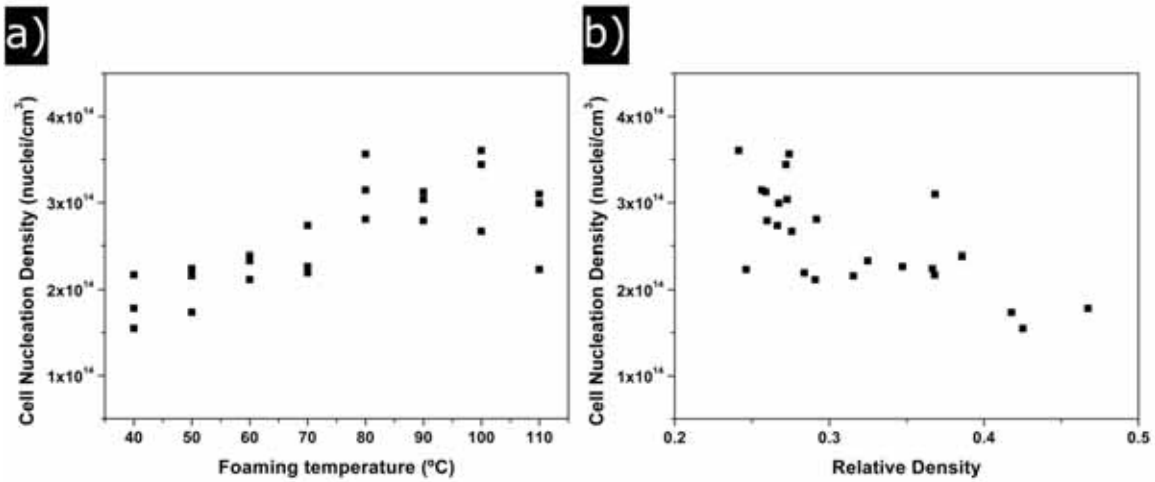

Figure 7. (**a**) change of cell nucleation density with foaming temperature; (**b**) change of cell nucleation density with relative density.

Figure 7a shows N_0 as a function of the foaming temperature. Cell nucleation density clearly increases between 40 °C and 80 °C, temperature at which the number of nucleation sites reaches its maximum value. Again, it is demonstrated that 110 °C is the upper limit

for the foaming temperature because N_0 drops again at this temperature. This is a behaviour opposite to that found for relative density (see **Figure 2a**). Between 40 °C and 80 °C, cell nucleation density grows due to a reduction in the energy barrier to create cells [8]. At higher temperatures, there is a competition between the higher nucleation rate and the emergence of degeneration mechanisms such as a coarsening, coalescence and/or collapse of the cellular structure. These last mechanisms seem to play a significant role when a temperature of 110 °C is used for foaming (cell nucleation density is reduced).

In short, the reduction in relative density is a result of an increase in the number of nucleation sites when the foaming temperature increases (**Figure 7b**). Cells created reach very similar sizes at any of the temperatures tested, so the increase in the volume of the samples produced at high temperatures is the result of having more cells (two times more cells) of equal size.

4.1.1. Open Cell Content

Figure 8 shows the relationship between the open cell content and the relative density. Samples with high relative densities present low contents of open cells. As density decreases, the open cell content increases up to a maximum value of 100%. Therefore, low density samples present a totally interconnected gas phase.

In previous sections, it has been proved that high temperatures are needed to decrease the relative density. These high temperatures imply a decrease in the polymer viscosity that causes cell wall ruptures during the expansion process.

Cell wall thickness has been measured to be constant, so it seems that there exists a minimum thickness value below which cell walls start to break down.

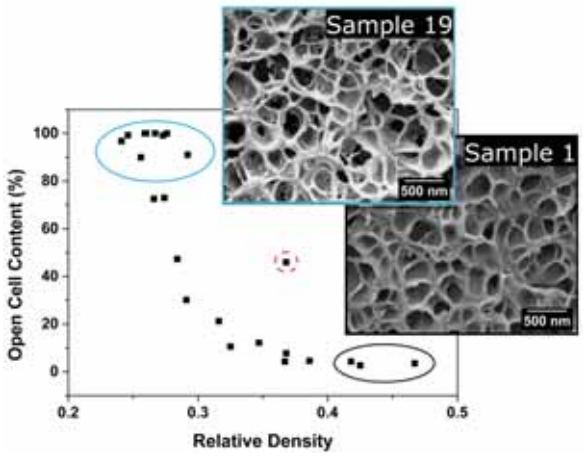

Figure 8. Open cell content as a function of relative density.

4.2. Solid Phase

As a consequence of the evolution in the gaseous phase, the topology of the solid part of the cellular material is also modified. With the purpose of determining these modifications, parameters such as the cell wall thickness and the fraction of solid mass in the struts have been analysed. Mean cell wall thickness is almost constant for all the

analysed materials (**Table 1**). In contrast, f_s is strongly modified when density is reduced (**Figure 9**). When a cellular material reduces its relative density, increasing as a consequence its expansion ratio, it is common to expect a reduction in the cell wall thickness.

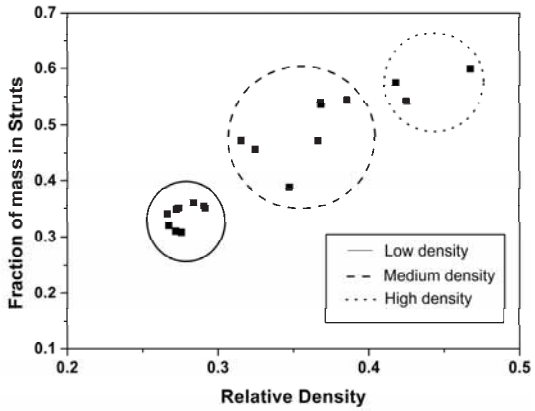

Figure 9. Fraction of mass in the struts with respect to relative density.

For example, in PU foams, it has been observed that a reduction in relative density implies drainage from the cell walls to the struts [35]. Then, cell walls become thinner as relative density decreases, reaching a minimum value at which coalescence starts to occur.

The results in **Figure 9** and **Table 1** demonstrate that a reduction in relative density results in totally different effects for nanocellular PMMA. As ρ_r decreases, the cell wall thickness remains constant, while the fraction of mass in the struts becomes smaller.

As it is shown in **Figures 9 and 10**, samples in this paper can be divided into three groups, taking into account their relative density and fraction of material in the struts: low density nanocellular materials, medium density nanocellular materials, and higher density ones. In order to clearly show the modifications in the local thickness, one example of the histograms of the local techiest for each group is included in **Figure 10**.

Modifications between different groups are clear. As it can be appreciated, mass fraction in the struts decreases as relative density falls. In fact, while in the high density materials, the struts have a clearly higher thickness, whereas in the low density nanocellular polymers, the struts have a thickness similar to that of the cell walls. In addition, the thickness distribution becomes narrow as the density is reduced. For low density materials, strut thickness is similar to cell wall thickness, which explains the fact that we were not able to accurately measure f_s for the materials with the lowest densities.

Therefore, this analysis has proven that the key point in density reduction is to increase the foaming temperature, a parameter that induces a higher number of cells. This density reduction takes place by keeping constant the values of cell size and the cell wall thickness but reducing the fraction of material in the struts and increasing the interconnectivity of the cells.

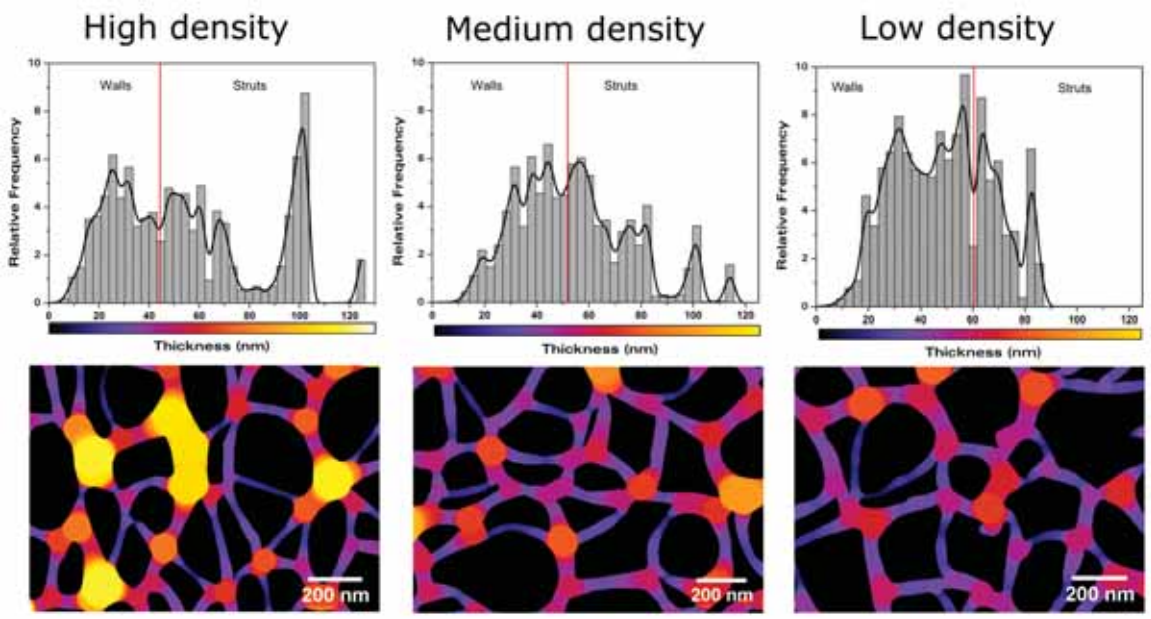

Figure 10. Solid phase distribution for high (Sample 1), medium (Sample 8) and low density samples (Sample 21).

4.2.1. Confinement Effect

As previously reported, there exist significant differences between the glass transition temperature of the nanocellular PMMA materials and that of the bulk material. This fact has been previously observed, and it is attributed to a confinement effect of the polymer matrix [36]. When the cellular polymers evolve from microcellular to nanocellular, higher cell densities, smaller cell sizes, and thinner cell walls, between 22 and 36 nm in our case, are obtained.

The size of these cell walls is of the same order of magnitude as the polymeric chain length, resulting in a confinement of the polymer within cell walls. This confinement restricts the mobility of the polymeric chains, making the T_g of the foamed material higher than the T_g of the solid precursor.

The importance of the confinement effect has recently been reported. It has been demonstrated that nanocellular materials present enhanced physical properties (modulus of elasticity, shore hardness), in comparison to microcellular ones, and this seems to be due, in part, to the confinement effect [18].

For the materials in this paper, c cell wall thickness remains constant independently of the relative density. Meanwhile, ΔT_g change in the studied range of relative densities (**Figure 11**). ΔT_g increases when the relative density is reduced, from 4 °C for the cellular materials with highest densities to 11 °C for cellular materials with the lowest densities.

Confinement effect is related to the solid phase of the cellular polymer, so although the cell wall thickness remains constant, it has been observed that f_s changes with ρ_r. **Figure 11b** shows that there is a clear relation between ΔT_g and the fraction of material in the struts. Reducing this value increases the ΔT_g values.

All the samples present confinement effect because thickness of the cell walls are of the same order of magnitude as that of PMMA chains. However, high density materials present a higher proportion of solid phase in the struts. In those areas, molecular mobility increases due to its higher size. As the struts size becomes smaller (i.e., density is reduced), the confinement starts to take part also in this part of the solid phase. This results in an increase of the confinement effect as relative density is reduced.

When a second measurement of the glass transition temperature is performed, after erasing the thermal history (**Table 1**), no differences between the nanocellular PMMA and the solid sheets are observed. This can be explained because when the nanocellular cellular structure disappears as a consequence of the increase in the temperature of the cellular material above its glass transition temperature (this was confirmed by performing SEM images of the samples after erasing the thermal history), the confinement effect disappears.

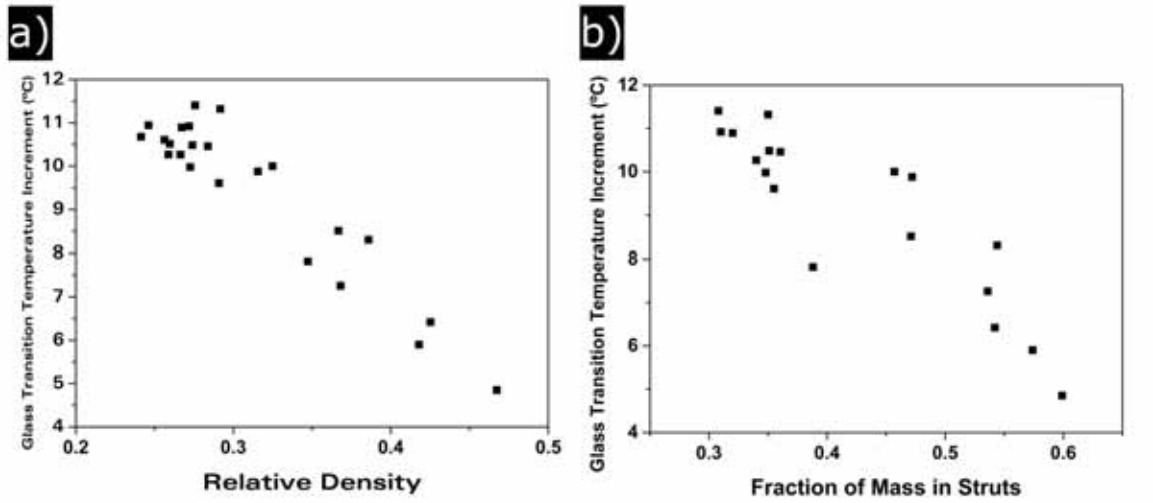

Figure 11. (**a**) glass transition temperature increment as a function of relative density; (**b**) glass transition temperature as a function of the fraction of mass in struts.

5. Conclusions

Low density nanocellular polymers have been fabricated using a PMMA homopolymer as raw material by means of the optimization of the foaming parameters. A wide range of relatives densities have been achieved, from 0.47 for 40 °C of foaming temperature to 0.24 for 90 °C of foaming temperature. A complete analysis of the cellular structure has been carried out, leading to a complete correlation process–density–structure. On the one hand, it has been found that cell sizes remain almost constant for all the samples, the increase of cell nucleation density being the key factor in the reduction of relative density. An increase in the foaming temperature from 40 °C to 90 °C increases the cell nucleation density by a factor of two, resulting in a reduction of the relative density of the same magnitude. In addition, it has been found that reducing the relative density increases the cells' connectivity, and, in fact, for low relative density materials, the open cell content is 100%. On the other hand, whereas cell wall thickness is almost constant for all the produced material, maintaining a low value between 22 and 36 nm, the fraction of

mass in the struts radically drops when the foaming temperature is increased and therefore when the relative density is reduced. Finally, it has been confirmed that the production of these nanocellular polymers with thin cell walls and struts results in a confinement effect of the polymeric matrix. The reduction of strut sizes when density is reduced causes a significant increase of this effect.

Acknowledgments: Financial assistance from the Ministerio de Economía y Competitividad MINECO and Fondo Europeo de Desarrollo Regional (FEDER) programs (MAT 2012-34901) MINECO, FEDER, UE (MAT2015-69234-R) and the Junta de Castile and Leon (VA035U13) are gratefully acknowledged. Financial support from Junta of Castile and Leon grant Q4718001C (Judith Martín-de León) and Formación de personal Universitario (FPU) grant FPU14/02050 (Victoria Bernardo) from the Spanish Ministry of Education are gratefully acknowledged.

Author Contributions: Judith Martín-de León, Victoria Bernardo and Miguel Ángel Rodríguez-Pérez conceived and designed the experiments. Judith Martín-de León and Victoria Bernardo performed the experiments. Judith Martín-de León analyzed the data. Judith Martín-de León, Victoria Bernardo and Miguel Ángel Rodríguez-Pérez revised the results obtained. Judith Martín-de León wrote the paper and Miguel Ángel Rodríguez-Pérez revised it.

Conflicts of Interest: The founding sponsors had no role in the design of the study; in the collection, analyses, or interpretation of data; in the writing of the manuscript, and in the decision to publish the results.

References

[1] Eaves, D. *Handbook of Polymer Foams*; Rapra Technology Limited: Shawbury, Shrewsbury, Shropshire, UK, **2004**.

[2] Sun, H.; Mark, J. E. Preparation, characterization, and mechanical properties of some microcellular polysulfone foams. *Journal of Applied Polymer Science* **2002**, *86*, 1692–1701.

[3] Arora, K. A.; Lesser, A. J.; McCarthy, T. J. Preparation and Characterization of Microcellular Polystyrene Foams Processed in Supercritical Carbon Dioxide. *Macromolecules* **1998**, *31*, 4614–4620.

[4] Kumar, V.; Weller, J. E. A Process to Produce Microcellular PVC. *International Polymer Processing* **1993**, *1*, 73–80.

[5] Parks, K. L.; Beckman, E. J. Genetration of Microcellular Polyurethane Foams via Polymerization in Carbon Dioxide . II : Foam Formation and Characterization. *Polymer Engineering and Science* **1996**, *36*, 2417–2431.

[6] Xing, Z.; Wu, G.; Huang, S.; Chen, S.; Zeng, H. Preparation of microcellular cross-linked polyethylene foams by a radiation and supercritical carbon dioxide approach. *The Journal of Supercritical Fluids* **2008**, *47*, 281–289.

[7] Reglero Ruiz, J. A.; Viot, P.; Dumon, M. Microcellular foaming of polymethylmethacrylate in a batch supercritical CO 2 process: Effect of microstructure on compression behavior. *Journal of Applied Polymer Science* **2010**, *118*, 320–331.

[8] Kumar, V.; Weller, J. Production of Microcellular Polycarbonate Using Carbon Dioxide for Bubble Nucleation. *Journal of Engineering for Industry* **1994**, *116*, 413–420.

[9] Shimbo, M.; Higashitani, I.; Miyano, Y. Mechanism of strength improvement of foamed plastics having fine cell. *Journal of Cellular Plastics* **2007**, *43*, 157–167.

[10] Nadella, K.; Kumar, V. Tensile and flexural properties of solid-state microcellular ABS panels. *Experimental Analysis of Nano and Engineering …* **2007**, *22*, 765–766.

[11] Juntunen, R. P.; Kumar, V.; Weller, J. E.; Bezubic, W. P. Impact strength of high density microcellular poly(vinyl chloride) foams. *Journal of Vinyl and Additive Technology* **2000**, *6*, 93–99.

[12] Collias, D. I.; Baird, D. G.; Borggreve, R. J. . Impact toughening of polycarbonate by microcellular foaming. *Polymer* **1994**, *35*, 3978–3983.

[13] Bureau, M. N. Fracture Toughness of High Density Polycarbonate Microcellular Foams. *Journal of Cellular Plastics* **2006**, *42*, 229–240.

[14] Kumar, V.; VanderWel, M.; Weller, J.; Seeler, K. a. Experimental Characterization of the Tensile Behavior of Microcellular Polycarbonate Foams. *Journal of Engineering Materials and Technology* **1994**, *116*, 439.

[15] Notario, B.; Pinto, J.; Rodriguez-Perez, M. A. Nanoporous polymeric materials: A new class of materials with enhanced properties. *Progress in Materials Science* **2016**, *78–79*, 93–139.

[16] Costeux, S. CO 2 -blown nanocellular foams. *Journal of Applied Polymer Science* **2014**, *131*, n/a-n/a.

[17] Miller, D.; Kumar, V. Microcellular and nanocellular solid-state polyetherimide (PEI) foams using sub-critical carbon dioxide II. Tensile and impact properties. *Polymer* **2011**, *52*, 2910–2919.

[18] Notario, B.; Pinto, J.; Rodriguez-Perez, M. a. Towards a new generation of polymeric foams: PMMA nanocellular foams with enhanced physical properties. *Polymer* **2015**, *63*, 116–126.

[19] Schmidt, D.; Raman, V. I.; Egger, C.; du Fresne, C.; Schädler, V. Templated cross-linking reactions for designing nanoporous materials. *Materials Science and Engineering: C* **2007**, *27*, 1487–1490.

[20] Notario, B.; Pinto, J.; Solorzano, E.; De Saja, J. A.; Dumon, M.; Rodriguez-Perez, M. A. Experimental validation of the Knudsen effect in nanocellular polymeric foams. *Polymer (United Kingdom)* **2015**, *56*, 57–67.

[21] Gibson, L. J.; Ashby, M. F. *Cellular solids: Structure and Properties*; 2nd ed.; Cambridge: Cambridge University Press.: United States, **1997**.

[22] Guo, H.; Nicolae, A.; Kumar, V. Solid-state poly(methyl methacrylate) (PMMA) nanofoams. Part II: Low-temperature solid-state process space using CO2 and the resulting morphologies. *Polymer* **2015**, *70*, 231–241.

[23] Hedrick, J. L.; Carter, K. R.; Cha, H. J.; Hawker, C. J.; DiPietro, R. A.; Labadie, J. W.; Miller, R. D.; Russell, T. P.; Sanchez, M. I.; Volksen, W.; Yoon, D. Y.; Mercerreyes, D.; Jerome, R.; McGrath, J. E. High-temperature polyimide nanofoams for microelectronic applications. *Reactive & Functional Polymers* **1996**, *30*, 43–53.

[24] Martini-Vvedensky, J. J. E.; Suh, N. N. P.; Waldman, F. F. a. Microcellular closed cell foams and their method of manufacture. *US Patent 4,473,665* **1984**.

[25] Changchun Zhou 1 Sriharsha S. Sundarram 1, Wei Li 1*, N. V. 2; Zhou, C.; Vaccaro, N.;

Sundarram, S. S.; Li, W. Fabrication and Characterization of Polyetherimide Nanofoams using Supercritical CO2. *Journal of Cellular Plastics* **2012**, *48*, 239–255.

[26] Guo, H.; Kumar, V. Some thermodynamic and kinetic low-temperature properties of the PC-CO2 system and morphological characteristics of solid-state PC nanofoams produced with liquid CO2. *Polymer* **2015**, *56*, 46–56.

[27] Pinto, J.; Dumon, M.; Pedros, M.; Reglero, J.; Rodriguez-Perez, M. A. Nanocellular CO2 foaming of PMMA assisted by block copolymer nanostructuration. *Chemical Engineering Journal* **2014**, *243*, 428–435.

[28] Costeux, S.; Khan, I.; Bunker, S. P.; Jeon, H. K. Experimental study and modeling of nanofoams formation from single phase acrylic copolymers. *Journal of Cellular Plastics* **2014**, *51*, 197–221.

[29] Zhai, W.; Yu, J.; Wu, L.; Ma, W.; He, J. Heterogeneous nucleation uniformizing cell size distribution in microcellular nanocomposites foams. *Polymer* **2006**, *47*, 7580–7589.

[30] Costeux, S.; Jeon, M. H.; Bunker, T. S.; Khan, I. Nanocellular foams from acrylic polymers : experiments and modeling. *FOAMS 2012 Conference* **2012**, 1–6.

[31] Guo, H.; Kumar, V. Solid-state poly(methyl methacrylate) (PMMA) nanofoams. Part I: Low-temperature CO2 sorption, diffusion, and the depression in PMMA glass transition. *Polymer* **2015**, *57*, 157–163.

[32] Tang, M.; Du, T.-B.; Chen, Y.-P. Sorption and diffusion of supercritical carbon dioxide in polycarbonate. *The Journal of Supercritical Fluids* **2004**, *28*, 207–218.

[33] Pinto, J.; Solorzano, E.; Rodriguez-Perez, M. a.; de Saja, J. a. Characterization of the cellular structure based on user-interactive image analysis procedures. *Journal of Cellular Plastics* **2013**, *49*, 555–575.

[34] Kumar, V.; Suh, N. P. A process for making microcellular thermoplastic parts. *Polymer Engineering and Science* **1990**, *30*, 1323–1329.

[35] Pardo-Alonso, S.; Solórzano, E.; Brabant, L.; Vanderniepen, P.; Dierick, M.; Van Hoorebeke, L.; Rodríguez-Pérez, M. A. 3D Analysis of the progressive modification of the cellular architecture in polyurethane nanocomposite foams via X-ray microtomography. *European Polymer Journal* **2013**, *49*, 999–1006.

[36] Reglero Ruiz, J. A.; Dumon, M.; Pinto, J.; Rodriguez-Pérez, M. A. Low-density nanocellular foams produced by high-pressure carbon dioxide. *Macromolecular Materials and Engineering* **2011**, *296*, 752–759.

5.3. References

[1] Guo, H.; Nicolae, A.; Kumar, V. Solid-state poly(methyl methacrylate) (PMMA) nanofoams. Part II: Low-temperature solid-state process space using CO2 and the resulting morphologies. *Polymer* **2015**, *70*, 231–241.

[2] Guo, H.; Kumar, V. Some thermodynamic and kinetic low-temperature properties of the PC-CO2 system and morphological characteristics of solid-state PC nanofoams produced with liquid CO2. *Polymer* **2015**, *56*, 46–56.

[3] Guo, H.; Nicolae, A.; Kumar, V. Solid-state microcellular and nanocellular polysulfone foams. *Journal of Polymer Science, Part B: Polymer Physics* **2015**, *53*, 975–985.

[4] Guo, H.; Nicolae, A.; Kumar, V. Fabrication of high temperature polyphenylsulfone nanofoams using high pressure liquid carbon dioxide. *Cellular Polymers* **2016**, *35*, 119–142.

[5] Guo, H. Solid-state Polymer Nanofoams. **2015**.

[6] Miller, D.; Kumar, V. Microcellular and nanocellular solid-state polyetherimide (PEI) foams using sub-critical carbon dioxide II. Tensile and impact properties. *Polymer* **2011**, *52*, 2910–2919.

Chapter 6

Influence of the polymeric matrix

"Ilusos que hoy arrojan a la fuente sus monedas, realistas que no dudan en mojarse y cogerlas."

LOVG

INDEX

6.1. Introduction

The properties of the polymer matrix, particularly the glass transition temperature, T_g, and the viscosity, η, were claimed to play a significant role in the final cellular structure of nanocellular polymers (See Chapter 2, section 2.4.1).

However, the literature barely supports these claims, due to the lack of experiments in this field for systems with homogeneous nucleation (See **Figure 2.26** in Chapter 2). The pursued purpose in Chapter 6 is to analyze the effect of the characteristics of the PMMA matrix on the obtained cellular structure. This study is combined with the influence of the production parameters on the nanocellular PMMA produced. Additionally, the foaming mechanisms involved in nanocellular polymers production are also investigated.

The described study is presented in the article "Martín-de León, J. .; Bernardo, V.; Laguna-Gutiérrez, E.; Rodríguez-pérez, M. A. Influence of the rheological behaviour of PMMA on the cellular structure of nanocellular materials. *Paper sent*." attached in the following section.

In this work, three different PMMA grades have been used. They are characterized by presenting different viscosities and glass transition temperatures. A set of nanocellular materials are produced from those three materials by using a set of production conditions. Thus, saturation temperatures of 24 and -32 °C were used combined with saturation pressures ranging from 6 to 31 MPa. On the other hand, the foaming temperature was also varied between 25 and 80 °C.

The analysis of the solubility, S, diffusivity, D, and cellular structure (relative density, ρ_r, cell size, ϕ, cell nucleation density, N_0, and open cell content, O_v), for all those experiments, results in a complete study, as illustrates in **Figure 6.1**.

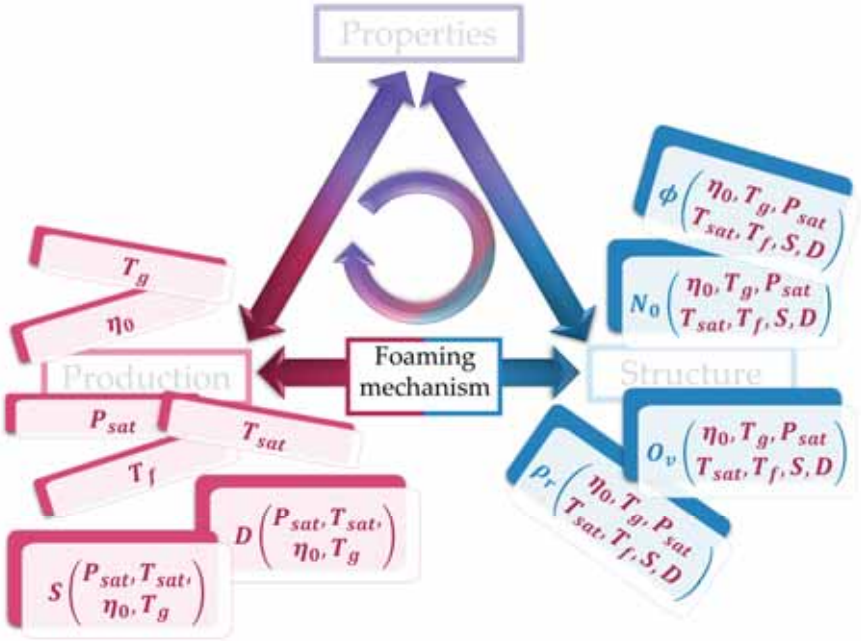

Figure 6.1. Established relationships in Chapter 6.

So, solubility and diffusivity are related to the production parameters as well as with the raw materials properties $\left(S(P_{sat}, T_{sat}, \eta_0, T_g)D(P_{sat}, T_{sat}, \eta_0, T_g)\right)$ .In addition, parameters defining the cellular structure are linked with the production parameters, the polymer matrix properties, and with solubility and diffusivity; $\rho_r(\eta_0, T_g, P_{sat}, T_{sat}, D, S)$; $N_0(\eta_0, T_g, P_{sat}, T_{sat}, D, S)$; $\phi(\eta_0, T_g, P_{sat}, T_{sat}, D, S)$; $O_v(\eta_0, T_g, P_{sat}, T_{sat}, D, S)$.

The obtained relationships have been justified theoretically by using a model developed by Costeux et al. [1] that allows obtaining further understanding on the foaming mechanism governing the production of nanocellular materials.

6.2. Influence of the rheological behaviour of PMMA on the cellular structure of nanocellular materials.

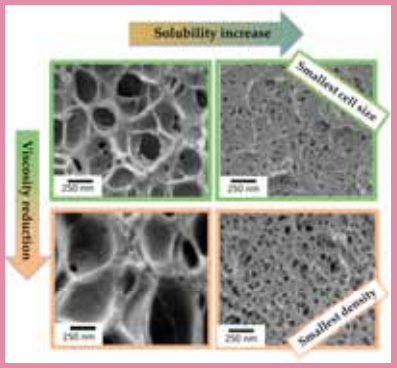

Cellular structure of nanocellular PMMA, produced by gas dissolution foaming process, is controlled through the viscosity of the polymeric matrix. When reducing the cell size below 100 nm by using high solubilities, the reduction of the viscosity is a key factor for reducing the density. Low viscous PMMA leads to cells of 75 nm combined with a relative density of 0.24.

INFLUENCE OF THE RHEOLOGICAL BEHAVIOUR OF PMMA ON THE CELLULAR STRUCTURE OF NANOCELLULAR MATERIALS.

Judith Martín-de León, Victoria Bernardo, Ester Laguna-Gutierrez, M.A. Rodriguez-Pérez

Cellular Materials Laboratory (CellMat), Universidad de Valladolid, 47011, Spain

CellMat Technologies S.L., Paseo de Belén 9A, 47011 Valladolid, Spain

Correspondence to: Judith Martín-de León (E-mail: *jmadeleon@fmc.uva.es*)

Abstract

Three different grades of polymethylmethacrylate (PMMA) with different rheological properties have been used for the production of nanocellular materials by means of gas dissolution foaming. The influence of both, the viscosity of the different polymers and the production parameters, on the final cellular structure has been studied using a wide range of saturation and foaming conditions. Foaming conditions affect in a similar way to all the materials. It has been found that an increase of the foaming temperature results in less dense nanocellular materials, with higher cell nucleation densities. In addition, it has been found that a lower viscosity leads to materials with a lower relative density but larger cell sizes and smaller cell nucleation densities, those differences being more noticeable for the condictions in which low solubilities are reached. It has been possible to produce nanocellular materials with relative densities of 0.24 combined with cell sizes of 75 nm and cell nucleation densities of 10^{15} nuclei/cm^3 using the PMMA with the lowest viscosity. While minimum cell sizes of around 14 nm and maximum cell nucleation densities of $3.5{\cdot}10^{16}$ nuclei/cm^3 with relative densities of 0.4 have been obtained with the most viscous one.

Keywords: nanocellular PMMA, viscosity, rheology, gas dissolution foaming.

1. Introduction

Nowadays the constant evolution of technology requires the production of materials with tailor-made properties. Cellular polymers are very present in this evolution due to an uncommon combination of properties combined with their low weight and therefore the possibility of reducing costs. Particularly, microcellular polymers have gained increasing importance since their discovery in the early 1980s [1], because of their enhanced mechanical properties in comparison with conventional cellular polymers, their higher thermal stability or their reduced thermal conductivity [2,3]. These improvements have encouraged scientifics in the field of cellular materials to further reduce the cell size with the aim of obtain better materials. Thus, nanocellular polymers were born, bringing with them a new enhancement of the mechanical properties such as a further reduction of the thermal conductivity as well as new and promising properties such as the possibility of producing transparent cellular polymers [4–6].

Even though nanocellular polymers are in general better than microcellular polymers, their interesting properties also depend on the cell size and the density among other characteristics (such as open cell content or anisotropy). For instance, Knudsen effect starts to be significant for cell sizes smaller than 100 nm. In addition, thermal conductivity of nanocellular polymers starts to be competitive with the ones currently in the market for relative densities smaller than 0.15. On the other hand, when referring to the transparency of those materials, more demanding requirements are needed, cell sizes smaller than 50 nm are needed, and it also expected that this property would strongly depend on the material density.

Therefore, it is mandatory to acquire a fine control of the process to design nanocellular polymer with the right density and cell size, and in this sense, it is also needed to find simple approaches to obtain that control. In particular, it has been proven that the viscosity of the polymer matrix is crucial for all the steps in the production of cellular and microcellular materials; that is, nucleation, growth, degeneration mechanisms of the cellular structure and stabilization are affected by this property of the solid material [7–9]. The viscosity of the base material can be easily modified during the polymerization process or by using fillers or chain extenders, among others. Taking into account the previous results for cellular polymers and microcellular polymers, it could be a simple way to obtain nanocellular materials with different cellular structures for given production conditions.

The study of the production of nanocellular materials has been carried out by using different polymer matrices such as polycarbonate (PC) [10], polyphenylsulfone (PPSU) [11], polyetherimide (PEI) [11], or one of the most promising ones, polymethylmethacrylate (PMMA) [12]. With this last one, multiple strategies have been followed trying to optimize the final cellular structure. One strategy has been the use of different copolymers based on PMMA, for example, PMMA/MAM blends (PMMA with block copolymer poly(methyl methacrylate)-co-poly(butyl acrylate)-co-poly(methyl methacrylate) (MAM))[13,14] or P(MMA-co-EMA)(a random copolymer of MMA with

50wt% ethyl methacrylate) [15]. Another one has been the use of nanocomposites with nanometric particles such as sepiolites [16] or silica particles [17]. Finally, the modification of the production parameters has also been studied to achieve an optimum cellular structure and density [12,18,19].

However, studies regarding the influence of the viscosity of the base material on the final cellular structure are hard to find in the bibliography. As far as authors know there exists only two previous reports. In the first one Forest et al. discussed this topic [20]. PMMA/MAM blends were used in this work. Despite the nanocellular structure was governed by the presence of MAM phase due to a heterogeneous nucleation process, it was demonstrated that the viscosity of the used PMMA phase affected the final cellular structure, being favorable having a low viscosity to reach low densities, but not so low to prevent coalescence leading to the loss of the nanocellular structure. On the other hand, Costeux et al. [21]presented the cellular structure of several blends of polymers with different viscosity. A lower viscosity it is also claimed to leads to smaller relative density. However, results were not directly correlated with the viscosity of the final blend.

An important difference of the present work from that of Forest et al. [20], apart from the much broader processing conditions tested in our case, is that in the systems analyzed here homogeneous nucleation will take place, and this type of nucleation could also depend on the properties of the base polymer. Refering to the work of Costeux et al. one step foaming is usedn in the process, moreover polymer blends instead of single polymers were used. This leads to the no possibility of relate the obtained results with the viscosity of the system due to the behaviour of this viscosity under gas pressure were different for each polymer. In this work all those contributions are removed by using different polymers separately in a two step gas disolution foaming process.

Bearing the previous concepts in mind the main target of this work is to study the influence of both, the rheological properties of homogeneous PMMA grades and the production parameters, on the final cellular structure. A complete relationship between the properties of the polymer matrix, the production parameters, and the final cellular structure has been established. It has also been found that the rheological properties of the polymer can be used to fine-tune the cellular structure of the nanocellular polymer.

2. Materials and methods

2.1. Materials

Three different grades of polymethylmethacrylate (PMMA) have been used for this study: V825T, 7N, and 6N. V825T was kindly supplied by ALTUGLAS® International (Colombes, France) in the form of pellets, while 7N and 6N were gently provided by PLEXIGLAS® Evonik Industries (Essen, Germany). All the materials used present a density (ρ) of 1.19 g/cm^3 (measured at 23 °C and 50% HR). They will be named as HV, MV, and LV as it is explained in section 3.1.

Medical grade CO_2 (99.9% purity) was used as a blowing agent.

2.2. Samples production

Pellets have been used to produce compression moulded sheets of 2 mm in thickness using a hot plate press from Remtex (Barcelona, Spain). Before this process, PMMA was dried at 80 °C for 4 hours to eliminate any moisture in the polymer. The compression moulded process comprises three steps; first of all, PMMA was heated at 250 °C for 9 minutes without applying any pressure. Secondly, the material was pressed under constant pressure of 11 MPa for one minute. Finally, the 2 mm thick layer was cooled down at room temperature and under 11 MPa of pressure.

The obtained cylindrical sheets were cut into 20 x 20 x 2 mm^3 samples to proceed with the foaming experiments.

The same procedure was used for the production of samples 1 mm thick for rheological measurements.

2.3. Foaming tests

Different cellular materials were produced using gas dissolution foaming process. This process consists on three steps. Firstly, in the saturation step; the samples are saturated, during enough time (t_{sat}) to reach the solubility limit in all the volume of the sample, under a certain saturation pressure (P_{sat}) and saturation temperature (T_{sat}) of CO_2. Secondly, the pressure is released, and the samples are transferred to the last step, the foaming step. The time between the pressure release and foaming is called desorption time (t_d). During the third step, samples are immersed in a thermal bath at the foaming temperature (T_f) during the foaming time (t_f) to promote the foaming process.

In this work two different set-ups were used, one for saturation experiments at room temperature and another one to perform experiments using saturation temperatures below room temperature.

For the room temperature experiments, a pressure vessel (model PARR 4681) provided by Parr Instrument Company (Moline, IL, USA) was used. Moreover, to provide the desired pressure, the system comprises a pump (model SFT-10) supplied by Supercritical Fluid Technologies Inc. (Newark, DE, USA).

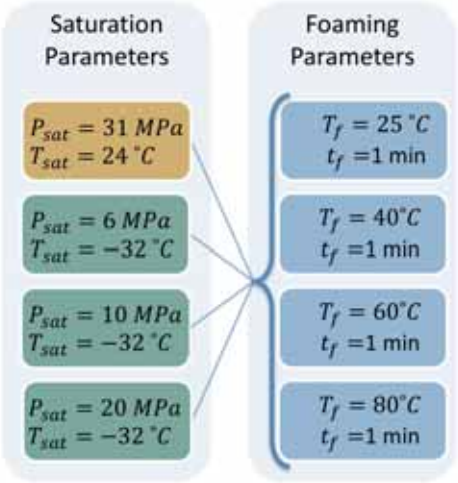

Figure 1. Production conditions for the cellular materials produced in this work.

For the experiments carried out at low temperature, a pressure vessel (model PARR 4760) has been employed. This autoclave was also provided by Parr Instrument Company (Moline, IL, USA) and it is placed inside a freezer that allows reaching temperatures from -15 °C to -32 °C.

For all saturation experiments, samples were foamed in thermal baths (J.P. Selecta Model 600685, Grupo Selecta, Barcelona, Spain).

As it is shown in **Figure 1**, different saturation parameters, as well as different foaming conditions were used in this work. For saturation parameters, four different conditions were used. The experiments with 31 MPa and 24 °C of saturation conditions were performed in the room temperature set-up by saturating for 24h. In this particular system, the pressure drop rate was 100MPa/s. On the other hand, the experiments at -32 °C and saturation pressures of 6, 10 and 20 MPa were carried out in the set-up for low-temperature saturation. Saturation time was 15 days, and the pressure drop rates were 10, 31 and 75 MPa/s respectively.

Moreover, for each of these saturation parameters, four different foaming conditions were used. Samples were foamed during 1 minute at temperatures of 25, 40, 60 and 80 °C. Desorption time was 2 and 1 minute respectively for the room temperature and low-temperature set-ups. In short, sixteen different conditions have been used for each material to study their influence on the final cellular structure.

2.4. Characterization techniques

2.4.1. Glass transition temperature

The glass transition temperature (T_g) was determined by using a Mettler DSC30 differential-scanning calorimeter previously calibrated with indium. The value of this temperature was considered as the mid-point of the drop in the thermogram that characterizes this transition. The selected weight for all the samples was 5 mg. Samples were heated from 20 °C to 160 °C at 10 °C/min.

2.4.2. Solubility and diffusivity

Solubility is defined as the amount of gas uptake and has been determined as the percentage of weight increment of each sample due to gas sorption. The desorption curve (mass lost vs. time) was registered by using a Mettler-Toledo balance and was used to extrapolate to zero time the mass of the samples after saturation. This value is considered as the mass of the sample when it is fully saturated, from which the solubility of the material is calculated [22].

Moreover, the desorption curve was used to determine the desorption diffusivity using the slope method [23]

2.4.3. Density

The density of the solid samples (ρ_s) was determined using a gas pycnometer (Mod. AccuPyc II 1340, Micromeritics, Norcross, GA, USA). The density of the foamed samples

has been measured with a density determination kit for an AT261 Mettler-Toledo balance considering the water displacement method based on Archimedes' principle. Solid skins of the nanocellular polymers were removed before these measurements by polishing more than 200 μm in each side of the samples.

Relative density (ρ_r) was defined as the ratio between ρ_f and ρ_s ($\rho_r = \rho_f/\rho_s$).

2.4.4. Open Cell Content

To measure the percentage of open cells in the cellular materials, that is the open cell content (O_v), a gas pycnometer (Mod. AccuPyc II 1340, Micromeritics) has been used by following the procedure described in ASTM D6226-10 standard. This amount is given by **Equation 1**:

$$O_v = \frac{V - V_p - V_s}{V(1 - \rho_r)} \qquad (1)$$

Where V is the geometric volume of the sample (determined by means of $V = m/\rho$ with an AT261 Mettler- Toledo balance), V_p is the volume determined by the pycnometer and V_s considers the exposed cells at the surface of the sample, value that is negligible for nanocellular materials. To determine V_p a pressure scan from 0.2 MPa to 1.3 MPa was performed measuring the volume for each pressure. This leads to a set of volumes as a function of the pressure, up to a certain point the volume become constant, meaning that no more gas is able to penetrate inside the cells of the material. V_p is calculated as the average value of those last constant measured volumes.

2.4.5. Scanning Electron Microscopy

The cellular structure of the samples was visualized with an ESEM Scanning Electron Microscope (QUANTA 200 FEG, Hillsboro, OR, USA). The samples were prepared for the visualization following different steps. Firstly, they were fractured after immersion in liquid nitrogen. Then, they were coated with 5 nm of gold by using a sputter coater (model SDC 005, Balzers Union, Balzers, Liechtenstein). Finally, they were observed with the ESEM.

The cellular structure was analyzed with a software based on ImageJ/FIJI [24] obtaining the cell size (Φ), the standard deviation of the cell size distribution (SD) and the cell nucleation density (N_0) (calculated by using Kumar's method [25]) of each cellular material. SEM images were taken along the thickness of each sample to ensure homogeneity. At least three different images and more than 200 cells per material were analyzed. The results presented in the paper are the mean value of all these results.

2.4.6. Polymers rheology

Zero shear viscosity η_0 was determined by shear rheology. The measurements were carried out in a stress-controlled rheometer, AR 2000 EX from TA instruments. Solid cylindrical samples were prepared by compression moulding using the procedure explained in section 2.2. Dynamic shear viscosity measurements were performed at 230

°C under a nitrogen atmosphere and using a parallel plates geometry of R = 25 mm in diameter and a fixed gap of h = 1 mm. The angular frequency range was $0.01 < w < 100\ rad/s$, and a strain of 6% was used. From the dynamic shear viscosity measurements, the zero shear viscosity has been calculated as the value of the complex viscosity at low frequencies in the Newtonian plateau [26].

3. Results

3.1. Thermal properties

To determine the differences between the three solid PMMAs under study, the glass transition temperature, and the zero-shear viscosity has been evaluated. As can be seen in **Table 1**, the materials present significant differences in terms of those two magnitudes.

Table 1. Cell nucleation density, cell size and SD/ Φ for the produced samples.

Material	Glass transition temperature (°C)	Zero shear viscosity (Pa·s)
HV	114.4	7095
MV	109.3	3800
LV	98.6	1587

PMMA V 825T is the one presenting the higher values (High Viscosity material, HV), with a glass transition temperature of 114.4 °C and a zero-shear viscosity of 7095 Pa·s. while 7N (Medium Viscosity, MV) and 6N (Low Viscosity, LV) have smaller values with a T_g of 109 and 99 °C respectively and a zero-shear viscosity of 3800 and 1587 Pa·s. Then, there is 15 °C difference between the Tg of the HV and LV materials. In addition, the ratio of viscosities at 230 °C is significant, the HV has a 2.4 times higher viscosity than the MV grade and a value 4.5 times higher than the LV grade.

Those changes in the physical properties of the raw materials will be essential to understand the different behaviour of each material under the foaming process.

3.2. Solubility and diffusivity

As it was proven in previous works [12], the solubility and diffusivity of CO_2 changes with the used saturation conditions. In order to study this change with the used saturation conditions and to establish the differences between materials, both magnitudes were determined as explained in section 2.4.2.

Figure 2a shows the solubility of the materials under study for the four saturation conditions used. As expected, the results show that a change in the saturation temperature from 24 °C to -32 °C, leads to a significant increase in the solubility for the three used polymers. On the other hand, when fixing the saturation temperature in -32°C an increase in the saturation pressure also results in a solubility increase. The highest values reached are around 45 % for the used PMMAs when the saturation conditions are 20 MPa and -32 °C.

If the differences among materials are analyzed, it can be said that for the experiments carried out at low saturation temperatures the three materials show very similar values of the solubility, however, for the experiment at 24°C, the material with the lowest viscosity shows a higher solubility. In this last case, the PMMA less viscous (LV) shows a solubility close to 36 wt.% while HV and MV materials remain in values near 31%.

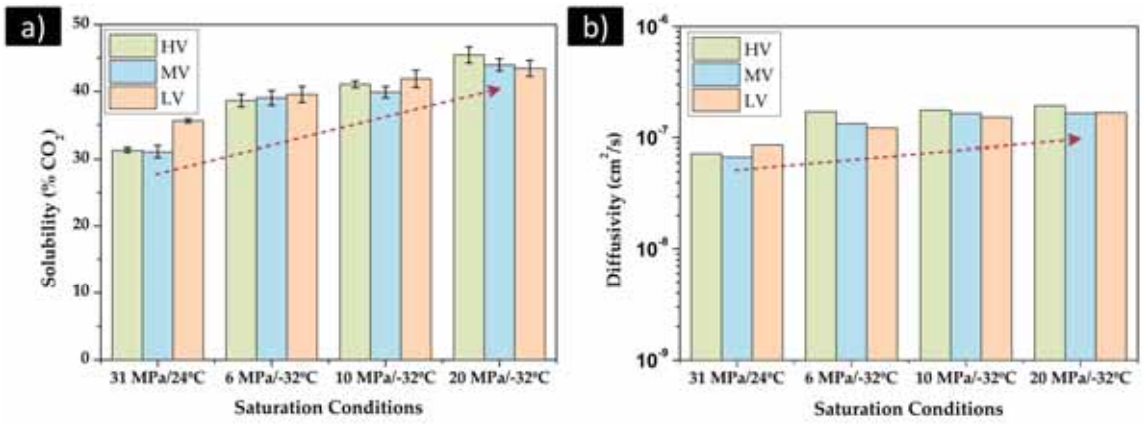

Figure 2. a) Solubility of the three PMMA as a function of the saturation conditions. **b)** Desorption diffusivity of the three PMMA as a function of the saturation conditions. Arrows indicate the increase of both magnitudes.

The changes measured in solubility as a function of saturation conditions are expected. The first significant change is the variation when the saturation temperature is reduced from 24 °C to -32°C. Taking into account the dependence of the solubility with the saturation temperature [27] (Equation 2) and considering that PMMA is a CO_2-philic material and therefore its Helmholtz energy (ΔH_s) is negative, it makes sense that a reduction in the saturation temperature results in an important increase of the solubility.

$$S = S_0 \exp\left(-\frac{\Delta H_s}{RT}\right) \qquad (2)$$

Also, when maintaining the saturation temperature at -32 °C, an increase in the saturation pressure increases the amount of gas uptake which is in agreement with previous results for similar systems [13,28,29].

Differences between materials can be explained by considering the physical mechanisms taking place during the gas sorption. Solubility depends on the polar interaction between the gas and the polymer and on the free volume available in the PMMA. The relative weight of these two contributions depends on the saturation temperature. At low saturation temperatures, the polar interactions between the gas and the polymer are more important while at high saturation temperatures the influence of the polar interactions decreases and the free volume of the polymer has a more substantial influence on the solubility [30].

Considering the previous information, it is possible to explain the obtained results. When using a saturation temperature of 24 °C the free volume of each polymer should be playing a major role in the solubility results. The free volume of a polymer has been

proved to be proportional to $T_{sat} - T_g$ [31], then by using the same saturation temperature, the free volume for LV is higher than the one in MV and HV (attending to the values of T_g showed in **Table 1**) and due to this, the solubility of LV is higher. On the other hand, when saturation temperature is decreased up to -32 °C, free volume loses importance with respect to polar interactions, then, considering that the three materials are PMMA based polymers, values of solubility should be similar for all of them.

The desorption diffusivity (**Figure 2b)** increases with the solubility being the values similar for the three materials under study. A higher solubility results in a higher CO_2 concentration gradient between the sample and the atmosphere, leading to a fast desorption [32].

3.3. Relative density and cellular structure

Figure 3 shows representative SEM images of the samples produced using the three raw materials.

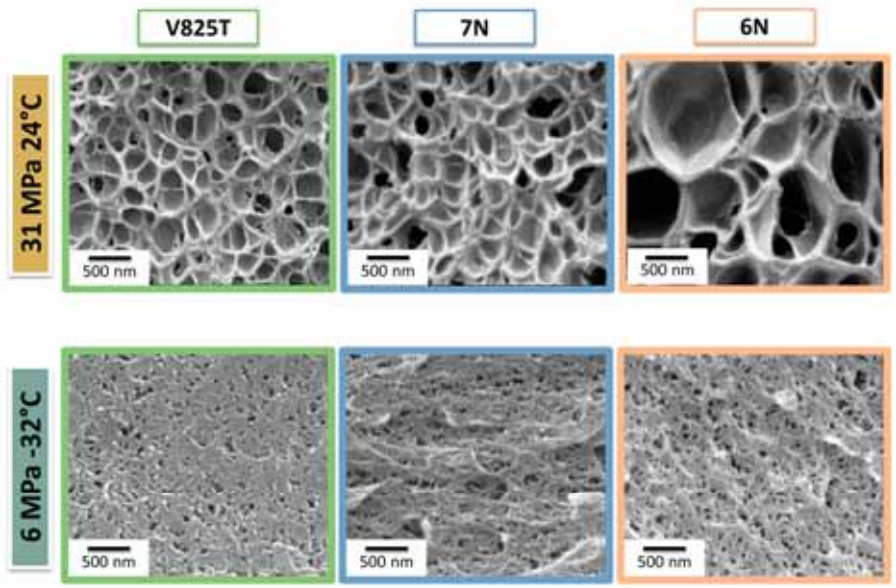

Figure 3. SEM micrographs for the three materials for two saturation conditions (30 MPa 25 °C and 6MPa -32 °C) foamed at 60°C during 1 minute.

Herein, it can be seen that all the produced materials show a homogeneous nanocellular structure, but there are clear differences when changing the process parameters or the characteristics of the PMMA.

This section is centered in the in-depth study of the influence of both the production parameters and the rheological properties of the PMMA on the final cellular structure.

3.3.1. Influence of the production parameters

3.3.1.1. Solubility influence

As is it noticeable in **Figure 3,** considerable differences in the cellular structure of the PMMAs are found when the saturation conditions and, consequently, the solubility is modified. To illustrate this fact the cell nucleation density, the cell size, the relative density,

and the open cell content have been studied as a function of the solubility for all the foaming conditions. To show these results a foaming temperature of 60 °C has been selected (**Figure 4**) being the tendency very similar for the other foaming temperatures (see supporting information).

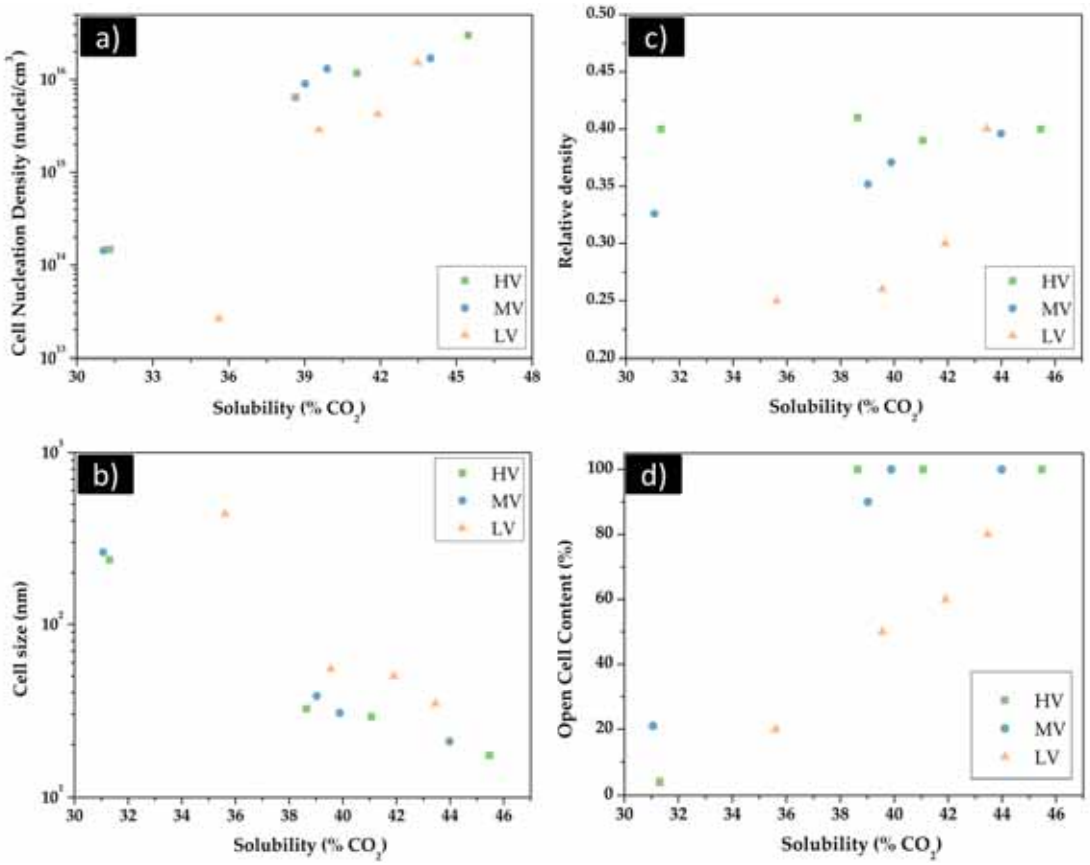

Figure 4. a) Cell nucleation density as a function of the solubility **b)** Cell size as a function of the solubility. **c)** Relative density as a function of the solubility. **d)** Open Cell Content as a function of the solubility.

For the three grades of PMMA, cell nucleation density increases with the solubility while the value of the cell size is reduced. The most significant change is detected in the first increase of the solubility, from values between 33 % and 36 % to values of 39 % of CO_2 uptake. Although the saturation pressure, between these two levels, decreases from 31 to 6 MPa, the decrease of the saturation temperature from 24 °C to -32 °C results in an increase of almost two orders of magnitude in the cell nucleation density of all the materials while the cell size decreases around five times. As it can be seen the cell size reduces from a hundred of nanometers to tens of nanometers.

A further increase in the solubility caused by an increase in the saturation pressure (when the saturation temperature is fixed in -32 °C), produces an additional increment of the cell nucleation density. It increases up to values higher than 10^{16} nuclei/cm^3 for the three materials while cell size is reduced to values of around 15 nm for HV material, 20 nm for MV and around 30 nm for LV.

Those changes in the cellular structure affect the relative density (**Figure 4c**). However, the trends are, in this case, different depending on the PMMA under study. When the attention is fixed in PMMA HV, it can be seen that the relative density remains almost constant in a value of around 0.4 independently of the saturation conditions. However, for LV and MV materials, this situation changes, and the relative density raises when the solubility becomes higher, it means that as the solubility increases the ability to expand seems to be reduced for these two materials.

These results can be understandable considering that both a change in cell nucleation density as well as a change in the cell size affect the relative density. Increasing the number of nucleation points implies to create more gas phase per unit of volume, which could lead to a reduction in the relative density. On the other hand, a reduction of the cell size implies a decrease in the gas phase proportion so an increase in the relative density. Both contributions compete in the evolution of the relative density. Thus, when increasing the solubility in High Viscous PMMA, an equilibrium is reached between the rise in the cell nucleation density and the reduction of the cell size. While for the materials with Medium and Low viscosities, the contribution to the relative density given by the reduction of the cell size is more significant than the one given by the increase of the cell nucleation density leading to an increase of the relative density when solubility increases.

Considering the graph in **Figure 4d**, the different ability of the cellular materials to expand is closely linked with the open cell content of the produced materials. A lower solubility leads to materials with a small open cell content, while high ones lead to completely interconnected cellular structures for PMMA HV and MV, and medium to high open cell contents for the LV material. It has been previously reported [33], that the interconnectivity of the cellular structure promotes faster desorption of the gas, preventing further expansion. So those cellular materials with an intermediate or a closed cell cellular structure present a high ability to expand and therefore lower relative densities. In short, an increase of the solubility leads to materials with a higher number of interconnected and smaller cells, and therefore with a higher relative density. A deeper study of the influence of the type of material is performed in section 3.3.2.

3.3.1.2. Influence of the foaming parameters.

As it is indicated in section 3.1, the glass transition temperature is different for the three used materials. For this reason, in order to study the influence of the foaming temperature in the final cellular structure, the relative density for all the saturation conditions have been represented as a function of the difference between the Tg and the foaming temperature ($T_g - T_f$). As it can be seen in **Figure 5**, the relative density strongly depends on this temperature difference. It seems clear that an increase in the foaming temperature, which corresponds to a decrease in the $T_g - T_f$ value, results in a decrease of the relative density for all the materials under study independently of the saturation conditions. This dependence was already demonstrated for PMMA V825T for a solubility of 31% [18].

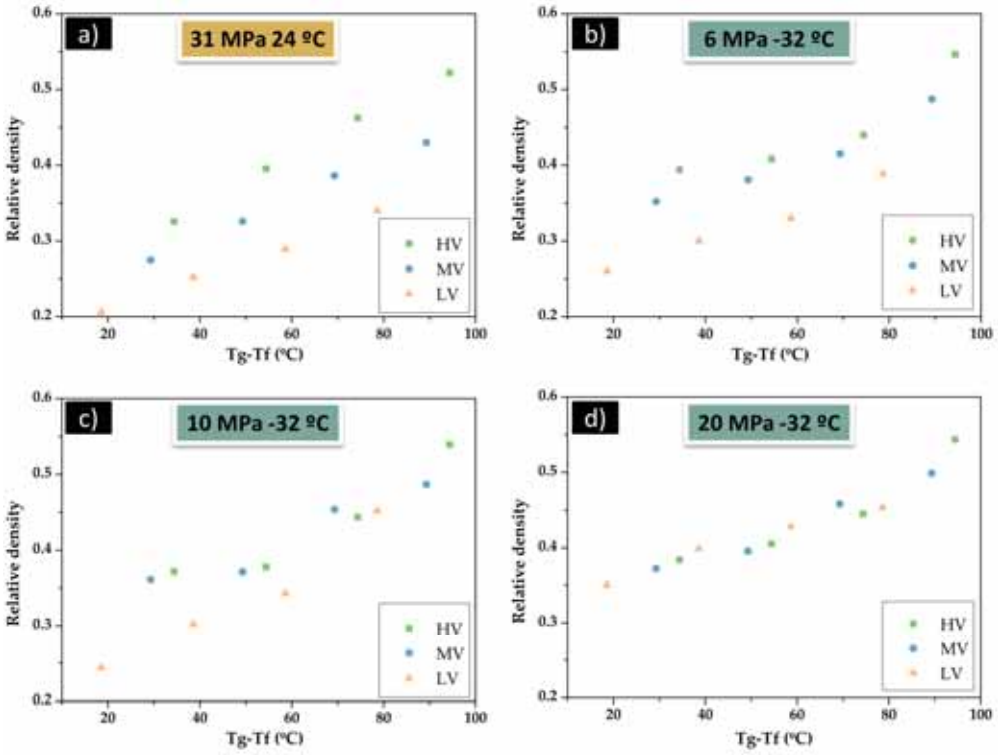

Figure 5. Relative density as a function of difference between the glass transition temperature and the foaming temperature for all the saturation conditions.

Changes between saturation conditions are also observed in **Figure 5**. The diffusion of gas inside the polymer implies the reduction of the T_g, up to the so-called effective glass transition temperature $T_{g_{eff}}$. This reduction is the result of an increase in the polymer chains mobility when the gas occupies the free volume of the polymer. Solubility for HV and MV are similar so the $T_{g_{eff}}$ is spected to be similar for both of them, in fact a similar tendency is observed when increasing the foaming temperature. Material with the Lowest Viscosity present higher solubilities but for saturation conditions of 20 MPa and -32 °C, which presumably leads to the smallest $T_{g_{eff}}$ that could be then reason for the different tendency observed in **Figure 5 a), b), c).**

On the other hand, the results of **Figure 5** may give the idea that a higher foaming temperature will decrease the relative density for all the used PMMA, but it was experimentally observed that an increase of the foaming temperature up to 100 °C, leads to the degeneration of the cellular structure for all the materials and saturation conditions except in the case of 31 MPa and 24 °C. In this last condition degeneration occurs at 110°C [33])

To understand the reasons for this clear modification of relative density, the cellular structure of all the materials has been characterized.

Figure 6 shows both the cell nucleation density and cell size as a function of relative density for two different saturation conditions, 31 MPa and 24 °C and 20 MPa and -32°C. Those results allow explaining the reduction of the relative density that was observed

when the foaming temperature was increased (**Figure 5**). This reduction of the relative density is mainly connected to an increase of the number of nucleation points, while the cell size is maintained almost constant. When talking about the materials saturated at 31 MPa and 24 °C, HV goes from cell sizes of 200 nm and cell nucleation densities of $1.5 \cdot 10^{14}$ nuclei/cm^3 for 0.5 of relative density to cell sizes of 225 nm and cell nucleation densities of $3.5 \cdot 10^{14}$ nuclei/cm^3, that means that N_0 is doubled while cell size slightly increases. Similarly, for LV PMMA that changes from $1.8 \cdot 10^{13}$ nuclei/cm^3 when the relative density is 0.34 to $3.3 \cdot 10^{13}$ nuclei/cm^3 when it decreases to 0.21, while cell sizes is between 450 and 490 nm for all the densities. The same can be said when saturating at 20 MPa and -32 °C, where cell nucleation densities are doubled between the density extremes while cell size is maintaining around 17 nm for HV PMMA, 20 nm for MV PMMA and around 35 nm for LV PMMA. Similar were also observed for the saturation conditions of 6 MPa -32°C and 10 MPa -32° (see supporting information).

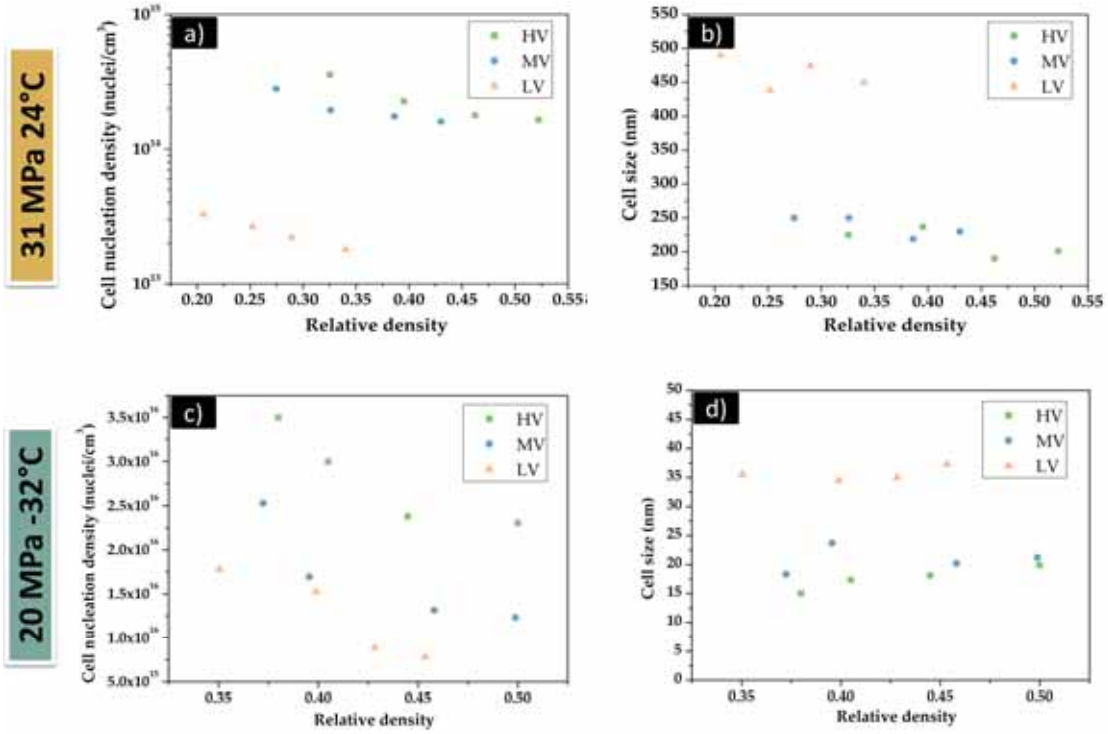

Figure 6. a) Cell nucleation density as a function of the relative density for 31 MPa and 24 °C of saturation conditions. **b)** Cell size as a function of the relative density for 31 MPa and 24 °C of saturation conditions. **c)** Cell nucleation density as a function of the relative density for 20 MPa and -32 °C of saturation conditions. **d)** Cell size as a function of the relative density for 20 MPa and -32 °C of saturation conditions.

Summing up, the reduction of the relative density is mainly caused by an increase of the cell nucleation density triggered by an increase of the foaming temperature. This is a common trend for all the PMMAs under study. In particular, a change in the foaming temperature from 25 °C to 80 °C allows increasing the cell nucleation density by two times while cell size remains almost constant. This way, in the more extreme saturation conditions, 20 MPa and -32 °C, it is possible to achieve values of N_0 as high as 10^{16} nuclei/cm^3 and cell sizes smaller than 40 nm for all the materials under study.

In short, it can be said that the foaming temperature has a substantial effect on the nanocellular materials produced by using PMMA as polymer matrix. An increase of the foaming temperature results in a rise of the cell nucleation density while the cell size is maintained, this is reflected in a reduction of the density of the final cellular material (**Figure 5**).

3.3.2. Influence of the rheological properties of PMMA

Along the previous section it has become evident that, although the trends with the process parameters are very similar for all the analyzed materials, there are clear differences in the absolute values of the foam characteristics depending on the type of PMMA. This section is focused on the study of the modifications of the final cellular structure as a function of the zero-shear viscosity of the raw polymers.

Figure 7 shows those differences; the relative density, the cell nucleation density and the cell size of all the produced materials (for all the conditions in **Figure 1**), have been plotted as a function of the zero-shear viscosity. It seems clear that the zero-shear viscosity is establishing some boundaries that are different for each material and foam characteristic.

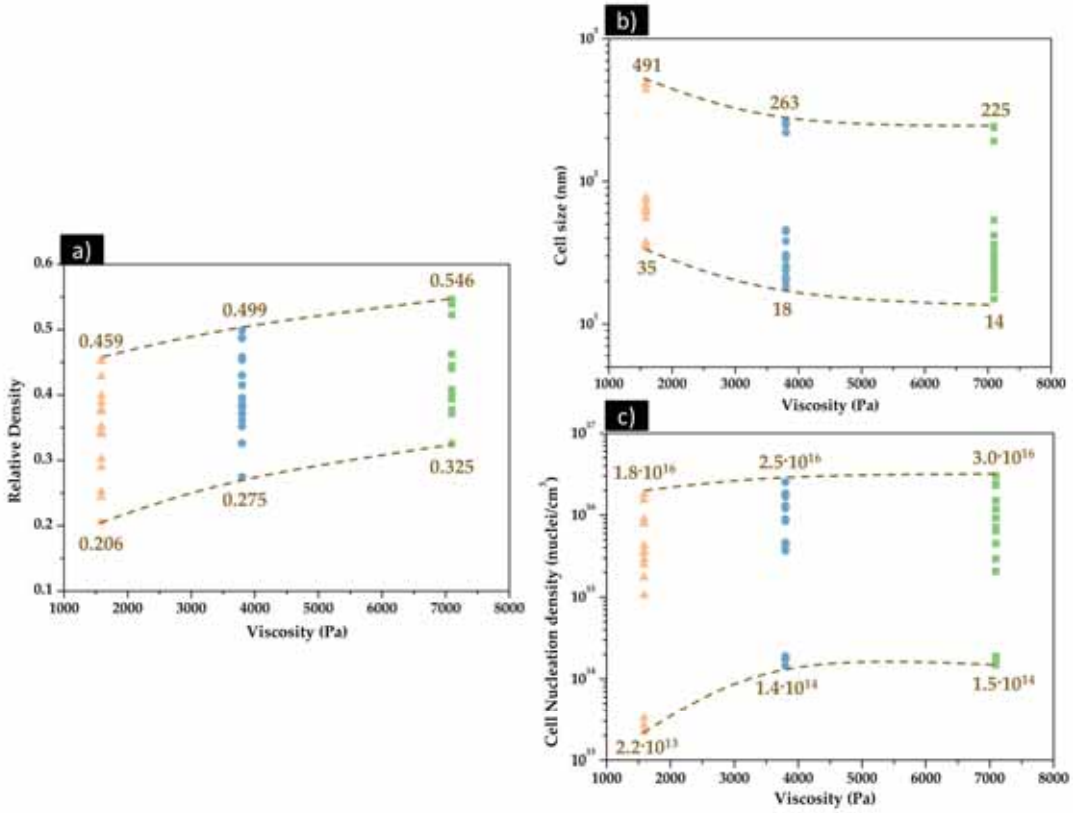

Figure 7. a) Relative density as a function of the zero-shear viscosity **b)** Cell Size as a function of the zero-shear viscosity. **c)** Cell nucleation density as a function of the zero-shear viscosity. The data for all the experiments performed have been included in these plots. For a given viscosity and polymer, the different data were obtained by modifying the saturation conditions and the foaming temperature.

The material that allows reaching a smaller density is the Low Viscous one, while the ability to expand is harder with the rise of the viscosity of the raw PMMA matrix. Thus, with the material LV, a density as low as 0.21 has been reached while for HV the minimum density produced in this work has been 0.33.

On the other hand, a smaller zero-shear viscosity makes possible to have a broader range of cell nucleation densities and cell sizes available. Then, it is possible to have materials with cell sizes from 491 nm to 35 nm and N_0 from $2.2 \cdot 10^{13}$ to $1.8 \cdot 10^{16}$ nuclei/cm^3 when working with LV; while this range is reduced to 225-14 nm and $1.5 \cdot 10^{14}$ to $3 \cdot 10^{16}$ nuclei/cm^3 with HV. Nonetheless, a higher viscosity allows reaching higher cell nucleation densities and lower cell sizes.

It is also important to notice that differences between materials are more pronounced at low solubilities (**Figure 6**) causing that the lower limit in the cell nucleation density (corresponding to the saturation conditions of 31 MPa 24 °C) is more variable among the three materials. In addition, the upper limit in the cell size (also for 31 MPa and 24 °C) presents more differences between materials than the lower one (20 MPa and -32 °C). In conclusion, at high solubilities, the three materials behave more similar in terms of cellular structure characteristics.

In order to understand the previous results, it is necessary to deepen in the nucleation mechanisms. It has been already proven that the classical nucleation theory (CNT) although providing correct trends, is useless to predict absolute data in nanocellular polymers. Moreover, viscoelastic effects are not considered in CNT. Costeux et al. [34] proposed a model based on CNT, this new model introduces some necessary changes for the understanding of nanocellular foaming.

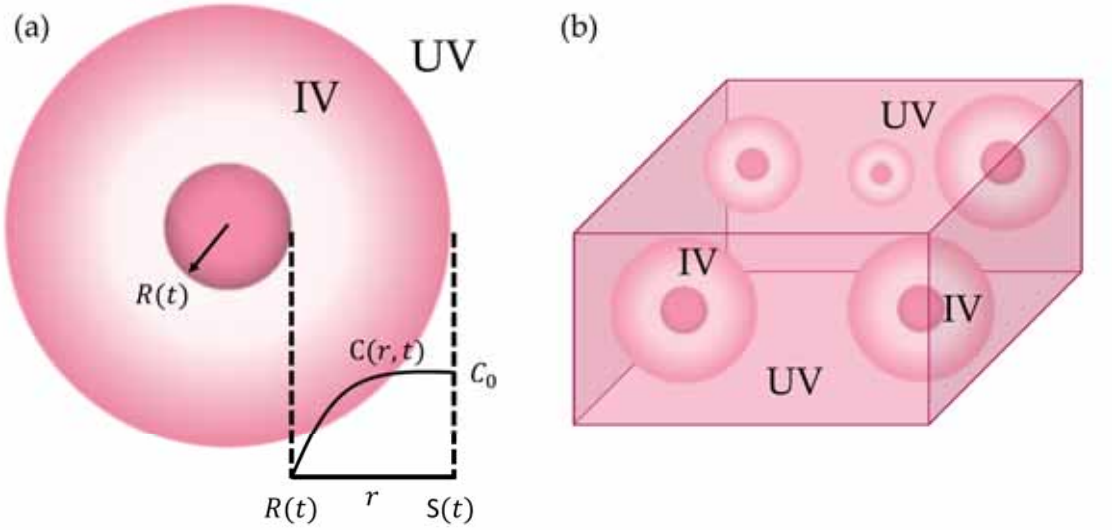

Figure 8. The concept of influence volume (IV)in the nucleation of nanocellular foams.

This theory introduces a new concept, the influence volume (IV). This new idea states that when a stable nucleus is formed, the surrounding gas molecules start to diffuse into this nucleus. This diffusion leads to a gas concentration gradient from the nucleus surface, as it is shown in **Figure 8a**. Thus, near the surface of the nascent cell, the concentration of

gas is smaller, increasing as moving away from the surface up to reach the value C_0 corresponding to the solubility achieved during the saturation step. The influence volume is defined as the halo of diffusing gas.

The success of this theory lies on two main aspects; the first one assumes that new nucleus can only be stable generated in the uninfluenced volume of the polymer (**Figure 8b**), this is because inside the influence volume the gas molecules diffuse preferable into the already stable one. This leads to a smaller nucleation ratio that agrees with experimental data. Additionally, the introduction of IV allos condidering in the model that nucleation does not occur instantaneously, allowing to introduce the influence of parameters such as viscosity, diffusivity or pressure drop rate on the cellular structure.

Taking into account this theory, the differences detected between the materials produced using PMMAs with different viscosities can be discussed.

Influence of the viscosity in the nucleation

The IV model assumes non-instantaneous nucleation, that means that cells nucleated first grows in detriment of the surrounding ones. Consequently, a higher Influence Volume will decrease the nucleation rate. That means that a slow growth rate of the initial nuclei is beneficial for the creation of new stable nuclei; this slow growth is promoted by high viscosity. A more viscous polymer provides more resistance to cell growth slowing down the increase of the influence volume and therefore leading to higher nucleation density. This contribution is given by the Schmidt number [35] that measures the relative effects of viscous diffusion over mass diffusion:

$$N_{Sc} = \frac{\mu}{\rho D} \qquad (3)$$

Where μ is the viscosity of the polymer/gas mixture, ρ is the density and D is the diffusion parameter.

Then, assuming the same amount of gas, the HV PMMA can produce a higher number of nucleation points than MV and LV because the influence volume is maintained smaller during the nucleation phase. This reasoning explains the results obtained at low saturation temperatures where the solubility of the three materials is similar.

On the other hand, when saturating at room temperature, the solubility of LV PMMA is around a 5% higher than the one of the HV and MV materials, which according to CNT will lead to a higher N_0. However, this higher solubility also results in a lower $T_{g_{eff}}$ and therefore a lower viscosity. According to the obtained results, this lower viscosity would lead to a large IV, that prevents the formation of a higher number of nucleation sites, resulting in a smaller cell nucleation density for the materials with lower viscosities.

Influence of the viscosity in cells growing.

One of the most common equations describing the growth rate of a single cell is [34,36]:

$$\frac{dR}{dt} = \frac{\Delta P \cdot R}{4\eta} - \frac{\gamma}{2\eta} \qquad (4)$$

With γ the interfacial tension between the gas bubble and the polymer, ΔP pressure difference between the inner part of the samples and the environment, and η the viscosity of the polymer/gas mixture.

Herein a decrease in the viscosity leads to the increase of the growth rate, which means that nuclei with the same size will grow faster in LV PMMA. Explaining the results in **Figure 7b**, that shows that LV PMMA presents higher cell sizes for any used condition.

On the other hand, the ability for cell growth and therefore the ability to reduce the relative density has been experimentally proved to be reduced as the amount of gas increases independently on the used polymer. This result can be again explained with the IV concept. Considering the equation 4, an increase in ΔP will lead to a faster cell growth that will consume faster the IV that is providing gas to the cell. Moreover, the nucleation rate is proportional to the exponential of $1/\Delta P^2$ meaning that the rate of nucleation is higher that growing rate. In conclusion, the gas is consumed in creating more cells that grows faster and less, due to the rapid decrease of IV. An interconnected cellular structure accompanies this fact. When the cells become open, the gas fast diffuses out of the cellular structure and then further growth is prevented.

In conclusion, the ability of the material to expand is strongly determined by the viscosity of the polymer, being possible to leads smaller relative densities as the viscosity decreases. However, this expansion ability decreases with an increase of the solubility, being more difficult to achieve lower densities when cell size is reduced.

Finally, the stabilization of the cellular structure should be done at a temperature lower than the effective glass transition of the polymer to freeze the cellular structure. If the foaming temperature or the foaming time is too high, degeneration mechanisms appear during growing, and the structure collapses. For the materials under study, this happens when the foaming temperature is fixed at 100 °C for the materials with low and medium viscosity and at 110°C for the material with a higher viscosity.

Maps in **Figure 8** show the wide range of cellular materials produced in this work. Moreover, data from the bibliography of nanocellular PMMA with cell sizes below 100 nm are shown. The combination of using materials with different rheological properties and the use of different saturation and foaming conditions, has allowed producing materials with characteristics not reported before.

On the one hand, the most viscous material is capable of reaching the highest nucleation densities and the lowest cell sizes, but the minimum relative density achievable is around 0.37. On the other hand, PMMA LV covers regions of the materials maps (**Figure 8**) only reported before by Costeux et al. by using a copolymer of P(MMA-co-EMA) [15].

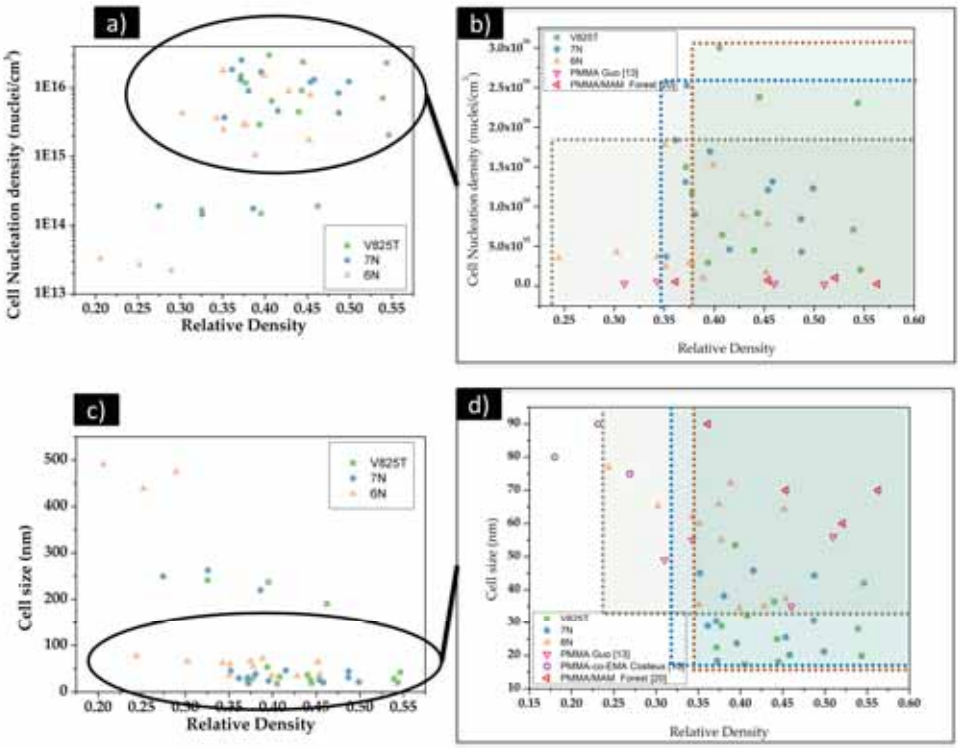

Figure 8. Maps of all the produced materials.

This study brings versatility to the production of nanocellular PMMA with a wide range of cell sizes, from 14 to 500 nm. On the one hand, the selection of the viscosity of the PMMA allows controlling the final characterizes of the foams inside certain boundaries that have been established.

4. Conclusions

The influence of the viscosity of PMMA on the density and cellular structure of nanocellular polymers produced by gas dissolution foaming have been studied. It has been proven that the viscosity affects the different steps, nucleation growing and stabilization, playing a key role on the density and final the cellular structure obtained.

It has been demonstrated that a lower viscosity leads to a smaller number of nucleation points even for larger solubilities. This effect can be attributed to the ability of the viscosity to control the Influence Volume; a higher viscosity slows down the evolution of IV leading to the creation of a higher number of cells. Moreover, the viscosity plays an essential role on the growing process, being beneficial to have low viscosity for further expansion, being these effects more pronounced at low solubilities.

Solubility is influenced by the production parameters, also playing an important role on the obtained cellular materials. A high solubility makes smaller the differences between polymers increasing the nucleation rate, reducing the growth of the cells and creating interconnected cellular structures.

On the other hand, with the same solubility, a change in the foaming conditions allows obtaining a wide range of cellular structures and densities. An increase in the

foaming temperature leads to materials with almost the same cell size but a higher cell nucleation density resulting in a lower relative density.

In this work, by combining the use of raw materials with difference viscosities and different production parameters, nanocellular materials with cell sizes in the range of 14 to 500 nm and cell nucleation densities from 10^{13} to 10^{16} nuclei/cm^3 have been produced. Between all these materials, we can highlight the production of a material with 75 nm of cell size and 10^{15} nuclei/cm^3 combined with a relative density of 0.24 using a low viscosity PMMA. On the other hand, using the high viscosity material is has been possible to produce a nanocellular polymers with 14 nm of cell size, $3.5 \cdot 10^{16}$ nuclei/cm^3 and a relative density of 0.4.

It has been proved that a proper control of the rheological properties of the PMMA is essential to fine-tune the cellular structure of nanocellular polymers.

Acknowledgments

Financial assistance from MINECO, FEDER, UE (MAT2015-69234-R), the Junta of Castile and Leon (VA275P18) and Spanish Ministry of Science, Innovation and Universities (RTI2018-098749-B-I00) are gratefully acknowledged. Financial support from FPU grant FPU14/02050 (V. Bernardo) from the Spanish Ministry of Education and Junta of Castile and Leon grant (J. Martín-de León) are gratefully acknowledged. Financial support from MINECO PTQ-16-08248 (E. Laguna-Gutierrez is gratefully acknowledged

5. References

[1] Kumar, V.; Suh, N. P. A process for making microcellular parts. *Polymer Engineering & Science* **1990**, *30*, 1323–1329.

[2] Shimbo, M.; Higashitani, I.; Miyano, Y. Mechanism of strength improvement of foamed plastics having fine cell. *Journal of Cellular Plastics* **2007**, *43*, 157–167.

[3] Kumar, V.; Weller, J. E.; Ma, M.; Montecillo, R.; Kwapisz, R. R. The Effect of Additives on Microcellular PVC Foams: Part II. Tensile Behaviour. *Cellular Polymers* **1998**, *17*, 350–361.

[4] Notario, B.; Pinto, J.; Solorzano, E.; De Saja, J. A.; Dumon, M.; Rodriguez-Perez, M. A. Experimental validation of the Knudsen effect in nanocellular polymeric foams. *Polymer (United Kingdom)* **2015**, *56*, 57–67.

[5] Notario, B.; Pinto, J.; Rodriguez-Perez, M. a. Towards a new generation of polymeric foams: PMMA nanocellular foams with enhanced physical properties. *Polymer* **2015**, *63*, 116–126.

[6] Martin-de Leon, J.; Bernardo, V.; Rodriguez-Perez, M. A. Key Production Parameters to Obtain Transparent Nanocellular PMMA. *Macromolecular Materials and Engineering* **2017**, 1700343(1)-1700343(5).

[7] Liao, R.; Yu, W.; Zhou, C. Rheological control in foaming polymeric materials: I. Amorphous polymers. *Polymer* **2010**, *51*, 568–580.

[8] Leung, S. N.; Wong, A.; Guo, Q.; Park, C. B.; Zong, J. H. Change in the critical nucleation radius and its impact on cell stability during polymeric foaming processes. *Chemical Engineering Science* **2009**, *64*, 4899–4907.

[9] Ludwiczak, J.; Frackowiak, S.; Łuzny, R. Effect of recycling on the cellular structure of polylactide in a batch process. *Cellular Polymers* **2018**, *37*, 69–79.

[10] Guo, H.; Kumar, V. Some thermodynamic and kinetic low-temperature properties of the PC-CO2 system and morphological characteristics of solid-state PC nanofoams produced with liquid CO2. *Polymer* **2015**, *56*, 46–56.

[11] Bernardo, V.; Martín-De León, J.; Rodríguez-Pérez, M. A. Production and characterization of nanocellular polyphenylsulfone foams. *Materials Letters* **2016**, *178*, 155–158.

[12] Guo, H.; Kumar, V. Solid-state poly(methyl methacrylate) (PMMA) nanofoams. Part I: Low-temperature CO2 sorption, diffusion, and the depression in PMMA glass transition. *Polymer* **2015**, *57*, 157–163.

[13] Pinto, J.; Dumon, M.; Pedros, M.; Reglero, J.; Rodriguez-Perez, M. A. Nanocellular CO2 foaming of PMMA assisted by block copolymer nanostructuration. *Chemical Engineering Journal* **2014**, *243*, 428–435.

[14] Bernardo, V.; Martin-de Leon, J.; Laguna-Gutierrez, E.; Catelani, T.; Pinto, J.; Athanassiou, A.; Rodriguez-Perez, M. A. Understanding the role of MAM molecular weight in the production of PMMA/MAM nanocellular polymers. *Polymer* **2018**, *153*, 262–270.

[15] Costeux, S.; Jeon, M. H.; Bunker, T. S.; Khan, I. NANOCELLULAR FOAMS FROM ACRYLIC POLYMERS : EXPERIMENTS AND MODELING. *FOAMS 2012 Conference* **2012**, 1–6.

[16] Costeux, S.; Zhu, L. Low density thermoplastic nanofoams nucleated by nanoparticles. *Polymer* **2013**, *54*, 2785–2795.

[17] Bernardo, V.; Martín-de León, J.; Laguna-Gutiérrez, E.; Rodríguez-Pérez, M. Á. PMMA-sepiolite nanocomposites as new promising materials for the production of nanocellular polymers. *European Polymer Journal* **2017**, *96*, 10–26.

[18] Martín-de León, J.; Bernardo, V.; Rodríguez-Pérez, M. Low Density Nanocellular Polymers Based on PMMA Produced by Gas Dissolution Foaming: Fabrication and Cellular Structure Characterization. *Polymers* **2016**, *8*, 265.

[19] Pinto, J.; Reglero-Ruiz, J. A.; Dumon, M.; Rodriguez-Perez, M. A. Temperature influence and CO2 transport in foaming processes of poly(methyl methacrylate)–block copolymer nanocellular and microcellular foams. *The Journal of Supercritical Fluids* **2014**, *94*, 198–205.

[20] Forest, C.; Chaumont, P.; Cassagnau, P.; Swoboda, B.; Sonntag, P. Nanofoaming of PMMA using a batch CO2 process: Influence of the PMMA viscoelastic behaviour. *Polymer* **2015**, *77*, 1–9.

[21] Costeux, S.; Bunker, S. P.; Jeon, H. K. Homogeneous nanocellular foams from styrenic-acrylic polymer blends. *Journal of Materials Research* **2013**, *28*, 2351–2365.

[22] Guo, H.; Nicolae, A.; Kumar, V. Solid-state poly(methyl methacrylate) (PMMA) nanofoams. Part II: Low-temperature solid-state process space using CO2 and the resulting morphologies. *Polymer* **2015**, *70*, 231–241.

[23] Crank, J. *The mathematics of diffusion*; Oxford University Press, **1975**.

[24] Pinto, J.; Solorzano, E.; Rodriguez-Perez, M. a.; de Saja, J. a. Characterization of the cellular structure based on user-interactive image analysis procedures. *Journal of Cellular Plastics* **2013**, *49*, 555–575.

[25] Kumar, V.; Suh, N. P. A process for making microcellular thermoplastic parts. *Polymer Engineering and Science* **1990**, *30*, 1323–1329.

[26] Laguna-Gutierrez, E.; Van Hooghten, R.; Moldenaers, P.; Angel Rodriguez-Perez, M. Effects of extrusion process, type and content of clays, and foaming process on the clay exfoliation in HMS PP composites. *Journal of Applied Polymer Science* **2015**, *132*, 1–12.

[27] Wilfried, W. Model calculation of the temperature dependence of small molecule diffusion in high polymers. **1968**, *63*, 1080–1085.

[28] Handa, Y. P.; Zhan, Z.; Wong, B. Solubility, diffusivity, and retrograde vitrification in PMMA-CO2, and development of sub-micron cellular structures. *Cellular polymers* **2001**, *20*, 1–16.

[29] Martín-de León, J.; Bernardo, V.; Rodríguez-Pérez, M. Á. Key Production Parameters to Obtain Transparent Nanocellular PMMA. *Macromolecular Materials and Engineering* **2017**, *3*, 1700343.

[30] Rindfleisch, F.; DiNoia, T. P.; McHugh, M. A. Solubility of Polymers and Copolymers in Supercritical CO 2. *The Journal of Physical Chemistry* **1996**, *100*, 15581–15587.

[31] Kaufman, H. S.; Falcetta, J. J.; Falcetta, J. J. *Introduction to polymer science and technology : an SPE textbook*; Wiley, **1977**.

[32] Tang, M.; Du, T.-B.; Chen, Y.-P. Sorption and diffusion of supercritical carbon dioxide in polycarbonate. *The Journal of Supercritical Fluids* **2004**, *28*, 207–218.

[33] Martín-de León, J.; Bernardo, V.; Rodríguez-Pérez, M. ángel Low density nanocellular polymers based on PMMA produced by gas dissolution foaming: Fabrication and cellular structure characterization. *Polymers* **2016**, *8*.

[34] Costeux, S.; Khan, I.; Bunker, S. P.; Jeon, H. K. Experimental study and modeling of nanofoams formation from single phase acrylic copolymers. *Journal of Cellular Plastics* **2014**, *51*, 197–221.

[35] Bergman, T. L.; Incropera, F. P. *Fundamentals of heat and mass transfer.*; Wiley, **2011**.

[36] Khan, I.; Adrian, D.; Costeux, S. A model to predict the cell density and cell size distribution in nano-cellular foams. *Chemical Engineering Science* **2015**, *138*, 634–645.

6.2.1. Suporting Information

INFLUENCE OF THE RHEOLOGICAL BEHAVIOUR OF PMMA ON THE CELLULAR STRUCTURE OF NANOCELLULAR MATERIALS.

Judith Martín-de León, Victoria Bernardo, Ester Laguna-Gutierrez, M.A. Rodriguez-Pérez

Cellular Materials Laboratory (CellMat), Universidad de Valladolid, 47011, Spain

CellMat Technologies S.L., Paseo de Belén 9A, 47011 Valladolid, Spain

Correspondence to: Judith Martín-de León (E-mail: *jmadeleon@fmc.uva.es*)

6. Solubility influence

The influence of the solubility on the obtained cellular structure has been studied for the four used foaming conditions. Thus, the cell nucleation density, the cell size the relative density and the cell nucleation density have been represented as a function of the solubility for 25, 40 60 and 80 °C of foaming temperature.

Results at $T_f = 60°C$ were included in the manuscript, herein the comparison between different foaming temperatures are included (**Figures S1, S2, S3** and **S4**).

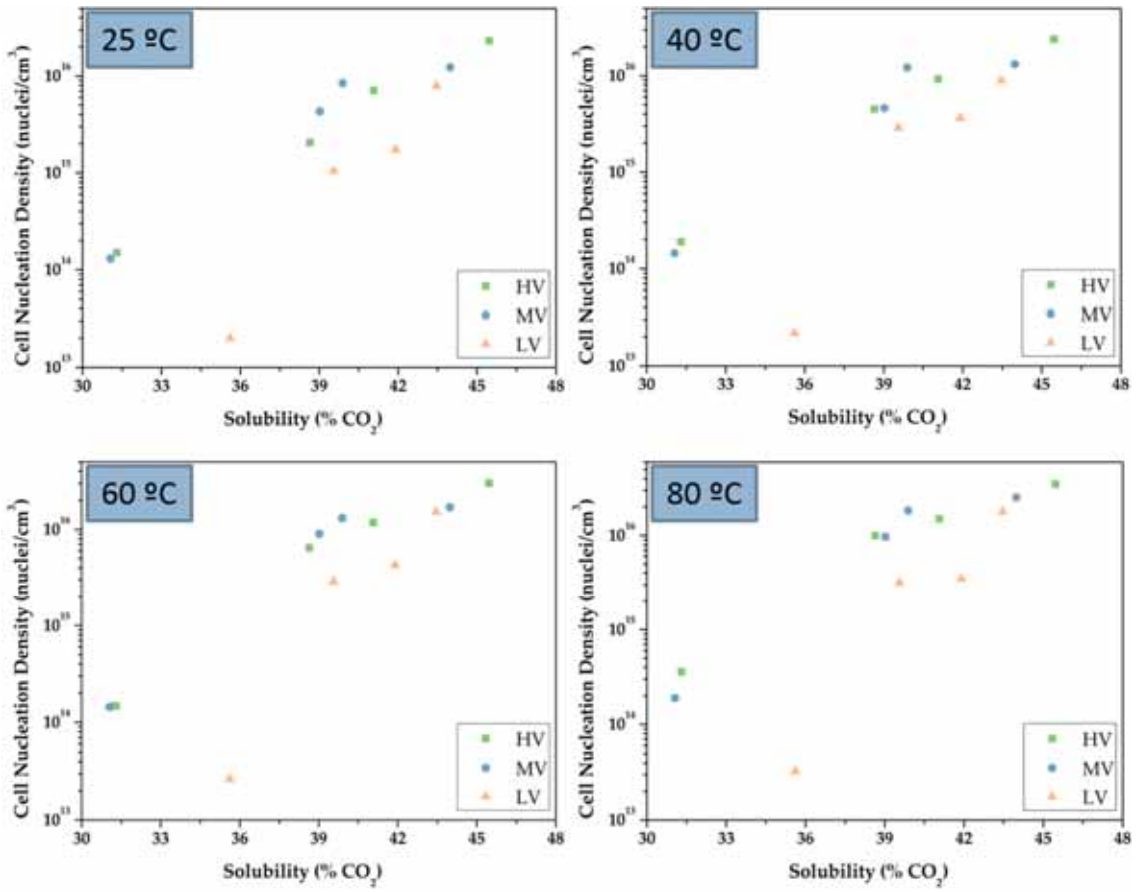

Figure S1. Cell nucleation density as a function of the solubility for 25 °C, 40 °C, 60°C and 80°C of foaming temperature.

Figures S1 and **S**2 show that tendencies observed for the cell nucleation density and the cell size are the same for all the foaming conditions. While the cell nucleation increases with the solubility rise, the cell size decreases. Differences between materials are also the same for the four foaming conditions. The highest viscous PMMA leads to higher cell nucleation densities combined with smaller cell sizes.

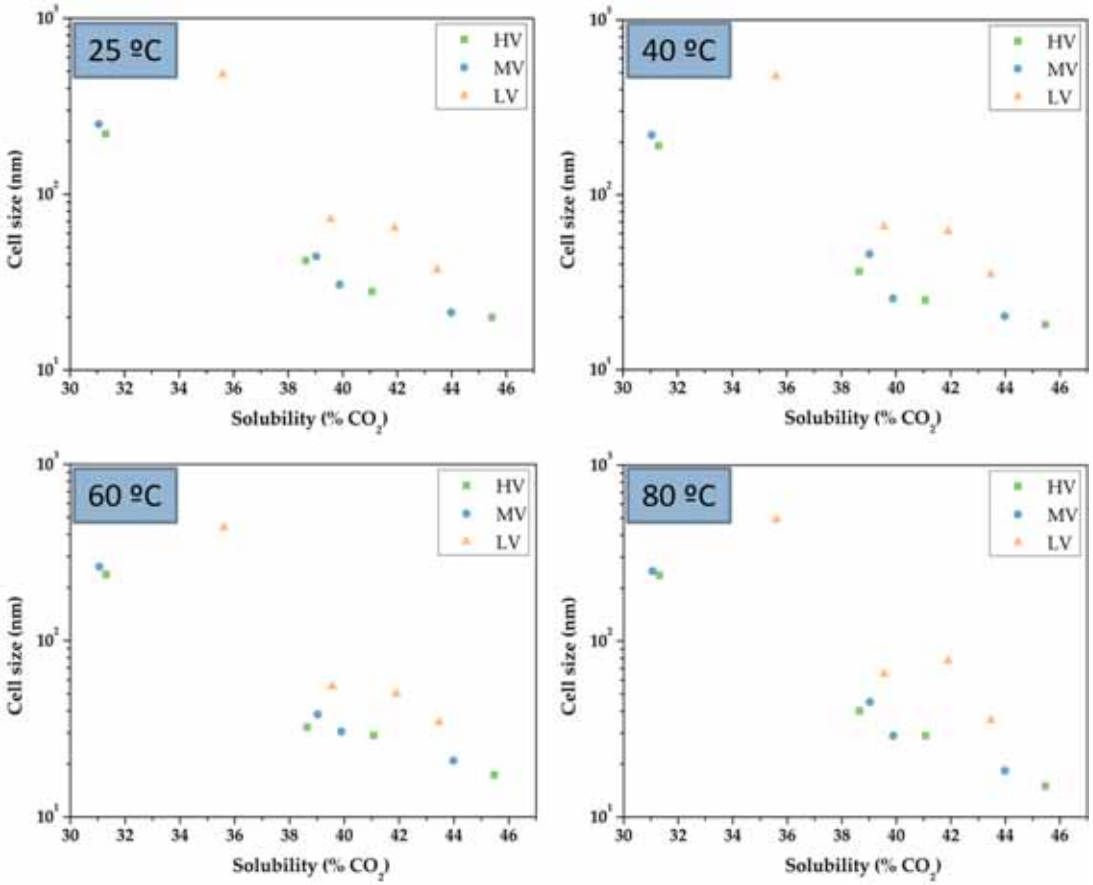

Figure S2. Cell size as a function of the solubility for 25 °C, 40 °C, 60°C and 80°C of foaming temperature.

Those changes in the cell size and cell nucleation density are translated in modifications in the relative density (**Figure S3**). As it was discussed in the manuscript, changes in the cell nucleation density and the cell size compensate in HV PMMA leading to no variation of the relative density with the solubility. On the other hand, in MV and LV PMMA an increase of the solubility leads to less ability for expansion, that means materials with higher relative densities.

However, changes between foaming temperatures are herein evident. The minimum foaming temperature leads to the higher relative density for all the materials while 80 °C of foaming temperature result in the lowest relative densities, fact showed in **Figure 5**. While for 25 °C of foaming temperature HV materials have a relative density of 0.5, this value decreases below 0.4 when foaming at 80°C. Similarly, for LV PMMA, which relative density ranges between 0.35 and 0.45 when foaming at 25 °C, and from 0.20 to 0.35 when foaming at 80 °C. So the expansion is optimized with a higher foaming temperature.

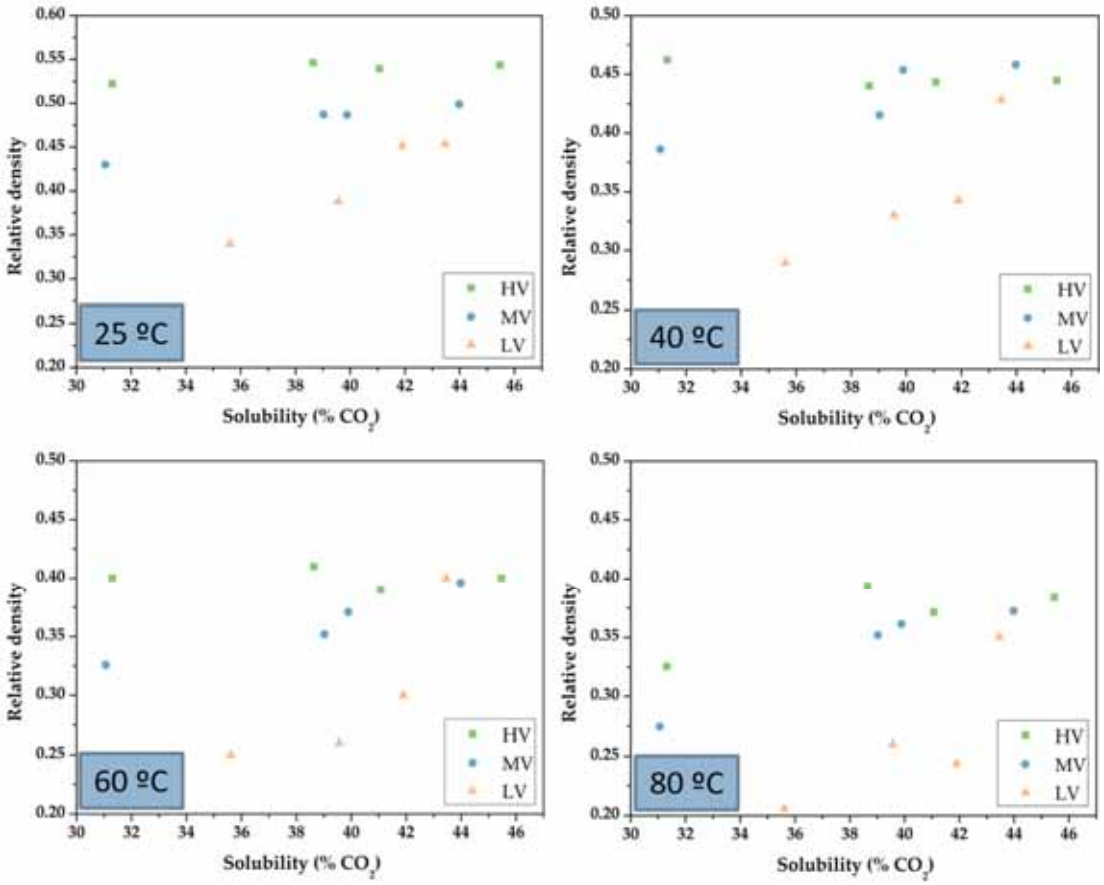

Figure S3. Relative density as a function of the solubility for 25 °C, 40 °C, 60°C and 80°C of foaming temperature.

As discussed in the manuscript the expansion ability is closely related to the open cell content of the materials (**Figure S4**). PMMAs with a completely open cellular structure is harder expand due to the gas, vital for the expansion, diffuses out eassiliy through the open pores.

For 25, 40 and 60 °C the material with the lowest viscosity shows values of open cell smaller than 100%. This indicates that this PMMA can further expand, being possible to reduce its relative density easily. When foaming at 80 °C the obtained cellular structures for all the solubilities are entirely open, indicating that this is the limit for this material. As explained in the paper 100 °C of foaming temperature leads to a degeneration of the cellular structure.

On the other hand, MV and HV show open cellular structures in all the foaming temperatures ranges for solubilities higher than 36%. This fact explains the difficulty of those materials to expand in comparison with LV. Conversely, for low solubilities, the open cell content is smaller than 100% for those two materials, even at 80 °C. This indicates that further expansion could be achieved with an increase in the foaming temperature for those two PMMAs. This fact was previously reported for HV PMMA showing a minimum relative density of 0.24 when foaming at 100°C [1].

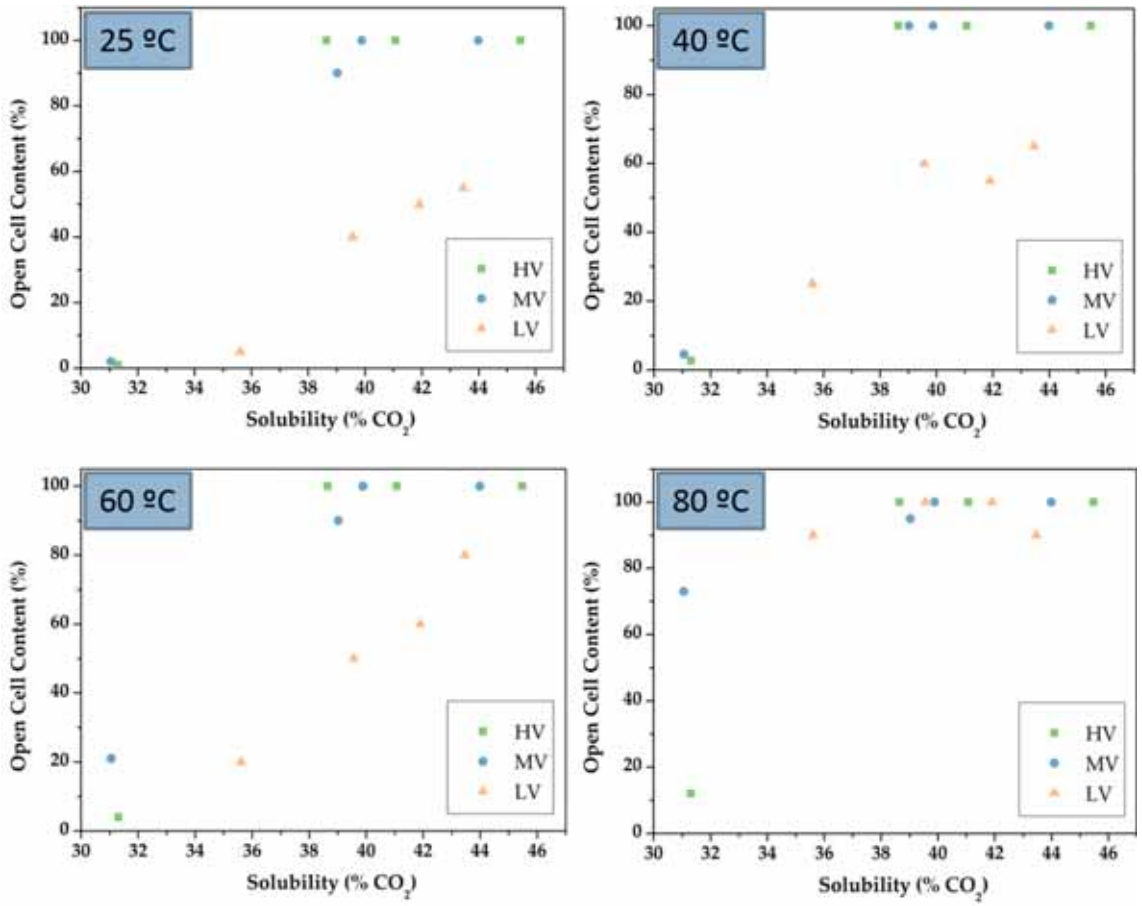

Figure S4. Open cell content as a function of the solubility for 25 °C, 40 °C, 60°C and 80°C of foaming temperature.

It can be then concluded that the general behavior with solubility is the same independently on the foaming conditions. An increase of the solubility enhances the cell nucleation density and decreases the cell size, leading to a smaller ability of expansion.

Changes between the three degrees of PMMA are attributed to the different viscosity as explained in section 3.3.2 of the manuscript.

7. Influence of the foaming parameters

Section 3.3.1.2 in the manuscript shows the influence of the foaming parameters in the cellular structure. The dependence of the relative density with the foaming temperature is showed for the four used saturation conditions. It was discussed that an increase in the foaming temperature leads to a reduction in the relative density. This reduction is justified by an increase in the cell nucleation density with the foaming temperature rise while the cell size remains constant.

The manuscript shows the cell nucleation density and the cell size as a function of the relative density for the two extreme saturation conditions. In **Figure S5** the graphs for P_{sat} =10 MPa, T_{sat} = -32°C and P_{sat} 6 MPa, T_{sat} = -32°C are shown.

For both conditions, the discussion in the manuscript can be verified. The reduction in relative density is given by an increase in the cell nucleation density when the foaming temperature becomes higher.

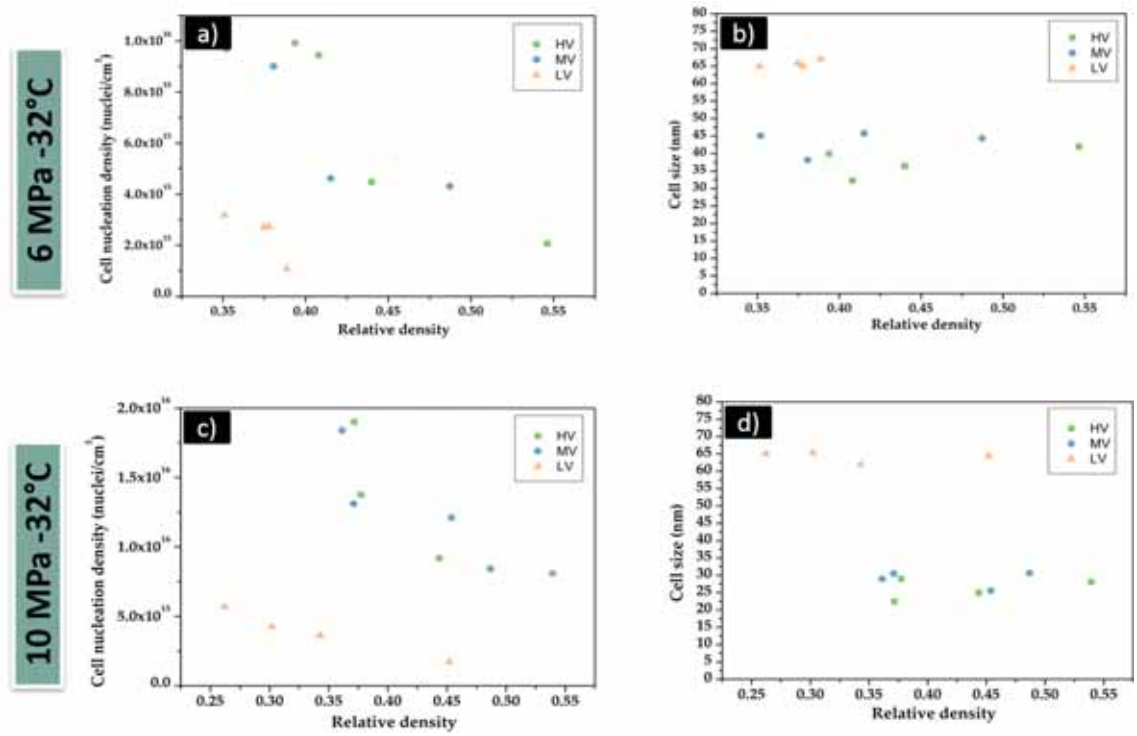

Figure S5. Open cell content as a function of the solubility for 25 °C (a), 40(b), 60°C (c) and 80°C (d) of foaming temperature.

Saturating at 6 MPa and -32 °C leads to constant cell sizes of around 65 nm for LV and around 40 nm for HV and MV independently on the relative density, while the cell nucleation density increases in one order of magnitude from the highest ρ_r to the lower one.

A similar situation is found when saturating at 10 MPa and -32 °C of saturation pressure and temperature respectively.

Differences between the three degrees of PMMA are justified with the different viscosity of the three PMMA as discussed in section 3.3.2 of the manuscript.

8. References

[1] Martín-de León, J.; Bernardo, V.; Rodríguez-Pérez, M. Low Density Nanocellular Polymers Based on PMMA Produced by Gas Dissolution Foaming: Fabrication and Cellular Structure Characterization. *Polymers* **2016**, *8*, 265.

6.3. References

[1] Costeux, S.; Khan, I.; Bunker, S. P.; Jeon, H. K. Experimental study and modeling of nanofoams formation from single phase acrylic copolymers. *Journal of Cellular Plastics* **2014**, *51*, 197–221.

Chapter 7

Gas dissolution process customization

"La felicidad solo es real cuando se comparte."

Christopher McCandless

INDEX

7.1. Introduction

Gas dissolution foaming process was firstly used in the earlys '80 for the production of microcellular materials. Since then, this process has been reproduced with very small modifications. Thus, different process parameters have been changed for the production of nanocellular materials but maintaining intact the scheme of the process. However, when in-deep explore the production of nanocellular materials, this process presents some limitations. For example, foaming in thermal bath allows the free expansion of the cellular polymer resulting in bent samples. On the other hand, some production parameters lead to materials with internal microcellular defects hard to remove if the process remains inalterable.

With the acquired knowledge described in previous chapters, Chapter 7 aims at presenting some alterations of the original gas dissolution foaming process leading to materials with characteristics not previously achieved. Two papers explaining those modifications are attached in the sections below.

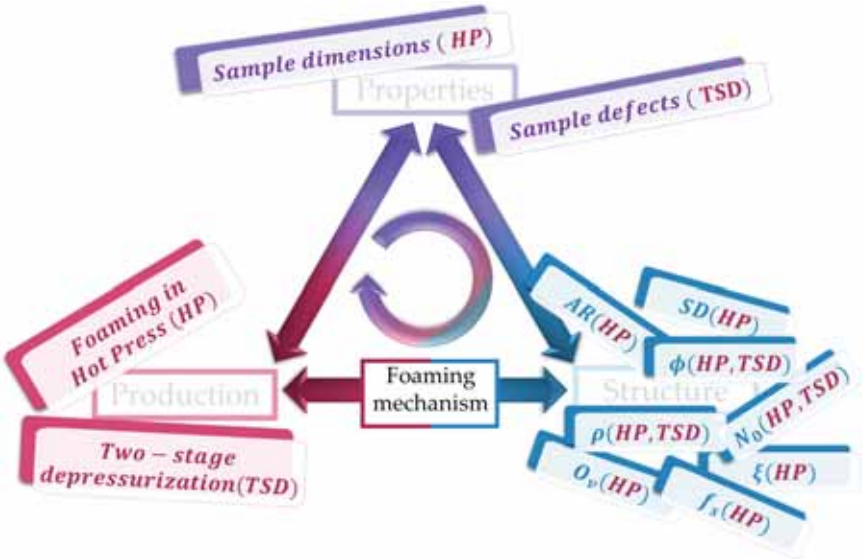

Figure 7.1. Established relationships in Chapter 7.

In the first one "Martín-de León, J.; Bernardo, V.; Cimavilla-Román, P.; Pérez-Tamarit, S.; Rodríguez-Pérez, M. A. Overcoming the Challenge of Producing Large and Flat Nanocellular Polymers: A Study with PMMA. *Advanced Engineering Materials* **2019**, 1–8.", the foaming step, usually carried out in a thermal bath, is substituted by foaming in a hot press (HP). This allows the production of nanocellular PMMA with a flat shape and dimensions not reported before in the literature for nanocellular polymers (sizes of 100 x 100 x 6 mm^3) (**Sample dimensions (HP)**). In addition, the cellular structure of the materials produced using the hot press (HP) is compared with the produced in a thermal bath. The influence of changing this process in the relative density, the cell nucleation density, the cell size, the standard deviation of the cell size distribution, the anisotropy ratio, the fraction of mass in struts, the cell wall thickness, and the open cell content is established. $\boldsymbol{\rho_r(HP), N_0(HP), \phi(HP), SD(HP), AR(HP), f_s(HP), \xi(HP), O_v(HP)}$.

The second one "Two-stage depressurization in one step foaming process: the production of nanocellular materials free of defects" describes how a depressurization in stages (TSD) helps to remove defects in nanocellular materials (produced through gas dissolution foaming. The cellular structure, cell nucleation density, cell size, and relative density is analyzed as a function of the introduced changes in the process $\boldsymbol{\rho_r(TSD), N_0(TSD), \phi(TSD)}$. Moreover, an analysis of the foaming mechanisms taking place during the nucleation and growing of the nanocellular materials is carried out.

7.2. Overcoming the challenge of producing large and flat nanocellular polymers: a study with PMMA.

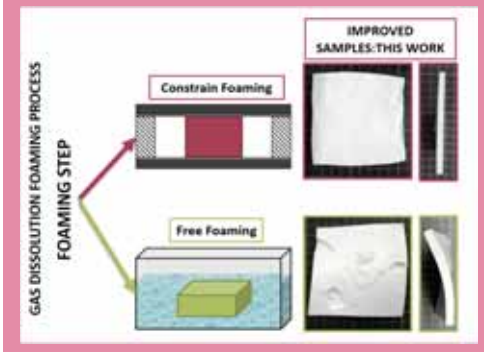

Large and flat nanocellular PMMA parts (sizes of 100 x 100 x 6 mm³) have been produced by foaming in a hot press. Obtained cellular structures are comparable to those materials foamed through the common method (thermal bath). Moreover, tuneable densities can be obtained by modifying the foaming parameters.

OVERCOMING THE CHALLENGE OF PRODUCING LARGE AND FLAT NANOCELLULAR POLYMERS: A STUDY WITH PMMA.

Judith Martín-de León, Victoria Bernardo, Paula Cimavilla-Román, Saúl Pérez Tamarit, Miguel Ángel Rodríguez-Pérez

Cellular Materials Laboratory (CellMat), Universidad de Valladolid, 47011, Spain

Correspondence to: Judith Martín-de León (E-mail: *jmadeleon@fmc.uva.es*)

Abstract

Although nanocellular polymers are interesting materials with improved properties in comparison with conventional or microcellular polymers, the production of large and flat parts of those materials is still challenging.

Herein, gas dissolution foaming process is used to produce large and flat nanocellular polymethylmethacrylate samples. In order to do that, the foaming step is performed in a hot press. The methodology is optimized to produce flat samples with dimensions of 100 x 100 x 6 mm³, relative densities in the range 0.25-0.55 and cell sizes around 250 nm.

Additionally, foaming parameters are modified to study their influence on the final cellular structure, and the materials produced in this paper are compared with samples produced by using a most conventional approach in which foaming step is conducted in a thermal bath.

Results obtained show that an increment in the foaming temperature leads to a reduction in relative density and an increase of cell nucleation density. Moreover, differences in the final cellular structure for materials produced by both foaming routes are studied, proving that although there exist some differences, the mechanisms

governing the nucleation and growing are the same in both processes, leading to the production of homogeneous materials with very similar cellular structures.

Keywords: Nanocellular polymers, PMMA, foaming, flat samples, gas dissolution foaming.

1. Introduction

Microcellular polymers have been implemented at the industrial level thanks to the successful scaling-up of the production process. Nowadays, large parts of microcellular plastics are produced by means of extrusion or injection molding. [1,2]

Although it has been proved that nanocellular polymers perform better than microcellular materials, their production is yet restricted to the laboratory scale, and most of the works on this topic have produced small samples that are not necessarily flat. However, it is already known that nanocellular materials present a smaller thermal conductivity due to Knudsen effect [3], they also present enhanced mechanical properties, [4] and recently, it has been proved that they can have some new and interesting properties such as transparency. [5]

All these properties together make nanocellular polymers the perfect candidates to substitute microcellular materials in sectors like the building sector, the automotive one, in high-performance applications or in new applications where microcellular materials have no place. However, in order to substitute microcellular materials, it is mandatory to be able to produce nanocellular polymers at a larger-scale.

Gas dissolution foaming process is the most common production method to obtain nanocellular polymers. [6] It consists of three steps, saturation, desorption and the last one, foaming, where samples usually are free foamed in a thermal bath. However, this foaming method does not allow producing large and flat nanocellular polymers, being the dimensions typically smaller than 30 x 30 x 4 mm^3. [5,7–9] Some previous studies have modified the last step of the gas dissolution foaming by proposing a constrained foaming process, where the sample is placed between the two heated plates of a hydraulic press. Nadella et al. proposed this method for the production of flat microcellular panels from polymethylmethacrylate (PMMA), polystyrene (PS) and acrylonitrile butadiene styrene (ABS). [10] A similar process was also used by Gedler et al. for the production of graphene-filled polycarbonate composite microcellular foams. [11]

However, to the best of our knowledge, this foaming approach has not been previously used for the production of nanocellular polymers, in which due to the higher amount of gas dissolved in the polymer and the critical requirement of not promoting coalescence during growing the process is more critical. This work aims at presenting. for the first time. the methodology required to produce larger and flat samples of nanocellular PMMA using a constrained foaming approach in a hot press. Besides, the results obtained in terms of densities and cellular structures are compared with those obtained by using the conventional approach of foaming the samples in a thermal bath.

2. Materials and methods

2.1. Materials

The material used in this study was polymethylmethacrylate (PMMA). The specific polymer, V825T, has been kindly supplied, in the forms of pellets, by ALTUGLAS® International (Colombes, France). The density (ρ) of this polymer is 1.19 g/cm^3 (measured at 23 °C and 50% HR), and its glass transition temperature (T_g) is 114 °C (measured by DSC).

Medical grade CO_2 (99.9% purity) was used as blowing agent.

2.2. Samples production

Solid samples of PMMA with dimensions of 60 x 60 x 4 mm^3 were produced. First of all, the pellets were dried for 4 hours at 80 °C and then solid precursors of 4 mm in thickness were produced using a hot plate press from Talleres Remtex. The compression molded process comprises two steps. Pellets were first heated at 250 °C for 9 minutes and then they were pressed under a constant pressure of 54 MPa for one minute. Finally, they were cooled down at room temperature under the same pressure.

Lastly, the sheets were cut into the desired dimensions for the foaming experiments (55 x 55 x 4 mm^3).

2.3. Foaming tests

Nanocellular materials were produced by using the gas dissolution foaming process. The set up used for this purpose consists of a high-pressure vessel (model PARR 4681) provided by Parr Instrument Company (Moline, IL, USA) working at a maximum pressure of 40 MPa. An accurate pressure pump controller (model SFT-10), provided by Supercritical Fluid Technologies Inc. (Newark, DE, USA), is available to pressurize the system. Finally, for the foaming step, a hot/cold plate hydraulic press (Talleres Remtex) was used.

The gas dissolution foaming process consists of three steps; saturation, desorption, and foaming. For the first step, samples are introduced in the pressure vessel under a high CO_2 pressure atmosphere. This process is extended in time until the sample is fully saturated. Then the pressure is fast released.After a desorption time (time between depressurization and foaming) the sample is foamed in a hot press.

To prevent the expansion of the sample during the desorption time samples were immediately immersed in ice after releasing the pressure..

The scheme showed in **Figure 1** has been followed to foam the samples. The saturated sample is introduced between two steel plates, two aluminum foil sheets and a steel mold of 4 mm in thickness.

The two steel plates had been previously heated to the desired foaming temperature, while the aluminum foil sheets stay at room temperature in order to prevent any foaming until the sample is under pressure. The steel mold works as a guard to avoid compressing

the samples below their initial thickness of 4 mm. Afterward, all the layers are introduced between the hot plates of the press, preheated at the foaming temperature, and an initial pressure of 5.4 kPa is applied. As it is discussed later in the results section the level of this pressure is an important parameter to consider. After the foaming time, the pressure is fast released, and the sample is stabilized.

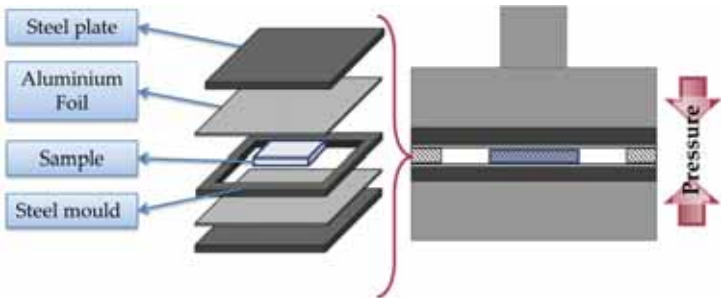

Figure 1. Scheme of the foaming step in a hot press.

In this study, the following parameters for the different steps have been chosen. A pressure (p_{sat}) of 31 MPa and a temperature (T_{sat}) of 25 °C were selected for the saturation step. Saturation time was selected to be 24 h for all the experiments. [7]The pressure release was carried out with an electrovalve with Kv = 1.1 l/min. at a pressure drop rate of 100 MPa/s. Desorption time was three minutes for all the experiments. Finally, foaming conditions were modified; foaming temperatures from 40 to 110 °C have been tested and foaming times of 0.5 min and 1 min were used for each temperature.

Results were compared with those obtained for a set of foamed samples produced using the same saturation conditions, pressure release and desorption time but foaming using a thermal bath at temperatures from 40 to 110 °C with foaming times of 1 and 2 min. [12]

2.4. Characterization techniques

2.4.1. Density

Relative density (ρ_r), defined as the ratio between the density of the foamed samples (ρ_f) and the density of the solid samples (ρ_s), has been determined for all the samples. ρ_s has been measured using a gas pycnometer (Mod. AccuPyc II 1340, Micromeritics, Norcross, GA, USA). On the other hand, previously to determine ρ_f, samples were polished in order to remove the solid outer skin (0.5 mm of each side of the samples were removed). Then ρ_f was measured using a density determination kit for an AT261 Mettler-Toledo balance using the water displacement method, based on Archimedes' principle.

2.4.2. Solubility

Solubility, defined as the amount of gas uptake, was calculated as the percentage of weight increment of the sample due to the gas sorption. The desorption curve after saturation (mass lost vs. time plot) was registered with a Mettler-Toledo balance and was used to extrapolate to zero time the mass of the samples after saturation. This value is

considered as the mass of the sample when it is fully saturated, i.e., the solubility of the material. [13] With the previously mentioned saturation conditions ((p_{sat}) of 31 MPa and a temperature (T_{sat}) of 25 °C) the reached solubility was 31 ± 0.3 %.

2.4.3. Scanning Electron Microscopy

The cellular structure was visualized with an ESEM Scanning Electron Microscope (QUANTA 200 FEG, Hillsboro, OR, USA). Before the visualization, samples were fractured in liquid nitrogen to preserve the original cellular structure. Then they were coated with gold by using a sputter coater (model SDC 005, Balzers Union, Balzers, Liechtenstein).

Cell size in 3D(Φ), the standard deviation of the cell size distribution divided by the cell size (SD/ Φ), the cell nucleation density (N_0) (calculated by using Kumar's method [6]) and the anisotropy ratio (AR) were measured to characterize the cellular structure. A software based on ImageJ/FIJI [14] was used for this purpose. Moreover, the mean cell wall thickness (ξ) and the fraction of mass in the struts (fs) were also measured to fully characterize the materials. Cell wall thickness was measured with ImageJ/FIJI directly from the micrographs, while fs was determined following the method described in a previous publication. [12]

2.4.4. Open Cell Content

The number of open cells in percentage (OC%) was measured using a gas pycnometer (Mod. AccuPyc II 1340, Micromeritics), according to ASTM D6226-10. E**quation 1** was used to calculate it, where V is the geometric volume of the sample, V_P is the volume measured by the pycnometer and V_s takes into account the exposed cells at the surface of the sample.

$$O_v(\%) = \frac{V - V_p - V_s}{V(1 - \rho_r)} \quad (1)$$

The external volume was determined as $V = m/\rho$ where m is the mass measured with an AT261 Mettler- Toledo balance and ρ is the density determined by the water-displacement method. V_P was determined by using the volume given by the pycnometer at different pressures (from 0.2 MPa to 1.3 MPa). From a certain pressure, this value becomes constant. V_P was taken as the mean value of these constant values. V_s can be neglected for nanocellular materials because this volume is proportional to the cell size.

2.4.5. Tomography analysis

The density distribution in the samples was measured by using X-ray Tomography. A homemade set-up with a maximum resolution of 2.5 microns was used to acquire the X-ray tomographies of the samples. [15,16]

This method allows detecting in a non-destructive way the presence of internal defects. In addition, it is also possible, to calculate a density profile. This technique allows determining the 3D distribution of attenuation coefficients (μ) that depends mainly on the

density of the materials and the constituent elements. As both gas and polymer are composed mainly by carbon, nitrogen, hydrogen, and oxygen, it is possible to conclude that in our case the attenuation coefficient only depends on materials density without losing generality. As the spatial resolution is not enough to resolve the cellular structure of the analyzed materials, the determined attenuation coefficient in every point of the space (voxel) is a linear combination of the attenuation coefficients of solid (μ_s) and gas (μ_g) constituents in that volume (**Equation 2**).

$$\mu = X_s\mu_s + (1 - X_g)\mu_g \tag{2}$$

Where X_s is the volumetric fraction of solid in the considered voxel.

The next step consists of determining the attenuation coefficients of both solid and gas. To this end, a two points calibration process has been implemented (**Figure 2**).

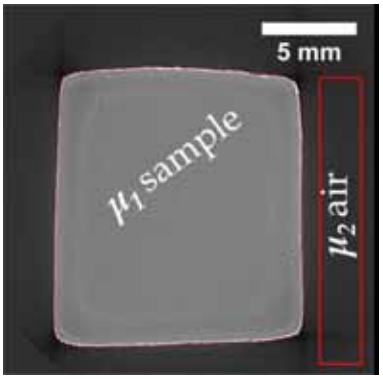

Figure 2. Reconstructed slice of one of the samples showing the two employed zones for the attenuation coefficient calibration.

The first point (μ_1) is the result of calculating the average attenuation coefficient of the sample considering the full scanned volume. After that, we obtain a first relationship between μ_1 , μ_s and μ_g by means of the relative density of the scanned material (ρ_r) (**Equation 3**).

$$\mu_1 = \rho_r\mu_s + (1 - \rho_r)\mu_g \tag{3}$$

The second point (μ_2) is selected out of the sample, consequently is the attenuation coefficient of air. As stated above, since the attenuation coefficient mainly depends on the constituent elements, we can consider that this attenuation coefficient is similar to μ_g (**Equation 4**).

$$\mu_2 \approx \mu_g \tag{4}$$

With these two last equations (2 and 3), it is possible to finally determine the attenuation coefficient of the solid (μ_s) (**Equation 5**).

$$\mu_s = \frac{\mu_1 - (1 - \rho_r)\mu_2}{\rho_r} \tag{5}$$

Including now the attenuation coefficients of both solid and gas, the relative density in any point of the sample ($\rho_r(\vec{r})$) can be calculated (**Equation 6**) knowing directly the corresponding attenuation coefficient ($\mu(\vec{r})$) in that point and those from pure solid and gas calculated using the two selected zones and the equations 3 and 4.

$$\rho_r(\vec{r}) = \frac{\mu(\vec{r}) - \mu_g}{\mu_s - \mu_g} \quad (6)$$

3. Results

3.1. External appearance and internal homogeneity of the samples

Besides their larger dimensions, all samples produced by means of foaming in a hot press present a flat and homogeneous shape independently of the foaming temperature, being the surface of the sample free of defects. In the thermal bath as the foaming temperature is increased it is more difficult to maintain the flat shape due to the higher expansion ratio. An example of this is shown in **Figure 3b,** where two samples foamed at 100 °C for 1 minute following the two-different foaming routes are shown. For this foaming temperature, the cellular materials have expanded around 4 times with respect the solid precursor (**Figure 3a**). As it can be observed, while the material produced in the hot press preserve the flat shape, samples produced using the thermal bath are entirely bent and present a significant number of superficial holes.

In order to explore the internal homogeneity of the nanocellular materials, tomography and SEM experiments were performed.

Figure 3c shows the 3D density distribution for the samples foamed at 60 °C for 1 minute, as well as a graph showing the relative density of the sample as a function of the thickness. Samples foamed at 60°C during 1 minute were chosen for tomography experiments because as it is shown in **Figure 3b** thermal bath samples foamed at 100°C presented defects that made more difficult to obtain high-quality tomographic images. For these experiments, the outer surface of the sample was not removed in order to evaluate the modification of the density near the outer surfaces. The upper and the lower part of the hot press foamed samples correspond to those parts in contact with the aluminium foil.

By analysing the tomography results the expected behavior for the gas dissolution foaming process can be appreciated; [17,18] The central part of the sample is homogeneous and similar for both cellular materials having the lowest density (purplish tones), then when approaching the outer surfaces, the relative density increases up to 1 (yellow tone) indicating the densest zone corresponding to the solid skin.

Nevertheless, it is near the surface where some differences can be appreciated between the two types of samples.. The sample foamed in the thermal bath presents a smooth transition from the inner part to the outer skin. However, the sample foamed in the hot press present a more abrupt transition. For this last material, density along the thickness remains constant even near the surface, and therefore near to the solid skin.

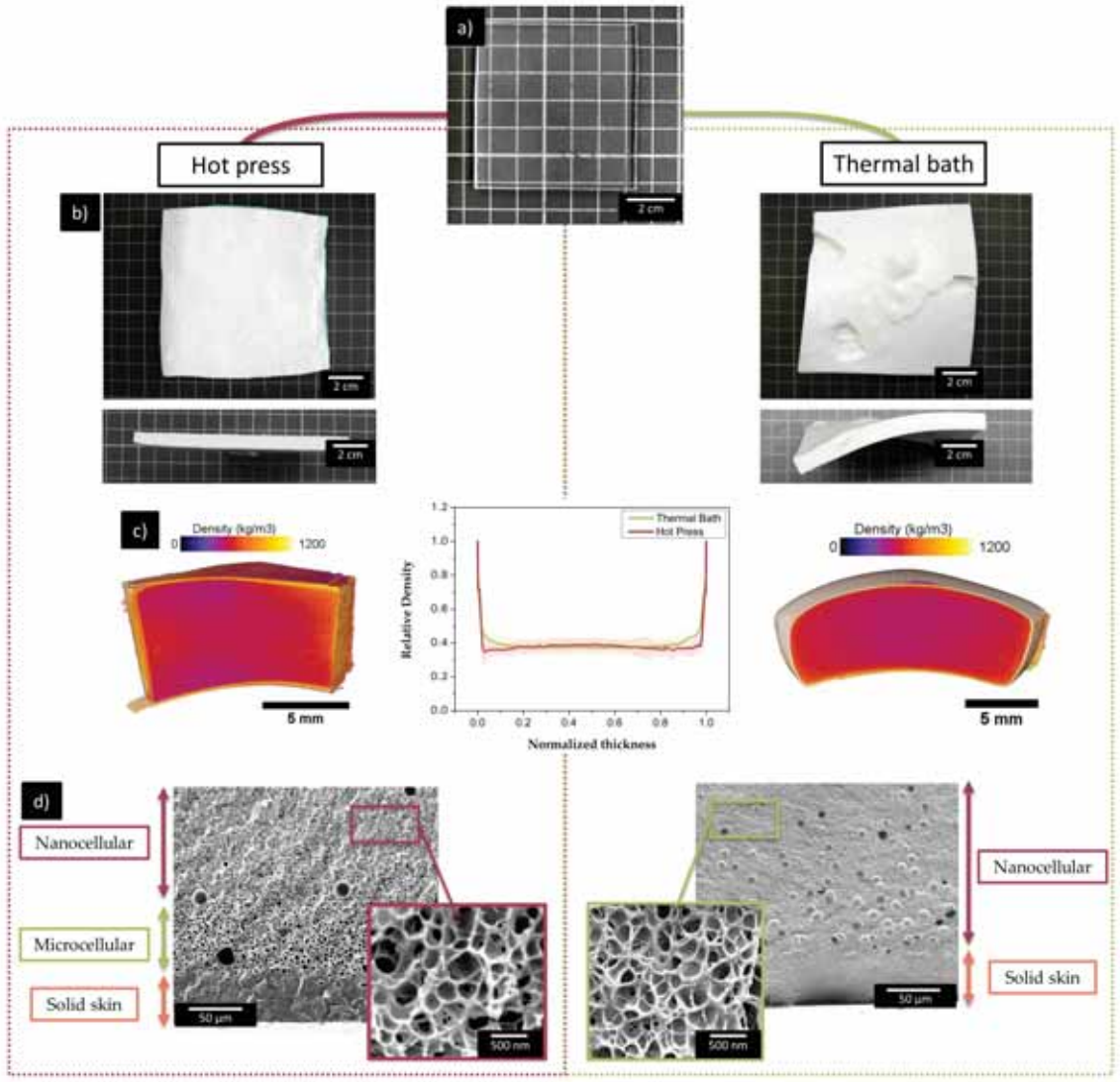

Figure 3. a) Photograph of a solid precursor **b)** Photograph of the foamed samples at 100 °C and 1 min. **c)** Tomography of the foamed samples at 60 °C and 1 min. **d)** SEM images of the foamed samples at 60 °C and 1 min with two different magnifications.

To understand this result, it is necessary to analyze the SEM images (**Figure 3d**). Micrographs with a lower magnification show the samples near the surface. Differences are clear, the sample produced in the hot press shows a a transition containing microcells between the solid skin and the nanocellular core. In the sample foamed in the thermal bath, this microcellular transition is almost non-existent, and the number of nanocells gradually decreases up to the solid skin, being this the cause of the soft change in the relative density. However, in the hot press, the microcellular transition makes it possible to maintain the relative density almost constant until the appearance of the solid skin.

Nevertheless, those differences are only shown in the edges of the sample. The central part of the material shows a homogeneous cellular structure (observed in the high magnification SEM images) and therefore an uniform density.

As shown in **Figure 3d** hot press materials present cell sizes in the nanometric range, very similar to those shown in nanocellular materials foamed in a thermal bath. [12]

The explanation of all of this can be found in the thermal transference of both foaming methods. A scheme is shown in **Figure 4**. In the thermal bath, the temperature of the water is faster transmitted to the sample due to the higher thermal conductivity of this fluid in comparison with air. It means that at a time t_1 the sample is uniformly hot at a temperature T_b smaller than the final temperature (T_f). The sample homogeneously increases it temperature until reaches T_f at a time t_2.

On the other hand, the heating of the sample in the hot press is less homogeneous- At a time t_1, the external parts of the sample heat rapidly at a temperature near T_f, while the center of the sample is cooler, at a temperature $T_p < T_b$. This situation evolves up to a time t_2 where the sample is homogeneous at a temperature T_f.

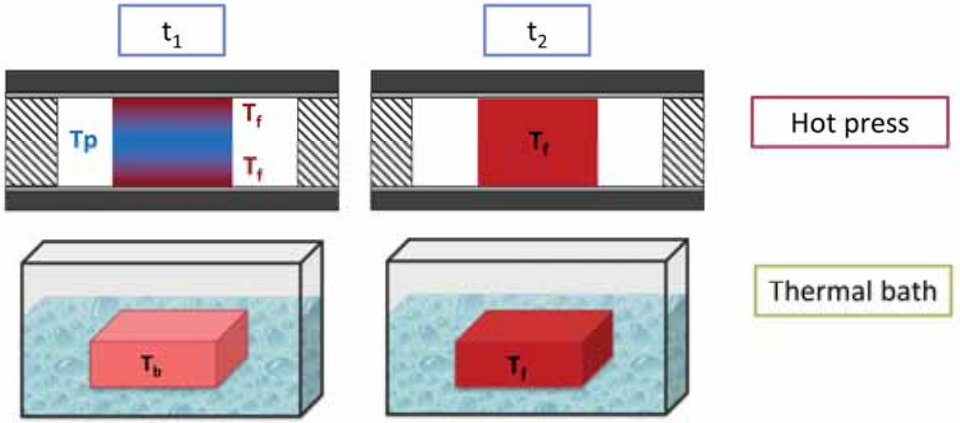

Figure 4. Scheme of the heat transfer for both foaming methods.

This leads to the results observed in **Figure 3**. The edges of the samples foamed in the hot press remain longer at a temperature T_f than those ones of the thermal bath samples, resulting in a coalescence of the cells near the surface that creates the microcellular transition between the solid skin and the center of the sample.

As a summary of this section, it can be concluded that the produced materials present a high homogeneity, with slight differences in the density distribution that only affects the areas near the outer skin. A more detailed comparison between the cellular structures in the central region of the samples is included in the following sections.

3.2. Comparison with thermal bath samples

3.2.1. Influence of the foaming parameters

In order to establish the differences between the two different foaming processes, the change in the final cellular structure in the inner part of the samples as a consequence of modifying the foaming parameters has been studied for samples produced by the two methods.

Table 1. Cellular structure characteristics for all the produced samples.

Foaming Method	Foaming Temperature	ϱ_r	N_0 (nuclei/cm3)	φ (nm)	SD/φ	AR	f_s	ξ(nm)	OC(%)
Hot Press	40.00	0.50	$1.48 \cdot 10^{14}$	258.40	0.34	1.18	0.66	31.75	5.94
Hot Press	60.00	0.40	$1.42 \cdot 10^{14}$	276.69	0.39	1.12	0.59	33.45	43.47
Hot Press	80.00	0.31	$2.02 \cdot 10^{14}$	277.36	0.38	1.00	0.58	29.74	73.23
Hot Press	100.00	0.27	$2.39 \cdot 10^{14}$	257.32	0.37	1.08	0.40	28.15	72.99
Hot Press	110.00	0.31	$2.84 \cdot 10^{14}$	239.74	0.38	0.99	0.42	25.65	76.97
Thermal Bath	40.00	0.47	$1.78 \cdot 10^{14}$	211.83	0.45	1.24	0.60	25.52	3.48
Thermal Bath	60.00	0.39	$2.38 \cdot 10^{14}$	207.41	0.42	1.21	0.54	25.93	4.53
Thermal Bath	80.00	0.27	$3.56 \cdot 10^{14}$	208.12	0.45	1.21	0.35	22.89	72.93
Thermal Bath	100.00	0.27	3.44E+14	203.86	0.41	1.18	-	27.66	100.00
Thermal Bath	110.00	0.25	2.23E+14	261.08	0.43	1.19	-	28.34	99.21

[a)] The missing data for f_s is due to the impossibility of measuring this value in those samples. [12]

Samples foamed for one minute, and different foaming temperatures from 40 to 110 °C were selected for this purpose, and all their characteristics are shown in **Table 1**.

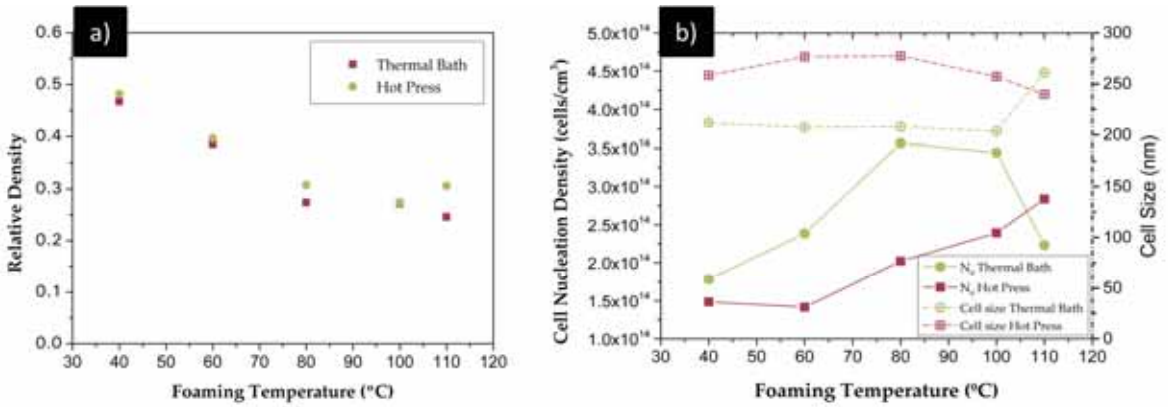

Figure 5. a) Relative density as a function of the foaming temperature. **b)** Cell size and cell nucleation density as a function of the foaming temperature. Foaming time was 1 minute for all the samples under study.

An increase in the foaming temperature is promoting a decrease in the relative density of all the samples (**Figure 5a**). In fact, it decreases in a very similar way for the two different foaming methods, starting from around 0.5 when the foaming temperature is 40 °C and decreasing up to values below 0.3 for temperatures above 80 °C. The differences in density

between the two foaming methods are almost negligible in all the temperature range under study, except ay 110°C.

To understand the trends measured for the relative density, attention must be paid to **Figure 5b** in which cell size and cell nucleation density values are summarized. Although changes in relative density are similar for both approaches, some differences in the parameters defining the final cellular structure can be appreciated. Without considering the highest foaming temperature (110 °C), in which cell degeneration mechanisms appear for the samples produced using the thermal bath, it can be asserted that cell size remains constant for both foaming routes when the foaming temperature rises, while cell nucleation density increases. In addition, it is clearly observed that materials produced in the hot press, present values of cell nucleation densities smaller than those foamed in a thermal bath and cell sizes slightly higher.

The cell size distributions are included in **Figure 6** for samples foamed at 60, 80 and 100°C. The higher values of cell size for the materials produced in the hot press are a consequence of cell size distributions that are slightly shifted to the right .

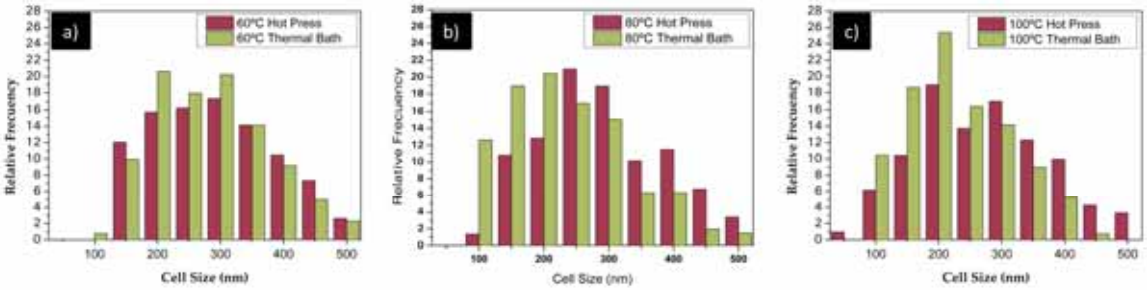

Figure 6. Cell size distributions for samples foamed in a thermal bath and in a hot press at 60 (a), 80 (b) and 100 °C (c). The foaming time was 1 minute for all the samples.

Additionally, SD/ Φ and the anisotropy ratio AR can be observed in **Table 1**. Both magnitudes present smaller values for the samples foamed in the hot press. It means that although the cell size distribution is shifted to higher values in the hot press samples, the distribution is narrower for those samples and moreover, attending to AR they present a smaller anisotropy.

Although classical nucleation theory cannot be used for predicting absolute values of cell size or cell nucleation densities in nanocellular materials, it is possible to explain using this theory the general tendencies observed in our materials [19]. So in order to understand the differences between both foaming routes, the classical homogeneous nucleation theory has been used. [20] For the formation of a nuclei, it is necessary to overcome an energetic barrier given by **Equation 7.** Also, CNT states that there exists a critical radius below which nuclei do not grow into cells **(Equation 8**).

$$W = \frac{16\gamma^3}{3\,\Delta P^2} \tag{7}$$

$$R_{cr} = \frac{2\gamma}{\Delta P} \tag{8}$$

Both are functions, among others, of the difference between the pressure inside the bubble and the surrounding system $\Delta P = P_{bub} - P_{sys}$.

When there exists stress in the surroundings of the bubbles the expression for the pressure increment is given by **Equation 9.** [21][22]

$$\Delta P = P_{bub} - \left(P_{sys} + \Delta P_{local}\right) \quad (9)$$

If the surroundings of the nucleation point experience compressive stress, then ΔP_{local} is positive, resulting in an increase of the critical radius as well as the energy barrier for homogeneous nucleation.

This is precisely what is happening in the materials foamed in the hot press; the pressure imposed by the hydraulic press is generating compressive stress that leads to cellular structures with a smaller number of nucleation points than those free foamed in a thermal bath.

For this reason, the control of the parameters of this new foaming process is critical; the applied pressure in the press has to be high enough to maintain the flatness of the sample but not as high to prevent in a significant extend bubble formation.

On the other hand, the foaming in a hot press presents additional advantages; as anisotropy ratio indicates it, cellular materials produced by this route are more isotropic than those ones foamed in a thermal bath. As it was aforementioned, solid precursors are produced by compressing the samples in the Z direction. This generates some tensions that result in a small anisotropy when the sample is free foamed in a thermal bath. However, in the hot press, while applying the pressure the sample is able to grow only in the XY plane, removing this anisotropy effect.

This method is also beneficial when foaming at very high temperatures due to heat transfer. As it was shown in **Figure 4** although the surfaces of the sample heated faster, the total heat transfer is slower than in the thermal bath, so when the foaming temperature is as high as 110 °C the cellular structure degenerates in the thermal bath (**Figure 5b**) because the matrix easily acquires this temperature and due to the low viscosity coalescence of the cells appears, obtaining a final cellular material with less and bigger cells. In the same conditions, the time for this to happen in the hot press is higher, being possible to still produce nanocellular materials at this temperature and short times of foaming. Therefore, the processing window is wider in the hot press when the foaming temperature is close to the glass transition temperature.

3.2.2. Foaming process-cellular structure-density relationship

In this section, the changes in the cellular structure are related to the changes in the relative density, in order to investigate in more detail, the two foaming routes.

For the foaming in a thermal bath, it was proved that the mechanism responsible of the reduction of the relative density when foaming temperature increases was the rise in the number of nucleation points while cell size remains constant. This can be observed in

Figure 7 together with the data obtained for the hot press foaming that follow a very similar trend. Therefore, it is possible to conclude that the mechanism governing the reduction of the relative density is the same for both foaming routes. Additionally, the hypothesis exposed in the previous section is also visible in this graph, samples foamed in the hot press are not able to reach values of cell nucleation density as high as those obtained in the thermal bath.

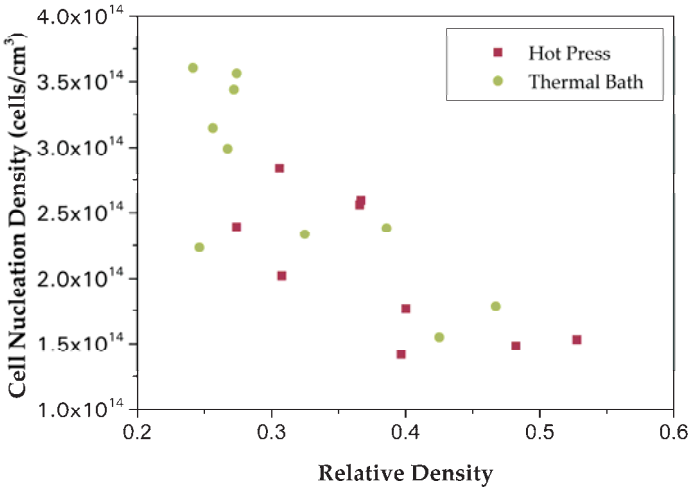

Figure 7. Cell Nucleation density as a function of the relative density for samples foamed by the two approaches.

In addition, as it can be seen in **Figure 8a** the reduction of relative density leads to other changes in the cellular structure. As relative density decreases the fraction of mass in the struts becomes smaller for both foaming processes. On the other hand, open cell content (**Figure 8b**) increases with the reduction of relative density. For samples presenting the same relative density, slightly higher values of open cell content are found in the hot press samples. However, completely open cell samples have not been produced using the hot press because the minimum relative density achieved is not as small as the one achieved in the thermal bath.

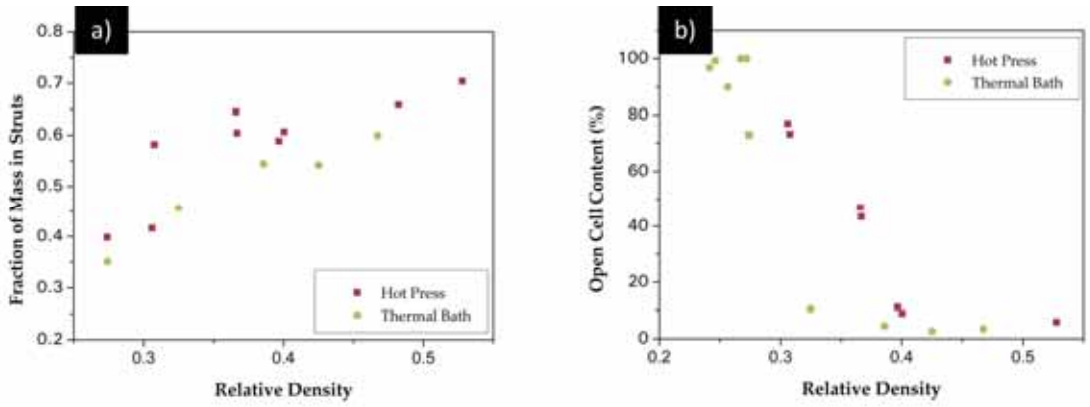

Figure 8.a) Fraction of mass in the struts as a function of the relative density. **b)** Open cell content as a function of the relative density.

This result indicates that the growth in the Z direction is more abrupt in the case of foaming in the hot press. As it is well known the effective glass transition (T_{geff}) decreases

with the amount of gas uptake. During the foaming, the gas is diffusing out resulting in a gradual increase of the T_{geff}. When foaming in a thermal bath, this increase is accompanied by a homogeneous growing in all the directions. Nonetheless, in the hot press, the expansion in the Z direction occurs at a higher $T_{geff,}$ meaning that the polymer is in a more rigid state, this leads to a faster and more abrupt growing in the Z direction, the polymer is deformed at a faster velocity resulting in higher open cell content. On the other hand, this higher T_{geff} allows the cells to grow less in this direction than in the thermal bath (smaller anisotropy).

4. Conclusions

Large and flat nanocellular PMMA parts (sizes of 100 x 100x 6 mm^3) have been produced using the gas dissolution foaming process by replacing the common foaming last step of the process consisting on heating the saturated material in a thermal bath by foaming in a hot press.

It has been demonstrated that the nanocellular samples produced in the hot press are very homogeneous both in density and cellular structure.

The cellular structure of the samples foamed in the press is tuneable by changing the foaming temperature. An increase of it leads to smaller relative densities due to an increase in the cell nucleation density. This reduction in the relative density also causes a decrease in the fraction of mass in the struts and an increase of the open cell content. It has been proved that these mechanisms are the same governing the process when the materials are foamed in a thermal bath.

Even though samples produced in the hot press present a slightly inferior number of nucleation sites due to the applied pressure, it is possible to produce nanocellular materials with cell sizes smaller than 250 nm and relative densities lower than 0.3.

Therefore, we have proved the concept of producing flat nanocellular polymers with significant sizes. The approach followed could be upscaled to produce even larger samples by using larger solid precursors and a press with a larger surface.

Acknowledgements

Financial assistance from MINECO, FEDER, UE (MAT2015-69234-R) and the Junta de Castile and Leon (VA275P18) are gratefully acknowledged. Financial support from FPU grant FPU14/02050 (V. Bernardo) from the Spanish Ministry of Education and Junta of Castile and Leon grant (J. Martín-de León and P. Cimavilla-Román) are gratefully acknowledged.

References

[1] Thiagarajan, C.; Sinha, V.; Sriraman, R.; Pattanayak, A.; Kumar, M. Nano Mechanics of Engineered Foam for Super Structural , Thermal and Optical Properties. **2006**.

[2] Singh, I.; Gandhi, A.; Biswal, M.; Mohanty, S.; Nayak, S. K. Multi-Stage recycling induced morphological transformations in solid-State microcellular foaming of polystyrene. *Cellular*

Polymers **2018**, *37*, 121–149.

[3] Notario, B.; Pinto, J.; Solorzano, E.; De Saja, J. A.; Dumon, M.; Rodriguez-Perez, M. A. Experimental validation of the Knudsen effect in nanocellular polymeric foams. *Polymer (United Kingdom)* **2015**, *56*, 57–67.

[4] Notario, B.; Pinto, J.; Rodriguez-Perez, M. A. Nanoporous polymeric materials: A new class of materials with enhanced properties. *Progress in Materials Science* **2016**, *78–79*, 93–139.

[5] Martín-de León, J.; Bernardo, V.; Rodríguez-Pérez, M. Á. Key Production Parameters to Obtain Transparent Nanocellular PMMA. *Macromolecular Materials and Engineering* **2017**, *3*, 1700343.

[6] Kumar, V.; Suh, N. P. A process for making microcellular thermoplastic parts. *Polymer Engineering and Science* **1990**, *30*, 1323–1329.

[7] Guo, H.; Kumar, V. Solid-state poly(methyl methacrylate) (PMMA) nanofoams. Part I: Low-temperature CO2 sorption, diffusion, and the depression in PMMA glass transition. *Polymer* **2015**, *57*, 157–163.

[8] Kumar, V.; Weller, J. Production of Microcellular Polycarbonate Using Carbon Dioxide for Bubble Nucleation. *Journal of Engineering for Industry* **1994**, *116*, 413–420.

[9] Bernardo, V.; Martín-De León, J.; Rodríguez-Pérez, M. A. Production and characterization of nanocellular polyphenylsulfone foams. *Materials Letters* **2016**, *178*, 155–158.

[10] Nadella, K.; Kumar, V.; Li, W. Constrained solid-state foaming of microcellular panels. *Cellular Polymers* **2005**, *24*, 71–90.

[11] Gedler, G.; Antunes, M.; Velasco, J. I. Polycarbonate foams with tailor-made cellular structures by controlling the dissolution temperature in a two-step supercritical carbon dioxide foaming process. *Journal of Supercritical Fluids* **2014**, *88*, 66–73.

[12] Martín-de León, J.; Bernardo, V.; Rodríguez-Pérez, M. Low Density Nanocellular Polymers Based on PMMA Produced by Gas Dissolution Foaming: Fabrication and Cellular Structure Characterization. *Polymers* **2016**, *8*, 265.

[13] Guo, H.; Kumar, V. Some thermodynamic and kinetic low-temperature properties of the PC-CO2 system and morphological characteristics of solid-state PC nanofoams produced with liquid CO2. *Polymer* **2015**, *56*, 46–56.

[14] Pinto, J.; Solorzano, E.; Rodriguez-Perez, M. a.; de Saja, J. a. Characterization of the cellular structure based on user-interactive image analysis procedures. *Journal of Cellular Plastics* **2013**, *49*, 555–575.

[15] Solórzano, E.; Pinto, J.; Pardo, S.; Garcia-Moreno, F.; Rodriguez-Perez, M. A. Application of a microfocus X-ray imaging apparatus to the study of cellular polymers. *Polymer Testing* **2013**, *32*, 321–329.

[16] Pérez-Tamarit, S.; Solórzano, E.; Hilger, A.; Manke, I.; Rodríguez-Pérez, M. A. Multi-scale tomographic analysis of polymeric foams: A detailed study of the cellular structure. *European Polymer Journal* **2018**, *109*, 169–178.

[17] Pinto, J.; Pardo, S.; Solórzano, E.; Rodríguez-Pérez, M. a.; Dumon, M.; de Saja, J. a. Solid Skin Characterization of PMMA/MAM Foams Fabricated by Gas Dissolution Foaming over a Range of Pressures. *Defect and Diffusion Forum* **2012**, *326–328*, 434–439.

[18] Kumar, V.; Weller, J. E. Model for the unfoamed skin on microcellular foams. *Polymer Engineering and Science* **1994**, *34*, 169–173.

[19] Costeux, S. CO2 -blown nanocellular foams. *Journal of Applied Polymer Science* **2015**, *132*, 41293–41293.

[20] Gibson, L. J.; Ashby, M. F. *Cellular solids: Structure and Properties*; 2nd ed.; Cambridge: Cambridge University Press.: United States, **1997**.

[21] Albalak, R. J.; Tadmor, Z.; Talmon, Y. Polymer melt devolatilization mechanisms. *AIChE Journal* **1990**, *36*, 1313–1320.

[22] Leung, S. N. S. Mechanism of Cell Nucleation, Growth and Coarsening in Plastic Foaming: Theory, Simulation and Experiments. *Ph.D. thesis* **2009**, 239.

7.3. Two-stage depressurization in one step foaming process: the production of nanocellular materials free of defects.

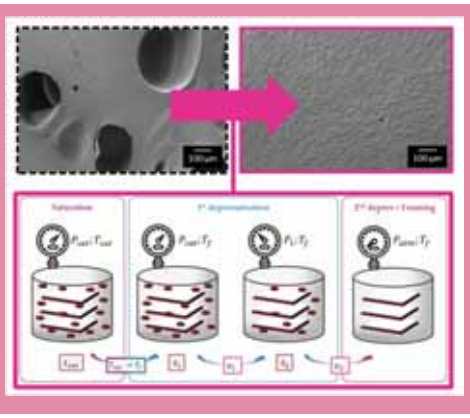

A new production method is presented for the production of nanocellular PMMA free of internal defects. A depressurization step carried out in two stages, leads to control an abrupt growing avoiding micrometric defects. Nanocellular structures were compared with those ones obtained in the common one step depressurization process. Moreover, the foaming mechanisms have been studied in-deep.

TWO-STAGE DEPRESSURIZATION IN ONE STEP FOAMING PROCESS: THE PRODUCTION OF NANOCELLULAR MATERIALS FREE OF DEFECTS.

Judith Martín-de León, Victoria Bernardo, Miguel Ángel Rodriguez-Pérez

Cellular Materials Laboratory (CellMat), Universidad de Valladolid, 47011, Spain

Correspondence to: Judith Martín-de León (E-mail: *jmadeleon@fmc.uva.es*)

Abstract

Nanocellular polymethylmethacrylate has been produced through a newly proposed method; a two-stage depressurization one-step foaming process. This method, based on the gas dissolution foaming process, modify the depressurization step and allows controlling the pressure during cells growth, avoiding this way, the production of micrometric defects. Three grades of PMMA, as well as different production parameters, were tested in order to study the influence on the final cellular structure. Moreover, cellular structures were compared with those produced in the standard foaming process. Additionally, this work allows understanding and experimentally validating the foaming mechanisms taking place during the production of nanocellular materials.

Keywords: Nanocellular PMMA, , one step foaming, pressure drop, pressure drop rate

5. Introduction

Nanocellular polymers were born around ten years ago as an attempt to improve the properties of microcellular materials. In general terms, nanocellular polymers are those presenting cells in the nanometric scale and cell nucleation densities higher than 10^{14} cells/cm^3 [1,2].

Since its discovery, nanocellular materials have been produced by following multiple strategies, and therefore, a wide range of results have been obtained. Thus, different polymeric matrix and cell sizes, cell nucleation densities, and relative densities in a wide range have been obtained up to now.

Among all those works presented in the literature, it is worthy highlighting the results obtained by Costeux et al. through heterogeneous nucleation. On the one hand, by mixing PMMA and PMMA-co-EA with nanosilicas, they achieved nanocellular materials with relative densities smaller than 0.23 and minimum cell sizes of 95 nm. On the other hand, by mixing PMMA-co-EMA with POSS, they produced nanocellular materials with cell sizes ranging 100 nm combined with a relative density of 0.16. [3]. Conversely, when working with homogeneous nucleation, the best results up to now were presented by Martín-de León et al. presenting a nanocellular material based on PMMA with cell sizes around 75 nm with a relative density of 0.24.

Although the reported results are exciting, moving forward in this field (i.e reducing the density while keeping the cells in the nanoscale) is increasingly tricky. On the one hand, gas dissolution foaming process leads to some limitations hard to solve, which are even more complicated to solve due to the lack of knowledge of the foaming mechanism in nanocellular polymers. On the other hand, in many cases when reducing the density, the materials produced present internal defects and microcells which origin is not clear today, being these defects a potential source of failure in mechanical testing and depending on the size and number of theses defects could also increase the thermal conductivity.

In this work, a new production approach, based on the one-step foaming process, has been developed for the production of nanocellular materials. This new method has led to the removal of defects observed in nanocellular materials under certain production conditions. Moreover, the production parameters of this new processing route were modified in order to optimize it as a function of the viscosity of the polymer matrix.

Moreover, the foaming mechanism taking place during the production of nanocellular materials have been studied. Thus, nucleation and cell growth were analysed using a nucleation theory developed by Costeux et al. [4] that allows understanding the physical phenomena taking place during the production process of nanocellular materials.

6. Materials and methods

6.1. Materials

Three grades of polymethylmethacrylate (PMMA) have been used in this work: 6N, 7N, and V825T. All of them were supplied in the form of pellets by PLEXIGLAS® Evonik Industries (Essen, Germany) in the case of grades 7N and 6N, and by ALTUGLAS® International (Colombes, France) in the case of V825T.

The density (ρ) of the three degrees is 1.19 g/cm^3 (measured at 23 °C and 50% HR). Their glass transition temperature (T_g) and zero-shear viscosity (η_0), determined as explained in sections 2.4.1 and 2.4.2, respectively, are presented in **Table 1**. The three

materials present different characteristics being the PMMA V825T the one with the highest viscosity accompanied with the highest glass transition temperature. Moreover, the 6N is the one with the lowest T_g and viscosity.

According to these characteristics, they will be named as high viscosity (HV), medium viscosity (MV), and low viscosity (LV) materials.

Table 1. Glass transition temperature and zero shear viscosity of the PMMAs under study.

Material	Glass transition temperature (°C)	Zero shear viscosity (Pa·s)
V825T (HV)	114.4	7095
7N (MV)	109.3	3800
6N (LV)	98.6	1587

Additionally, medical grade CO_2 (99.9% purity) was used as a blowing agent in gas dissolution foaming process.

6.2. Samples production

Solid samples of dimensions 20 x 20 x 4 mm^3 were produced using compression moulding .

Firstly, pellets were dried at 80 ºC for 4 hours to remove the remaining moisture inf the material. Afterward, they were compression moulded in a hot plate press from Remtex (Barcelona, Spain) using a mould of a size of 68 x 68 x 4 mm^3, and by following the next steps. First of all, the material was heated at 250 ºC for 9 minutes. Then, the polymer presents enough mobility to adapt to the mould, so a pressure of 42 MPa was applied for an additional minute while maintaining the temperature at 250 ºC. Finally, the sample was cooled down to room temperature for 4 minutes applying the same pressure.

The solid precursors were finally machined to the desired dimensions (20 x 20 x 4 mm^3) for the foaming tests.

6.3. Foaming Tests

Cellular materials have been produced by following the method described in **Figure 1**. This scheme represents a modified one-step gas dissolution foaming process.

One step gas dissolution foaming process [5] consists of three steps, saturation, depressurization, and finally stabilization. Firstly, the polymer is saturated with carbon dioxide (CO_2) under certain conditions of pressure (P_{sat}) and a saturation temperature (T_{sat}). Once the polymer is fully saturated, the gas is fast released up to reaching atmospheric pressure. This creates a huge instability in the gas-polymer system that results in phase-separation, that is, the creation of nucleation points.

When the gas diffuses into the polymer, it triggers a reduction in the glass transition temperature of the polymer up to a lower one, the so-called effective glass transition $T_{g_{eff}}$[6]. Then, if the saturation is performed at a T_{sat} higher than $T_{g_{eff}}$, it happens that,

when the gas is released nucleation and growing occurs simultaneously [5]. Finally, samples are stabilized to prevent further foaming.

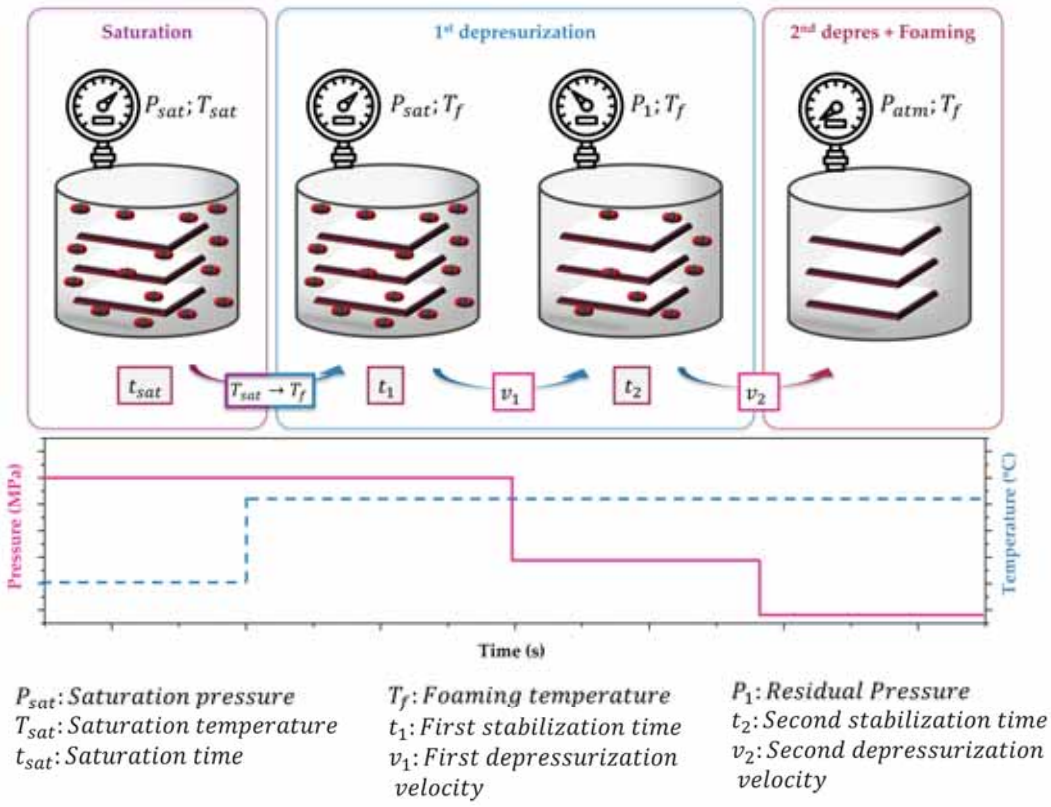

Figure 1. Scheme of the foaming process.

In this work, the one-step foaming process has been modified as follows (**Figure 1**). Firstly, saturation is performed under P_{sat} and a saturation temperature smaller than the effective glass transition. Afterward, the temperature is increased up to a foaming temperature (T_f) (see **Figure 1**), higher than $T_{g_{eff}}$ during a stabilization time t_1. Then, a first partial depressurization up to a residual pressure P_1 is carried out at a depressurization velocity v_1. This situation is maintained during a time t_2, and finally, the gas is completely released in a second depressurization at a velocity v_2.

As T_f is higher than the effective glass transition temperature, the polymer can grow when the pressure is completely released. The proposed method has been named as two-stage depressurization one-step foaming (TSD foaming).

Foaming tests were performed in a system that comprises a pressure vessel (model PARR 4681) provided by Parr Instrument Company (Moline, IL, USA). This one is connected to a pump (model SFT-10) supplied by Supercritical Fluid Technologies Inc. (Newark, DE, USA) responsible for providing the desired pressure to the system. Additionally, a clamp heater connected to a temperature controller CAL 3000 is used to adjust the temperature of the system. Finally, an electrovalve with $K_v = 1.1$ L/min allows to fast release the pressure.

In this work, six different experiments have been carried out in the described system by using the conditions shown in **Table 1.** Saturation conditions were fixed to be 31 MPa and 24 °C. According to the literature, this saturation conditions leads to solubilities higher than 30 % for the three used materials that result in cells in the nanometric scale for all of them when the comventional two steps gas dissolution process is used [7]. Then a two-stage depressurization was carried out by using two different partial pressures P_1, 17 and 7 MPa. Additionally, this was done for two different foaming temperatures 50, and 100 °C.

Table 2. Foaming conditions of the different test.

Test	P_{sat} (MPa)	T_{sat} (°C)	P_1 (MPa)	T_f (°C)	t_1 (min)	v_1 (MPa/s)	t_2 (min)	v_2 (MPa/s)
T1	31	24	16.6	50	1	100	5	50
T2	31	24	6.8	50	1	100	5	0.2
T3	31	24	-	50	1	100	5	-
T4	31	24	17.3	100	1	100	5	50
T5	31	24	6.9	100	1	100	5	0.2
T6	31	24	-	100	1	100	5	-

As can be seen in **Figure 2** and **Table 2**, the pressure drop rate is equivalent for both used P_1. In the first case, the pressure decreases from 31 MPa to 5 MPa leading to a depressurization rate $v_1 = 100\ MPa/s$, and then pressure recovers up to $P_1 = 17\ MPa$ **(Figure 2a**). In the second case, the pressure falls up to 5 MPa and maintains its value being $P_1 = 5\ MPa$. This effect was achieved by changing the opening time of the electrovalve.

Stabilization times t_1 and t_2 have been chosen to be 1 and 5 minutes for all the experiments.

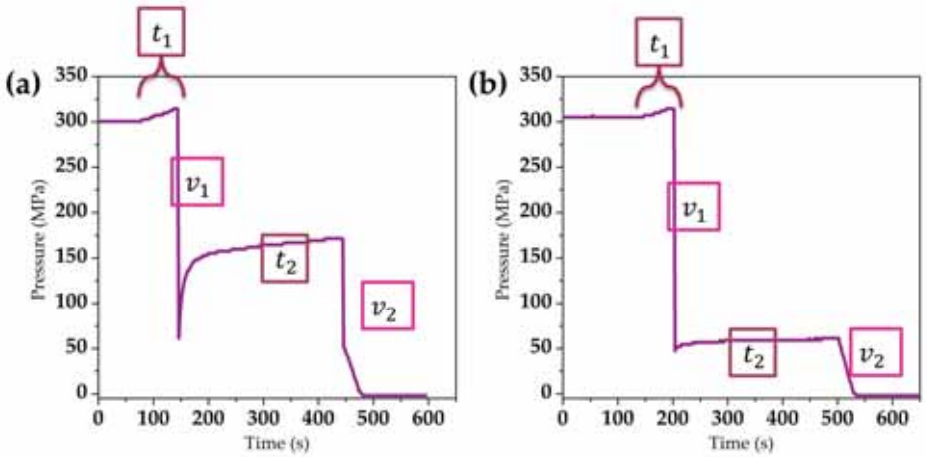

Figure 2. Pressure vs. time graphs for the partial depressurizations. **a)** corresponding to experiment T1. **b)** corresponding to experiment T2. Experiments T4 and T5 were equal to T1 and T2 respectively.

Two additional experiments (T3 and T6) were carried out with a single depressurization with the aim of comparison. In both of them, the pressure is completely

released after t_1 leaving the samples 5 minutes at the foaming temperature and atmospheric pressure to finally stabilize them in water.

After the foaming, samples were removed from the pressure vessel in less than 30 seconds and then stabilised in water at room temperature.

6.4. Characterization Techniques

6.4.1. Glass transition temperature

A differential-scanning calorimeter model Metler DSC30, previously calibrated with indium, was used for the measurement of the glass transition temperature. With an amount of sample of 5 mg, the thermogram was obtained by heating from 20 °C to 160 °C at 10 °C/min. The value for the T_g was calculated as the mid-point of the drop in the thermogram that characterizes this transition.

6.4.2. Polymers rheology

Shear rheology for the three used materials was carried out in a stress-controlled rheometer, AR 2000 EX from TA Instruments. Zero shear viscosity, η_0 was determined through this technique.

To perform the measurements, solid cylindrical samples were produced by compression moulding (section 2.2). Dynamic shear viscosity measurements were performed at 230 °C under a nitrogen atmosphere and using a parallel plates geometry of R = 25 mm in diameter and a fixed gap of h = 1 mm. The angular frequency range was $0.01 < w < 100\, rad/s$, and a strain of 6% was used. The zero shear viscosity has been calculated as the value of the complex viscosity at low frequencies in the Newtonian plateau [8] from the dynamic shear viscosity measurements.

6.4.3. Depressurization velocity determination

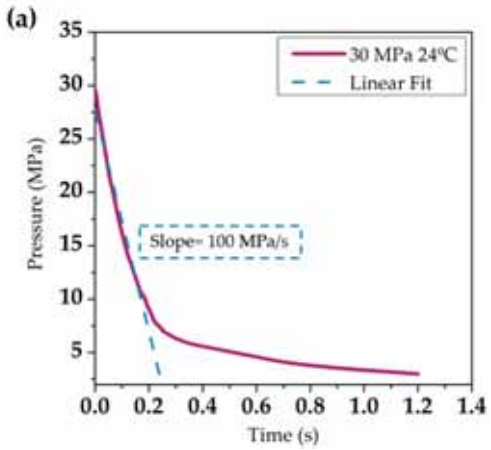

Figure 3. Example of pressure vs. time graph in the moment of depressurization.

To accurately determine the depressurization velocity data pressure was recorded by using a sampling frequency of 0.001 s. The depressurization velocity is considered as the slope of the first linear part of the graph (**Figure 3**).

6.4.4. Density

The density of solid samples (ρ_s) were measured through a gas pycnometer (Mod. AccuPyc II 1340) provided by Micromeritics, Norcross, GA, USA. While the density of cellular materials ρ_f was measured by using the density determination kit of an AT261 Mettler-Toledo balance and considering the water displacement method, based on Archimedes' principle.

Prior to those measurements, cellular materials were polished to remove the solid outer skin (around 200 μm were removed from each side). Finally, the relative density ρ_r is calculated as the ratio between the cellular material density and the solid one.

6.4.5. Scanning Electron Microscopy

Cellular structure was visualized using an ESEM Scanning Electron Microscope (FlexSEM1000 provided by HITACHI). In order to correctly visualize the samples, it is needed to fracture them in liquid nitrogen to preserve the original cellular structure. Then, they were coated in gold with a sputter coater (model SDC 005, Balzers Union, Balzers, Liechtenstein), and finally, they were visualized.

The cellular structure was analyzed using a software based on ImageJ/FIJI [9]. Thus, the cell size (ϕ) the standard deviation of the cell size distribution (SD), the parameter SD/ϕ and the cell nucleation density (N_0) were determined for each produced material. N_0 was calculated by following the Kumar's method [10].

7. Results

7.1. Cellular structure

7.1.1. External appearance

In order to analyse the aspect of the produced cellular materials (homogeneity and defects) SEM images at low magnifications were taken as it is shown in **Figure 4**.

The first row in the image, that means **Figure 4.a), b) and c),** corresponds to the materials produced in test T3, that means by following the standard one-step process. Both degrees MV and LV exhibit some big holes in the millimetric scale. That means, under these production conditions, the production of nanocellular materials with PMMA degrees MV and LV leads to samples with millimetric defects. When compared those results with the obtained when foaming by following a two-stage depressurization (esperiment T1), defects disappear as it is shown in **Figure 4.d), e), f)**. It is also interesting to point out that this behaviour also depends on the used material; thus, the one with the highest viscosity can be produced free of defects following both production routes.

Same results are obtained for the rest of the tests, so materials in test T3 and T6 show those big holes, while in the rest ones, produced samples are completely homogeneous.

Those findings can be justified by means of the foaming mechanisms that relate the foaming conditions with the cellular structure, as it is discussed in section 3.2.

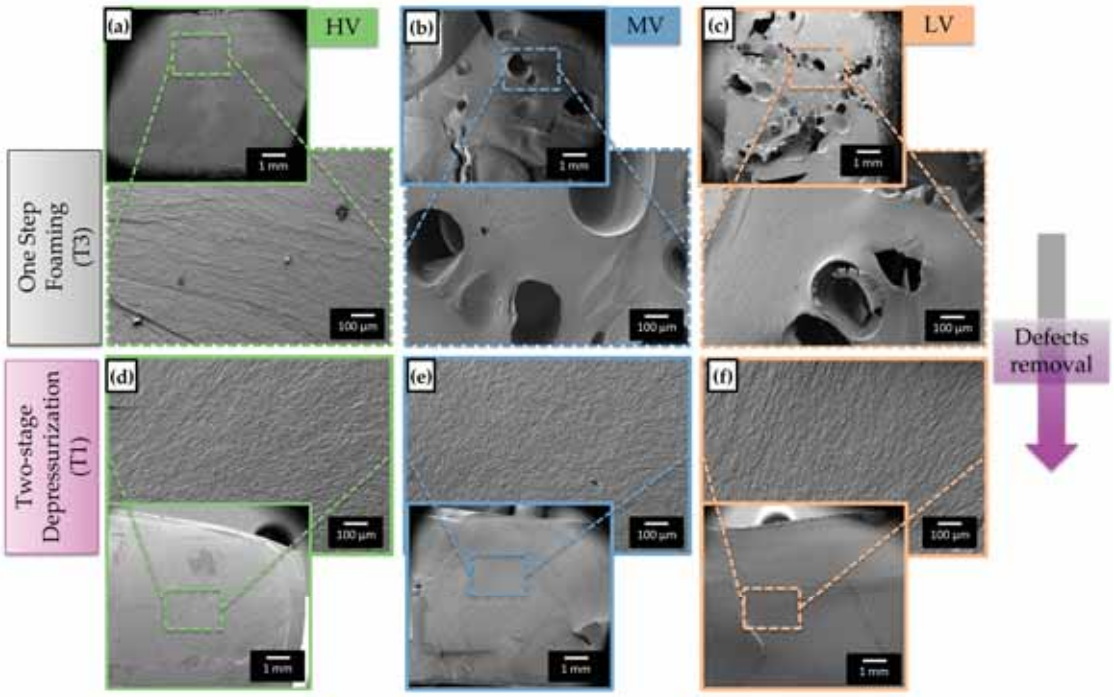

Figure 4. Low magnification SEM images for the visualization of defects. First row for materials produced in test T3 **a)** HV**, b)** MV and **c)** LV**.** Second row for materials produced in T1 **a)** HV**, b)** MV and **c)** LV.

So herein, it can be concluded that the new proposed process (TSD foaming) makes it possible to produce nanocellular materials completely free of defects. On the other hand, this procedure also affects the nanocellular structure of the samples as it is discussed in the following section.

7.1.2. Nanocellular structure

Figure 5 shows the cellular structure of the different materials.

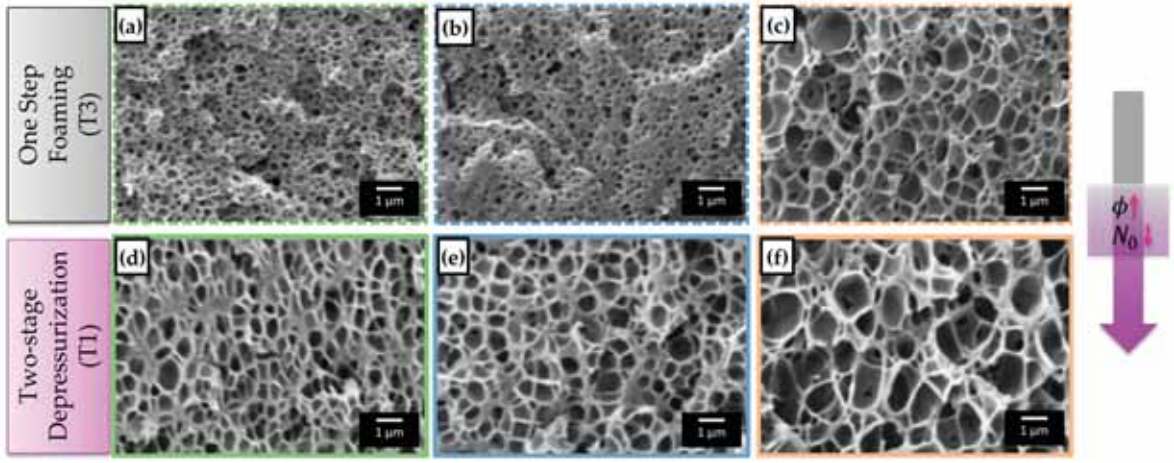

Figure 5. SEM images for the visualization of the internal nanocellular structure. First row for materials produced in test T3 **a)** HV**, b)** MV and **c)** LV**.** Second row for materials produced **in T1 a)** HV**, b)** MV and **c)** LV.

A nanocellular structure can be observed independently on the used route. For the samples produced through the one-step process, a homogeneous cellular structure is found when an area between the mentioned defects (**Figure 5. a), b)** and **c)**) is analysed. On the other hand, samples produced through the defined new process present a nanocellular structure as that shown in **Figure 5. d), f)** and **g)**, which is homogeneous along the thickness of the sample. This was proven by taking SEM images in different regions of the materials.

Although both processes lead to a nanocellular structure, there exists a clear difference between both ones for the three used PMMA. **Figure 5** shows that the TSD process (second row) leads to higher cell sizes and lower cell nucleation densities. In order to in-deep analyse those changes, relative density, cell size, and cell nucleation density were measured and plotted as a function of the residual pressure P_1 (**Figure 6**). Experiments with $P_1 = 0\ MPa$ correspond to one-step foaming tests (T3 and T6).

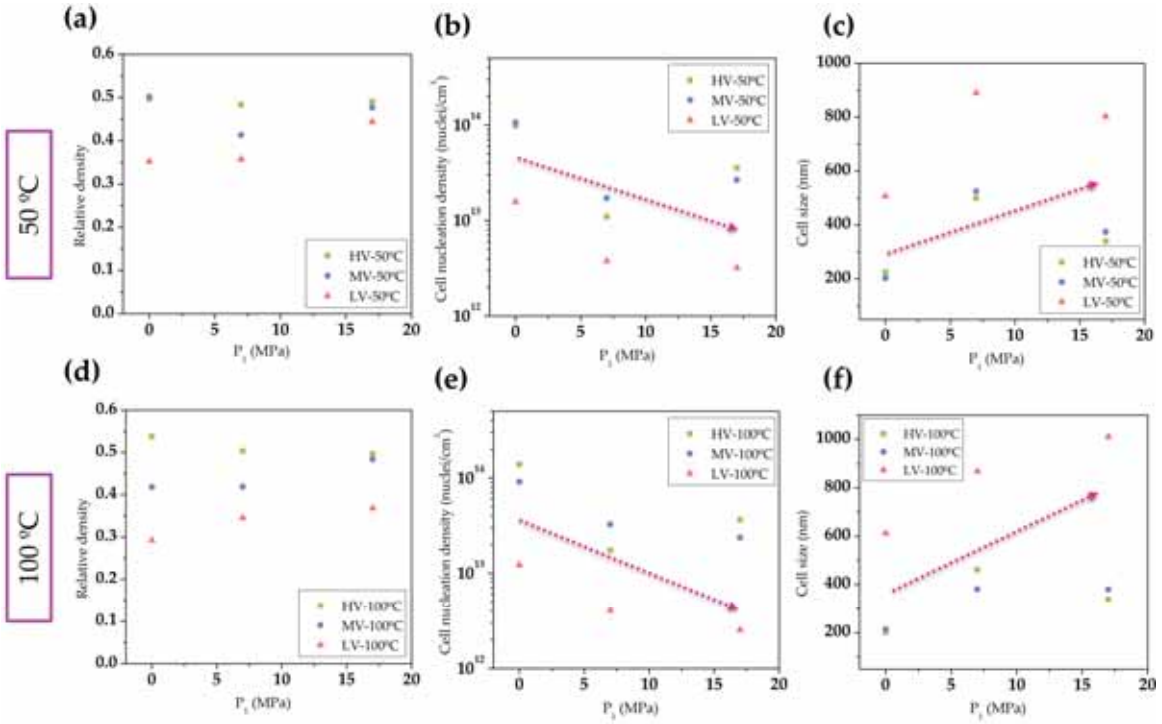

Figure 6. Graphs corresponding to 50 °C of foaming temperature: a) Relative density as a function of P_1 b) Cell nucleation density as a function of P_1c) Cell size as a function of P_1. Graphs corresponding to 100 °C of foaming temperature: d) Relative density as a function of P_1 e) Cell nucleation density as a function of P_1f) Cell size as a function of P_1. Arrows indicate the change of tendency between one-step foaming and two-stage one-step foaming.

First of all, the effect of changing from a single depressurization to a partial one will be studied. Single depressurization leads to higher cell nucleation densities and smaller

cell sizes. Thus, the cell nucleation density decreases over half an order of magnitude, while the cell size almost doubles its size for the three materials.

Any obvious effect is observed when studying the effect of changing the process in the relative density (**Figure 6.a)** and **d)**). This is because, relative density depends on both, the cell nucleation density and the cell size. This relationship is established through the following equation [11]:

$$\frac{1}{\rho_r} = 1 + \left(\frac{N_0 \phi^3 \pi}{6}\right) \quad (1)$$

So, while a decrease in the cell nucleation density increases the relative density, an increase in the cell size leads to a reduction of this parameter. Therefore, results regarding relative density are the consequence of the competition between those two parameters. Overall, it could be stated that the relative density of HV PMMA is around 0.5, the one of MV PMMA ranges between 0.5 and 0.4 and for LV PMMA is between 0.4 and 0.3. Those differences between materials are attributed to their different rheological properties as it was previously studied [12].

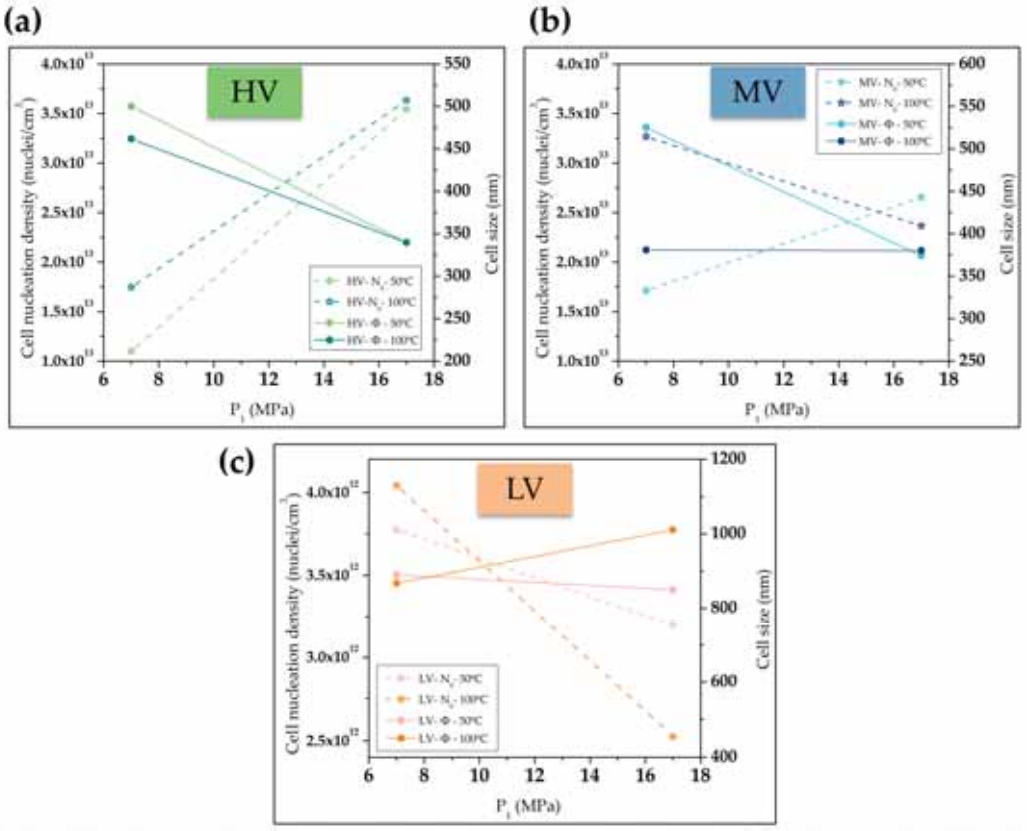

Figure 7. Change in the cell nucleation density and the cell size as a function of the residual pressure, for **a)** HV PMMA **b)** MV PMMA and **c)** LV PMMA.

Once the effect of modifying the process was studied, the attention is focussed in the analysis of the two-stages depressurization one-step foaming. So, the effect of changing the process parameters in this process will be herein analysed.

Figure 7 shows the changes observed in the cellular structure, cell nucleation density, and cell size when modifying the residual pressure between first and second depressurization for both foaming temperatures. Focusing on HV PMMA a higher residual pressure, that means, by following a process as the one shown in **Figure 2.a)**, results in higher cell nucleation density and smaller cell size independently on the foaming temperature. On the other hand, when using $T_f = 100\,°C$ the cell nucleation density is higher, and the cell size smaller than when using 50 °C.

Considering MV PMMA, the tendency with the residual pressure is the same when the foaming temperature is 50 °C, although when increasing the saturation temperature up to 100 °C, the tendency is reversed. Thus, when foaming at 100 °C, a higher residual pressure leads to smaller cell nucleation densities and slightly higher cell sizes.

For LV PMMA this reversed tendency is the one governing. So independently of working at $T_f = 50°C\ or\ 100\,°C$ and increase in P_1 leads to smaller cell nucleation densities and higher cell sizes.

Concluding, the new proposed process leads to nanocellular materials free of defects, although the cell size is increased, and the cell nucleation density decreased with respect to the common one-step process. On the other hand, obtained results when changing the production parameters in the two-stages depressurization process, depend on the used polymeric matrix.

Foaming mechanisms are discussed in the next section to understand the obtained results.

7.2. Discussion of the foaming mechanisms

To deal with the foaming mechanisms, an improved model developed from the classic nucleation theory (CNT) will be used. This model was presented by Costeux et al. [4], on the basis of the concept of Influence Volume proposed by Shafi et al. [13,14] This model allows adapting the CNT to the production of nanocellular polymers, and introduce the influence of parameters such as pressure drop rate, diffusivity or viscosity in the produced cellular structure.

The differences obtained when producing nanocellular materials by using PMMA with different viscosity were already explained employing this theory in a previous work [12].

The key parameter in this theory is, as previously mentioned, the influence volume. When a nucleus starts to grow the gas around it begins to diffuse into these nuclei. This results in a smaller gas concentration near the bubble surface that grows as goes away from the bubble. This halo of depleting gas is called Influence Volume (IV)[5].

According to this theory, new nuclei can be only stable out of this IV, because any nuclei formed inside IV will disappear at the expense of the already created one. For this reason, the growth rate of IV strongly determines the cellular structure. Moreover, this

rate is influenced by parameters such as the pressure drop rate, the viscosity, or the diffusivity.

To understand the obtained results, the following equations will be considered, so nucleation density in this model is described by:

$$N_0 = \int_0^t N_{hom} V_L dt \tag{2}$$

where N_{hom} is the homogeneous nucleation ratio given by CNT theory (**equation 3**) and V_L is the non-influenced volume at a time t, that means, this factor introduces the evolution of IV with time.

$$N_{hom} = f_0 C_0 \exp\left(-\frac{\Delta G_{hom}}{k_B T_f}\right) \tag{3}$$

Homogeneous nucleation is then related to, f_0 that is the frequency factor of gas molecules joining the nucleus, C_0 the concentration of gas in the polymer, k_B the Boltzmann constant, T_f is the gas temperature in the moment of the foaming and ΔG_{hom} is Gibbs free energy barrier defined as:

$$\Delta G_{hom} = \frac{16\pi\gamma^3}{3\Delta P^2} \tag{4}$$

Being γ the interfacial tension between the gas bubble and the polymer, and ΔP the difference between the gas pressure and the solid phase one.

On the other hand, the growth rate is described through equation 5, that defines the change in the bubble radius, R, with time.

$$\frac{dR}{dt} = \frac{\Delta P \cdot R}{4\eta} - \frac{\gamma}{2\eta} \tag{5}$$

Up to now, what it is well established for CNT is that maximization of the solubility, the pressure drop, and the foaming temperature affect positively to cell nucleation density (equation 3). However, to clarify how the influence volume affects this parameter, it is vital to consider the influence of diffusivity, viscosity, and depressurization velocity in IV.

When considering diffusivity, a faster velocity of the gas inside the material means that CO_2 diffuses faster to the nascent nucleus, resulting in more rapid growth of the Influence Volume. This reduces the time available for nucleation and therefore, reduces the cell nucleation density.

Conversely, the viscosity has the opposite effect, acting as a retardant for nucleation and growing. A higher viscosity makes it difficult for the nuclei to growth, decreasing the velocity of growing of IV, and therefore increasing the available time for nucleation. So a higher viscosity enhances the cell nucleation density.

Finally, changes induced by a different depressurization rate are very similar to those produced by changing the pressure drop. A higher pressure drop rate means that in every

moment, ΔP is higher, leading to the creation of more nucleus. As nucleation and growing are simultaneous, it should be considered that according to equation 5, the growth rate is also faster. But while nucleation density is proportional to the exponential of $1/\Delta P^2$, the growth rate is linearly proportional to the pressure drop. So the increase in the nucleation rate is much higher than the growth rate. In conclusion, a faster depressurization rate improves the nucleation rate.

7.2.1. Responsible mechanisms of changes in the nanocellular structure

From one-step foaming to two-stage depressurization one-step foaming

The first point is to understand when nucleation and growing occurs. As explained in section 2.3 in one-step foaming, both mechanisms take place simultaneously when the pressure is released. In the case of two-stage depressurization one-step foaming, this situation changes. Any pressure drop leads to the creation of nucleation points, attending to equation 3; so in both depressurizations, nucleation points are created. Although they are not allowed to grow until the complete release of the pressure. This fact is asserted due to experimental evidence. As it was shown in **Figure 5**, samples produced through this method do not present a second population of cells, meaning that nucleation points created in the first depressurization do not grow before the ones created in the second one. So, in this TSD foaming process, nuclei are produced in both pressure drops while growing takes place in the second one.

Taking this into consideration, differences in the internal cellular structure between both processes can be analysed. Differences are schematized in **Figure 9**. So by considering the same polymeric matrix foamed at the same temperature parameters influencing the cellular structure are ΔP, v, and D.

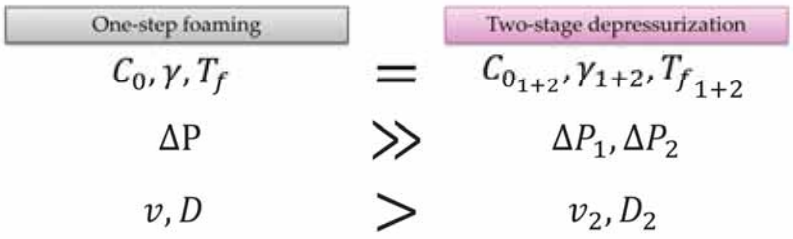

Figure 9. Scheme of differences between parameters influencing the cellular structure in one-step foaming and two-stage depressurization one-step foaming.

Regarding pressure difference, ΔP in the one-step process is higher than any of the two pressures drops in the proposed new method. So attending to equation 6, due to the exponential dependence of nucleation with this parameter the pressure difference in single depressurization leads to a higher N_0 independently on how ΔP_1 and ΔP_2 are distributed.

$$\Delta P > \Delta P_1, \Delta P_2 \rightarrow \exp(\Delta P) \gg \exp(\Delta P_1) + \exp(\Delta P_2) \rightarrow N_0 \gg N_{0_1} + N_{0_2} \quad (6)$$

A higher final depressurization velocity also enhances the nucleation rate, as previously explained. Conversely, diffusivity increases with pressure, being this parameter the only negatively influencing nucleation in one step process in comparison with the TSD process.

So due to the strong dependence of cell nucleation density with the pressure drop, it is clear that this is the primary mechanism making higher the cell nucleation density in the one-step process. In conclusion, starting from the same pressure, a two-stage depressurization reduces the number of nucleation points with a consequent increase of the cell size.

However, the understanding of the foaming mechanism makes it possible to theorize that in order to equalize the results, the solution is to increase the initial saturation pressure in this new process.

Differences triggered by changing the residual pressure

When working with the TSD process, the situation is the one shown in **Figure 10**. As it was shown in **Table 1**, and **Figure 2,** the first pressure drop is equivalent independently on the used residual pressure. Therefore it can be assumed that the number of nucleation points created in this first pressure drop is also comparable.

High residual pressure		Low residual pressure
$C_{0_H}, \gamma_H, T_{f_H}, \Delta P_{1_H}$	$=$	$C_{0_L}, \gamma_L, T_{f_L}, \Delta P_{1_L}$
$\Delta P_{2_H}, v_{2_H}, D_{2_H}$	$>$	$\Delta P_{2_L}, v_{2_L}, D_{2_L}$

Figure 10. Scheme of differences between parameters influencing the cellular structure when changing the residual pressure in two-stage one-step foaming.

It is in the second part of the process when discrepancies are found. It should be taking into account that in this second depressurization, nucleation and growing are simultaneous processes. As it can be seen in **Figure 10**, the pressure drop and the pressure drop rate are higher for higher residual pressure, contributing positively to the nucleation density. Conversely, the higher diffusivity also observed for higher residual pressure, reduces the number of nucleation points. On the other hand, the increase in the three parameters is raising the cell growth rate.

Taking into account that the highest pressure drop occurs in the first depressurization, herein the differences between ΔP in the second step are not so significant, so there exists a real competition between all those parameters, pressure drop, depressurization velocity, and diffusivity, that also depends on the used material. In order to consider the contribution of each parameter, the proposed model introduces two constants. The first one, N_p gives account of the competition between the depressurization velocity and the diffusivity [4], that as explained before, have opposite effects in nucleation density. The expression of this number is given by equation 7.

$$N_p = \frac{r_c^2}{D}\frac{dP_{liq}}{dt} \quad (7)$$

Which means that the pressure drop rate needs to be fast enough in comparison with diffusivity, to prevent the growth of IV that decreases the nucleation rate.

On the other hand, as previously commented, this also depends on the viscosity of the gas/polymer system. If the viscosity is high enough, it slows down the effect of the diffusivity, struggles against cells growth. If viscosity decreases, there is not any obstacle to cell growth, and the increment of IV mainly depends on the diffusivity. This contribution is given by the Schmidt number [15] (equation 8).

$$N_{Sc} = \frac{\mu}{\rho D} \quad (8)$$

In conclusion, the same pressure drop, depressurization velocity, and diffusivity will have a different effect on different polymers, that is the case presented in this work (**Figure 11**).

For the highest viscous PMMA, as it can be seen in **Figure 7,** a higher P_1 leads to higher cell nucleation density and smaller cell size. Meaning that $N_{p_H} > N_{p_L}$ for all the polymers due to this number only depends on the process parameters. Moreover, this result indicates that the viscosity in this polymer is high enough to cancels out the effects of a higher diffusivity. So $N_{SC_H} < N_{p_H}$. In addition, higher temperature leads to higher cell nucleation densities in this material, as equation 3 suggests.

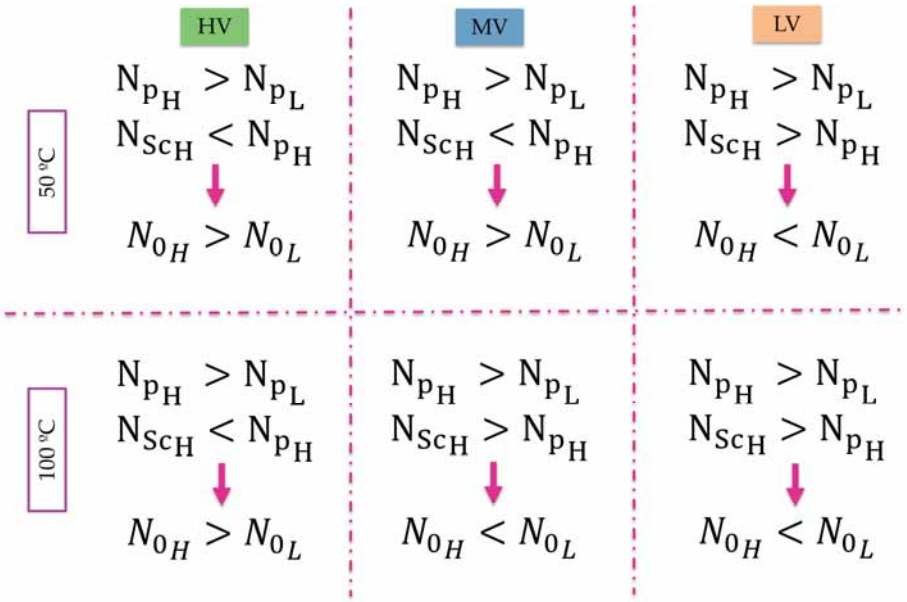

Figure 11. Scheme of the competition between $N_p$and N_{Sc} for the different materials and foaming conditions.

When working at 50 °C with MV PMMA, this situation remains the same. But the increase in the foaming temperature up to 100 °C is also accompanied by a decrease in the

viscosity of the system and an increase in the diffusivity. So when increasing the foaming temperature the smith number for the highest P_1 is not longer smaller than N_p. And the situation reverts, cells density decreases when increasing the residual pressure.

Predictably, LV material, present such slow viscosity that even at 50 °C of foaming temperature $N_{SC_H} > N_{p_H}$. So a smaller residual pressure is better to enhance the nucleation.

7.2.2. Responsible mechanisms for defects removal

The critical point for the removal of the defects can be now easily found. And the solution is gas pressure. In one-step foaming, when the foaming starts, the gas pressure is so high that the polymer is suddenly under enormous tension. Moreover, getting back to **Figure 9,** diffusivity is also higher when depressurization is done in one single step. That means that the gas takes advantage of any initial defect of the material, that join together with the high pressure cannot be supported if the viscosity of the polymer is not enough. This situation leads to cracks and defects as those shown in Figure 4. For HV material, the viscosity is high enough to prevent those big defects, while as viscosity decreases, there is not any barrier for defect propagation.

With the proposed method, the pressure of gas when the material is allowed to grow is smaller; this fact itself accompanied by a slower diffusivity leads to smothering growth.

In conclusion, two-stage depressurization one-step foaming leads to nanocellular materials free of defects, although there is a reduction of cell nucleation density that should be compensated by the use of different saturation parameters.

8. Conclusions

A new production method for nanocellular materials is proposed in this work. Two-stage depressurization one-step process, modifies the depressurization step of the commonly used one-step foaming process. This modification allows removing micrometric and milimetrics defects appearing in some materials when foaming at certain conditions.

Thus, depressurization has been carried out in two stages, allowing to produce nanocellular PMMA free of defects, from materials with different viscosities. Moreover, the obtained cellular structures were compared with those produced through a simple one-step process. The new method leads to higher cell sizes and smaller cell nucleation densities. The analysis of the foaming mechanisms playing a role in this process has led to conclude that a lower pressure of gas when the nucleation points start to grow is beneficial to avoid the generation of defects. On the other hand, in order to obtain comparable cellular structures with the ones obtained through one-step process, an increase in the saturation pressure would be enough.

On the other hand, modifications in the parameters of this new method were carried out, so the depressurization stages were modified. It can be concluded that the obtained

results depend on the viscosity of the used polymer. Higher residual pressures will be beneficial for polymers presenting a high viscosity, while for those with lower viscosity, a lower residual pressure enhances the nucleation density.

Acknowledgments:

Financial assistance from MINECO, FEDER, UE (MAT2015-69234-R), the Junta of Castile and Leon (VA275P18) and Spanish Ministry of Science, Innovation and Universities (RTI2018-098749-B-I00) are gratefully acknowledged. Financial support from FPU grant FPU14/02050 (V. Bernardo) from the Spanish Ministry of Education and Junta of Castile and Leon grant (J. Martín-de León) are gratefully acknowledged.

9. References

[1] Costeux, S. CO 2 -blown nanocellular foams. *Journal of Applied Polymer Science* **2014**, *131*, n/a-n/a.

[2] Notario, B.; Pinto, J.; Rodriguez-Perez, M. A. Nanoporous polymeric materials: A new class of materials with enhanced properties. *Progress in Materials Science* **2016**, *78–79*, 93–139.

[3] Costeux, S.; Zhu, L. Low density thermoplastic nanofoams nucleated by nanoparticles. *Polymer* **2013**, *54*, 2785–2795.

[4] Costeux, S.; Khan, I.; Bunker, S. P.; Jeon, H. K. Experimental study and modeling of nanofoams formation from single phase acrylic copolymers. *Journal of Cellular Plastics* **2014**, *51*, 197–221.

[5] Urbanczyk, L.; Calberg, C.; Detrembleur, C.; Jérôme, C.; Alexandre, M. Batch foaming of SAN/clay nanocomposites with scCO2: A very tunable way of controlling the cellular morphology. *Polymer* **2010**, *51*, 3520–3531.

[6] Kumar, V. Some thermodynamic and kinetic low-temperature properties of the PC-CO 2 system and morphological characteristics of solid-state PC nanofoams produced with liquid CO 2.

[7] Martín-de León, J.; Bernardo, V.; Rodríguez-Pérez, M. Low Density Nanocellular Polymers Based on PMMA Produced by Gas Dissolution Foaming: Fabrication and Cellular Structure Characterization. *Polymers* **2016**, *8*, 265.

[8] Laguna-Gutierrez, E.; Van Hooghten, R.; Moldenaers, P.; Angel Rodriguez-Perez, M. Effects of extrusion process, type and content of clays, and foaming process on the clay exfoliation in HMS PP composites. *Journal of Applied Polymer Science* **2015**, *132*, 1–12.

[9] Pinto, J.; Solorzano, E.; Rodriguez-Perez, M. a.; de Saja, J. a. Characterization of the cellular structure based on user-interactive image analysis procedures. *Journal of Cellular Plastics* **2013**, *49*, 555–575.

[10] Kumar, V.; Suh, N. P. A process for making microcellular thermoplastic parts. *Polymer Engineering and Science* **1990**, *30*, 1323–1329.

[11] Kumar, V.; Suh, N. P. A process for making microcellular parts. *Polymer Engineering & Science* **1990**, *30*, 1323–1329.

[12] León, J. M.; Bernardo, V.; Laguna-gutiérrez, E.; Rodríguez-pérez, M. Á. Influence of the rheological behaviour of PMMA on the cellular structure of nanocellular materials. *Paper sent* 1–16.

[13] Shafi, M. a; Lee, J. G.; Flumerfelt, R. W. Prediction of cellular structure in free expansion polymer foam processing. *Polymer Engineering and Science* **1996**, *36*, 1950–1959.

[14] Shafi, M. A.; Joshi, K.; Flumerfelt, R. W. Bubble size distributions in freely expanded polymer foams. *Chemical Engineering Science* **1997**, *52*, 635–644.

[15] Bergman, T. L.; Incropera, F. P. *Fundamentals of heat and mass transfer.*; Wiley, **2011**.

Chapter 8

Properties of nanocellular materials

"Cuanto más talento tiene un hombre, más grande es su poder de corromper a los demás."

Aldous Huxley

INDEX

8.1. Introduction

Previous chapters are focused on the study of the understanding of the relationships between process and cellular structure and on the understanding of the foaming mechanisms.

Chapter 8 aims at obtaining the relationship between production-cellular structure and some of the properties of nanocellular materials (**Figure 8.1**).

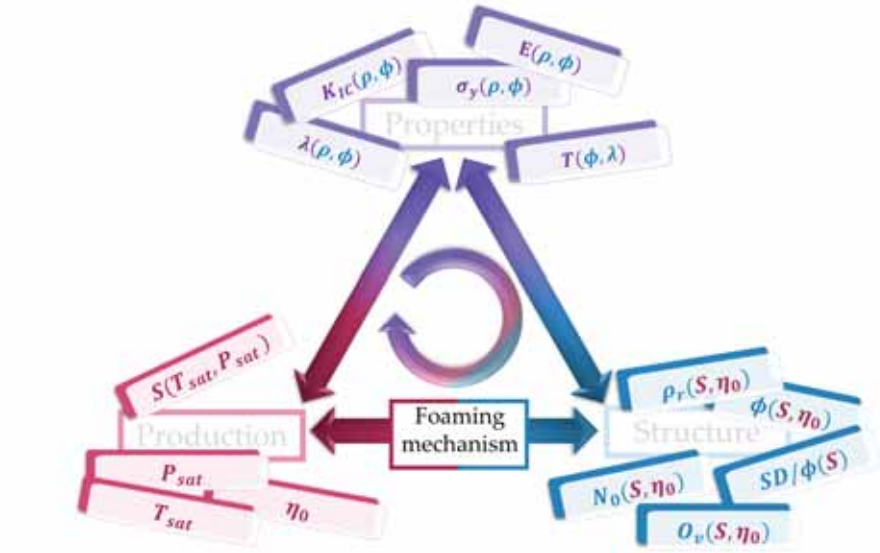

Figure 8.1. Established relationships in Chapter 8.

So, by using the acquired knowledge in the production of nanocellular materials, a wide range of materials with different cellular structures (cell sizes, cell nucleation densities) and relative densities can be produced, and therefore, their properties can be characterized and related with this structure.

Thus, the optical, mechanical, and thermal conductivity of produced nanocellular materials are discussed herein. Two papers are included, the first one "Martín-de León, J.; Pura, J. L.; Bernardo, V.; Rodríguez-Pérez, M. A. Transparent nanocellular PMMA: Characterization and modeling of the optical properties. *Polymer* **2019**, *170*, 16–23." aims at characterizing the optical properties of transparent nanocellular PMMA. So transmittance, T, for nanocellular materials with cell sizes smaller than 50 nm is experimentally measured determining the dependence with the cell size and with the used wavelength $T(\phi,\lambda)$. Furthermore, a theoretical model developed in this thesis to predict the transmittance is also explained. This model allows obtaining a better understanding of the physical phenomena taking place during visible light-nanocellular materials interaction.

The second paper, "Martín-de León, J.; Loock, F. Van; Bernardo, V.; Fleck, N. A.; Rodriguez-Perez, M. A. The influence of cell size on the mechanical properties of nanocellular PMMA. *Paper sent* **2019**" presents the mechanical properties of nanocellular PMMA with cell sizes smaller than 50 nm for the first time. The dependence with the cell size, relative density, as well as with the used polymer matrix is herein studied. So

materials with cell sizes from the micro to the nanoscale are produced and the Young´smodulus,E, the yield stress, σ_y, and the fracture toughness, K_{IC}, are measured. This allows obtaining the relationship of all these properties with the parameters of the cellular structure and therefore with the production process; $E(\phi, \rho_r)$, $\sigma_y(\phi, \rho_r)$, $K_{IC}(\phi, \rho_r)$ **(Figure 8.1)**.

Finally, an extra section is included to discuss the thermal conductivity of the produced materials. Nanocellular materials are well known to present a reduced thermal conductivity. Herein the experimental thermal conductivity, λ , of nanocellular PMMA is experimentally measured and compared with the one of microcellular PMMA. The dependence with the cell size and with the relative density are herein studied, $\lambda(\phi, \rho_r)$ Moreover, theoretical values are calculated, helping to understand the mechanisms allowing the thermal conductivity reduction in nanocellular PMMA.

8.2. Transparent nanocellular PMMA: Characterization and modeling of the optical properties.

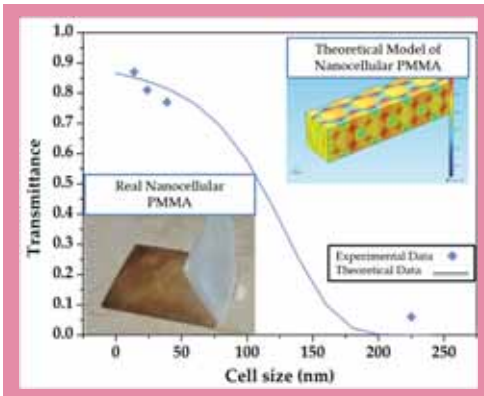

Transmittance of nanocellular PMMA with cell sizes below 50 nm is experimentally and theoretically characterized. A theoretical model is developed that permits to understand the physical phenomena taking place during the light-nanocellular materials interaction. The dependence of the transmittance with the cell size and the used wavelength is then determined both experimentally and theoretically.

TRANSPARENT NANOCELLULAR PMMA: CHARACTERIZATION AND MODELING OF THE OPTICAL PROPERTIES.

Judith Martín-de León, Jose Luis Pura, Victoria Bernardo, Miguel Ángel Rodriguez-Pérez

Cellular Materials Laboratory (CellMat), Universidad de Valladolid, 47011, Spain

Gds Optronlab, Condensed Matter Physics Department, Universidad de Valladolid, 47011, Spain

Correspondence to: Judith Martín-de León (E-mail: *jmadeleon@fmc.uva.es*)

Abstract

In this work, the optical properties of transparent nanocellular polymethylmethacrylate (PMMA) have been studied, experimental and theoretically. Transmittance measurements of samples presenting different cell sizes (14, 24, 39 and 225 nm) and a constant relative density of around 0.45 have been carried out obtaining values as high as 0.94 for the sample with the smaller cell size and a thickness of 0.05 mm. In addition, the light absorption coefficient has been measured as a function of cell size and wavelength. It has been found that the transmittance has a strong dependence with the wavelength, presenting these transparent materials Rayleigh scattering. On the other hand, the transmission of visible light through these nanocellular materials has been modelled for the first time. The developed model reproduces with good accuracy the trends observed in the experimental results and provides remarkable insights into the physics mechanisms controlling the optical behavior of these materials.

Keywords: Transparent, nanocellular polymer, modelling.

1. Introduction

Nanocellular polymers are nowadays the spotlight of numerous studies in the field of cellular materials science. This is due to the fact that it has been proved recently that they present new and improved properties in comparison with those presented by conventional or micro cellular materials[1]. Nanocellular polymers have the expected advantages of cellular materials, such as weight reduction and therefore the possibility of saving raw materials[2], excellent stiffness and strength to weight ratio and in addition some improved properties due to their reduced cell size such as a reduced thermal conductivity and a very high surface to volume ratio[3,4]. Besides, nanocellular polymers can present characteristics utterly unknown to date in the cellular polymers field. One of these new characteristics recently discovered is that nanocellular polymers can present a transparent character[5]. All these properties make nanocellular polymers materials with a high potential because they can combine properties never seen together before, being possible to use them in new sectors and possibly in still unknown applications. Some possible applications have been proposed in previous papers such as the possibility of producing super-insulating windows, combining the transparent character of the material and its low thermal conductivity[6]. Additionally, transparent nanocellular polymers could also be used to replace transparent solid polymer films used in many applications, such as the protective layer of electronic device screens, photo frames or in medical applications such as contact lenses. By using a transparent nanocellular polymer instead of a solid film, it would be possible to save in raw material cost and weight due to their reduced density.

In our previous work[5], some transparent nanocellular PMMA samples were produced for the first time using the gas dissolution foaming technique. This goal was accomplished by reaching a very high CO_2 solubility in the material. The increase in solubility was obtained by means of reducing up to -32 °C the saturation temperature. With this temperature and by changing the saturation pressures from 6 to 20 MPa, samples with cell sizes from 14 nm to 39 nm were obtained and its transparency was demonstrated using optical images. However, although it has been proved that the production of this type of materials is achievable, as far as the authors know, there is only one precedent in which the optical properties of these materials is reported. S. Pérez-Tamarit et al. published the transmittance of a single sample with a cell size of 25 nm and 1 mm of thickness [7]. In addition, the modelling of the optical behavior of nanocellular polymers has not been previously reported.

In this work, a detailed characterization of the optical transmittance of a collection of transparent nanocellular PMMA with different cell sizes and thickness is provided, together with a theoretical model that describes the interaction of visible light with this type of nanocellular material.

1. Materials and Methods

1.1. Materials

Pellets of polymethylmethacrylate V825T (PMMA) were supplied by ALTUGLAS® International (Colombes, France). The material presents a density of $\rho = 1.19\ g/cm^3$

(measured at 23 °C and 50% relative humidity) a glass transition temperature of T_g = 114.5 ° (measured by DSC) and a molecular weight M_n = 43 kg/mol and M_w=83 kg/mol.

Medical grade CO_2 (99.9% purity) was used as the blowing agent for the foaming experiments.

1.2. Samples Preparation

Solid sheets of PMMA were first produced from the initial pellets by using a hot plate press. Pellets were heated at 250°C for 9 minutes, then the material was pressed under a constant pressure of 35 MPa for an additional minute. Lastly, sheets were cooled down at room temperature under the same pressure. Samples of 75 x 75 x 4 mm^3 were obtained and then cut to the desired dimensions (30 x 30 x 4 mm^3) for the foaming experiments.

Gas dissolution foaming process[8] has been used to produce transparent nanocellular PMMA[9]. These foaming tests were carried out in a pressure vessel (model PARR 4760) provided by Parr Instrument Company (Moline, IL, USA) placed inside a freezer that allows reaching temperatures from -15 °C to -32 °C. Moreover, the pressure system comprises a pump (model SFT-10) supplied by Supercritical Fluid Technologies Inc. (Neward, DE, USA). After saturation, samples were foamed in thermal baths (J.P. Selecta Model 600685, Grupo Selecta, Barcelona, Spain).

The processing parameters of the gas dissolution process were chosen according to a previous work [5] with the main objective of obtaining cellular materials with cell sizes below 50 nm and relatives densities around 0.4. Saturation temperature was -32 °C for all the experiments, while three different saturation pressures were used (6, 10 and 20 MPa). Saturation time was 15 days[10] in order to ensure the complete saturation of the samples. After the complete saturation, the pressure was released at a ratio of 10, 31 and 75 MPa/s respectively (the pressure versus time curves and the way to obtain the pressure drop rate is provided in the supporting information (**Figure S1**). Foaming parameters were 40 °C for the foaming temperature and 2 minutes for the foaming time. The time between the release of the pressure in the vessel and the foaming of the samples was 1 minute in all experiments.

Moreover, a sample with a cell size closer to the wavelength of visible light (around 200 nm) has been produced and used as a reference. A pressure vessel (model PARR 4681) provided by Parr Instrument Company (Moline, IL, USA) was used for this purpose. Process parameters were chosen in order to obtain the desired cell size and relative density, taking into account a previous work[11]. The process parameters were 30 MPa and 25 °C as saturation parameters and 40 °C, 1 min as foaming parameters. In this case, the depressurization rate was 100MPa/s and the desorption time was 3 minutes.

Finally, thin plane-parallel sheets were obtained from the foamed samples with a precision cutting machine (Mod.1000 IsoMet). Homogenous and uniform samples of various thicknesses (from 0.05 to 1 mm) and sizes of 3 x 3 cm^2 were obtained for the transmittance measurements. The surface quality of all the samples were comparable,

because all of them were produced using the same method. SEM images of the surface quality of the samples have been include in the supporting information (**Figure S3**).

1.3. Characterization Techniques

1.3.1. Density

The density of the solid PMMA (ρ_s) was determined with a gas pycnometer (Mod. AccuPyc II 1340, Micromeritics, Norcross, GA, USA). For the density of cellular materials (ρ_f), a density determination kit for an AT261 Mettler-Toledo balance was used, the relative density was determined with the water displacement method, based on Archimedes' principle. Before performing this measurement, the solid skins of the samples were removed (more than 200 μm on each side). The density of the thin slices used for the optical measurements were the same of that of the bulk sample without solid skins. Relative density (ρ_r) is defined as follows: ($\rho_r = \rho_f/\rho_s$).

1.3.2. Scanning electron microscopy

Cellular structure was visualized with an ESEM Scanning Electron Microscope (QUANTA 200 FEG, Hillsboro, OR, USA). In order to obtain these images, samples were first cooled in liquid nitrogen to preserve the original cellular structure in the fracture. Then, they were coated with gold by using a sputter coater (model SDC 005, Balzers Union, Balzers, Liechtenstein). In order to characterize the cellular structure, a software based on ImageJ/FIJI[12] was used. The cell nucleation density (N_0) was determined using the Kumar's theoretical method[13], while the cell size distribution and the average cell size (ϕ) was determined by averaging the size of more than 200 cells . Moreover, the standard deviation of the cell size distribution (SD) was determined and finally the parameter SD/ϕ was calculated. This parameter allows evaluating the homogeneity of each cell size distribution.

1.3.3. X-Ray radiography

In order to ensure that the thin sheets of nanocellular materials under study are free of defects, X-ray radiographs were taken by using a home-made-X-ray imaging equipment with 3 microns of spatial resolution[14].

1.3.4. Transmittance measurements

Transmittance measurements were carried out to determine the transparency of the cellular materials. Transmittance ($T = I/I_0$) is defined as the ratio between the transmitted intensity reaching the detector (I) and the incident one (I_0). The transmittance of the cellular materials (T_c) were normalized by the transmittance of the solid PMMA (T_s) (this value is around 0.95 for every thickness and wavelength), so the experimental values of transmittance given in this work are defined as $T = T_c/T_s$.

The device for these transmittance measurements consists of three different lasers (blue: 450 nm, green: 532 nm and red: 650nm, 10mW) acting as light sources, and a photodiode joined to an integrating sphere with a 12.5 mm window (PRW0505, Gigahertz-Optik) connected to a photometer (X94, Gigahertz- Optik) working as light detector.

Samples are placed directly in the window of the integrating sphere to collect all the light scattered by the samples. The laser-detector distance was 30 mm fixing the size of the laser beam at the surface of the sample (2 mm).

1.3.5. UV-VIS

The dependence of the transmittance with the wavelength was measured using an ultraviolet spectrometer (UV-2102 PC, Shimadzu), that allows measuring the transmittance for wavelengths in the range from 400 nm to 800 nm. The experiments were performed with an aperture of the slit of 1 nm. The spectrometer was used in the energy mode in order to amplify the signal by a factor of 2. Solid PMMA and nanocellular materials were measured. The energy measured when solid PMMA was used as sample was taken as the incident energy while the measured with the nanocellular samples was considered as the transmitted energy, being the transmittance the ratio between both measurements. Samples were placed as near as possible to the detector, but because of the set-up in this equipment there exists a distance between the sample and the detector (around 2 cm), so the transmittance values measured in this equipment cannot be taken as absolute, because some of the transmitted light does not reach the detector. Due to this fact, these measurements were only used to evaluate the effect of wavelength on the transmittance.

1.3.6. Modeling

Light transmission process through nanocellular materials has been modeled. The primary objective of this modeling has been calculating the transmittance theoretically. The commercial software COMSOL Multiphysics has been used for the modeling purposes.

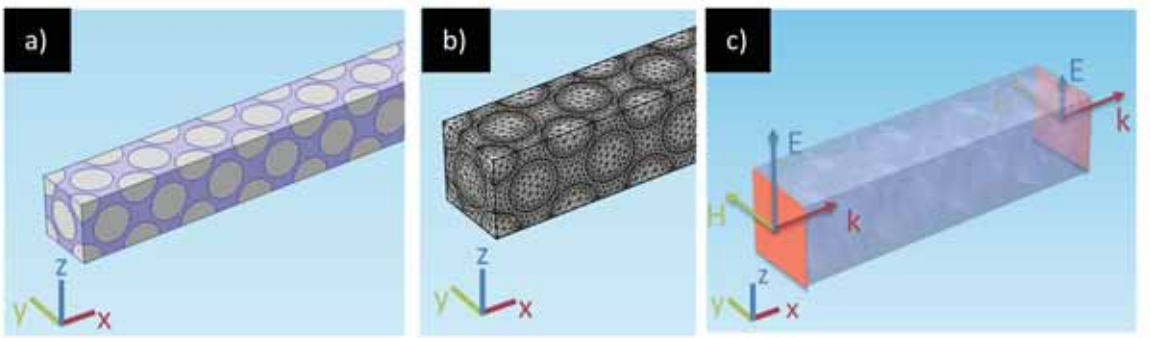

Figure 1. a) Nanocellular material simulation. **b)** Meshing of the material. **c)** Representation of the electromagnetic field.

First of all, nanocellular PMMA has been modeled; samples are simulated as an infinite plane film. This is performed by starting with a parallelepiped which length in the x-direction has been considered the thickness of the sample. Then, symmetry conditions are applied in the y and z directions to simulate the infinite plane sample and to maintain the computational cost at a minimum. Nanocellular materials have been modeled as biphasic materials formed by a solid matrix of PMMA (introducing the data of the

refractive index (n=1.49) and the dielectric constant (ϵ=2.22) of the material, given by the manufacturer) and a second air phase formed by the cells.

As it can be seen in **Figure 1.a**, cells have been represented by spheres with fcc packaging (because together with the hexagonal packaging this is the more compact one). The pore size is homogeneous and can be selected as required, the density of the sample is also tuneable by compacting the packing of spheres, but because of a geometric limitation there exists a minimum relative density of around 0.26, below of which the cell wall disappears, and cells join together. The mesh (**Figure 1.b**) is defined to be smaller than a tenth of the used wavelength and smaller than the selected cell size, to ensure enough resolution in the calculations. Once the main parameters of the material are selected (thickness, density, and cell size) an automatically generated tetrahedral mesh, for both the solid matrix and pores, was created. This mesh creates more elements in the interfaces between the pores and the solid PMMA, and less in the homogeneous phases, air or solid. This allows reaching a higher resolution with the minimum computational cost.

In order to study the interaction of light with these cellular structures, the module of COMSOL Multiphysics Electromagnetic Waves in Frequency Domain was used. This module solves the Maxwell equations for the propagation of light of a fixed wavelength, travelling in the x-direction of the nanocellular polymer. One face of the sample was homogeneously illuminated (**Figure 1c**) by a linearly polarized plane wave of the selected wavelength and with 1 W of power.

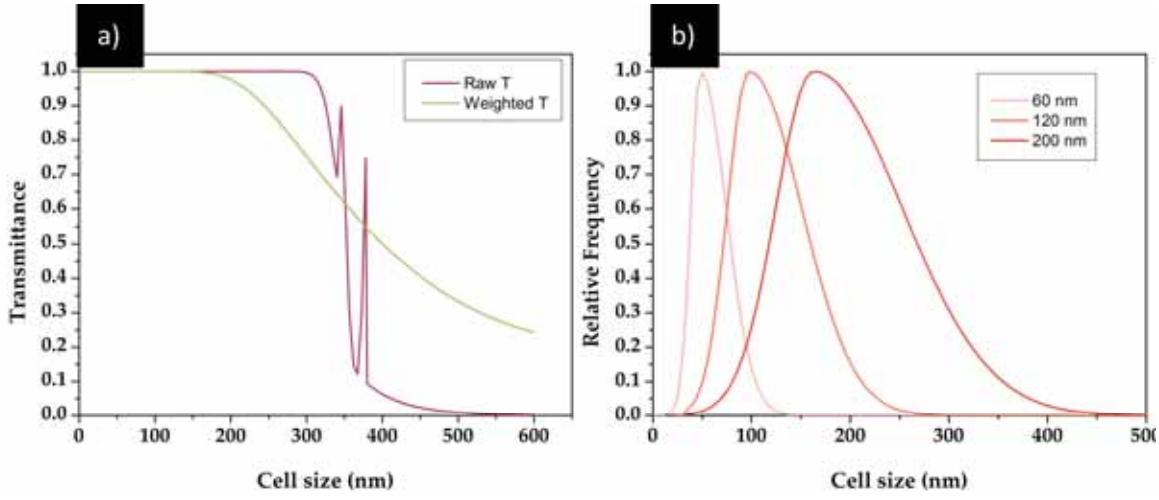

Figure 2.a) Raw transmittance and Weighted transmittance as a function of the cell size. **2.b)** Cell size distributions calculated for different mean cell sizes.

Then, the light intensity on the opposite face is calculated, thus obtaining the transmittance. As it can be seen in **Figure 1c**, due to the scattering of light in the medium, the intensity of the electromagnetic wave has been reduced in the area under analysis.

When this process is carried out for materials with different cell sizes and a fixed density and thickness, a curve like that represented in **Figure 2a** (raw T) is obtained. This

curve has been corrected in order to obtain a realistic transmittance (curve weighted T in **Figure 2.a.**).

To obtain raw T, it has been considered that samples present a uniform cell size (**Figure 1**), which means that all cells in the sample have the same size. This idea is not representing a real cellular material, because they all have a cell size distribution. Moreover, using materials with homogeneous cell sizes leads to resonances. As it can be seen in **Figure 2a**. , there are some peaks in the curve raw T appearing as a result of the coupling of the wavelength with the pore size and the sample length. To solve this artifact, samples with a real cell size distribution must be considered. Cell size distributions of the samples produced experimentally in this work are known, these distributions have been fitted to an asymmetric Gaussian distribution (**Equation 1**), where u and v are the width of each side of the distribution, ϕ is the cell size and $\bar{\phi}$ is the average cell size. Then, by adjusting the parameters u and v with the known distributions, it has been possible to obtain the cell size distribution for each mean cell size (the results of these fitting are shown in the supporting information, **Figure S5**).

$$\begin{cases} \exp -\dfrac{(\phi-\bar{\phi})^2}{u^2} \; when \; \phi < \bar{\phi} \\ \exp -\dfrac{(\phi-\bar{\phi})^2}{v^2} \; when \; \phi > \bar{\phi} \end{cases} \qquad \textbf{Eq.1}$$

Finally, a convolution between raw T (T_ϕ) and the cell size distributions has been calculated to obatin the weighted curve T ($T_{\bar{\phi}}$).

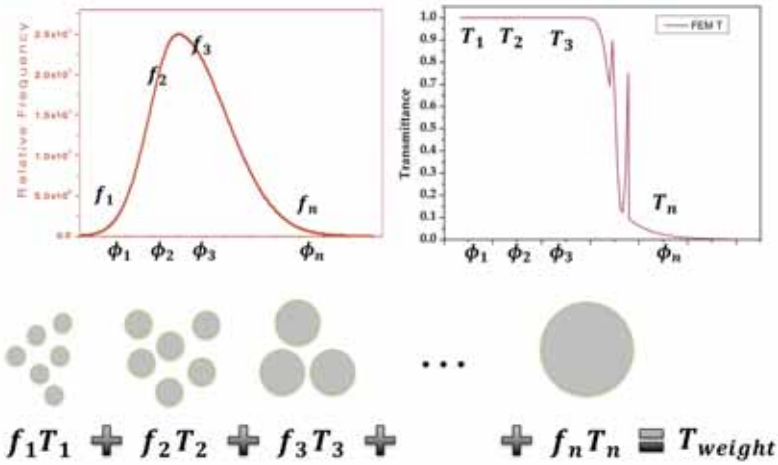

Figure 3. Explanation of how the transmittance for a given cell size is combined with the cell size distributions.

This convolution is explained in **Figure 3**. If the cell size distribution is known, the solution can be obtained using a superposition of the contribution of each cell size. Cells with a size Φ1 and a transmittance T1 will contribute proportionally to the number of these cells that are present in the cellular material. It means they contribute with their relative frequency f1. This is the same for each cell size so if we know the transmittance for each cell size the transmittance of the whole material can be obtained as the addition of each transmittance multiplied by its contribution, it means multiplied by the relative frequency.

It means that for a given mean cell size, the transmittance has been calculated by using **Equation 2**. Where f_ϕ are the normalized relative frequency of the cell size and T_ϕ is the computed transmittance for each cell size.

$$T_{\bar{\phi}} = \sum_{\phi} f_\phi T_\phi \qquad \textbf{Eq.2}$$

On the other hand, the scattering behaviour of one single cell has been studied. In this case, the model is formed by an infinite bulk PMMA with a single spherical pore at the origin. The model is surrounded by a spherical Perfectly Matched Layers to avoid secondary reflections on the boundaries. The sample is then illuminated by a 532 nm plane wave traveling in the x-direction and polarized along the z-axis. Once the scattering problem is solved, the far-field output is studied to understand the scattering behaviour as a function of the pore diameter.

2. Results

2.1. Cellular Structure

As it was presented in our previous works[5,11] the use of 30 MPa and 25 °C as saturation conditions lead to solubilities around 31 %, while the use of low saturation temperatures (-32°C) allows reaching solubilities of CO_2 as high as 48 %. This results in a change in the cell size from 200 nm when the saturation temperature is 25 °C to cell sizes below 50 nm when saturation temperature is below zero. In this work, in order to produce materials with different cell sizes, three different saturation pressures were used, (6, 10 and 20 MPa), while fixing the saturation temperature at -32 °C. Afterward, all samples were foamed at 40 °C for 2 minutes. All these process conditions lead to samples with the characteristics shown in **Table 1.** SEM images can be found in the supplementary information (**Figure S2**).

Table 1. Cell nucleation density, cell size and SD/ Φ for the produced samples.

Saturation conditions	Relative density	N_0 (nuclei/cm³)	Cell size (Φ) (nm)	SD/ϕ
30 MPa 25 °C	0.47	$1.8 \cdot 10^{14}$	213	0.45
6 MPa -32 °C	0.47	$7.7 \cdot 10^{15}$	39	0.35
10 MPa -32 °C	0.46	$1.2 \cdot 10^{16}$	24	0.28
20 MPa -32 °C	0.46	$4.0 \cdot 10^{16}$	14	0.22

As it can be seen, samples with a similar relative density (between 0.46 and 0.47) but different cellular structures have been obtained by using the previously described conditions. Thus, samples with cell sizes from 213 nm to 14 nm and with cell nucleation densities from $1.8 \cdot 10^{14}$ nuclei/cm³ to $4.0 \cdot 10^{16}$ nuclei/cm³ respectively are available for the transmittance experiments. It is also important to notice the change in the parameter SD/ϕ indicating the width of the cell size distribution. It is noticed that as cell size becomes smaller, the cell size distribution becomes clearly narrower.

2.2. X-Ray radiographs

Radiographies of all samples were taken to select homogeneous samples free of defects for the characterization of the optical properties. **Figure 4** shows some examples. Samples a) and b) are completely homogeneous while c) has some defects and d) has zones with different opacity (i.e., different density and/or thickness). Samples behaving as samples c) and d) were not used in the optical measurements, taking into account only those samples showing radiographies similar to those of samples a) or b).

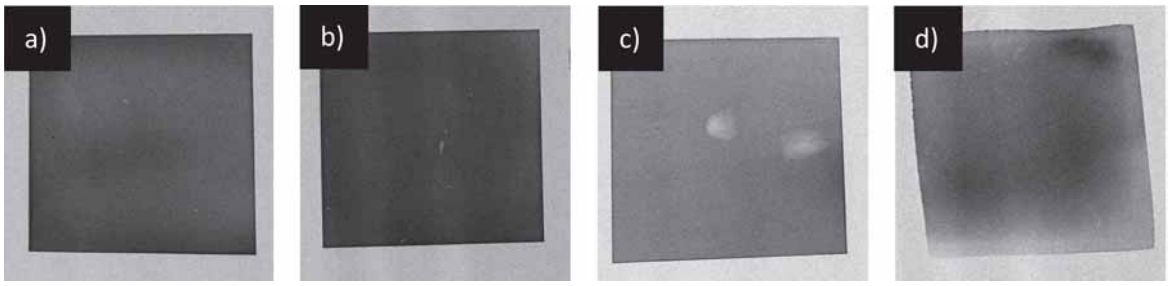

Figure 4. X-Ray radiography of different samples.

2.3. Transmittance

2.3.1. Cell size dependence

In this section, the results obtained using the green laser (532 nm) are presented and discussed. The resulted trends with the red and blue lasers were similar. (see supporting information).

Table 2 shows the transmittance results for samples with different cell sizes and thickness. The change between cellular PMMA with 225 nm of cell size and those with cell sizes below 50 nm is evident. While the first sample is almost opaque to green light, showing a transmittance near zero even for a thickness as low as 0.05 mm, the values for the rest of the samples are significantly higher. In particular, at low thickness, some of the samples present values higher than 0.90.

Table 2. Transmittance of samples with different cell size and thickness for a wavelength of 532 nm.

Cell size (nm)	Thickness 0.05 mm	Thickness 0.1 mm	Thickness 0.2 mm	Thickness 0.5 mm	Thickness 1 mm
225	0.09	0.06	0.04	0.02	0.01
39	0.88	0.81	0.74	0.53	0.36
24	0.92	0.85	0.84	0.56	0.41
14	0.94	0.92	0.83	0.66	0.48

In addition, the change between the three samples with less than 50 nm is remarkable. Sample with a mean cell size of 14 nm reach values of transmittance as high as 0.94 with 0.05 mm of thickness, while for the 39 nm sample this value is reduced down to 0.88. In addition, when the thickness increases up to 1 mm transmittance values become smaller, but not at all negligible. For the 14 nm sample, the transmittance is still 0.5 for 1 mm in thickness, which is a high value in comparison with the one presented by the sample with a cell size of 225 nm

According to scattering theories, the maximum particle size for the light to pass through is one-tenth of the wavelength[15]. This means that for a wavelength of 532 nm the maximum cell size for the sample to be transparent is around 50 nm. This is in accordance with the showed results, where only samples below 50 nm have a significant transmittance. Moreover, the cell size distribution needs to be considered to understand the results, the sample with a cell size of 39 nm has a broader cell size distribution than the sample with a cell size of 14 nm, that means that in the sample with a higher mean cell size there are some cells with sizes higher than 50 nm that are reducing the total transmittance.

In conclusion, to maximize the transmittance of the cellular materials, it is essential to minimize the cell size as well as narrowing the cell size distribution.

2.3.2. Dependence of the transmittance with the thickness

By representing $Ln(T)$ as a function of the thickness **Figure 5,** it can be seen that the relationship between the transmittance and the thickness (l) of the sample follow an exponential behaviour:

$$T = e^{-\mu l} \qquad \textbf{Eq.3}$$

where μ is a coefficient that can be related with the light that it not passing through the material.

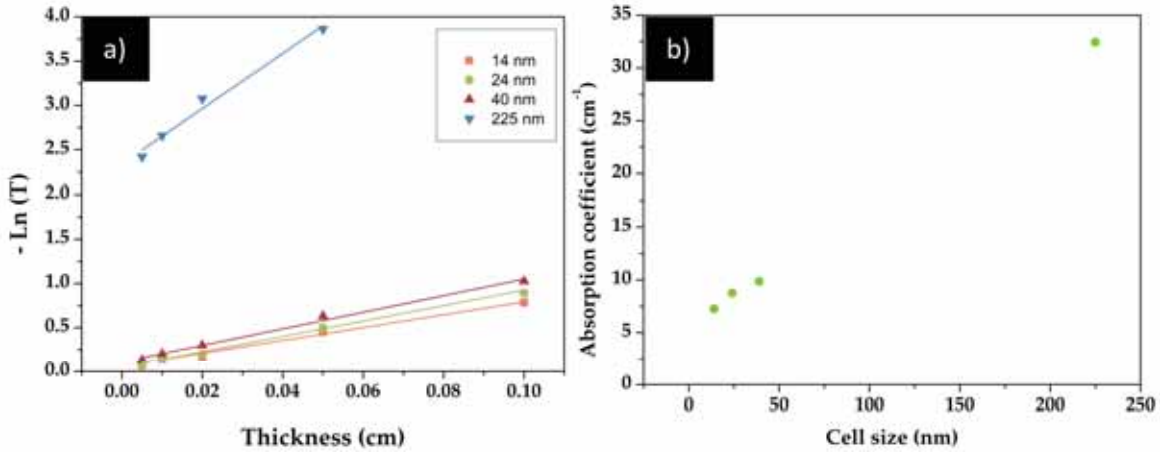

Figure 5. a) Exponential fitting for the experimental results for a wavelength of 532 nm **b)** Absorption coefficient as a function of cell size for a wavelength of 532 nm.

The obtained results for a wavelength of 532 nm are presented in **Figure 5**, from which it can be deduced that transmittance has an exponential behaviour with the thickness in all the samples under study. It means that the μ coefficient can be then obtained from the slope of the curve of each material, being possible to determine the value of transmittance for any thickness. Moreover, large differences between the samples have been obtained, showing that μ increases as cell size becomes higher (**Figure 5b**). In accordance with what has been discussed so far, this fact shows that as cell size increases, less light can pass through the sample. The results for the other wavelengths followed the same trends and have been included in the supporting information (**Figure S4**).

2.3.3. Wavelength dependence

The effect of the light wavelength on the transmittance of the samples was studied in the samples of 0.2 mm in thickness by means of a UV-VIS spectrometer. A continuous transmittance curve from 400 nm to 800 nm of wavelength was obtained. **Figure 4** shows the results for the samples with cell sizes smaller than 50 nm. The results for the sample with a cell size of 225 nm are not given because of the very small transmittance of these samples that made impossible detecting light by the UV-VIS equipment used in this research.

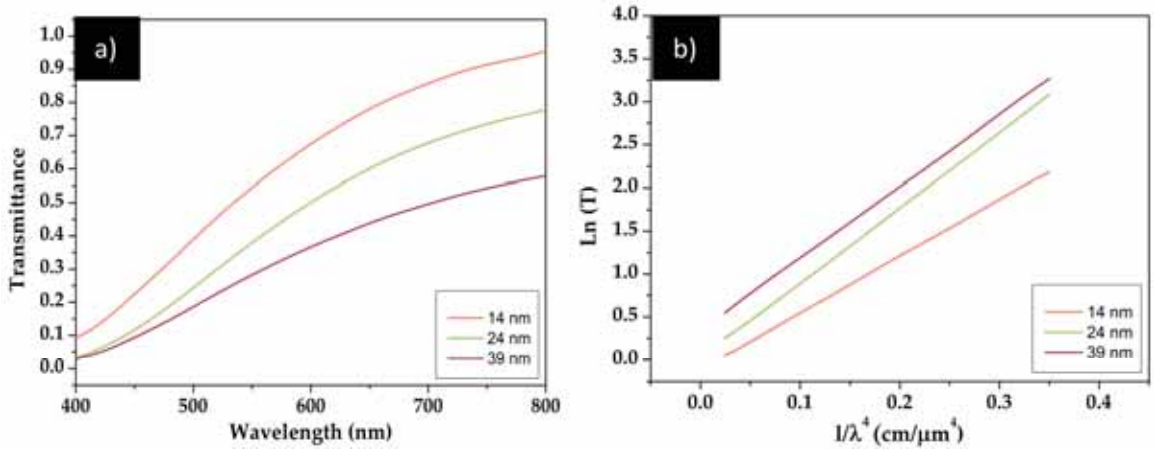

Figure 6. a) Transmittance as a function of the wavelength for the three samples with cells sizes smaller than 50 nm. **b)** Linearization of equation 4 to observe the λ^{-4} dependence.

As it can be seen in **Figure 6a**, the wavelength has a strong effect on the transmittance of the samples; small wavelengths are less likely to travel through the samples than the higher ones. It means the red light goes across the cellular material easily than blue light. This effect has been previously observed in transparent silica aerogels[16], and these materials are similar to the nanocellular PMMA produced in this work as far as cell size and transparency of the base material are concerned. This strong wavelength dependence was attributed to Rayleigh scattering in previous works studying this effect in aerogels[16,17,18,19]. Rayleigh scattering occurs when the light interacts with objects smaller than about a tenth of the wavelength. The intensity of the scattered light depends, according to Rayleigh law, on λ^{-4}, and the transmittance can be calculated according to Equation 4[20]:

$$T = Ae^{-\frac{Bl}{\lambda^4}} \qquad \textbf{Eq.4}$$

Where A and B are constants. The $Ln(T)$ as a function of l/λ^4 has been presented in **Figure 6b.** As it can be observed, straight lines are obtained which means that the nanocellular PMMA samples with cell sizes below 50 nm present Rayleigh scattering as it was previously demonstrated for silica aerogels.

2.4. Modeling

2.4.1. Cell size dependence

The transmittance as a function of the cell size has been modelled for cell sizes from 5 to 250 nm. This modeling has been carried out for a relative density of 0.47 and by fixing a sample thickness of 1.22 μm. This sample thickness has been chosen because it is the maximum that can be solved with the necessary precision and affordable computation times. So as to obtain the transmittance for different thicknesses **Equation 5**, derived from **Equation 3**, was used. Where T_0 is the calculated transmittance for an initial thickness l_0 and T is the transmittance for a new thickness l.

$$T = T_0^{\frac{l}{l_0}} \qquad \textbf{Eq.5}$$

This equation allows obtaining the transmittance for any thickness from the calculated data. The results obtained for four different thicknesses (from 0.1 to 1 mm) and for a wavelength of 532 nm are shown in **Figure 7b** The tendency with the cell size is clear: below 50 nm the transmittance is high, while when this value of cell size becomes higher, the transmittance sharply decreases up to reach 0 for cells between 125 and 200 nm depending of the sample thickness.

The experimental results are compared with the results from the modelling in **Figure 6b.** The results show that both, experimental and theoretical data, clearly fit and show the same trends, which demonstrates that the proposed model can predict the transmittance values.

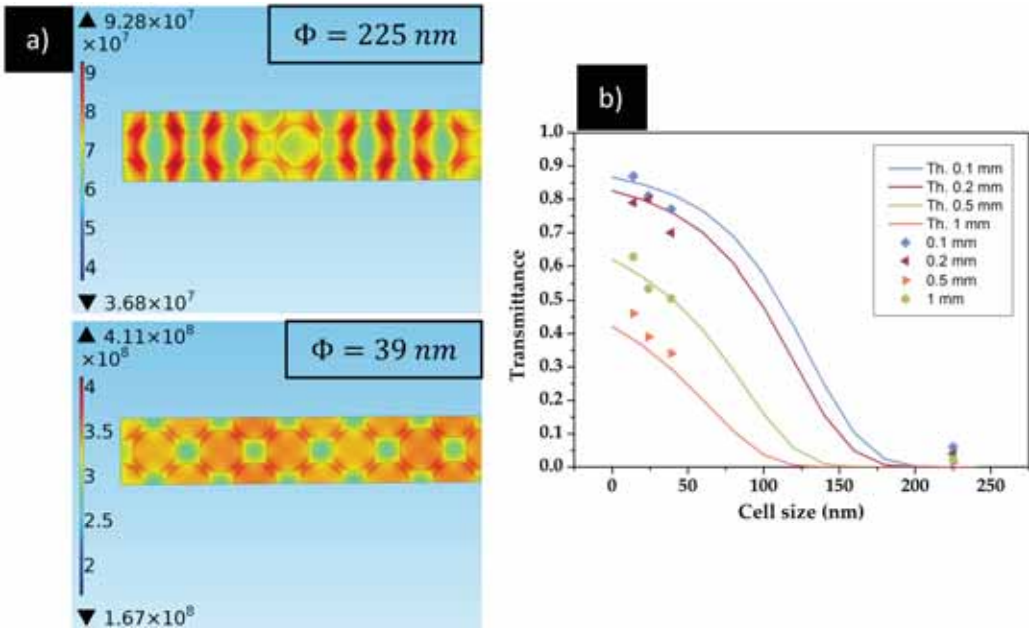

Figure 7.a) Spatial Distribution of electrical field modulus for 39 nm and 225 nm samples (wavelength of 532 nm). **b)** Theoretical and Experimental transmittance as a function of cell size (wavelength of 532 nm).

Also, using Comsol Multiphysics, a representation of the special distribution of the modulus of the electric field can be obtained for samples with different cell sizes (**Figure 7a**). The results for a sample with a cell size of 225 nm and a sample with a cell size of 39 nm are included in this figure. Differences between samples are clear, scale bars of the

intensity of the electric field (V/m) are shown in the figure, these values cannot be taken as absolutes because they should be compared with the initial intensity, but they can be used qualitatively.

When the pore size is small enough, the electromagnetic field is allowed to travel through the cells, and the intensity inside the cells and in the solid phase is similar. It seems that the electromagnetic field is traveling in a continuous way through the material and the scattering due to the presence of the cells is negligible. While when the pore size is larger than 100 nm, the electromagnetic field cannot enter the cells, the electromagnetic field is only traveling through solid PMMA, and the scattering is much higher.

2.4.2. Wavelength dependence

In order to study the variation of the transmittance with the wavelength, samples with a relative density of 0.47 and different cell sizes have been modelled, by varying the wavelength from 400 to 800 nm. When this modeling was carried out resonances like those shown in the previous section were observed. To overcome this problem, samples with different lengths from 1μm to 1.4μm (in steps of 0.05μm) were considered to eliminate the resonances and then an average of the transmittance was calculated. The refractive index and dielectric constants were considered here as constants because the minimum change they have in the range under study did not introduce any change in the transmittance values.

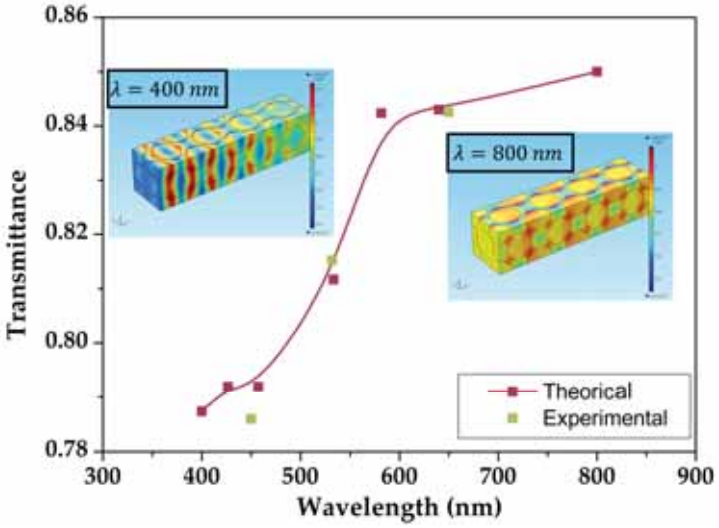

Figure 8. Theoretical and experimental results of the transmittance as a function of wavelength together with two images showing the electric field modulus.

Figure 8 shows both a graph transmittance vs. wavelength and images showing the electric field distribution for a sample of cell size 39 nm and 0.1 mm in thickness. Obtained results verify what it was observed in the experimental section, there exists a strong dependence of the transmittance with the light wavelength. As it can be seen, the electromagnetic field is not allowed to enter the cells, suffering a strong scattering along the sample when using an incident light of 400 nm. However, this effect is not observed with the 800 nm light. In this case, light travels from cell to cell and scattering is not

discernible. This results in a much higher transmittance at higher wavelengths than at smaller ones.

In addition, these data have also been compared with the experimental ones. In this section, the experimental data obtained by means of the three different lasers are used. As it is observed in **Figure 8,** the model reproduces the behaviour experimentally obtained, validating once again the proposed model.

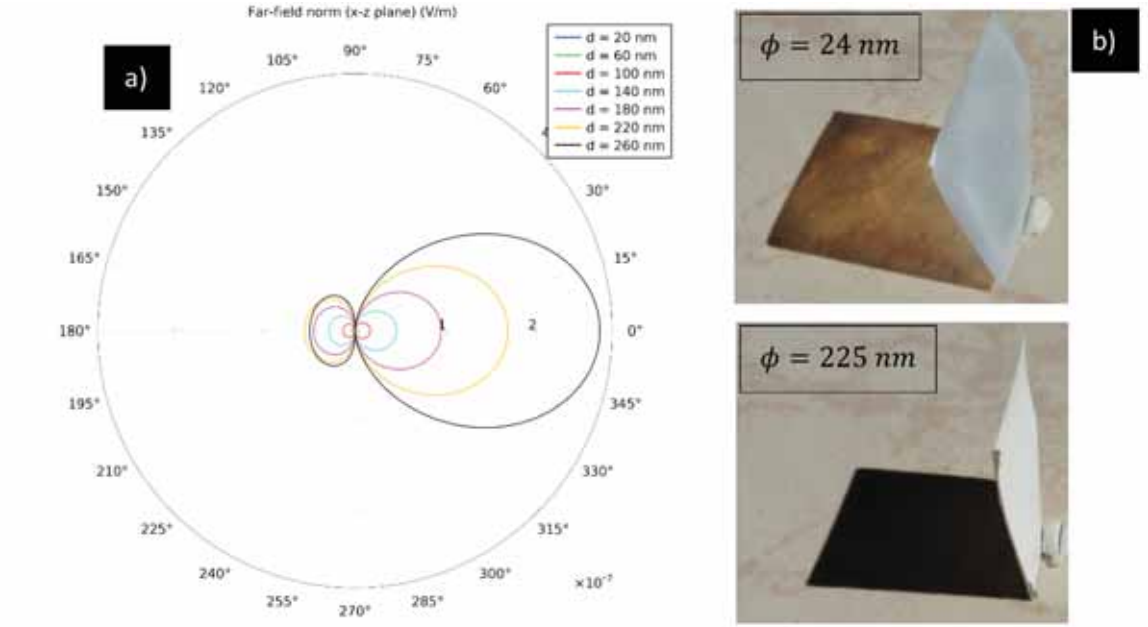

Figure 9.a) Far-field diagram of a unique pore surrounded by PMMA illuminated with light with a wavelength of 532 nm. **b)** optical images of the transmission of light through real samples with the same relative density and different cell sizes.

To fully understand the physics behind the obtained results, an additional simulation was carried out. A unique air cell surrounded by PMMA was modeled and then illuminated with linearly polarized light with a traveling in the x-direction and polarized in the z-direction of a wavelenght of 532 nm, then the behaviour of light depending on the cell size was studied. **Figure 9a** shows a far-field diagram, i.e., a polar plot of the intensity of the radiation field, that is, the light scattered by the system in each direction. In the diagram, 0° corresponds to the light scattered in the forward direction (x-positive-axis) while 180° corresponds to backscattered light. Large differences between cell sizes are appreciable; on the one hand, the amount of scattered light decreases abruptly when cell size becomes smaller, on the other hand, the scattering mechanism is also different for different cell sizes.

These differences result in visible effects when the light passes through real samples (**Figure 9b**). The results shown in **Figure 9** reinforce the discussion above; when a cell is clearly smaller than the wavelength, the cell acts as an electric dipole for the electromagnetic field, as it can be seen two lobes appear in the far-field diagram, which is the typical behaviour of a dipole. This effect is known as the Rayleigh effect. Moreover, the amount of scattered light is very small in comparison with higher pores. This leads to

a real transparent sample that when the light illuminates allow most of the light passing through it and the small amount that it is Rayleigh-scattered make the sample to acquire a bluish tone while the light passing through becomes red (this is due to the strong dependence of wavelength of this type of scattering). When pores start to be larger but still comparable to the wavelength Mie scattering takes part, the pore acts then like a dipole deformed in the forward direction. In addition, the amount of scattered light is very high resulting in an opaque sample (**Figure 9b**).

3. Conclusions

Transparent nanocellular PMMA with cell sizes from 14 nm to 39 nm and relative densities around 0.47 have been optically characterized. The transmittance of these materials has been compared with the one of an opaque sample with a cell size of 225 nm. It has been found that while the 225 nm sample presents values of transmittance near zero for all the used thickness, transmittances as high as 0.94 are achievable when the cell size is 14 nm, and the thickness of the sample is 0.05 mm. Moreover, this sample is able to maintain a transmittance near 0.5 when the thickness of the sample is 1 mm. On the other hand, the dependence on the wavelength was determined to be λ^{-4}, presenting these transparent materials Rayleigh scattering.

All this has been theoretically modelled; the model was able to predict the trends showed by the experimental results. The presence of Rayleigh scattering has also been predicted by this model. Therefore, we can conclude that for the first time, a theoretical model allows understanding the mechanisms taking place in the transmission of visible light in nanocellular polymers. This model allows calculating the transmittance for any cell size, thickness, and density and for any visible wavelength.

Acknowledgments

Financial support from the Junta of Castile and Leon grant (J. Martín-de León), FPU grant FPU14/00916 (J.L. Pura) and FPU grant FPU14/02050 (V. Bernardo) from the Spanish Ministry of Education are gratefully acknowledged. Financial assistance from MINECO, FEDER, UE (MAT2015-69234-R) and the Junta de Castile and Leon (VA275P18) are gratefully acknowledged.

4. References

1.B. Notario, J. Pinto, M. A. Rodriguez-Perez, *Prog. Mater. Sci.* **2016**, *78–79*, 93–139.

2.N. J. Mills, *Polymer (Guildf).* **1993**, *34*, 2237.

3.D. Miller, V. Kumar, *Polymer (Guildf).* **2011**, *52*, 2910–2919.

4.B. Notario, J. Pinto, E. Solorzano, J. A. De Saja, M. Dumon, M. A. Rodriguez-Perez, *Polym. (United Kingdom)* **2015**, *56*, 57–67.

5.J. Martín-de León, V. Bernardo, M. Á. Rodríguez-Pérez, *Macromol. Mater. Eng.* **2017**, *3*, 1700343.

6.H. Guo, V. Kumar, *Polymer (Guildf).* **2015**, *56*, 46–56.

7.S. Pérez-Tamarit, B. Notario, E. Solórzano, M. A. Rodriguez-Perez, *Mater. Lett.* **2018**, *210*, 39–41.

8.I. Singh, A. Gandhi, M. Biswal, S. Mohanty, S. K. Nayak, *Cell. Polym.* **2018**, *37*, 121–149.

9.V. Kumar, N. P. Suh, *Polym. Eng. Sci.* **1990**, *30*, 1323–1329.

10.H. Guo, V. Kumar, *Polymer (Guildf).* **2015**, *57*, 157–163.

11.J. Martín-de León, V. Bernardo, M. Rodríguez-Pérez, *Polymers (Basel).* **2016**, *8*, 265.

12.J. Pinto, E. Solorzano, M. a. Rodriguez-Perez, J. a. de Saja, *J. Cell. Plast.* **2013**, *49*, 555–575.

13.V. Kumar, N. P. Suh, *Polym. Eng. Sci.* **1990**, *30*, 1323–1329.

14.E. Solórzano, J. Pinto, S. Pardo, F. Garcia-Moreno, M. A. Rodriguez-Perez, *Polym. Test.* **2013**, *32*, 321–329.

15.D. J. Lockwood, in *Encycl. Color Sci. Technol.* (Ed.: R. Luo), Springer Berlin Heidelberg, Berlin, Heidelberg, **2014**, pp. 1–12.

16.A. A. Pisal, A. Venkateswara Rao, *J. Porous Mater.* **2017**, *24*, 685–695.

17.A. J. Hunt, P. Berdahl, *Mater. Res. Soc. Symp. Proceeding* **1984**, *32*, 275–280.

18.A. Soleimani Dorcheh, M. H. Abbasi, *J. Mater. Process. Technol.* **2008**, *199*, 10–26.

19.S. B. Riffat, G. Qiu, *Int. J. Low-Carbon Technol.* **2013**, *8*, 1–6.

20.Wanqing Cao, A. J. Hunt, *J. Non. Cryst. Solids* **1994**, *176*, 18–25.

8.2.1. Supporting information

TRANSPARENT NANOCELLULAR PMMA: CHARACTERIZATION AND MODELING OF THE OPTICAL PROPERTIES.

Judith Martín-de León, Jose Luis Pura, Victoria Bernardo, Miguel Ángel Rodríguez-Pérez

Cellular Materials Laboratory (CellMat), Universidad de Valladolid, 47011, Spain

Gds Optronlab, Condensed Matter Physics Department, Universidad de Valladolid, 47011, Spain

Correspondence to: Judith Martín-de León (E-mail: *jmadeleon@fmc.uva.es*)

2. Depressurization velocity

To determine the depressurization rate, the pressure versus time curves during the release of the pressure were measured (**Figure S1).** Then depressurization rate was calculated as the slope of the curve in the first pressure drop.

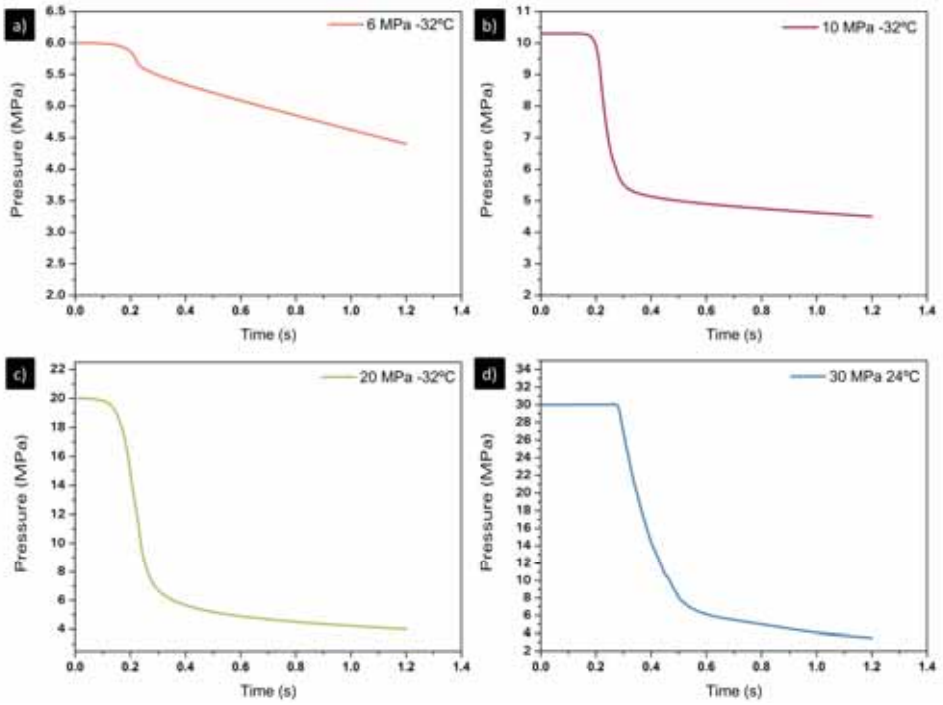

Figure S1. Pressure versus time curves for different saturation conditions. **a)** 6 MPa -32 °C. **b)** 10 MPa -32 °C **c)** 20 MPa -32 °C. **d)** 31 MPa 24 °C.

3. Homogeneity of the samples

3.1. Internal cellular structure

So as to proceed with the experimental measurements of the transmittance it is important to ensure the homogeneity of the cellular structure of the produced materials. To ensure this homogeneity, additionally to the X-ray experiments, SEM images of all the samples were taken at different magnifications and in different regions of the nanocellular materials, as it is shown in **Figure S2**.

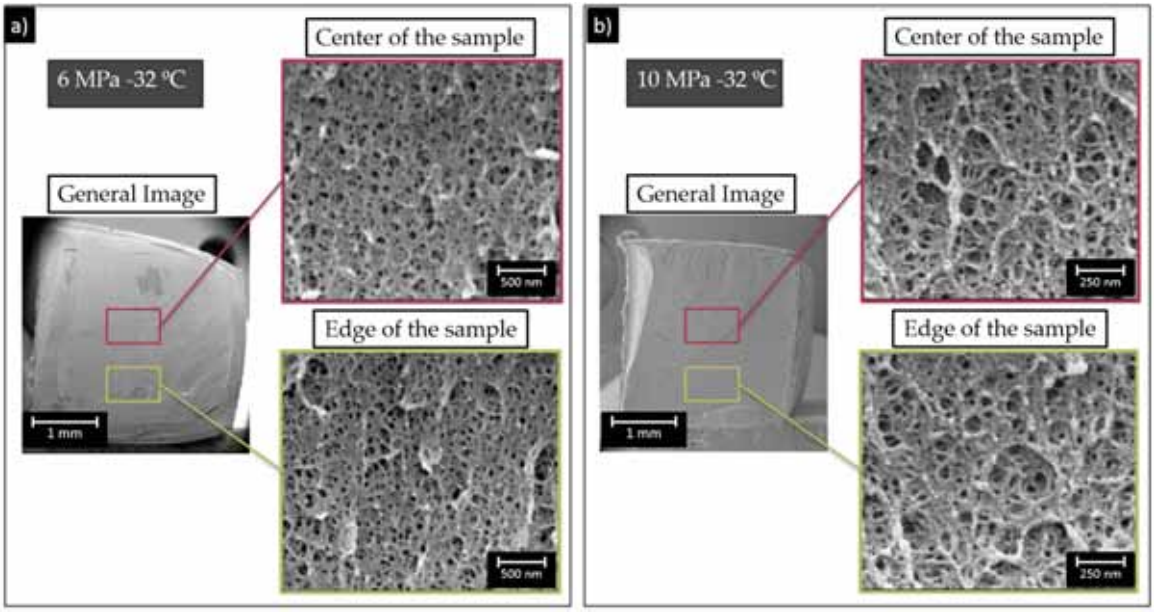

Figure S2. SEM micrographs for two of the samples under study.

As it can be seen, a first general image of the sample is taken, to ensure that is free of macroscopic or microscopic defects. After that, different micrographs are taken along the sample and with the same magnification, at this way three images of the centre of the sample and two of each edge are taken and analysed. This method ensures the homogeneity of the sample along the thickness.

The values given in the manuscript describing the cellular structure are the mean value of all the images taken in the center of the samples

3.2. Surface of the samples

As the layers for experimental measurements were cut with a saw, it is important to ensure that the effect introduced by this fact, is the same independently on the thickness of the samples or on the cellular structure.

For this reason, SEM images of the surfaces of different layers were taken as it is shown in **Figure S3**.

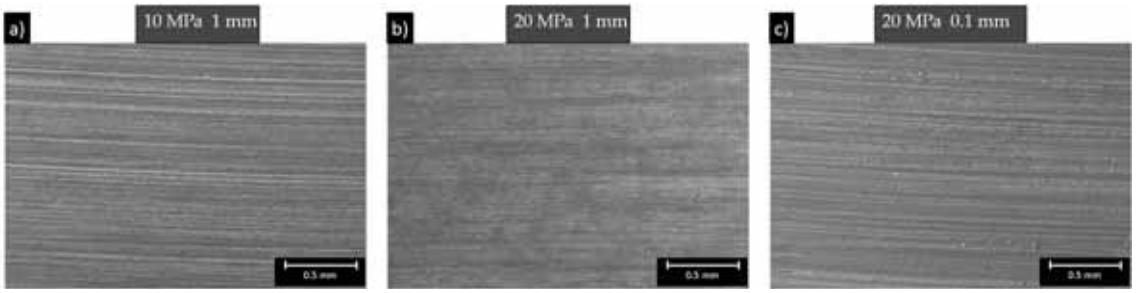

Figure S3. SEM micrographs of the surface of the nanocellular foams cut to a different thickness.

It can be appreciated that the surface of all the samples present a similar morphology, therefore the possible effect of this surface on the transmission measurements should be similar for all the materials under study.

4. Cell size dependence

Transmittance measurements were performed with three wavelengths 450 nm, 532 nm and 650 nm. **Table S1** and **S2** show the results obtained for the red and blue lasers respectively. As it was presented for the green laser in the paper, the differences between cell sizes are clear. The cellular material with 14 nm of cell size is the one with the highest transmittance for all the thicknesses. When the thickness is 0.05 mm, transmittance is as high as 0.96 for the red laser, and 0.74 nm for the blue one. As the thickness is increased this value decreases, but it remains quite high showing a transmittance of 0.58 for the sample of 1 mm and the 650 nm light. The samples presenting 24 nm and 39 nm of cell size also have a good transmittance, showing all of them values clearly below the transmittance of the sample with a cell size of 225 nm.

Table S1. Transmittance of samples with different cell sizes and thicknesses for a wavelength of 650 nm.

Cell size (nm)	Thickness 0.05 mm	Thickness 0.1 mm	Thickness 0.2 mm	Thickness 0.5 mm	Thickness 1 mm
225	0.09	0.07	0.05	0.02	0.02
39	0.91	0.83	0.80	0.66	0.44
24	0.93	0.88	0.86	0.64	0.49
14	0.96	0.93	0.91	0.75	0.58

Table S2. Transmittance of samples with different cell sizes and thicknesses for a wavelength of 450 m.

Cell size (nm)	Thickness 0.05 mm	Thickness 0.1 mm	Thickness 0.2 mm	Thickness 0.5 mm	Thickness 1 mm
225	0.06	0.04	0.03	0.01	0.01
39	0.63	0.51	0.45	0.27	0.13
24	0.69	0.63	0.59	0.30	0.16
14	0.74	0.70	0.60	0.33	0.18

On the other hand, it is also appreciable the change of the transmittance with the wavelength. Differences between both Tables are clear. The highest values correspond to the red laser, while the transmittance for the green one (showed in the paper) and the blue one are smaller. These results reveal again the strong dependence of the transmittance values with the wavelength.

5. Absorption coefficient for different wavelengths.

Figure S4 shows the μ coefficient for the three used wavelengths as a function of cell size. As it has been explained in the paper, when the size increases the μ coefficient also increases The same behavior can be found for the different wavelengths under study.

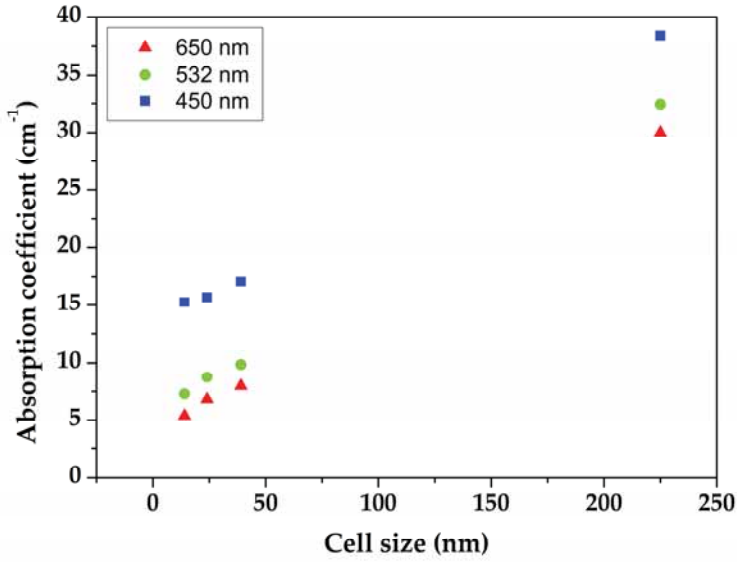

Figure S4. Absorption coefficient for the three used wavelengths.

Moreover, the effect of the wavelength can be also observed in the data. The μ coefficient is smaller for the higher wavelengths.

6. Cell size distribution for any cell size

In order to obtain the cell size distribution for any cell size, a mathematical treatment of the experimental data has been carried out.

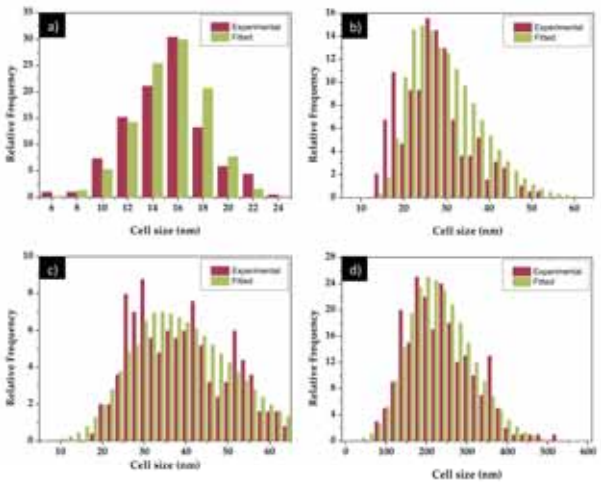

Figure S5. Experimental and fitted cell size distribution for the cellular materials with cell sizes of 14, 24, 39 nm and 225 nm.

The initial data are the experimental cell size distributions of the cellular materials produced in this paper. **Figure S5** shows those distributions for the samples with cell sizes of 14 nm, 24 nm, 39 nm and 225 nm. Those distributions were fitted to an asymmetric Gaussian distribution (**Equation S1**) by selecting the parameters u, v and $\bar{\phi}$ that better reproduces the experimental curves for the different cell sizes. Then, the green distributions showed in **Figure S5** were obtained.

$$\begin{cases} \exp -\dfrac{(\phi-\bar{\phi})^2}{u^2} \; when \; \phi < \bar{\phi} \\ \exp -\dfrac{(\phi-\bar{\phi})^2}{v^2} \; when \; \phi > \bar{\phi} \end{cases} \qquad \textbf{Eq.S1}$$

At that point, three linear regression were obtained by representing those three parameters (u, v and $\bar{\phi}$) with respect to the cell size (**Figure S6.a**). These linear fittings allow obtaining these three parameters for any cell size and therefore by using **Equation S1** the cell size distribution for any cell size can be obtained (**Figure S6.b**)

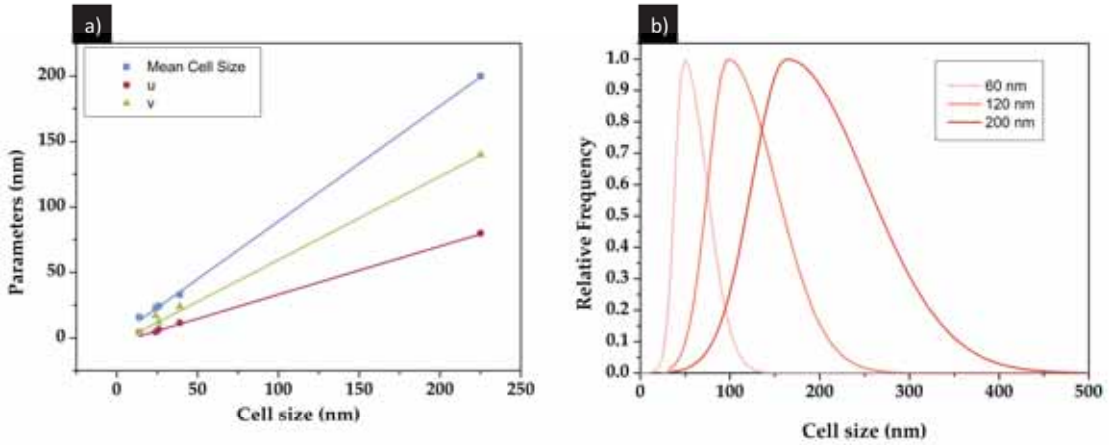

Figure S6.a Linear fitting for the parameters of equation S1. **S6b.** Cell size distribution theoretically calculated for three different cell sizes.

8.3. The influence of cell size on the mechanical properties of nanocellular PMMA.

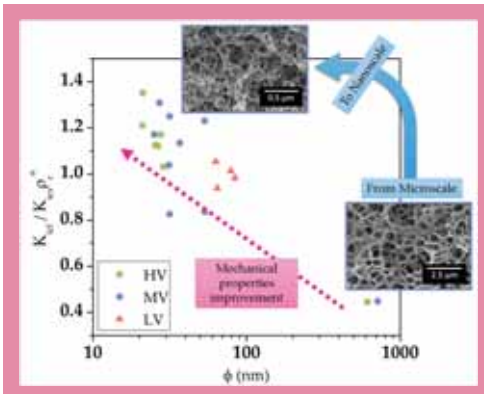

Mechanical properties of nanocellular PMMA are measured. Materials with cell sizes from the micro to the nanoscale (cell sizes lower than 50 nm) are tested through uniaxial compression and single edge notch bend tests. The Young´s modulus, the yield stress, and the fracture toughness are studied. It is found a significant increase of fracture toughness when cell size is reduced to the nanoscale.

THE INFLUENCE OF CELL SIZE ON THE MECHANICAL PROPERTIES OF NANOCELLULAR PMMA.

Judith Martín-de León, Frederik Van Loock, Victoria Bernardo, Norman A. Fleck, Miguel Ángel Rodriguez-Pérez

Cellular Materials Laboratory (CellMat), Universidad de Valladolid, 47011, Spain

Engineering Department, University of Cambridge, Trumpington Street, CB2 1PZ Cambridge, United Kingdom

Correspondence to: Judith Martín-de León (E-mail: *jmadeleon@fmc.uva.es*)

Abstract

Solid-state foaming experiments are conducted on three grades of polymethyl methacrylate (PMMA). Nanocellular PMMA foams are manufactured with an average cell size ranging from 20 nm to 84 nm and a relative density between 0.37 and 0.5. For benchmarking purposes, additional microcellular PMMA foams with an average cell size close to 1 μm and relative density close to that of the nanocellular foams are manufactured. Uniaxial compression tests and single edge notch bend tests are conducted on the PMMA foams. The measured Young's modulus and yield strength of the PMMA foams are independent of cell size whereas the fracture toughness of the PMMA foam increases with decreasing average cell size from the micron range to the nanometer range.

Keywords: Mechanical properties, nanocellular polymer, PMMA.

7. Introduction

Polymeric foams occupy a unique regime of material property space [1], and consequently are attractive candidates for a wide range of applications in the automotive,

aerospace, and construction industry [2]. Most commercially available polymeric foams are produced by liquid foaming process such as extrusion foaming or injection moulding. However, solid-state foaming or gas dissolution foaming can be employed to produce microcellular foams, of cell size on the order of 1 μm to 10 μm [3]. Microcellular foams offer a 10 % to 30 % weight reduction compared to conventional macrocellular foams of identical tensile strength and impact resistance and are used in niche applications such as the soles of running shoes and in automobile interior parts [4,5].

The continued development of solid-state foaming has allowed researchers to produce nanocellular foams, that is nanofoams, with an average cell size in the nanometric range [6,7]. It has been suggested that this relatively new class of porous polymers may exhibit superior mechanical and thermal properties per unit mass compared to micro- or macrocellular foams [8]. Both experimental and theoretical studies have confirmed the superior thermal insulation capability of nanocellular foams by exploitation of the Knudsen effect [9,10]. In contrast, only a few studies report the mechanical properties of nanocellular foams in comparison to microcellular and conventional macrocellular foams. Miller and Kumar performed uniaxial tensile tests on nanocellular and microcellular polyetherimide (PEI) foams of identical relative densities [11]. They found that PEI nanocellular foams have an increased tensile failure strength and failure strain compared to their microcellular counterparts, whereas the measured Young's modulus was independent of cell size. Sharudin and Ohshima [12] reported that the tensile yield strength of polypropylene-based (PP) nanocellular foams, of relative density 0.5-0.8, is close to that of the solid parent polymer; however, the tensile failure strain of the nanocellular foam was less than that of the solid polymer. Notario et al. [13] found the Charpy impact energy of a polymethyl methacrylate (PMMA) nanocellular foam exceeds that of a microcellular PMMA foam. They attributed this to the fact that the average size of the cell walls between the nano-sized cells is in the order of the size of the individual PMMA chains. Guo [14] conducted uniaxial tensile tests on polycarbonate (PC) nanocellular and microcellular foams and demonstrated that the Young's modulus and tensile ductility are independent of cell size, whereas the yield strength increases with diminishing cell size for a fixed value of relative density. Bernardo et al. [15] found that the Young's modulus, yield strength and fracture toughness of nanocellular composites made from PMMA and sepiolite particles were dependent upon the concentration and the dispersion of the particles, but independent of cell size.

In broad terms, data on the mechanical properties of nanocellular materials are limited. In particular, the mechanical properties of nanocellular PMMA of cell size below 50 nm have not yet been reported. In the present study, nanocellular PMMA foams are produced with an average cell size ranging from 20 nm to 84 nm and a relative density between 0.37 and 0.5. Additional microcellular PMMA foams are manufactured with relative densities close to the relative density of the nanocellular foams. Uniaxial compression and single edge notch bend tests are conducted on the nanocellular and microcellular foams to obtain the Young's modulus E, yield strength σ_y, and fracture toughness K_{Ic}. The dependence of E, σ_y, and K_{Ic} upon cell size and relative density is presented and discussed.

8. Materials and methods

8.1. Materials

Solid-state foaming experiments are conducted on three PMMA grades: V 825T, 7N, and 6N. V 825T was provided in the form of pellets from ALTUGLAS® International (Colombes, France), while 7N and 6N are provided in the form of pellets from PEXIGLAS® Evonik Industries (Essen, Germany). The three grades have a density ρ_s equal to 1 190 kg m^{-3} (as measured at 23 °C and at 50% relative humidity). The zero-shear viscosity η_0 (as measured by shear rheology, see section 2.4.4 below), and the glass transition temperature T_g (as measured by differential scanning calorimetry (DSC), see section 2.4.3 below) of the PMMA grades are summarized in **Table 1**. V 825T will be named as high viscosity PMMA (HV), 7N as medium viscosity (MV) and 6N as low viscosity PMMA (LV).

Table 1. Measured properties of the three PMMA grades used in this study.

Material	η_0 (Pa·s)	T_g (°C)
V 825T (HV)	7095	114.5
7N (MV)	3800	109.3
6N (LV)	1587	98.58

8.2. Production of the foaming precursors

The PMMA pellets were first dried at 80 °C for 4 hours to remove remnant moisture. Then, the pellets were made molten by heating them up to 250 °C in a hot press for 600 s. Next, the pellets were compacted at a pressure equal to 42 MPa and a temperature of 250 °C for 60 s. The resulting sheets were cooled to room temperature with the pressure of 42 MPa maintained. Cuboid-shaped foaming precursor samples of dimensions 68 x 13 x 4 mm^3 were machined from the compression moulded sheets.

8.3. Gas dissolution foaming experiments

Foaming experiments on the HV, MV and LV PMMA grades were performed using a pressure vessel (model PARR 4681) provided by Parr Instrument Company (Moline, IL, USA). The system has a pressure controller model SFT-10, provided by Parr Instrument Company (Moline, IL, USA) and a temperature controller (CAL 3300). Medical grade CO_2 (> 99.9% purity) was used as the blowing agent for the foaming tests. A two-step solid-state foaming process was employed, as detailed in Martín-de Leon et al. [16]. The precursor samples were held in the pressure vessel at a constant CO_2 saturation pressure p_{sat} equal to 31 MPa, and at a constant saturation temperature T_{sat} equal to 25℃ for 24 hours in order to ensure saturation of the CO_2 within the PMMA. Additional foaming tests were conducted by saturating the PMMA precursor samples in a pressure vessel (model PARR 4760), provided by Parr Instrument Company (Moline, IL, USA), and placed inside a freezer. Saturation experiments were done at constant T_{sat} ranging from -15 °C to -32 °C and a constant p_{sat} ranging from 6 MPa to 31 MPa. After saturation, the pressure was rapidly released to atmospheric pressure with an instantaneous pressure drop rate close

to 100 MPa s^{-1} for the samples saturated at T_{sat} = 25℃ and p_{sat} = 31 MPa, whereas a pressure drop rate of 10 MPa s^{-1} to 70 MPa s^{-1} for all other saturation conditions. The samples were then foamed in a hot press (Remtex, Barcelona) at a foaming temperature equal to 60℃ for a foaming time close to 60 s, resulting in flat foamed samples suitable for mechanical testing [17].

8.4. Characterization Techniques

8.4.1. Density

The density of the solid precursors ρ_s was measured through pycnometry using a gas pycnometer (Mod. AccuPyc II 1340, Micromeritics, Norcross, GA, USA). In contrast, the density of the foams ρ_f was measured with the water displacement-based density determination kit of an AT261 Mettler-Toledo balance. A surface layer of depth 200 μm was removed by polishing to ensure that the solid skin (of thickness well below 100 μm) was absent before the density measurements on the foams were made. All the testing, including the measurement of the mechanical properties, was performed in samples in which the solid skin was removed. The relative density of each sample ρ_r was determined via:

$$\rho_r = \frac{\rho_f}{\rho_s} \quad (1)$$

8.4.2. Cellular Structure

Foam samples were fractured in liquid nitrogen and coated with a layer of gold of 5 nm thickness by a sputter coater (model SDC 005, Balzers Union, Balzers, Liechtenstein). Micrographs of the coated fracture surfaces were obtained by a scanning electron microscope (QUANTA 200 FEG, Hillsboro, OR, USA). SEM micrographs were analysed by using a dedicated in-house software based on ImageJ/FIJI [18]. The cell size ϕ and the cell nucleation density N_0 (as calculated via the method of Kumar [19]) were measured for each foam sample. The homogeneity of the produced samples was determined by inspection of the SEM micrographs across the thickness of the cellular material. More than 200 cells were considered, from multiple micrographs per foam sample, to obtain quantitative values of the cellular structure characteristics.

8.4.3. Glass transition temperature

The glass transition temperature T_g of the as-foamed and solid samples was measured by differential scanning calorimetry DSC (Mettler DSC3 differential-scanning calorimeter). To achieve this, samples of mass 5 mg were machined from the foam blocks and heated from T = 20 ˚C to T = 160 ˚C at 0.17 ˚C s^{-1}. The value for T_g was identified as the mid-point of the observed transition on the heat flow versus temperature curve. The difference between the measured glass transition temperature $T_{g,f}$ of a foam sample made from a given PMMA grade and the measured glass transition temperature $T_{g,s}$ of the solid PMMA precursor of the same grade is written as:

$$\Delta T_g = T_{g,f} - T_{g,s} \quad (2)$$

8.4.4. Polymers Rheology

The zero-shear viscosity η_0 of the used polymers was measured by shear rheology in a stress-controlled rheometer, (AR 2000 EX from TA instruments). Solid cylindrical samples were prepared by compression moulding as explained in section 2.2. Dynamic shear viscosity measurements were performed with a parallel plates geometry of R = 25 mm and a fixed gap of h = 1 mm at a temperature of 230 °C in a nitrogen atmosphere. The angular frequency ω ranged between 0.01 $s^{-1}$and 100 s^{-1}, and measurements were conducted at a shear strain equal to 0.06. The value of the zero shear viscosity was taken as the value of the complex viscosity at low frequencies in the Newtonian plateau [20].

8.4.5. Open Cell Content

The open cell content of the foamed samples was measured by gas pycnometry (Mod. AccuPyc II 1340, Micromeritics) with nitrogen in accordance with the ASTM D6226-15 standard [22]. The open cell content ratio (O_v), is defined as the ratio of the volume of open cells to the total cell volume of a foam, and is given by:

$$O_v = \frac{V - V_p - V_s}{V(1 - \rho_r)} \quad (3)$$

where V is the geometric volume of the sample, as determined via the water-displacement method, V_p is the volume determined by the pycnometer and V_s corresponds to the value of the volume of the exposed cells at the surface of the sample; V_s is assumed to be negligible for the microcellular and nanocellular foams. The value for V_p is obtained via a pressure scan in the pycnometer from 0.2 MPa to 1.3 MPa. The resulting pycnometric volume versus pressure curve becomes close to independent of pressure when the open, interconnected pores in the foam are completely filled with gas. The pressure-independent value for the pycnometric volume is taken as V_p to calculate O_v via Eq. 3.

8.4.6. Mechanical tests

Uniaxial compression tests were conducted on the solid and foamed PMMA. Compression specimens of dimensions 10 x 10 x 4 mm^3 were machined from each foamed and solid sample. At least three compression tests are performed for each foamed sample and solid PMMA grade. The compression tests were conducted on a screw-driven test bench (Instron 5584 electromechanical testing machine) at room temperature. The samples were compressed in a direction perpendicularly to the compression moulding direction of the PMMA sheets prior to foaming and with a cross-head speed equal to 0.083 mm s^{-1}, resulting in a strain rate equal to 8.3 x 10^{-4} s^{-1} for all compression tests. The displacement of the material elements along the compression direction was measured with a laser extensometer.

Single edge notch three point bending (SENB) tests were performed at room temperature with a screw-driven test bench at a constant crosshead speed of 0.167 mm s-

[1]. Singe edge notch bend specimens were cuboids with in-plane dimensions 60 x 13.6 mm^2 and thickness close to 4 mm. A sharp pre-crack was made at the end of a sawed notch by tapping with a razor blade. At least 6 specimens were tested for each PMMA grade and each foamed sample. The critical mode I stress intensity factor K_{Ic} was calculated as a measure for the fracture toughness in accordance with the ASTM D5045-14 standard [21].

9. Results

9.1. Cellular materials characterization

A representative set of SEM micrographs of the nanocellular foams made from the three PMMA grades are shown in **Figure 1.** Additional micrographs for the microcellular foams are included**.** The foamed samples were found to have a homogeneous morphology.

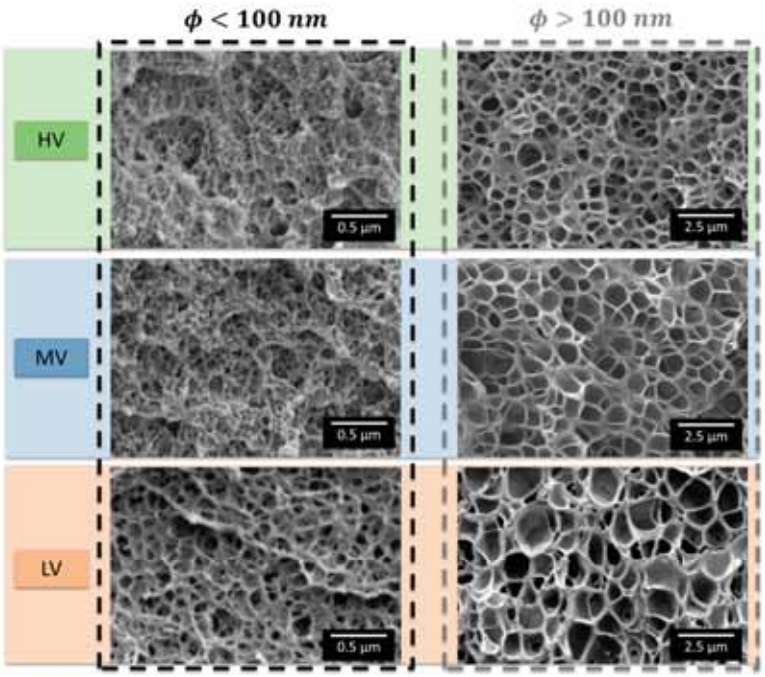

Figure 1. SEM micrographs showing the cellular structure of a selection of foamed PMMA samples. Saturation conditions of 10 MPa and -32 ˚C were used for the samples with cell sizes below 100 nm; 30 MPa and 24 ˚C were used for the samples with cell sizes above 100 nm.

The samples which were saturated at room temperature during the foaming tests resulted in foams with an average cell size exceeding 100 nm and with a cell nucleation density around 10^{12} to 10^{13} nuclei/cm^3, while saturation at temperatures below 0 ˚C resulted in nanocellular materials with an average void size below 100 nm and cell nucleation densities ranging 10^{15}-10^{16} nuclei/cm^3. These results are consistent with the observation of Martín-de León et al. [22] who found that saturation temperatures below 0 °C lead to a CO_2 solubility above 40 wt% and nanocellular materials with cell size close to 50 nm and cell nucleation density close to 10^{16} nuclei/cm^3. In contrast, saturating PMMA at room temperature with a CO_2 pressure equal to 30 MPa results in a CO_2 solubility close

to 31 wt%, and cellular materials with cell sizes above 100 nm [22,23]. The observed differences between the cellular materials made from the different PMMA grades when subjected to identical saturation and foaming conditions can be attributed to the different zero shear viscosity of the grades [22].

The measured average cell size ϕ of the produced nanocellular and microcellular foams is plotted as a function of the measured relative density ρ in **Figure 2.** Nanocellular foams with cell size between 20 nm and 84 nm and of relative density between 0.37 and 0.53 were produced from the three PMMA grades. In addition, microcellular foams of each grade were manufactured with an average cell size in the order of 1 μm and relative density close to the relative density of the nanocellular foams. Contours of equal values for the open cell content are included in the cell size versus relative density plot shown in **Figure 2a.** The microcellular foams are predominantly closed-celled in nature in within the explored range of relative densities in this study, whereas the nanocellular foams are open-celled. In addition, contours of equal values for the difference in glass transition temperature ΔT_g are plotted on the cell size versus relative density diagram shown in **Figure 2b.** The value of ΔT_g increases with decreasing value of cell size and, as demonstrated by Martin-de León [23], the value of ΔT_g may be used as a measure for the confinement of the solid material separating the micro- or nano-sized voids.

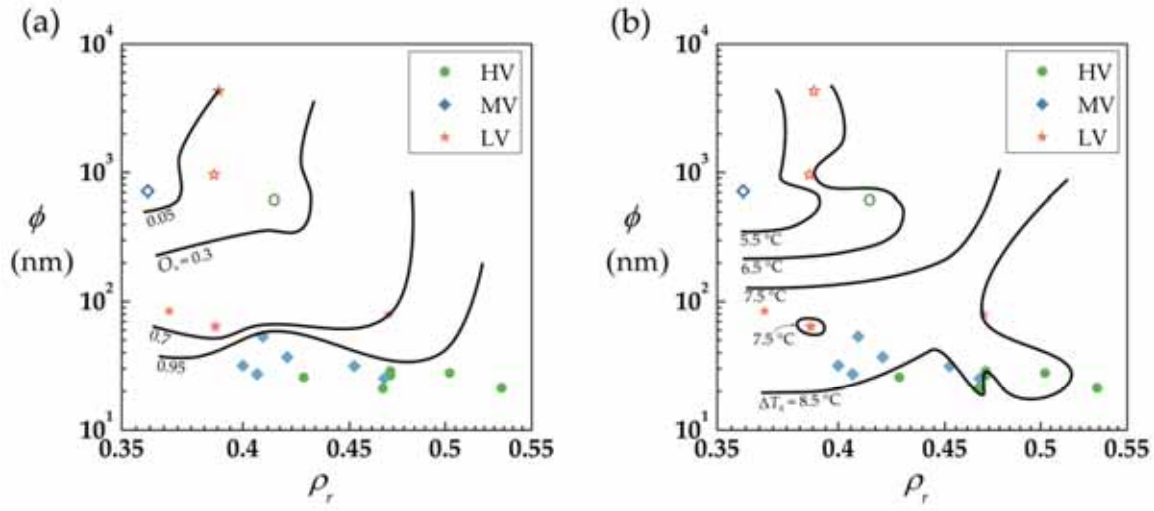

Figure 2. The measured average cell size versus the measured relative density of the PMMA foams with contours for (a) the value of the open cell content O_v and for (b) the value of the the difference in glass transition temperature ΔT_g, as defined in Eq. (2). The closed symbols refer to the nano-cellular foams, whereas the open symbols denote the microcellular foams. (The contourplots were constructed via the griddata and contour functions in Matlab).

9.2. Mechanical properties

3.2.1 Stress-strain curves

A nominal stress σ_n versus nominal strain ε_n curve for the solid PMMA HV in uniaxial compression is shown in **Figure 3**. Representative σ_n - ε_n curves for the microcellular and nanocellular HV foams of close to identical relative density are included in **Figure 3.**

The structural response of the solid and foamed samples of the three grades is similar. There is an initial linear, elastic region until the yield point, after which a small degree of softening occurs [24]. Softening is followed by a plateau in stress and subsequent hardening [1]. The compression tests were terminated at a nominal strain close to 0.4; no specimen failure was observed prior to completion of the tests. The elastic modulus E was calculated from the slope of the initial linear region, while the compressive yield strength σ_y was deduced from the peak load before the plateau in stress is observed.

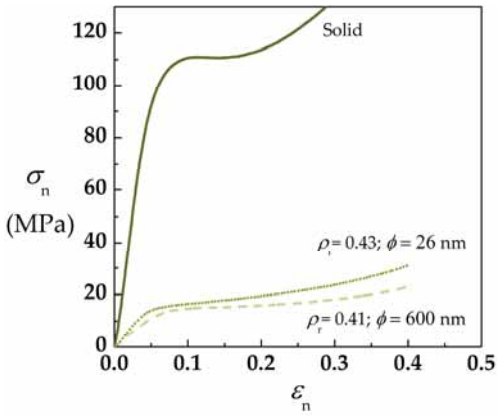

Figure 3. A representative set of nominal stress versus nominal strain curves for the V825T solid and the foamed PMMA. Experiments were terminated at a nominal strain close to 0.4.

9.2.1. Mechanical properties of the solid PMMA grades

The Young's modulus of the solid PMMA grades was found to be close to 2.2 GPa (and observed to be independent of material grade). The value for the fracture toughness, as obtained via the SENB tests, is plotted versus the measured value of the yield strength in **Figure 4.**

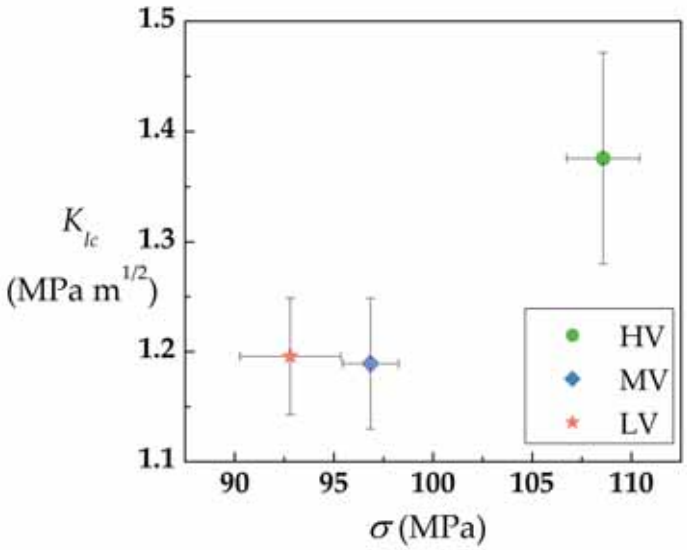

Figure 4. The measured fracture toughness versus yield strength of the three PMMA grades. The error bars correspond to an uncertainty level of one standard deviation.

The value for the yield strength and the fracture toughness of the MV and LV grades are close to identical, whereas the yield strength (and fracture toughness) of the HV grade was found to be close to 20 % higher than that of the MV and LV grades. This may be attributed to the measured higher glass transition temperature of the HV grade compared to the MV and LV grades, see **Table 1** [24].

9.2.2. Mechanical properties of the PMMA foams

The measured values of E, σ_y, and K_{Ic} for each foamed sample made from a given PMMA grade were normalised with respect to the values for E, σ_y, and K_{Ic} of the solid materials of the same grade:

$$E_r = \frac{E_f}{E_s} \tag{4}$$

$$\sigma_{y,r} = \frac{\sigma_{y,f}}{\sigma_{y,s}} \tag{5}$$

$$K_{Ic,r} = \frac{K_{Ic,f}}{K_{Ic,s}} \tag{6}$$

where $E_r, \sigma_{y,r}$ *and* $K_{Ic,r}$ are the relative young modulus, yield strength and fracture toughness of a foam respectively, $E_f, \sigma_{y,f}$ *and* $K_{Ic,f}$ are the measured properties of the foams and $E_s, \sigma_{y,s}$ *and* $K_{Ic,s}$ are the properties of the solid PMMA.

The measured values for the relative modulus E_r and for the relative yield strength σ_y of the nanocellular and microcellular PMMA foams are plotted as a function of the measured relative density in **Figs. 5a** and **5b**, respectively. The values of E_r and σ_y are found to be independent of cell size within the explored range of relative density and cell size.

According to the model of Gibson and Ashby, the relative modulus of open-celled foams scales with the relative density as follows [25]:

$$E_r = C_1 \rho_r^2 \tag{7}$$

Gibson and Ashby fitted Eq. 7 to data for open-celled polymeric foams in the literature and suggested that the value for the fitting constant C_1 equals unity. The E_r versus ρ_r curve predicted by Eq. (7) is plotted in **Figure 5a** assuming $C_1 = 1$. The slope of the curve predicted by Eq. (7) corresponds to the slope of the measured E_r versus ρ_r curve. Equation (7) is fitted to the measured E_r versus ρ_r curve, resulting in $C_1 = 0.7$. The predicted E_r versus ρ_r curve by Eq. (7) with $C_1 = 0.7$ is included in **Figure 5a.**

Likewise, the relative yield strength of open-celled foams scales with the relative density as follows [25]:

$$\sigma_{y,r} = C_2 \rho_r^{\frac{3}{2}} \quad (8)$$

where C_2 is a constant of proportionality equal to 0.3 as suggested by Gibson and Ashby. The predicted $\sigma_{y,r}$ versus ρ_r curve by Eq. (8) by assuming $C_2 = 0.3$ is shown in **Figure 5b**. Again, the slope of the $\sigma_{y,r}$ versus ρ_r predicted by Eq. (8) is in agreement with the slope of the measured $\sigma_{y,r}$ versus ρ_r curve. Equation (8) is fitted to the measured $\sigma_{y,r}$ data, resulting in $C_2 = 0.47$. The predicted $\sigma_{y,r}$versus ρ_r curve by Eq. (8) with $C_2 = 47$ is included in **Figure 5.**

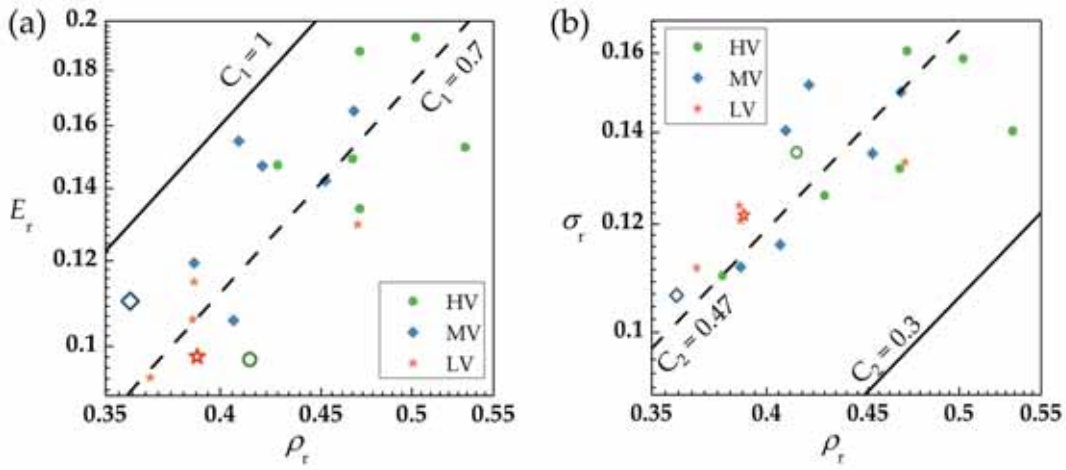

Figure 5 (a) The measured relative Young's modulus E_r as a function of the relative density ρ_r and(**b)** the measured relative yield strength σ_y as a function of the relative density. The closed symbols refer to the nanocellular foams (ϕ < 100 nm), whereas the open symbols refer to the microcellular foams (ϕ > 100 nm). The predicted E_r versus ρ_r curve by Eq. (7) is plotted in (a) with $C_1 = 1$ (solid line) and $C_1 = 0.7$ (dashed line). The $\sigma_{y,r}$ versus ρ_r curve predicted by Eq. (8) is included in (b) with $C_1 = 0.3$ (solid line) and $C_2 = 0.47$ (dashed line).

The measured relative fracture toughness $K_{Ic,r}$ of the nanocellular and microcellular PMMA foams is plotted as a function of the measured relative density in **Figure 6a.** The measured values for $K_{Ic,r}$ of the microcellular foams are lower than those of the nanocellular foams with close to identical relative density. Hence, we deduce that, within the explored range of relative density, the relative fracture toughness increases when the average cell size of the PMMA foams decreases from the micro-sized range to the nano-sized range: a cell size effect is observed.

The model of Maiti and Ashby [26] may be used to predict the normalised fracture toughness of open-celled foams as a function of relative density:

$$\overline{K}_{Ic} = \frac{K_{Ic}}{\sigma_{y,s}\sqrt{\pi\phi}} = C_3 \rho_r^{\frac{3}{2}} \quad (9)$$

where C_3 is equal to 0.65 according to the work of Maiti and Ashby [26]. The measured values for the normalised fracture toughness of the PMMA foams is shown in **Fig 6b**.

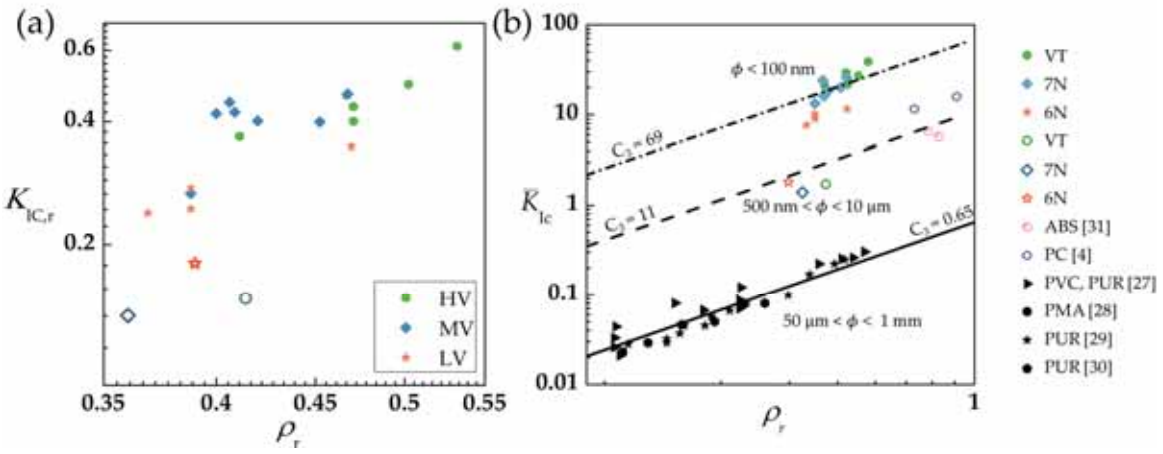

Figure 6. (a) The measured relative fracture toughness $K_{Ic,r}$ as a function of the relative density ρ_r. The closed symbols refer to the nanocellular foams (ϕ < 100 nm), whereas the open symbols refer to the microcellular foams (ϕ > 100 nm). (b) The measured normalised fracture toughness $\overline{K}_{Ic}$ as a function of relative density. Reported values for $\overline{K}_{Ic}$ for macrocellular and microcellar foams in the literature are plotted as a function of relative density. The curves predicted by Eq. (9) are included for selected values of C_3.

Reported values for $\overline{K}_{Ic}$ in the literature for macrocellular and microcellular polymeric foams are plotted as a function of relative density in **Figure 6b** [4,27–31]. The $\overline{K}_{Ic}$ versus ρ_r curve of the macrocellular data is well approximated by Eq. (9) taking $C_3 = 0.65$. The slope of the nanocellular and microcellular $\overline{K}_{Ic}$ versus ρ_r curve is in agreement with the slope predicted by Eq. 9. As a result of the observed cell size effect, the value for C_3 is found to be a function of cell size: the measured $\overline{K}_{Ic}$ versus ρ_r curve for the microcellular and nanocellular PMMA foams is predicted with reasonable accuracy via Eq. (9) by assuming $C_3 = 11$ and $C_3 = 69$, respectively.

10. Conclusions

Nanocellular and microcellular foams are manufactured from three different grades of PMMA via the solid-state foaming route. The relative density of the foams ranges between 0.37 and 0.5. Uniaxial compression tests and single edge notch bend tests are conducted on the foams and the solid PMMA. The measured values of the Young's modulus, yield strength, and fracture toughness of the foams were normalised with respect to the measured values of the solid PMMA grades. The relative fracture toughness was found to be dependent upon cell size: the relative fracture toughness of a foam of a given relative density increases when the average void size decreases from the micro-sized range to the nano-sized range. In contrast, no dependence of the relative Young's modulus and the relative yield strength upon cell size was observed within the explored range of relative density and cell size.

Acknowledgements

Financial assistance from MINECO, FEDER, UE (MAT2015-69234-R), the Junta of Castile and Leon (VA275P18) and Spanish Ministry of Science, Innovation and Universities (RTI2018-098749-B-I00) are gratefully acknowledged. Financial support from FPU grant

FPU14/02050 (V. Bernardo) from the Spanish Ministry of Education and Junta of Castile and Leon grant (J. Martín-de León) are gratefully acknowledged

11. References

[1] Gibson, L. J.; Ashby, M. F. *Cellular solids: Structure and Properties*; 2nd ed.; Cambridge: Cambridge University Press.: United States, **1997**.

[2] Buist, J. M. Cellular Polymers. In *Fire and Cellular Polymers*; Springer, Dordrecht, **1986**; pp. 5–23.

[3] Kumar, V.; Suh, N. P. A process for making microcellular parts. *Polymer Engineering & Science* **1990**, *30*, 1323–1329.

[4] Bureau, M. N. Fracture Toughness of High Density Polycarbonate Microcellular Foams. *Journal of Cellular Plastics* **2006**, *42*, 229–240.

[5] Sun, H.; Sur, G.; Mark, J. Microcellular foams from polyethersulfone and polyphenylsulfonePreparation and mechanical properties. *European Polymer Journal* **2002**, *38*, 2373–2381.

[6] Costeux, S.; Jeon, M. H.; Bunker, T. S.; Khan, I. NANOCELLULAR FOAMS FROM ACRYLIC POLYMERS : EXPERIMENTS AND MODELING. *FOAMS 2012 Conference* **2012**, 1–6.

[7] Notario, B.; Pinto, J.; Rodriguez-Perez, M. A. Nanoporous polymeric materials: A new class of materials with enhanced properties. *Progress in Materials Science* **2016**, *78–79*, 93–139.

[8] Schmidt, D.; Raman, V. I.; Egger, C.; du Fresne, C.; Schädler, V. Templated cross-linking reactions for designing nanoporous materials. *Materials Science and Engineering: C* **2007**, *27*, 1487–1490.

[9] Wang, G.; Wang, C.; Zhao, J.; Wang, G.; Park, C. B.; Zhao, G. Modelling of thermal transport through a nanocellular polymer foam: Toward the generation of a new superinsulating material. *Nanoscale* **2017**, *9*, 5996–6009.

[10] Notario, B.; Pinto, J.; Solorzano, E.; De Saja, J. A.; Dumon, M.; Rodriguez-Perez, M. A. Experimental validation of the Knudsen effect in nanocellular polymeric foams. *Polymer (United Kingdom)* **2015**, *56*, 57–67.

[11] Nadella, K.; Kumar, V. Tensile and flexural properties of solid-state microcellular ABS panels. *Experimental Analysis of Nano and Engineering* **2007**, *22*, 765–766.

[12] Sharudin, R. W. B.; Ohshima, M. CO2-Induced Mechanical Reinforcement of Polyolefin-Based Nanocellular Foams. *Macromolecular Materials and Engineering* **2011**, *296*, 1046–1054.

[13] Notario, B.; Pinto, J.; Rodriguez-Perez, M. a. Towards a new generation of polymeric foams: PMMA nanocellular foams with enhanced physical properties. *Polymer* **2015**, *63*, 116–126.

[14] Guo, H. Solid-state Polymer Nanofoams, **2015**.

[15] Bernardo, V.; Martín-de León, J.; Laguna-Gutiérrez, E.; Rodríguez-Pérez, M. Á. PMMA-sepiolite nanocomposites as new promising materials for the production of nanocellular polymers. *European Polymer Journal* **2017**, *96*, 10–26.

[16] Martín-de León, J.; Bernardo, V.; Rodríguez-Pérez, M. Á. Low density nanocellular polymers based on PMMA produced by gas dissolution foaming: Fabrication and cellular structure characterization. *Polymers* **2016**, *8*, 265.

[17] Martín-de León, J.; Bernardo, V.; Cimavilla-román, P.; Angel, M. Overcoming the Challenge of Producing Large and Flat Nanocellular Polymers : A Study with PMMA l P. **2019**, *1900148*, 1–8.

[18] Pinto, J.; Solorzano, E.; Rodriguez-Perez, M. a.; de Saja, J. a. Characterization of the cellular structure based on user-interactive image analysis procedures. *Journal of Cellular Plastics* **2013**, *49*, 555–575.

[19] Kumar, V.; Suh, N. P. A process for making microcellular thermoplastic parts. *Polymer Engineering and Science* **1990**, *30*, 1323–1329.

[20] Laguna-Gutierrez, E.; Van Hooghten, R.; Moldenaers, P.; Angel Rodriguez-Perez, M. Effects of extrusion process, type and content of clays, and foaming process on the clay exfoliation in HMS PP composites. *Journal of Applied Polymer Science* **2015**, *132*, 1–12.

[21] International, A. D5045 − 14. Standard Test Methods for Plane-Strain Fracture Toughness and Strain Energy Release Rate of Plastic Materials.

[22] León, J. M.; Bernardo, V.; Laguna-gutiérrez, E.; Rodríguez-pérez, M. Á. Influence of the rheological behaviour of PMMA on the cellular structure of nanocellular materials. *Paper sent* 1–16.

[23] Martín-de León, J.; Bernardo, V.; Rodríguez-Pérez, M. ángel Low density nanocellular polymers based on PMMA produced by gas dissolution foaming: Fabrication and cellular structure characterization. *Polymers* **2016**, *8*.

[24] Van Loock, F.; Fleck, N. A. Deformation and failure maps for PMMA in uniaxial tension. *Polymer* **2018**, *148*, 259–268.

[25] Ashby, M. F.; Medalist, R. F. M. The mechanical properties of cellular solids. *Metallurgical Transactions A* **2007**, *14*, 1755–1769.

[26] Maiti, S. K.; Ashby, M. F.; Gibson, L. J. Fracture toughness of brittle cellular solids. *Scripta Metallurgica* **1984**, *18*, 213–217.

[27] Kabir, M. E.; Saha, M. C.; Jeelani, S. Tensile and fracture behavior of polymer foams. *Materials Science and Engineering: A* **2006**, *429*, 225–235.

[28] Maiti, S. K.; Ashby, M. F.; Gibson, L. J. Fracture toughness of brittle cellular solids. **1984**, *18*, 213–217.

[29] McIntyre, A.; Anderton, G. E. Fracture properties of a rigid polyurethane foam over a range of densities. *Polymer* **1979**, *20*, 247–253.

[30] Fowlkes, C. W. Fracture toughness tests of a rigid polyurethane foam. *International Journal of Fracture* **1974**, *10*, 99–108.

[31] Gómez-Monterde, J.; Schulte, M.; Ilijevic, S.; Hain, J.; Sánchez-Soto, M.; Santana, O. O.; Maspoch, M. L. Effect of microcellular foaming on the fracture behavior of ABS polymer. *Journal of Applied Polymer Science* **2016**, *133*, 1–10.

8.4. Thermal conductivity

8.4.1. Cellular materials characteristics

Several nanocellular materials were produced to characterize its thermal conductivity. All of them were produced from solid precursors with 4 mm in thickness obtained as detailed in chapter 3 section 3.3.1. The characteristics of those cellular materials are presented in **Table 8.1.** As it can be seen, three different ranges of cell sizes have been produced for thermal conductivity measurements.

Thus, microcellular materials (HV[1]) with cell sizes around 20 μm have been produced using saturation pressures of 10 MPa and saturation temperatures of 24 ºC. Moreover, two different sets of nanocellular PMMA were used. On the one hand, materials with cell sizes around 225 nm were produced (HV[2]) following the route explained in paper 3 (P3). On the other hand, materials produced for testing the mechanical properties, with cell sizes below 50 nm (HV[3] and MV[3]) have been used herein. The production method of these materials are explained in P8 section 2.3.

Table 8.1. Characteristics of the cellular materials used for the thermal conductivity measurements. The foaming time was 1 minute for all the samples.

Material	P_{sat} (MPa)	T_{sat} (°C)	T_f (°C)	ρ_r	ϕ (nm)	N_0 $(nuclei/cm^3)$
HV[1]	10	24	60	0.427	16570	$5.55{\cdot}10^{8}$
HV[1]	10	24	80	0.414	18350	$4.08{\cdot}10^{8}$
HV[1]	10	24	100	0.297	19710	$7.07{\cdot}10^{8}$
HV[1]	10	24	100	0.267	19940	$6.22{\cdot}10^{8}$
HV[1]	10	24	100	0.210	25880	$3.92E{\cdot}10^{8}$
HV[2]	31	24	40	0.407	224.6	$2.00{\cdot}10^{14}$
HV[2]	31	24	60	0.336	221	$2.34{\cdot}10^{14}$
HV[2]	31	24	80	0.273	227	$3.15{\cdot}10^{14}$
HV[2]	31	28	80	0.220	387	$1.14{\cdot}10^{14}$
HV[3]	20	-32	60*	0.427	26	$1.65{\cdot}10^{16}$
HV[3]	10	-32	60*	0.509	28	$1.34{\cdot}10^{16}$
MV[3]	6	-15	60*	0.35	53	$4.06{\cdot}10^{15}$
MV[3]	6	-32	60*	0.443	31	$1.06{\cdot}10^{16}$
MV[3]	10	-32	60*	0.398	37	$3.93{\cdot}10^{15}$
MV[3]	20	-32	60*	0.463	25	$1.84{\cdot}10^{16}$

*Samples foamed in the hot press as explained in P5 section 2.3.

Additionally, relative densities from 0.2 to 0.5 were achieved thanks to the modification of the foaming parameters.

8.4.2. Thermal conductivity measurements

Thermal conductivity measurements at ambient conditions were carried out in a thermal conductivity equipment TPS 2500 S, as explained in Chapter 3 section 3.4.9. Obtained results are presented in **Figure 8.1.** It is important to indicate here that the data

given by this equipment, based on the transient plane source method (TPS), can be used to establish a relative comparison between the materials, but they cannot be considered as absolute values. It is known that in general, the TPS approach over-estimates the thermal conductivity of thermal insulating materials.

For a constant relative density, when decreasing the cell size from the micro to the nanoscale cellular materials reduce their thermal conductivity as expected. Thus materials with cell sizes around 225 nm present a clear reduction with respect microcellular ones. This reduction is enhanced when the cell size drops below 50 nm (**Figure 8.1b**).

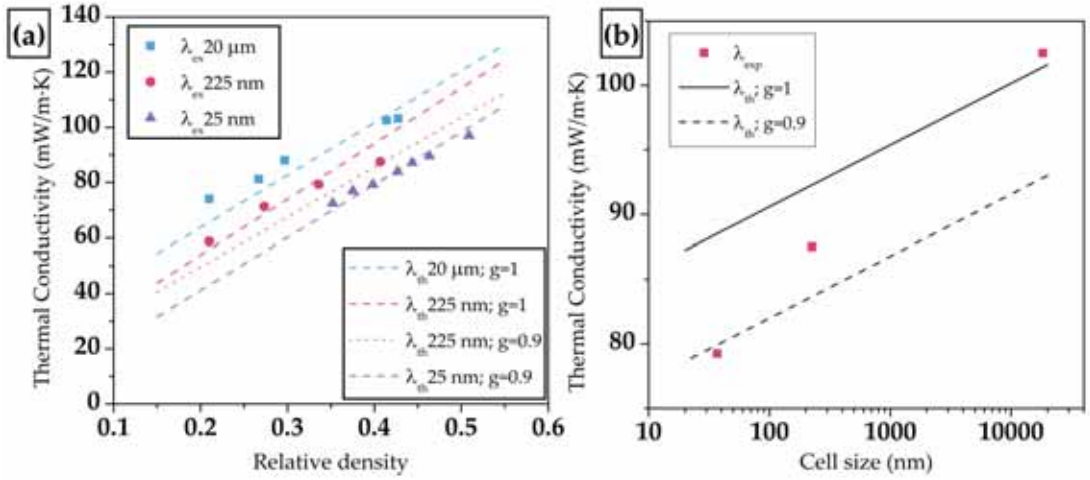

Figure 8.1. a) Experimental and theoretical thermal conductivities of the samples showed in **table 8.1**. **b)** Experimental and theoretical thermal conductivities for a constant relative density of 0.4.

To understand where those differences come from the theoretical conductivity was calculated through the following equation:

$$\lambda_t = \lambda_g + \lambda_s + \lambda_c + \lambda_r \tag{8.1}$$

As explained in Chapter 2 section 2.5.2, convection inside the pores (λ_c) can be neglected for cells smaller than 2 mm. On the other hand, for relative densities higher than 0.2, the radiation term can also be neglected. So, taking into account the Ashby´s model and considering the Knudsen effect, the conductivity for nanocellular materials can be obtained from equation 8.2 (as already explained in Chapter 2 section 2.5.2):

$$\lambda_t = \lambda_g + \lambda_s = g\lambda'_s\left(1 - V_g\right) + \lambda'_g V_g \tag{8.2}$$

$$\lambda'_g = \frac{\lambda'_{g0} V_g}{(1 + 2\beta k_n)} \tag{8.3}$$

where λ'_{g0} is the thermal conductivity of the gas (26 mW/m·K for air at room temperature and atmospheric pressure), β is a parameter that considers the energy transfer when a gas

molecule collides with the solid phase (about 1.64 for air) and l_g is the mean free path of the gas molecules (70 nm for air at room temperature) and finally ϕ is the cell size.

When data fit with a factor g=1, it can be asserted that the reduction in the thermal conductivity is justified by the confinement of the gas phase inside the cells, it means the Knudsen effect. However, when the cell size is reduced, the structural factor should be reduced up to 0.9 in order to obtain a good agreement between experimental and theoretical values (see **Figure 8.1b**).

Therefore, these measurements support the fact of a double contribution in the reduction in thermal conductivity, the first one due to the confinement in the gaseous phase and a second one attributed to the confinement in the solid phase as previously discussed in the bibliography.

Chapter 9

Conclusions and future work

"Son tiempos difíciles para los soñadores."

Amélie

INDEX

9.1. Conclusions

After presenting the obtained results (chapter 4 to chapter 8), chapter 9 collects the main conclusions extracted from each of those. Then, a section explaining the conclusions about the foaming mechanisms has been added. The obtained data are also compared with those of the literature in section 9.3, and finally, some ideas about the future work are included in section 9.4.

9.1.1. Chapter 4

Chapter 4 focused on measuring how saturation process takes place and on analyzing the influence of saturation and depressurization parameters on the cellular structure of nanocellular PMMA produced through homogeneous nucleation, as it is shown in **Figure 9.1**.

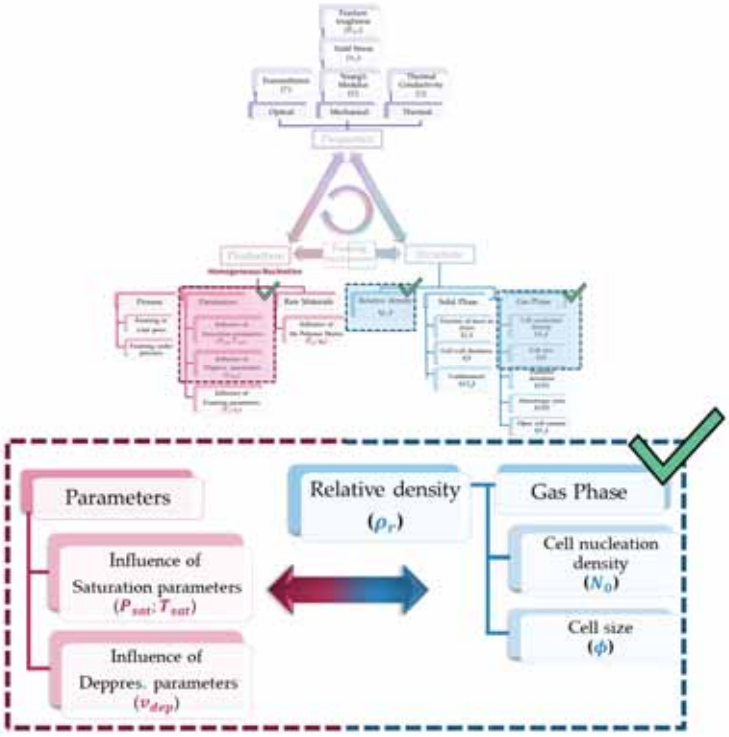

Figure 9.1. Main objectives of Chapter 4.

This analysis was carried out by means of two scientific papers; the first one (P1[1]) presents an innovative set-up for monitoring gas diffusion process through neutron radiography and tomography. The main findings and conclusions extracted from this study are as follows:

⇒ **Diffusion experiments** of gas under high pressures atmospheres (up to 20 MPa) **can be monitored through neutron tomography (Figure 9.2) and radiography** being possible to determine:

- In-situ solubility curves of CO_2 in PMMA and PS through a developed calibration method.

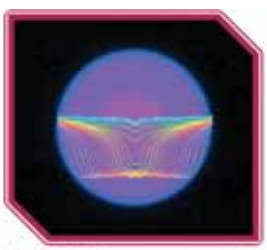

Figure 9.2. Neutron tomography of CO_2 diffusion in PMMA.

- In-situ swelling curves of PMMA by monitoring the morphological changes of the polymer.
- The temporal evolution of the gas diffusion profile in PMMA (**Figure 9.2**).
- The sorption diffusivity and saturation times.

⇒ Solubility of CO_2 in PMMA:
- Increases with the saturation pressure by following a dual law for saturation pressures from 10 to 20 MPa and 40°C of saturation temperature.
- Decreases with an increase of the saturation temperature, when saturating at 15 MPa and 40 and 60 °C, according to an Arrhenius type equation.

⇒ Sorption diffusivity of CO_2 in PMMA:
- Increases with the saturation pressure for saturation pressures from 10 to 20 MPa and 40 °C of saturation temperature, by following a grade 2 polynomial function.
- Increases with the saturation temperature by following an Arrhenius type equation (working at 15 MPa and 40 and 60 °C of saturation conditions).

⇒ During sorption experiments PMMA suffers a volume increment known as swelling that:
- Increases with the solubility and the foaming temperature.
- The increment of volume is between 24 and 30 % when working at pressures from 10 to 20 MPa and temperatures from 40 to 60 °C.

The second scientific paper (P2 [2]) aims at relating changes in the saturation parameters with the obtained cellular structure, leading to the following conclusions:

⇒ A decrease in the saturation temperature from 24 °C to -32 °C (and saturation pressures of 31 MPa and 6 MPa respectively) leads to an increase in the solubility of CO_2 in PMMA from 31 wt. % to 39 wt. %.

⇒ By maintaining constant the saturation temperature in -32 °C, an increase in the saturation pressure from 6 MPa to 20 MPa leads to rising on the solubility of CO_2 in PMMA from 39 to 48 wt.%.

⇒ This solubility increase leads to a significant increase in the cell nucleation density and a decrease in the cell size:
- Solubilities of 48 wt.% of CO_2 allows the production of nanocellular PMMA with a cell nucleation density of $7 \cdot 10^{16}$ nuclei/cm^3 and a cell size of 14 nm. The relative density of these materials is 0.4.

⇒ The decrease of the cell size below 50 nm leads to **the first semi-transparent nanocellular polymers ever reported** (**Figure 9.3**):
- Decreasing the cell size from 40 nm to 14 nm leads to higher transparency.

Figure 9.3. Transparent PMMA

The influence of the depressurization parameters was also studied in this chapter, including some experiments on this topic. The following conclusions were obtained:

⇒ By fixing the saturation parameters in 31 MPa and 24 °C, the foaming parameters in 25 °C and 5 minutes, an increment in the depressurization velocity leads to improved cellular structures:

- A depressurization drop rate of 98 Pa/s in comparison with 22 and 17 MPa/s produce smaller cell sizes (218 nm in comparison with 237 and 250 nm), higher cell nucleation densities ($1.6 \cdot 10^{14}$ nuclei/cm^3 in comparison with $1.3 \cdot 10^{14}$ and $1.2 \cdot 10^{14}$ nuclei/cm^3).

9.1.2. Chapter 5

Chapter five aimed at completing the study about the impact of the production parameters on the cellular structure. In this chapter, it was analyzed the effect of the foaming conditions (foaming temperature and foaming time). An in-deep analysis of the cellular structure was carried out, leading to an understanding of the foaming mechanisms responsible for the measured changes (**Figure 9.4**).

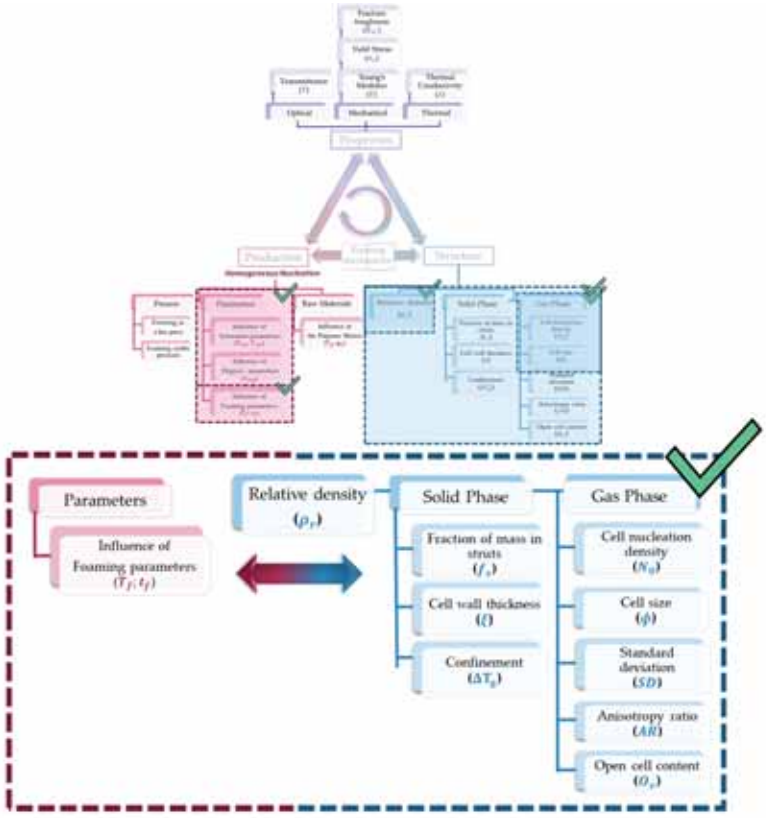

Figure 9.4. Main Objectives of Chapter 5.

The results were presented in a scientific article (P3 [3]) whose main findings are listed as follows:

⇒ While using a saturation pressure of 31 MPa and a saturation temperature of 24 °C in PMMA (obtaining a solubility of 31 wt.% of CO_2), an increase in the foaming

temperature from 40 °C to 100 °C leads to the following changes in the cellular structure:

- An increase in the cell nucleation density from $2 \cdot 10^{14}$ nuclei/cm^3 when foaming at 40 °C to almost $4 \cdot 10^{14}$ nuclei/cm^3 when foaming at 100 °C.
- Almost any changes in the cell size, obtaining values around 225 nm for all the produced materials.
- A reduction in the relative density from values around 0.4 for the lowest foaming temperature to values as low as 0.24 when foaming at 100°C.

⇒ 110 °C of foaming temperature is the limit temperature for the production of nanocellular PMMA with those saturation conditions (using the PMMA grade of this paper, HV material): degeneration mechanisms appear when foaming at this temperature for 5 minutes, observing a decrease in the cell size up to 184 nm and an increase in the relative density up to 0.54.

⇒ An increase in the foaming time from 1 to 5 minutes has the same effect that an increase in the foaming temperature. For example, when using a foaming temperature of 40 °C an increase of the foaming time from 1 to 5 minutes results in a reduction of the relative density from 0.47 to 0.37, an increase in the cell nucleation density from $1.8 \cdot 10^{14}$ nuclei/cm^3 to $2.2 \cdot 10^{14}$ nuclei/cm^3 while the cell size is almost constant ranging between 212 and 225 nm.

⇒ The reduction of the relative density results in additional changes in the cellular structure of nanocellular PMMA:

- The open cell content increases with the decrease of the relative density. Completely connected cellular structures are produced for relative densities smaller than 0.3.
- While the cell wall thickness remains constant, around 25 nm, for all the produced materials, **the fraction of mass in struts (Figure 9.5), firstly determined for nanocellular materials, is reduced as relative density becomes smaller.**

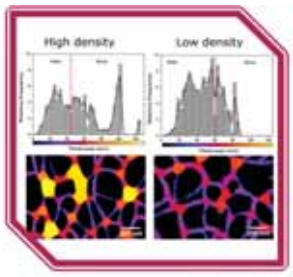

Figure 9.5. Technique to measure fraction of mass in struts.

⇒ The analysis of the obtained results allowed obtaining a better understanding of the foaming mechanisms:

- Relative density reduction is a consequence of cell nucleation density increase. The density is halved when increasing the temperature from 40 °C to 100 °C because cell nucleation density doubles while cell size remains constant.
- Relative density is no longer reduced below 0.24, probably because a further reduction in density is stopped by the opening of the cellular structure. No further reduction of relative density below 0.24 is achieved due to the gas diffusing out through the completely open cells, stopping the growing.
- The reduction of the fraction of mass in struts as a result of the decrease in relative density involves an increase in the solid confinement of nanocellular

PMMA. This confinement is quantified through the increment in the glass transition temperature in comparison with that of the solid precursor used for foaming, and it reaches 11 °C for the materials presenting the lowest relative densities.

9.1.3. Chapter 6

Once the influence of the production parameters on the cellular structure of PMMA has been studied in chapters 4 and 5, the impact of changing the properties of the used polymeric matrix was explored in Chapter 6 (**Figure 9.6**).

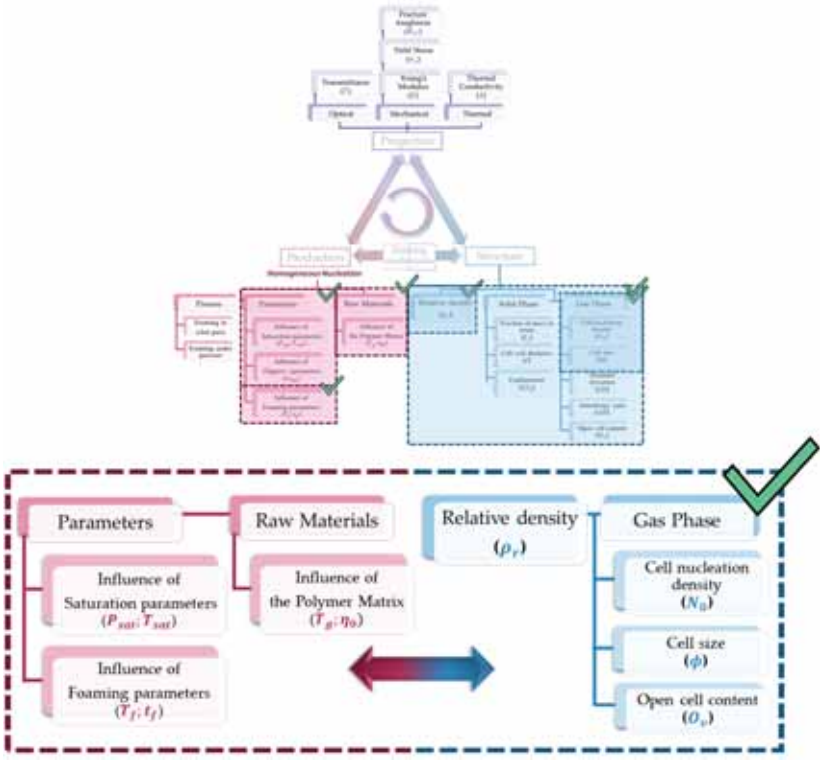

Figure 9.6. Main objective of Chapter 6.

The findings were presented in the form of a scientific article (P4 [4]) where three different PMMA grades with different viscosities from 1587 Pa·s to 7095 Pa·s and different glass transition temperatures from 99 °C to 114 °C were used. At the same time, the production process parameters were also modified.

The work developed in this chapter leads to the following conclusions:

⇒ Solubility is highly influenced by the process parameters and the used polymer matrix:

- A smaller viscosity of the polymer and/or a lower glass transition temperature matrix leads to higher solubilities, especially when saturating at room temperature.
- When using saturation conditions of 31 MPa and 24 °C solubilities range from 31 wt.% for the more viscous polymer to 36 wt.% for the less viscous one. When changing the saturation conditions to 20 MPa and -32 °C, solubilities raises to

values around 45 wt.% for all the polymers, being the differences between them reduced.

⇒ Desorption diffusivity increases with solubility independently on the polymer viscosity from values around $7 \cdot 10^{-8}$ cm^2/s to values around $2 \cdot 10^{-7}$ cm^2/s.

⇒ The cellular structure is strongly affected by the solubility resulting in the same tendencies independently on the polymer viscosity:

- Cell nucleation density increases in two orders of magnitude when solubility changes from the smallest to the highest value.
  - For HV PMMA and MV PMMA cell nucleation density increases from 10^{14} nuclei/cm^3 to 10^{16} nuclei/cm^3 when solubility goes from 31 % to around 45 wt.%.
  - For LV PMMA cell nucleation density increases from 10^{13} nuclei/cm^3 to 10^{16} nuclei/cm^3 when solubility rises from 36 wt.% to around 44 wt.%.
- Cell size is divided by ten, going from the hundreds of nanometers to the tens of nanometers when solubility changes from the smallest to the highest value.
- It is difficult to decrease the relative density when solubility increases.
- Open cell content increases with solubility up to reach completely connected cellular structures.
  - For the two polymers with the higher viscosity, this takes place for solubilities above 38%.
  - The cellular structure of the less viscous material opens more gradually. Thus, interconnectivity is 20% when solubility is 36 wt.%, around 50% when solubility rises to 40 wt.% until reaching values of near 80% when solubility is 44 wt.%.

⇒ Foaming parameters modify the cellular structure similarly regardless of the viscosity and the solubility:

- An increase in the foaming temperature from 25 °C to 80 °C reduces the relative density.
  - For PMMA grade HV with 31 wt.% of gas, relative density reduces from 0.5 to 0.3 when increasing the foaming temperature from 25 to 80 °C. While with around 45 wt.% of CO_2 relative density decreases from 0.55 to 0.38.
  - For PMMA grade LV with 36 wt.% of gas, relative density reduces from 0.3 to 0.2 when increasing the foaming temperature from 25 to 80 °C. While with around 45 wt.% of CO_2 relative density decreases from 0.45 to 0.35.
- Cell nucleation density increases while cell size remains constant when the foaming temperature becomes higher.
  - For PMMA grade HV with 31 wt.% of gas CO_2 cell nucleation density increases from $1.7 \cdot 10^{14}$ nuclei/cm^3 to $3.6 \cdot 10^{14}$ nuclei/cm^3 when increasing the foaming temperature from 25 to 80 °C. While with around 45 wt.%

of CO_2 cell nucleation density increases from $2.2 \cdot 10^{16}$ nuclei/cm^3 to $3.5 \cdot 10^{16}$ nuclei/cm^3.

- For PMMA grade MV with 36 wt.% of gas, cell nucleation density increases from $1.8 \cdot 10^{13}$ nuclei/cm^3 to $3.3 \cdot 10^{13}$ nuclei/cm^3 when increasing the foaming temperature from 25 to 80 °C. While with around 45 wt.% of CO_2 cell nucleation density increases from $7.9 \cdot 10^{15}$ nuclei/cm^3 to $1.8 \cdot 10^{16}$ nuclei/cm^3

⇒ Although the observed tendencies are the same for the three grades, viscosity strongly affects the final cellular structure of nanocellular PMMA:

- Whatever the solubility, a smaller viscosity allows reaching lower relative densities, while higher viscosity leads to smaller cell sizes and higher cell nucleation densities.

⇒ Taking advantage of high solubilities and different viscosities, **nanocellular materials produced in this chapter through homogeneous nucleation showed cellular structures never reported before**:

- PMMA with the lowest viscosity has led to the production of nanocellular PMMA with **75 nm of cell size, a cell nucleation density of 10^{15} nuclei/cm^3 combined with a relative density of 0.24** (**Figure 9.7**).
- PMMA with the highest viscosity allows producing a nanocellular material with **14 nm of cell size, $3.5 \cdot 10^{16}$ nuclei/cm^3, and a relative density of 0.4** (**Figure 9.7**).

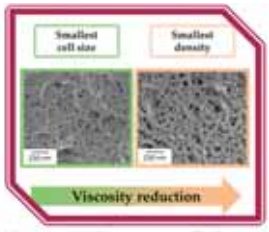

Figure 9.7. Best nanocellular materials from homogeneous polymers.

⇒ Foaming mechanisms have been studied, leading to the following conclusions:

- The reduction of relative density when increasing the foaming temperature is driven by an increase in the cell nucleation density.
- Open cell structures prevent further foaming leading to higher relative density materials.
- Differences in the cellular structure powered by different viscosity are attributed to the effect of the viscosity on the Influence Volume (IV):
  - A higher viscosity slows down the evolution of IV, leading to larger nucleation times and therefore, the creation of a higher number of cells.
  - Viscosity plays an essential role in the growing process, being beneficial to have low viscosity for further expansion. This effect is more pronounced at low solubilities.

9.1.4. Chapter 7

Chapter 7 analyzed several modifications of the conventional two steps gas dissolution foaming process (**Figure 9.8**).

Two scientific papers were included, presenting alternatives to the original production process that affect the shape and the cellular structure of the produced materials.

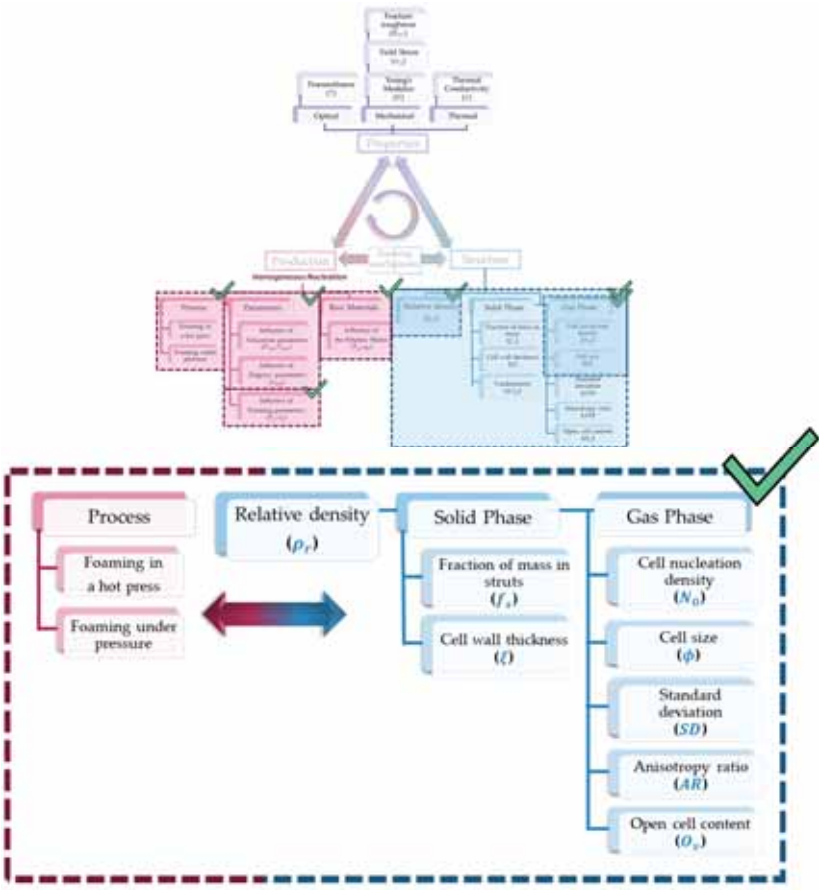

Figure 9.8. Main Objectives of Chapter 7

The first scientific article (P5 [5]) reports the production of nanocellular materials by carrying out the foaming step in a hot press instead of a thermal bath. A set of foaming experiments have led to conclude the following:

⇒ **It is possible to produce large and flat nanocellular PMMA parts (sizes of 100 x 100x 6 mm³) through the gas dissolution foaming process by carrying out the foaming step in a hot press** (**Figure 9.9**). Nanocellular materials with cell size smaller than 250 nm and relative densities lower than 0.3 have been produced.

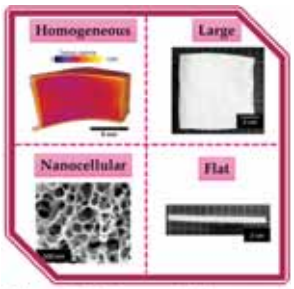

Figure 9.9. Large and flat parts of nanocellular PMMA

⇒ The cellular structure of the produced samples is homogeneous and similar to the ones obtained when the materials are foamed in a thermal bath (**Figure 9.9**). However, some small differences have been detected:

- Samples present a slightly inferior number of nucleation sites due to the applied pressure. Nucleation sites for samples foamed in the hot press range

from $1.5 \cdot 10^{14}$ nuclei/cm^3 to $2.8 \cdot 10^{14}$ nuclei/cm^3 while the foamed in thermal bath present values going from $1.8 \cdot 10^{14}$ nuclei/cm^3 to $3.6 \cdot 10^{14}$ nuclei/cm^3.

- Cell size is slightly higher for the materials produced in the hot press, with values between 240 nm and 277 nm in comparison with cell sizes between 204 nm and 261 nm produced when foaming in a thermal bath.

⇒ Increases the foaming temperature results in the same effects observed for the foaming in a thermal bath:

- Higher cell nucleation density. It increases from $1.5 \cdot 10^{14}$ nuclei/cm^3 when foaming at 40 ˚C to $2.8 \cdot 10^{14}$ nuclei/cm^3 when foaming at 80 ˚C.
- The increase in the cell nucleation density implies the reduction of the relative density from 0.5 to 0.31.
- The fraction of mass in the struts reduces from 0.66 when foaming at 40ºC to 0.42 when foaming at 80ºC.
- The open cell content increases, presenting a value of 6% when foaming at 40 ˚C and a value of 77 % when the foaming temperature is 80 ˚C.

In the second scientific paper (P6 [6]), a new process modification is presented. In this case, the depressurization process of the one-step foaming is modified. Thus, a method with a two-stage depressurization is developed. This work resulted in the following key results:

⇒ **It is possible to remove the micrometric and millimetric defects appearing in some nanocellular PMMA structures for some conditions, through the two-stage depressurization** (**Figure 9.10**)

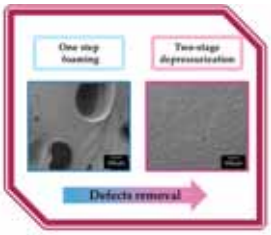

Figure 9.10. Removal of micrometric defects

⇒ The obtained cellular structures are nanocellular, and they are comparable with those produced using the standard one-step process, although:

- Larger cells and smaller cell nucleation densities are achieved:
  - For PMMA grades HV and MV cell size increases from around 200 nm to values higher than 300 nm when foaming at 50 ˚C, while cell nucleation density decreases from $1 \cdot 10^{14}$ nuclei/cm^3 to around $3 \cdot 10^{13}$ nuclei/cm^3.
  - For PMMA grades LV cell size increases from around 500 nm to values higher than 800 nm when foaming at 50 ˚C, while cell nucleation density decreases from $1 \cdot 10^{13}$ nuclei/cm^3 to $3 \cdot 10^{12}$ nuclei/cm^3.

⇒ A change in the production parameters of the proposed method leads to the following results:

- A higher residual pressure leads to different results as a function of the viscosity of the foamed material:
  - For high viscosity PMMA matrix, it enhances the cell nucleation density.
  - For low viscosity PMMA matrix, it reduces the cell nucleation density.

⇒ The analysis of the foaming mechanisms in this particular process allows obtaining some further insights about the foaming of nanocellular polymers:

- A lower pressure of the gas during the growing process of nanocellular materials is beneficial to avoid the generation of defects.
- When performing a two-stage depressurization process, there exists a strong competition between parameters governing the nucleation and growing. Thus, diffusivity, depressurization rate, and viscosity compete.
  - High depressurization rate and high viscosity enhance the nucleation, while high diffusivity decreases it. The final result depends on this competition.

After the analysis of the conclusions of chapters 4, 5, 6, and 7, it can be asserted that the relationship illustrated in **Figure 9.11** has been fulfilled. The production process of nanocellular materials has been exhaustively explored. Thus, modifications in the process parameters, in the used matrix and in the process itself have been carried out; simultaneously to a comprehensive analysis of the cellular structure.

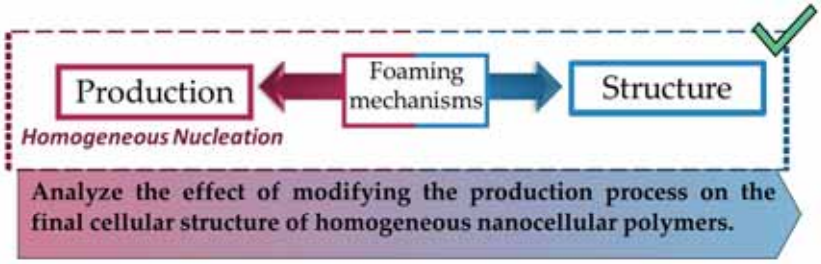

Figure 9.11. Relationships analyzed in Chapters 4, 5, 6, and 7.

Also, foaming mechanisms taking place during the production of nanocellular PMMA has been analysed through nucleation theories.

The first objective proposed in this thesis can be considered fulfilled.

9.1.5. Chapter 8

Chapter 8 aimed at fulfilling the second objective proposed in Chapter 1 (**Figure 9.12**).

The properties of the nanocellular materials have been described in this chapter. Thus, the optical, mechanical, and thermal conductivity have been presented.

The optical properties of semi-transparent nanocellular PMMA are characterized in a scientific study (P7 [7]) leading to the following findings:

⇒ Transmittance of nanocellular PMMA experimentally measured depends on:

- The cell size, having the cellular material with 225 nm almost zero transmittance while transmittances as high as 0.94 are achievable for the smallest cell size (14 nm) a relative density of 0.45 and a sample thickness of 0.05 mm.
- The used wavelength to the minus fourth power, indicating the presence of Rayleigh scattering.

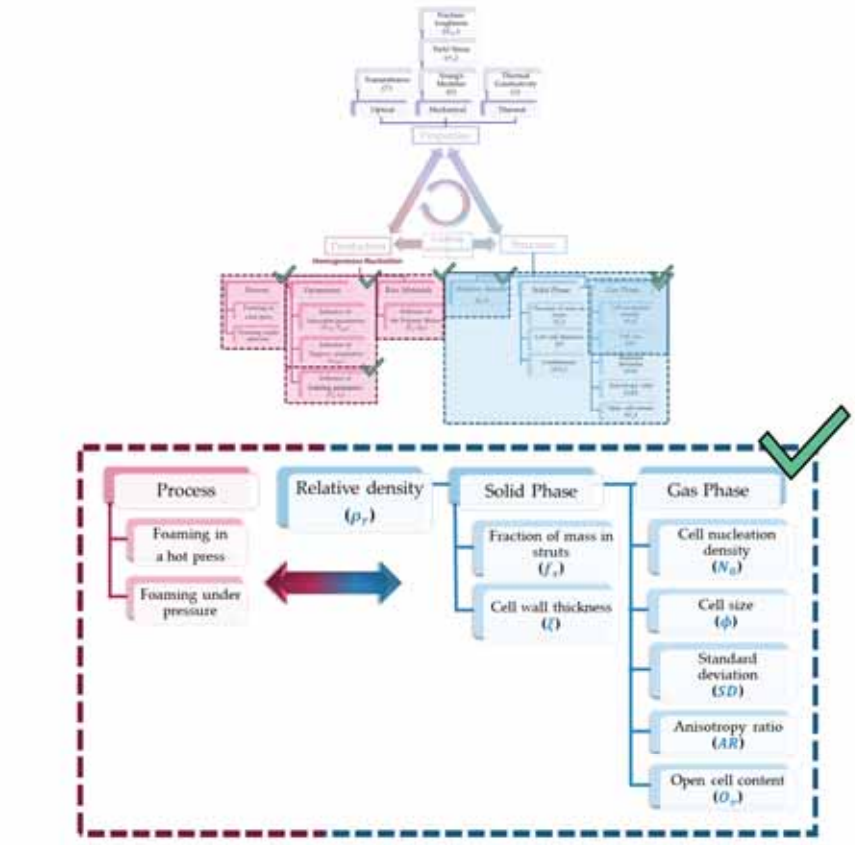

Figure 9.12. Main objectives of Chapter 8.

⇒ **The physical mechanisms taking place in the light-nanocellular polymer interaction can be understood thanks to the first developed model on this topic** (**Figure 9.13**) that has allowed obtaining the following additional information:

- When the material has a cell size smaller than 1/10 of the wavelength of light, visible light preferably travels through the gaseous phase.
- Experimental values and measured trends with the cell size and the used wavelength are reproduced with this model.
- It is possible to calculate the transmittance for any cell size, thickness, density, and visible wavelength.

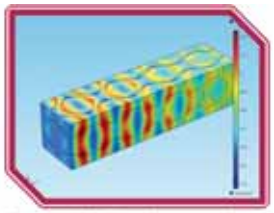

Figure 9.13. First theoretical model for light transmission in nanocellular PMMA.

Regarding the mechanical properties, different tests carried out for nanocellular PMMA with different cellular structures are presented in the second scientific work of this chapter (P8 [8]). Thus, the mechanical properties of cellular materials with similar densities and cell sizes from the micro to the nanoscale (from 3 microns to 30 nm) have been tested. The main conclusions are listed below:

⇒ The relative Young's modulus and the relative yield strength are independent on the cell size in the studied range of cell sizes and for a relative density around 0.4.

⇒ The relative fracture toughness almost doubles when decreasing the cell size from the micro to the nanoscale.

Finally, the thermal conductivity of nanocellular materials with cell sizes from 20 microns to 25 nm has been measured, concluding that:

⇒ Samples with cell sizes in the nanometric range present Knudsen effect being their thermal conductivity smaller than the one of microcellular materials.

⇒ An additional reduction on the thermal conductivity is observed in nanocellular PMMA that has been attributed to a modification of the conductivity through the solid phase.

In conclusion, the properties of nanocellular materials have been experimentally proven to present differences when compared with the one of microcellular polymers.

Those findings make it possible to establish the relationship between the properties of nanocellular materials and their cellular structure. This, together with the previously studied relationships between the cellular structure and the production process, was the second objective of this thesis (**Figure 9.14**).

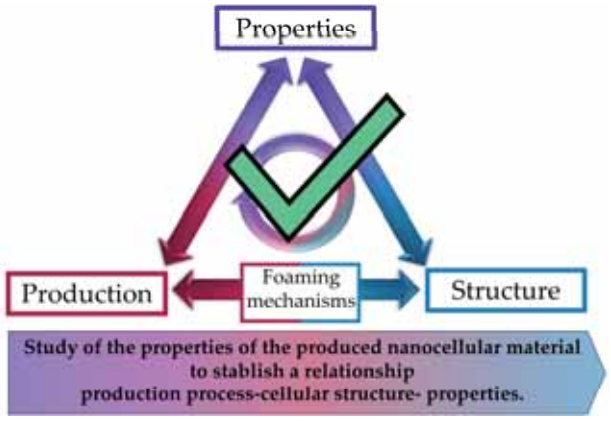

Figure 9.14. Fulfilled relationships in this thesis.

9.2 Foaming mechanisms

To understand the previous conclusions, **the foaming mechanisms taking place during nucleation and growing have been analyzed through nucleation theory** concluding the following:

⇒ In order to understand the foaming mechanisms, it is essential to improve the classical nucleation theory (CNT).

- The concept of influence volume has been included in this thesis in order to consider the impact of diffusivity pressure drop rate and viscosity.
- The introduction of the influence volume leads to assuming that nucleation does not occur instantaneously:
  - A slower increase in the influence volume leads to higher nucleation times and therefor, to higher nucleation densities.

⇒ To correctly estimate the final characteristics of the cellular structure, classical nucleation theory, and changes in the influence volume should be considered.
  - Nucleation density is maximized, and cell size minimized by:
    - A rise in the solubility, given by either an increase of saturation pressure or a decrease of saturation temperature.
    - A slower growth of the influence volume that can be achieved through:
      - High depressurization rates.
      - High viscosities.
      - Small desorption diffusivities.
  - Relative density is minimized through:
    - High foaming temperatures
    - Low viscosities.

⇒ The perfect equilibrium could be reached by combining all the previous knowledge, being possible to produce on demand the desired nanocellular material.

All the concluded before can be summarized in **Table 1**. This table shows the requirements to produce nanocellular materials from a homogeneous polymer employing a two-step gas dissolution foaming process. It is assumed that maximum nucleation densities and minimum cell sizes combined with a minimum ρ_r are required.

Table 1. Scheme of the influence of the production parameters in a two-step gas dissolution foaming process and used matrix to produce nanocellular materials with low relative densities. The script **–** indicates that there is not a direct influence between the parameter and the expected result.

	Saturation		Depressurization		Foaming		Matrix	
	P_{sat}	T_{sat}	v_d	t_d	T_f	t_f	η	T_g
Max. N_0	↑	**↓**	↑	↓	↑*	↑*	**↑**	↑
Min. ϕ	↑	**↓**	↑	↓	-	↑*	**↑**	↑
Min. ρ_r	-	-	-	-	**↑***	↑*	**↓**	↓

***** Those parameters should be maximized up to a limit when degeneration of the cellular structure takes place.

Those parameters having a greater influence have been marked with larger and bold arrows. Thus, the optimum nanocellular material will be achieved by maximizing the saturation pressure, the pressure drop rate, the foaming temperature and time and minimizing the saturation temperature, the desorption time and by the use of a polymer

with a balanced viscosity and glass transition temperature allowing to reach a high expansion without compromising the nucleation density and cell size.

9.3 Comparison with literature data

Materials produced in this thesis has been compared with the previous reported nanocellular polymers in the literature, produced by using both homogeneous and heterogeneous nucleation. The cell size as a function of the relative density has been represented for all of them, as **Figure 9.15** shows.

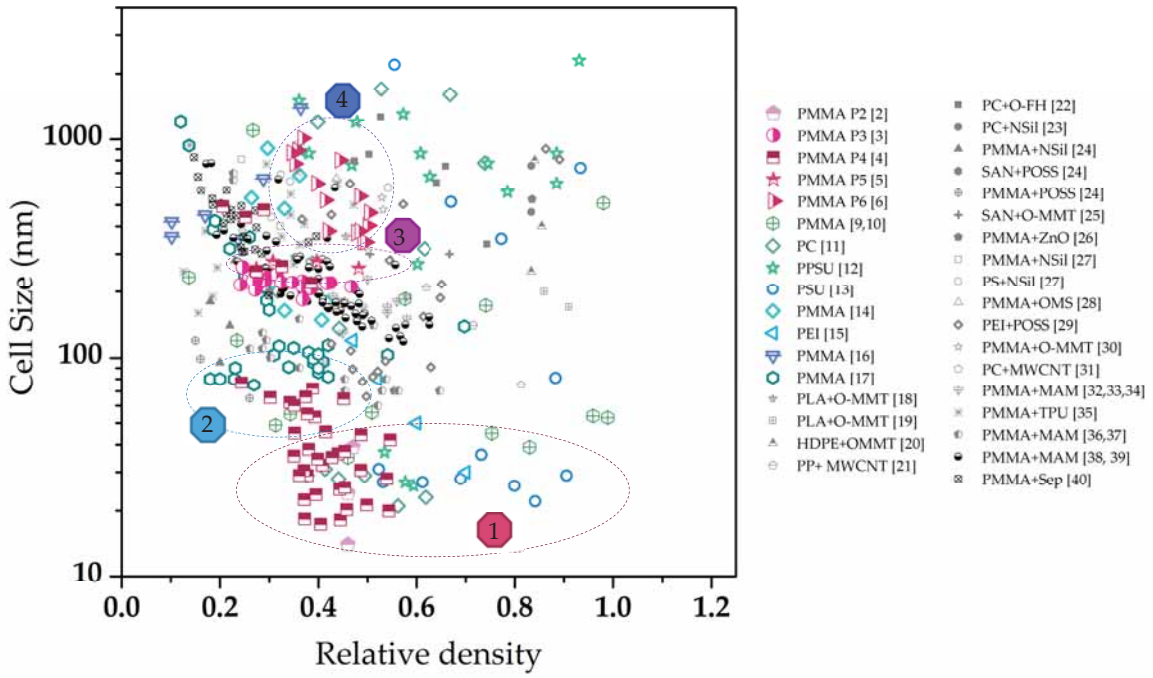

Figure 9.15. Cell size as a function of the relative density for nanocellular materials produced in this thesis and the ones reported in the bibliography produced by using homogeneous and heterogeneous nucleation.

It can be seen that the nanocellular PMMA (pinkish points) produced in this thesis share characteristics with the previous literature data. Thus, in the map of **Figure 9.15,** most of the points corresponding to the data in this thesis are in regions previously covered for other authors. However, some materials show a combination of cell sizes and relative densities not previously reported. Focusing on the lower cell size region (1), it can be seen that materials produced in paper P2 and P4 present cell sizes below 20 nm, reported for the first time for nanocellular polymers [2,4]. In those works, the combination of low saturation temperatures and high saturation pressures with different grades of PMMA leads to the production of those nanocellular materials with cell sizes below 20 nm. Guo et al. [11] reported the closest data by using polycarbonate as matrix and homogeneous nucleation. Those materials hadcell sizes of 21 nm combined with a relative density of 0.56. When working with PSU and PPSU Guo et al. also achieved small cell sizes of 22 nm and 26 nm respectively with relative densities of 0.84 and 0.59 [12,13].

In addition to the small cell size, nanocellular PMMA presented herein show the lowest achieved relative density for cell sizes below 30 nm as it can be seen in region 1 of **Figure 9.15.**

Focusing now in the region 2 of the map, it can be seen that nanocellular PMMA presented in paper P4 with a cell size of 75 nm and a relative density of 0.24, can compete with the materials in the literature showing the lowest cell size combined with the lowest relative density. Firstly, nanocellular polymers produced through homogeneous nucleation are considered. Thus, Costeux et al. reported a nanocellular PMMA copolymer (PMMA-co-EA) reported a relative density of 0.18 with a material presenting cell sizes around 80 nm. However, when the cell size is 75 nm relative density increases up to 0.27 [17]. Meaning that nanocellular PMMA produced in this thesis present the smallest cell size join to the lowest relative density for a nanocellular polymer produced using homogeneous nucleation. On the other hand, by working with heterogeneous nucleation (PMMA with added POSS nanoparticles), Costeux et al. produced a material with a cell size of 65 nm and a relative density of 0.26 that improves the data of this work [24].

Additionally, to the commented regions, nanocellular PMMA having cellular structures comparable to the ones previously reported but with enhanced characteristics have been produced in this thesis (regions 3 and 4 in the map). Large and flat samples of PMMA with dimensions never reported before were showed in P5 [5]. These samples show cellular structures comparable to the nanocellular polymers in the bibliography (cell sizes around 250 nm and relative densities between 0.5 and 0.3). So, produced materials are similar to some of the nanocellular PMMA of Bernardo et al. [39,40] produced through heterogeneous nucleation (using MAM) with cell sizes from 200 nm to 300 nm and relative densities from 0.23 to 0.47 and with dimensions of 20 x 10 x 4 mm^3. Pinto et al. also produced nanocellular PMMA by following the heterogeneous nucleation route with cell sizes around 250 nm and relative densities around 0.5 but with dimensions of 50 x 15 x 3 mm^3 [33].

Finally, materials in region 4 is a group of nanocellular PMMA completely free of defects (previously proved to lead to nanocellular materials with defects (P4)). They show cellular structures with cell sizes from 300 nm to 1 μm, and relative densities from 0.5 to 0.34 comparable to other nanocellular polymers in the literature, produced through homogeneous nucleation such as the PMMA of Costeux et. al [14] or through heterogeneous PMMA, such as the PMMA with TPU produced by Wang et. al [35].

9.4. Future work

The developed thesis opens many possibilities to further study. So, different investigations lines are proposed:

⇒ Further increase of the saturation pressure: the use of saturation pressures higher than 31 MPa should enhance the solubility of the materials. When working at low saturation

temperatures diffusivity decreases leading to large saturation times. The use of high saturation pressures could lead to overcoming this drawback, being possible to obtain similar cellular structures in reduced times.

⇒ Explore the combination of high saturation pressures (higher than 31 MPa) with high saturation temperatures: this would open the possibility of produce nanocellular materials with cell sizes smaller than 50 nm through a one-step process. This approach could lead to a reduction of the relative density of the materials or a reduction of their solid skin.

⇒ Evaluate the effect of the depressurization rate for a wider range of production conditions and with larger differences in the depressurization rates: this effect has been only studied for particular saturation conditions in this work, and no additional data is shown in the literature. Thus a more in-depth study should be carried out.

⇒ Further explore the two-step depressurization process: processing parameters should be in-deeper studied. Thus, the saturation pressure should be increased in order to produce materials free of defects with smaller cell sizes. Moreover, additional foaming temperatures or residual pressures should be tested as well as the effect of performing additional steps in the depressurization.

⇒ Broaden the range of used polymer matrix: new polymeric matrixes can be explored. Thus, PMMA with different properties can be tested, being interesting to study the effect of the molecular weight or the crosslinking on the final cellular structure. It would also be interesting the production of nanocellular materials from blends of different PMMA matrixes. In addition, different polymers could be used in the different production routes proposed in the thesis.

⇒ Continue exploring new production routes: the studied alternative production routes have led to interesting results. Properties such as the transparency of the nanocellular materials or the thermal conductivity should enhance with a reduction of their relative density, so new production routes based on the gas dissolution foaming process could be developed aiming at producing nanocellular materials with enhanced cellular structures and lower densities

⇒ In deep study of the foaming mechanisms: more experiments are needed for validating the theoretical models and to develop a more detailed theory about the production of nanocellular materials.

⇒ Study of the transmittance of nanocellular materials with smaller relative density: the use of polymeric matrixes with smaller viscosity leads to materials with smaller relative densities, fact that should enhance the transparency of nanocellular materials. Experimental measurements should be carried out to prove this hypothesis.

⇒ Model theoretically the transmittance of different nanocellular materials: the developed model allows calculating the transmittance for materials with different characteristics. The raw materials properties for producing the optimum transparent nanocellular materials could be estimated.

⇒ Further study of the mechanical properties of nanocellular materials: the developed study could be extended to materials with different cell sizes and smaller relative densities and other mechanical properties.

⇒ Perform more thermal conductivity measurements: produced samples could be measured in vacuum conditions to validate the Knudsen effect. The measurements should be broadened to a wider range of cell sizes and relative densities.

9.5. References

[1] Martín-de León, J.; Cimavilla-Román, P.; Bernardo, V.; Solórzano, E.; Rodríguez-Pérez, M. A. Cold neutron transmission for in-situ analysis of gas diffusion in polymers. *Paper sent* **2019**.

[2] Martín-de León, J.; Bernardo, V.; Rodríguez-Pérez, M. Á. Key Production Parameters to Obtain Transparent Nanocellular PMMA. *Macromolecular Materials and Engineering* **2017**, *302*.

[3] Martín-de León, J.; Bernardo, V.; Rodríguez-Pérez, M. Low Density Nanocellular Polymers Based on PMMA Produced by Gas Dissolution Foaming: Fabrication and Cellular Structure Characterization. *Polymers* **2016**, *8*, 265.

[4] León, J. M.; Bernardo, V.; Laguna-gutiérrez, E.; Rodríguez-pérez, M. Á. Influence of the rheological behaviour of PMMA on the cellular structure of nanocellular materials. *Paper sent* 1–16.

[5] Martín-de León, J.; Bernardo, V.; Cimavilla-Román, P.; Pérez-Tamarit, S.; Rodríguez-Pérez, M. Á. Overcoming the Challenge of Producing Large and Flat Nanocellular Polymers: A Study with PMMA. *Advanced Engineering Materials* **2019**, 1–8.

[6] Martín-de León, J.; Bernardo, V.; Rodríguez-pérez, M. Á. Two stage depressurization in one step foaming process: the production of nanocellular materials free of defects. *Paper sent* **2019**.

[7] Martín-de León, J.; Pura, J. L.; Bernardo, V.; Rodríguez-Pérez, M. Á. Transparent nanocellular PMMA: Characterization and modeling of the optical properties. *Polymer* **2019**, *170*, 16–23.

[8] Martín-de León, J.; Van Loock, F.; Bernardo, V.; Fleck, N. A.; Rodríguez-Pérez, M. A. The influence of cell size on the mechanical properties of nanocellular PMMA.

[9] Guo, H.; Kumar, V. Solid-state poly(methyl methacrylate) (PMMA) nanofoams. Part I: Low-temperature CO2 sorption, diffusion, and the depression in PMMA glass transition. *Polymer* **2015**, *57*, 157–163.

[10] Guo, H.; Nicolae, A.; Kumar, V. Solid-state poly(methyl methacrylate) (PMMA) nanofoams. Part II: Low-temperature solid-state process space using CO2 and the resulting morphologies. *Polymer* **2015**, *70*, 231–241.

[11] Guo, H.; Kumar, V. Some thermodynamic and kinetic low-temperature properties of the PC-CO2 system and morphological characteristics of solid-state PC nanofoams produced with liquid CO2. *Polymer* **2015**, *56*, 46–56.

[12] Guo, H.; Nicolae, A.; Kumar, V. Fabrication of high temperature polyphenylsulfone nanofoams using high pressure liquid carbon dioxide. *Cellular Polymers* **2016**, *35*, 119–142.

[13] Guo, H.; Nicolae, A.; Kumar, V. Solid-state microcellular and nanocellular polysulfone foams. *Journal of Polymer Science, Part B: Polymer Physics* **2015**, *53*, 975–985.

[14] Costeux, S.; Khan, I.; Bunker, S. P.; Jeon, H. K. Experimental study and modeling of nanofoams formation from single phase acrylic copolymers. *Journal of Cellular Plastics* **2014**, *51*, 197–221.

[15] Miller, D.; Chatchaisucha, P.; Kumar, V. Microcellular and nanocellular solid-state polyetherimide (PEI) foams using sub-critical carbon dioxide I. Processing and structure. *Polymer* **2009**, *50*, 5576–5584.

[16] Handa, Y. P.; Zhan, Z.; Wong, B. Solubility, diffusivity, and retrograde vitrification in PMMA-CO2, and development of sub-micron cellular structures. *Cellular polymers* **2001**, *20*, 1–16.

[17] Costeux, S.; Bunker, S. P.; Jeon, H. K. Homogeneous nanocellular foams from styrenic-acrylic polymer blends. *Journal of Materials Research* **2013**, *28*, 2351–2365.

[18] Fujimoto, Y.; Ray, S. S.; Okamoto, M.; Ogami, A.; Yamada, K.; Ueda, K. Well-Controlled Biodegradable Nanocomposite Foams : From Microcellular to Nanocellular. *Macromolecular Rapid Communications* **2003**, *24*, 457–461.

[19] Ema, Y.; Ikeya, M.; Okamoto, M. Foam processing and cellular structure of polylactide-based nanocomposites. *Polymer* **2006**, *47*, 5350–5359.

[20] Lee, Y. H.; Park, C. B.; Wang, K. H. HDPE-Clay Nanocomposite Foams Blown with Supercritical CO2. *Journal of Cellular Plastics* **2005**, *41*, 487–502.

[21] Ameli, A.; Nofar, M.; Park, C. B. Polypropylene / carbon nanotube nano / microcellular structures with high dielectric permittivity , low dielectric loss , and low percolation threshold. **2014**, *1*.

[22] Zhai, W.; Yu, J.; Wu, L.; Ma, W.; He, J. Heterogeneous nucleation uniformizing cell size distribution in microcellular nanocomposites foams. *Polymer* **2006**, *47*, 7580–7589.

[23] Ito, Y.; Yamashita, M.; Okamoto, M. Foam Processing and Cellular Structure of Polycarbonate-Based Nanocomposites. **2006**, 773–783.

[24] Costeux, S.; Zhu, L. Low density thermoplastic nanofoams nucleated by nanoparticles. *Polymer* **2013**, *54*, 2785–2795.

[25] Urbanczyk, L.; Calberg, C.; Detrembleur, C.; Jérôme, C.; Alexandre, M. Batch foaming of SAN/clay nanocomposites with scCO2: A very tunable way of controlling the cellular morphology. *Polymer* **2010**, *51*, 3520–3531.

[26] Pinto, J.; Morselli, D.; Bernardo, V.; Notario, B.; Fragouli, D.; Rodriguez-Perez, M. A.; Athanassiou, A. Nanoporous PMMA foams with templated pore size obtained by localized in situ synthesis of nanoparticles and CO 2 foaming. *Polymer* **2017**, *124*, 176–185.

[27] Liu, S.; Zoetebier, B.; Hulsman, L.; Zhang, Y.; Duvigneau, J.; Vancso, G. J. Nanocellular polymer foams nucleated by core-shell nanoparticles. *Polymer* **2016**, *104*.

[28] Yang, J.; Huang, L.; Zhang, Y.; Chen, F.; Fan, P.; Zhong, M.; Yeh, S. A new promising nucleating agent for polymer foaming: Applications of ordered mesoporous silica particles in polymethyl methacrylate supercritical carbon dioxide microcellular foaming. *Industrial and Engineering Chemistry Research* **2013**, *52*, 14169–14178.

[29] Yu, H.; Lei, Y.; Yu, X.; Wang, X.; Liu, T.; Luo, S. Solid-state polyetherimide (PEI) nanofoams: the influence of the compatibility of nucleation agent on the cellular morphology. *Journal of Polymer Research* **2016**, *23*, 121.

[30] Realinho, V.; Antunes, M.; Martínez, A. B.; Velasco, J. I. Influence of nanoclay concentration on the CO 2 diffusion and physical properties of PMMA montmorillonite microcellular foams. *Industrial and Engineering Chemistry Research* **2011**, *50*, 13819–13824.

[31] Monnereau, L.; Urbanczyk, L.; Thomassin, J. M.; Alexandre, M.; Jérôme, C.; Huynen, I.; Bailly, C.; Detrembleur, C. Supercritical CO2and polycarbonate based nanocomposites: A critical issue for foaming. *Polymer* **2014**, *55*, 2422–2431.

[32] Pinto, J.; Dumon, M.; Pedros, M.; Reglero, J.; Rodriguez-Perez, M. A. Nanocellular CO2 foaming of PMMA assisted by block copolymer nanostructuration. *Chemical Engineering Journal* **2014**, *243*, 428–435.

[33] Pinto, J.; Reglero-ruiz, J. A.; Dumon, M.; Rodriguez-Perez, M. A. Temperature influence and CO2 transport in foaming processes of poly (methyl methacrylate)– block copolymer nanocellular and microcellular foams. *The Journal of Supercritical Fluids* **2014**, *94*, 198–205.

[34] Pinto, J.; Dumon, M.; Rodriguez-Perez, M. A.; Garcia, R.; Dietz, C. Block Copolymers Self-Assembly Allows Obtaining Tunable Micro or Nanoporous Membranes or Depth Filters Based on PMMA; Fabrication Method and Nanostructures. *The Journal of Physical Chemistry C* **2014**, *118*, 4656–4663.

[35] Wang, G.; Zhao, J.; Mark, L. H.; Wang, G.; Yu, K.; Wang, C.; Park, C. B.; Zhao, G. Ultra-tough and super thermal-insulation nanocellular PMMA/TPU. *Chemical Engineering Journal* **2017**, *325*, 632–646.

[36] Forest, C.; Chaumont, P.; Cassagnau, P.; Swoboda, B.; Sonntag, P. CO2 nano-foaming of nanostructured PMMA. *Polymer* **2015**, *58*, 76–87.

[37] Forest, C.; Chaumont, P.; Cassagnau, P.; Swoboda, B.; Sonntag, P. Nanofoaming of PMMA using a batch CO2 process: Influence of the PMMA viscoelastic behaviour. *Polymer* **2015**, *77*, 1–9.

[38] Bernardo, V.; Martin-de Leon, J.; Pinto, J.; Catelani, T.; Athanassiou, A.; Rodriguez-Perez, M. A. Low-density PMMA/MAM nanocellular polymers using low MAM contents: Production and characterization. *Polymer* **2019**, *163*, 115–124.

[39] Bernardo, V.; Martin-de Leon, J.; Laguna-Gutierrez, E.; Catelani, T.; Pinto, J.; Athanassiou, A.; Rodriguez-Perez, M. A. Understanding the role of MAM molecular weight in the production of PMMA/MAM nanocellular polymers. *Polymer* **2018**, *153*, 262–270.

[40] Bernardo, V.; Martín-de León, J.; Laguna-Gutiérrez, E.; Rodríguez-Pérez, M. Á. PMMA-sepiolite nanocomposites as new promising materials for the production of nanocellular polymers. *European Polymer Journal* **2017**, *96*, 10–26.